Mathematical Problems in Engineering

Theory, Methods, and Applications

Editor-in-Chief: José Manoel Balthazar

Special Issue
Nonlinear Vibrations, Stability Analysis, and Control

Guest Editors: Carlo Cattani, Alexander Seyranian, and Irina Trendafilova

Hindawi Publishing Corporation
http://www.hindawi.com

Volume 2010

Nonlinear Vibrations, Stability Analysis, and Control

Mathematical Problems in Engineering

Nonlinear Vibrations, Stability Analysis, and Control

Guest Editors: Carlo Cattani, Alexander Seyranian, and Irena Trendafilova

Contents

Hindawi Publishing Corporation
Mathematical Problems in Engineering
Volume 2010, Article ID 873047, 2 pages
doi:10.1155/2010/873047

Editorial

Nonlinear Vibrations, Stability Analysis, and Control

Carlo Cattani,[1] Alexander Seyranian,[2] and Irina Trendafilova[3]

[1] *Department of Pharmaceutical Sciences (diFarma), University of Salerno, Via Ponte Don Melillo, 84084 Fisciano, Italy*
[2] *Institute of Mechanics, Moscow State Lomonosov University, 119192 Moscow, Russia*
[3] *Department of Mechanical Engineering, University of Strathclyde, Glasgow, UK*

Correspondence should be addressed to Carlo Cattani, ccattani@unisa.it

Received 24 October 2010; Accepted 24 October 2010

Important advances in mathematics, physics, biology, economics, and engineering science have shown the importance of the analysis of nonlinear vibrations, instabilities, and strongly coupled dynamical behavior.

New investigation tools enable us to better understand the dynamic behavior of more complex structures. However, the increasing interest in mechanical structures with extreme performances has propelled the scientific community toward the search for solutions of complex problems and systems exhibiting strong nonlinearities. As a consequence, there is an increasing demand for both high-performance, nonlinear structural components as well as advanced multidisciplinary and multiscale mathematical models and methods.

It should be kept in mind that linearity is one of the properties of dynamic systems which is very rarely fulfilled. Nonetheless, if the system under consideration is not strongly nonlinear, then the methods of spectral and correlation analysis can be applied and will lead to sensible results describing a linear approximation of the system at hand. But there are cases of strongly nonlinear systems for which the output signal might not be even proportional to the input. This is a very important problem if one is trying to determine, for example, extreme values of the system response like in cases of catastrophic structural failure prediction. In such cases of strong nonlinear behavior, the system nonlinearities should be taken into account. When dealing with phenomena involving large amplitude and/or high frequency vibrations or a great number of coupled oscillators, the classical methods of linear dynamics have to be replaced by new specific mathematical tools.

In this special issue, the current state of nonlinear structural dynamic models in vibration analysis, stability analysis, and control has been reviewed. Known methods for analysis of nonlinear and oscillating systems at a macroscopic scale have been explored in

some new problems, and some new techniques have been applied to complex structures as well.

There are thirty five papers, collected in this special issue on Nonlinear vibrations, stability analysis, and control, that are shedding light on a wide range of topics; however, they do not cover all rich contents of these important fields.

Mathematical models and methods for nonlinear and strongly coupled (correlated) oscillating systems and for distributed-parameter structures have been investigated and improved in the following main topics:

(i) vibration analysis of distributed-parameter and multibody systems, parametric models,

(ii) global methods, wavelet methods, and fractal analysis for spatially and temporally coupled oscillators,

(iii) nonlinear time series methods for dynamic systems,

(iv) control of nonlinear vibrations and bifurcations, control of chaos in vibrating systems is as well as transient chaos chaotic oscillators and bifurcations.

(v) Micro- and nano-vibrating structural systems.

This special issue deals with interesting and modern problems in vibrations, stability, and control. Some of these papers investigate theoretical problems while others are devoted to more practical applications. Some papers deal with structural engineering methods and applications such as stochastic finite elements, laminated composite plates, Jeffcott rotor, Euler-Bernoulli and magnetic beams, vehicle-pipes-soil vibration, gear transmission, and compressor vibrations. Others are devoted to biomechanical applications: cardiovascular system, ossicular chain, and human standing model, while some papers discuss oscillations, stability, and control problems in challenging topics, such as quantum interaction, financial systems, and energy production.

The collection of papers in this special issue covers a very wide range of applications ranging from purely mathematical tools for engineering problems to applications of nonlinear dynamics tools for human and economic problems. Some of the papers are dedicated to mathematical methods based on nonlinear dynamics tools, for example, wavelets for solving different mathematical and engineering problems. Others concentrate on specific nonlinear systems with well-expressed nonlinear behavior and offer methods for their analysis. The special issue contains studies on different engineering applications of nonlinear dynamic systems for the analysis of the behavior of essential structural components like beams, plates, and pipes. Some papers offer nonlinear-dynamics-based analysis of important machinery components and applications, for example, rotors, gear transmissions, vehicle vibrations, power transmission lines, hydraulic systems, compressors, gas stations, controllers. Medical, human, climate, and financial applications of nonlinear dynamics tools are considered also.

In all these papers, the authors efforts succeeded in showing the importance of nonlinear vibrations, stability, and control topics in opening new frontiers for challenging future researches.

Carlo Cattani
Alexander Seyranian
Irina Trendafilova

Hindawi Publishing Corporation
Mathematical Problems in Engineering
Volume 2010, Article ID 408418, 22 pages
doi:10.1155/2010/408418

Research Article

Shannon Wavelets for the Solution of Integrodifferential Equations

Carlo Cattani

Department of Pharmaceutical Sciences (diFarma), University of Salerno, Via Ponte Don Melillo, 84084 Fisciano, Italy

Correspondence should be addressed to Carlo Cattani, ccattani@unisa.it

Received 30 December 2009; Accepted 17 February 2010

Academic Editor: Alexander P. Seyranian

Shannon wavelets are used to define a method for the solution of integrodifferential equations. This method is based on (1) the Galerking method, (2) the Shannon wavelet representation, (3) the decorrelation of the generalized Shannon sampling theorem, and (4) the definition of connection coefficients. The Shannon sampling theorem is considered in a more general approach suitable for analysing functions ranging in multifrequency bands. This generalization coincides with the Shannon wavelet reconstruction of $L_2(\mathbb{R})$ functions. Shannon wavelets are C^∞-functions and their any order derivatives can be analytically defined by some kind of a finite hypergeometric series (connection coefficients).

1. Introduction

In recent years wavelets have been successfully applied to the wavelet representation of integro-differential operators, thus giving rise to the so-called wavelet solutions of PDE and integral equations. While wavelet solutions of PDEs can be easily find in a large specific literature, the wavelet representation of integro-differential operators cannot be considered completely achieved and only few papers discuss in depth this question with particular regards to methods for the integral equations. Some of them refer to the Haar wavelets [1–3] to the harmonic wavelets [4–9] and to the spline-Shannon wavelets [10–13]. These methods are mainly based on the Petrov-Galerkin method with a suitable choice of the collocation points [14]. Alternatively to the collocation method, there has been also proposed, for the solution of PDEs, the evaluation of the differential operators on the wavelet basis, thus defining the so-called connection coefficients [6, 15–21].

Wavelets [22] are localized functions which are a useful tool in many different applications: signal analysis, data compression, operator analysis, PDE solving (see, e.g.,

[15, 23] and references therein), vibration analysis, and solid mechanics [23]. Very often wavelets have been used only as any other kind of orthogonal functions, without taking into consideration their fundamental properties. The main feature of wavelets is, in fact, their possibility to split objects into different scale components [22, 23] according to the multiscale resolution analysis. For the $L_2(\mathbb{R})$ functions, that is, functions with decay to infinity, wavelets give the best approximation. When the function is localized in space, that is, the bottom length of the function is within a short interval (function with a compact support), such as pulses, any other reconstruction, but wavelets, leads towards undesirable problems such as the Gibbs phenomenon when the approximation is made in the Fourier basis. Wavelets are the most expedient basis for the analysis of impulse functions (pulses) [24, 25].

Among the many families of wavelets, Shannon wavelets [17] offer some more specific advantages, which are often missing in the others. In fact, Shannon wavelets

(1) are analytically defined;

(2) are infinitely differentiable;

(3) are sharply bounded in the frequency domain, thus allowing a decomposition of frequencies in narrow bands;

(4) enjoy a generalization of the Shannon sampling theorem, which extend to all range of frequencies [17]

(5) give rise to the connection coefficients which can be analytically defined [15–17] for any order derivatives, while for the other wavelet families they were computed only numerically and only for the lower order derivatives [18, 19, 21].

The (Shannon wavelet) connection coefficients are obtained in [17] as a finite series (for any order derivatives). In Latto's method [18, 20, 21], instead, these coefficients were obtained only (for the Daubechies wavelets) by using the inclusion axiom but in approximated form and only for the first two-order derivatives. The knowledge of the derivatives of the basis enables us to approximate a function and its derivatives and it is an expedient tool for the projection of differential operators in the numerical computation of the solution of both partial and ordinary differential equations [6, 15, 23, 26].

The wavelet reconstruction by using Shannon wavelets is also a fundamental step in the analysis of functions-operators. In fact, due to their definition Shannon wavelets are box functions in the frequency domain, thus allowing a sharp decorrelation of frequencies, which is an important feature in many physical-engineering applications. In fact, the reconstruction by Shannon wavelets ranges in multifrequency bands. Comparing with the Shannon sampling theorem where the frequency band is only one, the reconstruction by Shannon wavelets can be done for functions ranging in all frequency bands (see, e.g., [17]). The Shannon sampling theorem [27], which plays a fundamental role in signal analysis and applications, will be generalized, so that under suitable hypotheses a few set of values (samples) and a preliminary chosen Shannon wavelet basis enable us to completely represent, by the wavelet coefficients, the continuous signal and its frequencies.

The Shannon wavelet solution of an integrodifferential equation (with functions localized in space and slow decay in frequency) will be computed by using the Petrov-Galerkin method and the connection coefficients. The wavelet coefficients enable to represent the solution in the frequency domain singling out the contribution to different frequencies.

This paper is organized as follows. Section 2 deals with some preliminary remarks and properties of Shannon wavelets also in frequency domain; the reconstruction of a function is given in Section 3 together with the generalization of the Shannon sampling theorem;

the error of the wavelet approximation is computed. The wavelet reconstruction of the derivatives of the basis and the connection coefficients are given in Section 4. Section 5 deals with the Shannon wavelet solution of an integrodifferential equation and an example is given at last in Section 6.

2. Shannon Wavelets

Shannon wavelets theory (see, e.g., [16, 17, 28, 29]) is based on the scaling function $\varphi(x)$ (also known as sinc function)

$$\varphi(x) = \operatorname{sinc} x \stackrel{\text{def}}{=} \frac{\sin \pi x}{\pi x} = \frac{e^{\pi i x} - e^{-\pi i x}}{2\pi i x}, \tag{2.1}$$

and the corresponding wavelet [16, 17, 28, 29]

$$\begin{aligned} \psi(x) &= \frac{\sin \pi(x - 1/2) - \sin 2\pi(x - 1/2)}{\pi(x - 1/2)} \\ &= \frac{e^{-2i\pi x}\left(-i + e^{i\pi x} + e^{3i\pi x} + ie^{4i\pi x}\right)}{(\pi - 2\pi x)}. \end{aligned} \tag{2.2}$$

From these functions a multiscale analysis [22] can be derived. The dilated and translated instances, depending on the scaling parameter n and space shift k, are

$$\begin{aligned} \varphi_k^n(x) &= 2^{n/2}\varphi(2^n x - k) = 2^{n/2}\frac{\sin \pi(2^n x - k)}{\pi(2^n x - k)} \\ &= 2^{n/2}\frac{e^{\pi i(2^n x - k)} - e^{-\pi i(2^n x - k)}}{2\pi i(2^n x - k)}, \end{aligned} \tag{2.3}$$

$$\begin{aligned} \psi_k^n(x) &= 2^{n/2}\ \frac{\sin \pi(2^n x - k - 1/2) - \sin 2\pi(2^n x - k - 1/2)}{\pi(2^n x - k - 1/2)} \\ &= \frac{2^{n/2}}{2\pi(2^n x - k + 1/2)}\sum_{s=1}^{2} i^{1+s}e^{s\pi i(2^n x - k)} - i^{1-s}e^{-s\pi i(2^n x - k)} \end{aligned} \tag{2.4}$$

respectively.

2.1. Properties of the Shannon Scaling and Wavelet Functions

By a direct computation it can be easily seen that

$$\varphi_k^0(h) = \delta_{kh}, \quad (h, k \in \mathbb{Z}), \tag{2.5}$$

with δ_{kh} Kroneker symbol, so that

$$\varphi_k^0(x) = 0, \quad x = h \neq k \quad (h, k \in \mathbb{Z}), \tag{2.6}$$

$$\psi_k^n(x) = 0, \quad x = 2^{-n}\left(k + \frac{1}{2} \pm \frac{1}{3}\right), \quad (n \in \mathbb{N}, k \in \mathbb{Z}). \tag{2.7}$$

It is also

$$\lim_{x \to 2^{-n}(h+1/2)} \psi_k^n(x) = -2^{n/2}\delta_{hk}. \tag{2.8}$$

Thus, according to (2.5), (2.8), for each fixed scale n, we can choose a set of points x:

$$x \in \{h\} \cup \left\{2^{-n}\left(h + \frac{1}{2} \pm \frac{1}{3}\right)\right\}, \quad (n \in \mathbb{N}, h \in \mathbb{Z}), \tag{2.9}$$

where either the scaling functions or the wavelet vanishes, but it is important to notice that when the scaling function is zero, the wavelet is not and viceversa. As we shall see later, this property will simplify the numerical methods based on collocation point.

Since they belong to $L_2(\mathbb{R})$, both families of scaling and wavelet functions have a (slow) decay to zero; in fact, according to their definition (2.3), (2.4)

$$\lim_{x \to \pm\infty} \varphi_k^n(x) = 0, \qquad \lim_{x \to \pm\infty} \psi_k^n(x) = 0, \tag{2.10}$$

it can be also easily checked that for a fixed x_0

$$\begin{gathered} \varphi_{k+1}^n(x_0) < \varphi_k^n(x_0), \quad \frac{\varphi_{k+1}^n(x_0)}{\varphi_k^n(x_0)} = \frac{2^n x - k}{2^n x - k + 1} < 1, \\ \frac{\psi_{k+1}^n(x_0)}{\psi_k^n(x_0)} = \frac{2^{n+1}x - 2k - 1}{2^{n+1}x - 2k - 3} \times \frac{2\sin(\pi(2^n x - k)) - 1}{2\sin(\pi(2^n x - k)) + 1}. \end{gathered} \tag{2.11}$$

Since

$$\begin{gathered} \lim_{x \to \infty} \frac{2^{n+1}x - 2k - 1}{2^{n+1}x - 2k - 3} = 1, \\ 2\sin(\pi(2^n x - k)) - 1 < 2\sin(\pi(2^n x - k)) + 1, \end{gathered} \tag{2.12}$$

it is

$$\lim_{x \to \infty} \frac{\psi_{k+1}^n(x)}{\psi_k^n(x)} < 1. \tag{2.13}$$

Analogously we have

$$\begin{gathered}\frac{\psi_k^{n+1}(x_0)}{\psi_k^n(x_0)} = \frac{\sqrt{2}(2^{n+1}x-2k-1)}{2^{n+2}x-2k-1} \times \frac{\cos(\pi(2^{n+1}x-k)) - \sin(2\pi(2^{n+1}x-k))}{\cos(\pi(2^n x-k)) - \sin(2\pi(2^n x-k))}, \\ \lim_{x\to 2^{-n}(k+1/2)} \frac{\psi_{k+1}^{n+1}(x)}{\psi_k^n(x)} = \frac{2\sqrt{2}(\cos k\pi - \sin 2k\pi)}{(2k-1)\pi} = \frac{(-1)^k 2\sqrt{2}}{(2k-1)\pi}, \quad \left|\frac{(-1)^k 2\sqrt{2}}{(2k-1)\pi}\right| < 1.\end{gathered} \tag{2.14}$$

The maximum and minimum values of these functions can be easily computed. The maximum value of the scaling function $\varphi_k^0(x)$ can be found in correspondence of $x = k$

$$\max\left[\varphi_k^0(x_M)\right] = 1, \quad x_M = k. \tag{2.15}$$

The min value of $\varphi_k^0(x)$ can be computed only numerically and it is

$$\min\left[\varphi_k^0(x)\right] \cong \varphi_k^0(x_m) = \frac{\sin\sqrt{2}\pi}{\sqrt{2}\pi}, \quad x_m = k - 1 \pm \sqrt{2}. \tag{2.16}$$

The minimum of the wavelet $\psi_k^n(x)$ can be found in correspondence of the middle point of the zeroes (2.7) so that

$$\min\left[\psi_k^n(x_m)\right] = -2^{n/2}, \quad x_m = 2^{-n-1}(2k+1), \tag{2.17}$$

and the max values of $\psi_k^n(x)$ are

$$\max\left[\psi_k^n(x_M)\right] = 2^{n/2}\frac{3\sqrt{3}}{\pi}, \quad x_M = \begin{cases} -2^{-n}\left(k+\dfrac{1}{6}\right), \\ \dfrac{2^{-n-1}}{3}(18k+7). \end{cases} \tag{2.18}$$

2.2. Shannon Wavelets Theory in the Fourier Domain

Let

$$\hat{f}(\omega) = \widehat{f(x)} \stackrel{\text{def}}{=} \frac{1}{2\pi}\int_{-\infty}^{\infty} f(x)e^{-i\omega x}\,\mathrm{d}x \tag{2.19}$$

be the Fourier transform of the function $f(x) \in L_2(\mathbb{R})$, and

$$f(x) = 2\pi\int_{-\infty}^{\infty} \hat{f}(\omega)e^{i\omega x}\,\mathrm{d}\omega \tag{2.20}$$

its inverse transform.

The Fourier transform of (2.1), (2.2) gives us

$$\widehat{\varphi}(\omega) = \frac{1}{2\pi}\chi(\omega + 3\pi) = \begin{cases} \dfrac{1}{2\pi}, & -\pi \le \omega < \pi \\ 0, & \text{elsewhere,} \end{cases} \tag{2.21}$$

and [17]

$$\widehat{\varphi}(\omega) = \frac{1}{2\pi}e^{-i\omega}\left[\chi(2\omega) + \chi(-2\omega)\right] \tag{2.22}$$

with

$$\chi(\omega) = \begin{cases} 1, & 2\pi \le \omega < 4\pi, \\ 0, & \text{elsewhere.} \end{cases} \tag{2.23}$$

Analogously for the dilated and translated instances of scaling/wavelet function, in the frequency domain, it is

$$\begin{aligned} \widehat{\varphi}_k^n(\omega) &= \frac{2^{-n/2}}{2\pi}e^{-i\omega k/2^n}\chi\left(\frac{\omega}{2^n} + 3\pi\right), \\ \widehat{\varphi}_k^n(\omega) &= -\frac{2^{-n/2}}{2\pi}e^{-i\omega(k+1/2)/2^n}\left[\chi\left(\frac{\omega}{2^{n-1}}\right) + \chi\left(\frac{-\omega}{2^{n-1}}\right)\right]. \end{aligned} \tag{2.24}$$

It can be seen that

$$\chi(\omega + 3\pi)\left[\chi\left(\frac{\omega}{2^{n-1}}\right) + \chi\left(\frac{-\omega}{2^{n-1}}\right)\right] = 0 \tag{2.25}$$

so that by using the function $\widehat{\varphi}_k^0(\omega)$ and $\widehat{\varphi}_k^n(\omega)$ there is a decorrelation into different non-overlapping frequency bands.

For each $f(x) \in L_2(\mathbb{R})$ and $g(x) \in L_2(\mathbb{R})$, the inner product is defined as

$$\langle f, g\rangle \stackrel{\text{def}}{=} \int_{-\infty}^{\infty} f(x)\overline{g(x)}\mathrm{d}x, \tag{2.26}$$

which, according to the Parseval equality, can be expressed also as

$$\langle f, g\rangle \stackrel{\text{def}}{=} \int_{-\infty}^{\infty} f(x)\overline{g(x)}\mathrm{d}x = 2\pi\int_{-\infty}^{\infty} \widehat{f}(\omega)\overline{\widehat{g}(\omega)}\mathrm{d}\omega = 2\pi\left\langle \widehat{f}, \widehat{g}\right\rangle, \tag{2.27}$$

where the bar stands for the complex conjugate.

With respect to the inner product (2.26). The following can be shown. [16, 17]

Theorem 2.1. *Shannon wavelets are orthonormal functions, in the sense that*

$$\left\langle \psi_k^n(x), \psi_h^m(x) \right\rangle = \delta^{nm}\delta_{hk}, \tag{2.28}$$

With δ^{nm}, δ_{hk} being the Kroenecker symbols.

For the proof see [17]. Moreover we have [16, 17].

Theorem 2.2. *The translated instances of the Shannon scaling functions $\varphi_k^n(x)$, at the level $n = 0$, are orthogonal, in the sense that*

$$\left\langle \varphi_k^0(x), \varphi_h^0(x) \right\rangle = \delta_{kh}, \tag{2.29}$$

being $\varphi_k^0(x) \stackrel{\text{def}}{=} \varphi(x-k)$.

See the proof in [17].

The scalar product of the (Shannon) scaling functions with respect to the corresponding wavelets is characterized by the following [16, 17].

Theorem 2.3. *The translated instances of the Shannon scaling functions $\varphi_k^n(x)$, at the level $n = 0$, are orthogonal to the Shannon wavelets, in the sense that*

$$\left\langle \varphi_k^0(x), \psi_h^m(x) \right\rangle = 0, \quad m \geq 0, \tag{2.30}$$

being $\varphi_k^0(x) \stackrel{\text{def}}{=} \varphi(x-k)$.

Proof is in [17].

3. Reconstruction of a Function by Shannon Wavelets

Let $f(x) \in L_2(\mathbb{R})$ be a function such that for any value of the parameters $n, k \in \mathbb{Z}$, it is

$$\left| \int_{-\infty}^{\infty} f(x)\varphi_k^0(x)\mathrm{d}x \right| \leq A_k < \infty, \qquad \left| \int_{-\infty}^{\infty} f(x)\psi_k^n(x)\mathrm{d}x \right| \leq B_k^n < \infty, \tag{3.1}$$

and $\mathcal{B} \subset L_2(\mathbb{R})$ the Paley-Wiener space, that is, the space of band limited functions, that is,

$$\operatorname{supp} \hat{f} \subset [-b, b], \quad b < \infty. \tag{3.2}$$

According to the sampling theorem (see, e.g., [27] and references therein) we have the following.

Theorem 3.1 (Shannon). *If $f(x) \in L_2(\mathbb{R})$ and* supp $\widehat{f} \subset [-\pi, \pi]$, *the series*

$$f(x) = \sum_{k=-\infty}^{\infty} \alpha_k \varphi_k^0(x) \tag{3.3}$$

uniformly converges to $f(x)$, and

$$\alpha_k = f(k). \tag{3.4}$$

Proof (see also [17]). In order to compute the values of the coefficients we have to evaluate the series in correspondence of the integer:

$$f(h) = \sum_{k=-\infty}^{\infty} \alpha_k \varphi_k^0(h) \overset{(2.5)}{=} \sum_{k=-\infty}^{\infty} \alpha_k \delta_{kh} = \alpha_h, \tag{3.5}$$

having taken into account (2.5).

The convergence follows from the hypotheses on $f(x)$. In particular, the importance of the band limited frequency can be easily seen by applying the Fourier transform to (3.3):

$$\begin{aligned} \widehat{f}(\omega) &= \sum_{k=-\infty}^{\infty} f(k) \widehat{\varphi}_k^0(x) \\ &\overset{(2.24)}{=} \frac{1}{2\pi} \sum_{k=-\infty}^{\infty} f(k) e^{-i\omega k} \chi(\omega + 3\pi) \\ &= \frac{1}{2\pi} \chi(\omega + 3\pi) \sum_{k=-\infty}^{\infty} f(k) e^{-i\omega k} \end{aligned} \tag{3.6}$$

so that

$$\widehat{f}(\omega) = \begin{cases} \dfrac{1}{2\pi} \displaystyle\sum_{k=-\infty}^{\infty} f(k) e^{-i\omega k}, & \omega \in [-\pi, \pi] \\ 0, & \omega \notin [-\pi, \pi]. \end{cases} \tag{3.7}$$

In other words, if the function is band limited (i.e., with compact support in the frequency domain), it can be completely reconstructed by a discrete Fourier series. The Fourier coefficients are the values of the function $f(x)$ sampled at the integers. □

As a generalization of the Paley-Wiener space, and in order to generalize the Shannon theorem to unbounded intervals, we define the space $\mathcal{B}_\psi \supseteq \mathcal{B}$ of functions $f(x)$ such that the integrals

$$\begin{aligned} \alpha_k &\overset{\text{def}}{=} \left\langle f(x), \varphi_k^0(x) \right\rangle \overset{(2.27)}{=} \int_{-\infty}^{\infty} f(x)\overline{\varphi_k^0(x)}\mathrm{d}x, \\ \beta_k^n &\overset{\text{def}}{=} \left\langle f(x), \psi_k^n(x) \right\rangle \overset{(2.27)}{=} \int_{-\infty}^{\infty} f(x)\overline{\psi_k^n(x)}\mathrm{d}x \end{aligned} \tag{3.8}$$

exist and are finite. According to (2.26), (2.27), it is in the Fourier domain that

$$\begin{aligned} \alpha_k &\overset{\text{def}}{=} \int_{-\infty}^{\infty} f(x)\varphi_k^0(x)\mathrm{d}x \overset{(14)}{=} 2\pi\langle \widehat{f(x)}, \widehat{\varphi_k^0(x)}\rangle = 2\pi \int_{-\infty}^{\infty} \widehat{f}(\omega)\overline{\varphi_k^0(\omega)}\mathrm{d}\omega \\ &\overset{(2.24)}{=} 2\pi \int_{-\infty}^{\infty} \widehat{f}(\omega)\frac{1}{2\pi}e^{i\omega k}\chi(\omega+3\pi)\mathrm{d}\omega \overset{(2.23)}{=} \int_{-\pi}^{\pi} \widehat{f}(\omega)e^{i\omega k}\mathrm{d}\omega, \\ \beta_k^n &\overset{\text{def}}{=} \int_{-\infty}^{\infty} f(x)\psi_k^n(x)\mathrm{d}x \overset{(2.27)}{=} 2\pi\langle \widehat{f(x)}, \widehat{\psi_k^n(x)}\rangle \\ &\overset{(2.24)}{=} -2\pi \int_{-\infty}^{\infty} \widehat{f}(\omega)\frac{2^{-n/2}}{2\pi}e^{i\omega(k+1/2)/2^n}\left[\chi\left(\frac{\omega}{2^{n-1}}\right)+\chi\left(\frac{-\omega}{2^{n-1}}\right)\right]\mathrm{d}\omega \\ &\overset{(2.23)}{=} -2^{-n/2}\left[\int_{2^n\pi}^{2^{n+1}\pi} \widehat{f}(\omega)e^{i\omega(k+1/2)/2^n}\mathrm{d}\omega + \int_{-2^{n+1}\pi}^{-2^n\pi} \widehat{f}(\omega)e^{i\omega(k+1/2)/2^n}\mathrm{d}\omega\right], \end{aligned} \tag{3.9}$$

so that

$$\begin{aligned} \alpha_k &= \int_{-\pi}^{\pi} \widehat{f}(\omega)e^{i\omega k}\mathrm{d}\omega \\ \beta_k^n &= -2^{-n/2}\left[\int_{2^n\pi}^{2^{n+1}\pi} \widehat{f}(\omega)e^{i\omega(k+1/2)/2^n}\mathrm{d}\omega + \int_{-2^{n+1}\pi}^{-2^n\pi} \widehat{f}(\omega)e^{i\omega(k+1/2)/2^n}\mathrm{d}\omega\right]. \end{aligned} \tag{3.10}$$

For the unbounded interval, let us prove the following.

Theorem 3.2 (Shannon generalized theorem). *If $f(x) \in B_\psi \subset L_2(\mathbb{R})$ and* $\operatorname{supp} \widehat{f} \subseteq \mathbb{R}$, *the series*

$$f(x) = \sum_{h=-\infty}^{\infty} \alpha_h \varphi_h^0(x) + \sum_{n=0}^{\infty}\sum_{k=-\infty}^{\infty} \beta_k^n \psi_k^n(x) \tag{3.11}$$

converges to $f(x)$, with α_h and β_k^n given by (3.8) *and* (3.10). *In particular, when* $\operatorname{supp} \widehat{f} \subseteq [-2^{N+1}\pi, 2^{N+1}\pi]$, *it is*

$$f(x) = \sum_{h=-\infty}^{\infty} \alpha_h \varphi_h^0(x) + \sum_{n=0}^{N}\sum_{k=-\infty}^{\infty} \beta_k^n \psi_k^n(x). \tag{3.12}$$

Proof. The representation (3.11) follows from the orthogonality of the scaling and Shannon wavelets (Theorems 2.1, 2.2, and 2.3). The coefficients, which exist and are finite, are given by (3.8). The convergence of the series is a consequence of the wavelet axioms. □

It should be noticed that

$$\operatorname{supp} \widehat{f} = [-\pi, \pi] \bigcup_{n=0,\ldots,\infty} \left[-2^{n+1}\pi, -2^{n}\pi\right] \cup \left[2^{n}\pi, 2^{n+1}\pi\right], \tag{3.13}$$

so that for a band limited frequency signal, that is, for a signal whose frequency belongs to the band $[-\pi, \pi]$, this theorem reduces to the Shannon sampling theorem. More in general, the representation (3.11) takes into account more frequencies ranging in different bands. In this case we have some nontrivial contributions to the series coefficients from all bands, ranging from $[-2^{N}\pi, 2^{N}\pi]$:

$$\operatorname{supp} \widehat{f} = [-\pi, \pi] \bigcup_{n=0,\ldots,N} \left[-2^{n+1}\pi, -2^{n}\pi\right] \cup \left[2^{n}\pi, 2^{n+1}\pi\right]. \tag{3.14}$$

In the frequency domain, (3.11) gives

$$\begin{aligned}
\widehat{f}(\omega) &= \sum_{h=-\infty}^{\infty} \alpha_h \widehat{\varphi}_h^0(\omega) + \sum_{n=0}^{\infty} \sum_{k=-\infty}^{\infty} \beta_k^n \widehat{\psi}_k^n(\omega) \\
\widehat{f}(\omega) &\overset{(2.24)}{=} \frac{1}{2\pi} \sum_{h=-\infty}^{\infty} \alpha_h e^{-i\omega h} \chi(\omega + 3\pi) \\
&\quad - \frac{1}{2\pi} \sum_{n=0}^{\infty} \sum_{k=-\infty}^{\infty} 2^{-n/2} \beta_k^n e^{-i\omega(k+1/2)/2^n} \left[\chi\left(\frac{\omega}{2^{n-1}}\right) + \chi\left(\frac{-\omega}{2^{n-1}}\right)\right].
\end{aligned} \tag{3.15}$$

That is,

$$\begin{aligned}
\widehat{f}(\omega) = \frac{1}{2\pi} \chi(\omega + 3\pi) \sum_{h=-\infty}^{\infty} \alpha_h e^{-i\omega h} \\
- \frac{1}{2\pi} \chi\left(\frac{\omega}{2^{n-1}}\right) \sum_{n=0}^{\infty} \sum_{k=-\infty}^{\infty} 2^{-n/2} \beta_k^n e^{-i\,\omega(k+1/2)/2^n} \\
- \frac{1}{2\pi} \chi\left(\frac{-\omega}{2^{n-1}}\right) \sum_{n=0}^{\infty} \sum_{k=-\infty}^{\infty} 2^{-n/2} \beta_k^n e^{-i\,\omega(k+1/2)/2^n}.
\end{aligned} \tag{3.16}$$

Moreover, taking into account (2.5), (2.7), we can write (3.11) as

$$f(x) = \sum_{h=-\infty}^{\infty} f(h) \varphi_h^0(x) - \sum_{n=0}^{\infty} \sum_{k=-\infty}^{\infty} 2^{-n/2} f_n\left(2^{-n}\left(k + \frac{1}{2}\right)\right) \psi_k^n(x) \tag{3.17}$$

with

$$f_n(x) \stackrel{\text{def}}{=} \sum_{k=-\infty}^{\infty} \langle f(x), \psi_k^n(x) \rangle \psi_k^n(x). \tag{3.18}$$

3.1. Error of the Shannon Wavelet Approximation

Let us fix an upper bound for the series of (3.11) in a such way that we can only have the approximation

$$f(x) \cong \sum_{h=-K}^{K} \alpha_h \varphi_h^0(x) + \sum_{n=0}^{N} \sum_{k=-S}^{S} \beta_k^n \psi_k^n(x). \tag{3.19}$$

This approximation can be estimated by the following

Theorem 3.3 (Error of the Shannon wavelet approximation). *The error of the approximation* (3.19) *is given by*

$$\begin{aligned} &\left| f(x) - \sum_{h=-K}^{K} \alpha_h \, \varphi_h^0(x) + \sum_{n=0}^{N} \sum_{k=-S}^{S} \beta_k^n \psi_k^n(x) \right| \\ &\quad \le \left| f(-K-1) + f(K+1) - \frac{3\sqrt{3}}{\pi} \left[f\left(2^{-N-1}\left(-S - \frac{1}{2}\right)\right) + f\left(2^{-N-1}\left(S + \frac{3}{2}\right)\right) \right] \right|. \end{aligned} \tag{3.20}$$

Proof. The error of the approximation (3.19) is defined as

$$\begin{aligned} &f(x) - \sum_{h=-K}^{K} \alpha_h \varphi_h^0(x) + \sum_{n=0}^{N} \sum_{k=-S}^{S} \beta_k^n \psi_k^n(x) \\ &\quad = \sum_{h=-\infty}^{-K-1} \alpha_h \, \varphi_h^0(x) + \sum_{h=K+1}^{\infty} \alpha_h \varphi_h^0(x) + \sum_{n=N+1}^{\infty} \left[\sum_{k=-\infty}^{-S-1} \beta_k^n \psi_k^n(x) + \sum_{k=S+1}^{\infty} \beta_k^n \psi_k^n(x) \right]. \end{aligned} \tag{3.21}$$

Concerning the first part of the r.h.s, it is

$$\begin{aligned} \sum_{h=-\infty}^{-K-1} \alpha_h \, \varphi_h^0(x) + \sum_{h=K+1}^{\infty} \alpha_h \varphi_h^0(x) &\le \max_{x \in \mathbb{R}} \left[\sum_{h=-\infty}^{-K-1} \alpha_h \varphi_h^0(x) + \sum_{h=K+1}^{\infty} \alpha_h \varphi_h^0(x) \right] \\ &= \sum_{h=-\infty}^{-K-1} \alpha_h \, \varphi_h^0(h) + \sum_{h=K+1}^{\infty} \alpha_h \, \varphi_h^0(h) \\ &\stackrel{(2.5)}{=} \sum_{h=-\infty}^{-K-1} \alpha_h + \sum_{h=K+1}^{\infty} \alpha_h \stackrel{(3.3)}{=} \sum_{h=-\infty}^{-K-1} f(h) + \sum_{h=K+1}^{\infty} f(h), \end{aligned} \tag{3.22}$$

and since $f(x) \in L_2(\mathbb{R})$ is a decreasing function,

$$\sum_{h=-\infty}^{-K-1} \alpha_h \varphi_h^0(x) + \sum_{h=K+1}^{\infty} \alpha_h \varphi_h^0(x) \leq f(-K-1) + f(K+1). \tag{3.23}$$

Analogously, it is

$$\begin{aligned}
&\sum_{n=N+1}^{\infty} \left[\sum_{k=-\infty}^{-S-1} \beta_k^n \psi_k^n(x) + \sum_{k=S+1}^{\infty} \beta_k^n \psi_k^n(x) \right] \leq \max_{x\in\mathbb{R}} \sum_{n=N+1}^{\infty} \left[\sum_{k=-\infty}^{-S-1} \beta_k^n \psi_k^n(x) + \sum_{k=S+1}^{\infty} \beta_k^n \psi_k^n(x) \right] \\
&\overset{(2.18)}{=} \sum_{n=N+1}^{\infty} \left[\sum_{k=-\infty}^{-S-1} \beta_k^n \psi_k^n \left(\frac{2^{-n-1}(18k+7)}{3} \right) + \sum_{k=S+1}^{\infty} \beta_k^n \psi_k^n \left(\frac{2^{-n-1}(18k+7)}{3} \right) \right] \\
&= \sum_{n=N+1}^{\infty} \left[\sum_{k=-\infty}^{-S-1} \beta_k^n 2^{n/2} \frac{3\sqrt{3}}{\pi} + \sum_{k=S+1}^{\infty} \beta_k^n 2^{n/2} \frac{3\sqrt{3}}{\pi} \right] = \frac{3\sqrt{3}}{\pi} \sum_{n=N+1}^{\infty} 2^{n/2} \left[\sum_{k=-\infty}^{-S-1} \beta_k^n + \sum_{k=S+1}^{\infty} \beta_k^n \right] \\
&\overset{(3.17)}{=} -\frac{3\sqrt{3}}{\pi} \sum_{n=N+1}^{\infty} 2^{n/2} \left[\sum_{k=-\infty}^{-S-1} 2^{-n/2} f\left(2^{-n}\left(k+\frac{1}{2}\right)\right) + \sum_{k=S+1}^{\infty} 2^{-n/2} f\left(2^{-n}\left(k+\frac{1}{2}\right)\right) \right],
\end{aligned} \tag{3.24}$$

so that

$$\sum_{n=N+1}^{\infty} \left[\sum_{k=-\infty}^{-S-1} \beta_k^n \psi_k^n(x) + \sum_{k=S+1}^{\infty} \beta_k^n \psi_k^n(x) \right] \leq -\frac{3\sqrt{3}}{\pi} \left[f\left(2^{-N-1}\left(-S-\frac{1}{2}\right)\right) + f\left(2^{-N-1}\left(S+\frac{3}{2}\right)\right) \right] \tag{3.25}$$

from where (3.20) follows. □

4. Reconstruction of the Derivatives

Let $f(x) \in L_2(\mathbb{R})$ and let $f(x)$ be a differentiable function $f(x) \in C^p$ with p sufficiently high. The reconstruction of a function $f(x)$ given by (3.11) enables us to compute also its derivatives in terms of the wavelet decomposition:

$$\frac{\mathrm{d}^\ell}{\mathrm{d}x^\ell} f(x) = \sum_{h=-\infty}^{\infty} \alpha_h \frac{\mathrm{d}^\ell}{\mathrm{d}x^\ell} \varphi_h^0(x) + \sum_{n=0}^{\infty} \sum_{k=-\infty}^{\infty} \beta_k^n \frac{\mathrm{d}^\ell}{\mathrm{d}x^\ell} \psi_k^n(x), \tag{4.1}$$

so that, according to (3.11), the derivatives of $f(x)$ are known when the derivatives

$$\frac{\mathrm{d}^\ell}{\mathrm{d}x^\ell} \varphi_h^0(x), \qquad \frac{\mathrm{d}^\ell}{\mathrm{d}x^\ell} \psi_k^n(x) \tag{4.2}$$

are given.

Indeed, in order to represent differential operators in wavelet bases, we have to compute the wavelet decomposition of the derivatives:

$$\begin{aligned}\frac{\mathrm{d}^{\ell}}{\mathrm{d}x^{\ell}}\varphi_h^0(x) &= \sum_{k=-\infty}^{\infty}\lambda_{hk}^{(\ell)}\ \varphi_k^0(x),\\ \frac{\mathrm{d}^{\ell}}{\mathrm{d}x^{\ell}}\psi_h^m(x) &= \sum_{n=0}^{\infty}\sum_{k=-\infty}^{\infty}\gamma^{(\ell)}{}_{hk}^{mn}\psi_k^n(x),\end{aligned} \tag{4.3}$$

being

$$\lambda_{kh}^{(\ell)} \stackrel{\text{def}}{=} \left\langle \frac{\mathrm{d}^{\ell}}{\mathrm{d}x^{\ell}}\varphi_k^0(x), \varphi_h^0(x)\right\rangle, \qquad \gamma^{(\ell)}{}_{kh}^{nm} \stackrel{\text{def}}{=} \left\langle \frac{\mathrm{d}^{\ell}}{\mathrm{d}x^{\ell}}\psi_k^n(x), \psi_h^m(x)\right\rangle \tag{4.4}$$

the connection coefficients [15–21, 26, 29] (or refinable integrals).

Their computation can be easily performed in the Fourier domain, thanks to the equality (2.27). In fact, in the Fourier domain the ℓ-order derivative of the (scaling) wavelet functions is

$$\widehat{\frac{\mathrm{d}^{\ell}}{\mathrm{d}x^{\ell}}\varphi_k^n(x)} = (i\omega)^{\ell}\widehat{\varphi}_k^n(\omega), \qquad \widehat{\frac{\mathrm{d}^{\ell}}{\mathrm{d}x^{\ell}}\psi_k^n(x)} = (i\omega)^{\ell}\widehat{\psi}_k^n(\omega), \tag{4.5}$$

and according to (2.24),

$$\begin{aligned}\widehat{\frac{\mathrm{d}^{\ell}}{\mathrm{d}x^{\ell}}\varphi_k^n(x)} &= (i\omega)^{\ell}\frac{2^{-n/2}}{2\pi}e^{-i\omega k/2^n}\chi\left(\frac{\omega}{2^n}+3\pi\right),\\ \widehat{\frac{\mathrm{d}^{\ell}}{\mathrm{d}x^{\ell}}\psi_k^n(x)} &= -(i\omega)^{\ell}\frac{2^{-n/2}}{2\pi}e^{-i\omega(k+1/2)/2^n}\left[\chi\left(\frac{\omega}{2^{n-1}}\right)+\chi\left(-\frac{\omega}{2^{n-1}}\right)\right].\end{aligned} \tag{4.6}$$

Taking into account (2.27), we can easily compute the connection coefficients in the frequency domain

$$\lambda_{kh}^{(\ell)} = 2\pi\left\langle \widehat{\frac{\mathrm{d}^{\ell}}{\mathrm{d}x^{\ell}}\varphi_k^0(x)}, \widehat{\varphi_h^0(x)}\right\rangle, \qquad \gamma^{(\ell)}{}_{kh}^{nm} = 2\pi\left\langle \widehat{\frac{\mathrm{d}^{\ell}}{\mathrm{d}x^{\ell}}\psi_k^n(x)}, \widehat{\psi_h^m(x)}\right\rangle \tag{4.7}$$

with the derivatives given by (4.6).

If we define

$$\mu(m) = \operatorname{sign}(m) = \begin{cases}1, & m>0,\\ -1, & m<0,\\ 0, & m=0,\end{cases} \tag{4.8}$$

the following has been shown [16, 17].

Theorem 4.1. *The any order connection coefficients* $(4.4)_1$ *of the Shannon scaling functions* $\varphi_k^0(x)$ *are*

$$\lambda_{kh}^{(\ell)} = \begin{cases} (-1)^{k-h}\dfrac{i^\ell}{2\pi}\displaystyle\sum_{s=1}^{\ell}\dfrac{\ell!\pi^s}{s![i(k-h)]^{\ell-s+1}}\left[(-1)^s-1\right], k\neq h, \\ \dfrac{i^\ell\pi^{\ell+1}}{2\pi(\ell+1)}\left[1+(-1)^\ell\right], k=h, \end{cases} \tag{4.9}$$

or, shortly,

$$\begin{aligned} \lambda_{kh}^{(\ell)} &= \frac{i^\ell\pi^\ell}{2(\ell+1)}\left[1+(-1)^\ell\right]\left(1-\left|\mu(k-h)\right|\right) \\ &\quad + (-1)^{k-h}\left|\mu(k-h)\right|\frac{i^\ell}{2\pi}\sum_{s=1}^{\ell}\frac{\ell!\pi^s}{s![i(k-h)]^{\ell-s+1}}\left[(-1)^s-1\right]. \end{aligned} \tag{4.10}$$

For the proof see [17].

Analogously for the connection coefficients $(4.4)_2$ we have the following.

Theorem 4.2. *The any order connection coefficients* $(4.7)_2$ *of the Shannon scaling wavelets* $\psi_k^n(x)$ *are*

$$\begin{aligned} {\gamma^{(\ell)}}_{kh}^{nm} &= \delta^{nm}\Bigg\{ i^\ell\left(1-\left|\mu(h-k)\right|\right)\frac{\pi^\ell 2^{n\ell-1}}{\ell+1}\left(2^{\ell+1}-1\right)\left(1+(-1)^\ell\right) \\ &\quad + \mu(h-k)\sum_{s=1}^{\ell+1}(-1)^{[1+\mu(h-k)](2\ell-s+1)/2}\,\frac{\ell!i^{\ell-s}\pi^{\ell-s}}{(\ell-s+1)!|h-k|^s}(-1)^{-s-2(h+k)}2^{n\ell-s-1} \\ &\quad \times\left\{2^{\ell+1}\left[(-1)^{4h+s}+(-1)^{4k+\ell}\right]-2^s\left[(-1)^{3k+h+\ell}+(-1)^{3h+k+s}\right]\right\}\Bigg\}, \end{aligned} \tag{4.11}$$

respectively, for $\ell\geq 1$, *and* ${\gamma^{(0)}}_{kh}^{nm} = \delta_{kh}\delta^{nm}$.

For the proof see [17].

Theorem 4.3. *The connection coefficients are recursively given by the matrix at the lowest scale level:*

$${\gamma^{(\ell)}}_{kh}^{nn} = 2^{\ell(n-1)}{\gamma^{(\ell)}}_{kh}^{11}. \tag{4.12}$$

Moreover it is

$${\gamma^{(2\ell+1)}}_{kh}^{nn} = -{\gamma^{(2\ell+1)}}_{hk}^{nn}, \qquad {\gamma^{(2\ell)}}_{kh}^{nn} = {\gamma^{(2\ell)}}_{hk}^{nn}. \tag{4.13}$$

If we consider a dyadic discretisation of the x-axis such that

$$x_k = 2^{-n}\left(k+\frac{1}{2}\right), \quad k\in\mathbb{Z} \tag{4.14}$$

according to (2.8), the $(4.3)_2$ at dyadic points $x_k = 2^{-n}(k+1/2)$ becomes

$$\left[\frac{\mathrm{d}}{\mathrm{d}x}\psi_k^n(x)\right]_{x=x_k} = -2^{n/2}\sum_{h=-\infty}^{\infty}\gamma'^{nn}_{kh}. \tag{4.15}$$

For instance, in $x_1 = 2^{-1}(1+1/2)$

$$\left[\frac{\mathrm{d}}{\mathrm{d}x}\psi_1^1(x)\right]_{x=x_1=3/4} = -2^{1/2}\sum_{h=-\infty}^{\infty}\gamma_{1h}^{11} \cong -2^{1/2}\sum_{h=-2}^{2}\gamma_{1h}^{11} = -2^{1/2}\left(\frac{1}{6}+\frac{1}{4}\right) = -\frac{5\sqrt{2}}{12}. \tag{4.16}$$

Analogously it is

$$\varphi_k^n\left(2^{-n}\left(k+\frac{1}{2}\right)\right) = \frac{2^{1+n/2}}{\pi}, \quad k\in\mathbb{Z}, \tag{4.17}$$

from where, in $x_k = (k+1/2)$, it is

$$\left[\frac{\mathrm{d}}{\mathrm{d}x}\varphi_k^0(x)\right]_{x=x_k} = \frac{2}{\pi}\sum_{h=-\infty}^{\infty}\lambda_{kh}. \tag{4.18}$$

5. Wavelet Solution of the Integrodifferential Equation

Let us consider the following linear integrodifferential equation:

$$A\frac{\mathrm{d}u}{\mathrm{d}x} = B\int_{-\infty}^{\infty}k(x,y)u(y)\mathrm{d}y + u(x) + q(x) \quad (A,B\in\mathbb{R}), \tag{5.1}$$

which includes as special cases the integral equation $(A = 0, B\neq 0)$ and the differential equation $(A\neq 0, B = 0)$. When $A = B = 0$, there is the trivial solution $u(x) = -q(x)$.

It is assumed that the kernel is in the form:

$$k(x,y) = f(x)g(y), \tag{5.2}$$

and the given functions $f(x)\in L_2(\mathbb{R})$, $g(x)\in L_2(\mathbb{R})$, $q(x)\in L_2(\mathbb{R})$, so that, according to (3.11)

$$\begin{aligned} f(x) &= \sum_{h=-\infty}^{\infty} f_h\varphi_h^0(x) + \sum_{n=0}^{\infty}\sum_{k=-\infty}^{\infty} f_k^n\psi_k^n(x), \\ g(x) &= \sum_{h=-\infty}^{\infty} g_h\varphi_h^0(x) + \sum_{n=0}^{\infty}\sum_{k=-\infty}^{\infty} g_k^n\psi_k^n(x), \\ q(x) &= \sum_{h=-\infty}^{\infty} q_h\varphi_h^0(x) + \sum_{n=0}^{\infty}\sum_{k=-\infty}^{\infty} q_k^n\psi_k^n(x), \end{aligned} \tag{5.3}$$

with the wavelet coefficients $f_h, f_k^n, g_h, g_k^n, q_h, q_k^n$ given by (3.8).

The analytical solution of (5.1) can be obtained as follows.

Theorem 5.1. *The solution of* (5.1), *in the degenerate case* (5.2), *in the Fourier domain is*

$$\widehat{u}(\omega) = \frac{2\pi\ B\langle \widehat{g}(\omega), \widehat{q}(\omega)/(Ai\omega - 1)\rangle}{(1 - 2\pi B)\left\langle \widehat{g}(\omega), \widehat{f}(\omega)/(Ai\omega - 1)\right\rangle} \frac{\widehat{f}(\omega)}{Ai\omega - 1} + \frac{\widehat{q}(\omega)}{Ai\omega - 1}. \tag{5.4}$$

Proof. The Fourier transform of (5.1), with kernel as (5.2), is

$$\begin{aligned} A\widehat{\frac{\mathrm{d}u}{\mathrm{d}x}} &= B\widehat{f(x)}\int_{-\infty}^{\infty} g(y)u(y)\mathrm{d}y + \widehat{u(x)} + \widehat{q(x)}, \\ Ai\omega\,\widehat{u}(\omega) &= 2\pi B\widehat{f}(\omega)\langle \widehat{g}(\omega), \widehat{u}(\omega)\rangle + \widehat{u}(\omega) + \widehat{q}(\omega), \\ \widehat{u}(\omega) &= 2\pi B\frac{\widehat{f}(\omega)}{(Ai\omega - 1)}\langle \widehat{g}(\omega), \widehat{u}(\omega)\rangle + \frac{\widehat{q}(\omega)}{(Ai\omega - 1)}, \end{aligned} \tag{5.5}$$

that is,

$$\widehat{u}(\omega) = 2\pi B\frac{\widehat{f}(\omega)}{(Ai\omega - 1)}\langle \widehat{g}(\omega), \widehat{u}(\omega)\rangle + \frac{\widehat{q}(\omega)}{(Ai\omega - 1)}. \tag{5.6}$$

By the inner product with $\widehat{g}(\omega)$ there follows

$$\langle \widehat{g}(\omega), \widehat{u}(\omega)\rangle = 2\pi B\left\langle \widehat{g}(\omega), \frac{\widehat{f}(\omega)}{(Ai\omega - 1)}\right\rangle\langle \widehat{g}(\omega), \widehat{u}(\omega)\rangle + \left\langle \widehat{g}(\omega), \frac{\widehat{q}(\omega)}{(Ai\omega - 1)}\right\rangle, \tag{5.7}$$

so that

$$\langle \widehat{g}(\omega), \widehat{u}(\omega)\rangle = \frac{\langle \widehat{g}(\omega), \widehat{q}(\omega)/(Ai\omega - 1)\rangle}{(1 - 2\pi B)\left\langle \widehat{g}(\omega), \widehat{f}(\omega)/(Ai\omega - 1)\right\rangle}. \tag{5.8}$$

If we put this equation into (5.6), we get (5.4). □

Although the existence of solution is proven, the computation of the Fourier transform could not be easily performed. Therefore the numerical computation is searched in the wavelet approximation.

The wavelet solution of (5.1) can be obtained as follows: it is assumed that the unknown function and its derivative can be written as

$$\begin{aligned} u(x) &= \sum_{h=-\infty}^{\infty} \alpha_h \varphi_h^0(x) + \sum_{n=0}^{\infty} \sum_{k=-\infty}^{\infty} \beta_k^n \psi_k^n(x), \\ \frac{\mathrm{d}u}{\mathrm{d}x} &= \sum_{h=-\infty}^{\infty} \alpha_h \frac{\mathrm{d}}{\mathrm{d}x} \varphi_h^0(x) + \sum_{n=0}^{\infty} \sum_{k=-\infty}^{\infty} \frac{\mathrm{d}}{\mathrm{d}x} \beta_k^n \psi_k^n(x) \\ &\overset{(4.3)}{=} \sum_{h=-\infty}^{\infty} \alpha_h \sum_{s=-\infty}^{\infty} \lambda'_{hs} \varphi_s^0(x) + \sum_{n=0}^{\infty} \sum_{k=-\infty}^{\infty} \beta_k^n \sum_{m=0}^{\infty} \sum_{s=-\infty}^{\infty} \gamma'^{nm}_{sk} \psi_s^m(x), \end{aligned} \tag{5.9}$$

and the integral can be written as

$$\int_{-\infty}^{\infty} g(y) u(y) \mathrm{d}y = \langle g, u \rangle = \sum_{h=-\infty}^{\infty} \alpha_h g_h + \sum_{n=0}^{\infty} \sum_{k=-\infty}^{\infty} \beta_k^n g_k^n. \tag{5.10}$$

There follows the system

$$\begin{aligned} &\sum_{h=-\infty}^{\infty} \alpha_h \sum_{s=-\infty}^{\infty} \lambda'_{hs} \varphi_s^0(x) + \sum_{n=0}^{\infty} \sum_{k=-\infty}^{\infty} \beta_k^n \sum_{m=0}^{\infty} \sum_{s=-\infty}^{\infty} \gamma'^{nm}_{sk} \psi_s^m(x) \\ &\quad = \sum_{h=-\infty}^{\infty} \alpha_h \varphi_h^0(x) + \sum_{n=0}^{\infty} \sum_{k=-\infty}^{\infty} \beta_k^n \psi_k^n(x) \\ &\qquad + \left[\sum_{h=-\infty}^{\infty} \alpha_h g_h + \sum_{n=0}^{\infty} \sum_{k=-\infty}^{\infty} \beta_k^n g_k^n \right] \left[\sum_{h=-\infty}^{\infty} f_h \varphi_h^0(x) + \sum_{n=0}^{\infty} \sum_{k=-\infty}^{\infty} f_k^n \psi_k^n(x) \right] \\ &\qquad + \sum_{h=-\infty}^{\infty} q_h \varphi_h^0(x) + \sum_{n=0}^{\infty} \sum_{k=-\infty}^{\infty} q_k^n \psi_k^n(x), \end{aligned} \tag{5.11}$$

and, according to the definition of the connection coefficients,

$$\begin{aligned} &\sum_{h=-\infty}^{\infty} \alpha_h \sum_{s=-\infty}^{\infty} \lambda'_{hs} \varphi_s^0(x) + \sum_{n=0}^{\infty} \sum_{k=-\infty}^{\infty} \sum_{s=-\infty}^{\infty} \beta_k^n \gamma'^{nn}_{sk} \psi_s^n(x) \\ &\quad = \sum_{h=-\infty}^{\infty} \alpha_h \varphi_h^0(x) + \sum_{n=0}^{\infty} \sum_{k=-\infty}^{\infty} \beta_k^n \psi_k^n(x) \\ &\qquad + \left[\sum_{h=-\infty}^{\infty} \alpha_h g_h + \sum_{n=0}^{\infty} \sum_{k=-\infty}^{\infty} \beta_k^n g_k^n \right] \left[\sum_{h=-\infty}^{\infty} f_h \varphi_h^0(x) + \sum_{n=0}^{\infty} \sum_{k=-\infty}^{\infty} f_k^n \psi_k^n(x) \right] \\ &\qquad + \sum_{h=-\infty}^{\infty} q_h \varphi_h^0(x) + \sum_{n=0}^{\infty} \sum_{k=-\infty}^{\infty} q_k^n \psi_k^n(x). \end{aligned} \tag{5.12}$$

By the inner product and taking into account the orthogonality conditions (Theorems 2.1, 2.2, and 2.3) it is

$$\sum_{h=-\infty}^{\infty} \alpha_h \lambda'_{hk} = \alpha_k + \left[\sum_{h=-\infty}^{\infty} \alpha_h g_h + \sum_{n=0}^{\infty} \sum_{h=-\infty}^{\infty} \beta_h^n g_h^n \right] f_k + q_k, \tag{5.13}$$

or

$$\sum_{h=-\infty}^{\infty} (\lambda'_{hk} - \delta_{hk} - g_h f_k) \alpha_h = \left[\sum_{n=0}^{\infty} \sum_{h=-\infty}^{\infty} \beta_h^n g_h^n \right] f_k + q_k, \quad (k \in \mathbb{Z}). \tag{5.14}$$

Analogously, it is

$$\sum_{n=0}^{\infty} \sum_{k=-\infty}^{\infty} \beta_k^n \, \gamma'^{nj}_{kr} = \beta_r^j + \left[\sum_{h=-\infty}^{\infty} \alpha_h g_h + \sum_{n=0}^{\infty} \sum_{k=-\infty}^{\infty} \beta_k^n g_k^n \right] f_r^j + q_r^j \tag{5.15}$$

or, according to (4.11), and rearranging the indices

$$\sum_{h=-\infty}^{\infty} \beta_h^n (\gamma'^{nn}_{hk} - \delta_{hk}) - f_k^n \sum_{m=0}^{\infty} \sum_{h=-\infty}^{\infty} \beta_h^m g_h^m = f_k^n \sum_{h=-\infty}^{\infty} \alpha_h g_h + q_k^n. \tag{5.16}$$

Thus the solution of (5.1) is $(5.9)_1$ with the wavelet coefficients given by the algebraic system

$$\begin{gathered} \sum_{h=-\infty}^{\infty} (\lambda'_{hk} - \delta_{hk} - g_h f_k) \alpha_h = \left[\sum_{n=0}^{\infty} \sum_{h=-\infty}^{\infty} \beta_h^n g_h^n \right] f_k + q_k \quad (k \in \mathbb{Z}), \\ \sum_{h=-\infty}^{\infty} \beta_h^n (\gamma'^{nn}_{hk} - \delta_{hk}) - f_k^n \sum_{m=0}^{\infty} \sum_{h=-\infty}^{\infty} \beta_h^m g_h^m = f_k^n \sum_{h=-\infty}^{\infty} \alpha_h g_h + q_k^n \quad (n \in \mathbb{N}, k \in \mathbb{Z}) \end{gathered} \tag{5.17}$$

and up to a fixed scale of approximation N, S:

$$\begin{gathered} \sum_{h=-S}^{S} (\lambda'_{hk} - \delta_{hk} - g_h f_k) \alpha_h = \left[\sum_{n=0}^{N} \sum_{h=-S}^{S} \beta_h^n g_h^n \right] f_k + q_k \quad (k \in \mathbb{Z}), \\ \sum_{h=-S}^{S} \beta_h^n (\gamma'^{nn}_{hk} - \delta_{hk}) - f_k^n \sum_{m=0}^{N} \sum_{h=-S}^{S} \beta_h^m g_h^m = f_k^n \sum_{h=-N}^{N} \alpha_h g_h + q_k^n \quad (n \in \mathbb{N}, k \in \mathbb{Z}). \end{gathered} \tag{5.18}$$

6. Example

Let us consider the following equation:

$$\frac{\mathrm{d}u}{\mathrm{d}x} = \int_{-\infty}^{\infty} e^{-x^2-|y|} u(y)\,\mathrm{d}y - \frac{x}{|x|} u(x) - e^{-x^2} \tag{6.1}$$

with the condition

$$u(0) = 1. \tag{6.2}$$

The analytical solution, as can be directly checked, is

$$u(x) = e^{-|x|}. \tag{6.3}$$

Since

$$f(x) = e^{-x^2}, \qquad g(x) = e^{-|x|}, \qquad q(x) = -e^{-x^2} \tag{6.4}$$

belong to $L_2(\mathbb{R})$, let us find the wavelet approximation by assuming that also $u(x)$ belongs to $L_2(\mathbb{R})$, so that they can be represented according to (5.3), (5.9).

At the level of approximation $N = 0, S = 0$, from (5.3) we have

$$\begin{gathered} f(x) = e^{-x^2} \cong 0.97\varphi_0^0(x), \qquad g(x) = e^{-|x|} \cong 0.80\varphi_0^0(x) + 0.04\psi_0^0(x), \\ q(x) = -e^{-x^2} \cong -0.97\varphi_0^0(x), \end{gathered} \tag{6.5}$$

so that

$$f_0 = 0.97, \qquad f_0^0 = 0, \qquad g_0 = 0.80, \qquad g_0^0 = 0.04, \qquad q_0 = -0.97, \qquad q_0^0 = 0. \tag{6.6}$$

System (5.18) becomes

$$\begin{gathered} (\lambda'_{00} - \delta_{00} - g_0 f_0)\alpha_0 = \beta_0^0 g_0^0 f_0 + q_0, \\ \beta_0^0\left(\gamma'^{00}_{00} - \delta_{00}\right) - f_0^0 \beta_0^0 g_0^0 = f_0^0 \alpha_0 g_0 + q_0^0, \end{gathered} \tag{6.7}$$

and, since $\lambda'_{00} = 0$ and $\gamma'^{00}_{00} = 0$, according to (6.6) we have

$$\begin{gathered} -1 - 0.80 \times 0.97\alpha_0 = -0.97, \\ -\beta_0^0 = 0, \end{gathered} \tag{6.8}$$

whose solution is

$$\alpha_0 = 0.548, \qquad \beta_0^0 = 0, \tag{6.9}$$

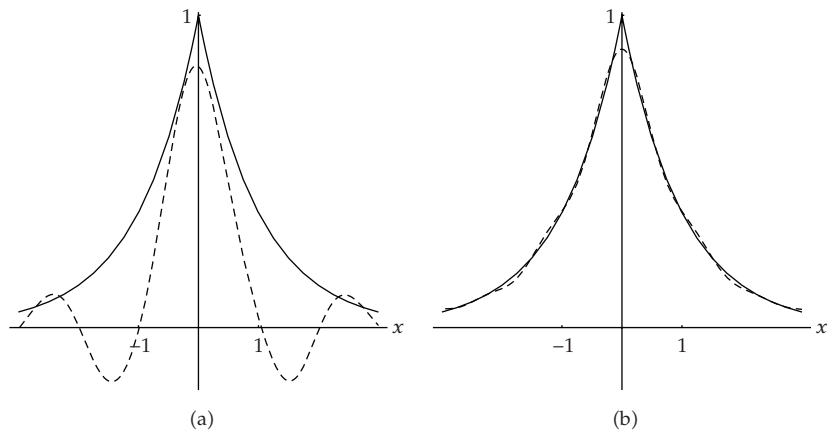

Figure 1: Wavelet approximations (shaded) of the analytical solution (plain) of (6.1) obtained by solving (5.17).

so that

$$u(x) \cong 0.548\varphi_0^0(x). \tag{6.10}$$

As expected, the approximation is very row (Figure 1(a)); in fact in order to get a satisfactory approximation we have to solve system (5.18) at least at the levels $N = 0, S = 5$ as shown in Figure 1(b).

7. Conclusion

In this paper the theory of Shannon wavelets combined with the connection coefficients methods and the Petrov-Galerkin method has been used to find the wavelet approximation of integrodifferential equations. Among the main advantages there is the decorrelation of frequencies, in the sense that the differential operator is splitted into its different frequency bands.

References

[1] H.-T. Shim and C.-H. Park, "An approximate solution of an integral equation by wavelets," *Journal of Applied Mathematics and Computing*, vol. 17, no. 1-2-3, pp. 709–717, 2005.

[2] U. Lepik, "Numerical solution of evolution equations by the Haar wavelet method," *Applied Mathematics and Computation*, vol. 185, no. 1, pp. 695–704, 2007.

[3] U. Lepik, "Solving fractional integral equations by the Haar wavelet method," *Applied Mathematics and Computation*, vol. 214, no. 2, pp. 468–478, 2009.

[4] C. Cattani and A. Kudreyko, "Application of periodized harmonic wavelets towards solution of egenvalue problems for integral equations," *Mathematical Problems in Engineering*, vol. 2010, Article ID 570136, 8 pages, 2010.

[5] C. Cattani and A. Kudreyko, "Harmonic wavelet method towards solution of the Fredholm type integral equations of the second kind," *Applied Mathematics and Computation*, vol. 215, no. 12, pp. 4164–4171, 2010.

[6] S. V. Muniandy and I. M. Moroz, "Galerkin modelling of the Burgers equation using harmonic wavelets," *Physics Letters A*, vol. 235, no. 4, pp. 352–356, 1997.

[7] D. E. Newland, "Harmonic wavelet analysis," *Proceedings of the Royal Society of London A*, vol. 443, pp. 203–222, 1993.

[8] J.-Y. Xiao, L.-H. Wen, and D. Zhang, "Solving second kind Fredholm integral equations by periodic wavelet Galerkin method," *Applied Mathematics and Computation*, vol. 175, no. 1, pp. 508–518, 2006.

[9] S. Yousefi and A. Banifatemi, "Numerical solution of Fredholm integral equations by using CAS wavelets," *Applied Mathematics and Computation*, vol. 183, no. 1, pp. 458–463, 2006.

[10] Y. Mahmoudi, "Wavelet Galerkin method for numerical solution of nonlinear integral equation," *Applied Mathematics and Computation*, vol. 167, no. 2, pp. 1119–1129, 2005.

[11] K. Maleknejad and T. Lotfi, "Expansion method for linear integral equations by cardinal B-spline wavelet and Shannon wavelet as bases for obtain Galerkin system," *Applied Mathematics and Computation*, vol. 175, no. 1, pp. 347–355, 2006.

[12] K. Maleknejad, M. Rabbani, N. Aghazadeh, and M. Karami, "A wavelet Petrov-Galerkin method for solving integro-differential equations," *International Journal of Computer Mathematics*, vol. 86, no. 9, pp. 1572–1590, 2009.

[13] A. Mohsen and M. El-Gamel, "A sinc-collocation method for the linear Fredholm integro-differential equations," *ZAMP*, vol. 58, no. 3, pp. 380–390, 2007.

[14] N. Bellomo, B. Lods, R. Revelli, and L. Ridolfi, *Generalized Collocation Methods: Solutions to Nonlinear Problem*, Modeling and Simulation in Science, Engineering and Technology, Birkhäuser, Boston, Mass, USA, 2008.

[15] C. Cattani, "Harmonic wavelets towards the solution of nonlinear PDE," *Computers & Mathematics with Applications*, vol. 50, no. 8-9, pp. 1191–1210, 2005.

[16] C. Cattani, "Connection coefficients of Shannon wavelets," *Mathematical Modelling and Analysis*, vol. 11, no. 2, pp. 117–132, 2006.

[17] C. Cattani, "Shannon wavelets theory," *Mathematical Problems in Engineering*, vol. 2008, Article ID 164808, 24 pages, 2008.

[18] A. Latto, H. L. Resnikoff, and E. Tenenbaum, "The evaluation of connection coefficients of compactly supported wavelets," in *Proceedings of the French-USA Workshop on Wavelets and Turbulence*, Y. Maday, Ed., pp. 76–89, Springer, New York, NY, USA, June 1992.

[19] E. B. Lin and X. Zhou, "Connection coefficients on an interval and wavelet solutions of Burgers equation," *Journal of Computational and Applied Mathematics*, vol. 135, no. 1, pp. 63–78, 2001.

[20] J. Restrepo and G. K. Leaf, "Wavelet-Galerkin discretization of hyperbolic equations," *Journal of Computational Physics*, vol. 122, no. 1, pp. 118–128, 1995.

[21] C. H. Romine and B. W. Peyton, "Computing connection coefficients of compactly supported wavelets on bounded intervals," Tech. Rep. ORNL/TM-13413, Oak Ridge, Computer Science and Mathematical Division, Mathematical Sciences Section, Oak Ridge National Laboratory, 1997, http://citeseer.ist.psu.edu/romine97computing.html .

[22] I. Daubechies, *Ten Lectures on Wavelets*, vol. 61 of *CBMS-NSF Regional Conference Series in Applied Mathematics*, SIAM, Philadelphia, Pa, USA, 1992.

[23] C. Cattani and J. Rushchitsky, *Wavelet and Wave Analysis as Applied to Materials with Micro or Nanostructure*, vol. 74 of *Series on Advances in Mathematics for Applied Sciences*, World Scientific, Singapore, 2007.

[24] E. Bakhoum and C. Toma, "Mathematical transform of travelling-wave equations and phase aspects of quantum interaction," *Mathematical Problems in Engineering*, vol. 2010, Article ID 695208, 15 pages, 2010.

[25] G. Toma, "Specific differential equations for generating pulse sequences," *Mathematical Problems in Engineering*, vol. 2010, Article ID 324818, 11 pages, 2010.

[26] C. Cattani, "Harmonic wavelet solutions of the schrödinger equation," *International Journal of Fluid Mechanics Research*, vol. 5, pp. 1–10, 2003.

[27] S. Unser, "Sampling-50 years after Shannon," *Proceedings of the IEEE*, vol. 88, no. 4, pp. 569–587, 2000.

[28] C. Cattani, "Shannon wavelet analysis," in *Proceedings of the International Conference on Computational Science (ICCS '07)*, Y. Shi, et al., Ed., vol. 4488 of *Lecture Notes in Computer Science Part II*, pp. 982–989, Springer, Beijing, China, May 2007.

[29] E. Deriaz, "Shannon wavelet approximation of linear differential operators," *Institute of Mathematics of the Polish Academy of Sciences*, no. 676, 2007.

Hindawi Publishing Corporation
Mathematical Problems in Engineering
Volume 2010, Article ID 560429, 14 pages
doi:10.1155/2010/560429

Research Article

Variance Bound of ACF Estimation of One Block of fGn with LRD

Ming Li[1] and Wei Zhao[2]

[1] *School of Information Science & Technology, East China Normal University, No. 500, Dong-Chuan Road, Shanghai 200241, China*
[2] *University of Macau, Avenue Padre Tomás Pereira, Taipa, Macau, China*

Correspondence should be addressed to Ming Li, ming lihk@yahoo.com

Received 19 September 2009; Accepted 4 November 2009

Academic Editor: Carlo Cattani

This paper discusses the estimation of autocorrelation function (ACF) of fractional Gaussian noise (fGn) with long-range dependence (LRD). A variance bound of ACF estimation of one block of fGn with LRD for a given value of the Hurst parameter (H) is given. The present bound provides a guideline to require the block size to guarantee that the variance of ACF estimation of one block of fGn with LRD for a given H value does not exceed the predetermined variance bound regardless of the start point of the block. In addition, the present result implies that the error of ACF estimation of a block of fGn with LRD depends only on the number of data points within the sample and not on the actual sample length in time. For a given block size, the error is found to be larger for fGn with stronger LRD than that with weaker LRD.

1. Introduction

ACF analysis, or equivalently spectral analysis according to the Wiener-Khintchine theorem, plays a role in many areas of sciences and technologies (see, e.g., [1, 2]), such as structural engineering [3–7]. In engineering, ACF or its Fourier transform (power spectrum density function (PSD)) can only be estimated according to a given record length in measurement. Note that the random load simulated in a laboratory test may be generated based on a predetermined ACF or PSD; see, for example, [8–13]. Thus, the quality of ACF or PSD estimation has great impact on structure analysis and design.

The literature of error analysis (mainly, bias, and variance) of ACF/PSD estimation of an ordinary random process is quite rich; see, for example, [1, 2, 14–19]. By ordinary random processes, we mean that the ACF and PSD of a process are ordinary functions except the Dirac delta function that is the ACF of white noise.

Note that processes with LRD or long-memory substantially differ from ordinary processes [20]. By LRD, we mean that the ACF of a process is nonsummable in the discrete case or nonintegrable in the continuous case [20]. Hence, its PSD should be considered in the sense of generalized function over the Schwartz space of test functions. FGn introduced in [21] is a widely used model of stationary fractal time series, which has found increasingly wide applications in many fields of sciences and technologies, ranging from hydrology to network traffic; see, for example, [22–45]. Note that the statistics of a zero mean Gaussian process are completely determined in terms of its ACF. Therefore, when using fGn-type load in structural engineering, the method to assure the quality of its ACF estimation is desired. In passing, we mention that, in the field of the Internet, ACF estimation of fGn-type teletraffic is utilized for detection of distributed denial-of-service flood attacks [32].

In the field, [46] discussed the statistical error of the structure function of Gaussian random fractals, and [47] studied the bias of the sample autocorrelations of fractional noise. This paper aims at providing a variance bound of the ACF estimation of one block of fGn.

An ACF is usually estimated on a block-by-block basis [1, 10, 13], where block size means the number of data points of a block of sample. Note that the ACF estimation of different blocks may be different, resulting in the estimation error caused by sectioning. The error resulted from sectioning can be reduced by the skill of averaging [1]. Different from conventional methods to reduce errors based on averaging, this research studies how to determine the size of one block according to a given degree of accuracy of ACF estimation of fGn with LRD.

Intuitively, if the size of one block is large enough, the ACF estimation will be independent of the start point for sectioning the block. Let N be the block size of fGn with LRD. The aim of this paper is to provide a formula to calculate the variance bound of ACF estimation of fGn with LRD for a given N and a given value of H.

The remaining article is organized as follows. Section 2 presents an error bound of ACF estimation of one block of fGn with LRD. Discussions are given in Section 3. Finally, Section 4 concludes the paper.

2. Variance Bound of ACF Estimation of One Block of fGn with LRD

2.1. Preliminaries

Let $B(t)$ be ordinary Brownian motion (Bm) for $t \geq 0$ and $B(0) = 0$ [48]. The stationary white noise can be taken as $B'(t)$, which is the derivative of $B(t)$ in the domain of generalized functions. Let ${}_0D_t^{-v}$ be the Riemann-Liouville integral operator [49, 50]. Then,

$$ {}_0D_t^{-v} B'(t) = \frac{1}{\Gamma(v)} \int_0^t (t-u)^{v-1} dB(u), \tag{2.1} $$

where Γ is the Gamma function. Replacing ν with $H + 1/2$ in (2.1) yields

$$ {}_0D_t^{-(H+1/2)} B'(t) = \frac{1}{\Gamma(H+1/2)} \int_0^t (t-u)^{H-1/2} dB(u) \triangleq B_H^0(t). \tag{2.2} $$

In the above expression, $B_H^0(t)$ is termed the Riemann-Liouville fractional Brownian motion (fBm) and $0 < H < 1$. This fBm is self-similar but does not have stationary increments. In

passing, it is noted that the fBm described in the sense of the Riemann-Liouville fractional integral can be explained as the response of a fractional system, the impulse response of which is $t^{H-1/2}/\Gamma(H+1/2)$ under the excitation of white noise from a view of the theory of linear fractional systems discussed in [51, 52].

Following Mandelbrot and van Ness [21], the fBm that is self-similar and has stationary increments is defined for $t > 0$ by

$$B_H(t) - B_H(0) = \frac{1}{\Gamma(H+1/2)} \left\{ \begin{array}{c} \displaystyle\int_{-\infty}^{0} \left[(t-u)^{H-0.5} - (-u)^{H-0.5} \right] dB(u) \\ \displaystyle + \int_{0}^{t} (t-u)^{H-0.5} dB(u) \end{array} \right\}, \tag{2.3}$$

where $B_H(0) = b_0$ is the starting value at time 0. If $b_0 = 0$, $B_{1/2}(t) = B(t)$. Hence, fBm generalizes Bm. The fBm expressed by (2.3) is the fractional integral of $B(t)$ in the sense of Weyl (see [49, 50] for the details of the fractional Weyl integral operator).

FGn is the increment process of fBm. It is stationary and self-affine with parameter H. Let $X(t)$ be fGn in the continuous case. Then, the ACF of $X(t)$ is given by

$$r(\tau) = \frac{\sigma^2 \varepsilon^{2H-2}}{2} \left[\left(\frac{|\tau|}{\varepsilon} + 1 \right)^{2H} + \left| \frac{|\tau|}{\varepsilon} - 1 \right|^{2H} - 2 \left| \frac{\tau}{\varepsilon} \right|^{2H} \right], \quad \tau \in \mathbb{R}, \tag{2.4}$$

where $0 < H < 1$, $\sigma^2 = (H\pi)^{-1}\Gamma(1-2H)\cos(H\pi)$ is the intensity of fGn, and $\varepsilon > 0$ is used by regularizing fBm so that the regularized fBm is differentiable [21, pages 427-428]. The PSD of $X(t)$ is given by (Li and Lim [53])

$$S(\omega) = \sigma^2 \sin(H\pi)\Gamma(2H+1)|\omega|^{1-2H}. \tag{2.5}$$

Letting $\varepsilon = 1$ and replacing $\tau \in \mathbb{R}$ by $k \in \mathbb{Z}$ in (2.4) yields the ACF of the discrete fGn (dfGn):

$$r(k) = \frac{\sigma^2}{2} \left[(|k|+1)^{2H} + ||k|-1|^{2H} - 2|k|^{2H} \right], \quad k \in \mathbb{Z}. \tag{2.6}$$

Recall that a stationary Gaussian process with ACF $r(\tau)$ is of LRD if [20]

$$\int_0^\infty r(\tau) d\tau = \infty; \tag{2.7}$$

otherwise it is of short-range dependence (SRD). Another definition of LRD is given as follows. For asymptotically large time scales, if

$$r(\tau) \sim \tau^{-\beta}, \quad \beta \in (0,1) \text{ as } \tau \longrightarrow \infty, \tag{2.8}$$

then the process is of LRD.

Note that the expression $0.5[(k+1)^{2H} - 2k^{2H} + (k-1)^{2H}]$ described in (2.6) is the finite second-order difference of $0.5(k)^{2H}$. Approximating it with the second-order differential of $0.5(k)^{2H}$ yields

$$0.5\left[(k+1)^{2H} - 2k^{2H} + (k-1)^{2H}\right] \approx H(2H-1)(k)^{2H-2}. \tag{2.9}$$

Expressing β in (2.8) by the Hurst parameter H gives $\beta = 2 - 2H$, or

$$H = 1 - \frac{\beta}{2}. \tag{2.10}$$

The LRD condition expressed by H therefore is $0.5 < H < 1$. The larger the H value, the stronger the long-range persistence.

FGn contains three subclasses of time series. In the case of $0.5 < H < 1$, $r(\tau)$ is positive and finite for all τ. It is monotonously decreasing but nonintegrable. In fact, from the ACF of dfGn described by (2.9), one immediately has $\sum_0^\infty k^{2H-2} = \infty$. Thus, for $0.5 < H < 1$, the corresponding fGn is of LRD. For $H \in (0, 0.5)$, the integral of $r(\tau)$ is zero. Hence, fGn is of SRD in this case. Moreover, $r(\tau)$ changes its sign and becomes negative for some τ proportional to ε in the parameter domain [21, page 434]. FGn reduces to white noise when $H = 0.5$.

Note that if $r(\tau)$ is sufficiently smooth on $(0, \infty)$ and if

$$r(0) - r(\tau) \sim c|\tau|^{\alpha} \quad \text{for } |\tau| \longrightarrow 0, \tag{2.11}$$

where c is a constant, then one has the fractal dimension of $X(t)$ as

$$D = 2 - \frac{\alpha}{2}; \tag{2.12}$$

see, for example, [54–57]. The local irregularity of the sample paths is measured by α, which can be regarded as the fractal index of the process. Thus, the behaviour of $r(\tau)$ near the origin determines the local irregularity or the local self-similarity of the sample paths. The larger the D value, the higher the local irregularity.

Now, in the case of $\varepsilon = 1$, we apply the binomial series to $r(\tau)$. Then, one has

$$r(0) - r(\tau) \sim c|\tau|^{2H} \quad \text{for } |\tau| \longrightarrow 0. \tag{2.13}$$

Therefore, one immediately gets

$$D = 2 - H. \tag{2.14}$$

Hence, H measures both LRD and self-similarity of fGn. In other words, the local properties of fGn are reflected in the global ones as remarked by Mandelbrot [58, page 27].

Figures 1(a) and 1(b) give the plots of the ACFs of fGn with LRD and SRD in the case of $\varepsilon = 1$, respectively.

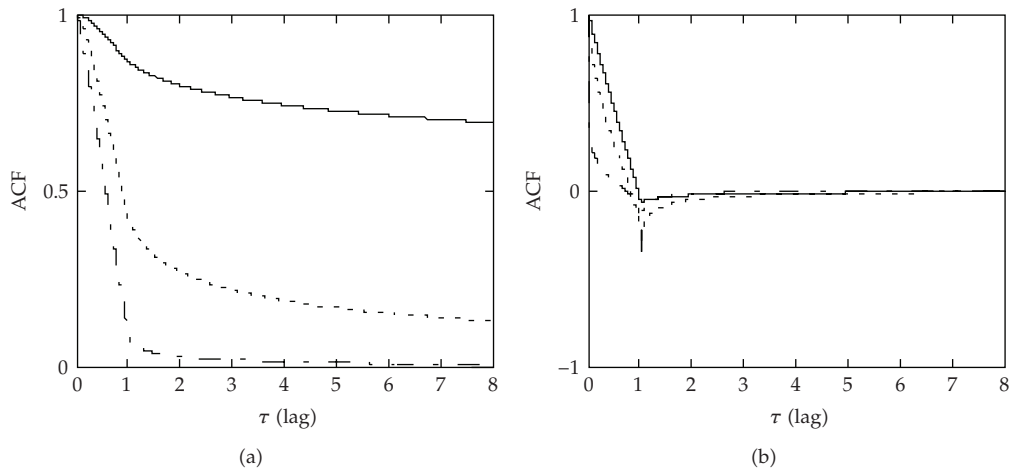

Figure 1: Plots of ACF of fractional Gaussian noise. (a) ACF of fGn with LRD. Solid line is for $H = 0.95$, dot line is for $H = 0.75$, and dadot line is for $H = 0.55$. (b) ACF of fGn with SRD. Solid line is for $H = 0.45$, dot line is for $H = 0.25$, and dadot line is for $H = 0.05$.

2.2. Variance Bound

In practical terms, the number of measured data points within a sample of fGn is finite. Let a positive integer N be the number of data points of a measured sample of dfGn sequence $x(i)$. Then, the ACF of $x(i)$ is estimated by

$$R(k) = \frac{1}{N}\sum_{i=1}^{N} x(i)x(i+k). \tag{2.15}$$

Usually, for $l, m \in \mathbb{Z}_+$,

$$\frac{1}{N}\sum_{i=mN}^{(m+1)N} x(i)x(i+k) \neq \frac{1}{N}\sum_{i=lN}^{(l+1)N} x(i)x(i+k). \tag{2.16}$$

Therefore, $R(k)$ is a random variable.

Let $M^2(R)$ be the mean square error in terms of R. Denote $R(k)$ by $R(k; H, N)$. The aim of the statistical error analysis in this research is to derive a relationship between $M^2(R)$ and N as well as H so as to establish a reference guideline for requiring N under the conditions that the bound of $M^2(R)$ and the value of H are given.

Theorem 2.1. *Let $x(i)$ be dfGn series with LRD. Let $r(k)$ be the true ACF of $x(i)$. Let N be the number of data points of a sample sequence. Let $R(k)$ be an estimate of $r(k)$. Let $\mathrm{Var}(R)$ be the variance of R. Then,*

$$\mathrm{Var}(R) \leq \frac{4|\Gamma(1-2H)|^2\cos^2(H\pi)(2H-1)^2}{\pi^2 N}\sum_{i=1}^{N}(i)^{4H-4}. \tag{2.17}$$

Proof. Mathematically, $r(k)$ is computed over infinite interval [1, 2, 59]:

$$r(k) = E[x(i)x(i+k)] = \lim_{N\to\infty} \frac{1}{N}\sum_{i=0}^{N} x(i)x(i+k). \tag{P-1}$$

In practice, $r(k)$ can only be estimated with a finite sequence. Therefore,

$$r(k) \approx R(k) = \frac{1}{N}\sum_{i=N_0}^{N_0+N} x(i)x(i+k), \tag{P-2}$$

where N_0 is the start point.

Let $b^2(R)$ be the bias of R. Then, $M^2(R) = E[(r-R)^2] = \mathrm{Var}(R) + b^2(R)$. Since

$$E[R(\tau)] = \frac{1}{N}\sum_{i=N_0}^{N_0+N} E[x(i)x(i+k)] = \frac{1}{N}\sum_{i=N_0}^{N_0+N} r(k) = r(k), \tag{P-3}$$

$R(k)$ is the unbiased estimate of $r(k)$ and $M^2(R) = \mathrm{Var}(R)$ accordingly. We need to express $\mathrm{Var}(R)$ by the following proposition to prove the theorem. □

Proposition 2.2. *Let $x(i)$ be dfGn with LRD. Let $r(k)$ be the true ACF of $x(i)$. Let N be the number of data points of a sample sequence. Let $R(k)$ be an estimate of $r(k)$. Let Var(R) be the variance of R. Suppose that $r(k)$ is monotonously decreasing and $r(k) \geq 0$. Then,*

$$\mathrm{Var}(R) \leq \frac{4}{N}\sum_{i=0}^{N} r^2(k). \tag{P-4}$$

Proof. As $\mathrm{Var}(R) = E\{[R - E(R)]^2\} = E(R^2) - E^2(R)$, according to (P-3), one has

$$\mathrm{Var}(R) = E\left(R^2\right) - r^2. \tag{P-5}$$

Expanding $E(R^2)$ yields

$$\begin{aligned} E\left(R^2\right) &= E\left\{\left[\frac{1}{N}\sum_{N_0}^{N_0+N} x(i)x(i+k)\right]^2\right\} \\ &= E\left[\frac{1}{N^2}\sum_{N_0}^{N_0+N} x(i_1)x(i_1+k)\sum_{N_0}^{N_0+N} x(i_2)x(i_2+k)\right] \\ &= E\left[\frac{1}{N^2}\sum_{N_0}^{N_0+N}\sum_{N_0}^{N_0+N} x(i_1)x(i_2)x(i_1+k)x(i_2+k)\right] \\ &= \frac{1}{N^2}\sum_{N_0}^{N_0+N}\sum_{N_0}^{N_0+N} E[x(i_1)x(i_2)x(i_1+k)x(i_2+k)]. \end{aligned} \tag{P-6}$$

Thus,

$$\mathrm{Var}(R) = \frac{1}{N^2} \sum_{N_0}^{N_0+N} \sum_{N_0}^{N_0+N} E[x(i_1)x(i_2)x(i_1+k)x(i_2+k)] - r^2(k). \tag{P-7}$$

Let

$$\begin{aligned} X_1 &= x(n_1), \\ X_2 &= x(n_2), \\ X_3 &= x(n_1+k), \\ X_4 &= x(n_2+k). \end{aligned} \tag{P-8}$$

Then,

$$E[x(n_1)x(n_2)x(n_1+k)x(n_2+k)] = E(X_1X_2X_3X_4). \tag{P-9}$$

Since x is Gaussian, random variables X_1, X_2, X_3, and X_4 have a joint-normal distribution and $E(X_1X_2X_3X_4) = m_{12}m_{34} + m_{13}m_{24} + m_{14}m_{23}$, where

$$\begin{aligned} m_{12} &= E[x(n_1)x(n_2)] = r(n_2 - n_1), \\ m_{13} &= E[x(n_1)x(n_1+k)] = r(k), \\ m_{14} &= E[x(n_1)x(n_2+k)] = r(n_2 - n_1 + k), \\ m_{23} &= E[x(n_2)x(n_1+k)] = r(n_1 - n_2 + k), \\ m_{24} &= E[x(n_2)x(n_2+k)] = r(k), \\ m_{34} &= E[x(n_1)x(n_2+k)] = r(n_2 - n_1). \end{aligned} \tag{P-10}$$

Therefore,

$$\begin{aligned} &\frac{1}{N^2} \sum_{N_0}^{N_0+N} \sum_{N_0}^{N_0+N} E[x(i_1)x(i_2)x(i_1+k)x(i_2+k)] \\ &\quad = \frac{1}{N^2} \sum_{N_0}^{N_0+N} \sum_{N_0}^{N_0+N} E(X_1X_2X_3X_4) \\ &\quad = \frac{1}{N^2} \sum_{N_0}^{N_0+N} \sum_{N_0}^{N_0+N} (m_{12}m_{34} + m_{13}m_{24} + m_{14}m_{23}) \end{aligned} \tag{P-11}$$

$$= \frac{1}{N^2}\sum_{N_0}^{N_0+N}\sum_{N_0}^{N_0+N} r^2(i_2-i_1)+r^2(k)+r(i_2-i_1+k)r(i_1-i_2+k)$$

$$= \frac{1}{N^2}\sum_{N_0}^{N_0+N}\sum_{N_0}^{N_0+N} r^2(i_2-i_1)+r(i_2-i_1+k)r(i_1-i_2+k)+r^2(k). \tag{2.18}$$

According to (P-6), the variance is expressed as

$$\mathrm{Var}(R) = \frac{1}{N^2}\sum_{N_0}^{N_0+N}\sum_{N_0}^{N_0+N} r^2(i_2-i_1)+r(i_2-i_1+k)r(i_1-i_2+k). \tag{P-12}$$

Replacing (i_2-i_1) with i in the above expression yields

$$\mathrm{Var}(R) = \frac{1}{N^2}\sum_{i_1=N_0}^{N_0+N}\sum_{i=N_0}^{N_0-N_1+N} r^2(i)+r(i+k)r(-i+k) = \frac{1}{N^2}\sum_{i_1=N_0}^{N_0+N}\sum_{i=N_0}^{N_0-N_1+N} f(i), \tag{P-13}$$

where $f(i)=r^2(i)+r(i+k)r(-i+k)$. Without losing generality, let $N_0=0$. Then, the above becomes

$$\mathrm{Var}(R) = \frac{1}{N^2}\sum_{i=0}^{N}(N-i)f(i)+\frac{1}{N^2}\sum_{i=-N}^{0}(N+i)f(i). \tag{P-14}$$

Since ACF is an even function, the above expression is written by

$$\begin{aligned}\mathrm{Var}(R) &= \frac{2}{N^2}\sum_{i=0}^{N}(N-i)f(i) = \frac{2}{N^2}\sum_{i=0}^{N}(N-i)\left[r^2(i)+r(i+k)r(-i+k)\right]\\ &\le \frac{2}{N}\sum_{i=0}^{N}\left|1-\frac{i}{N}\right|\left|r^2(i)+r(i+k)r(-i+k)\right|\\ &\le \frac{2}{N}\sum_{i=0}^{N}\left|r^2(i)+r(i+k)r(-i+k)\right| \le \frac{4}{N}\sum_{i=0}^{N}r^2(i).\end{aligned} \tag{2.19}$$

Therefore, Proposition 2.2 holds.

Now, replacing $r(k)$ with (2.6) yields

$$\mathrm{Var}(R) \le \frac{4}{N}\sum_{i=0}^{N}r^2(i) \le \frac{4}{N}\sum_{i=1}^{N}r^2(i) \le \frac{\sigma^4}{N}\sum_{i=1}^{N}\left[(i+1)^{2H}-2i^{2H}+(i-1)^{2H}\right]^2. \tag{P-15}$$

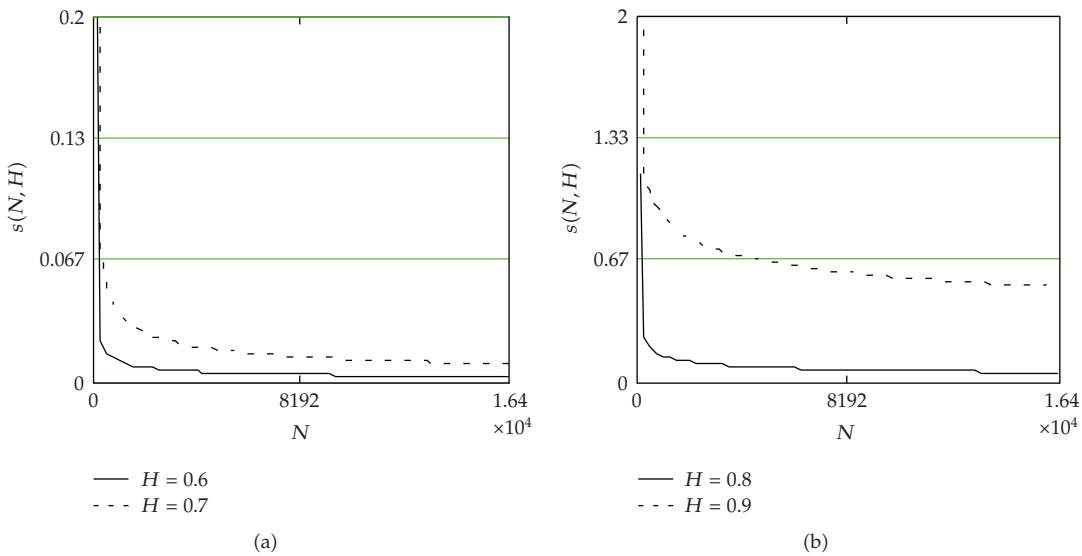

Figure 2: Error bound $s(N, H)$. (a) $H = 0.60, 0.70$. (b) $H = 0.80, 0.90$.

According to (2.9), replacing $[(i+1)^{2H} - 2i^{2H} + (i-1)^{2H}]$ on the right hand of the above expression by $(i)^{2H}$, we have

$$\mathrm{Var}(R) \leq \frac{4|\Gamma(1-2H)|^2 \cos^2(H\pi)(2H-1)^2}{\pi^2 N} \sum_{i=1}^{N} (i)^{4H-4}. \tag{2.20}$$

Theorem results. □

The above formula represents an upper bound of $\mathrm{Var}(R)$. Denote by $s(N, H)$ the bound of standard deviation. Then,

$$s(N, H) = \frac{2\Gamma(1-2H)\cos(H\pi)|2H-1|}{\pi} \sqrt{\frac{1}{N} \sum_{i=1}^{N} (i)^{4H-4}}. \tag{2.21}$$

We illustrate $s(N, H)$ in terms of N by Figure 2 for $H = 0.60, 0.70, 0.80$, and 0.90.

From Figure 2, we see that $s(N, H_1) > s(N, H_2)$ for $H_1 > H_2$, meaning that the error of ACF estimation of fGn is larger with stronger LRD than that with weaker LRD.

3. Discussions

3.1. To Avoid Misleading Result of ACF Estimation

Recall that processes with LRD substantiality differ from those with SRD [20]. Therefore, possible SRD signs of an ACF estimate of an fGn series that is of LRD may be taken as a misleading result of ACF estimation.

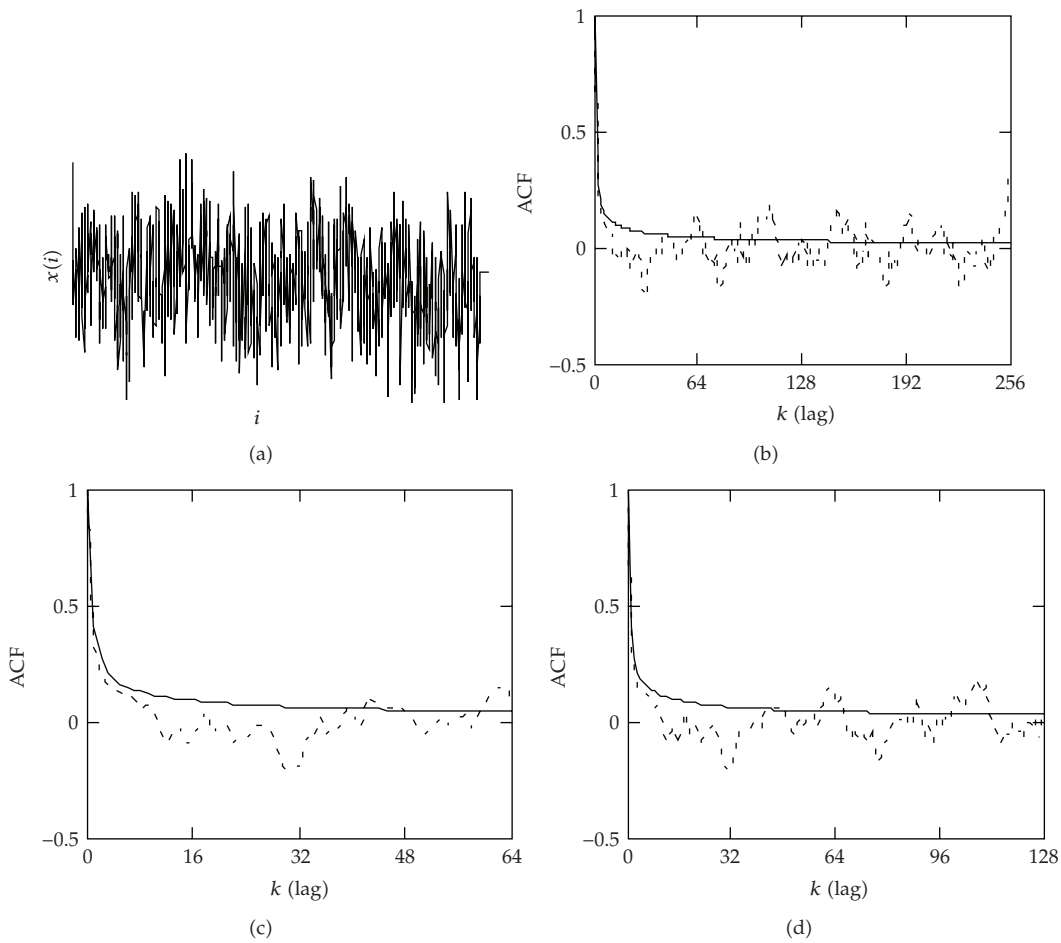

Figure 3: Case study. Solid line: theoretic ACF of fGn. Dot line: ACF estimate. (a) FGn with $H = 0.75$. (b) AFC estimate for $N = 256$. (c) The first 64 points of Figure 3(b). (d) The first 128 points of Figure 3(b).

Suppose that we have a block of fGn with $H = 0.75$. Hence, this series is of LRD. Figure 3(a) shows an fGn series with $H = 0.75$, which is synthesized with the method given in [60].

Assume the block size $N = 256$. Then, we have $\mathrm{Var}(R) \leq 0.015$ according to Theorem 2.1. The dotted line in Figure 3(b) indicates its ACF estimation with $N = 256$ and the solid line in Figure 3(b) shows the theoretical ACF of fGn with $H = 0.75$. We note that the error regarding the ACF estimate reflected by the dotted line in Figure 3(b) is severe because many points of the dotted line are negative. Thus, it may probably confuse the property of the positive correlation (i.e., LRD) of the data being processed. Consequently, by the dotted line in Figure 3(b), one might likely be misled to take the data being processed (Figure 3(a)) as SRD. Figures 3(c) and 3(d) show the first 64 and 128 points of Figure 3(b), respectively. They again show the possible confusions caused by severe estimation error.

Now we increase the block size such that $N = 2048$. Then, one has $\mathrm{Var}(R) \leq 2.5 \times 10^{-3}$ according to (2.17). In this case, the ACF estimation is indicated by the dotted line in Figure 4(a). Comparing Figure 4(a) to Figure 3(b), we see that the error of ACF estimation is

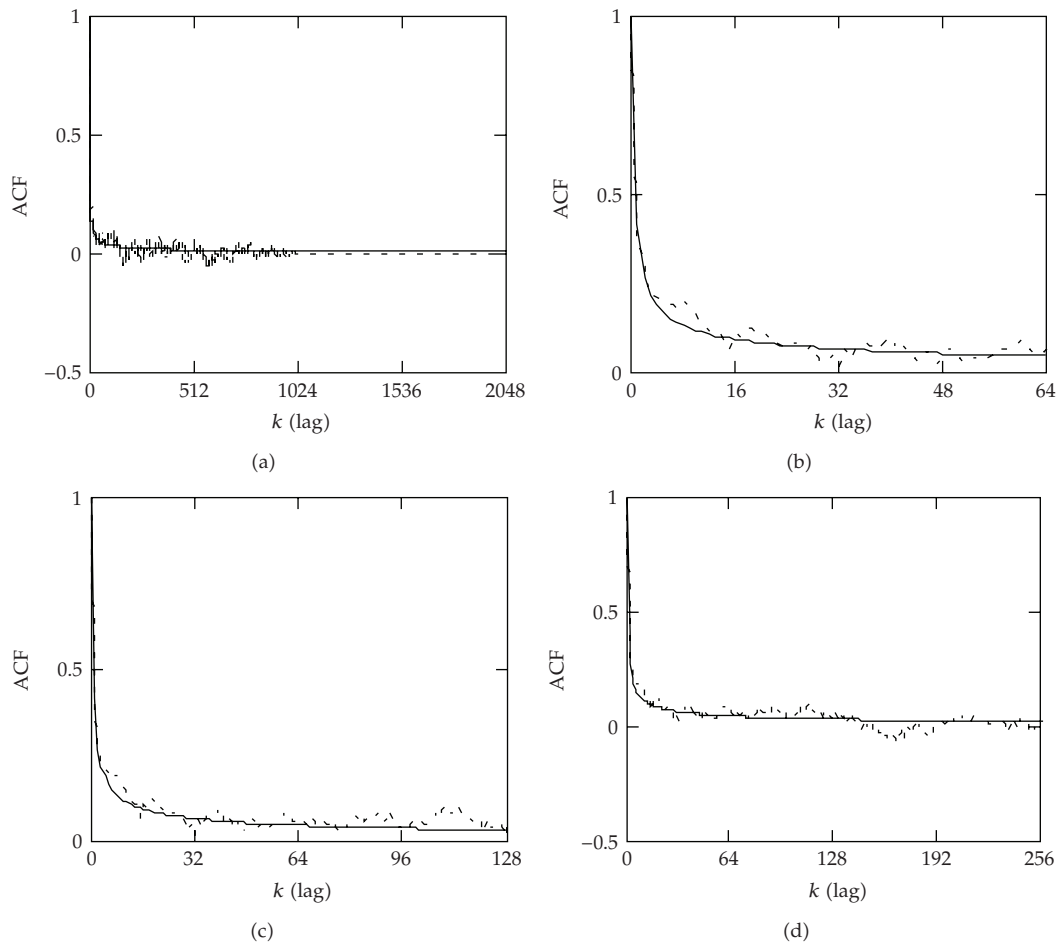

Figure 4: Solid line: theoretic ACF of FGN. Dot line: ACF estimate. (a) ACF estimate of fGn with $H = 0.75$ for $N = 2048$. (b) The first 64 points of Figure 4(b). (c) The first 128 points of Figure 4(b). (d) The first 256 points of Figure 4(b).

considerably reduced when N increases to 2048 because most data points of the ACF estimate are positive. Figures 4(b), 4(c), and 4(d) give the plots of the first 64, 128, and 256 points of Figure 4(a), respectively. They evidently interpret the improvement of the quality of ACF estimation of one block of fGn with LRD by increasing the block size.

From the above, one sees that the accuracy of ACF estimate of fGn with LRD can be increased if the block size increases. Therefore, in addition to the direct way to increase the record length, increasing the sampling rate in measurement of fGn to be processed may yet be a way to increase the accuracy of the ACF estimation in the case that the block size is given.

3.2. One Block Estimation

The previous discussions regarding ACF estimation of fGn with LRD do not relate to averaging. In fact, once the block size N is such that it meets the required accuracy according to Theorem 2.1, the ACF estimation is independent of the start point of the block. That is, for

any $N_0 \in \mathbb{Z}_+$, $(1/N)\sum_{i=N_0}^{N_0+N} x(i)x(i+k)$ yields an ACF estimate, the error of which is bounded based on Theorem 2.1. Further, we note that the discussed ACF estimation does not relate to sectioning. As a matter of fact, for each $m \in \mathbb{Z}_+$, $(1/N)\sum_{i=mN}^{(m+1)N} x(i)x(i+k)$ yields an ACF estimate, the error of which is bounded by (2.17).

3.3. Remarks

In the field of fractional order signal processing (see, e.g., [61]), [62] recently introduced a method to obtain a reliable estimation of H based on fractional Fourier transform for processing very long experimental time series locally. It is worth noting that the present error bound in this paper may yet be an explanation why the reliable estimation of H discussed in [62] requires long series.

Finally, we note that the ACF estimate expressed by (2.15) is biased one. However, that does not matter because the present variance bound relates to the fluctuation of the ACF estimate regardless of whether it is biased or not.

4. Conclusions

We have established an error bound of ACF estimation of one block of fGn with LRD. It has been shown that the error does not depend on the absolute length of the sample but only relies on the number of data points, that is, the block size N, of the sample. The error of an ACF estimate of fGn with stronger LRD is larger than that with weaker LRD for a given N. The discussed ACF estimation is not related to averaging. The accuracy of an ACF estimate of a block of fGn with LRD can be guaranteed once the block size is selected according to (2.17) without the relation to sectioning.

Acknowledgment

This work was supported in part by the National Natural Science Foundation of China under the project Grant nos. 60573125, 60873264, and 60873102.

References

[1] S. K. Mitra and J. F. Kaiser, *Handbook for Digital Signal Processing*, John Wiley & Sons, New York, NY, USA, 1993.
[2] J. S. Bendat and A. G. Piersol, *Random Data: Analysis and Measurement Procedure*, John Wiley & Sons, New York, NY, USA, 3rd edition, 2000.
[3] I. Elishakoff and R. H. Lyon, *Random Vibration Status and Recent Developments*, vol. 14 of *Studies in Applied Mechanics*, Elsevier, New York, NY, USA, 1986.
[4] A. Preumont, *Random Vibration and Spectral Analysis*, vol. 33 of *Studies in Applied Mechanics*, Kluwer, London, UK, 1993.
[5] J. J. Jensen and M. Dogliani, "Wave-induced ship hull vibrations in stochastic seaways," *Marine Structures*, vol. 9, no. 3-4, pp. 353–387, 1996.
[6] X.-K. Gu, J.-J. Hu, and J.-W. Shen, "The frequency characteristics of ship vertical wave bending moments," *Shipbuilding of China*, vol. 41, no. 1, pp. 31–38, 2000 (Chinese).
[7] D. Benasciutti and R. Tovo, "Spectral methods for lifetime prediction under wide-band stationary random processes," *International Journal of Fatigue*, vol. 27, no. 8, pp. 867–877, 2005.
[8] Technical Software Consultants Limited, "FLAPS: Fatigue Laboratory Applications Package, Version 01:03," Instron 2165035, UK.

[9] M. Li, "An optimal controller of an irregular wave maker," *Applied Mathematical Modelling*, vol. 29, no. 1, pp. 55–63, 2005.
[10] M. Li, "An iteration method to adjusting random loading for a laboratory fatigue test," *International Journal of Fatigue*, vol. 27, no. 7, pp. 783–789, 2005.
[11] M. Li, "Experimental stability analysis of a test system for doing fatigue tests under random loading," *Journal of Testing and Evaluation*, vol. 34, no. 4, pp. 364–367, 2006.
[12] M. Li, Y.-S. Wu, B.-H. Xu, W. Jia, and W. Zhao, "An on-line correction technique of random loading with a real-time signal processor for a laboratory fatigue test," *Journal of Testing and Evaluation*, vol. 28, no. 5, pp. 409–414, 2000.
[13] M. Li, B.-H. Xu, and Y.-S. Wu, "An H_2-optimal control of random loading for a laboratory fatigue test," *Journal of Testing and Evaluation*, vol. 26, no. 6, pp. 619–625, 1998.
[14] F. H. C. Marriott and J. A. Pope, "Bias in the estimation of autocorrelations," *Biometrika*, vol. 41, pp. 390–402, 1954.
[15] E. Jakeman, E. R. Pike, and S. Swain, "Statistical accuracy in the digital autocorrelation of photon counting fluctuations," *Journal of Physics A*, vol. 4, no. 4, pp. 517–534, 1971.
[16] J. Pickands III, "Spectral estimation with random truncation," *The Annals of Mathematical Statistics*, vol. 41, no. 1, pp. 44–58, 1970.
[17] U. Grenander, "Bandwidth and variance in estimation of the spectrum," *Journal of the Royal Statistical Society Series B*, vol. 20, no. 1, pp. 152–157, 1958.
[18] D. J. Thomson, "Spectrum estimation and harmonic analysis," *Proceedings of the IEEE*, vol. 70, no. 9, pp. 1055–1096, 1982.
[19] M. Li, "A method for requiring block size for spectrum measurement of ocean surface waves," *IEEE Transactions on Instrumentation and Measurement*, vol. 55, no. 6, pp. 2207–2215, 2006.
[20] J. Beran, *Statistics for Long-Memory Processes*, vol. 61 of *Monographs on Statistics and Applied Probability*, Chapman & Hall, New York, NY, USA, 1994.
[21] B. B. Mandelbrot and J. W. van Ness, "Fractional Brownian motions, fractional noises and applications," *SIAM Review*, vol. 10, no. 4, pp. 422–437, 1968.
[22] H. E. Hurst, "Long-term storage capacity of reservoirs," *Transactions of American Society of Civil Engineers*, vol. 116, pp. 770–808, 1951.
[23] B. B. Mandelbrot and J. R. Wallis, "Noah, Joseph and operational hydrology," *Water Resources Research*, vol. 4, no. 5, pp. 909–918, 1968.
[24] S. M. Barbosa, M. J. Fernandes, and M. E. Silva, "Long-range dependence in North Atlantic sea level," *Physica A*, vol. 371, no. 2, pp. 725–731, 2006.
[25] A. J. Lawrance and N. T. Kottegoda, "Stochastic modelling of riverflow time series," *Journal of the Royal Statistical Society-Series A*, vol. 140, no. 1, pp. 1–47, 1977.
[26] M. Radziejewski and Z. W. Kundzewicz, "Fractal analysis of flow of the river Warta," *Journal of Hydrology*, vol. 200, no. 1–4, pp. 280–294, 1997.
[27] B. B. Mandelbrot, *Gaussian Self-Affinity and Fractals*, Selected Works of Benoit B. Mandelbrot, Springer, New York, NY, USA, 2002.
[28] W. Stallings, *High-Speed Networks TCP/IP and ATM Design Principles*, chapter 8, Prentice-Hall, Upper Saddle River, NJ, USA, 1998.
[29] M. Li, "An approach to reliably identifying signs of DDOS flood attacks based on LRD traffic pattern recognition," *Computers and Security*, vol. 23, no. 7, pp. 549–558, 2004.
[30] B. B. Mandelbrot, *Gaussian Self-Affinity and Fractals*, Selected Works of Benoit B. Mandelbrot, Springer, New York, NY, USA, 2002.
[31] J. Levy-Vehel, E. Lutton, and C. Tricot, Eds., *Fractals in Engineering*, Springer, Berlin, Germany, 1997.
[32] M. Li and W. Zhao, "Detection of variations of local irregularity of traffic under DDOS flood attack," *Mathematical Problems in Engineering*, vol. 2008, Article ID 475878, 11 pages, 2008.
[33] M. Li, "Modeling autocorrelation functions of long-range dependent teletraffic series based on optimal approximation in Hilbert space-A further study," *Applied Mathematical Modelling*, vol. 31, no. 3, pp. 625–631, 2007.
[34] M. Li, "Change trend of averaged Hurst parameter of traffic under DDOS flood attacks," *Computers & Security*, vol. 25, no. 3, pp. 213–220, 2006.
[35] C. Cattani, "Shannon wavelets theory," *Mathematical Problems in Engineering*, vol. 2008, Article ID 164808, 24 pages, 2008.
[36] E. G. Bakhoum and C. Toma, "Relativistic short range phenomena and space-time aspects of pulse measurements," *Mathematical Problems in Engineering*, vol. 2008, Article ID 410156, 20 pages, 2008.

[37] C. Cattani, "Harmonic wavelet analysis of a localized fractal," *International Journal of Engineering and Interdisciplinary Mathematics*, vol. 1, no. 1, pp. 35–44, 2009.
[38] P. Abry, P. Borgnat, F. Ricciato, A. Scherrer, and D. Veitch, "Revisiting an old friend: on the observability of the relation between long range dependence and heavy tail," *Telecommunication Systems*, 2009.
[39] M. Li, W.-S. Chen, and L. Han, "Correlation matching method of the weak stationarity test of LRD traffic," *Telecommunication Systems*, 2009.
[40] L. Janowski and P. Owezarski, "Assessing the accuracy of using aggregated traffic traces in network engineering," *Telecommunication Systems*, 2009.
[41] C. Li and W. Zhao, "Stochastic performance analysis of non-feedforward networks," *Telecommunication Systems*, 2009.
[42] M. Li, "Fractal time series—a tutorial," *Mathematical Problems in Engineering*, vol. 2010, Article ID 157264, 26 pages, 2010.
[43] M. Li and W. Zhao, "Representation of a stochastic traffic bound," *IEEE Transactions on Parallel & Distributed Systems*, 2009, http://doi.ieeecomputersociety.org/10.1109/TPDS.2009.162.
[44] K.-L. Tian and M. Li, "A reliable anomaly detector against low-rate DDOS attack," *International Journal of Electronics and Computers*, vol. 1, no. 1, pp. 1–6, 2009.
[45] C. Cattani, "Harmonic wavelet approximation of random, fractal and high frequency signals," *Telecommunication Systems*. In press.
[46] E. Jakeman and D. L. Jordan, "Statistical accuracy of measurements on Gaussian random fractals," *Journal of Physics D*, vol. 23, no. 4, pp. 397–405, 1990.
[47] P. Newbold and C. Agiakloglou, "Bias in the sample autocorrelations of fractional noise," *Biometrica*, vol. 30, no. 3, pp. 698–702, 1990.
[48] T. Hida, *Brownian Motion*, vol. 11 of *Applications of Mathematics*, Springer, New York, NY, USA, 1980.
[49] A. A. Kilbas, H. M. Srivastava, and J. J. Trujillo, *Theory and Applications of Fractional Differential Equations*, vol. 204 of *North-Holland Mathematics Studies*, Elsevier Science, Amsterdam, The Netherlands, 2006.
[50] K. S. Miller and B. Ross, *An Introduction to the Fractional Calculus and Fractional Differential Equations*, A Wiley-Interscience Publication, John Wiley & Sons, New York, NY, USA, 1993.
[51] M. D. Ortigueira, "Introduction to fractional linear systems, part I: continuous-time systems," *IEE Proceedings: Vision, Image and Signal Processing*, vol. 147, no. 1, pp. 62–70, 2000.
[52] M. D. Ortigueira and A. G. Batista, "A fractional linear system view of the fractional brownian motion," *Nonlinear Dynamics*, vol. 38, no. 1–4, pp. 295–303, 2004.
[53] M. Li and S. C. Lim, "A rigorous derivation of power spectrum of fractional Gaussian noise," *Fluctuation and Noise Letters*, vol. 6, no. 4, pp. C33–C36, 2006.
[54] R. J. Adler, *The Geometry of Random Fields*, Wiley Series in Probability and Mathematical Statistic, John Wiley & Sons, New York, NY, USA, 1981.
[55] P. Hall and R. Roy, "On the relationship between fractal dimension and fractal index for stationary stochastic processes," *The Annals of Applied Probability*, vol. 4, no. 1, pp. 241–253, 1994.
[56] G. Chan, P. Hall, and D. S. Poskitt, "Periodogram-based estimators of fractal properties," *The Annals of Statistics*, vol. 23, no. 5, pp. 1684–1711, 1995.
[57] J. T. Kent and A. T. A. Wood, "Estimating the fractal dimension of a locally self-similar gaussian process by using increments," *Journal of the Royal Statistical Society Series B*, vol. 59, no. 3, pp. 679–699, 1997.
[58] B. B. Mandelbrot, *The Fractal Geometry of Nature*, W. H. Freeman, New York, NY, USA, 1982.
[59] G. A. Korn and T. M. Korn, *Mathematical Handbook for Scientists and Engineers*, McGraw-Hill, New York, NY, USA, 1961.
[60] M. Li and C.-H. Chi, "A correlation-based computational model for synthesizing long-range dependent data," *Journal of the Franklin Institute*, vol. 340, no. 6-7, pp. 503–514, 2004.
[61] Y. Chen, R. Sun, and A. Zhou, "An overview of fractional order signal processing (FOSP) techniques," in *Proceedings of the ASME International Design Engineering Technical Conferences & Computers and Information in Engineering Conference (IDETC/CIE '07)*, vol. 5, pp. 1205–1222, Las Vegas, Nev, USA, September 2007, DETC2007-34228.
[62] Y.-Q. Chen, R. Sun, and A. Zhou, "An improved Hurst parameter estimator based on fractional Fourier transform," *Telecommunication Systems*, 2009.

Hindawi Publishing Corporation
Mathematical Problems in Engineering
Volume 2010, Article ID 695208, 15 pages
doi:10.1155/2010/695208

Research Article

Mathematical Transform of Traveling-Wave Equations and Phase Aspects of Quantum Interaction

Ezzat G. Bakhoum[1] and Cristian Toma[2]

[1] *Department of Electrical and Computer Engineering, University of West Florida, 11000 University Parkway, Pensacola, FL 32514, USA*
[2] *Faculty of Applied Sciences, Politechnica University, Hagi-Ghita 81, 060032 Bucharest, Romania*

Correspondence should be addressed to Ezzat G. Bakhoum, ebakhoum@uwf.edu

Received 28 July 2009; Accepted 30 August 2009

Academic Editor: Carlo Cattani

The traveling wave equation is an essential tool in the study of vibrations and oscillating systems. This paper introduces an important extension to the Fourier/Laplace transform that is needed for the analysis of signals that are represented by traveling wave equations. Another objective of the paper is to present a mathematical technique for the simulation of the behavior of large systems of optical oscillators.

1. Introduction

The Fourier and the Laplace transforms are great mathematical tools that have served science well for nearly two centuries. Recently, however, the Fourier/Laplace transform has become increasingly inadequate for treating one specific class of signals, namely, signals represented by traveling wave equations. The Fourier/Laplace transform is essentially a tool for time domain to frequency domain translation, and vice versa. In that transformation, the dependence of each component of the original signal on time is described by a time-related constant: the angular frequency ω. The transformation then maps the time domain into the ω domain, essentially by finding correlations between the original signal and an infinite set of pure sinusoidal signals. Those correlations collectively become a "frequency-domain" representation of the signal. In the class of signals represented by traveling-wave equations, however, the signal has existence in *two* domains: the time domain t and the spatial domain x. More specifically, the signal has dependence on two propagation constants: the temporal propagation constant ω, and the spatial propagation constant k [1, 2]. Hence, a

transformation is needed to map the behavior of the signal in the $x - t$ domain into the $k - \omega$ domain. The Fourier/Laplace transform only maps the t domain into the ω domain and is incapable of performing the 2×2 mapping that is required in this case. Here, it is important to point out that the transform known as the "multidimensional Fourier transform" [3], used extensively in image processing applications, is still a 1×1 mapping process. By its definition, the "multidimensional Fourier transform" cannot perform a transformation of a signal that has simultaneous existence in both the time and the spatial domains.

The first objective of this paper is to present an important extension to the Fourier/Laplace transform that will allow the 2×2 mapping that is required in the case of traveling-wave signals to be performed. Another objective of the paper is to demonstrate that certain partial fraction decomposition and differentiation techniques can obviate the need for complex computations to simulate the behavior of large systems of optical oscillators. More particularly, some optical phenomena, such as the phenomenon of optical echo, are very hard to simulate without using physical variables corresponding to the internal states of a great number of atoms. Typically, such simulations require complex (order N^2, where N is the number of atoms) computations. We demonstrate that this problem can be fundamentally solved in a much simpler manner by using derivative-taking procedures for symbolic polynomials.

2. A Dual-Domain Extension for the Fourier/Laplace Transform

Signals that physically propagate in various media are usually represented by traveling-wave equations, the most basic of which is the simple sinusoidal traveling wave [1, 2]:

$$f(x,t) = \sin(kx - \omega t), \tag{2.1}$$

where ω is the usual temporal propagation constant and where $k = 2\pi/\lambda$ is the spatial propagation constant. The usual Fourier transform for a signal that exists only in the time domain is given by [4, 5]

$$f(\omega) = \int_{-\infty}^{\infty} f(t) e^{-j\omega t} dt. \tag{2.2}$$

We first define a companion to the Fourier transform for signals that are defined only in the spatial domain:

$$f(k) = \int_{-\infty}^{\infty} f(x) e^{+jkx} dx. \tag{2.3}$$

This transform maps the x domain into the propagation constant (k) domain. We now introduce a 2×2 dual-domain transform as follows:

$$f(k,\omega) = \iint_{-\infty}^{\infty} f(x,t) e^{j(kx-\omega t)} dx\, dt. \tag{2.4}$$

Notice that the Fourier transform measures the correlations between the signal $f(t)$ and an infinite set of pure sinusoidal signals in the time domain, while the transform of (2.4) measures the correlations between the signal $f(x,t)$ and an infinite set of pure sinusoidal *traveling* waves. This is the main difference between the transform of (2.4) and the other known extensions to the Fourier transform.

To write the one-sided version of the transform in (2.4) (which will be equivalent to the Laplace transform), we first decompose the exponential term as follows:

$$e^{j(kx-\omega t)} = e^{\gamma x} e^{-st}, \tag{2.5}$$

where $\gamma = jk$ and $s = j\omega$. The one-sided transform will now be written as follows:

$$f(k,\omega) = \iint_0^\infty f(x,t) e^{\gamma x} e^{-st} dx\, dt. \tag{2.6}$$

We can now clearly see that this dual-domain transform differs from the basic Laplace transform in that an extra exponential term $e^{\gamma x}$ is introduced, with γ being an imaginary number representation of the spatial propagation constant k. The basic Laplace transform contains the imaginary number s only, which is a representation of the temporal propagation constant ω.

3. Dual-Domain Transforms of Some Well-Known Propagating Signals

We will now demonstrate how the dual-domain transform is calculated for various propagating signals. The transforms of two well-known signals, specifically, the propagating sinusoid and the propagating unit-step function are calculated here as examples.

3.1. *Transform of* $f(x,t) = \sin(ax - bt)$

By using the well-known decomposition

$$\sin\theta = \frac{e^{j\theta} - e^{-j\theta}}{2j} \tag{3.1}$$

and carrying out the integration in (2.6) in a straightforward manner, the dual-domain transform of $f(x,t) = \sin(ax - bt)$ is found to be the following:

$$f(k,\omega) = \frac{as + b\gamma}{(s^2 + b^2)(\gamma^2 + a^2)}. \tag{3.2}$$

We can clearly see that if $a = 0$, this transform reverts to the Laplace transform, with the presence of $\gamma = jk$ in the denominator. Essentially, what we get in that case will be the Laplace transform of $\sin bt$, mapped into the k domain.

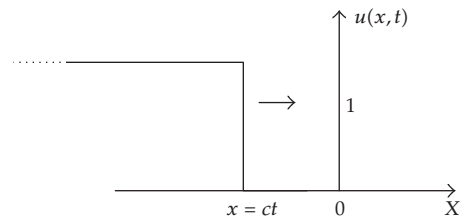

Figure 1: A propagating unit step function.

3.2. *Transform of a Propagating Unit Step Function* $f(x,t) = u(x - ct)$

A propagating unit step function $u(x - ct)$ is shown in Figure 1. The velocity of propagation of the wave is c.

Here, due to the positive exponent of $e^{\gamma x}$ in (2.6), we will reverse the order of the limits on the integrals in order to obtain a meaningful result. Specifically, the time domain will be assumed to extend from $-\infty$ to 0 and the x domain will be assumed to extend from $-\infty$ to ct. The transform of (2.6) will now be written as

$$f(k,\omega) = \int_{t=-\infty}^{t=0} \int_{x=-\infty}^{x=ct} 1 \cdot e^{\gamma x} e^{-st} dx\, dt. \tag{3.3}$$

The result is

$$f(k,\omega) = \frac{1}{\gamma(\gamma c - s)}. \tag{3.4}$$

We can again easily observe that if the propagation velocity $c = 0$, the Laplace transform of a stationary unit step function is obtained, with the presence of an extra factor of $1/\gamma$ that represents the mapping into the k domain.

4. Dual-Domain Transform Theorems

We will now present two important theorems related to the dual-domain transform. Those theorems, namely, the phase-shift theorem and the convolution theorem, are straightforward extensions to the corresponding theorems of the Fourier/Laplace transforms.

4.1. *The Phase-Shift Theorem*

The dual-domain transform of a signal that is phase shifted by a phase $\phi = k\Delta x - \omega\Delta t$, where Δx and Δt are shifts along the x and t dimensions, respectively, is given by

$$D\left[f(x - \Delta x,\ t - \Delta t)\right] = e^{j\phi} f(k,\omega), \tag{4.1}$$

where $f(k,\omega) = D[f(x,t)]$ is the dual-domain transform of $f(x,t)$.

Proof. One has

$$D\left[f(x-\Delta x, t-\Delta t)\right] = \iint_0^\infty f(x-\Delta x, t-\Delta t)e^{\gamma x}e^{-st}dx\,dt. \tag{4.2}$$

Let $(t-\Delta t)=\tau$ and $(x-\Delta x)=\delta$, so that $dt=d\tau$ and $dx=d\delta$. Hence

$$\begin{aligned} D\left[f(x-\Delta x, t-\Delta t)\right] &= \iint_0^\infty f(\delta,\tau)e^{\gamma(\delta+\Delta x)}e^{-s(\tau+\Delta t)}d\tau\,d\delta \\ &= e^{(\gamma\Delta x - s\Delta t)}\iint_0^\infty f(\delta,\tau)e^{\gamma\delta}e^{-s\tau}d\tau\,d\delta \\ &= e^{j(k\Delta x-\omega\Delta t)}f(k,\omega). \end{aligned} \tag{4.3}$$

□

4.2. The Convolution Theorem

A signal $z(x,t)$, the dual-domain transform of which is given by $z(k,\omega)=y(k,\omega)h(k,\omega)$, where $y(k,\omega)$ and $h(k,\omega)$ are the transforms of another signal and a transfer function, respectively, is given by

$$z(x,t) = \iint_{-\infty}^\infty y(\delta,\tau)h(x-\delta,\ t-\tau)d\delta\,d\tau. \tag{4.4}$$

Proof. $z(x,t)$ will be given by the inverse dual-domain transform of $y(k,\omega)h(k,\omega)$, that is,

$$\begin{aligned} z(x,t) &= D^{-1}\left[y(k,\omega)h(k,\omega)\right] \\ &= \iint_{-\infty}^\infty y(k,\omega)h(k,\omega)e^{-j(kx-\omega t)}dk\,d\omega. \end{aligned} \tag{4.5}$$

But

$$y(k,\omega) = \iint_{-\infty}^\infty y(\delta,\tau)e^{j(k\delta-\omega\tau)}d\delta\,d\tau. \tag{4.6}$$

Hence

$$z(x,t) = \iint_{-\infty}^\infty\iint_{-\infty}^\infty y(\delta,\tau)e^{j(k\delta-\omega\tau)}d\delta\,d\tau h(k,\omega)e^{-j(kx-\omega t)}dk\,d\omega. \tag{4.7}$$

By interchanging the order of the double integrals, we have

$$\begin{aligned} z(x,t) &= \iint_{-\infty}^{\infty} y(\delta,\tau)\left[\iint_{-\infty}^{\infty} h(k,\omega)e^{-j[k(x-\delta)-\omega(t-\tau)]}dk\,d\omega\right]d\delta\,d\tau \\ &= \iint_{-\infty}^{\infty} y(\delta,\tau)h(x-\delta,\ t-\tau)d\delta d\tau. \end{aligned} \tag{4.8}$$

□

5. Example Application: Transfer Function of a Wireless Communication Channel with Multiple Phase Shifts

The transfer function characteristics of urban wireless communications channels are very important for cellular phone and wireless multimedia applications [6–8]. The high-frequency signals that travel through such channels are all represented by traveling wave equations, and each signal suffers from various phase shifts that collectively result in "fading effects" as the signal travels through the channel. Characterizing the behavior of a channel by means of a transfer function has always been a challenging problem, mainly because the Fourier/Laplace transform can only provide a transfer function representation in the frequency domain, that is, the ω domain, while the behavior of the channel in reality must ultimately be described in *both* the ω and the k domains. We will now proceed to obtain such a dual-domain transfer function for a wireless communication channel by using the dual-domain transform, and important new conclusions about the behavior of such channels will be reached.

According to the phase-shift theorem (4.1), a signal that encounters multiple phase shifts in a wireless communication channel will be represented by the sum

$$A_0e^{j\phi_0}f(k,\omega) + A_1e^{j\phi_1}f(k,\omega) + A_2e^{j\phi_2}f(k,\omega) + \cdots \tag{5.1}$$

at the output of the channel, where ϕ_i are the various phase shifts and where A_i are the amplitudes of the phase-shifted components. The transfer function (TF) of the channel is therefore given by

$$\mathrm{TF} = \frac{\text{Channel Output}}{f(k,\omega)} = A_0e^{j\phi_0} + A_1e^{j\phi_1} + A_2e^{j\phi_2} + \cdots. \tag{5.2}$$

By expanding each exponential term as a power series and rearranging the equation, we get

$$\mathrm{TF} = (A_0 + A_1 + \cdots) + j\left(A_0\phi_0 + A_1\phi_1 + \cdots\right) + \frac{j^2}{2!}\left(A_0\phi_0^2 + A_1\phi_1^2 + \cdots\right) + \cdots. \tag{5.3}$$

For comparison, the single-domain Laplace transform of a rectangular pulse in the time domain is given by [5]

$$f(\omega) = C_0 - C_1s + C_2s^2 - \cdots, \tag{5.4}$$

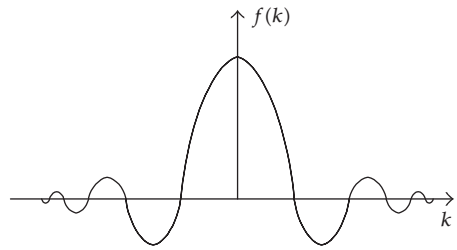

Figure 2: Behavior of the multipath wireless channel in the k domain.

where C_i are constants. It is clear that while (5.4) is a power series in $j\omega$, (5.3) is a power series in $j\phi$. This means that (5.3) is the transform of pulse-like characteristics in the time domain *and* pulse-like characteristics in the spatial domain. This is a very important conclusion, since it was previously assumed that multipath wireless channels exhibit pulse-like characteristics in the time domain only [6]. The pulse-like behavior of the channel in the spatial domain will be then described by a *sinc* function in the k domain, as shown in Figure 2.

The conclusion therefore is that the channel acts as a band-pass filter in *both* the frequency domain and the propagation constant k domain. This conclusion has substantial implications for the analysis of multipath wireless channels and will be further developed and investigated in a subsequent report in a specialized communications journal.

6. Aspects Regarding the Propagation of Traveling Waves Corresponding to Wave Functions. Phase Loss due to Multiple Quantum Interaction

We can extend our study at quantum phenomena by taking into account the fact that the expression $(kx - \omega t)$ corresponds also to the phase of a wave function describing the propagation of a free quantum particle.

According to the statistical interpretation of quantum theory, the wave function is representing just a mathematical model suitable for statistical interpretation. In the David Bohm interpretation of quantum theory, the wave function is a real wave in configuration space. This interpretation is also in accordance with measurements aspects of interaction of wave-trains with observer's material medium [9]. Due to these reasons, the phase of the traveling quantum wave requires a more detailed analysis, the dynamical aspect having to be taken into consideration.

Let us consider the propagation of an electron in a central symmetric electrostatic (Coulomb) field. According to the standard quantum analysis (based on second quantification theory, describing creation and annihilation of particles) the central symmetric electrostatic field should be decomposed (using the Fourier transformation) in a set of waves with a certain angular frequency ω and a certain wave vector k:

$$A_\mu^e(x_0, \vec{x}) = \frac{1}{(2\pi)^2} \int dq A_\mu^e(q) \exp -iqx, \tag{6.1}$$

where the product qx stands for

$$qx = q_0 x_0 - \vec{q}\vec{x} \tag{6.2}$$

with x_0 representing the time coordinate, $\vec{x} = x_1, x_2, x_3$ representing to the vector of position, q_0 representing the angular frequency ,and $\vec{q} = q_1, q_2, q_3$ representing the wave vector. The measurement system is chosen so as $c = 1$, $h/(2\pi) = 1$ for performing a better correspondence from the angular frequency to the energy and from the wave vector to the momentum of the quantum particle (see [10] for more details).

The quantities $A_\mu^e(x)$ and $A_\mu^e(p)$ do not correspond to standard photons, and for this reason they cannot be substituted by operators as required by second quantification theory. However, experimental facts have shown that the electromagnetic field effect can be studied using the perturbations method from quantum theory.

Using this method [10] the matrix element (for the first-order of perturbation) corresponding to the electromagnetic interaction between the electron and the electromagnetic field is represented by,

$$S_{fi}^{(1)} = -ie \int dx \overline{v}_{r'}^{(+)}(\vec{p}_f) \exp ip_f x \int dq A_\mu^e(q) \gamma_\mu \exp -iqx v_r^{(-)}(\vec{p}_i) \exp -ip_i x, \tag{6.3}$$

which can be also written as,

$$S_{fi}^{(1)} = -ie \int dq \overline{v}_{r'}^{(+)}(\vec{p}_f) \gamma_\mu A_\mu^e(q) v_r^{(-)}(\vec{p}_i) \delta(q - p_f + p_i). \tag{6.4}$$

In both previous equations the expression $A_\mu^e \gamma_\mu$ corresponds to the sum:

$$A_\mu^e \gamma_\mu = A_0^e \gamma_0 + \sum_{n=1}^{3} A_n^e \gamma_n, \tag{6.5}$$

where A_μ^e represents the cuadrivector of the electromagnetic field and γ_μ represents the Dirac matrices (its argument corresponds to the energy and momentum conservation laws).

If the electromagnetic field does not depend on time, the cuadripotential $A_\mu^e(x)$ can be presented as

$$A_\mu^e(x) = A_\mu^e(\vec{x}) = \frac{1}{(2\pi)^{3/2}} \int dq \exp i\vec{q}\vec{x} A_\mu^e(\vec{q}), \tag{6.6}$$

which shows that the virtual photons composing the electromagnetic field have a nonzero value just for the momentum (the energy corresponding to quantity q_0 being equal to zero). As a consequence, the matrix element for the first-order of perturbation can be written as

$$S_{fi}^{(1)} = -ie \int dq \overline{v}_{r'}^{(+)}(\vec{p}_f) \gamma_\mu A_\mu^e(\vec{q}) v_r^{(-)}(\vec{p}_i) \delta(\vec{q} - \vec{p}_f + \vec{p}_i) \delta(p_{f0} - p_{i0}). \tag{6.7}$$

By performing the integration on dq, it results

$$S_{fi}^{(1)} = -ie\overline{v}_{r'}^{(+)}(\vec{p}_f)\gamma_\mu A_\mu^e(\vec{q})v_r^{(-)}(\vec{p}_i)\delta(p_{f0} - p_{i0}). \tag{6.8}$$

For the coulombian electrostatic field with central symmetry $A_\mu^e(\vec{x}) = 0$; it results

$$eA_0^e(r) = -\frac{Q}{r}, \tag{6.9}$$

where Q represents the electrical negative charge. The previous equation can be also written (in p representation) as

$$eA_0^e(r) = -\int \frac{Q}{r} \exp iqr\, dr = \frac{4\pi Q}{\vec{q}^2}. \tag{6.10}$$

As a consequence, the matrix element for the first-order of perturbation in case of coulombian field with central symmetry can be written as:

$$S_{fi}^{(1)} = -ie\overline{v}_{r'}^{(+)}(\vec{p}_f)\gamma_0 A_0^e(\vec{q})v_r^{(-)}(\vec{p}_i)\delta(p_{f0} - p_{i0}), \tag{6.11}$$

which can be also written as

$$S_{fi}^{(1)} = -i\overline{v}_{r'}^{(+)}(\vec{p}_f)\gamma_0 v_r^{(-)}(\vec{p}_i)\left[eA_0^e(\vec{q})\right]\delta(p_{f0} - p_{i0}). \tag{6.12}$$

According to standard interpretation of quantum theory, this first-order element from perturbation method is connected to the probability of an interaction between an electron with initial momentum $\vec{p}_i$ and energy p_{i0} and a virtual photon with momentum $\vec{q}$ so as to result an electron with momentum $\vec{p}_f$ and energy p_{f0}. This interaction can be also represented using Feynman diagrams. By analyzing higher orders of matrix element (presented in an intutive manner using the same Feynman diagrams) some supplementary phenomena can be also explained, as elastic diffusion of photons by electrons, the annihilation of an electron-positron pair in two photons, the generation of an electron-positron pair by photons, the emission of two photons by an electron, the emission of brehmstrahlung radiation by electrons and positrons and so on.

However, for describing the whole interaction of an electron in a central symmetrical electrostatic field (so as to determine the trajectory of the associated wave-train) we can consider that the electron has to undergo multiple interactions with such virtual photons until the action of the exterior field vanishes (such multiple interactions being allowed by quantum mechanics). According to the quantum laws, each interaction transform the initial electron (corresponding to a certain wave train) into a new wave-train (the final electron) with different characteristics (another momentum and energy), and so on.

However, we should take also into account the fact that the wave-train associated to a quantum particle has not just a statistical interpretation. The Bohm-Aharonov effect has shown that a certain phase should also be associated to such a wave-train. Considering

that the wave-train corresponding to an electron undergoes a set of interactions with virtual photons, it results that a certain transient time is required by each interaction, so as physical quantities as wavelength and angular fequency to be defined on a certain time interval (these quantities being used by the formula of matrix elements of interaction). This transient time causes a phase-loss for the initial wave-train, while the timelength of stabilized oscillations (corresponding to the new-generated wave-train associated to the final photon) is represented (in a classical dynamical model) by the difference between the timelength of the initial wave-train and the transient time. Considering that no supplementary stabilized oscillations are added by each interaction (this means that quantum interaction does not generate any output wave-train after the input wave-train has vanished) it results that a very great number of interactions of the initial electron in a central symmetrical electrostatic (coulombian) field would cause a great number of phase loss (each interaction substracting a certain transient time), and, finally, the timelength of the wave-train associated to the final electron tends to zero. This corresponds to a vanishing phenomena for the initial electron in contradiction with experimental facts.

7. Nonlinear Phenomena of Phase-Loss Compensation for Propagating Wave-Trains in Quantum Physics: The Need of a Certain Material Reference System

At an extended analysis of propagating phenomena in quantum physics, we can notice that an approach based on second quantification laws leads to the same aspects of phase-loss (or shortened timelength) of a propagating wave-train due to multiple interactions along its trajectory in different situations, such as the interaction of a propagating free electron with its own electromagnetic field (implying renormalization of electron mass using higher orders of perturbation theory) and the generation of virtual electron-positron pairs due to the interaction of an electron with a weak exterior electromagnetic field (analyzed by taking into account higher order of perturbation theory, implying renormalization of electron charge) [10].

For justifying the fact that the phase-loss does not appear in experimental phenomena of such propagating beams (as presented above), we can take into consideration a possible phenomenon of phase-addition, consisting in an addition of supplementary oscillations *after* the initial wave-train has vanished. According to mathematical dynamical models, this corresponds to a dead-time transient phenomenon. As a consequence, a kind of internal memory should be associated to the space interval where the interaction occurs, generating an output signal even after the input signal has disappeared.

Another possibility consists in taking into account (from the same dynamical point of view) a resonance phenomena, considering that the initial wave-train can generate (as in a resonant phenomenon) oscillations with amplitude above a certain threshold. When the initial wave-train (similar to an input signal) disappears, these oscillations will become damped oscillations able to generate a final wave-train (similar to an output signal) as long as their amplitude is above a certain threshold. As in the case of the previous dynamical model, this mathematical model requires also an internal memory of the threshold level and of certain state variables able to generate resonant oscillations.

Both possibilities previously presented have a common feature: a certain delay time appears at each interaction, and thus the overall delay time should be connected with the wave-train velocity.

However, the phase-loss phenomenon can be avoided (as a theoretical result) if the whole trajectory is considered to be determined by just one Lagrangean function for the whole interaction of the electron with the electromagnetic field, implying the dynamical equations:

$$\begin{gathered}\left(-\frac{\partial^2}{\partial t^2}+\nabla^2\right)A_\mu(x)=-e\overline{\psi}\gamma_\mu\psi,\\ \left(i\gamma_\mu\frac{\partial}{\partial x_\mu}-e\gamma_\mu A_\mu\psi(x)\right)-m\psi(x)=0,\\ \overline{\psi}(x)\left(i\gamma_\mu\frac{\partial}{\partial x_\mu}+e\gamma_\mu A_\mu\right)+m\overline{\psi}(x)=0\end{gathered}\tag{7.1}$$

[10]. Thus the wave-function corresponding to the electron and the electromagnetic field is modified in a continuous manner along its trajectory. However, this possible solution is based on quantum laws of first quantification theory, all phenomena corresponding to second quantification (involving creation and annihilation of particles) being neglected. Yet we have to take into account the fact that the exterior electromagnetic field has usually a higher magnitude and a slow time variation as compared to the energy and velocity of the interacting electron. So it is quite naturally to consider that a certain exterior field (more important at a macrosopic scale) is determining the evolution of the electron wave-train, and thus appears the need of a certain reference system which acts upon the wave-trains corresponding to quantum particles. This assumption is supported also by the lack of reversibility for diffraction phenomena in quantum physics. We can notice an electron diffraction phenomenon when an electron beam interacts with a motionless crystal lattice, but we cannot imagine a diffraction phenomenon for the atoms of a crystal lattice when a moving lattice interacts with a motionless spatial distribution of electrons.

8. Phase Aspects and Quantum Dynamics of Cooperative Phenomena: Formal Logic Problems for Cooperative Quantum Phenomena

Our study upon quantum dynamics and phase aspects should be extended by taking into consideration multiparticle cooperative phenomena in quantum physics involving emission of electromagnetic field, while key issues as transition from a set of single particle quantum states to a global cooperative state can be noticed. For example, the photonic echo phenomenon is based on the rephasing that can occur in an inhomogeneously broadened atomic system, when the motion of the Bloch vectors is reversed following the initial dephasing of the atomic dipoles. For the beginning, we consider a group of atoms whose Bloch vectors in the rotating frame have the direction along the y' axis at the zero moment of time. We consider also that the rotating frame has the angular frequency ω_0 (the central frequency of the inhomogeneous line). In time, the Bloch vectors of the atoms will precess clockwise or counter-clockwise around the z' axis, depending whether their natural angular frequencies are either greater or less than ω_0. In time a dephasing phenomenon occurs, the atomic Bloch vectors being distributed almost uniformly around the x', y' plane. The initial macroscopic moment becomes zero, and the system does not radiate.

By applying a short, intense π pulse at time moment τ a reversal of the y' coordinate appears, the motion of the atomic Bloch vectors is reversed, and the vectors would be aligned again at a certain time moment 2τ. As a consequence, the atomic system generates a high-intensity echo pulse at time moment 2τ. This is the basic principle of both spin echo phenomenon and photon echo phenomenon [11].

Usually, a preparatory $\pi/2$ pulse (from the superradiance states point of view) is applied to the active medium at the initial moment of time. Mathematically, the property of the reference pulse of being a $\pi/2$ pulse is represented by the relation

$$\eta E_I \Delta t_I = \frac{\pi}{2}, \tag{8.1}$$

where E_I stands for the amplitude of the electric field, Δt_I stands for its timelength and η represents a parameter depending on frequency. The condition for the main optical pulse of being a π pulse is represented by the relation

$$\eta E_M \Delta t_M = \pi, \tag{8.2}$$

where E_M stands for the electric field of this signal, Δt_M stands for its timelength, and η represents the same parameter depending on frequency.

A basic feature of the high-intensity pulse (the photonic echo pulse) is represented by its power. Unlike amplified optical pulses by stimulated emission (with the power of emergent pulse proportional to N), the power of the photonic echo pulse is proportional to N^2 where N represents the number of atoms involved in the emission of this high-intensity pulse. This feature can be derived using the formalism of superradiant states $|r, m\rangle$, where r stands for the cooperative quantum number and m is proportional to the unperturbed Hamiltonian function for the ensemble of atoms (due to the the similarities with quantic angular momentum theory, $|m| < r < N/2$). According to this similarities, when the state of the atomic system is described by the state $|r, m\rangle$, the intensity of the emitted pulse is

$$I(r, m) = (r + m)(r - m + 1)I_0. \tag{8.3}$$

If all atoms involved in light emission are in excited state, $r = m = N/2$ and the intensity of emitted pulse is equal to

$$I\left(\frac{N}{2}, \frac{N}{2}\right) = NI_0, \tag{8.4}$$

where I_0 stands for the intensity of an optical pulse emitted by a single atom ($r = m = 1/2$). It can be shown that the maximum for the emission rate is obtained for $m = 1/2$ and greater values of r; while m is also equal to $(N_+ - N_-)$ (N_+ representing the number of atoms in excited state and N_- representing the number of atoms in ground state) it results that $m = 0$

or $m = 1$ and $r = N/2$. In this case the intensity of emitted pulse is

$$I\left(\frac{N}{2},0\right) = I\left(\frac{N}{2},1\right) = \left(\frac{N}{2}\right)\left(\frac{N}{2}+1\right)I_0 \tag{8.5}$$

being proportional (for large N) with N^2.

These aspects can be also explained (in an intuitive manner) using classical electromagnetics. When all atoms radiate independently, it can be considered that the phase ϕ and angular frequency ω of emitted electric field are not the same and thus the average value of the intensity corresponds to a sum of $a_k^2 E_k^2/2$ terms (all terms having the form $a_i a_k E_i E_k/2$ vanish while they correspond to alternating functions). It can be also argued that different orientation of Bloch vectors for a great number of atoms imply a null result for the sum of these vectors from the very beginning. On the contrary, when all atoms radiate in a cooperative manner, it can be considered that their emitted electric field has the same phase and angular frequency and thus the electric field E generated by all atoms is represented by a sum $E_1 + E_2 + \cdots + E_N$ and the intensity of the emitted electric field is represented by $(E_1 + E_2 + \cdots + E_N)^2$. For $E_1 = E_2 = \cdots = E_N$ it results that the intensity of the emitted electric field is proportional to N (in the first case) and to N^2 (in the second case). It can be also argued that the situation when all Bloch vectors are aligned corresponds to a great global dipole momentum for the entire system of atoms, and thus the emitted radiation has the same phase.

However, an important question regarding phase appears for these cases: which is the angular frequency of the emitted field for the photonic echo phenomenon? Is there a certain angular frequency or should we consider the emitted field as a mixture of waves with different characteristics? If we consider that we deal with a cooperative phenomenon, it seems logical to search for a certain angular frequency and a certain phase for the whole emitted field (as in the case of correlated photon emission, when two photons act as a single entity even when they are situated at large distances). Thus the emission would be similar to a single photon emission and interference phenomena could be noticed further (according to the Dirac principle that a photon interacts just with itself). Yet this affirmative answer generates another question: under which circumstances an ensemble of atoms can be studied using the quantum formalism of superradiant states, instead of analyzing a superposition of atoms with independent emission? According to formal logic in physics, an interference phenomenon can either occur or not. However, it is quite difficult to imagine that a certain parameter of the ensemble could suddenly generate the transition to a single quantum state when it reaches a specific value (so as interference phenomena to occur). This aspect is similar to the problem of defining a certain material reference system which performs the Lorentz transformation upon a received wave-train [9]: which are the requirements for a certain material reference system (as related to the parameters of the received wave-train)? (see [12] for the theoretical case when the energy of the received wave is comparable to the rest energy of the atoms composing the material medium). More probably, some correlation techniques with past events are required, and thus phase correlation aspects could appear. The phase correlation represents also the main technique for creating and controlling cooperative phenomena (when some spatially distributed particles or atoms can be described by a single quantum function at a certain moment of time, and possible transitions are controlled by imposing phase coincidence).

9. Simulating High-Intensity Superradiant Pulses Using Derivative Procedures and Partial Fraction Decomposition

A step forward in looking for an adequate mathematical model should consist in finding a mathematical quantity proportional to $(N/2)(N/2-1)$; this step must be performed in a similar manner used for passing from coordinates representation to momentum representation in quantum theory, by the aid of Fourrier transformation (the basic variables being changed) [13]. We can easily notice that the derivatives of different order for $f = p^{N/2}$ are direct proportional to $N/2, (N/2)(N/2-1), \ldots$. according to

$$\frac{df}{dp} = \left(\frac{N}{2}\right)p^{N/2-1},$$
$$\frac{d^2 f}{dp^2} = \left(\frac{N}{2}\right)\left(\frac{N}{2}-1\right)p^{N/2-2}. \tag{9.1}$$

It can be noticed that the coefficient of final monomial $p^{N/2-2}$ equals $(N/2)(N/2-1)$ which represents the ratio of the intensity $I(N/2, N/2)$ of the photonic echo pulse emitted from the state $r = m = N/2$ to the intensity I_0 of the pulse emitted independently by a single atom (similar to derivative procedures presented in [14]). In an intuitive manner, p can be considered as an operator of creation (as in second quantification formula) and the $N/2$ exponent symbolizes the creation of the quantum superradiant state with quantum number $r = N/2$ as a result of $N/2$ successive application of p operator upon an initial preliminary state (with $r = 0$). The same derivative procedure could be used for obtaining the eigenvalue of the square of the angular momentum $\hat{L}^2 = L(L+1)$ according to

$$\left(\frac{\partial^2}{\partial p^2}\right)p^{L+1} = (L+1)Lp^{L-2} \tag{9.2}$$

and considering an eigenvalue the coefficient of the resulting monomial.

For the case of nonsuperradiant states the ensemble of atoms could be described using a function f as

$$f = \sum_i (p - \varphi_i), \tag{9.3}$$

where φ_i stands for the specific phase difference for each atom. While the power of p equals unity, a second-order differentiation $\partial^2 f/\partial p^2$ yields zero, and no superradiant pulse appears.

10. Conclusions

This paper has presented an important extension to the Fourier/Laplace transform that is needed for the analysis of signals that are represented by traveling wave equations. Specific mathematical technique for the simulation of the behavior of large systems of optical oscillators was obtained. Signals described by traveling wave equations are typically characterized by a spatial propagation constant, k, in addition to the usual temporal

propagation constant ω. The Fourier/Laplace transform can only perform mapping of the time domain t into the ω domain (or frequency domain), and is incapable of performing the more general 2×2 mapping of the $x - t$ domain into the $k - \omega$ domain. The new extension introduced here allows for that general 2×2 mapping to be performed. This study has also emphasized the importance of phase dynamics aspects for traveling wave-trains in multiple interaction phenomena in quantum physics. It was shown that a phase-loss phenomenon should appear due to transient time, implying an annihilation of the quantum particle due to multiple interactions. The absence of this phenomenon in experimental results is explained by a possible correlation between the trajectory and phase of the quantum wave-train before interaction and the trajectory and phase of the quantum wave-train after the corresponding quantum particle has undergone the interaction. The need of a certain exterior reference system acting upon the quantum wave-train is also presented (based on some diffraction aspects). Finally it is shown that some interference aspects of the photonic echo phenomenon imply the need of considering that superradiant quantum states for an ensemble of atoms can either exist or not. Using a specific differentiation technique for symbolic polynomials corresponding to phase difference of each atom, a useful formalism for determining the condition for generating a superradiant pulse and its intensity is obtained.

References

[1] W. H. Hayt and J. A. Buck, *Engineering Electromagnetics*, McGraw Hill, New York, NY, USA, 2006.

[2] R. Feynmam, R. Leighton, and M. Sands, *The Feynman Lectures on Physics*, vol. 2, Addison Wesley, Reading, Mass, USA, 1977.

[3] J. S. Lim, *Two-Dimensional Signal and Image Processing*, Prentice Hall, Upper Saddle River, NJ, USA, 1990.

[4] T. W. Korner, *Fourier Analysis*, Cambridge University Press, Cambridge, UK, 2nd edition, 1989.

[5] J. E. Marsden and M. J. Hoffman, *Basic Complex Analysis*, W. H. Freeman, New York, NY, USA, 2nd edition, 1987.

[6] T. S. Rappaport, *Wireless Communications*, Prentice Hall, Upper Saddle River, NJ, USA, 1996.

[7] V. K. Garg and J. E. Wilkes, *Wireless and Personal Communications Systems*, Prentice Hall, Upper Saddle River, NJ, USA, 1996.

[8] V. K. Garg, *Wireless Network Evolution*, Prentice Hall, Upper Saddle River, NJ, USA, 2002.

[9] E. Bakhoum and C. Toma, "Relativistic short range phenomena and space-time aspects of pulse measurements," *Mathematical Problems in Engineering*, vol. 2008, Article ID 410156, 20 pages, 2008.

[10] N. Nelipa, *Physique des Particules Elementaires*, MIR, Moscou, Russia, 1981.

[11] L. Mandel and E. Wolf, *Optical Coherence and Quantum Optics*, Cambridge University Press, Cambridge, UK, 1995.

[12] A. Toma, S. Pusca, and C. Morarescu, "Spatial aspects of interaction between high-energy pulses and waves considered as suddenly emerging phenomena," in *Proceedings of the 1st International Conference on Computational Science and Its Applications (ICCSA '06)*, vol. 3980 of *Lecture Notes Computer Science*, pp. 839–846, Glasgow, UK, May 2006.

[13] P. Sterian and C. Toma, "Methods for presenting key concepts in physics for MS students by photon-MD program," *Bulgarian Journal of Physics*, vol. 27, no. 4, pp. 27–30, 2000.

[14] Th. Toma, S. Pusca, and C. Morarescu, "Simulating superradiant laser pulses using partial fraction decomposition and derivative procedures," in *Proceedings of the 1st International Conference on Computational Science and Its Applications (ICCSA '06)*, vol. 3980 of *Lecture Notes Computer Science*, pp. 779–784, Glasgow, UK, May 2006.

Hindawi Publishing Corporation
Mathematical Problems in Engineering
Volume 2010, Article ID 584863, 19 pages
doi:10.1155/2010/584863

Research Article

Stochastic Finite Element for Structural Vibration

Mo Wenhui

Mechanical Department, Hubei University of Automotive Technology, Shiyan 442002, China

Correspondence should be addressed to Mo Wenhui, hustmwh@sina.com

Received 17 December 2009; Revised 7 May 2010; Accepted 2 June 2010

Academic Editor: Carlo Cattani

This paper proposes a new method of calculating stochastic field. It is an improvement of the midpoint method of stochastic field. The vibration equation of a system is transformed to a static problem by using the Newmark method and the Taylor expansion is extended for the structural vibration analysis with uncertain factors. In order to develop computational efficiency and allow for efficient storage, the Conjugate Gradient method (CG) is also employed. An example is given, respectively, and calculated results are compared to validate the proposed methods.

1. Introduction

Material properties, geometry parameters, and applied loads of the structure are assumed to be stochastic. Although the finite element method analysis of complicated structures has become a generally widespread and accepted numerical method, regarding the given factors as constants cannot apparently correspond to the reality of a structure. In order to enhance computational accuracy, the influence of random factors must be considered.

Many physics parameters of material possess spatial variability, such as Young's modulus and Poisson's ratio, so we should regard them as stochastic fields. Stochastic field discretization is the problem that various stochastic finite element methods need to resolve, but discrete form of stochastic field plays the decisive influence on the calculation and computational accuracy of stochastic finite element. The simplest discretization is the midpoint method (MSF) [1]. The stochastic field is described by a single random variable replacing the value of the field at a central point of the mesh. The local average method of the stochastic field describes the stochastic field of an element in terms of the spatial average. The local average method of rectangle element is described by the mean, variance, and covariance [2]. It can be extended for 3D [3]. The stochastic field of nonrectangular element is described by the mean vector and covariance matrix using Gaussian quadrature [4]. The stochastic

field can be described by the shape function and nodal values, and it is necessary to know the related function [5]. Making use of the Karhunen-Loeve expansion, stochastic field is represented by series expansion [6]. When stiffness matrices are deduced, a weighted integral method is adopted to consider stochastic field of material parameters [7, 8]. When stochastic field is expressed by series expansion, the optimal linear-estimation method is applied to make the error of variance minimum [9].

The direct Monte Carlo simulation of the stochastic finite element method (DSFEM) requires a large number of samples, which requires much calculation time [10]. Monte Carlo simulation by applying the Neumann expansion (NSFEM) enhances computational efficiency and saves storage in such a way that the NSFEM combined with Monte Carlo simulation enhances the finite element model advantageously [11]. The preconditioned Conjugate Gradient method (PCG) applied in the calculation of stochastic finite elements can also enhance computational accuracy and efficiency [12]. According to first-order or second-order perturbation methods, calculation formulas can be obtained [5, 11, 14–16, 18–20, 22]. The result is called the PSFEM and has been adopted by many authors.

The PSFEM is often applied in dynamic analysis of structures and the second-order perturbation technique has been proved to be efficient [5]. Dynamic reliability of a frame is calculated by the SFEM and response sensitivity is formulated in the context of stiffness and mass matrix condensation [16]. When load actions are treated as stochastic processes, vibration of the structure is resolved by the PSFEM [17]. The PSFEM is an adequate tool for nonlinear structural dynamics. Nonlinearities due to material and geometrical effects have also been included [18]. By forming a new dynamic shape function matrix, dynamic analysis of the spatial frame structure is presented by the PSFEM [19]. The NSFEM is introduced in dynamic analysis within the framework of a Monte Carlo simulation [20]. The NSFEM is applied to the dynamic response of a random structure system and results are compared with those from the PSFEM and the DSFEM [21]. With the aid of the PSFEM, a stochastic formulation for nonlinear dynamic analysis of a structure is presented [22].

An improved midpoint method of stochastic field (IMSF) is presented. The IMSF is more accurate than the MSF. The Newmark method transforms differential equations into linear equations. The IMSF is used and the structural vibrations for a linear system are computed by the Taylor expansion method, the CG method, and the PCG method of stochastic finite element (TSFEM, CG, PCG). The TSFEM, the CG, and the PCG based on the MSF are called the MTSFEM, the MCG, and the MPCG. An example demonstrates the superiority of the proposed methods.

2. Improved Midpoint Method of Stochastic Field

When finite element method is used, structure is divided into small elements whose number is appropriate. In this paper, Young's modulus is assumed to be a Gaussian process. When element is appropriately small, Young's modulus of an element is described by a variable. The Young's modulus of structure is described by a group of variables. Without loss of generality, it is supposed that the structure is divided into elements of m nodes and n nodes. The Young's modulus of node within element e of m nodes is expressed by $a_{em1}, a_{em2}, \ldots, a_{emm}$. The Young's modulus of midpoint within element e of m nodes is expressed by a_{eml}. The Young's modulus of node within element f of n nodes is expressed by $a_{fn1}, a_{fn2}, \ldots, a_{fnn}$. The Young's modulus of midpoint within element f of n nodes is expressed by a_{fnl}.

The Young's modulus within element e is defined as

$$a_e = \frac{a_{em1} + a_{em2} + \cdots + a_{emm} + a_{eml}}{m+1}. \tag{2.1}$$

Its mean is

$$\begin{aligned} \mu_e &= \mu\left(\frac{a_{em1} + a_{em2} + \cdots + a_{emm} + a_{eml}}{m+1}\right) \\ &= \frac{\mu_{aem1} + \mu_{aem2} + \cdots + \mu_{aemm} + \mu_{aeml}}{m+1}, \end{aligned} \tag{2.2}$$

where the means of Young's modulus at the first node, the second node,..., the mth node of element e are expressed by $\mu_{aem1}, \mu_{aem2}, \ldots, \mu_{aemm}$.The mean of Young's modulus at the midpoint of element e is expressed by μ_{aeml}.

The Young's modulus within element f is defined as

$$a_f = \frac{a_{fn1} + a_{fn2} + \cdots + a_{fnn} + a_{fnl}}{n+1}. \tag{2.3}$$

Its mean is

$$\begin{aligned} \mu_f &= \mu\left(\frac{a_{fn1} + a_{fn2} + \cdots + a_{fnn} + a_{fnl}}{n+1}\right) \\ &= \frac{\mu_{afn1} + \mu_{afn2} + \cdots + \mu_{afnn} + \mu_{afnl}}{n+1}, \end{aligned} \tag{2.4}$$

where the means of Young's modulus at the first node, the second node,...,the nth node of element f are expressed by $\mu_{afn1}, \mu_{afn2}, \ldots, \mu_{afnn}$. The mean of Young's modulus at the midpoint of element f is expressed by μ_{afnl}.

The covariance of Young's modulus between two elements that each has m nodes is obtained by

$$\begin{aligned}
\operatorname{Cov}(a_e, a_{e'}) &= \operatorname{Cov}\left(\frac{a_{em1} + a_{em2} + \cdots + a_{emm} + a_{eml}}{m+1}, \frac{a_{e'm1} + a_{e'm2} + \cdots + a_{e'mm} + a_{e'ml}}{m+1}\right) \\
&= \frac{1}{(m+1)^2}[\operatorname{Cov}(a_{em1}, a_{e'm1} + a_{e'm2} + \cdots + a_{e'mm} + a_{e'ml}) \\
&\qquad + \operatorname{Cov}(a_{em2} + \cdots a_{emm} + a_{eml}, a_{e'm1} + a_{e'm2} + \cdots + a_{e'mm} + a_{e'ml})] \\
&= \frac{1}{(m+1)^2}[\operatorname{Cov}(a_{em1}, a_{e'm1}) + \operatorname{Cov}(a_{em1}, a_{e'm2}) \\
&\qquad + \cdots + \operatorname{Cov}(a_{em1}, a_{e'mm}) + \operatorname{Cov}(a_{em1}, a_{e'ml})] \\
&\quad + \frac{1}{(m+1)^2}\operatorname{Cov}(a_{em2} + \cdots + a_{emm} + a_{eml}, a_{e'm1} + a_{e'm2} + \cdots + a_{e'mm} + a_{e'ml}) \\
&= \frac{1}{(m+1)^2}\left(\sum_{g_1=1}^{m}\sum_{g_2=1}^{m}\operatorname{Cov}(a_{emg_1}, a_{e'mg_2})\right) + \frac{1}{(m+1)^2}\left(\sum_{g_1=1}^{m}\operatorname{Cov}(a_{emg_1}, a_{e'ml})\right) \\
&\quad + \frac{1}{(m+1)^2}\left(\sum_{g_2=1}^{m}\operatorname{Cov}(a_{eml}, a_{e'mg_2}) + \operatorname{Cov}(a_{eml}, a_{e'ml})\right),
\end{aligned} \tag{2.5}$$

where $\operatorname{Cov}(a_{emg_1}, a_{e'mg_2})$ = the covariance of Young's modulus between node $g_1 (g_1 = 1, 2, \ldots, m)$ of element e and node g_2 $(g_2 = 1, 2, \ldots, m)$ of element e', $\operatorname{Cov}(a_{emg_1}, a_{e'ml})$ = the covariance of Young's modulus between node g_1 of element e and the midpoint of element e', $\operatorname{Cov}(a_{eml}, a_{e'mg_2})$ = the covariance of Young's modulus between the midpoint of element e and node g_2 of element e', and $\operatorname{Cov}(a_{eml}, a_{e'ml})$ = the covariance of Young's modulus between the midpoint of element e and the midpoint of element e'.

The covariance of Young's modulus between two elements is given in Appendix A.

Using covariance matrix, the correlation of Young's modulus between any two elements is given by

$$C_{aa} = \begin{pmatrix} \operatorname{Cov}(a_1, a_1) & \operatorname{Cov}(a_1, a_2) & \cdots & \operatorname{Cov}(a_1, a_N) \\ \operatorname{Cov}(a_2, a_1) & \operatorname{Cov}(a_2, a_2) & \cdots & \operatorname{Cov}(a_2, a_N) \\ \vdots & \vdots & & \vdots \\ \operatorname{Cov}(a_N, a_1) & \operatorname{Cov}(a_N, a_2) & \cdots & \operatorname{Cov}(a_N, a_N) \end{pmatrix}. \tag{2.6}$$

A Gaussian vector $\vec{a} = [a_1, a_2, \ldots, a_N]^T$ is generated

$$\vec{a} = LZ. \tag{2.7}$$

$Z = [Z_1, Z_2, \ldots, Z_N]^T$ consists of N Gaussian random variables with mean zero and unit standard deviation. The Cholesky matrix L can be obtained through a decomposition of the covariance matrix; therefore,

$$\begin{aligned} \mu\left[ZZ^T\right] &= I, \\ LL^T &= C_{aa}. \end{aligned} \tag{2.8}$$

I is the identity matrix. The generation of vector $\vec{a}$ must satisfy the covariance matrix

$$\begin{aligned} \mu\left[\vec{a}\,\vec{a}^T\right] &= \mu\left[LZ(LZ)^T\right] \\ &= L\mu\left[ZZ^T\right]L^T = C_{aa}. \end{aligned} \tag{2.9}$$

Once the decomposition has been completed, different samples of vector $\vec{a}$ can be acquired easily by (2.7). Thus, it is possible that Monte Carlo simulation resolves problem of stochastic finite element.

3. Dynamic Analysis of Finite Element

For a linear system, the dynamic equilibrium equation is given by

$$[M]\{\ddot{\boldsymbol{\delta}}\} + [C]\{\dot{\boldsymbol{\delta}}\} + [K]\{\boldsymbol{\delta}\} = \{F\}, \tag{3.1}$$

where $\{\ddot{\delta}\}, \{\dot{\delta}\}, \{\delta\}$ are the acceleration, velocity, and displacement vectors. $[M], [K]$, and $[C]$ are the global mass, stiffness, and damping matrices obtained by assembling the element variables in global coordinate system.

By using the Newmark method, (3.1) becomes

$$\{\delta_{t+\Delta t}\} = \left[\widetilde{K}\right]^{-1}\left\{\widetilde{F}_{t+\Delta t}\right\}, \tag{3.2}$$

where $\{\delta_{t+\Delta t}\}[\widetilde{K}]$ and $\{\widetilde{F}_{t+\Delta t}\}$ indicate the displacement vector, stiffness matrix and load vector at time $t + \Delta t$. $[\widetilde{K}]$ and $\{\widetilde{F}_{t+\Delta t}\}$ are given in Appendix B.

4. Dynamic Analysis of Structure Based on CG

Equation (3.2) can be rewritten as

$$\left[\widetilde{K}\right]\{\delta_{t+\Delta t}\} = \left\{\widetilde{F}_{t+\Delta t}\right\}. \tag{4.1}$$

Using (2.7), (2.8), and (2.9), N_1 samples of vector $\vec{a}$ are produced. N_1 matrices $[\widetilde{K}]$ and N_1 (4.1) are generated. For linear vibrations, (4.1) is a system of linear equations. The CG is

an adequate method for solving large systems of linear equations. It can be accomplished as follows.

first, select appropriate solution as initial values

$$\{\delta_{t+\Delta t}\}^{(0)} = \left(\delta^{(0)}{}_{(t+\Delta t)_1}, \delta^{(0)}{}_{(t+\Delta t)_2}, \ldots, \delta^{(0)}{}_{(t+\Delta t)_{N_1}}\right)^T; \tag{4.2}$$

calculate the first residual vector

$$r^{(0)} = \left\{\widetilde{F}_{t+\Delta t}\right\} - \left[\widetilde{K}\right]\{\delta_{t+\Delta t}\}^{(0)} \tag{4.3}$$

and vector

$$p^{(0)} = \left[\widetilde{K}\right]^T r^{(0)} \tag{4.4}$$

where $[\widetilde{K}]^T$ is the transposed matrix;

for $\widetilde{i} = 0, 1, 2, \ldots, n_2 - 1$, iterate step by step as follows:

$$\begin{aligned}
\alpha_{\widetilde{i}} &= \frac{\left(\left[\widetilde{K}\right]p^{(\widetilde{i})}, r^{(\widetilde{i})}\right)}{\left(\left[\widetilde{K}\right]p^{(\widetilde{i})}, \left[\widetilde{K}\right]p^{(\widetilde{i})}\right)} = \frac{\left(p^{(\widetilde{i})}, \left[\widetilde{K}\right]^T r^{(\widetilde{i})}\right)}{\left(\left[\widetilde{K}\right]p^{(\widetilde{i})}, \left[\widetilde{K}\right]p^{(\widetilde{i})}\right)} \\
&= \frac{\left(\left[\widetilde{K}\right]^T r^{(\widetilde{i})}, \left[\widetilde{K}\right]^T r^{(\widetilde{i})}\right)}{\left(\left[\widetilde{K}\right]p^{(\widetilde{i})}, \left[\widetilde{K}\right]p^{(\widetilde{i})}\right)}, \\
\{\delta_{t+\Delta t}\}^{(\widetilde{i}+1)} &= \{\delta_{t+\Delta t}\}^{(\widetilde{i})} + \alpha_{\widetilde{i}} p^{(\widetilde{i})}, \\
r^{(\widetilde{i}+1)} &= r^{(\widetilde{i})} - \alpha_{\widetilde{i}}\left[\widetilde{K}\right]p^{(\widetilde{i})}, \\
\beta_{\widetilde{i}+1} &= \frac{\left(\left[\widetilde{K}\right]^T r^{(\widetilde{i}+1)}, \left[\widetilde{K}\right]^T r^{(\widetilde{i}+1)}\right)}{\left(\left[\widetilde{K}\right]^T r^{(\widetilde{i})}, \left[\widetilde{K}\right]^T r^{(\widetilde{i})}\right)}, \\
p^{(\widetilde{i}+1)} &= \left[\widetilde{K}\right]^T r^{(\widetilde{i}+1)} + \beta_{\widetilde{i}+1} p^{(\widetilde{i})}.
\end{aligned} \tag{4.5}$$

This process stops only if r^{n_2} is small enough.

Vectors $\{\delta_{t+\Delta t}\}_1, \{\delta_{t+\Delta t}\}_2, \ldots, \{\delta_{t+\Delta t}\}_{N_1}$ are solutions of N_1 (4.1). The mean of $\{\delta_{t+\Delta t}\}$ is given by

$$\mu\{\delta_{t+\Delta t}\} = \frac{\{\delta_{t+\Delta t}\}_1 + \{\delta_{t+\Delta t}\}_2 + \cdots + \{\delta_{t+\Delta t}\}_{N_1}}{N_1}. \tag{4.6}$$

The variance of $\{\delta_{t+\Delta t}\}$ is given by

$$\mathrm{Var}\{\delta_{t+\Delta t}\} = \frac{1}{N_1 - 1}\sum_{i=1}^{N_1}\left(\{\delta_{t+\Delta t}\}_i - \mu\{\delta_{t+\Delta t}\}\right)^2. \tag{4.7}$$

Similarly, the mean and variance of vector $\{\delta_{t+i_1\Delta t}\}$ can be solved at time $t + i_1\Delta t$ step by step.

At time $t' = t + i_2\Delta t$ $(i_2 = 1, 2, \ldots, n_1)$, the stress for element d is given by

$$\{\sigma\} = [D][B]\left\{\delta_{t'}^{d}\right\}, \tag{4.8}$$

where $[D]$ = the material response matrix of element d, $[B]$ = the gradient matrix of element d and $\{\delta_{t'}{}^{d}\}$ = the element d nodal displacement vector at time t'.

Substituting N_1 samples of vector $\vec{a}$ into (4.8), vectors $\{\sigma\}_1, \{\sigma\}_2, \ldots, \{\sigma\}_{N_1}$ can be obtained.

The mean of $\{\sigma\}$ is given by

$$\mu\{\sigma\} = \frac{\{\sigma\}_1 + \{\sigma\}_2 + \cdots + \{\sigma\}_{N_1}}{N_1}. \tag{4.9}$$

The variance of $\{\sigma\}$ is given by

$$\mathrm{Var}\{\sigma\} = \frac{1}{N_1 - 1}\sum_{i=1}^{N_1}\left(\{\sigma\}_i - \mu\{\sigma\}\right)^2. \tag{4.10}$$

The CG belongs to methods of iteration that converge quickly. For practical purposes, PCG is applied to accelerate convergence.

5. Dynamic Analysis of Structure Based on the TSFEM

Young's modulus of the structure is given as function of N random variables $a_1, a_2, \ldots, a_N$. The partial derivative of (4.1) with respect to a_i is given by

$$\frac{\partial\{\delta_{t+\Delta t}\}}{\partial a_i} = \left[\widetilde{K}\right]^{-1}\left(\frac{\partial\left\{\widetilde{F}_{t+\Delta t}\right\}}{\partial a_i} - \frac{\partial\left[\widetilde{K}\right]}{\partial a_i}\{\delta_{t+\Delta t}\}\right), \tag{5.1}$$

where

$$\begin{aligned}\frac{\partial\left\{\widetilde{F}_{t+\Delta t}\right\}}{\partial a_i} &= \frac{\partial\{F_{t+\Delta t}\}}{\partial a_i} + \frac{\partial[M]}{\partial a_i}\left(b_0\{\delta_t\} + b_2\{\dot{\delta}_t\} + b_3\{\ddot{\delta}_t\}\right) \\ &\quad + [M]\left(b_0\frac{\partial\{\delta_t\}}{\partial a_i} + b_2\frac{\partial\{\dot{\delta}_t\}}{\partial a_i} + b_3\frac{\partial\{\ddot{\delta}_t\}}{\partial a_i}\right) \\ &\quad + \frac{\partial[C]}{\partial a_i}\left(b_1\{\delta_t\} + b_4\{\dot{\delta}_t\} + b_5\{\ddot{\delta}_t\}\right) \\ &\quad + [C]\left(b_1\frac{\partial\{\delta_t\}}{\partial a_i} + b_4\frac{\partial\{\dot{\delta}_t\}}{\partial a_i} + b_5\frac{\partial\{\ddot{\delta}_t\}}{\partial a_i}\right).\end{aligned} \tag{5.2}$$

After $\partial\{\delta_t\}/\partial a_i = q_0$, $\partial\{\dot{\delta}_t\}/\partial a_i = \dot{q}_0$, and $\partial\{\ddot{\delta}_t\}/\partial a_i = \ddot{q}_0$ are given, (5.2) can be calculated.

The partial derivative of (5.1) with respect to a_j is given by

$$\frac{\partial^2\{\delta_{t+\Delta t}\}}{\partial a_i \partial a_j} = \left[\widetilde{K}\right]^{-1}\left(\frac{\partial^2\left\{\widetilde{F}_{t+\Delta t}\right\}}{\partial a_i \partial a_j} - \frac{\partial\left[\widetilde{K}\right]}{\partial a_i}\frac{\partial\{\delta_{t+\Delta t}\}}{\partial a_j} - \frac{\partial\left[\widetilde{K}\right]}{\partial a_j}\frac{\partial\{\delta_{t+\Delta t}\}}{\partial a_i} - \frac{\partial^2\left[\widetilde{K}\right]}{\partial a_i \partial a_j}\{\delta_{t+\Delta t}\}\right), \tag{5.3}$$

where

$$\begin{aligned}\frac{\partial^2\left\{\widetilde{F}_{t+\Delta t}\right\}}{\partial a_i \partial a_j} &= \frac{\partial^2\{F_{t+\Delta t}\}}{\partial a_i \partial a_j} + \frac{\partial^2[M]}{\partial a_i \partial a_j}\left(b_0\{\delta_t\} + b_2\{\dot{\delta}_t\} + b_3\{\ddot{\delta}_t\}\right) \\ &\quad + \frac{\partial[M]}{\partial a_i}\left(b_0\frac{\partial\{\delta_t\}}{\partial a_j} + b_2\frac{\partial\{\dot{\delta}_t\}}{\partial a_j} + b_3\frac{\partial\{\ddot{\delta}_t\}}{\partial a_j}\right) \\ &\quad + \frac{\partial[M]}{\partial a_j}\left(b_0\frac{\partial\{\delta_t\}}{\partial a_i} + b_2\frac{\partial\{\dot{\delta}_t\}}{\partial a_i} + b_3\frac{\partial\{\ddot{\delta}_t\}}{\partial a_i}\right) \\ &\quad + [M]\left(b_0\frac{\partial^2\{\delta_t\}}{\partial a_i \partial a_j} + b_2\frac{\partial^2\{\dot{\delta}_t\}}{\partial a_i \partial a_j} + b_3\frac{\partial^2\{\ddot{\delta}_t\}}{\partial a_i \partial a_j}\right) \\ &\quad + \frac{\partial^2[C]}{\partial a_i \partial a_j}\left(b_1\{\delta_t\} + b_4\{\dot{\delta}_t\} + b_5\{\ddot{\delta}_t\}\right) \\ &\quad + \frac{\partial[C]}{\partial a_i}\left(b_1\frac{\partial\{\delta_t\}}{\partial a_j} + b_4\frac{\partial\{\dot{\delta}_t\}}{\partial a_j} + b_5\frac{\partial\{\ddot{\delta}_t\}}{\partial a_j}\right) \\ &\quad + \frac{\partial[C]}{\partial a_j}\left(b_1\frac{\partial\{\delta_t\}}{\partial a_i} + b_4\frac{\partial\{\dot{\delta}_t\}}{\partial a_i} + b_5\frac{\partial\{\ddot{\delta}_t\}}{\partial a_i}\right) \\ &\quad + [C]\left(b_1\frac{\partial^2\{\delta_t\}}{\partial a_i \partial a_j} + b_4\frac{\partial^2\{\dot{\delta}_t\}}{\partial a_i \partial a_j} + b_5\frac{\partial^2\{\ddot{\delta}_t\}}{\partial a_i \partial a_j}\right).\end{aligned} \tag{5.4}$$

Table 1: Comparison of error.

	The mean of vertical displacement at node 505	The variance of vertical displacement at node 505	The mean of horizontal stress at node 5	The variance of horizontal stress at node 5
PCG	2.95%	3.42%	4.31%	5.07%
CG	3.11%	3.84%	4.57%	5.24%
TSFEM	5.12%	6.01%	6.28%	7.17%
MPCG	7.14%	7.02%	8.67%	9.94%
MCG	7.23%	7.63%	8.82%	10.17%
MTSFEM	12.76%	13.27%	14.47%	16.53%

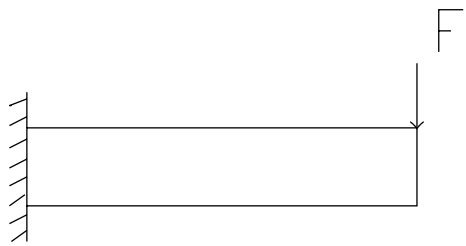

Figure 1: A cantilever beam.

After $\partial\{\delta_t\}/\partial a_j = q_1$, $\partial\{\dot{\delta}_t\}/\partial a_j = \dot{q}_1$, $\partial\{\ddot{\delta}_t\}/\partial a_j = \ddot{q}_1$, $\partial^2\{\delta_t\}/\partial a_i \partial a_j = r_0$, and $\partial^2\{\dot{\delta}_t\}/\partial a_i \partial a_j = \dot{r}_0$, $\partial^2\{\ddot{\delta}_t\}/\partial a_i \partial a_j = \ddot{r}_0$ are given, (5.4) can be calculated.

The displacement is expanded at the mean value point $\overline{a} = (\overline{a}_1, \overline{a}_2, \ldots, \overline{a}_i, \ldots, \overline{a}_{n_1})^T$ by means of a Taylor series. the mean of $\delta_{t+\triangle t}$ is obtained as

$$\mu\{\delta_{t+\Delta t}\} \approx \{\delta_{t+\Delta t}\}|_{a=\overline{a}} + \frac{1}{2}\sum_{i=1}^{N}\sum_{j=1}^{N} \frac{\partial^2\{\delta_{t+\Delta t}\}}{\partial a_i \partial a_j}\bigg|_{a=\overline{a}} \operatorname{Cov}(a_i, a_j), \tag{5.5}$$

where $\mu\{\delta_{t+\Delta t}\}$ expresses mean value $\delta_{t+\Delta t}$ and $\operatorname{Cov}(a_i, a_j)$ is the covariance between a_i and a_j.

The variance of $\delta_{t+\triangle t}$ is given by

$$\operatorname{Var}\{\delta_{t+\Delta t}\} \approx \sum_{i=1}^{N}\sum_{j=1}^{N} \frac{\partial\{\delta_{t+\Delta t}\}}{\partial a_i}\bigg|_{a=\overline{a}} \cdot \frac{\partial\{\delta_{t+\Delta t}\}}{\partial a_j}\bigg|_{a=\overline{a}} \cdot \operatorname{Cov}(a_i, a_j). \tag{5.6}$$

The velocity vector $\{\dot{\delta}_{t+\triangle t}\}$ and the acceleration vector $\{\ddot{\delta}_{t+\triangle t}\}$ are given in Appendix B. The partial derivative of $\ddot{\delta}_{t+\triangle t}$ with respect to a_i is given by

$$\frac{\partial\{\ddot{\delta}_{t+\Delta t}\}}{\partial a_i} = b_0\left(\frac{\partial\{\delta_{t+\Delta t}\}}{\partial a_i} - \frac{\partial\{\delta_t\}}{\partial a_i}\right) - b_2\frac{\partial\{\dot{\delta}_t\}}{\partial a_i} - b_3\frac{\partial\{\ddot{\delta}_t\}}{\partial a_i}. \tag{5.7}$$

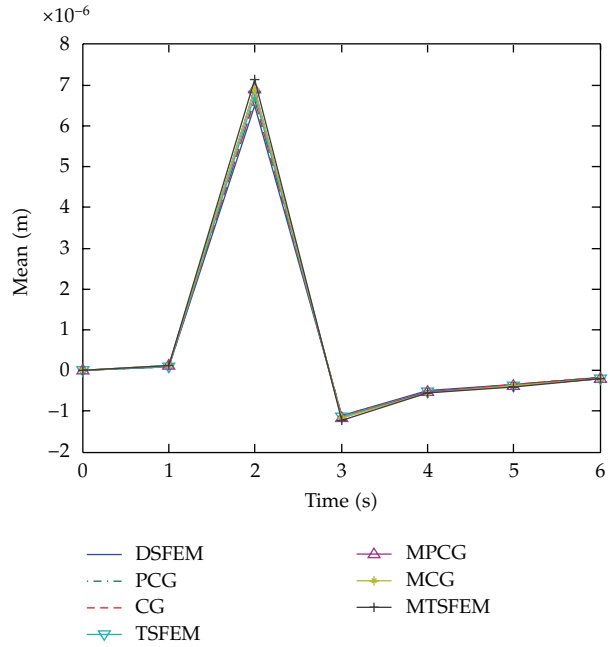

Figure 2: The mean of vertical displacement at node 505.

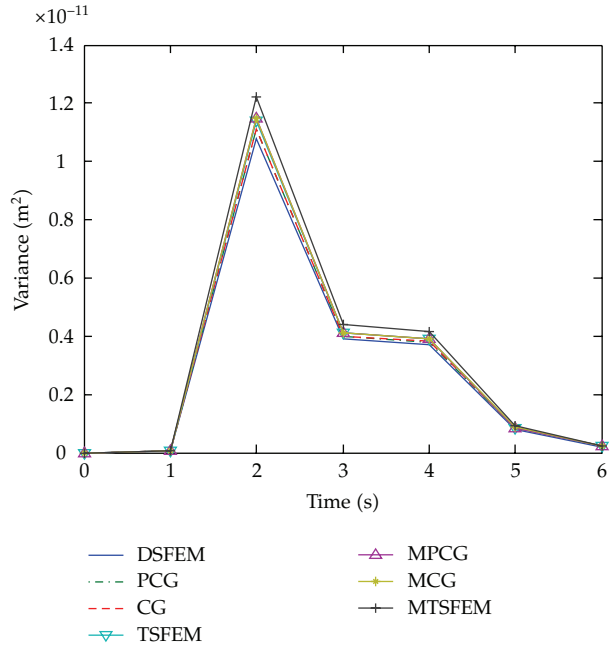

Figure 3: The variance of vertical displacement at node 505.

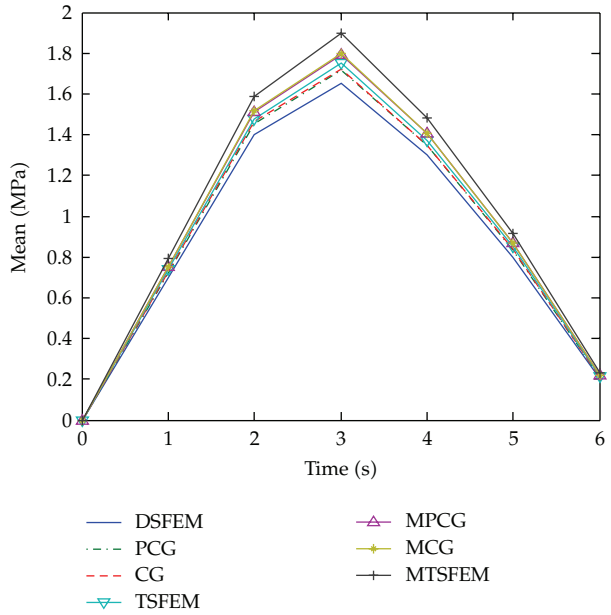

Figure 4: The mean of horizontal stress at node 5.

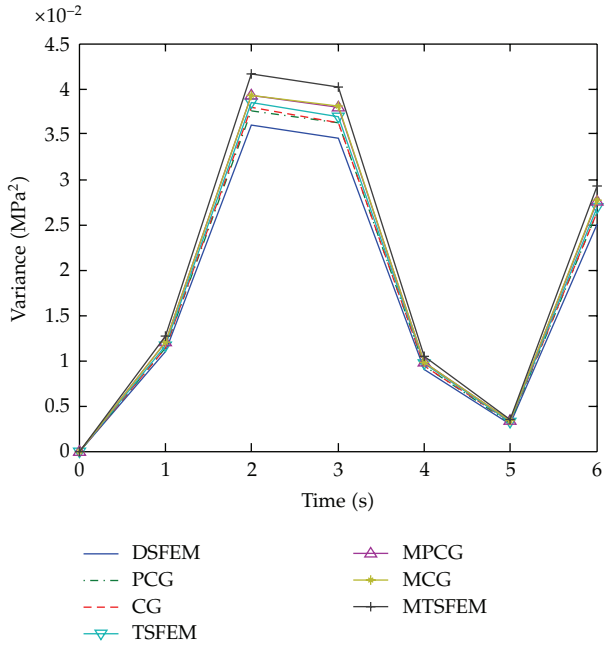

Figure 5: The variance of horizontal stress at node 5.

Table 2: Comparison of CPU time.

	DSFEM	PCG	CG	TSFEM	MPCG	MCG	MTSFEM
CPU time	4 h 32 m 47 s	1 h 15 m 43 s	1 h 47 m 36 s	10 h 45 m 34 s	1 h 7 m 23 s	1 h 36 m 31 s	4 h 12 m 17 s

h: hour; m: minute; s: second.

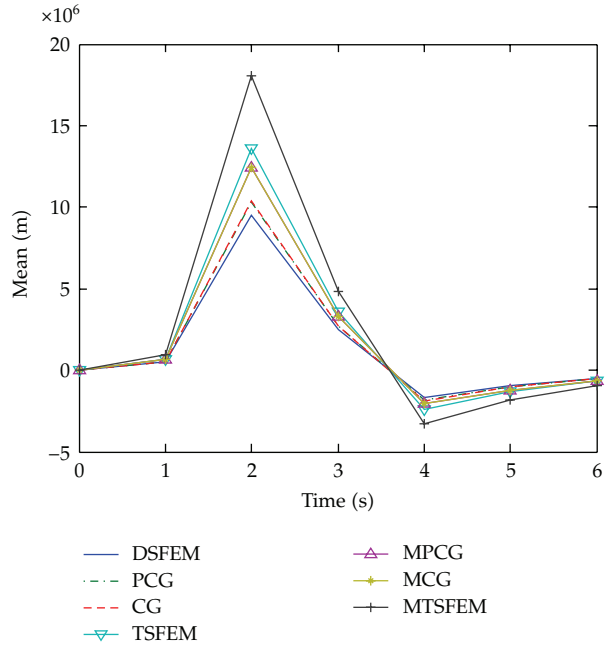

Figure 6: The mean of vertical displacement at node 505 for larger covariances.

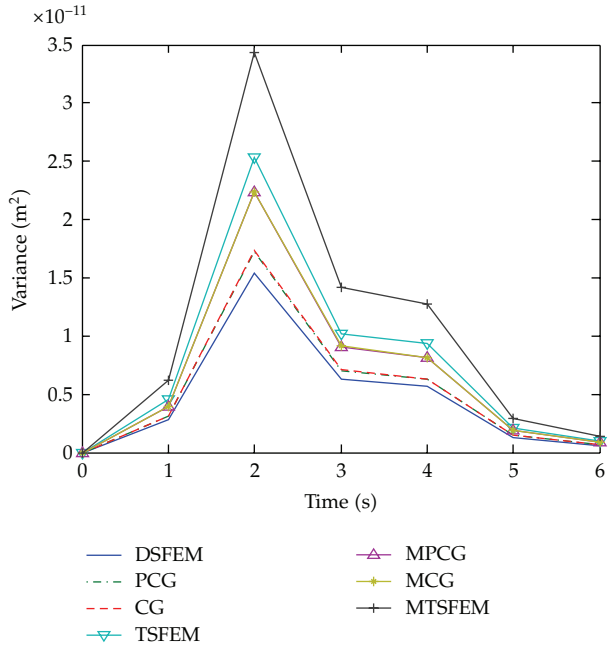

Figure 7: The variance of vertical displacement at node 505 for larger covariances.

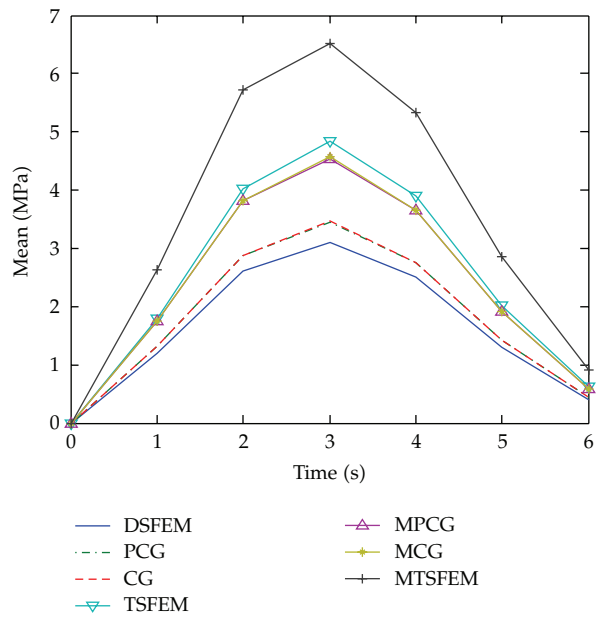

Figure 8: The mean of horizontal stress at node 5 for larger covariances.

Table 3: Comparison of error for larger covariances.

	The mean of vertical displacement at node 505	The variance of vertical displacement at node 505	The mean of horizontal stress at node 5	The variance of horizontal stress at node 5
PCG	9.27%	12.15%	11.43%	14.16%
CG	9.53%	12.37%	11.67%	14.41%
TSFEM	43.19%	64.28%	56.42%	76.39%
MPCG	31.42%	45.13%	47.16%	63.17%
MCG	31.75%	45.41%	47.43%	63.42%
MTSFEM	94.27%	125.74%	125.41%	162.43%

The partial derivative of $\dot{\delta}_{t+\Delta t}$ with respect to a_i is given by

$$\frac{\partial\{\dot{\delta}_{t+\Delta t}\}}{\partial a_i} = \frac{\partial\{\dot{\delta}_t\}}{\partial a_i} + b_6\frac{\partial\{\ddot{\delta}_t\}}{\partial a_i} + b_7\frac{\partial\{\ddot{\delta}_{t+\Delta t}\}}{\partial a_i}. \tag{5.8}$$

The partial derivative of (5.7) with respect to a_j is given by

$$\frac{\partial^2\{\ddot{\delta}_{t+\Delta t}\}}{\partial a_i \partial a_j} = b_0\left(\frac{\partial^2\{\delta_{t+\Delta t}\}}{\partial a_i \partial a_j} - \frac{\partial^2\{\delta_t\}}{\partial a_i \partial a_j}\right) - b_2\frac{\partial^2\{\dot{\delta}_t\}}{\partial a_i \partial a_j} - b_3\frac{\partial^2\{\ddot{\delta}_t\}}{\partial a_i \partial a_j}. \tag{5.9}$$

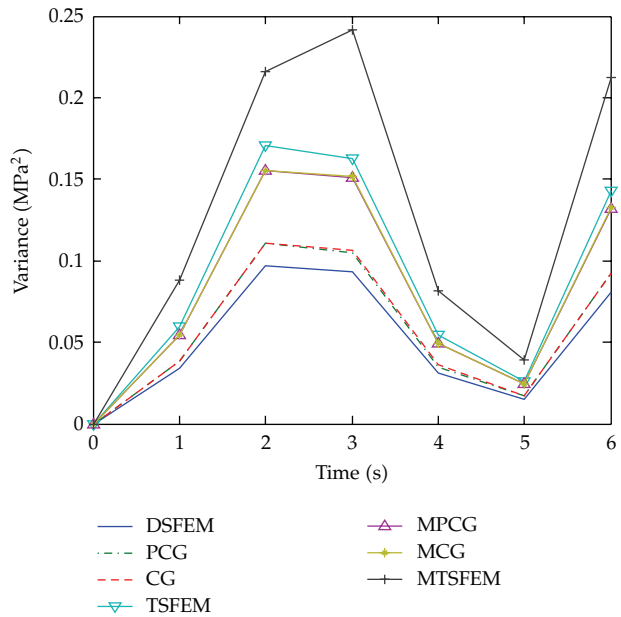

Figure 9: The variance of horizontal stress at node 5 for larger covariances.

The partial derivative of (5.8) with respect to a_j is given by

$$\frac{\partial^2\{\dot{\delta}_{t+\Delta t}\}}{\partial a_i \partial a_j} = \frac{\partial^2\{\dot{\delta}_t\}}{\partial a_i \partial a_j} + b_6 \frac{\partial^2\{\ddot{\delta}_t\}}{\partial a_i \partial a_j} + b_7 \frac{\partial^2\{\ddot{\delta}_{t+\Delta t}\}}{\partial a_i \partial a_j}. \tag{5.10}$$

Equations (5.7), (5.8), (5.9) and (5.10), must be calculated for the following iteration.

Then, the mean and variance of displacement are obtained at time $t + i_1 \Delta t$ ($i_1 = 2, 3, \ldots, n_1$) step by step.

The partial derivative of (4.8) with respect to a_i is given by

$$\frac{\partial\{\sigma\}}{\partial a_i} = \frac{\partial[D]}{\partial a_i}[B]\left\{\delta_{t'}^d\right\} + [D]\frac{\partial[B]}{\partial a_i}\left\{\delta_{t'}^d\right\} + [D][B]\frac{\partial\left\{\delta_{t'}^d\right\}}{\partial a_i}. \tag{5.11}$$

The partial derivative of (5.11) with respect to a_j is given by

$$\begin{aligned}\frac{\partial^2\{\sigma\}}{\partial a_i \partial a_j} = {} & \frac{\partial^2[D]}{\partial a_i \partial a_j}[B]\left\{\delta_{t'}^d\right\} + \frac{\partial[D]}{\partial a_i}\frac{\partial[B]}{\partial a_j}\left\{\delta_{t'}^d\right\} + \frac{\partial[D]}{\partial a_i}[B]\frac{\partial\left\{\delta_{t'}^d\right\}}{\partial a_j} \\ & + \frac{\partial[D]}{\partial a_j}\frac{\partial[B]}{\partial a_i}\left\{\delta_{t'}^d\right\} + [D]\frac{\partial^2[B]}{\partial a_i \partial a_j}\left\{\delta_{t'}^d\right\} + [D]\frac{\partial[B]}{\partial a_i}\frac{\partial\left\{\delta_{t'}^d\right\}}{\partial a_j} \\ & + \frac{\partial[D]}{\partial a_j}[B]\frac{\partial\left\{\delta_{t'}^d\right\}}{\partial a_i} + [D]\frac{\partial[B]}{\partial a_j}\frac{\partial\left\{\delta_{t'}^d\right\}}{\partial a_i} + [D][B]\frac{\partial^2\left\{\delta_{t'}^d\right\}}{\partial a_i \partial a_j}.\end{aligned} \tag{5.12}$$

The stress is expanded at mean value point $\overline{a} = (\overline{a}_1, \overline{a}_2, \ldots, \overline{a}_i, \ldots, \overline{a}_{n_1})^T$ by means of a Taylor series. By taking the expectation operator for two sides of the above (4.8), the mean of stress is obtained as

$$\mu\{\sigma\} \approx \{\sigma\}|_{a=\overline{a}} + \frac{1}{2}\sum_{i=1}^{N}\sum_{j=1}^{N} \frac{\partial^2\{\sigma\}}{\partial a_i \partial a_j}\bigg|_{a=\overline{a}} \mathrm{Cov}(a_i, a_j), \tag{5.13}$$

where $\mu\{\sigma\}$ expresses the mean of σ and $\mathrm{Cov}(a_i, a_j)$ is the covariance between a_i and a_j. The variance of σ is given by

$$\mathrm{Var}\{\sigma\} \approx \sum_{i=1}^{N}\sum_{j=1}^{N} \frac{\partial\{\sigma\}}{\partial a_i}\bigg|_{a=\overline{a}} \cdot \frac{\partial\{\sigma\}}{\partial a_j}\bigg|_{a=\overline{a}} \cdot \mathrm{Cov}(a_i, a_j). \tag{5.14}$$

6. Numerical Example

Figure 1 shows a cantilever beam. The length is 1 m, the width is 0.2 m, and the height is 0.05 m. The load subjected to the cantilever beam is 100sin(100t)N. Its material is the concrete. It is divided into 400 rectangle elements that have 505 nodes and 400 midpoints. Young's modulus is regarded as a stochastic process. For numerical calculation, the means of Young's modulus at each node and the midpoint within an element are $c_1(1.0 + \theta_1 x_i'/L)$. Horizontal coordinates of each node and the midpoint within an element are x_i'. The covariance of Young's modulus between any two nodes, between two midpoints and between each node and each midpoint are $c_2(1.0 + \theta_2 x_i/l)$. $c_1, c_2, \theta_1, \theta_2, l, L$ are constants. The distances between any two nodes, between two midpoints, and between each node and each midpoint are x_i. Figure 2 shows the mean of vertical displacement at node 505. the DSFEM simulates 100 samples. It is common knowledge that The DSFEM approaches the accurate solution gradually with the increase of the number of simulations. The DSFEM uses the Cholesky decomposition to solve linear equations and provides the reference solution. Figure 3 shows the variance of vertical displacement at node 505. Figure 4 shows the mean of horizontal stress at node 5. Figure 5 shows the variance of horizontal stress at node 5. Table 1 shows results obtained from the PCG, the CG, the TSFEM, the MPCG, the MCG and the MTSFEM compare with those of the DSFEM within six seconds. The PCG adopts the preconditioned Conjugate Gradient method to solve linear equations. The errors of the PCG, the CG and the TSFEM are smaller than those of the MPCG, the MCG, and the MTSFEM. The maximum error is obtained by the MTSFEM.The minimum error is produced by the PCG.Table 2 compares the CPU times of the above-mentioned methods when the cantilever beam has vibrated for six seconds.The PCG requires the least amount of CPU time. The MTSFEM requires the greatest amount of CPU time.

In order to test accuracy and computational efficiency of the above-mentioned methods, larger covariances of Young's modulus are selected. Figure 6 shows the mean of vertical displacement at node 505. Figure 7 shows the variance of vertical displacement at node 505. Figure 8 shows the mean of horizontal stress at node 5. Figure 9 shows the variance of horizontal stress at node 5.Table 3 indicates the errors of the above-mentioned methods compare to results of the DSFEM. The results produced by the PCG and the CG are close to those produced by the DSFEM. The TSFEM and the MTSFEM cannot achieve satisfactory results.

7. Conclusion

In this paper, improved midpoint method has the advantage of high accuracy. It can be conveniently applied to DSFEM, PSFEM, NSFEM, and CG. The mechanical vibration in a linear system is investigated by using the Taylor expansion. When Young's modulus is assumed to be a stochastic process, different samples of random variables are simulated. The combination of the CG method and Monte Carlo method makes this an effective method for analyzing a large vibration problem with the characteristics of high accuracy and quick convergence.

Appendices

A. Covariance of Young's Modulus between Two Elements

The covariance of Young's modulus between one element containing m nodes and another element containing n nodes is obtained by

$$\begin{aligned}
\operatorname{Cov}(a_e, a_f) &= \operatorname{Cov}\left(\frac{a_{em1} + a_{em2} + \cdots + a_{emm} + a_{eml}}{m+1}, \frac{a_{fn1} + a_{fn2} + \cdots + a_{fnn} + a_{fnl}}{m+1}\right) \\
&= \frac{1}{(m+1)(n+1)}\left[\operatorname{Cov}(a_{em1}, a_{fn1} + a_{fn2} + \cdots a_{fnn} + a_{fnl})\right. \\
&\qquad \left. + \operatorname{Cov}(a_{em2} + \cdots + a_{emm} + a_{eml}, a_{fn1} + a_{fn2} + \cdots a_{fnn} + a_{fnl})\right] \\
&= \frac{1}{(m+1)(n+1)}\left[\operatorname{Cov}(a_{em1}, a_{fn1}) + \operatorname{Cov}(a_{em1}, a_{fn2})\right. \\
&\qquad \left. + \cdots + \operatorname{Cov}(a_{em1}, a_{fnn}) + \operatorname{Cov}(a_{em1}, a_{fnl})\right] \\
&\quad + \frac{1}{(m+1)(n+1)}\operatorname{Cov}(a_{em2} + \cdots + a_{emm} + a_{eml}, a_{fn1} + a_{fn2} + \cdots + a_{fnn} + a_{fnl}) \\
&= \frac{1}{(m+1)(n+1)}\left(\sum_{g_1=1}^{m}\sum_{g_3=1}^{n}\operatorname{Cov}(a_{emg_1}, a_{fng_3})\right) \\
&\quad + \frac{1}{(m+1)(n+1)}\left(\sum_{g_1=1}^{m}\operatorname{Cov}(a_{emg_1}, a_{fnl})\right) \\
&\quad + \frac{1}{(m+1)(n+1)}\left(\sum_{g_3=1}^{n}\operatorname{Cov}(a_{eml}, a_{fng_3})\right) \\
&\quad + \frac{1}{(m+1)(n+1)}\operatorname{Cov}(a_{eml}, a_{fnl}),
\end{aligned} \tag{A.1}$$

where $\operatorname{Cov}(a_{emg_1}, a_{fng_3})$ = the covariance of Young's modulus between node g_1 ($g_1 = 1, 2, \ldots, m$) of element e and node g_3 ($g_3 = 1, 2, \ldots, n$) of element f, $\operatorname{Cov}(a_{emg_1}, a_{fnl})$ = the

covariance of Young's modulus between node g_1 of element e and the midpoint of element f, $\mathrm{Cov}(a_{eml}, a_{fng_3})$ = the covariance of Young's modulus between the midpoint of element e and node g_3 of element f, and $\mathrm{Cov}(a_{eml}, a_{fnl})$ = the covariance of Young's modulus between the midpoint of element e and the midpoint of element f.

The covariance of Young's modulus between two elements that each has n nodes is given by

$$\begin{aligned}\mathrm{Cov}(a_f, a_{f'}) = {} & \frac{1}{(n+1)^2}\left(\sum_{g_3=1}^{n}\sum_{g_4=1}^{n}\mathrm{Cov}(a_{fng_3}, a_{f'ng_4})\right) \\ & + \frac{1}{(n+1)^2}\left(\sum_{g_3=1}^{n}\mathrm{Cov}(a_{fng_3}, a_{f'nl})\right) \\ & + \frac{1}{(n+1)^2}\left(\sum_{g_4=1}^{n}\mathrm{Cov}(a_{fnl}, a_{f'ng_4}) + Cov(a_{fnl}, a_{f'nl})\right),\end{aligned} \tag{A.2}$$

where $\mathrm{Cov}(a_{fng_3}, a_{f'ng_4})$ = the covariance of Young's modulus between node g_3 ($g_3 = 1, 2, \ldots, n$) of element f and node g_4 ($g_4 = 1, 2, \ldots, n$) of element f', $\mathrm{Cov}(a_{fng_3}, a_{f'nl})$ = the covariance of Young's modulus between node g_3 of element f and the midpoint of element f', $\mathrm{Cov}(a_{fnl}, a_{f'ng_4})$ = the covariance of Young's modulus between the midpoint of element f and node g_4 of element f', and $\mathrm{Cov}(a_{fnl}, a_{f'nl})$ = the covariance of Young's modulus between the midpoint of element f and the midpoint of element f'.

B. Newmark Method

For ease of programming, the comprehensive calculation steps of the Newmark method are as follows.

In the initial calculation the matrices $[K]$, $[M]$, and $[C]$ are formed. The initial values $\{\delta_t\}$, $\{\dot{\delta}_t\}$, $\{\ddot{\delta}_t\}$ are given. After selecting step Δt and parameters γ, β, the following relevant parameters are calculated:

$$\begin{gathered}\gamma \geq 0.50, \quad \beta \geq 0.25(0.5+\gamma)^2, \\ b_0 = \frac{1}{\beta(\Delta t)^2}, \quad b_1 = \frac{\gamma}{\beta\Delta t}, \quad b_2 = \frac{1}{\beta\Delta t}, \\ b_3 = \frac{1}{2\beta} - 1, \quad b_4 = \frac{\gamma}{\beta} - 1, \quad b_5 = \frac{\Delta t}{2}\left(\frac{\gamma}{\beta} - 2\right), \\ b_6 = \Delta t(1-\gamma), \quad b_7 = \gamma\Delta t.\end{gathered} \tag{B.1}$$

The stiffness matrix is defined as

$$\left[\widetilde{K}\right] = [K] + b_0[M] + b_1[C]. \tag{B.2}$$

The stiffness matrix inversion $[\widetilde{K}]^{-1}$ is solved.

Calculation of each step time At time $t+\triangle t$, the load vector is defined as

$$\left\{\widetilde{F}_{t+\Delta t}\right\} = \{F_{t+\Delta t}\} + [M]\left(b_0\{\delta_t\} + b_2\{\dot{\delta}_t\} + b_3\{\ddot{\delta}_t\}\right) + [C]\left(b_1\{\delta_t\} + b_4\{\dot{\delta}_t\} + b_5\{\ddot{\delta}_t\}\right). \tag{B.3}$$

At time $t + \Delta t$, the displacement vector is given by

$$\{\delta_{t+\Delta t}\} = \left[\widetilde{K}\right]^{-1}\left\{\widetilde{F}_{t+\Delta t}\right\}. \tag{B.4}$$

At time $t + \Delta t$, the velocity vector and acceleration vector are obtained as

$$\begin{aligned}\left\{\ddot{\delta}_{t+\triangle t}\right\} &= b_0(\{\delta_{t+\Delta t}\} - \{\delta_t\}) - b_2\{\dot{\delta}_t\} - b_3\{\ddot{\delta}_t\},\\ \left\{\dot{\delta}_{t+\triangle t}\right\} &= \left\{\dot{\delta}_t\right\} + b_6\left\{\ddot{\delta}_t\right\} + b_7\left\{\ddot{\delta}_{t+\triangle t}\right\}.\end{aligned} \tag{B.5}$$

Vectors $\{\delta_{t+i_1\Delta t}\}$, $\{\dot{\delta}_{t+i_1\triangle t}\}$, and $\{\ddot{\delta}_{t+i_1\triangle t}\}$ are solved at time $t + i_1\Delta t$ $(i_1 = 2, 3, \ldots, n_1)$ step by step.

References

[1] A. Der Kiureghian and J.-B. Ke, "The stochastic finite element method in structural reliability," *Probabilistic Engineering Mechanics*, vol. 3, no. 2, pp. 83–91, 1988.

[2] E. Vanmarcke and M. Grigoriu, "Stochastic finite element analysis of simple beams," *Journal of Engineering Mechanics*, vol. 109, no. 5, pp. 1203–1214, 1983.

[3] S. Chakraborty and B. Bhattacharyya, "An efficient 3D stochastic finite element method," *International Journal of Solids and Structures*, vol. 39, no. 9, pp. 2465–2475, 2002.

[4] W. Q. Zhu, Y. J. Ren, and W. Q. Wu, "Stochastic FEM based on local averages of random vector fields," *Journal of Engineering Mechanics*, vol. 118, no. 3, pp. 496–511, 1992.

[5] W. K. Liu, T. Belytschko, and A. Mani, "Random field finite elements," *International Journal for Numerical Methods in Engineering*, vol. 23, no. 10, pp. 1831–1845, 1986.

[6] P. D. Spanos and R. Ghanem, "Stochastic finite element expansion for random media," *Journal of Engineering Mechanics*, vol. 115, no. 5, pp. 1035–1053, 1989.

[7] G. Deodatis, "Bounds on response variability of stochastic finite element systems," *Journal of Engineering Mechanics*, vol. 116, no. 3, pp. 565–585, 1990.

[8] M. Shinozuka and G. Deodatis, "Response variability of stochastic finite element systems," *Journal of Engineering Mechanics*, vol. 114, no. 3, pp. 499–519, 1988.

[9] C.-C. Li and A. Der Kiureghian, "Optimal discretization of random fields," *Journal of Engineering Mechanics*, vol. 119, no. 6, pp. 1136–1154, 1993.

[10] J. Astill, C. J. Nosseir, and M. Shinozuka, "Impact loading on structures with random properties," *Journal of Structural Mechanics*, vol. 1, no. 1, pp. 63–67, 1972.

[11] F. Yamazaki, M. Shinozuka, and G. Dasgupta, "Neumann expansion for stochastic finite element analysis," *Journal of Engineering Mechanics*, vol. 114, no. 8, pp. 1335–1354, 1988.

[12] M. Papadrakakis and V. Papadopoulos, "Robust and efficient methods for stochastic finite element analysis using Monte Carlo simulation," *Computer Methods in Applied Mechanics and Engineering*, vol. 134, no. 3-4, pp. 325–340, 1996.

[13] X. Q. Peng, L. Geng, W. Liyan, G. R. Liu, and K. Y. Lam, "A stochastic finite element method for fatigue reliability analysis of gear teeth subjected to bending," *Computational Mechanics*, vol. 21, no. 3, pp. 253–261, 1998.

[14] K. Handa and K. Andersson, "Application of finite element methods in the statistical analysis of structures," in *Proceedings of the 3rd International Conference on Structure Safety and Reliability*, Trondheim, Norway, 1981.
[15] T. Hisada and S. Nakagiri, "Role of the stochastic finite elenent method in structural safety and reliability," in *Proceedings of the 4th International Conference on Structure Safety and Reliability*, Kobe, Japan, 1985.
[16] S. Mahadevan and S. Mehta, "Dynamic reliability of large frames," *Computers and Structures*, vol. 47, no. 1, pp. 57–67, 1993.
[17] Q.-L. Zhang and U. Peil, "Random finite element analysis for stochastical responses of structures," *Computers and Structures*, vol. 62, no. 4, pp. 611–616, 1997.
[18] W. K. Liu, T. Belytschko, and A. Mani, "Probabilistic finite elements for nonlinear structural dynamics," *Computer Methods in Applied Mechanics and Engineering*, vol. 56, no. 1, pp. 61–81, 1986.
[19] Z. Lei and C. Qiu, "A dynamic stochastic finite element method based on dynamic constraint mode," *Computer Methods in Applied Mechanics and Engineering*, vol. 161, no. 3-4, pp. 245–255, 1998.
[20] S. Chakraborty and S. S. Dey, "A stochastic finite element dynamic analysis of structures with uncertain parameters," *International Journal of Mechanical Sciences*, vol. 40, no. 11, pp. 1071–1087, 1998.
[21] Z. Lei and C. Qiu, "Neumann dynamic stochastic finite element method of vibration for structures with stochastic parameters to random excitation," *Computers and Structures*, vol. 77, no. 6, pp. 651–657, 2000.
[22] Z. Lei and C. Qiu, "A stochastic variational formulation for nonlinear dynamic analysis of structure," *Computer Methods in Applied Mechanics and Engineering*, vol. 190, no. 5–7, pp. 597–608, 2000.

Hindawi Publishing Corporation
Mathematical Problems in Engineering
Volume 2010, Article ID 562539, 15 pages
doi:10.1155/2010/562539

Research Article

Nonlinear Free Vibration for Viscoelastic Moderately Thick Laminated Composite Plates with Damage Evolution

Y. F. Zheng and L. Q. Deng

College of Civil Engineering, Fuzhou University, Fuzhou 350108, China

Correspondence should be addressed to Y. F. Zheng, zheng_yufang@163.com

Received 22 December 2009; Accepted 20 March 2010

Academic Editor: Carlo Cattani

The nonlinear free vibration for viscoelastic cross-ply moderately thick laminated composite plates under considering transverse shear deformation and damage effect is investigated. Based on the Timoshenko-Mindlin theory, strain-equivalence hypothesis, and Boltzmann superposition principle, the nonlinear free vibration governing equations for viscoelastic moderately thick laminated plates with damage are established and solved by the Galerkin method, Simpson integration, Newton-Cotes, Newmark, and iterative methods. In the numerical results, the effects of transverse shear, material viscoelasticity, span-thickness ratio, aspect ratio, and damage effect on the nonlinear free vibrating frequency of the viscoelastic cross-ply moderately thick laminated plates are discussed.

1. Introduction

The structure will present the resonance phenomenon when the external excitation frequency is near to a certain natural frequency of the structure during the service life of the structures. Structure destructions caused by the resonance are prevalent in the practical engineering. The damage will emerge in the viscoelastic composite structures during the process of vibration and lead to the change of the dynamic behavior. When the damage develops, the structure will probably enter into the resonant state. As soon as the resonance appears, the stress values in the structure will increase, which will cause the development of the damage accelerate. Therefore, it is a very important research field to investigate the nonlinear dynamic behavior of viscoelastic laminated plates with damage effect.

Extensive studies have been made in dynamics of viscoelastic homogeneous structures. On the basis of the linear theory and the concept of the Lyapunov exponents, Aboudi and Cederbaum [1] investigated the dynamic stability of viscoelastic rectangular plates.

Librescu and Chandiramani [2] analyzed the dynamic stability of transversely isotropic viscoelastic plates. Sun and Zhang [3] investigated the chaotic behaviors of viscoelastic rectangular plates subjected to an in-plane periodic load and pointed out that the stability of the structure could be increased by adjusting the material parameters. Chen et al. [4] analyzed the steady-state response of the parametrically excited axially moving string constituted by the Boltzmann superposition principle. T. W. Kim and J. H. Kim [5] applied finite element analysis and the method of multiple scales to investigate the nonlinear vibrating frequency of viscoelastic laminated plates. Yu and Huang [6] presented a mathematical model for the vibration of a three-layered sandwich circular plate with viscoelastic core and discussed the effect of viscoelasticity on the frequency and amplitude. Relatively, few works have been devoted to study the effects of local damage and defects on the static and dynamic behavior of plates. Prabhakara and Datta [7, 8] analyzed the effect of the structural flaw on the natural frequency and buckling load of elastic plates subjected to a uniform in-plane load. Laura and Gutierrez [9] presented the linear fundamental frequency of transverse vibration for a damaged circular annular plate. However, the materials of the composite laminated plates have the property of viscoelasticity with the apparent creep phenomenon and relaxation characteristic, so it is very necessary to examine the influences of the damage effect on the nonlinear dynamics of viscoelastic laminated plates. Sheng and Cheng [10] used the history curve, phase trajectory diagram, Poincare map, bifurcation figure, and power spectrum to analyze the nonlinear dynamical properties of viscoelastic thick plate with damage. Fu et al. [11, 12] studied the nonlinear dynamic response of viscoelastic composite plate with transverse matrix cracks based on Schapery's 3D constitutive relationship. To author's work, Zheng and Fu [13] have studied the effect of local damage on the bifurcation and chaos of viscoelastic isotropic plates, and the nonlinear dynamic properties of viscoelastic isotropic plates and laminated plates with considering damage evolution [14–16].

In the present study, the nonlinear free vibration equations of the viscoelastic cross-ply moderately thick laminated composite plates with damage effect are established by applying Timoshenko-Mindlin theory, strain equivalence hypothesis, and Boltzmann superposition principle. By employing the standard linear solid model to express the viscoelastic material properties, Kachanov's approach to describe the damage evolution, and using the Galerkin method, Simpson integration, Newton-Cotes, Newmark method, and iterative procedure, the solutions of the problem are obtained. Numerical results are presented for different parameters.

2. Basic Equations

Consider a viscoelastic cross-ply rectangular plate having length a in the x direction, width b in the y direction, and thickness h in the z direction. The middle plane of the undeformed plate contains the x, y axes and the origin of the coordinate system is taken at the upper left corner of the plate. Based on Timoshenko-Mindlin kinematic hypotheses taking into account the transverse normal deformation, the displacement components u_1, u_2, and u_3 that include the effect of transverse shear deformation may be described by the following expressions [17]:

$$\begin{aligned} u_1(x,y,z,t) &= u(x,y,t) + z\varphi(x,y,t), \\ u_2(x,y,z,t) &= v(x,y,t) + z\psi(x,y,t), \\ u_3(x,y,z,t) &= w(x,y,t), \end{aligned} \tag{2.1}$$

where t is the time, u, v, and w are the values of u_1, u_2, and u_3 at the middle surface, and φ and ψ are rotation angles of the normal to the middle surface in the xz and yz planes, respectively. The nonlinear strain-displacement relationship can be written as

$$\begin{gathered}\varepsilon_x = \varepsilon_x^0 + z\kappa_x, \qquad \varepsilon_y = \varepsilon_y^0 + z\kappa_y, \qquad \varepsilon_{xy} = \varepsilon_{xy}^0 + z\kappa_{xy}, \\ \varepsilon_{xz} = \varphi + w_{,x}, \qquad \varepsilon_{yz} = \psi + w_{,y},\end{gathered} \tag{2.2}$$

where a comma denotes partial differentiation with respect to the corresponding coordinates and where

$$\begin{gathered}\varepsilon_x^0 = u_{,x} + \frac{1}{2}w_{,x}^2, \qquad \kappa_x = \varphi_{,x}, \\ \varepsilon_y^0 = v_{,y} + \frac{1}{2}w_{,y}^2, \qquad \kappa_y = \psi_{,y}, \\ \varepsilon_{xy}^0 = u_{,y} + v_{,x} + w_{,x}w_{,y}, \qquad \kappa_{xy} = \varphi_{,y} + \psi_{,x}.\end{gathered} \tag{2.3}$$

By applying the loading equivalent principle and assuming that the internal forces acting on any damaged section are the same as the ones before damage, the relationship between the effective stresses $\tilde{\sigma}_{ij}$ and the Cauchy stresses σ_{ij} is given as [18]

$$\begin{bmatrix}\tilde{\sigma}_x \\ \tilde{\sigma}_y \\ \tilde{\sigma}_{xy} \\ \tilde{\sigma}_{xz} \\ \tilde{\sigma}_{yz}\end{bmatrix} = \begin{bmatrix}\frac{1}{1-D_1} & 0 & 0 & 0 & 0 \\ 0 & \frac{1}{1-D_2} & 0 & 0 & 0 \\ 0 & 0 & \frac{1}{\sqrt{(1-D_1)(1-D_2)}} & 0 & 0 \\ 0 & 0 & 0 & \frac{1}{\sqrt{1-D_1}} & 0 \\ 0 & 0 & 0 & 0 & \frac{1}{\sqrt{1-D_2}}\end{bmatrix}\begin{bmatrix}\sigma_x \\ \sigma_y \\ \sigma_{xy} \\ \sigma_{xz} \\ \sigma_{yz}\end{bmatrix}, \tag{2.4}$$

where the anisotropic damage variables D_1 and D_2 are similarly defined as in [15, 16].

The above relation is expressed as follows:

$$\tilde{\boldsymbol{\sigma}} = \boldsymbol{\Lambda}\boldsymbol{\sigma}. \tag{2.5}$$

Employing the strain energy equivalence principle [19] and Boltzmann superposition principle [20], the stress-strain constitutive equations of the coupled viscoelastic/damage cross-ply laminated plates for the kth layer can be obtained in the following form:

$$\boldsymbol{\sigma}^{(k)}(t) = T^{(k)^{\mathrm{T}}}\boldsymbol{\Lambda}^{(k)^{-1}}\mathbf{Q}^{(k)}(0)\boldsymbol{\Lambda}^{(k)^{-1}}T^{(k)}\varepsilon^{(k)}(t) + T^{(k)^{\mathrm{T}}}\boldsymbol{\Lambda}^{(k)^{-1}}\int_0^t \dot{\mathbf{Q}}^{(k)}(t-\tau)\boldsymbol{\Lambda}^{(k)^{-1}}T^{(k)}\varepsilon^{(k)}(\tau)\mathrm{d}\tau \tag{2.6}$$

in which $\mathbf{Q}^{(k)}(t)$ is the time-dependent relaxation function and $\mathbf{Q}^{(k)}(0)$ is the initial Young's modulus of materials for the kth layer. For orthotropic viscoelastic materials and considering

that Poisson ratio contains constant, $T^{(k)}$ is the strain transformation relation for the kth layer, having

$$\mathbf{Q}^{(k)}(t) = \begin{bmatrix} \dfrac{E_1^{(k)}(t)}{1-\nu_{12}^{(k)}\nu_{21}^{(k)}} & \dfrac{\nu_{12}^{(k)}E_2^{(k)}(t)}{1-\nu_{12}^{(k)}\nu_{21}^{(k)}} & 0 & 0 & 0 \\ \dfrac{\nu_{12}^{(k)}E_2^{(k)}(t)}{1-\nu_{12}^{(k)}\nu_{21}^{(k)}} & \dfrac{E_2^{(k)}(t)}{1-\nu_{12}^{(k)}\nu_{21}^{(k)}} & 0 & 0 & 0 \\ 0 & 0 & G_{12}^{(k)}(t) & 0 & 0 \\ 0 & 0 & 0 & G_{13}^{(k)}(t) & 0 \\ 0 & 0 & 0 & 0 & G_{23}^{(k)}(t) \end{bmatrix},$$

$$\mathbf{T}^{(k)} = \begin{bmatrix} \cos^2\theta_k & \sin^2\theta_k & \sin\theta_k\cos\theta_k & 0 & 0 \\ \sin^2\theta_k & \cos^2\theta_k & -\sin\theta_k\cos\theta_k & 0 & 0 \\ -2\sin\theta_k\cos\theta_k & 2\sin\theta_k\cos\theta_k & \cos 2\theta_k & 0 & 0 \\ 0 & 0 & 0 & \cos\theta_k & \sin\theta_k \\ 0 & 0 & 0 & -\sin\theta_k & \cos\theta_k \end{bmatrix}, \tag{2.7}$$

where $c = \cos\theta_k$ and $s = \sin\theta_k$. θ_k is the angle measured from the fibre direction to coordinate axis ox for the kth layer; here $\theta_k = 0$ or $90°$

For simplification, (2.6) is rewritten as

$$\begin{aligned} \boldsymbol{\sigma}_1^{(k)} &= \mathbf{Q}^{d(k)} \otimes \varepsilon_1^{(k)}, \\ \boldsymbol{\sigma}_2^{(k)} &= \mathbf{Q}_*^{d(k)} \otimes \varepsilon_2^{(k)}, \end{aligned} \tag{2.8}$$

where the symbol ($\otimes$) is the Stieltjes convolution operation symbol, which is defined as

$$\begin{gathered} f \otimes g = \int_{-\infty}^{t} f(t-\tau)\mathrm{d}g(\tau) = f(0)g(t) + \int_0^t \dot{f}(t-\tau)g(\tau)\mathrm{d}\tau, \\ \boldsymbol{\sigma}_1^{(k)} = \left\{\sigma_x^{(k)}, \sigma_y^{(k)}, \sigma_{xy}^{(k)}\right\}^T, \qquad \boldsymbol{\sigma}_2^{(k)} = \left\{\sigma_{xz}^{(k)}, \sigma_{yz}^{(k)}\right\}^T, \\ \varepsilon_1{}^{(k)} = \left\{R_1^{(k)}\varepsilon_x, R_2^{(k)}\varepsilon_x, R_3^{(k)}\varepsilon_x, R_1^{(k)}\varepsilon_y, R_2^{(k)}\varepsilon_y, R_3^{(k)}\varepsilon_y, R_1^{(k)}\varepsilon_{xy}, R_2^{(k)}\varepsilon_{xy}, R_3^{(k)}\varepsilon_{xy}\right\}^T, \\ \varepsilon_2^{(k)} = \left\{R_4^{(k)}\varepsilon_{xz}, R_5^{(k)}\varepsilon_{xz}, R_4^{(k)}\varepsilon_{yz}, R_5^{(k)}\varepsilon_{yz}\right\}^T, \\ \mathbf{Q}^{d(k)} = \left[Q_{ij}^{d(k)}\right], \quad (i = 1,2,3,\ j = 1,2,\ldots,9), \qquad \mathbf{Q}_*^{d(k)} = \left[Q_{ij}^{d(k)}\right], \quad (i = 4,5,\ j = 1,2,3,4), \\ R_1^{(k)} = 1 - D_1^{(k)}, \qquad R_2^{(k)} = 1 - D_2^{(k)}, \qquad R_3^{(k)} = \sqrt{\left(1-D_1^{(k)}\right)\left(1-D_2^{(k)}\right)}, \\ R_4^{(k)} = \sqrt{\left(1-D_1^{(k)}\right)}, \qquad R_5^{(k)} = \sqrt{\left(1-D_2^{(k)}\right)}. \end{gathered} \tag{2.9}$$

The nonzero elements in $\mathbf{Q}^{d(k)}$ and $\mathbf{Q}_*^{d(k)}$ are given as

$$
\begin{gathered}
Q_{11}^{d(k)} = c^4 R_1^{(k)} Q_{11}^{(k)}, \qquad Q_{12}^{d(k)} = s^4 R_2^{(k)} Q_{22}^{(k)}, \qquad Q_{14}^{d(k)} = s^4 R_2^{(k)} Q_{12}^{(k)}, \qquad Q_{15}^{d(k)} = c^4 R_1^{(k)} Q_{12}^{(k)}, \\
Q_{21}^{d(k)} = c^4 R_2^{(k)} Q_{12}^{(k)}, \qquad Q_{22}^{d(k)} = s^4 R_1^{(k)} Q_{12}^{(k)}, \qquad Q_{24}^{d(k)} = s^4 R_1^{(k)} Q_{11}^{(k)}, \qquad Q_{25}^{d(k)} = c^4 R_2^{(k)} Q_{22}^{(k)}, \\
Q_{39}^{d(k)} = \left(c^2 - s^2\right)^2 R_3^{(k)} Q_{66}^{(k)}, \qquad Q_{41}^{d(k)} = c^2 R_4^{(k)} Q_{44}^{(k)}, \qquad Q_{42}^{d(k)} = s^2 R_5^{(k)} Q_{55}^{(k)}, \\
Q_{53}^{d(k)} = s^2 R_4^{(k)} Q_{44}^{(k)}, \qquad Q_{54}^{d(k)} = c^2 R_5^{(k)} Q_{55}^{(k)}.
\end{gathered}
\tag{2.10}
$$

As the classical plate theory, the stress resultants and couples are defined by

$$
\begin{gathered}
\left[N_x, N_y, N_{xy}\right] = \int_{-h/2}^{h/2} \left[\sigma_x^{(k)}, \sigma_y^{(k)}, \sigma_{xy}^{(k)}\right] \mathrm{d}z, \\
\left[Q_x, Q_y\right] = \int_{-h/2}^{h/2} \left[k_s \sigma_{xz}^{(k)}, k_s \sigma_{yz}^{(k)}\right] \mathrm{d}z, \\
\left[M_x, M_y, M_{xy}\right] = \int_{-h/2}^{h/2} \left[\sigma_x^{(k)}, \sigma_y^{(k)}, \sigma_{xy}^{(k)}\right] z \mathrm{d},
\end{gathered}
\tag{2.11}
$$

where, N_x, N_y, and N_{xy} are the membrane stress resultants per unit length, Q_x and Q_y are the transverse shear stress resultants per unit length, M_x, M_y, and M_{xy} are the bending and twisting moments per unit length, and k_s is the shear correction factor taking $k_s = 5/6$. Substituting (2.8) into (2.11), we can obtain

$$
\begin{gathered}
\begin{Bmatrix} \mathbf{N} \\ \mathbf{M} \end{Bmatrix} = \sum_{k=1}^{n} \begin{bmatrix} \mathbf{A}^{(k)} & \mathbf{B}^{(k)} \\ \mathbf{B}^{(k)} & \mathbf{D}^{(k)} \end{bmatrix} \otimes \begin{Bmatrix} \boldsymbol{\varepsilon}^{0(k)} \\ \boldsymbol{\kappa}^{0(k)} \end{Bmatrix}, \\
\begin{Bmatrix} Q_x \\ Q_y \end{Bmatrix} = \sum_{k=1}^{n} k_s \mathbf{C}^{(k)} \otimes \boldsymbol{\varepsilon}_2^{(k)},
\end{gathered}
\tag{2.12}
$$

where

$$
\begin{gathered}
\mathbf{N} = \left\{N_x, N_y, N_{xy}\right\}^T, \quad \mathbf{M} = \left\{M_x, M_y, M_{xy}\right\}^T, \\
\boldsymbol{\varepsilon}^{0(k)} = \left\{R_1^{(k)} \varepsilon_x^0, R_2^{(k)} \varepsilon_x^0, R_3^{(k)} \varepsilon_x^0, R_1^{(k)} \varepsilon_y^0, R_2^{(k)} \varepsilon_y^0, R_3^{(k)} \varepsilon_y^0, R_1^{(k)} \varepsilon_{xy}^0, R_2^{(k)} \varepsilon_{xy}^0, R_3^{(k)} \varepsilon_{xy}^0\right\}^T, \\
\boldsymbol{\kappa}^{0(k)} = \left\{R_1^{(k)} \kappa_x, R_2^{(k)} \kappa_x, R_3^{(k)} \kappa_x, R_1^{(k)} \kappa_y, R_2^{(k)} \kappa_y, R_3^{(k)} \kappa_y, R_1^{(k)} \kappa_{xy}, R_2^{(k)} \kappa_{xy}, R_3^{(k)} \kappa_{xy}\right\}^T,
\end{gathered}
\tag{2.13}
$$

and the elements in the coupled damaged stiffness tensors $\mathbf{A}^{(k)}$, $\mathbf{B}^{(k)}$, $\mathbf{D}^{(k)}$, and $\mathbf{C}^{(k)}$ are determined as

$$\begin{gathered}\left(A_{ij}^{(k)}, B_{ij}^{(k)}, D_{ij}^{(k)}\right) = \int_{z_{k-1}}^{z_k} Q_{ij}^{d(k)}\left(1, z, z^2\right)\mathrm{d}z \quad (i = 1,2,3,\ j = 1,2,\ldots,9), \\ C_{ij}^{(k)} = \int_{z_{k-1}}^{z_k} Q_{ij}^{d(k)}\mathrm{d}z \quad (i = 4,5,\ j = 1,2,3,4).\end{gathered} \tag{2.14}$$

Neglecting the effects of in-plane inertia, rotary inertia, and coupled normal-rotary inertia, the nonlinear equilibrium equations for moderately thick laminated plates are [21]

$$\begin{gathered}N_{x,x} + N_{xy,y} = 0, \\ N_{xy,x} + N_{y,y} = 0, \\ Q_{x,x} + Q_{y,y} + \left[N_x w_{,x} + N_{xy} w_{,y}\right]_{,x} + \left[N_{xy} w_{,x} + N_y w_{,y}\right]_{,y} = \rho_0 h \ddot{w}, \\ M_{x,x} + M_{xy,y} - Q_x = 0, \\ M_{y,y} + M_{xy,x} - Q_y = 0,\end{gathered} \tag{2.15}$$

where ρ_0 is the mass of unit volume. By substituting (2.12) into (2.15), and introducing the following dimensionless parameters:

$$\begin{gathered}\xi = \frac{x}{a}, \quad \eta = \frac{y}{b}, \quad \lambda = \frac{a}{b}, \quad \overline{\rho} = \frac{\rho_0 a^2}{t_1^2 E}, \quad H = \frac{a}{h}, \quad \tau = \frac{t}{t_1}, \quad U = \frac{au}{h^2}, \\ V = \frac{av}{h^2}, \quad W = \frac{w}{h}, \quad \mathbf{\Lambda} = H\varphi, \quad \Psi = H\psi, \quad \overline{A}_{ij}^{(k)} = \frac{A_{ij}^{(k)}}{Eh}, \quad \overline{B}_{ij}^{(k)} = \frac{B_{ij}^{(k)}}{Eh^2}, \\ \overline{D}_{ij}^{(k)} = \frac{D_{ij}^{(k)}}{Eh^3\mathrm{s}} \quad (i = 1,2,3,\ j = 1,2,\ldots,9), \quad \overline{C}_{ij}^{(k)} = \frac{C_{ij}^{(k)}}{Eh} \quad (i = 4,5,\ j = 1,2,3,4), \\ e_1^{(k)} = \frac{E_1^{(k)}(\tau)}{E}, \quad e_2^{(k)} = \frac{E_2^{(k)}(\tau)}{E}, \quad e_{12}^{(k)} = \frac{G_{12}^{(k)}(\tau)}{E}, \quad e_{13}^{(k)} = \frac{G_{13}^{(k)}(\tau)}{E}, \quad e_{23}^{(k)} = \frac{G_{23}^{(k)}(\tau)}{E},\end{gathered} \tag{2.16}$$

then, the dimensionless equilibrium equations of cross-ply laminated plates with the coupled effects of viscoelasticity and damage can be expressed as

$$\sum_{k=1}^{n}\left\{\sum_{i=1}^{2}\overline{A}_{1i}^{(k)}\otimes R_i^{(k)}\left(U_{,\xi\xi}+W_{,\xi}W_{,\xi\xi}\right)+\sum_{i=4}^{5}\lambda\overline{A}_{1i}^{(k)}\otimes R_{i-3}^{(k)}\left(V_{,\xi\eta}+\lambda W_{,\eta}W_{,\xi\eta}\right)+\sum_{i=1}^{2}\overline{B}_{1i}^{(k)}\otimes R_i^{(k)}\mathbf{\Lambda}_{,\xi\xi}\right.$$
$$+\lambda\sum_{i=4}^{5}\overline{B}_{1i}^{(k)}\otimes R_{i-3}^{(k)}\Psi_{,\xi\eta}+\lambda\overline{A}_{39}^{(k)}\otimes R_3^{(k)}\left(\lambda U_{,\eta\eta}+V_{,\xi\eta}+\lambda W_{,\eta}W_{,\xi\eta}+\lambda W_{,\xi}W_{,\eta\eta}\right)$$
$$\left.+\lambda\overline{B}_{39}^{(k)}\otimes R_3^{(k)}\left(\lambda\mathbf{\Lambda}_{,\eta\eta}+\Psi_{,\xi\eta}\right)\right\}=0,$$

$$\sum_{k=1}^{n}\left\{\overline{A}_{39}^{(k)}\otimes R_3^{(k)}\left(\lambda U_{,\xi\eta}+V_{,\xi\xi}+\lambda W_{,\eta}W_{,\xi\xi}+\lambda W_{,\xi}W_{,\xi\eta}\right)+\overline{B}_{39}^{(k)}\otimes R_3^{(k)}\left(\lambda\mathbf{\Lambda}_{,\xi\eta}+\Psi_{,\xi\xi}\right)\right.$$
$$+\lambda\sum_{i=1}^{2}\overline{A}_{2i}^{(k)}\otimes R_i^{(k)}\left(U_{,\xi\eta}+W_{,\xi}W_{,\xi\eta}\right)+\lambda^2\sum_{i=4}^{5}\overline{A}_{2i}^{(k)}\otimes R_{i-3}^{(k)}\left(V_{,\eta\eta}+\lambda W_{,\eta}W_{,\eta\eta}\right)$$
$$\left.+\lambda\sum_{i=1}^{2}\overline{B}_{2i}^{(k)}\otimes R_i^{(k)}\mathbf{\Lambda}_{,\xi\eta}+\lambda^2\sum_{i=4}^{5}\overline{B}_{2i}^{(k)}\otimes R_{i-3}^{(k)}\Psi_{,\eta\eta}\right\}=0,$$

$$\sum_{k=1}^{n}\left\{H^2k_s\sum_{i=1}^{2}\overline{C}_{4i}^{(k)}\otimes R_{i+3}^{(k)}\left(\mathbf{\Lambda}_{,\xi}+W_{,\xi\xi}\right)+H^2\lambda k_s\sum_{i=3}^{4}\overline{C}_{5i}^{(k)}\otimes R_{i+1}^{(k)}\left(\Psi_{,\eta}+\lambda W_{,\eta\eta}\right)\right.$$
$$+\left[\sum_{i=1}^{2}\overline{A}_{1i}^{(k)}\otimes R_i^{(k)}\left(U_{,\xi}+\frac{1}{2}W_{,\xi}^2\right)+\sum_{i=4}^{5}\overline{A}_{1i}^{(k)}\otimes R_{i-3}^{(k)}\left(\lambda V_{,\eta}+\frac{\lambda^2}{2}W_{,\eta}^2\right)\right.$$
$$\left.+\sum_{i=1}^{2}\overline{B}_{1i}^{(k)}\otimes R_i^{(k)}\mathbf{\Lambda}_{,\xi}+\lambda\sum_{i=4}^{5}\overline{B}_{1i}^{(k)}\otimes R_{i-3}^{(k)}\Psi_{,\eta}\right]W_{,\xi\xi}$$
$$+2\lambda\left[\overline{A}_{39}^{(k)}\otimes R_3^{(k)}\left(\lambda U_{,\eta}+V_{,\xi}+\lambda W_{,\xi}W_{,\eta}\right)+\overline{B}_{39}^{(k)}\otimes R_3^{(k)}\left(\lambda\mathbf{\Lambda}_{,\eta}+\Psi_{,\xi}\right)\right]W_{,\xi\eta}$$
$$+\lambda^2\left[\sum_{i=1}^{2}\overline{A}_{2i}^{(k)}\otimes R_i^{(k)}\left(U_{,\xi}+\frac{1}{2}W_{,\xi}^2\right)+\sum_{i=4}^{5}\lambda\overline{A}_{2i}^{(k)}\otimes R_{i-3}^{(k)}\left(V_{,\eta}+\frac{\lambda}{2}W_{,\eta}^2\right)\right.$$
$$\left.\left.+\sum_{i=1}^{2}\overline{B}_{2i}^{(k)}\otimes R_i^{(k)}\mathbf{\Lambda}_{,\xi}+\lambda\sum_{i=4}^{5}\overline{B}_{2i}^{(k)}\otimes R_{i-3}^{(k)}\Psi_{,\eta}\right]W_{,\eta\eta}\right\}-\overline{\rho}H^2\ddot{W}=0,$$

$$\sum_{k=1}^{n}\left\{\sum_{i=1}^{2}\overline{B}_{1i}^{(k)}\otimes R_i^{(k)}\left(U_{,\xi\xi}+W_{,\xi}W_{,\xi\xi}\right)+\sum_{i=4}^{5}\lambda\overline{B}_{1i}^{(k)}\otimes R_{i-3}^{(k)}\left(V_{,\xi\eta}+\lambda W_{,\eta}W_{,\xi\eta}\right)\right.$$
$$+\sum_{i=1}^{2}\overline{D}_{1i}^{(k)}\otimes R_i^{(k)}\mathbf{\Lambda}_{,\xi\xi}+\lambda\sum_{i=4}^{5}\overline{D}_{1i}^{(k)}\otimes R_{i-3}^{(k)}\Psi_{,\xi\eta}$$
$$+\lambda\overline{B}_{39}^{(k)}\otimes R_3^{(k)}\left(\lambda U_{,\eta\eta}+V_{,\xi\eta}+\lambda W_{,\eta}W_{,\xi\eta}+\lambda W_{,\xi}W_{,\eta\eta}\right)$$
$$\left.+\lambda\overline{D}_{39}^{(k)}\otimes R_3^{(k)}\left(\lambda\mathbf{\Lambda}_{,\eta\eta}+\Psi_{,\xi\eta}\right)-H^2k_s\sum_{i=1}^{2}\overline{C}_{4i}^{(k)}\otimes R_{i+3}^{(k)}\left(\mathbf{\Lambda}+W_{,\xi}\right)\right\}=0,$$

$$\sum_{k=1}^{n}\Bigg\{\overline{B}_{39}^{(k)}\otimes R_3^{(k)}\left(\lambda U_{,\xi\eta}+V_{,\xi\xi}+\lambda W_{,\eta}W_{,\xi\xi}+\lambda W_{,\xi}W_{,\xi\eta}\right)+\overline{D}_{39}^{(k)}\otimes R_3^{(k)}\left(\lambda\mathbf{\Lambda}_{,\xi\eta}+\Psi_{,\xi\xi}\right)$$
$$+\lambda\sum_{i=1}^{2}\overline{B}_{2i}^{(k)}\otimes R_i^{(k)}\left(U_{,\xi\eta}+W_{,\xi}W_{,\xi\eta}\right)+\lambda^2\sum_{i=4}^{5}\overline{B}_{2i}^{(k)}\otimes R_{i-3}^{(k)}\left(V_{,\eta\eta}+\lambda W_{,\eta}W_{,\eta\eta}\right)$$
$$+\lambda\sum_{i=1}^{2}\overline{D}_{2i}^{(k)}\otimes R_i^{(k)}\mathbf{\Lambda}_{,\xi\eta}+\lambda^2\sum_{i=4}^{5}\overline{D}_{2i}^{(k)}\otimes R_{i-3}^{(k)}\Psi_{,\eta\eta}-H^2k_s\sum_{i=3}^{4}\overline{C}_{5i}^{*(k)}\otimes R_{i+1}^{(k)}\left(\Psi+\lambda W_{,\eta}\right)\Bigg\}=0. \tag{2.17}$$

Suppose that all of the boundary conditions of the plate are simply supported. In such case, the dimensionless boundary conditions can be written as

$$\begin{aligned}\xi=0,1:&\quad U=V=W=\Psi=M_{\xi\xi}=0,\\ \eta=0,1:&\quad U=V=W=\mathbf{\Lambda}=M_{\eta\eta}=0.\end{aligned} \tag{2.18}$$

3. Solution Methodology

A solution for (2.17) in conjunction with the boundary condition (2.18) is sought in the following separable form:

$$\begin{aligned}U&=\sum_{m=1}^{\infty}\sum_{n=1,3,\ldots}^{\infty}f_u(\tau)\sin(2\pi m\xi)\sin(\pi n\eta),\\ V&=\sum_{m=1,3,\ldots}^{\infty}\sum_{n=1}^{\infty}f_v(\tau)\sin(\pi m\xi)\sin(2\pi n\eta),\\ W&=\sum_{m=1,3,\ldots}^{\infty}\sum_{n=1,3,\ldots}^{\infty}f_w(\tau)\sin(\pi m\xi)\sin(\pi n\eta),\\ \mathbf{\Lambda}&=\sum_{m=1,3,\ldots}^{\infty}\sum_{n=1,3,\ldots}^{\infty}f_\varphi(\tau)\cos(\pi m\xi)\sin(\pi n\eta),\\ \Psi&=\sum_{m=1,3,\ldots}^{\infty}\sum_{n=1,3,\ldots}^{\infty}f_\psi(\tau)\sin(\pi m\xi)\cos(\pi n\eta).\end{aligned} \tag{3.1}$$

Substituting (3.1) into the governing equations (2.17) and making use of the one-term approximation of the Galerkin method, we can transform the nonlinear integral-partial differential equations into the nonlinear integral-ordinary differential equations in terms of $f_u(\tau), f_v(\tau), f_w(\tau), f_\varphi(\tau)$, and $f_\psi(\tau)$. The domain is divided by square mesh into $M\times M$ divisions and the time τ is equally divided into small time segments $\Delta\tau$. The Simpson integral formula is used to compute the integrations with respect to the spatial coordinates and the Newton-Cotes trapezoidal rule is used to compute the integrations with respect to time.

Moreover, using the Newmark scheme, the acceleration item $\ddot{f}_w$ and velocity item $\dot{f}_w$ can be expressed as follows:

$$\begin{aligned} \ddot{f}_w^{(N)} &= \frac{4\left(f_w^{(N)} - f_w^{(N-1)}\right)}{(\Delta\tau)^2} - \frac{4\dot{f}_w^{(N-1)}}{\Delta\tau} - \ddot{f}_w^{(N-1)}, \\ \dot{f}_w^{(N)} &= \dot{f}_w^{(N-1)} + \frac{1}{2}\left[\ddot{f}_w^{(N-1)} + \ddot{f}_w^{(N)}\right]\Delta\tau, \end{aligned} \tag{3.2}$$

where $f_w^{(N)}$ denotes the value of $f_w(\tau)$ at the time $N\Delta\tau$. Through these treatings, (2.17) can be transformed into the nonlinear algebraic equations only with time. And the whole equations are iterated to seek solutions. At each step of the iteration, the nonlinear items are linearized. For example, at the step J, the nonlinear items may be transformed to

$$(X \cdot Y)_J = (X)_J \cdot (Y)_{J_P}, \tag{3.3}$$

where $(Y)_{J_P}$ is the average value of those obtained in the preceding two iterations. For the initial step of the iteration, it can be determined by using the quadratic extrapolation, that is,

$$(Y)_{J_P} = AA(Y)_{J-1} + BB(Y)_{J-2} + CC(Y)_{J-3}. \tag{3.4}$$

And for the different step of the iteration, the coefficients AA, BB, and CC can be expressed as follow:

$$\begin{aligned} J = 1&: \quad AA = 1, \quad BB = 0, \quad CC = 0, \\ J = 2&: \quad AA = 2, \quad BB = -1, \quad CC = 0, \\ J \geq 3&: \quad AA = 3, \quad BB = -3, \quad CC = 1. \end{aligned} \tag{3.5}$$

For every time step, the iteration lasts until the difference of the present value and the former is smaller than 0.1%; then continue the calculation of the next step.

4. Damage Evolution Equation

In the present research, the following damage evolution equation is employed [19, 22]:

$$\frac{\mathrm{d}D_i^{(k)}}{\mathrm{d}\tau} = \begin{cases} B_i\left(\dfrac{\sigma_i^{(k)}}{1 - D_i^{(k)}}\right)^{m_i}, & \sigma_i^{(k)} \geq \sigma_{D_i}^{(k)}, \\ 0, & \sigma_i^{(k)} < \sigma_{D_i}^{(k)}. \end{cases} \quad (i = 1, 2) \tag{4.1}$$

Table 1: Comparison of fundamental linear frequencies of laminated elastic plates ($a/h = 10$).

Reference [23]		Reference [24]		Present
SOT	CPT	FOT	TOT	FOT
12.527	15.104	12.163	11.958	12.2233

Here B_i and m_i are the material constants. $\sigma_{D_i}^{(k)}$ is the stress threshold value in the i direction at which the damage $D_i^{(k)}$ begins to grow, and

$$\sigma_1^{(k)} = \frac{1}{h^{(k)}} \int_{z_{k-1}}^{z_k} \tilde{\sigma}_x^{(k)} \mathrm{d}z, \qquad \sigma_2^{(k)} = \frac{1}{h^{(k)}} \int_{z_{k-1}}^{z_k} \tilde{\sigma}_y^{(k)} \mathrm{d}z. \tag{4.2}$$

Assume that there is no damage at initial time; thus, the damage values of all points are $D_1^{(k)}(0) = 0$ and $D_2^{(k)}(0) = 0$. When stopping iterative step J, we can obtain the five function values $f_u(\tau)$, $f_v(\tau)$, $f_w(\tau)$, $f_\varphi(\tau)$, and $f_\psi(\tau)$. Before continuing the next iterative step, it must determine whether the damage values of an arbitrary point of the plate develop. Therefore, firstly, the displacements of an arbitrary point of the plate can be obtained by using (3.1). Calculate the strains of an arbitrary point of the plate by using (2.2) and (2.3). Then, using (2.5), (2.8) and (4.2), $\sigma_1^{(k)}$and $\sigma_2^{(k)}$ can be obtained. Finally, use (4.1) to determine whether the damage grows. Suppose that $D_i^{(k)}(J)$ is the damage value of an arbitrary point for the kth layer in the i direction at the time $J\Delta\tau$. If $\sigma_i^{(k)} \geq \sigma_{D_i}^{(k)}$, then the damage value at the time $J\Delta\tau$ is

$$D_i^{(k)}(J) = D_i^{(k)}(J-1) + \dot{D}_i^{(k)}\left(D_i^{(k)}(J-1), \sigma_i^{(k)}\right)\Delta\tau. \tag{4.3}$$

and if $\sigma_i{}^{(k)} < \sigma_{D_i}^{(k)}$, then

$$D_i^{(k)}(J) = D_i^{(k)}(J-1). \tag{4.4}$$

5. Numerical Results

To ensure the accuracy and effectiveness of the present method, the fundamental frequencies of a three-layer symmetric cross-ply $[0°/90°/0°]$ laminated elastic plate without considering damage effect are solved firstly and the materials properties [23, 24] are given as $E_1 = 25E_2$, $G_{12} = G_{13} = 0.5E_2$, $G_{23} = 0.2E_2$, and $\nu_{12} = 0.25$. Define $\overline{\omega}_0 = (\omega_0 a^2/h)\sqrt{\rho_0/E_2}$, in which $\overline{\omega}_0$ and ω_0 are the dimensionless and dimensional linear frequencies of laminated elastic plates without damage, respectively. The fundamental frequencies are calculated and compared in Table 1 with those of [23, 24]. Table 1 shows that the present result approximately agrees with the result in [24] by the first-order shear-deformation theory (FOT). And for the moderately thick laminated plates, the FOT solution has small difference compared with the second-order shear-deformation theory (SOT) solution and third-order shear-deformation theory (TOT) solution, but large difference is compared with the classical plate theory (CPT). It is noted that the effect of the transverse shear deformation cannot be neglected for the moderately thick laminated plates.

Table 2: Effect of transverse shear on the nonlinear vibrating frequency Ω^* of laminated plates.

$w_{\max}/h$	Case	a/h			
		5	10	15	20
1	$T_s = 0, T_d = 0$	2.73182	1.33970	0.883711	0.677714
	$T_s = 0, T_d = 1$	2.38090	1.30900	0.872317	0.670063
	$T_s = 1, T_d = 0$	2.15917	1.21767	0.847933	0.649089
	$T_s = 1, T_d = 1$	1.90400	1.20830	0.840535	0.64502
2	$T_s = 0, T_d = 0$	3.92699	2.02683	1.36591	0.998917
	$T_s = 0, T_d = 1$	2.84119	1.74745	1.30736	0.991473
	$T_s = 1, T_d = 0$	3.69599	1.92329	1.32000	0.987922
	$T_s = 1, T_d = 1$	2.68778	1.65347	1.27967	0.981748

Consider the amplitudes and the frequencies varying with time and the viscoelasticity and damage developing with the increase of time, so we must elect the later vibrating period to be analyzed. Hence, the relationship of the average frequency and the maximum amplitude in the 20th period are presented. Also, assume that every layer has the same material and the identical thickness. The parameters used in numerical calculation are taken as

$$\begin{gathered}
e_1 = 9.75 + 0.25e^{-\alpha_1\tau}, \quad \alpha_1 = 0.022, \\
e_2 = 0.32 + 0.68e^{-\alpha_2\tau}, \quad \alpha_2 = 0.024, \quad \nu_{12} = 0.4, \\
e_{12} = 0.07 + 0.16e^{-\alpha_{12}\tau}, \quad \alpha_{12} = 0.026, \\
e_{13} = 0.07 + 0.16e^{-\alpha_{13}\tau}, \quad \alpha_{13} = 0.026, \\
e_{23} = 0.05 + 0.12e^{-\alpha_{23}\tau}, \quad \alpha_{23} = 0.026, \\
B_1 = 3.7 \times 10^{-12}\,\mathrm{MPa}^{-m_1}, \quad B_2 = 4.8 \times 10^{-11}\,\mathrm{MPa}^{-m_2}, \quad m_1 = m_2 = 3.
\end{gathered} \tag{5.1}$$

Define

$$\Omega^* = \Omega\sqrt{\frac{\rho_0 a^2}{E}}, \tag{5.2}$$

where Ω^* and Ω are the dimensionless and dimensional nonlinear free vibrating frequency of viscoelastic plates with damage, respectively.

Table 2 shows the effect of transverse shear deformation on the nonlinear free vibrating frequency of the viscoelastic cross-ply $[0°/90°/0°]$ laminated square plate with considering damage effect or without considering damage effect, in which $w_{\max}/h$ is the dimensionless maximum vibration amplitude of the center point of the plate (similarly below), T_s is the tracing constant which represents the influence of transverse shear when $T_s = 1$ and the effect is neglected when $T_s = 0$, as well as T_d is the tracing constant which represents the influence of damage when $T_d = 1$ and the effect is neglected when $T_d = 0$. From Table 2 it may be observed that the thicker the thickness of the laminated plate, the more significant the effect of transverse shear on the nonlinear free vibrating frequency of the laminated plate. And in all cases transverse shear results in a decrease of the vibrating frequency. Therefore, the effect of transverse shear deformation is considered in the following calculated examples.

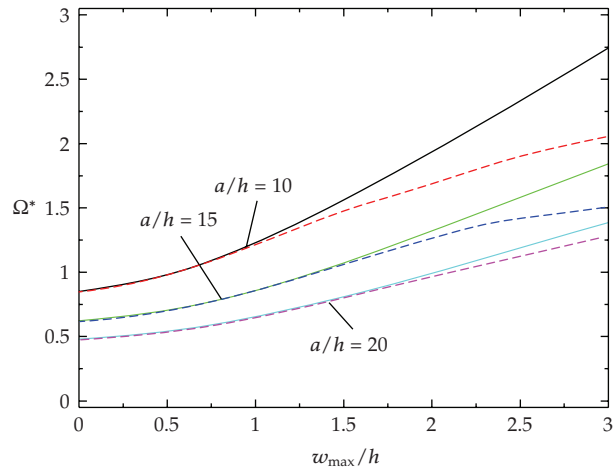

Figure 1: Effect of span-thickness ratio on the nonlinear amplitude-frequency curves of viscoelastic laminated plate.

Figure 1 shows the effect of span-thickness ratio a/h on the nonlinear free vibrating amplitude-frequency response curves of the viscoelastic cross-ply $[0°/90°/0°]$ laminated square plate. In Figure 1, the solid line denotes the undamaged condition, while the dashed line denotes the condition with damage evolution. It can be observed that with the decrease of the span-thickness ratio, namely, the increase of thickness of the plate, the nonlinear free vibrating frequency of the plate becomes bigger under a given vibration amplitude. Meanwhile, the frequency increases with increase of the vibration amplitude under a fixed span-thickness ratio. It can be also seen that the two curves with/without damage agree very well where the vibration amplitude is small. But with the increase of the vibration amplitude, the damage begins to appear and the accumulation velocity of the damage increases, which results in the stiffness of the plate becoming smaller. Accordingly, the nonlinear vibration frequency considering damage reduces remarkably than the result neglecting damage. Moreover, the less the span-thickness ratio of the plate is, the more the damage becomes, then the more the frequency descends.

Figure 2 displays the effect of aspect ratio λ on the nonlinear free vibrating amplitude-frequency response curves of the viscoelastic cross-ply $[0°/90°/0°]$ laminated plate. With the increase of the aspect ratio, that is, the width decreases under the condition that the length remains constant, the nonlinear free vibrating frequency of the plate becomes bigger. Similarly, under the given aspect ratio λ, the increase of the amplitude will expedite the accumulation velocity of the damage which will cause the more reduction in the stiffness of the plate. Consequently, the reduction of frequency caused by the damage will be more remarkable. The more the aspect ratio is, the more the frequency reduces.

The effect of material viscoelasticity parameter $\alpha(= \alpha_1 = \alpha_2 = \alpha_{12} = \alpha_{13} = \alpha_{23})$ on the nonlinear free vibrating frequency of the viscoelastic cross-ply $[0°/90°/0°]$ laminated square plate is listed in Table 3. The nonlinear free vibrating frequency of the laminated plate decreases with the higher value of the material viscoelasticity parameter. Due to the fact that viscoelastic material possesses dissipative nature and it acts as damping in the dynamic problems, it can improve the stability of the structure. Therefore, at the same condition, the higher viscoelasticity parameter can suppress the emergence of damage and

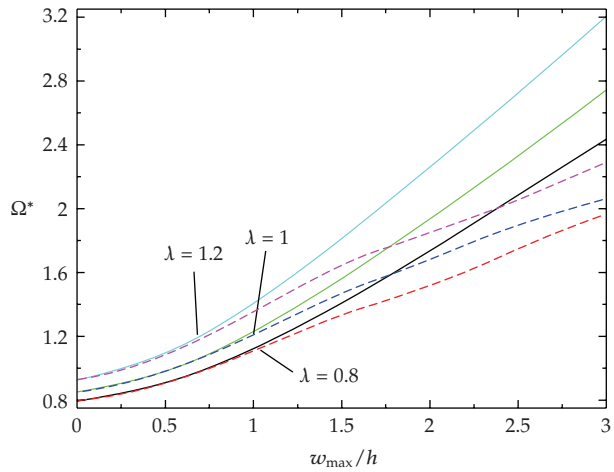

Figure 2: Effect of aspect ratio on the nonlinear amplitude-frequency curves of viscoelastic laminated plate ($a/h = 10$).

Table 3: Effect of viscoelasticity parameter on the nonlinear vibrating frequency Ω^* of laminated plates ($a/h = 15$).

α	Case	w_{max}/h				
		1	1.5	2	2.5	3
0	$T_d = 0$	0.850871	1.07477	1.35062	1.61494	1.85181
	$T_d = 1$	0.837562	1.04704	1.28289	1.46316	1.49701
0.5	$T_d = 0$	0.846744	1.06551	1.31475	1.56880	1.84306
	$T_d = 1$	0.838762	1.05061	1.25715	1.42693	1.49761
2	$T_d = 0$	0.820509	1.04718	1.28120	1.53075	1.79590
	$T_d = 1$	0.820229	1.04668	1.25565	1.42815	1.47021

cause the difference of the vibrating frequency between the damaged plate and undamaged plate decrease.

6. Conclusions

The nonlinear free vibration for viscoelastic cross-ply laminated composite plates under considering transverse shear deformation and damage effect has been investigated. The effects of transverse shear, material viscoelasticity, span-thickness ratio, aspect ratio, and damage effect on the nonlinear vibration of laminated plates have been discussed. In summary, the transverse shear effect on the nonlinear vibration of the viscoelastic laminated plates with damage is significant, especially, for the laminates with large thickness. This effect decreases the nonlinear frequency but does not change the general behavior of the nonlinear vibration in all cases. With the decrease of span-thickness ratio or increase of aspect ratio, the vibrating frequency increases, as well as the difference of vibration frequency between considering damage and neglecting damage becomes bigger. In addition, with the increase of the vibration amplitude, the damage begins to appear, the accumulation velocity of the damage increases, and the reduction of the vibrating frequency becomes more significant. The larger the material viscoelasticity, the smaller the reduction of the vibrating frequency.

Acknowledgments

The project was supported by the Young Technological Talents' Innovation Foundation of Fujian Province (2006F3077) and Scientific and Technical Development Foundation of Fuzhou University (2007-XQ-20).

References

[1] J. Aboudi and G. Cederbaum, "Dynamic stability analysis of viscoelastic plates by Lyapunov exponents," *Journal of Sound and Vibration*, vol. 139, no. 3, pp. 459–467, 1990.

[2] L. Librescu and N. K. Chandiramani, "Dynamic stability of transversely isotropic viscoelastic plates," *Journal of Sound and Vibration*, vol. 130, no. 3, pp. 467–486, 1989.

[3] Y. X. Sun and S. Y. Zhang, "Chaotic dynamic analysis of viscoelastic plates," *International Journal of Mechanical Sciences*, vol. 43, no. 5, pp. 1195–1208, 2001.

[4] L. Q. Chen, J. W. Zu, and J. Wu, "Steady-state response of the parametrically excited axially moving string constituted by the Boltzmann superposition principle," *Acta Mechanica*, vol. 162, no. 1–4, pp. 143–155, 2003.

[5] T. W. Kim and J. H. Kim, "Nonlinear vibration of viscoelastic laminated composite plates," *International Journal of Solids and Structures*, vol. 39, no. 10, pp. 2857–2870, 2002.

[6] S. C. Yu and S. C. Huang, "Vibration of a three-layered viscoelastic sandwich circular plate," *International Journal of Mechanical Sciences*, vol. 43, no. 10, pp. 2215–2236, 2001.

[7] D. L. Prabhakara and P. K. Datta, "Vibration and static stability characteristics of rectangular plates with a localized flaw," *Computers and Structures*, vol. 49, no. 5, pp. 825–836, 1993.

[8] D. L. Prabhakara and P. K. Datta, "Parametric instability characteristics of rectangular plates with localized damage subjected to in-plane periodic load," *Structural Engineering Review*, vol. 1, pp. 71–79, 1993.

[9] P. A. A. Laura and R. H. Gutierrez, "Transverse vibration of a damaged circular annular plate with a free edge," *Journal of Sound and Vibration*, vol. 241, no. 4, pp. 720–724, 2001.

[10] D. F. Sheng and C. J. Cheng, "Dynamical behaviors of nonlinear viscoelastic thick plates with damage," *International Journal of Solids and Structures*, vol. 41, no. 26, pp. 7287–7308, 2004.

[11] Y. Fu, P. Li, and Y. Zheng, "Analysis of nonlinear dynamic response for viscoelastic composite plate with transverse matrix cracks," *Acta Mechanica Solida Sinica*, vol. 17, no. 3, pp. 230–238, 2004.

[12] Y. Fu and Y. H. Lu, "Analysis of the nonlinear dynamic response of viscoelastic symmetric cross-ply laminated plates with transverse matrix crack," *Composite Structures*, vol. 72, no. 4, pp. 469–476, 2006.

[13] Y. F. Zheng and Y. Fu, "Effect of damage on bifurcation and chaos of viscoelastic plates," *International Journal of Nonlinear Sciences and Numerical Simulation*, vol. 6, no. 1, pp. 87–92, 2005.

[14] Y. F. Zheng and Y. Fu, "Effect of damage on nonlinear dynamic properties of viscoelastic rectangular plates," *Applied Mathematics and Mechanics*, vol. 26, no. 3, pp. 319–326, 2005.

[15] Y. F. Zheng and Y. Fu, "Nonlinear dynamic analysis of viscoelastic/damage behaviour for symmetric cross-ply laminated plates," *Advances in Vibration Engineering*, vol. 3, pp. 185–197, 2004.

[16] Y. F. Zheng and Y. Fu, "Analysis of nonlinear vibration for symmetric angle-ply laminated viscoelastic plates with damage," *Acta Mechanica Sinica*, vol. 21, no. 5, pp. 459–466, 2005.

[17] R. D. Mindlin, "Influences of rotatory inertia and shear inflexural motion of isotropic, elastic plates," *Journal of Applied Mechanics*, vol. 18, pp. 1031–1036, 1951.

[18] C. L. Chow and J. Wang, "An anisotropic theory of elasticity for continuum damage mechanics," *International Journal of Fracture*, vol. 33, no. 1, pp. 3–16, 1987.

[19] L. M. Kachanov, *Introduction to Continuum Damage Mechanics*, Martinus Nijhoff, Dordrecht, The Netherlands, 1986.

[20] A. C. Pipkin, *Lectures on Viscoelasticity Theory*, Springer, New York, NY, USA, 1986.

[21] Y. Nath and K. K. Shukla, "Non-linear transient analysis of moderately thick laminated composite plates," *Journal of Sound and Vibration*, vol. 247, no. 3, pp. 509–526, 2001.

[22] W. H. Zhang, *Numerical analysis of continuum damage mechanics*, Ph.D. thesis, University of New South Wales, Sydney, Australia, 1992.

[23] A. A. Khdeir and J. N. Reddy, "Free vibrations of laminated composite plates using second-order shear deformation theory," *Computers and Structures*, vol. 71, no. 6, pp. 617–626, 1999.

[24] L. Librescu, A. A. Khdeir, and D. Frederick, "A shear deformable theory of laminated composite shallow shell-type panels and their response analysis I: free vibration and buckling," *Acta Mechanica*, vol. 76, no. 1-2, pp. 1–33, 1989.

Hindawi Publishing Corporation
Mathematical Problems in Engineering
Volume 2010, Article ID 695025, 15 pages
doi:10.1155/2010/695025

Research Article

Identification of a Duffing Oscillator under Different Types of Excitation

E. Gandino and S. Marchesiello

Dipartimento di Meccanica, Politecnico di Torino, Corso Duca degli Abruzzi 24, 10129 Torino, Italy

Correspondence should be addressed to S. Marchesiello, stefano.marchesiello@polito.it

Received 11 January 2010; Revised 12 March 2010; Accepted 22 March 2010

Academic Editor: Carlo Cattani

In many engineering applications the dynamics may significantly be affected by nonlinear effects, which must be accounted for in order to accurately understand and robustly model the dynamics. From a practical point of view, it is very important to solve the *inverse problem* related to system identification and output prediction. In this paper the recently developed Nonlinear Subspace Identification (NSI) method is presented and applied to an oscillator described by the Duffing equation, with different types of excitation including random forces, which are demonstrated to be very suitable for the identification process. The estimates of system parameters are excellent and, as a consequence, the behaviour of the system, including the jump phenomena, is reconstructed to a high level of fidelity. In addition, the possible memory limitations affecting the method are overcome by the development of a novel algorithm, based on a specific computation of the QR factorisation.

1. Introduction

In many applications nonlinear effects may affect significantly the dynamics, even when the amplitude of the motion is sufficiently small. These dynamical effects must be accounted for in order to accurately understand and robustly model the dynamics.

In general, bifurcations of equilibrium positions or periodic orbits of nonlinear systems are the source of additional nonlinear features in the dynamics [1], which result in a qualitative change in the response and also in a substantial quantitative variation in oscillatory behaviour of the system. For example [2], in the externally excited pendulum a relatively small amplitude periodic attractor, under the variation of a control parameter (such as the frequency), may lose its stability at a saddle-node bifurcation in which the system may then start to oscillate with a relatively large amplitude.

Among essentially nonlinear dynamics caused by bifurcations [1], such as the possibility of multiple coexisting stable equilibrium positions (each with its own separate domain of attraction), this paper focuses on sudden nonlinear transitions between stable attractors (jumps) caused by nonlinear hysteresis phenomena.

Moving to the *inverse problem* of nonlinear systems, many studies have been recently conducted: in this case, system parameters are unknown and have to be estimated through an identification procedure, consisting in the development of mathematical models from input and output measurements performed on the real system.

Nonlinear system identification has been thoroughly investigated in recent years and many efforts have been spent leading to a large number of methods. An exhaustive list of the techniques elaborated to identify the behaviour of nonlinear dynamical systems is hard to write and, moreover, there is no general analysis method that can be applied to all systems in all circumstances. A comprehensive list describing the past and recent developments is given in [1].

One of the established techniques is the Restoring Force Surface (RFS) method, firstly introduced by Masri and Caughey [3]: this simple procedure allows a direct identification for single-degree-of-freedom (SDOF) nonlinear systems. There exist in the literature several applications of RFS method to experimental systems: in a recent paper [4], it is applied for the analysis of a nonlinear automotive damper. A similar approach is the Direct Parameter Estimation (DPE) method, which may be applied to multidegree-of-freedom (MDOF) nonlinear systems: a practical implementation of the procedure was made by Mohammad et al. [5].

Recent methods are suitable for identification of more complex nonlinear systems, in particular MDOF systems. One of them is the Conditioned Reverse Path (CRP) method, developed by Richards and Singh [6, 7]: this technique is based on the construction of a hierarchy of uncorrelated response components in the frequency domain, allowing the estimation of the coefficients of the nonlinearities away from the location of the applied excitation. One of the examples of experimental application is given by Kerschen et al. [8].

More recently, Adams and Allemang [9] proposed a frequency-domain method called Nonlinear Identification through Feedback of the Outputs (NIFO), which has demonstrated [10] some advantages with respect to the CRP, mainly due to the lighter conceptual and computing effort. This method exploits the spatial information and interprets nonlinear forces as unmeasured internal feedback forces.

Starting from the basic idea of NIFO, the Nonlinear Subspace Identification (NSI) method has been developed by Marchesiello and Garibaldi [11], showing a higher level of accuracy with respect to NIFO. NSI is a time-domain method which exploits the robustness and the high numerical performances of the subspace algorithms.

In this paper the NSI method is applied to a Duffing oscillator, which has been studied for many years as representative of many nonlinear systems [12]. This system can be considered in order to simply describe the sudden transitions between coexisting stable branches of solutions. For this type of system there are frequencies at which the vibration suddenly jumpsup or down, when it is excited harmonically with slowly changing frequency.

One of the main topics about the study of the Duffing oscillator consists in searching for analytical expressions of the jump frequencies and the amplitudes of vibration at these frequencies. For example, Worden [13] and Friswell and Penny [14] computed these points by using the harmonic balance method, while Malatkar and Nayfeh [15] determined the minimum excitation force required for the jump phenomenon to appear, by using a method based on the elimination theory of polynomials. A recent paper by Brennan et al. [16]

provides a full set of expressions determined by using the harmonic balance approach, as a link between the earlier analytical work and the later numerical studies.

In this paper the NSI estimates of system parameters are excellent and, as a consequence, the behaviour of the Duffing oscillator, including the jump phenomena, is reconstructed to a high level of fidelity.

In addition, the NSI method is enforced by the development of a new algorithm to compute the QR factorisation in a *Matlab* environment, in those cases in which the data matrix is too large to be stored or factorised. This new algorithm, which exploits some useful features of the Householder transformations, allows the NSI method to reach more accurate results in the parameter estimation.

2. Nonlinear Subspace Identification

2.1. Nonlinear Model

The adopted mathematical approach follows the one used in [11], in order to derive a mathematical model for a nonlinear dynamical system. The expression for a linear time-invariant system is first considered, as described by the following continuous state-space model:

$$\begin{aligned} \dot{x} &= A_c x + B_c u, \\ y &= Cx + Du, \end{aligned} \tag{2.1}$$

where the output $y(t)$ is a q-dimensional column vector, t is time, the input $u(t)$ is an m-dimensional column vector, and the order of the model, that is, the dimension of the state vector $x(t)$, is n.

A dynamical system with h degrees of freedom and with lumped nonlinear springs and dampers can be described by the following equation of motion:

$$M\ddot{z}(t) + C_v\dot{z}(t) + Kz(t) = f(t) - \sum_{j=1}^{p} \mu_j L_{nj} g_j(t) = f(t) + f_{nl}(t), \tag{2.2}$$

where M, C_v, and K are the mass, viscous damping, and stiffness matrices, respectively, $z(t)$ is the generalised displacement vector, and $f(t)$ is the generalised force vector, both of dimension h, at time t. Each of the p nonlinear components depends on the scalar nonlinear function $g_j(t)$, which specifies the class of the nonlinearity (e.g., Coulomb friction, clearance, quadratic damping, etc.), and on a scalar nonlinear coefficient μ_j. The vector L_{nj}, whose entries may assume the values 1, −1, or 0, is related to the location of the nonlinear element: it specifies the degrees-of-freedom joint by the jth nonlinear component and the sign of the term appearing in the equation of motion (2.2).

Written as in (2.2), the original system may be viewed as subjected to the external forces $f(t)$ and the internal feedback forces due to nonlinearities $f_{nl}(t)$, expressed as the sum of the p nonlinear components. This concept, already used in [9] to derive the NIFO frequency-domain method, is also on the basis of the present time-domain identification method.

Assuming that the measurements concern displacements only, the state-space formulation of the equation of motion, corresponding to a state vector chosen as $x = [z^T \quad \dot{z}^T]^T \in \mathbf{R}^{n\times 1}$ and to an input vector $u = [f(t)^T \quad -g_1(t) \quad \cdots \quad -g_p(t)]^T \in \mathbf{R}^{m\times 1}$, is

$$\begin{Bmatrix} \dot{z} \\ \ddot{z} \end{Bmatrix} = \begin{bmatrix} 0_{h\times h} & I_{h\times h} \\ -M^{-1}K & -M^{-1}C_v \end{bmatrix} \begin{Bmatrix} z \\ \dot{z} \end{Bmatrix} + \begin{bmatrix} 0_{h\times h} & 0_{h\times 1} & \cdots & 0_{h\times 1} \\ M^{-1} & M^{-1}\mu_1 L_{n1} & \cdots & M^{-1}\mu_p L_{np} \end{bmatrix} \begin{Bmatrix} f(t) \\ -g_1(t) \\ \vdots \\ -g_p(t) \end{Bmatrix}, \tag{2.3}$$

$$y = \begin{bmatrix} I_{h\times h} & 0_{h\times h} \end{bmatrix} \begin{Bmatrix} z \\ \dot{z} \end{Bmatrix} + \begin{bmatrix} 0_{h\times h} & 0_{h\times 1} & \cdots & 0_{h\times 1} \end{bmatrix} \begin{Bmatrix} f(t) \\ -g_1(t) \\ \vdots \\ -g_p(t) \end{Bmatrix}, \tag{2.4}$$

and matrices $A_c \in \mathbf{R}^{n\times n}, B_c \in \mathbf{R}^{n\times m}, C \in \mathbf{R}^{l\times n}$, and $D \in \mathbf{R}^{l\times m}$ of (2.1) are consequently defined.

Then the continuous model of (2.1) may be converted [11] into the following discrete state-space model:

$$\begin{aligned} x_{r+1} &= Ax_r + Bu_r, \\ y_r &= Cx_r + Du_r, \end{aligned} \tag{2.5}$$

where $A = \mathrm{e}^{A_c \Delta t} \in \mathbf{R}^{n\times n}$ and $B = (\mathrm{e}^{A_c \Delta t} - I)A_c^{-1}B_c \in \mathbf{R}^{n\times m}$.

2.2. Subspace Identification

Given a deterministic-stochastic state-space model with s measurements of the input and of the output

$$\begin{aligned} x_{r+1} &= Ax_r + Bu_r + w_r, \\ y_r &= Cx_r + Du_r + v_r, \end{aligned} \tag{2.6}$$

where w_r and v_r are unmeasurable vector signals called process error and measurement error, respectively, the subspace identification problem consists in estimating the model order n and the system matrices A, B, C, and D up to within a similarity transformation, which does not affect the parameter estimation.

In the "data-driven approach" [17] the input data are gathered in a block Hankel matrix

$$U_{0|2i-1} \stackrel{\text{def}}{=} \begin{bmatrix} u_0 & u_1 & \cdots & u_{j-1} \\ u_1 & u_2 & \cdots & u_j \\ \vdots & \vdots & \ddots & \vdots \\ u_{2i-1} & u_{2i} & \cdots & u_{2i+j-2} \end{bmatrix} \in \mathbf{R}^{2mi\times j}, \tag{2.7}$$

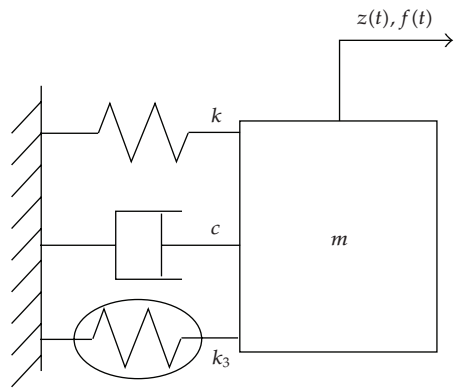

Figure 1: The nonlinear system described by the Duffing equation.

Table 1: System parameters.

m (kg)	k (N/m)	c (Ns/m)	k_3 (N/m^3)
1.3	800	1.3	1.5×10^6

where the number of block rows i is a user-defined index. The number of columns j is typically equal to $s - 2i + 1$, which implies that all given data are used. The output block Hankel matrix $Y_{0|2i-1} \in \mathbf{R}^{2li \times j}$ is defined in a similar manner by replacing u with y in (2.3).

Subspace methods take advantage of robust numerical techniques such as QR factorisation and Singular Value Decomposition (SVD) by using geometric tools such as the oblique projections of the row space of matrices. For a complete description of the estimating procedure see [17].

The nonlinear identification procedure is based on the computation of system parameters, once the state-space matrices A, B, C, and D have been estimated by a subspace method in the time domain. In fact, system parameters (included in M, C_v, K, and μ_j) are contained in the matrix

$$H_E(\omega) = D + C(\mathrm{i}\omega I - A_c)^{-1} B_c, \tag{2.8}$$

which is invariant under the similarity transformation corresponding to the application of a subspace method [11].

3. Application: The Duffing Equation

Consider the SDOF system with cubic hardening stiffness depicted in Figure 1, whose motion is described by the following Duffing equation:

$$m\ddot{z}(t) + c\dot{z}(t) + kz(t) + k_3 z^3(t) = f(t) \tag{3.1}$$

with system parameters summarized in Table 1. The strength, the type, and the location of the nonlinearity are defined respectively by the three scalar quantities $\mu_1 = k_3, g_1(t) = -z^3(t)$, and obviously $L_{n1} = 1$. The system is excited by two different types of force.

Table 2: Identification results: percentage error (100 · |estimated–actual|/actual).

	m	k	c	k_3
(Case 1-up) Upward sweep	4.63	4.01	4.04	5.86
(Case 1-down) Downward sweep	1.71	1.30	2.64	3.97
(Case 2) Random	0.13	0.54	0.73	0.73

Case 1. The first one is a linearly varying frequency sweep (of amplitude $A = 1$) between 3 and 6 Hz, applied for an upward (up) and a downward (down) frequency sweep.

Case 2. The second one is a zero-mean Gaussian random input whose r.m.s. is 20 N, selected so that the r.m.s. of the nonlinear force is equal to 67% of the corresponding linear stiffness force.

A fourth-order Runge-Kutta numerical integration (with a time step $\Delta t = 10^{-3}$ s) of the equation of motion has been performed and a total number of $s = 10^5$ samples has been generated (so $t_{\text{fin}} = 100$ s) and then corrupted by adding a zero-mean Gaussian noise (1% of the r.m.s. value of the output).

3.1. Identification

The invariant matrix $H_E(\omega)$, defined in (2.8), can be easily computed for $\omega = 0$:

$$H_E(0) = D - CA_c^{-1}B_c = \begin{bmatrix} 0 & 0 \end{bmatrix} - \begin{bmatrix} 1 & 0 \end{bmatrix} \begin{bmatrix} -\dfrac{c}{k} & -\dfrac{m}{k} \\ 1 & 0 \end{bmatrix} \begin{bmatrix} 0 & 0 \\ \dfrac{1}{m} & \dfrac{k_3}{m} \end{bmatrix} = \begin{bmatrix} \dfrac{1}{k} & \dfrac{k_3}{k} \end{bmatrix}. \tag{3.2}$$

From the eigenvalues of the system matrix A_c it is possible to obtain [18] estimates for the angular frequency ω_n of the undamped system and for the damping factor ζ, so that all system parameters can be estimated from (3.2) and from the following relationships:

$$\omega_n = \sqrt{\frac{k}{m}}, \qquad \zeta = \frac{c}{c_{\text{crit}}} = \frac{c}{2\sqrt{km}}. \tag{3.3}$$

It is observed here that in each of the identification procedures performed, the model order $n = 2$ is determined by inspecting a singular value plot (with $i = 60$ block rows), as shown in [11].

The identification results for all system parameters are presented in Table 2: the best estimates are obtained by applying a random input. In fact, for Case 1, it should be observed that the added noise is related to the r.m.s. of the entire time history, which is nonstationary; so, samples corresponding to small displacements are more deeply corrupted by noise and are consequently counterproductive for the identification procedure. This is shown in Figure 2 for Case 1-up, in which this concept is more evident because the system reaches higher values of response amplitudes (and then a higher r.m.s. of the time histories).

A slightly better result for Case 1 can be obtained by considering k_3 as depending on ω: for each ω, matrix $H_E(\omega)$ defined in (2.8) simply reduces to a vector $\overline{h}_E$ with two elements

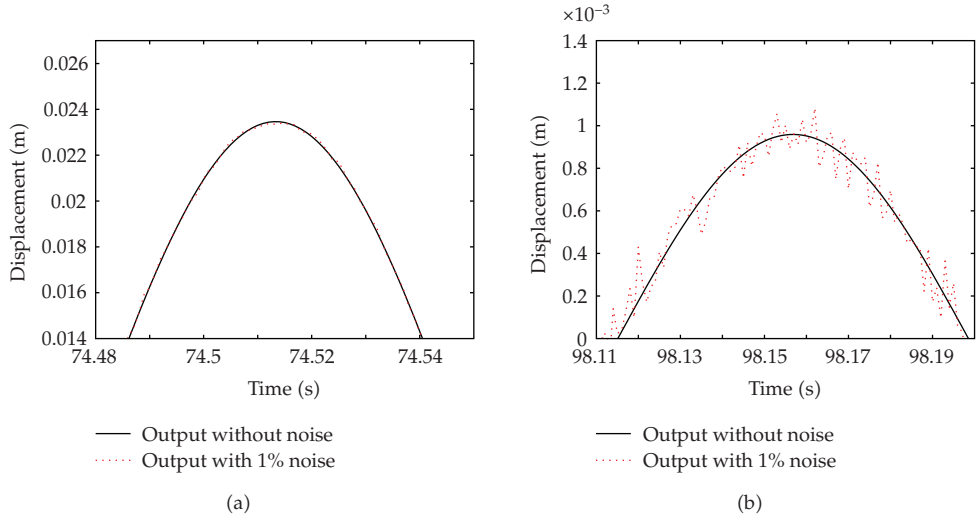

Figure 2: Effect of noise corruption for Case 1-up. The r.m.s. of the entire time history is 0.0088 m. (a) Zoom just before the jump-down (large amplitudes). (b) Zoom after the jump (small amplitudes).

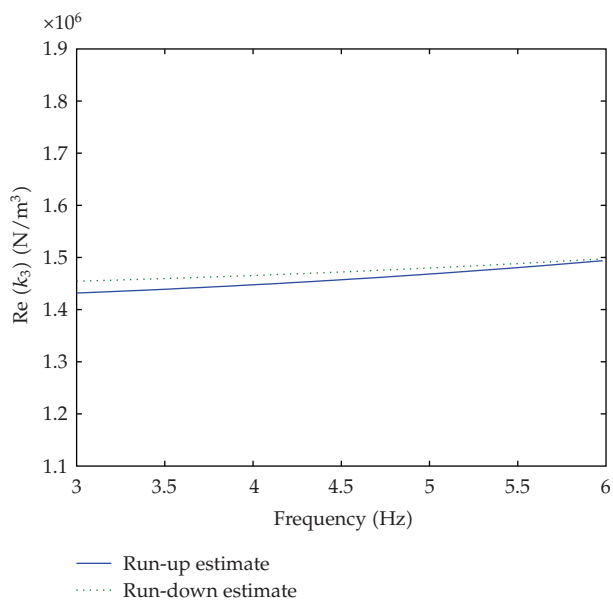

Figure 3: Real part of the estimated nonlinear coefficient k_3, in the frequency range considered.

as in (3.2), and it is possible to compute $k_3 = \overline{h}_E(2)/\overline{h}_E(1)$. The estimated coefficient of the nonlinear term is frequency dependent and complex, albeit its imaginary part is some orders of magnitude smaller than the real part. A single value can be obtained by performing a spectral mean in the frequency range from 3 to 6 Hz (Figure 3). In this way, the percentage errors related to the k_3 estimates become 2.74 for Case 1-up and 1.78 for Case 1-down. Note that this procedure is not applicable to get a spectral mean for k, because for $\omega > 0$ vector $\overline{h}_E$ is not defined as in (3.2).

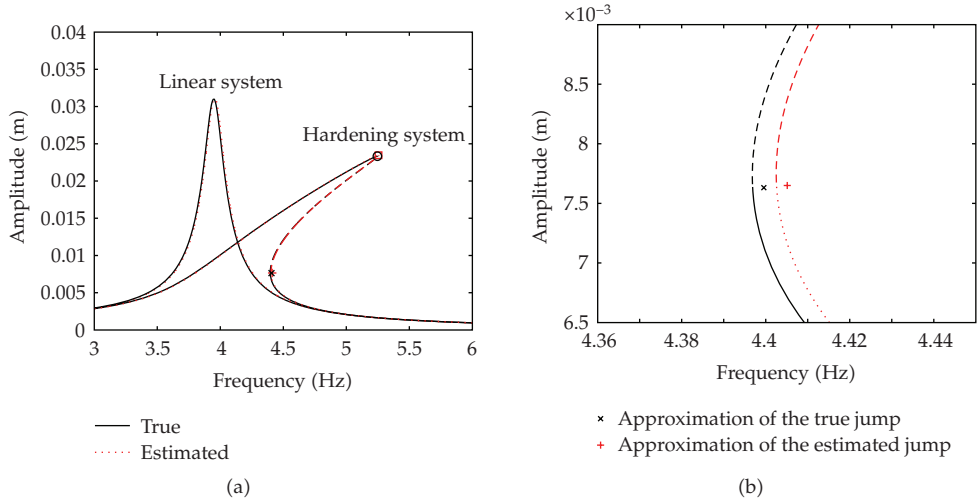

Figure 4: (a) Frequency response curves. The crosses and the circles denote the responses at the jump-up and jump-down frequencies, respectively. The dashed lines denote unstable solutions. (b) Zoom near the jump-up.

In Figure 4(a) the true Frequency Response Functions (FRFs) of the nonlinear and underlying linear system are shown in comparison with the NSI estimates, computed from the identified system parameters in Case 2. As a consequence of the results reported in Table 2, the curves are almost overlaid: an excellent agreement can be observed, even in estimating the jump-up and jump-down frequencies and responses. The values for the jump-down and the jump-up (Figure 4(b)) have been obtained from the approximate expressions derived in [16]: the approximation of the true jump is obtained with the real system parameters of Table 1 while the approximation of the estimated jump is obtained with the NSI estimates of Case 2.

3.2. Output Prediction

The NSI method presented in this paper is also attractive for its predictive capability. In fact, once the system matrices A, B, C, and D in (2.5) have been estimated, it is possible to predict the system behaviour when it is subject to a different type of excitation.

It is important to remark that recent methods such as CRP [6, 7] and NIFO [9] would require a second step to perform output prediction in a general case of MDOF systems. In fact, these methods only produce estimates of the underlying linear FRFs and of nonlinear coefficients. On the contrary, the NSI capability of predicting the output is intrinsic in its formulation, since a state-space model is used. In other words, system parameter estimation is not strictly necessary and this represents a great advantage of NSI in case of MDOF systems. However, for simplicity's sake, in this paper an SDOF numerical example is considered, so estimating system parameters out of state-space matrices is both possible and easy to perform.

Starting from the best estimates of system parameters, obtained through Case 2 identification procedure, it is possible to generate new time histories considering the system as excited by the frequency sweeps described in Case 1. Now the numerical integration has

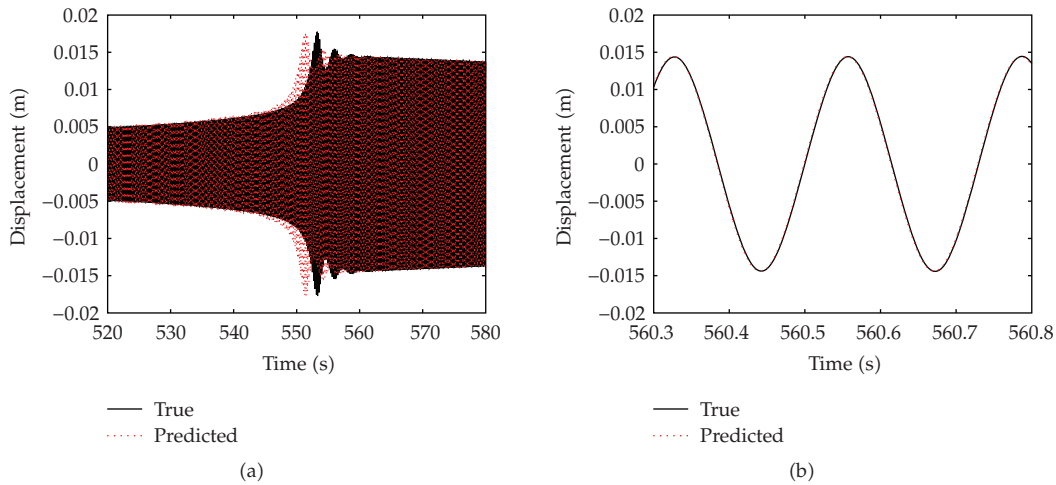

Figure 5: Downward prediction. (a) Comparison between true and predicted output, near the jump-up. (b) Zoom just after the jump.

been performed for $t_{\text{fin}} = 1000\,\text{s}$, in order to have a slower frequency sweep and to obtain a more accurate representation of jump phenomena.

In Figure 5 the results are shown, in terms of a comparison between the true (i.e., system parameters as in Table 1) and the predicted (i.e., identified system parameters) time histories, for Case 1-down. In Figure 5(a) it can be observed that the predicted jump-up occurs at a higher frequency (at a lower time instant in the downward sweep), as expected from the FRFs zoom shown in Figure 4(b). After the jump-up, this slight shift has no longer effect on the prediction: as shown in Figure 5(b), the true and the predicted output are almost overlaid just a few seconds after the jump. Notice the high global level of accuracy of the prediction results, albeit system parameters have been estimated starting from a time history corrupted by measurement noise.

4. QR Factorisation

A common feature in the implementation of all algorithms concerning the subspace methods is the following QR factorisation of a block Hankel matrix $\mathcal{H} \in \mathbf{R}^{j\times 2(m+l)i}$, constructed from all input and output measurements:

$$\mathcal{H} = \frac{1}{\sqrt{j}}\begin{bmatrix} U_{0|2i-1}^T & Y_{0|2i-1}^T \end{bmatrix} = \frac{1}{\sqrt{j}}\begin{bmatrix} U_{0|i-1}^T & U_{i|i}^T & U_{i+1|2i-1}^T & Y_{0|i-1}^T & Y_{i|i}^T & Y_{i+1|2i-1}^T \end{bmatrix} = \text{QR}, \tag{4.1}$$

where $R \in \mathbf{R}^{2(m+l)i\times 2(m+l)i}$ is an upper triangular matrix; note that, as shown in [17], the computation of the orthonormal matrix $Q \in \mathbf{R}^{j\times 2(m+l)i}$ is not needed.

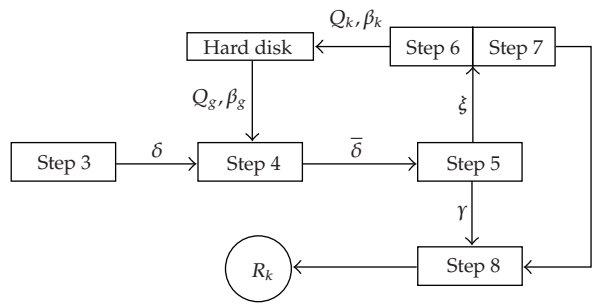

Figure 6: Flow chart representation of the new algorithm, from step (3) to step (8).

4.1. Memory Limitations

Assuming to work in a *Matlab* environment, matrix R in (4.1) should easily be computed through the standard "qr" function, after constructing the block Hankel matrix $\mathcal{H} \in \mathbf{R}^{j\times 2(m+l)i}$. This procedure is certainly valid and efficient for linear systems, because an accurate identification does not require the values of i and j to be so large to fall into the problem described below (typically $j \sim 10^4$ and i do not exceed some tens).

In order to apply subspace methods to nonlinear systems with satisfactory results, it is necessary to consider as many samples s as possible (so $j \approx s$ should be of the order of 10^5 or 10^6) and in particular to extend the index i to some hundreds, especially in presence of noisy measurements. The consequent problem consists in dealing with a matrix $\mathcal{H}$ which results in being too large to be stored nor factorised.

Therefore, it is clear that the NSI method undergoes severe limitations in its applicability, in particular as regards MDOF systems (increasing l) or systems having many nonlinear terms (increasing m).

4.2. New Algorithm

It is then necessary to conceive a new algorithm to compute the QR factorisation. This algorithm is based on *Matlab* commands "save" and "load", which allow to save and load variables directly from the hard disk, and the command "clear", useful to clean virtual memory.

Moreover, it is observed that the development of this new procedure exploits the particular structure of the matrix $\mathcal{H}$ to be factorised and the useful features of Householder transformations: in particular, from now on, Algorithms 1 and 2 reported in the appendix will be considered.

The new algorithm is described in the following and a flow chart representation is given in Figure 6.

(1) Load measured data y, representing the l system outputs, and the values of the external force f; compute from these data the vector u of the m system inputs.

(2) Choose the number of samples s for the identification procedure and the number of block rows i; this choice determinates the number of rows and columns of matrix $\mathcal{H}$, respectively, $j = s - 2i + 1$ and $d = 2(l + m)i$.

(3) Start a **Cycle 1**, $k = 1, \ldots, d$; define δ as the kth column of matrix $\mathcal{H}$. δ is constructed by using the input (if it is a column of submatrix $U^T_{0|2i-1}$) or output (if it is a column of submatrix $Y^T_{0|2i-1}$) data, as defined in (4.1).

(4) Start a **Cycle 2,** $g = 1, \ldots, k-1$; for each iteration g:

(a) "load" from the hard disk vector $Q_g = [v_g, \ldots, v_j]^T$;

(b) execute, on part $\tilde{\delta} = [\delta_g, \ldots, \delta_j]^T$ of vector δ, the transformations defined in Algorithm 2, also using number β_g; vector $\overline{\delta}$ is obtained;

(c) "clear" vector Q_g from virtual memory.

End of Cycle 2.

(5) Subdivide vector $\overline{\delta}$ into two vectors $\gamma = [\overline{\delta}_1, \ldots, \overline{\delta}_{k-1}]^T$ and $\xi = [\overline{\delta}_k, \ldots, \overline{\delta}_j]^T$. Make a copy ψ of vector ξ.

(6) Apply Algorithm 1 to vector ψ, which becomes the new $Q_k = [v_k, \ldots, v_j]^T$ obtaining also number β_k.

(7) Execute, on vector ξ, the transformations defined in Algorithm 2, in order to obtain the new vector $\xi = [\overline{\xi}_1, 0, \ldots, 0]$.

(8) Attain the kth column of matrix R, denoted here as R_k:

(a) construct vector $\tilde{R} = [\gamma \quad \overline{\xi}]^T \in \mathbf{R}^j$;

(b) truncate vector $\tilde{R}$, by eliminating all unnecessary zeros and keeping only the first d elements, in order to obtain $R_k \in \mathbf{R}^d$.

(9) "save" vectors Q_k and R_k on the hard disk, and "clear" them from the virtual memory.

End of Cycle 1.

(10) Reconstruct matrix R, by loading (load) the d columns R_k from the hard disk.

At the end of the algorithm, all saved vectors Q_k and R_k (and β also) will be deleted from the hard disk.

Note (referring in particular to step (3) of the above algorithm) that in this way it is not necessary to store the entire matrix $\mathcal{H}$, and the already discussed memory problems can be avoided. It is indeed sufficient to construct and factorise a new column for each iteration k of Cycle 1.

As a final consideration, it should be observed that this new algorithm does not present any limitations about the choice of index i and the number of samples s to be considered in the NSI procedure. The only limitation may be represented by a larger (depending on the system considered and on the choice of i and s) amount of time requested for the computation of matrix R.

4.3. Application

In order to test the new algorithm and to analyse the results of the NSI procedure exploiting it, the numerical application described in Section 3 is considered. Note that the previously

Table 3: Identification results (noise 1%): percentage error (100 · |estimated–actual|/actual).

i	m	k	c	k_3
60	0.13	0.54	0.73	0.73
90	0.13	0.33	0.57	0.49
120	0.08	0.13	0.15	0.21
180	0.07	0.11	0.33	0.18

Table 4: Identification results (noise 3%): percentage error (100 · |estimated–actual|/actual).

i	m	k	c	k_3
60	0.68	1.87	1.54	2.98
90	0.76	1.37	1.22	2.32
120	0.57	0.74	0.80	1.37
180	0.51	0.66	0.63	1.20

adopted $i = 60$ is the maximum index (for the calculator used for the computations) which allows to avoid the memory limitation problems described in Section 4.1. In fact, for larger values of i, *Matlab* goes out of memory and the NSI procedure with the standard "qr" function fails.

The same time histories ($s = 10^5$ samples) as in Section 3 are considered, and the NSI procedure with the novel algorithm is performed for higher values of the number of block rows i.

Since Table 2 shows that the best parameter estimations are obtained in Case 2 (Gaussian random input), the results presented in this section refer only to Case 2. Note also that in all the following tables the results obtained by choosing $i = 60$ are also reported for comparison purposes. For this value of i the results are the same as in Table 2, as expected: the novel algorithm does not alter the NSI results, it just proposes a useful way to compute matrix R in those cases in which *Matlab* produces an "out of memory" message. However it is observed that, when the standard *Matlab* "qr" function is still applicable, the novel algorithm is about 26 times slower because of its many savings and loadings from the hard disk.

Table 3 shows the identification results relative to an output corrupted by 1% of noise: it is clear that the percentage error in the estimates of k and k_3 decreases as i increases. This trend is not so evident for the estimates of m and c: this is due to the fact that these parameters are not directly estimated from matrix $H_E(\omega = 0)$, as k and k_{nl} in (3.2), but they depend on the estimates of k, ω_n, and ζ through the relationships of (3.3); this may cause a sort of error propagation or compensation. This remark is also valid for Tables 4 and 5.

From Table 3 it can also be observed that a value of $i = 60$ is anyway sufficient to obtain an excellent level of accuracy in the estimates, so the application of the new algorithm is not necessary.

The new algorithm appears to be more appealing when the output is corrupted by a higher level of noise: in this case it is necessary to increase the value of i in order to attain acceptable accuracy in the estimates, in particular as regards the nonlinear coefficient k_3.

For this reason, the previously generated output is corrupted by adding a higher percentage of zero-mean Gaussian random noise, and the results of the identification procedures are shown in Tables 4 and 5 for 3% and 5% noise, respectively. It can be observed that the index i required in order to obtain the same level of accuracy increases as the noise percentage increases.

Table 5: Identification results (noise 5%): percentage error (100 · |estimated–actual|/actual).

i	m	k	c	k_3
60	1.19	3.08	0.53	6.24
90	1.60	2.62	0.15	5.29
120	1.41	1.84	0.73	3.82
180	1.26	1.61	1.59	3.34

5. Conclusions

In this paper the NSI method is presented and applied to an oscillator described by the Duffing equation, in order to handle the *inverse problem* related to identification and output prediction.

It is shown that the best results in parameter estimation are obtained when the system is excited by a Gaussian random input, in particular in presence of a measurement noise. However, the NSI method is also applicable in case of a linearly varying frequency sweep: with this type of excitation jump phenomena are highlighted, but a reduced level of accuracy is attained.

The best parameter estimates are then exploited in order to predict the system behaviour when it is subject to a frequency sweep excitation: the output reconstruction is excellent, in particular as regards the amplitudes and the frequencies at which jump phenomena occur.

The predictive accuracy depends on the quality of parameter estimates, but their improving implies the need of processing a larger amount of data. To this purpose, the NSI method is enforced by the development of a new algorithm to compute the QR factorisation in a *Matlab* environment, in those cases in which the data matrix is too large to be stored or factorised.

Appendix

Householder Transformations

In this appendix some concepts, exploited in Section 4.2 to conceive a new useful algorithm to compute the QR factorisation of a matrix, are presented. For a detailed overview of Householder transformations (also known as elementary reflectors), see [19]. In particular, the algorithms presented below are a revised form of those contained in [19, pages 40-41].

Given a generic vector x different from zero, the Householder transformation

$$U = I - \beta u u^T \tag{A.1}$$

with $u = x + \sigma \cdot e_1$, $e_1 = [1, 0, \ldots, 0]^T$, $\sigma = \pm\|x\|_2$ and $\beta = 2/\|u\|_2^2$ yields the following relation:

$$Ux = -\sigma \cdot e_1. \tag{A.2}$$

It can be observed that the couple (u, β), formed of $n+1$ real numbers, is sufficient to uniquely determine matrix U, having n^2 elements. Thus, given a vector $x = [\xi_1, \xi_2, \ldots, \xi_n]^T$, it is possible

to write an efficient algorithm providing the quantities u (which is overwritten to x) and β (and also σ).

Algorithm 1. We have the following:

(1) $\eta \leftarrow \max\{|\xi_i|,\ i = 1, \ldots, n\}$

(2) $\sigma \leftarrow 0$

(3) **cycle 1**: $i = 1, \ldots n$

(4) if $|\xi_i| \geq \eta\sqrt{\text{eps}}$ then $\sigma \leftarrow \sigma + (\xi_i/\eta)^2$

(5) **end of cycle 1**

(6) $\sigma = \text{sgn}(\xi_1)\eta\sqrt{\sigma}$

(7) $\xi_1 \leftarrow \xi_1 + \sigma$

(8) $\beta \leftarrow 1/(\sigma \cdot \xi_1)$.

Note that *eps* stands for the lowest possible machine number, and that this algorithm avoids possible phenomena of *overflow*, *underflow,* and numerical cancellation.

The couple (u, β) determined through the above algorithm is sufficient to construct products of the form

$$UA = U[a_1, a_2, \ldots, a_n] = [Ua_1, Ua_2, \ldots, Ua_n]. \tag{A.3}$$

In fact, given the two vectors $u = [v_1, v_2, \ldots, v_n]^T$ and $a = [\alpha_1, \alpha_2, \ldots, \alpha_n]^T$, and the number β, the substitution of a with vector Ua can be computed in the following way.

Algorithm 2. We have the following:

(1) $\tau \leftarrow \beta \sum_{i=1}^{n} v_i\alpha_i$

(2) $\alpha_i \leftarrow \alpha_i - \tau \cdot v_i,\ \ i = 1, \ldots, n.$

As an application of the concepts introduced above, it is possible to construct $n - 1$ elementary reflectors $U_1, U_2, \ldots, U_{n-1}$ such that the new matrix

$$U_{n-1} \cdots U_2 U_1 A = Q^T A = R \tag{A.4}$$

is upper triangular; note the orthogonality of Q, which is a product of orthogonal matrices.

As a final observation, the QR factorisation can be computed even if matrix A is rectangular $m \times n$; in this case $A = \text{QR}$ with $Q \in \mathbf{R}^{m\times m}$ and $R \in \mathbf{R}^{m\times n}$ and the factorisation is attained with $r = \min\{m - 1, n\}$ elementary reflectors $U_1, U_2, \ldots, U_r$.

References

[1] G. Kerschen, K. Worden, A. F. Vakakis, and J.-C. Golinval, "Past, present and future of nonlinear system identification in structural dynamics," *Mechanical Systems and Signal Processing*, vol. 20, no. 3, pp. 505–592, 2006.

[2] M. S. Soliman, "Jump phenomena resulting in unpredictable dynamics in the driven damped pendulum," *International Journal of Non-Linear Mechanics*, vol. 31, no. 2, pp. 167–174, 1996.

[3] S. F. Masri and T. K. Caughey, "A nonparametric identification technique for nonlinear dynamic problems," *Journal of Applied Mechanics*, vol. 46, pp. 433–447, 1979.
[4] K. Worden, D. Hickey, M. Haroon, and D. E. Adams, "Nonlinear system identification of automotive dampers: a time and frequency-domain analysis," *Mechanical Systems and Signal Processing*, vol. 23, no. 1, pp. 104–126, 2009.
[5] K. S. Mohammad, K. Worden, and G. R. Tomlinson, "Direct parameter estimation for linear and nonlinear structures," *Journal of Sound and Vibration*, vol. 152, no. 3, pp. 471–499, 1992.
[6] C. M. Richards and R. Singh, "Identification of multi-degree-of-freedom non-linear systems under random excitations by the reverse-path spectral method," *Journal of Sound and Vibration*, vol. 213, pp. 673–708, 1998.
[7] C. M. Richards and R. Singh, "Feasibility of identifying non-linear vibratory systems consisting of unknown polynomial forms," *Journal of Sound and Vibration*, vol. 220, no. 3, pp. 413–450, 1999.
[8] G. Kerschen, V. Lenaerts, S. Marchesiello, and A. Fasana, "A frequency domain versus a time domain identification technique for nonlinear parameters applied to wire rope isolators," *Journal of Dynamic Systems, Measurement and Control*, vol. 123, no. 4, pp. 645–650, 2001.
[9] D. E. Adams and R. J. Allemang, "A frequency domain method for estimating the parameters of a non-linear structural dynamic model through feedback," *Mechanical Systems and Signal Processing*, vol. 14, no. 4, pp. 637–656, 2000.
[10] A. Fasana, L. Garibaldi, and S. Marchesiello, "Performances analysis of frequency domain nonlinear identification techniques," in *Proceedings of International Conference on Noise and Vibration Engineering (ISMA '04)*, pp. 2115–2128, Leuven, Belgium, September 2004.
[11] S. Marchesiello and L. Garibaldi, "A time domain approach for identifying nonlinear vibrating structures by subspace methods," *Mechanical Systems and Signal Processing*, vol. 22, no. 1, pp. 81–101, 2008.
[12] A. H. Nayfeh and D. T. Mook, *Nonlinear Oscillations*, Pure and Applied Mathematics, John Wiley & Sons, New York, NY, USA, 1979.
[13] K. Worden, "On jump frequencies in the response of the Duffing oscillator," *Journal of Sound and Vibration*, vol. 198, no. 4, pp. 522–525, 1996.
[14] M. I. Friswell and J. E. T. Penny, "The accuracy of jump frequencies in series solutions of the response of a duffing oscillator," *Journal of Sound and Vibration*, vol. 169, no. 2, pp. 261–269, 1994.
[15] P. Malatkar and A. H. Nayfeh, "Calculation of the jump frequencies in the response of s.d.o.f. nonlinear systems," *Journal of Sound and Vibration*, vol. 254, no. 5, pp. 1005–1011, 2002.
[16] M. J. Brennan, I. Kovacic, A. Carrella, and T. P. Waters, "On the jump-up and jump-down frequencies of the Duffing oscillator," *Journal of Sound and Vibration*, vol. 318, no. 4-5, pp. 1250–1261, 2008.
[17] P. van Overschee and B. De Moor, *Subspace Identification for Linear Systems: Theory, Implementation, Applications*, Kluwer Academic Publishers, Boston, Mass, USA, 1996.
[18] E. Reynders and G. De Roeck, "Reference-based combined deterministic-stochastic subspace identification for experimental and operational modal analysis," *Mechanical Systems and Signal Processing*, vol. 22, no. 3, pp. 617–637, 2008.
[19] G. H. Golub and C. F. Van Loan, *Matrix Computations*, vol. 3 of *Johns Hopkins Series in the Mathematical Sciences*, Johns Hopkins University Press, Baltimore, Md, USA, 1983.

Hindawi Publishing Corporation
Mathematical Problems in Engineering
Volume 2010, Article ID 657361, 14 pages
doi:10.1155/2010/657361

Research Article

Nonlinear Vibration Analysis for a Jeffcott Rotor with Seal and Air-Film Bearing Excitations

Yuefang Wang[1] and Xiaoyan Wang[2]

[1] *State Key Laboratory of Structural Analysis for Industrial Equipment, Dalian University of Technology, Dalian 116024, China*
[2] *Center for Research and Development, Shengyang Turbo-Machinery Cooperation, Shenyang 110142, China*

Correspondence should be addressed to Yuefang Wang, yfwang@dlut.edu.cn

Received 10 July 2009; Accepted 30 August 2009

Academic Editor: Carlo Cattani

The nonlinear coupling vibration and bifurcation of a high-speed centrifugal compressor with a labyrinth seal and two air-film journal bearings are presented in this paper. The rotary shaft and disk are modeled as a rigid Jeffcott rotor. Muszynska's model is used to express the seal force with multiple parameters. For air-film journal bearings, the model proposed by Zhang et al. is adopted to express unsteady bearing forces. The Runge-Kutta method is used to numerically determine the vibration responses of the disk center and the bearings. Bifurcation diagrams for transverse motion of the rotor are presented with parameters of rotation speed and pressure drop of the seal. Multiple subharmonic, periodic, and quasiperiodic motions are presented with two seal-pressure drops. The bifurcation characteristics show inherent interactions between forces of the air-film bearings and the seal, presenting more complicated rotor dynamics than the one with either of the forces alone. Bifurcation diagrams are obtained with parameters of pressure drop and seal length determined for the sake of operation safety.

1. Introduction

The motion stability of high-speed rotor systems has drawn extensive attention throughout the past several decades. It is now well known that the stability of the rotor's equilibrium can be lost as a result of the Hopf bifurcation, which leads to finite-amplitude whirls of oil-film inside the bearings. The mechanism of oil whips developed from escalating whirling motions has been thoroughly investigated both experimentally and theoretically (see, e.g., [1–4]). Several models have been developed to investigate oil-film forces of short bearings and bearings with finite lengths [5–9]. Various studies of the oil-film forces were carried out to present nonlinear vibrations, for example, super- and subharmonic motions, of the rotor system related to the bearing dynamics [10–12]. Aside from the bearing forces, seal forces

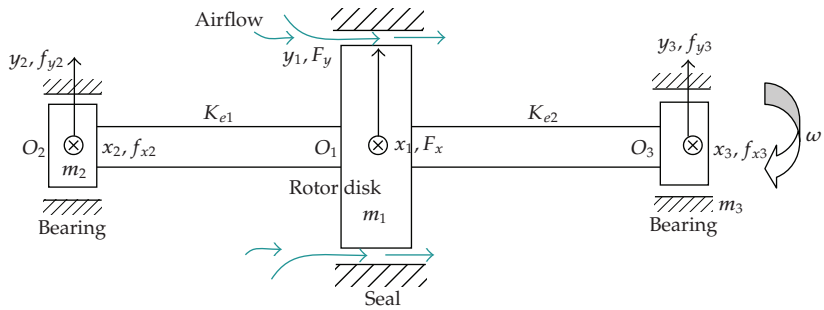

Figure 1: A Jeffcott rotor-seal-bearing system.

play significant roles in vibration and stability of air compressors and steam turbines. Seal forces are usually generated due to the fluid-solid interaction in the clearance between the shaft and the stator which may cause self-excited motions of the rotor. Previous investigations showed that the seal force provides not only supportive reactions to the rotor in the radial direction but also cross-coupling forces in the tangential direction that excites severe vibrations in some occasions. An effective model was proposed by Muszynska to express nonlinear seal forces based on experimental results [13, 14]. This model was later adopted by Ding et al. [15] in their study on the Hopf bifurcation of a symmetric rotor-seal system and by Hua et al. who numerically obtain the nonlinear vibration and bifurcation characteristics of an unbalanced rotor-seal system [16]. Similar research was provided in Zhang et al. [17] where subharmonic motions and bifurcation diagrams were demonstrated with parameter of rotation speed. In spite of the numerous publications that separately dealt with rotor-bearing and rotor-seal systems, very few literatures have been focused on the dynamics of rotor-seal-bearing systems which is a great concern of air-compressor and steam turbine engineers. It is worth emphasizing that the interaction between the seal and bearing excitations should not be ignored since complicated, large-amplitude motions can be developed for rotors of compressors and turbines.

The numerical analysis for nonlinear vibration and bifurcation behavior of a high-speed centrifugal compressor with a labyrinth seal and two journal bearings is presented in this paper. What differentiates the current rotor system from others is the application of air-film bearings rather than conventional oil-film journal bearings. Practically, compressors supported by this kind of bearings operate under circumstance where only inflammable lubricants (i.e., air or pure water) are allowed. It should be noticed that the air-film bearings complicate the dynamics of the rotor in two aspects: (1) since the viscosity of the air is very small, the amplitude of whirling orbit is remarkably large, which brings rich nonlinear characteristics into the rotor response; (2) the airflow inside the clearance of journals is much more irregular and turbulent than the oil-film bearings, which makes most of existent theories unable to provide realistic prediction of the bearing dynamics. In the first case, the vibration response is strongly nonlinear and must be solved numerically with consideration of both bearing and seal forces. In the second case, an effective model for unsteady air-film force should be adopted to express time-varying boundaries of the film that whirls rapidly around the journal center. In the present study, the oil-film force proposed by Zhang et al. [18, 19] is used to model the nonlinear, unsteady air-film excitation in the current study. For the seal force Muszynska's model is adopted with parameters of pressure drop, rotation speed, and seal length. The complexity in the rotor motion is demonstrated through bifurcation

diagrams with those parameters as well as through the Poincaré maps, time history of displacement, and rotor orbits. For seal pressure drop of 0.2 MPa the bifurcation sequence is given with increasing rotation speed, showing subharmonic motions of periodic-1, 12, 11, 10, 9, 8, 7 and quasiperiodic motions. The results are compared to the ones without bearing forces to present the interaction between the air-film bearing and the seal forces. Periods-4 and -11 bifurcations and quasiperiodic motion are observed with a 0.4 MPa pressure drop. The bifurcation diagrams of motion with parameters of pressure drop and length of the seal provide suitable values of these quantities for improvement of operation safety of the machinery. The intricacy in the motion's bifurcation presents complicated dynamics of the system in contrast to the rotors with either of bearing forces or of the seal excitations.

2. Problem Modeling

A Jeffcott rotor with a rigid disk, a segment of labyrinth seal, and two supporting air-film journal bearings is shown in Figure 1, where o_1 is the geometric center of the disk; o_2 and o_3 are centers of the left and right bearings. Denote by (x_1, y_1), (x_2, y_2), and (x_3, y_3) the displacements of the disk center, the left bearing, and the right journal bearing, respectively. The equation of motion of the system is expressed as follows:

$$\begin{gathered}
m_1\ddot{x}_1 + D_e(\dot{x}_1 - \dot{x}_2) + D_e(\dot{x}_1 - \dot{x}_3) + K_{e1}(x_1 - x_2) + K_{e2}(x_1 - x_3) = F_x + m_1 e\omega^2 \cos \omega t, \\
m_1\ddot{y}_1 + D_e(\dot{y}_1 - \dot{y}_2) + D_e(\dot{y}_1 - \dot{y}_3) + K_{e1}(y_1 - y_2) + K_{e2}(y_1 - y_3) = F_y - m_1 g + m_1 e\omega^2 \sin \omega t, \\
m_2\ddot{x}_2 + D_e(\dot{x}_2 - \dot{x}_1) + K_{e1}(x_2 - x_1) = f_{x2}, \\
m_2\ddot{y}_2 + D_e(\dot{y}_2 - \dot{y}_1) + K_{e1}(y_2 - y_1) = f_{y2} - m_2 g, \\
m_3\ddot{x}_3 + D_e(\dot{x}_3 - \dot{x}_1) + K_{e2}(x_3 - x_1) = f_{x3}, \\
m_3\ddot{y}_3 + D_e(\dot{y}_3 - \dot{y}_1) + K_{e2}(y_3 - y_1) = f_{y3} - m_3 g,
\end{gathered} \tag{2.1}$$

where m_1 is the mass of the disk; m_2 and m_3 are masses of the left and the right bearings. K_{e1} and K_{e2} are equivalent stiffness coefficients of the left and the right shafts; D_e is the factor of viscous damping; e is the mass unbalance of the disk; F_x and F_y are directional components of the seal force; $f_{x2,x3}$ and $f_{y2,y3}$ are directional force components of the left and the right bearings, respectively. ω is the rotation speed and g is the gravitational acceleration. The symmetry of the fluid field inside the seal clearance is destroyed as the rotor is perturbed from its equilibrium position with a nonzero rotation speed. Muszynska's model [13, 14] is used to express the seal forces in both x- and y-directions, as

$$\begin{Bmatrix} F_x \\ F_y \end{Bmatrix} = -\begin{bmatrix} K - m_f\tau^2\omega^2 & \tau\omega D \\ -\tau\omega D & K - m_f\tau^2\omega^2 \end{bmatrix} \begin{Bmatrix} x_1 \\ y_1 \end{Bmatrix} - \begin{bmatrix} D & 2\tau m_f\omega \\ -2\tau m_f\omega & D \end{bmatrix} \begin{Bmatrix} \dot{x}_1 \\ \dot{y}_1 \end{Bmatrix} - \begin{bmatrix} m_f & 0 \\ 0 & m_f \end{bmatrix} \begin{Bmatrix} \ddot{x}_1 \\ \ddot{y}_1 \end{Bmatrix}, \tag{2.2}$$

where K and D are coefficients of stiffness and damping of the air that flows through the seal clearance, respectively; m_f is the effective mass of the air; τ is the factor of average angular speed of fluid that rotates along with the rotor, determined by

$$\tau = \tau_0(1-\varepsilon)^b, \tag{2.3}$$

where τ_0 is the average angular speed for the unperturbed rotor; b is an empirical coefficient; $\varepsilon = \sqrt{x_{2,3}^3 + y_{2,3}^2}$ is the nondimensional amplitude of whirling motion of the bearings. The model of the bearing force adopted in the current study is the one proposed by Zhang et al. [18, 19] for unsteady oil-film journal bearings, expressed as follows:

$$f_x = -C_1\dot{\varepsilon} - C_2\left(\dot{\varphi} - \frac{\omega}{2}\right)\varepsilon, \qquad f_y = -C_2\dot{\varepsilon} - C_3\left(\dot{\varphi} - \frac{\omega}{2}\right)\varepsilon, \tag{2.4}$$

where $\dot{\varphi}$ is the whirling speed of the journal; C_1, C_2, and C_3 are damping coefficients of the lubricant [20]. Unlike most existent bearing theories that handle time-invariant boundaries of the lubricant film with, for example, the Gümbel condition and the π-oil-film assumption, the unsteady force model of (2.4) is capable of dealing with time-varying boundary of the film arising from large whirling velocity of the journal center, which is appropriate for weakly viscous systems with air- or water-film bearings such as the present one. Introducing the following nondimensional parameters:

$$\begin{gathered}
T = \omega t, \qquad X_1 = \frac{x_1}{c}, \qquad Y_1 = \frac{y_1}{c}, \\
X_{2,3} = \frac{x_{2,3}}{\delta}, \qquad Y_{2,3} = \frac{y_{2,3}}{\delta}, \\
X_1' = \frac{\dot{x}_1}{(\omega c)}, \qquad Y_1' = \frac{\dot{y}_1}{(\omega c)}, \\
X_{2,3}' = \frac{\dot{x}_{2,3}}{(\omega\delta)}, \qquad Y_{2,3}' = \frac{\dot{y}_{2,3}}{(\omega\delta)},
\end{gathered} \tag{2.5}$$

where $(\cdot)' \triangleq d(\cdot)/dT$ denotes the derivative of a quantity with respect to T, and c and δ are clearances of the seal and the journal bearings, respectively, the equation of motion is then rewritten as

$$\begin{aligned}
&X_1'' + \frac{2D_e + D}{(m_1+m_f)\omega}X_1' + \frac{2\tau m_f}{m_1+m_f}Y_1' - \frac{D_e\delta}{(m_1+m_f)\omega c}(X_2' + X_3') + \frac{K_{e1}+K_{e2}+K-m_f\tau^2\omega^2}{(m_1+m_f)\omega^2}X_1 \\
&\quad + \frac{\tau D}{(m_1+m_f)\omega}Y_1 - \frac{K_{e1}\delta}{(m_1+m_f)\omega^2 c}X_2 - \frac{K_{e2}\delta}{(m_1+m_f)\omega^2 c}X_3 = \frac{m_1 e}{(m_1+m_f)c}\cos T,
\end{aligned}$$

$$
\begin{aligned}
&Y_1'' - \frac{2\tau m_f}{m_1+m_f}X_1' + \frac{2D_e + D}{(m_1+m_f)\omega}Y_1' - \frac{D_e\delta}{(m_1+m_f)\omega c}(Y_2' + Y_3') - \frac{\tau D}{(m_1+m_f)\omega}X_1 \\
&\quad + \frac{K_{e1}+K_{e2}+K-m_f\tau^2\omega^2}{(m_1+m_f)\omega^2}Y_1 - \frac{K_{e1}\delta}{(m_1+m_f)\omega^2 c}Y_2 \\
&\quad - \frac{K_{e2}\delta}{(m_1+m_f)\omega^2 c}Y_3 = \frac{m_1 e}{(m_1+m_f)c}\sin T - \frac{m_1 g}{(m_1+m_f)\omega^2 c}, \\
&X_2'' - \frac{D_e c}{m_2\omega\delta}X_1' + \frac{D_e\omega\delta + S_0C_{11L}}{m_2\omega^2\delta}X_2' + \frac{S_0C_{12L}}{m_2\omega^2\delta}Y_2' - \frac{K_{e1}c}{m_2\omega^2\delta}X_1 \\
&\quad + \frac{2K_{e1}\delta - C_{2L}S_0}{2m_2\omega^2\delta}X_2 + \frac{C_{3L}S_0}{2m_2\omega^2\delta}Y_2 = 0, \\
&Y_2'' - \frac{D_e c}{m_2\omega\delta}Y_1' + \frac{S_0C_{12L}}{m_2\omega^2\delta}X_2' + \frac{D_e\omega\delta + S_0C_{22L}}{m_2\omega^2\delta}Y_2' - \frac{K_{e1}c}{m_2\omega^2\delta}Y_1 \\
&\quad + \frac{2K_{e1}\delta - C_{2L}S_0}{2m_2\omega^2\delta}Y_2 - \frac{C_{3L}S_0}{2m_2\omega^2\delta}X_2 = -\frac{g}{\omega^2\delta}, \\
&X_3'' - \frac{D_e c}{m_3\omega\delta}X_1' + \frac{D_e\omega\delta + S_0C_{11R}}{m_3\omega^2\delta}X_3' + \frac{S_0C_{12R}}{m_3\omega^2\delta}Y_3' - \frac{K_{e2}c}{m_3\omega^2\delta}X_1 \\
&\quad + \frac{2K_{e2}\delta - S_0C_{2R}}{2m_3\omega^2\delta}X_3 + \frac{S_0C_{3R}}{2m_3\omega^2\delta}Y_3 = 0, \\
&Y_3'' - \frac{D_e c}{m_3\omega\delta}Y_1' + \frac{S_0C_{12R}}{m_3\omega^2\delta}X_3' + \frac{D_e\omega\delta + S_0C_{22R}}{m_3\omega^2\delta}Y_3' - \frac{K_{e2}c}{m_3\omega^2\delta}Y_1 \\
&\quad - \frac{S_0C_{3R}}{2m_3\omega^2\delta}X_3 + \frac{2K_{e2}\delta - S_0C_{2R}}{2m_3\omega^2\delta}Y_3 = -\frac{g}{\omega^2\delta},
\end{aligned}
\tag{2.6}
$$

where l and r are length and radius of the bearing, respectively; μ is the dynamic viscosity of the lubricant; superscripts L and R represent the left and the right bearings, respectively, and

$$
\begin{aligned}
C_{11} &= C_1\cos^2\varphi + C_3\sin^2\varphi - 2C_2\sin\varphi\cos\varphi, \\
C_{12} &= C_{21} = C_2\left(\cos^2\varphi - \sin^2\varphi\right) + (C_1 - C_3)\sin\varphi\cos\varphi, \\
C_{22} &= C_1\sin^2\varphi + C_3\cos^2\varphi + 2C_2\sin\varphi\cos\varphi, \\
S_0 &= 6\mu\omega l r^3\delta^{-2}.
\end{aligned}
\tag{2.7}
$$

3. Subharmonic Motions and Bifurcation Behavior

Notice that parameters K, D, and τ and coefficients C_1, C_2, and C_3 are functions of displacements of the disk centers and the bearings. Hence, (2.6) is a group of highly nonlinear

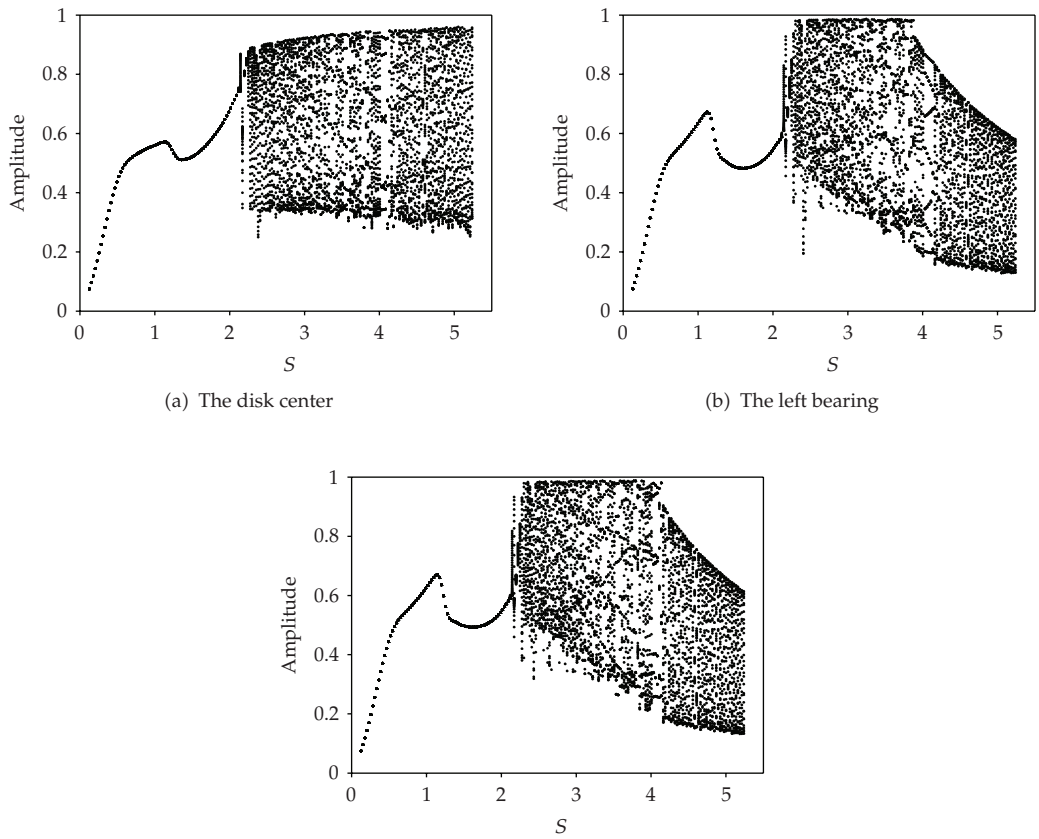

(a) The disk center

(b) The left bearing

(c) The right bearing

Figure 2: Bifurcation diagrams of the rotor system with seal and air-film excitations. $\Delta P = 0.2\,\text{MPa}$.

ordinary differential equations that can hardly be solved through conventional perturbation methods [21]. Instead, the vibration responses of the disk center and the two bearings are computed by using the fourth-order Runge-Kutta method with adaptive-step control to reduce local truncation error of every single step. The parameters selected for the current study are

$$\begin{gathered} m_1 = 50\,\text{kg}, \qquad m_2 = 3.5\,\text{kg}, \qquad m_3 = 3.5\,\text{kg}, \qquad D_e = 3000\,\text{N}\cdot\text{s/m}, \\ K_{e1} = 3.4635\times 10^6\,\text{N/m}, \qquad K_{e2} = 3.8127\times 10^6\,\text{N/m}, \\ e_1 = 0.2\,\text{mm}, \qquad r = 0.035\,\text{m}, \qquad l = 0.06\,\text{m}, \qquad c = 0.3\,\text{mm}, \qquad \delta = 0.3\,\text{mm}, \\ \mu = 1.47\times 10^{-5}\,\text{Pa}\cdot\text{s}, \qquad \tau_0 = 0.4, \qquad b = 0.45. \end{gathered} \tag{3.1}$$

Additionally, the length and radius of the seal are 0.102 m and 0.067 m, respectively. The system's parameters are chosen based on a single-staged centrifugal compressor manufactured by Shenyang Turbo-machinery Cooperation. To investigate the bifurcation we chose the rotation speed as the parameter under two pressure drops of the seal, that is, the

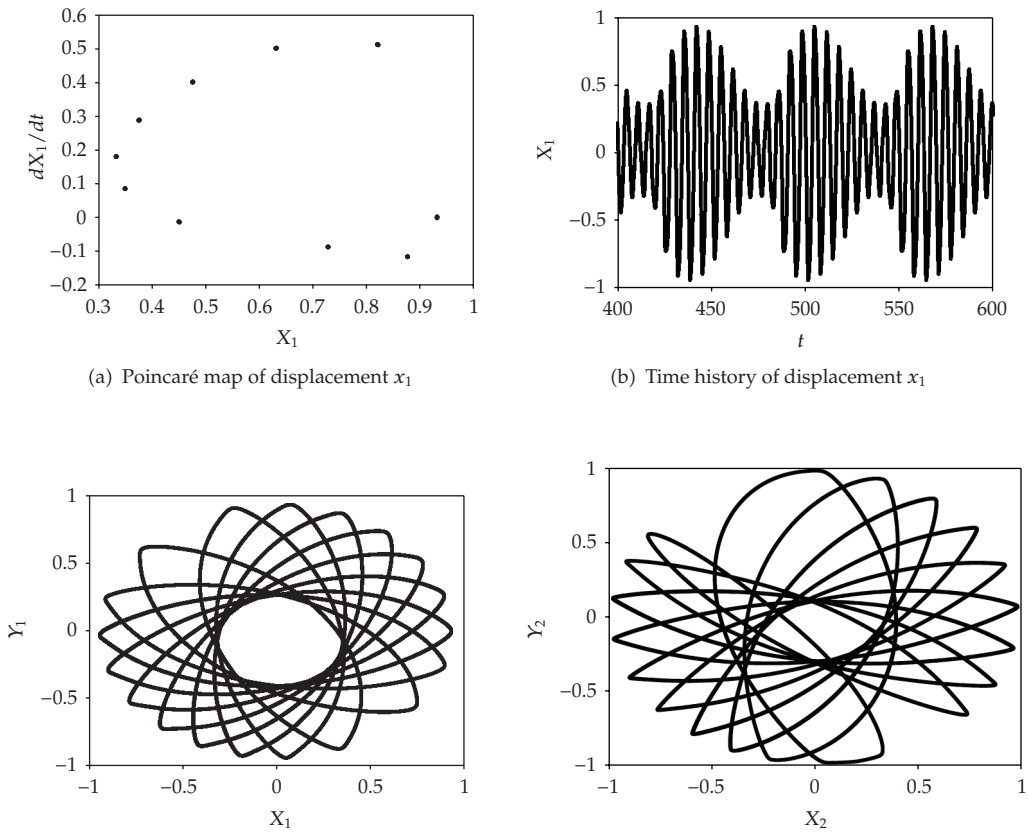

(a) Poincaré map of displacement x_1

(b) Time history of displacement x_1

(c) Orbit of the disk center

(d) Orbit of the left bearing

Figure 3: Motions of the rotor system with rotation speed $S = 3.355$.

pressure differences between the entrance and the exit of the seal. The initial displacements and velocities of the disk center and the two are $(0.01, 0)$.

Let pressure drop ΔP be 0.2 MPa. The bifurcation diagrams of displacement x are illustrated in Figure 2, where $S = \omega/\sqrt{(K_{e1} + K_{e2})/m_1}$ is the nondimensional rotation speed. In the current computation $S = 1$ corresponds to a rotation speed of 60.71 Hz or 3642.77 rpm.

It can be seen that the disk and the bearings are in motions of period-1, that is, motions with the same frequency as the rotation speed, when the rotation is slow. The primary resonance happens at $S = 1.1272$. The stability of the period-1 motions is lost at $S = 2.1496$, and the motion becomes quasiperiodic. Various subharmonic motions can be observed when the rotation speed is increased. A period-12 bifurcation takes place at $S = 3.1457$. Following that, the motions become quasiperiodic again with escalating rotation speed. At $S = 3.2505$ the displacements undergo a period-11 bifurcation and return quasiperiodic with higher S afterwards. A period-10 bifurcation is encountered with speed $S = 3.355$. The Poincaré map of displacement x_1 is presented in Figure 3(a) to show the existence of a periodic-10 motion. The time history of x_1 is illustrated in Figure 3(b), and the orbits of the disk center and the left bearing are shown in Figures 3(c) and 3(d), respectively. Further, a period-9 bifurcation is observed at $S = 3.5389$ followed by a period-8 bifurcation at $S = 3.8010$. The bifurcation cascade continues at $S = 4.0632$ when a period-7 bifurcation takes place. Following that,

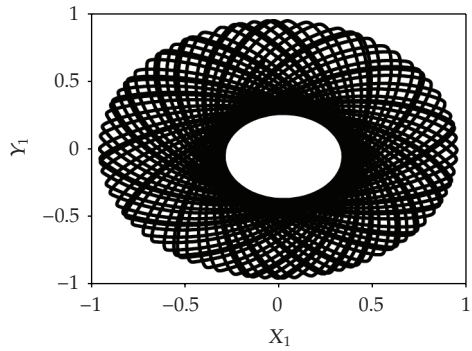

(a) Orbit of the disk center

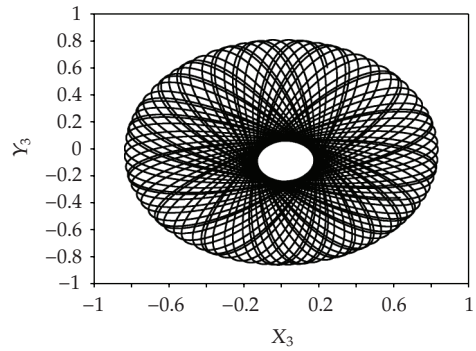

(b) Orbit of the right bearing

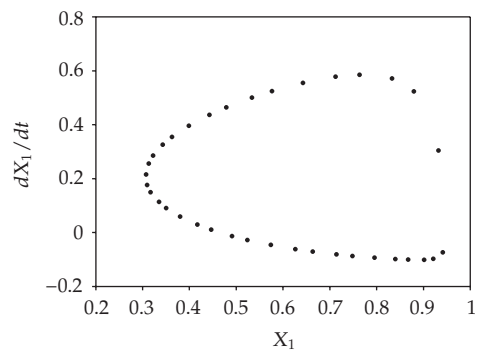

(c) Poincaré map of displacement x_1

Figure 4: Motions of the rotor system with rotation speed $S = 4.352$.

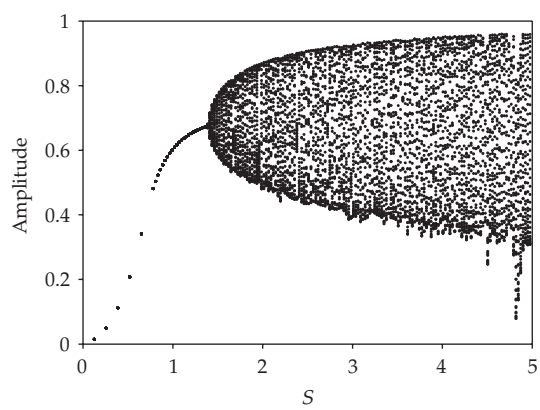

Figure 5: Bifurcation diagram of the disk center with rigid supports.

quasiperiodic motions are obtained with higher rotation speed. Figures 4(a), 4(b), and 4(c) depict the orbits of the disk center and the right bearing as well as the Poincaré map of displacement x_1 at $S = 4.352$, respectively.

To investigate the interaction between the bearing and the seal forces a comparative computation is carried out for a Jeffcott rotor with two rigid supports (hence, the seal force

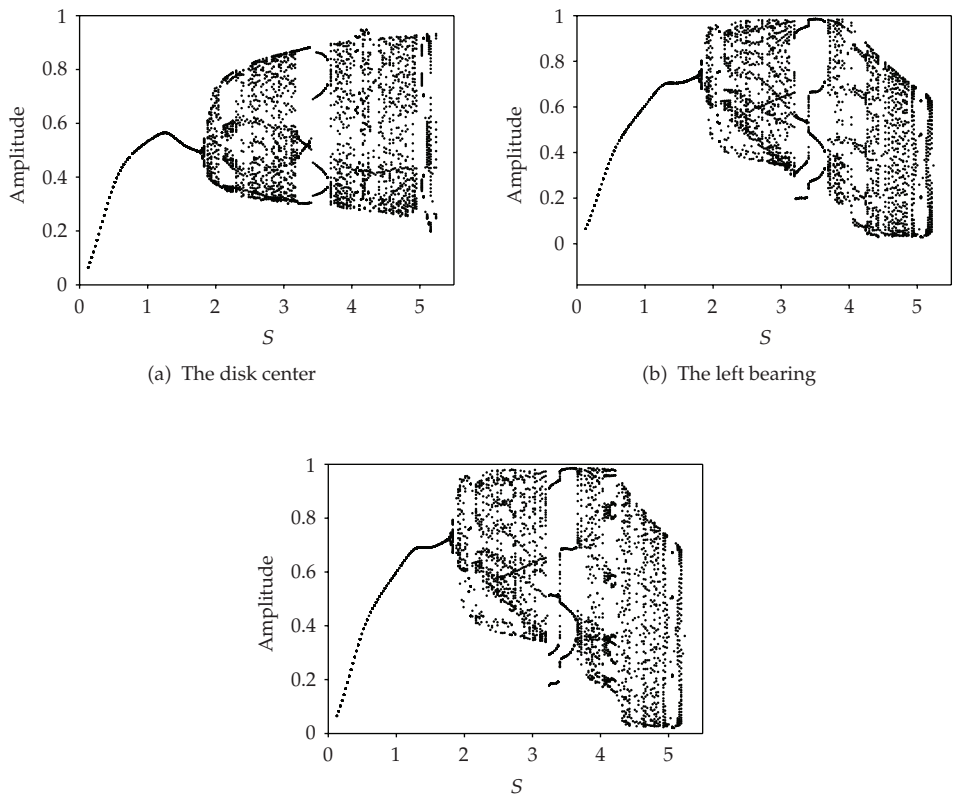

(a) The disk center

(b) The left bearing

(c) The right bearing

Figure 6: Bifurcation diagrams of the rotor system with seal and air-film excitations. $\Delta P = 0.4$ MPa.

is the only excitation of the system) and exactly the same geometrical and seal properties as aforementioned. The bifurcation diagram is shown in Figure 5. For rotation speed less than $S = 1.432$, the motion is period-1 with the same frequency as the rotation speed. With an increasing speed, the motion remains quasiperiodic up to $S = 3.52$, where a period-8 bifurcation is observed from the disk's displacements. The motions turns into quasiperiodic again with advancing rotation speed. The comparison between the responses to the coupling forces and to the seal force alone reveals rich bifurcating behavior of the system vibration: the interaction of the seal and the air-film forces results in more period-multiple bifurcations (see Figures 2(a) and 5).

We now change the pressure drop of the seal to 0.4 MPa. The bifurcation diagrams of displacement x of the disk and the two journal bearings are presented in Figure 6.

It is found that the x-directional displacements of the disk and the bearings are period-1 with small rotation speed. The primary resonance in the motion is found at $S = 1.2582$. Then, the bifurcation starts and the motions become quasiperiodic. A period-4 bifurcation takes place with speed $S = 2.0709$ followed by quasiperiodic motions as the rotor is accelerated. For speed $S \in [3.2243, 3.3816] \cup [3.4340, 3.6437]$ the motions are period-4. Figures 7(a) and 7(b) show the orbits of the disk center and the left bearing at $S = 3.4340$. Figure 7(c) depicts the Poincaré map of the disk motion. The motions become quasiperiodic with higher rotation speed. Figures 8(a) and 8(b) plot the orbits of the disk

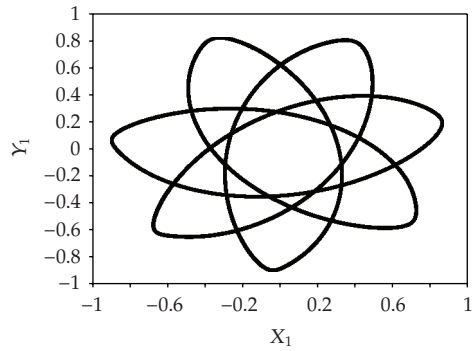

(a) Orbit of the disk center

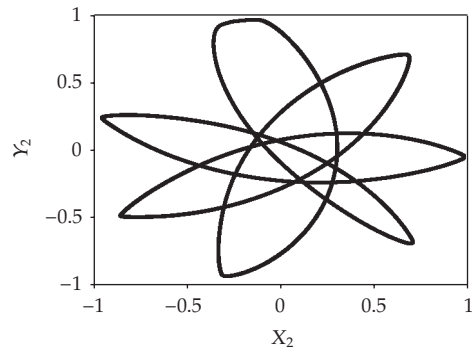

(b) Orbit of the left bearing

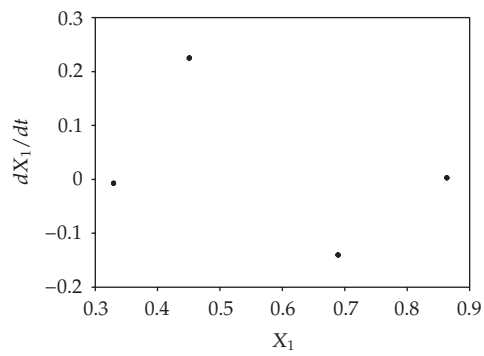

(c) Poincaré map of displacement x_1

Figure 7: Motions of the rotor system with rotation speed $S = 3.434$.

center and the right bearing at $S = 3.8797$. The Poincaré maps of displacements x_1 and x_3 are shown in Figures 8(c) and 8(d), respectively. A period-11 bifurcation is observed at $S = 4.2204$ followed by another series of quasiperiodic motions. With higher pressure-drop from the entrance to the exit of the seal, some previously notified bifurcations are not observed again. Nevertheless, the bifurcation behavior is still more complicated than the one with the seal force only.

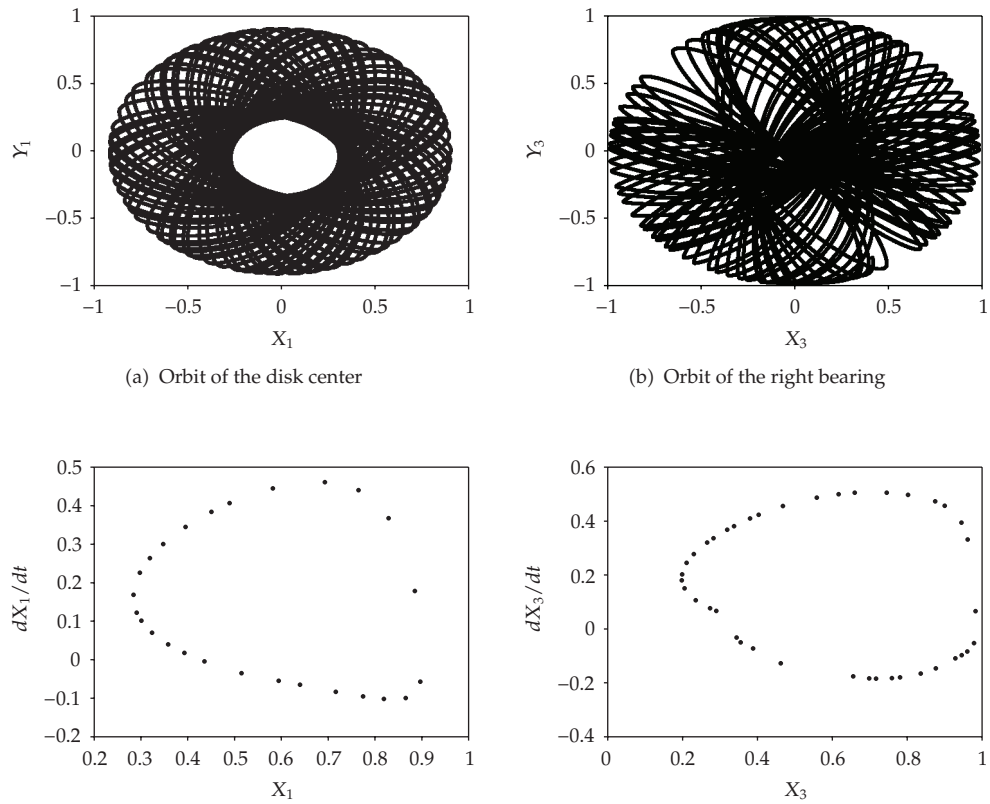

(a) Orbit of the disk center

(b) Orbit of the right bearing

(c) Poincaré map of displacement x_1

(d) Poincaré map of displacement x_3

Figure 8: Motions of the rotor with rotation speed $S = 3.8797$.

In the following analysis we adopt the pressure drop as the bifurcation parameter. Let rotation speed ω be 1200 rad/s. The bifurcation diagrams of x-displacements of the disk center and the left and the right bearings are presented in Figure 9. For low-pressure drops the motions are found quasiperiodic with large amplitude until $\triangle P$ up to 0.048 MPa. The motions of the disk center and the bearings then become period-1, and the amplitudes step up with the advancing pressure drop. The synchronous motions are lost at a critical drop ΔP = 0.168 MPa without undergoing primary resonances in the motions. The vibrations afterwards are basically quasiperiodic, and it is very difficult to distinguish the bifurcation points. The average amplitudes of the displacements remain almost unchanged with increasing pressure drops, showing the remarkable air-film whip in the journal bearings. This implies that the whole system cannot be stabilized by increasing the pressure drops larger than the critical value.

Finally, the evolution of the bifurcation in the rotor motions is investigated by taking the length of the seal as the control parameter. Let rotation speed ω be 1200 rad/s and let pressure drop ΔP be 0.2 MPa. The bifurcation diagrams of x-displacements of the disk center and the left and the right bearings are depicted in Figure 10. The period-1 motion is found for length: $0.082\,\text{m} \leq l \leq 0.098\,\text{m}$, where the orbital whirling motions grow monotonously with the increasing seal-length. Beyond this range of length, the motions are mainly quasiperiodic

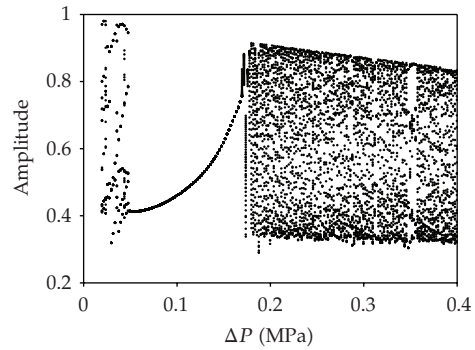

(a) The disk center

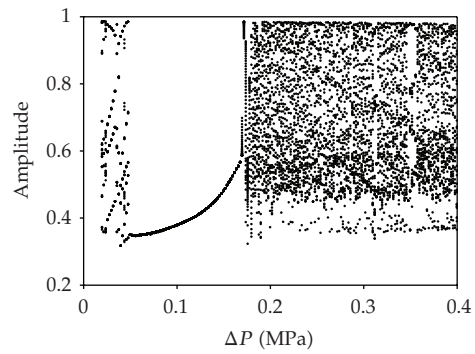

(b) The left bearing

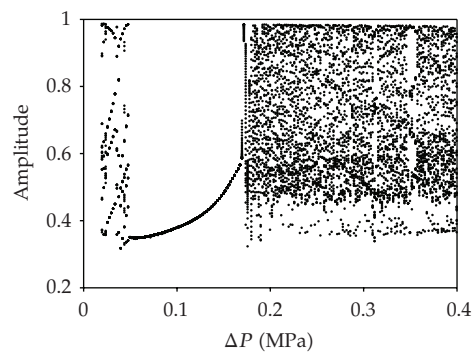

(c) The right bearing

Figure 9: Bifurcation diagram of the rotor with varying pressure drop. $\omega = 1200\,\text{rad/s}$.

with considerably large amplitudes. Therefore, a suitable length of seal should be chosen between 0.082 m and 0.098 m to keep the rotor distant from strong vibration responses that may jeopardize the safety of the machine in operation. From the manufacturer's point of view, a labyrinth seal with a medium length of between 0.082 m and 0.098 m is feasible for it can be conveniently processed, assembled, and positioned by using conventional tools.

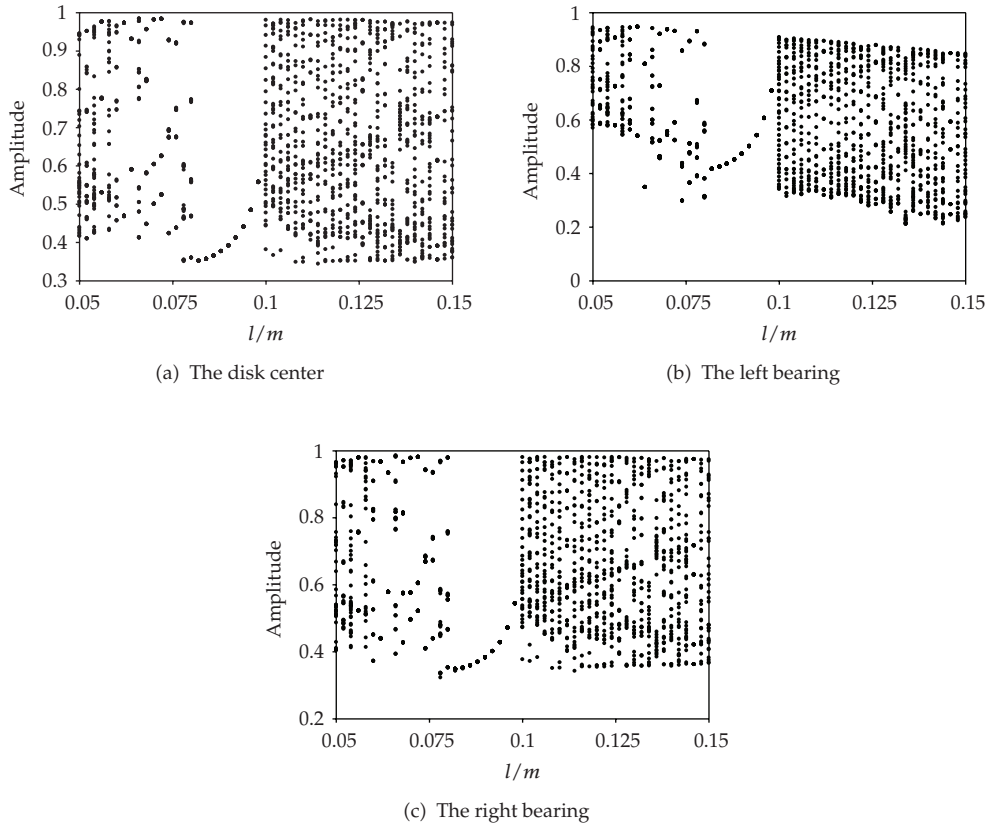

(a) The disk center

(b) The left bearing

(c) The right bearing

Figure 10: Bifurcation diagram of the rotor with varying seal-length. $\omega = 1200\,\text{rad/s}$; $\Delta P = 0.2\,\text{MPa}$.

4. Conclusions

The nonlinear coupling vibration excited by a labyrinth seal and two air-film journal bearing is investigated through numerical simulations for high-speed centrifugal compressors. The results obtained with various rotation speeds and seal pressure drops show complexity of nonlinear vibration and bifurcation behavior in the displacements of the rotor system. Further, the motions of the system reveal period-multiple bifurcations compared to the system excited only by the seal force, presenting an intricate interaction between the seal and the bearing forces. Suitable seal pressure drop and seal length are determined for the sake of operation safety through the bifurcation analysis for rotor displacements as well.

Acknowledgments

The authors gratefully acknowledge the Natural Science Foundation of China (Projects 10472021, 10721062), the Chinese National Programs for High Technology Research and Development (2007AA04Z405), and the State Key Development Program for Basic Research of China (Project 2009CB724300) for their fundings.

References

[1] B. L. Newkirk and H. D. Taylor, "Shaft whipping due to oil action in journal bearing," *General Electric Review*, vol. 28, pp. 559–568, 1925.

[2] J. W. Lund, "Spring and damping coefficients for the tilting pad journal bearing," *Transactions of the ASAE*, vol. 7, pp. 342–352, 1964.

[3] D. W. Childs, *Turbomachinery Rotordynamics: Phenomena, Modeling, and Analysis*, John Wiley & Sons, New York, NY, USA, 1993.

[4] E. Kramer, *Dynamics of Rotors and Foundations*, Springer, Berlin, Germany, 1993.

[5] L. San Andres, "Dynamic force and moment coefficients for short length annular seals," *Journal of Tribology*, vol. 115, no. 1, pp. 61–70, 1993.

[6] K. Kwanka, "Dynamic coefficients of stepped labyrinth gas seals," *Journal of Engineering for Gas Turbines and Power*, vol. 122, no. 3, pp. 473–477, 2000.

[7] J. K. Scharrer and D. W. Childs, "Theory versus experiment for the rotordynamic coefficients of labyrinth gas seals—part I: a two control volume model," *Journal of Vibration, Acoustics, Stress, and Reliability in Design*, vol. 110, no. 3, pp. 270–280, 1988.

[8] J. K. Scharrer and D. W. Childs, "Theory versus experiment for the rotordynamic coefficients of labyrinth gas seals—parts II: a comparison to experiment," *Journal of Vibration, Acoustics, Stress, and Reliability in Design*, vol. 110, no. 3, pp. 281–287, 1988.

[9] O. R. Marquette and D. W. Childs, "An extended three-control-volume theory for circumferentially-grooved liquid seals," *Journal of Tribology*, vol. 118, no. 2, pp. 276–285, 1996.

[10] F. F. Ehrich, "Subharmonic vibration of rotors in bearing clearance," ASME Paper no. 66-MD-1, 1966.

[11] F. F. Ehrich, "High order subharmonic response of high speed rotor in bearing clearance," *Journal of Vibration, Acoustics, Stress, and Reliability in Design*, vol. 110, pp. 695–702, 1988.

[12] D. E. Bently, "Forced subrotative speed dynamic action of rotating machinery," ASME Paper no. 74-PET-16, 1994.

[13] A. Muszynska, "Whirl and whip-rotor/bearing stability problems," *Journal of Sound and Vibration*, vol. 110, no. 3, pp. 443–462, 1986.

[14] A. Muszynska and D. E. Bently, "Frequency-swept rotating input perturbation techniques and identification of the fluid force models in rotor/bearing/seal systems and fluid handling machines," *Journal of Sound and Vibration*, vol. 143, no. 1, pp. 103–124, 1990.

[15] Q. Ding, J. E. Cooper, and A. Y. T. Leung, "Hopf bifurcation analysis of a rotor/seal system," *Journal of Sound and Vibration*, vol. 252, no. 5, pp. 817–833, 2002.

[16] J. Hua, S. Swaddiwudhipong, Z. S. Liu, and Q. Y. Xu, "Numerical analysis of nonlinear rotor-seal system," *Journal of Sound and Vibration*, vol. 283, no. 3–5, pp. 525–542, 2005.

[17] Y.-H. Zhang, J. Hua, Q.-Y. Xu, and X.-L. Zhang, "A new high precision direct integration scheme for nonlinear rotor-seal system," *Chinese Journal of Computational Mechanics*, vol. 22, no. 5, pp. 541–545, 2005 (Chinese).

[18] W. Zhang, H. S. Zhang, and X. F. Xu, "Study of general nonlinear formula of oil-film force acting on a journal with unsteady motion," in *Proceedings of the Asia-Pacific Vibration Conference*, Kyungju, Korea, 1997.

[19] W. Zhang and X. Xu, "Modeling of nonlinear oil-film force acting on a journal with unsteady motion and nonlinear instability analysis under the model," *International Journal of Nonlinear Sciences and Numerical Simulation*, vol. 1, no. 3, pp. 179–186, 2000.

[20] D. W. Childs, "Dynamic analysis of turbulent annular seals based on Hirs' lubrication equation," *Journal of Lubrication Technology*, vol. 105, no. 3, pp. 429–436, 1983.

[21] J.-H. He, "A review on some new recently developed nonlinear analytical techniques," *International Journal of Nonlinear Sciences and Numerical Simulation*, vol. 1, no. 1, pp. 51–70, 2000.

Hindawi Publishing Corporation
Mathematical Problems in Engineering
Volume 2010, Article ID 591786, 17 pages
doi:10.1155/2010/591786

Research Article

A Semianalytical Method for Nonlinear Vibration of Euler-Bernoulli Beams with General Boundary Conditions

Jian-She Peng,[1] Yan Liu,[2] and Jie Yang[3]

[1] *School of Industrial Manufacturing, Chengdu University, Sichuan 610106, China*
[2] *Department of Physics and Electronic Information, China West Normal University, Nanchong, Sichuan 637002, China*
[3] *School of Aerospace, Mechanical and Manufacturing Engineering, RMIT University, P.O. Box 71, Bundoora, Victoria 3083, Australia*

Correspondence should be addressed to Jie Yang, j.yang@rmit.edu.au

Received 31 December 2009; Revised 17 April 2010; Accepted 3 June 2010

Academic Editor: Carlo Cattani

This paper presents a new semianalytical approach for geometrically nonlinear vibration analysis of Euler-Bernoulli beams with different boundary conditions. The method makes use of Linstedt-Poincaré perturbation technique to transform the nonlinear governing equations into a linear differential equation system, whose solutions are then sought through the use of differential quadrature approximation in space domain and an analytical series expansion in time domain. Validation of the present method is conducted in numerical examples through direct comparisons with existing solutions, showing that the proposed semianalytical method has excellent convergence and can give very accurate results at a long time interval.

1. Introduction

Geometrically nonlinear vibration of beams with different boundary conditions has long been a subject receiving numerous research efforts, as evidenced by many analytical and numerical studies reported in the open literature. Woinowsky-Krieger [1] used the elliptic integral function to solve the nonlinear equation of motion for simply supported beams with immovable ends. Lewandowski [2] applied the Rayleigh-Ritz technique to the nonlinear vibration of beams. A comprehensive review in this field was given by Sathyamoorthy [3]. Sze et al. [4] applied incremental harmonic balance method for nonlinear vibration of axially moving beams. Gadagi and Benaroya [5] studied the dynamic response of an axially loaded tendon of a tension leg platform. Ibrahim and Somnay [6] solved the nonlinear dynamic analysis of an elastic beam isolator sliding on frictional supports. Ozkaya and Tekin

[7] analyzed the nonlinear vibrations of stepped beam system under different boundary conditions. Chen et al. [8] put forward the multidimensional Lindstedt-Poincare method for nonlinear vibration of axially moving beams. It is noted that many numerical investigations published so far employed step-by-step iterative time integration schemes to calculate the dynamic deflection response which requires a very small time step size in order to achieve the response with sufficient accuracy. This is inevitably computationally expensive. Another big concern associated with these iterative schemes is the error accumulation in each time step which may cause a huge loss of accuracy and sometimes numerical stability problem of the results in later time steps. To overcome this problem, several analytical and semianalytical approaches to the nonlinear vibration of beams which do not involve step-by-step time integration have been proposed; see, for example, those by Azrar et al. [9, 10], Leung and his coworkers [11–13], Lewandowski [14, 15], Nayfeh and his associates [16–18], and Ribeiro [19], to name just a few.

The differential quadrature method (DQM) is an efficient numerical approach developed by Bellman et al. [20] to solve linear and nonlinear differential equations. This method was later introduced to the structural analysis by Bert and his coworkers [21] and has been widely used in many structural engineering problems, including those in the nonlinear vibration of beams, plates, and shells; see, for example, the work by Zhong and Guo [22], Yang et al. [23, 24], Manaoach and Ribeiro [25], Hsu [26], and Tomasiello [27], among many others. Based on DQM approximation, this paper proposes a new semianalytic method for the geometrically nonlinear vibration of Euler-Bernoulli beams with different boundary conditions. The proposed method overcomes the disadvantage of error accumulation that occurs in conventional numerical methods involving iterative time integration and is therefore accurate and numerically stable even for a long time interval. The present paper is structured as follows: Section 2 briefly outlines the DQM rules. Section 3 gives a detailed description of mathematic formulations of the proposed semianalytical approach, starting with the transformation of the nonlinear governing equations into a group of linear differential equations by Linstedt-Poincare perturbation procedure which is followed by the semianalytical solution process for each perturbation equation by using DQM in space domain and an analytical series in the time domain. Section 4 presents some numerical results to validate the proposed method in both accuracy and convergence aspects through direct comparisons between the present results and existing solutions. Some concluding remarks are summarized in Section 4.

2. Mathematical Formulations

2.1. Perturbation Equations

Consider an isotropic, homogeneous slender beam of length L with uniform cross-section area subjected to a dynamic transverse load $\overline{q}(x,\overline{t})$. Let $\overline{u}$ and $\overline{w}$ be the displacements parallel to the x- and y-axes, $\overline{t}$ the time, and m denote the mass density. Based on classical Euler-Bernoulli beam theory and von-Karman nonlinear displacement-strain relationship, the geometrically nonlinear governing equations for flexural vibration of the beam can be derived as

$$\begin{gathered}\frac{\partial}{\partial x}\left[E\overline{A}\left(\frac{\partial\overline{u}}{\partial x}+\frac{1}{2}\left(\frac{\partial\overline{w}}{\partial x}\right)^2\right)\right]=0,\\ EI\frac{\partial^4\overline{w}}{\partial x^4}-E\overline{A}\left[\frac{\partial\overline{u}}{\partial x}+\frac{1}{2}\left(\frac{\partial\overline{w}}{\partial x}\right)^2\right]\frac{\partial^2\overline{w}}{\partial x^2}+m\frac{\partial^2\overline{w}}{\partial\overline{t}^2}=\overline{q}\left(x,\overline{t}\right),\end{gathered}\tag{2.1}$$

where E is the elastic modulus of the beam, and $\overline{A}$ and I are the area and the second moment of the cross section. The present analysis considers general boundary conditions, that is, the beam end may be either simply supported or clamped, with the following boundary conditions:

$$\begin{gathered}\overline{u} = 0, \quad \overline{w} = 0, \quad \overline{M}_x = 0 \quad \text{(simply supported)}, \\ \overline{u} = 0, \quad \overline{w} = 0, \quad \frac{d\overline{w}}{dx} = 0 \quad \text{(clamped)},\end{gathered} \tag{2.2}$$

where $\overline{M}_x$ is the bending moment of the beam. To facilitate the solution process of (2.1) by using the differential quadrature method in space domain, the following quantities are introduced:

$$\begin{gathered}u = \frac{\overline{u}}{\eta}, \quad w = \frac{\overline{w}}{\rho}, \quad \xi = \frac{x}{L}, \quad t = \omega\bar{t}, \quad q = \frac{L^4\overline{q}}{\rho EI}, \quad q = \varepsilon F, \\ p = \frac{\omega}{\omega_L}, \qquad \omega_L = \left(\frac{1}{L}\right)^2\sqrt{\frac{EI}{m}}, \qquad \rho^2 = \frac{I}{\overline{A}},\end{gathered} \tag{2.3}$$

where ω_L and ω refer to the linear and nonlinear frequencies of the beam, respectively, and ε is the small perturbation parameter. Substituting these quantities into (2.1) leads to dimensionless nonlinear governing equations as below

$$\begin{gathered}\frac{\partial^2 u}{\partial \xi^2} + \frac{\partial w}{\partial \xi}\frac{\partial^2 w}{\partial \xi^2} = 0, \\ \frac{\partial^4 w}{\partial \xi^4} - \left[\frac{\partial u}{\partial \xi} + \frac{1}{2}\left(\frac{\partial w}{\partial \xi}\right)^2\right]\frac{\partial^2 w}{\partial \xi^2} + p^2\frac{\partial^2 w}{\partial t^2} = \varepsilon F.\end{gathered} \tag{2.4}$$

Deflection w, axial displacement u, and frequency parameter p can be expanded into series forms in terms of a small perturbation parameter ε

$$w = w_1\varepsilon + w_3\varepsilon^3 + w_5\varepsilon^5 + \cdots, \tag{2.5}$$

$$u = u_2\varepsilon^2 + u_4\varepsilon^4 + \cdots, \tag{2.6}$$

$$p^2 = 1 + \varepsilon^2\sigma_2 + \varepsilon^4\sigma_4 + \cdots. \tag{2.7}$$

Inserting (2.5)–(2.7) into (2.4), and equating the terms of the same power of ε yield a series

of perturbation equations

$$\varepsilon^1: \quad \frac{\partial^4 w_1}{\partial \xi^4} + \frac{\partial^2 w_1}{\partial t^2} = F, \tag{2.8}$$

$$\varepsilon^2: \quad \frac{\partial^2 u_2}{\partial \xi^2} + \frac{\partial w_1}{\partial \xi}\frac{\partial^2 w_1}{\partial \xi^2} = 0, \tag{2.9}$$

$$\varepsilon^3: \quad \frac{\partial^4 w_3}{\partial \xi^4} - \frac{\partial u_2}{\partial \xi}\frac{\partial^2 w_1}{\partial \xi^2} - \frac{1}{2}\left(\frac{\partial w_1}{\partial \xi}\right)^2 \frac{\partial^2 w_1}{\partial \xi^2} + \frac{\partial^2 w_3}{\partial t^2} + \sigma_2 \frac{\partial^2 w_1}{\partial t^2} = 0, \tag{2.10}$$

$$\varepsilon^4: \quad \frac{\partial^2 u_4}{\partial \xi^2} + \frac{\partial w_1}{\partial \xi}\frac{\partial^2 w_3}{\partial \xi^2} + \frac{\partial w_3}{\partial \xi}\frac{\partial^2 w_1}{\partial \xi^2} = 0. \tag{2.11}$$

The initial conditions considered in the present study are

$$w_1(\xi, 0) = w_{10}, \qquad \frac{\partial w_1(\xi, 0)}{\partial t} = 0, \tag{2.12}$$

$$w_3(\xi, 0) = 0, \qquad \frac{\partial w_3(\xi, 0)}{\partial t} = 0, \tag{2.13}$$

where w_{10} refers to initial vibration amplitude. By making use of the dimensionless quantities and perturbation series defined above, the dimensionless form of the associated boundary conditions in each perturbation can also be obtained.

2.2. Differential Quadrature Method

According to the DQM rule, an unknown function $g(x)$ and its nth order derivative with respect to x can be approximated as the weighted linear sums of its function values at a number of sampling points in the x-axis as

$$g(x) = \sum_{i=1}^{N} g(x_i) L_i(x), \tag{2.14}$$

$$\left.\frac{d^n g(x)}{dx^n}\right|_{x=x_i} = \sum_{j=1}^{N} C_{ij}^{(n)} g(x_j) \quad (n = 1, \ldots, N-1), \tag{2.15}$$

where N is the total number of sampling points, $L_i(x)$ are Lagrange interpolation polynomials, and the weighting coefficients $C_{ij}^{(n)}$ can be calculated from recursive formulae [20, 21].

2.3. Semianalytical Solution of the 1st-Order Perturbation Equation

This study is focused on the nonlinear vibration due to an initial deflection. In such a case, the right-hand-side term in (2.8) $F = 0$. Hence, the first-order perturbation becomes

$$\frac{\partial^4 w_1}{\partial \xi^4} + \frac{\partial^2 w_1}{\partial t^2} = 0. \tag{2.16}$$

The solution of (2.16) can be readily obtained by separation of variables

$$w_1(\xi, t) = \sum_{m=0}^{N_s} T_{1m}(t)\phi_{1m}(\xi), \tag{2.17}$$

where N_s is the number of terms in the truncated time series,

$$T_{1m}(t) = \cos(p_m t) \tag{2.18}$$

is the solution in the time domain for the first-order perturbation equation, and p_m and $\delta_{1m}(\xi)$ are the frequency parameter and the associated mode shape function.

The transient deflection at an arbitrary sampling point "i" can be expressed as a cosine series with a supplementary term as

$$w_1(\xi_i, t) = \delta_0^i + \sum_{m=1}^{N_s} T_{1m}(t)\delta_{1m}^i \quad (i = 1, \ldots, N), \tag{2.19}$$

where $\delta_{1m}^i = \phi_{1m}(\xi_i)$ needs to be determined. The frequency parameter p_m of beams with different boundary conditions can be written in a general form as

$$p_m = \left[(m + j)\pi\right]^2 \tag{2.20}$$

in which $j = 0$ for a simply supported beam, $j = 1/2$ for a clamped beam, $j = -1/2$ for a beam clamped at one end and free at the other end, and $j = 1/4$ for a beam clamped at one end but simply supported at the other end.

Since $w_1(\xi_i, t)$ needs to satisfy the initial conditions in (2.12), one has

$$\delta_0^i = w_{10}^i - \sum_{m=1}^{N} \delta_{1m}^i. \tag{2.21}$$

The time domain function in (2.19) can be readily obtained as

$$w_1(\xi_i, t) = w_{10}^i + \sum_{m=1}^{N_s} (\cos p_{m1} t - 1) \quad \delta_{1m}^i \quad (i = 1, \ldots, N). \tag{2.22}$$

Differentiation of (2.22) with respect to time twice gives

$$\ddot{w}_1(\xi_i, t) = -\sum_{m=1}^{N_s} p_m^2 (\cos p_{m1} t) \delta_{1m}^i \quad (i = 1, \ldots, N). \tag{2.23}$$

The deflection response of the 1st-order perturbation equation can be determined by

$$w_1(\xi, t) = \sum_{i=1}^{N} w_1(\xi_i, t) L_i(\xi). \tag{2.24}$$

Substitution of (2.23) and application of DQM approximation (2.15) to (2.16) result in a semianalytical algebraic equation at an arbitrary sampling point

$$\sum_{j=1}^{N} C_{ij}^{(4)} \sum_{m=1}^{N_s} (\cos p_m t_k - 1) \delta_{1m}^j - p_1^2 \sum_{m=1}^{N_s} p_m^2 \cos(p_m t_k) \delta_{1m}^i = -\sum_{j=1}^{N} C_{ij}^{(4)} w_{10}^j \quad (i = 1, \ldots, N;\ k = 1, \ldots, N_s). \tag{2.25}$$

This linear equation system can be written in a matrix form as

$$[D_1]\{\delta_1\} = \{f_1\}, \tag{2.26}$$

where $[D_1]$ and $\{\delta_1\}$ are the coefficient matrix and unknown vector to be solved, and $\{f_1\}$ is the generalized load vector due to initial deflection. Once $\{\delta_1\}$ is determined from (2.26), the deflections at all of the sampling points can be calculated from (2.22) and the 1st-order deflection solution of the beam is then obtained from (2.24).

2.4. Semianalytical Solution of the 2nd-Order Perturbation Equation

To solve the 2nd-order perturbation equation (2.9), the unknown axial displacement u_2 is expressed as

$$u_2(\xi, t) = \sum_{m=1}^{N_s} T_{2m}(t) \phi_{2m}(\xi). \tag{2.27}$$

Substituting the 1st-order deflection solution and (2.27) into (2.9) yields

$$\sum_{m=1}^{N_s} T_{2m}(t) \frac{d^2 \phi_{2m}}{d\xi^2} = -\sum_{m=1}^{N_S} \sum_{n=1}^{N_S} T_{1m}(t) T_{1n}(t) \frac{d\phi_{1m}}{d\xi} \frac{d^2 \phi_{1n}}{d\xi^2}. \tag{2.28}$$

This gives

$$T_{2m} = -\frac{\sum_{n=1}^{N_s} T_{1m}T_{1n}\left(d\phi_{1m}/d\xi\right)\left(d^2\phi_{1n}/d\xi^2\right)}{d^2\phi_{2m}/d\xi^2}. \tag{2.29}$$

Therefore, (2.27) becomes

$$u_2(\xi,t) = \sum_{m=1}^{Ns}\sum_{n=1}^{Ns} T_{1m}T_{1n}\psi_{2mn}(\xi) \tag{2.30}$$

with

$$\psi_{2mn}(\xi) = -\frac{\left(d\phi_{1m}/d\xi\right)\left(d^2\phi_{1n}/d\xi^2\right)}{d^2\phi_{2m}/d\xi^2}\phi_{2m}. \tag{2.31}$$

From (2.30), the axial displacement u_2 at an arbitrary sampling point "i" is

$$u_2(\xi_i,t) = \sum_{m=1}^{N_s}\sum_{n=1}^{N_s} T_{1m}(t)T_{1n}(t)\delta_{2mn}^{i}. \tag{2.32}$$

Putting (2.30) into (2.9) and then applying DQM approximation, one has

$$\sum_{j=1}^{N} C_{ij}^{(2)}\sum_{m=1}^{N_s}\sum_{n=1}^{N_s} T_{1m}T_{1n}\delta_{2mn}^{j} = -\sum_{j=1}^{N} C_{ij}^{(1)}\sum_{m=1}^{N_s} T_{1m}\delta_{1m}^{j}\sum_{k=1}^{N} C_{ik}^{(2)}\sum_{n=1}^{N_s} T_{1n}\delta_{1n}^{k} \quad (i = 1,\ldots,N) \tag{2.33}$$

in a matrix form

$$[D_2]\cdot\{\delta_2\} = \{f_2\}. \tag{2.34}$$

Note that the right-hand-side term $\{f_2\}$ is the pseudodynamic force vector totally dependent on the 1st-order deflection solution already obtained. After the unknown vector $\{\delta_2\}$ composed of δ_{2mn}^{j} is determined from (2.34), u_2 can be calculated from the relationship

$$\psi_{2mn}(\xi) = \sum_{i=1}^{N} \delta_{2mn}^{i} L_i(\xi) \tag{2.35}$$

and (2.30).

2.5. Semianalytical Solution of the 3rd-Order Perturbation Equation

The 3rd-order perturbation equation (2.10) can be rewritten as

$$\frac{\partial^4 w_3}{\partial \xi^4} + \frac{\partial^2 w_3}{\partial t^2} = f(\xi, t), \tag{2.36}$$

where the right-hand-side term

$$f(\xi, t) = \left\{ \left[\frac{\partial u_2}{\partial \xi} + \frac{1}{2}\left(\frac{\partial w_1}{\partial \xi}\right)^2 \right] \right\} \frac{\partial^2 w_1}{\partial \xi^2} - \sigma_2 \frac{\partial^2 w_1}{\partial t^2}. \tag{2.37}$$

Substituting (2.17) and (2.30) into (2.37) gives

$$f(\xi, t) = \sum_{l=1}^{N_s} \sum_{m=1}^{N_S} \sum_{n=1}^{N_s} T_{1l} T_{1m} T_{1n} \varphi_{lmn} + \sum_{n=1}^{N_s} p_n^2 \sigma_2 T_{1n} \phi_{1n}, \tag{2.38}$$

where

$$\varphi_{lmn}(\xi) = \left\{ \frac{d\psi_{2lm}}{d\xi} + \frac{1}{2}\left[\frac{d\phi_{1l}}{d\xi} \frac{d\phi_{1m}}{d\xi} \right] \right\} \frac{d^2 \phi_{1n}}{d\xi^2}. \tag{2.39}$$

The solution of (2.36) can be readily obtained by the method of separation of variables

$$w_3(\xi, t) = \sum_{r=1}^{N_s} T_{3r}(t) \phi_{3r}(\xi). \tag{2.40}$$

It is evident from (2.16) and (2.36) that $\phi_{3m}(\xi)$ is the same as $\phi_{1m}(\xi)$. Therefore,

$$w_3(\xi, t) = \sum_{r=1}^{N_s} T_{3r}(t) \phi_{1r}(\xi), \tag{2.41}$$

and (2.36) becomes

$$\sum_{r=1}^{N_s} T_{3r}(t) \frac{\partial^4 \phi_{1r}}{\partial \xi^4} + \sum_{r=1}^{N_s} \frac{\partial^2 T_{3r}}{\partial t^2} \phi_{1r} = f(\xi, r). \tag{2.42}$$

From (2.16)–(2.18), one has

$$\frac{\partial^4 \phi_{1r}}{\partial \xi^4} = P_r^2 \phi_{1r}. \tag{2.43}$$

Expanding $f(\xi,t)$ into Fourier series in function ϕ_{1m}, (2.42) becomes

$$\sum_{r=1}^{N_s}\left[T_{3r}''+T_{3r}p_r^2\right]\phi_{1r}(\xi)=\sum_{r=1}^{N_s}f_r(\xi,t)\phi_{1r}(\xi) \tag{2.44}$$

which yields

$$T_{3r}''+T_{3r}p_r^2=f_r(\xi,t), \tag{2.45}$$

where right-hand-side term

$$\begin{gathered}
f_r(t)=\frac{1}{N_{3r}^2}\int_0^1 f(\xi,t)\phi_{1r}(\xi)d\xi=\sum_{l=1}^{N_s}\sum_{m=1}^{N_s}\sum_{n=1}^{N_s}a_{lmnr}T_{1l}T_{1m}T_{1n}+\sum_{n=1}^{N_s}\sigma_2 b_{nr}p_n^2T_{1n},\\
N_{3r}^2=\int_0^1\phi_{1r}^2(\xi)d\xi,\qquad a_{lmnr}=\frac{1}{N_{3r}^2}\int_0^1\varphi_{lmn}(\xi)\phi_{1r}(\xi)d\xi,\qquad b_{nr}=\frac{1}{N_{3r}^2}\int_0^1\phi_{1n}(\xi)\phi_{1r}(\xi)d\xi.
\end{gathered} \tag{2.46}$$

Since ϕ_{1r} are orthogonal functions, we have

$$b_{nr}=\begin{cases}0, & n\neq r,\\ \dfrac{1}{N_{3r}^2}\displaystyle\int_0^1\phi_{1r}\cdot\phi_{1r}(\xi)d\xi=1, & n=r.\end{cases} \tag{2.47}$$

To remove the secular terms in (2.43), $f_{3m}(t)$ is expanded as

$$\begin{aligned}
f_r(t)=&\left\{\sum_{l=1}^{Ns}\sum_{m=1}^{Ns}\sum_{n=1}^{Ns}\cos(p_l+p_m+p_n)ta_{lmnr}+\sum_{l=1}^{Ns}\sum_{m=1}^{Ns}\sum_{n=1}^{Ns}{}_{l\neq n,n\neq m}\cos(p_l+p_m-p_n)ta_{lmnr}\right.\\
&+\sum_{l=1}^{Ns}\sum_{m=1}^{Ns}\sum_{n=1}^{Ns}{}_{l\neq m,m\neq n}\cos(p_l-p_m+p_n)ta_{lmnr}\\
&\left.+\sum_{l=1}^{Ns}\sum_{m=1}^{Ns}\sum_{n=1}^{Ns}{}_{l\neq m,l\neq n}\cos(p_l-p_m-p_n)ta_{lmnr}\right\}\\
&+\left\{2\sum_{l=1}^{Ns}\sum_{m=1}^{Ns}{}_{l=n}\cos p_m ta_{lmlr}+2\sum_{l=1}^{Ns}\sum_{m=1}^{Ns}{}_{m=n}\cos p_l ta_{lmmr}+2\sum_{l=1}^{Ns}\sum_{n=1}^{Ns}{}_{l=m}\cos p_n ta_{llnr}\right.\\
&\left.+3\sum_{l=1}^{Ns}{}_{l=m=n}\cos p_l ta_{lllr}\right\}+p_r^2\sigma_{2r}\cos p_r t.
\end{aligned} \tag{2.48}$$

The following condition must be satisfied in order to remove the last two terms in (2.48),

$$\left\{2\sum_{l=1}^{Ns}\sum_{m=1}^{Ns}{}_{l=n}\cos p_m t a_{lmlr} + 2\sum_{l=1}^{Ns}\sum_{m=1}^{Ns}{}_{m=n}\cos p_l t a_{lmmr} + 2\sum_{l=1}^{Ns}\sum_{n=1}^{Ns}{}_{l=m}\cos p_n t a_{llnr} \right.$$
$$\left. +3\sum_{l=1}^{Ns}{}_{l=m=n}\cos p_l t a_{lllr}\right\} + p_r^2\sigma_{2r}\cos p_r t = 0. \tag{2.49}$$

The sum of the coefficients for $\cos(p_r t)$ must be zero, which gives the expressions of σ_2 for different values of m as

$$\sigma_{2r} = \frac{-1}{p_r^2}\left\{2\sum_{m=1}^{Ns}\left[a_{mrmr} + a_{rmmr} + a_{mmrr}\right] + 3a_{rrrr}\right\}. \tag{2.50}$$

Thus the term $f_{3m}(t)$ without secular terms is

$$f_r(t) = \left\{\sum_{l=1}^{Ns}\sum_{m=1}^{Ns}\sum_{n=1}^{Ns}\cos(p_l + p_m + p_n)t a_{lmnr} + \sum_{l=1}^{Ns}\sum_{m=1}^{Ns}\sum_{n=1}^{Ns}{}_{l\neq n, n\neq m}\cos(p_l + p_m - p_n)t a_{lmnr}\right.$$
$$+\sum_{l=1}^{Ns}\sum_{m=1}^{Ns}\sum_{n=1}^{Ns}{}_{l\neq m, m\neq n}\cos(p_l - p_m + p_n)t a_{lmnr}$$
$$\left.+\sum_{l=1}^{Ns}\sum_{m=1}^{Ns}\sum_{n=1}^{Ns}{}_{l\neq m, l\neq n}\cos(p_l - p_m - p_n)t\cdot a_{lmnr}\right\}. \tag{2.51}$$

Equation (2.45) can then be rewritten as

$$T_{3r}'' + T_{3r}p_r^2 = f_r(t). \tag{2.52}$$

From (2.13), the initial condition for (2.52) can be derived by using separation of variable method

$$T_{3r}(0) = \frac{dT_{3r}(0)}{dt} = 0. \tag{2.53}$$

The solution of (2.52) under the given initial condition (2.53) can be obtained through Laplace transform as

$$\begin{aligned}
T_{3r}(t) = {} & \sum_{l=1}^{M}\sum_{m=1}^{M}\sum_{n=1}^{M}\frac{\cos(p_r t)-\cos((p_l+p_m+p_n)t)}{(p_l+p_m+p_n)^2-p_r^2}\gamma_{lmnr} \\
& + \sum_{l=1}^{M}\sum_{m=1}^{M}\sum_{n=1}^{M}{}_{l\neq n, n\neq m}\frac{\cos(p_r t)-\cos((p_l+p_m-p_n)t)}{(p_l+p_m-p_n)^2-p_r^2}\gamma_{lmnr} \\
& + \sum_{l=1}^{M}\sum_{m=1}^{M}\sum_{n=1}^{M}{}_{l\neq m, m\neq n}\frac{\cos(p_r t)-\cos((p_l-p_m+p_n)t)}{(p_l-p_m+p_n)^2-p_r^2}\gamma_{lmnr} \\
& + \sum_{l=1}^{M}\sum_{m=1}^{M}\sum_{n=1}^{M}{}_{l\neq m, l\neq n}\frac{\cos(p_r t)-\cos((p_l-p_m-p_n)t)}{(p_l-p_m-p_n)^2-p_r^2}\gamma_{lmnr} \\
& \left(\text{where } \gamma_{lmnr} = \frac{1}{4}a_{lmnr}\right).
\end{aligned} \tag{2.54}$$

Finally, we have

$$w_3(\xi,t) = \sum_{r=1}^{Ns} T_{3r}(t)\phi_{1r}(\xi). \tag{2.55}$$

The deflections response of nonlinear free vibration of the beam is then calculated from

$$w = w_1\varepsilon + w_3\varepsilon^3 + \cdots \tag{2.56}$$

while the nonlinear frequency response, with higher-order terms being neglected, is given by (2.50) and (2.7) as

$$p_r^2 = 1 + \varepsilon^2\sigma_{2r}, \tag{2.57}$$

and the nonlinear frequency response can be obtained from

$$\left(\frac{\omega_r}{\omega_A}\right)^2 = 1 - \varepsilon^2\frac{1}{p_r^2}\left\{2\sum_{m=1}^{Ns}[a_{mrmr}+a_{rmmr}+a_{mmrr}]+3a_{rrrr}\right\}. \tag{2.58}$$

3. Numerical Results

To illustrate its efficiency and accuracy, the proposed semianalytical approach is used to study the nonlinear frequency and dynamic response of Euler-Bernoulli beams of rectangular cross section ($b \times h = 0.01\,\text{m} \times 0.02\,\text{m}$) under various boundary conditions with a given

Table 1: Normalized frequency ratio ω_n/ω_L for a simply supported beam.

A	$N = 9$	$N = 11$	$N = 13$	Woinowsky-Krieger [1]	Mei [28]
0.1	1.0009	1.0009	1.0009	1.0008	1.0009
0.2	1.0037	1.0037	1.0037	1.0038	1.0037
0.4	1.0149	1.0149	1.0149	1.0150	1.0148
0.6	1.0331	1.0331	1.0334	1.0380	1.0339
0.8	1.0580	1.0581	1.0588	1.0580	1.0578
1.0	1.0891	1.0893	1.0908	1.0890	1.0889
1.5	1.1893	1.1910	1.1932	1.1900	1.1902
2.0	1.3140	1.3201	1.3300	1.3160	1.3022

Table 2: Normalized frequency ratio ω_n/ω_L for a clamped beam.

A	$N = 9$	$N = 11$	$N = 13$	Mei [28]
0.1	1.0003	1.0003	1.0003	1.0003
0.2	1.0012	1.0012	1.0012	1.0012
0.4	1.0050	1.0047	1.0048	1.0048
0.6	1.0112	1.0106	1.0107	1.0107
0.8	1.0198	1.0187	1.0190	1.0190
1.0	1.0307	1.0290	1.0295	1.0296
1.5	1.0676	1.0640	1.0650	1.0653
2.0	1.1169	1.1100	1.1125	1.1135

initial vibration amplitude and zero-valued initial velocity. The dimensionless vibration amplitude is defined as $A = W/\rho$ (or $A = 6W/\sqrt{3}h$ for a rectangular beam) where W is the vibration amplitude at the midpoint of the beam. The parameters used herein are $L = 0.5\,\mathrm{m}$, $E = 150\,\mathrm{GPa}$, and $m = 8 \times 10^3\,\mathrm{kg/m^3}$. The results are presented in both tabular and graphical forms in terms of the normalized frequency ratio ω_n/ω_L and dimensionless dynamic deflections at the midpoint of the beam.

Among the sampling point distribution schemes available, a nonuniform distribution is chosen in the present analysis due to its excellent convergence [21, 26], that is,

$$x_k = \frac{1}{2}\left(1 - \cos\frac{k\pi}{N-1}\right) \quad (k = 0, 1, \ldots, N-1). \tag{3.1}$$

In what follows, the total number of sampling points in the space domain is $N = 11$, unless stated otherwise.

In Figures 1–3, the present solutions and exact solutions are represented by solid lines and circular dots, respectively.

3.1. Nonlinear Vibration Frequency

Tables 1, 2, and 3 list, respectively, the normalized fundamental frequency ratios ω_n/ω_L for a simply supported beam, a clamped beam, and a beam simply supported at one end but clamped at the other end at varying dimensionless vibration amplitudes $A = 0.1 \sim 2.0$. All beams exhibit typical "hard-spring" behavior, that is, the frequency ratio increases with an increase in vibration amplitude. Comparisons between the results with varying total number

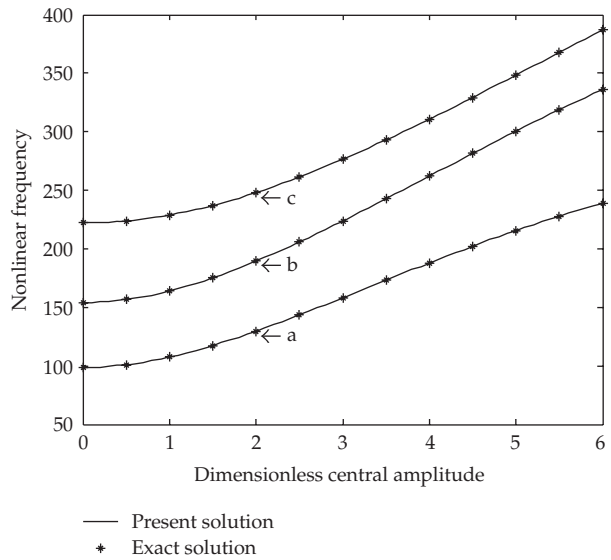

Figure 1: Nonlinear fundamental frequency versus dimensionless central amplitude relationship of beams with different boundary conditions.

of sampling points $N = 9, 11, 13$ show that the present method converges very well to produce very accurate results when $N \geq 11$. Our results are compared with the existing results obtained by using elliptic function [1] and the finite element method [28]. The relative errors, defined as

$$\frac{(\text{Present Solution} - \text{Existing Solution})}{\text{Existing Solution}} \times 100\%, \tag{3.2}$$

are also provided. Excellent agreement can be observed in these tables. The relationship between nonlinear fundamental frequency and dimensionless vibration amplitude ($A = 0.0 \sim 6.0$) of these three beams are shown in Figure 1 where curves a, b, and c are for a simply supported beam, a beam simply supported at one end but clamped at the other end, and a clamped beam. The scatter points represent the elliptical function results using the formulae provided by Woinowsky-Krieger [1]. As can be seen, the present results and the elliptical function results are almost identical. The clamped beam has the highest fundamental frequency with the lowest deflection while the simply supported beam has the smallest fundamental frequency and the largest deflection. This is because the end support of the clamped beam is much stronger than its simply supported counterpart.

3.2. Nonlinear Dynamic Response

Convergence study on the nonlinear dynamic response is conducted in both Tables 4 and 5 where central deflections of a simply supported beam at different time (in sec), calculated by using different total number of sampling points N in the space domain and different number of truncated series terms N_s in the time domain, are given and compared with the results calculated by using the formulae given by Woinowsky-Krieger [1]. The dimensionless

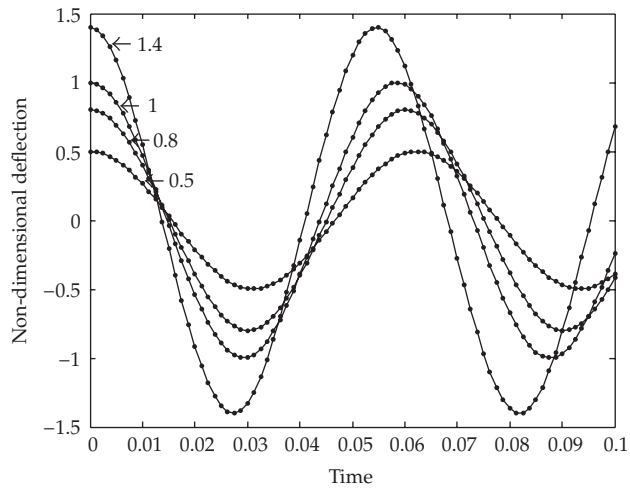

Figure 2: Nondimensional central deflection response of a simply supported beam under different initial vibration amplitudes.

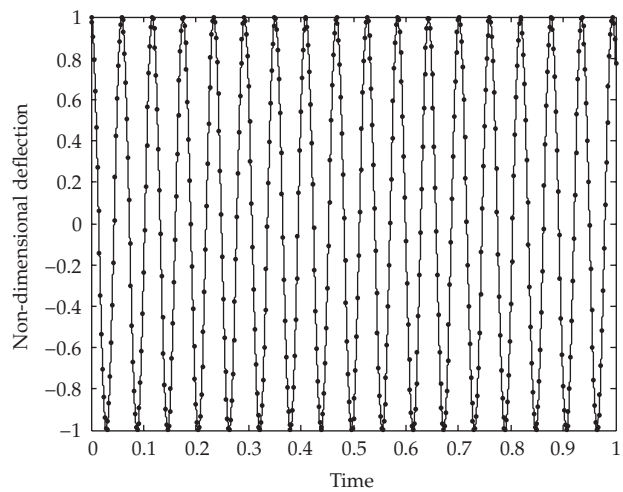

Figure 3: Nondimensional central deflection response of a simply supported beam.

Table 3: Normalized frequency ratio ω_n/ω_L for a beam simply supported at one end and clamped at the other end.

A	$N = 9$	$N = 11$	$N = 13$	Mei [28]
0.1	1.0006	1.0006	1.0006	1.0006
0.2	1.0026	1.0026	1.0026	1.0026
0.4	1.0103	1.0103	1.0103	1.0106
0.6	1.0230	1.0231	1.0231	1.0238
0.8	1.0404	1.0406	1.0407	1.0418
1.0	1.0624	1.0627	1.0628	1.0647
1.5	1.1346	1.1353	1.1355	1.1404
2.0	1.2272	1.2283	1.2286	1.2385

Table 4: Nonlinear central deflection response of a simply supported beam: solutions with varying number of terms in time domain series N_s.

Time (s)	$N_s = 1$	$N_s = 3$	$N_s = 5$	Woinowsky-Krieger [1]	Error 1	Error 2	Error 3
0.0050	0.8622	0.8566	0.8553	0.8533	1.0505	0.3895	0.2405
0.0100	0.4811	0.4720	0.4700	0.4665	3.1360	1.1828	0.7540
0.0150	−0.0420	−0.0398	−0.0395	−0.0404	3.7991	−1.6178	−2.2036
0.0300	−0.9965	−0.9939	−0.9942	−0.9963	0.0134	−0.2437	−0.2146
0.0400	−0.4060	−0.3952	−0.3938	−0.3928	3.3588	0.6230	0.2717
0.0450	0.1259	0.1240	0.1231	0.1210	4.0692	2.4780	1.7217
0.0550	0.9335	0.9300	0.9297	0.9286	0.5294	0.1543	0.1177
0.0650	0.7672	0.7596	0.7574	0.7545	1.6804	0.6677	0.3804
0.0750	−0.2086	−0.2022	−0.2010	−0.2009	3.8259	0.6691	0.0613
0.0850	−0.9596	−0.9547	−0.9549	−0.9566	0.3065	−0.2001	−0.1767
0.0900	−0.9698	−0.9655	−0.9657	−0.9676	0.2261	−0.2173	−0.1960
0.0950	−0.7113	−0.6999	−0.6983	−0.6974	1.9872	0.3496	0.1245
0.1000	−0.2477	−0.2404	−0.2390	−0.2387	3.7615	0.7006	0.1317

vibration amplitude is $A = 1.0$. Error 1, Error 2, and Error 3 in Table 4 indicate the relative error percentages between the exact solutions and the present results with $N = 9$ and $N_s = 1$, $N = 9$ and $N_s = 3$, $N = 9$ and $N_s = 5$ while Error 4, Error 5, and Error 6 in Table 5 are the relative error percentages between the exact solutions and the present results with $N = 9$ and $N_s = 3$, $N = 11$ and $N_s = 3$, $N = 13$ and $N_s = 3$. Our semianalytical solutions converge monotonically as N_s increases but nonmonotonically with an increasing N. However, the present method is capable of giving very accurate results with relative error less than 1.5% when $N_s \geq 3$ and $N \geq 11$. We have calculated the nonlinear dynamic response of beams with other end supports as well and found that the results exhibit the same convergence characteristics as observed in Tables 4 and 5. These results are, therefore, not detailed here.

Figure 2 depicts the nonlinear dynamic central deflection response of a simply supported beam with dimensionless initial deflection $w_{10} = 0.5\sin(\pi\xi)$, $0.8\sin(\pi\xi)$, $1.0\sin(\pi\xi)$, and $1.4\sin(\pi\xi)$. The time interval in this example is relatively short, that is, $t = 0 \sim 0.1$ sec. The result within a much longer time interval $t = 0 \sim 1$ sec is displayed in Figure 3 where $w_{10} = 1.0\sin(\pi\xi)$. $N = 11$ and $N_s = 3$ are used in these two examples. Again, the present results agree very well with the elliptical function solutions by Woinowsky-Krieger [1]. It is also seen that a bigger initial deflection magnitude results in larger vibration amplitude.

It is worthy of noting that unlike the conventional numerical integration schemes commonly used to calculate dynamic response whose accuracy is quickly degraded at later time steps due to the accumulation of numerical errors, the proposed technique does not involve iterative time integration and accumulative errors and is therefore able to give results with excellent accuracy even for a very long time interval, as demonstrated in Figure 3.

4. Conclusions

A new semianalytical method for geometrically nonlinear vibration analysis of Euler-Bernoulli beams with different boundary conditions is presented in this paper. The proposed method is based on the perturbation technique, differential quadrature approximation, and an analytical series expansion in the time domain. Numerical results show that this

Table 5: Nonlinear central deflection response of a simply supported beam: solutions with varying total number of sampling points N.

Time (s)	$N = 9$	$N = 11$	$N = 13$	Woinowsky-Krieger [1]	Error 4	Error 5	Error 6
0.0050	0.8566	0.8562	0.8562	0.8533	0.3895	0.3458	0.3484
0.0100	0.4720	0.4711	0.4712	0.4665	1.1828	0.9922	1.0026
0.0150	−0.0398	−0.0410	−0.0410	−0.0404	−1.6178	1.4624	1.4228
0.0300	−0.9939	−0.9967	−0.9967	−0.9963	−0.2437	0.0411	0.0378
0.0400	−0.3952	−0.3969	−0.3970	−0.3928	0.6230	1.0606	1.0657
0.0450	0.1240	0.1223	0.1223	0.1210	2.4780	1.0651	1.0839
0.0500	0.6106	0.6097	0.6097	0.6048	0.9513	0.7984	0.8054
0.0650	0.7596	0.7585	0.7586	0.7545	0.6677	0.5300	0.5335
0.0750	−0.2022	−0.2033	−0.2033	−0.2009	0.6691	1.1924	1.1903
0.0850	−0.9547	−0.9580	−0.9579	−0.9566	−0.2001	0.1391	0.1377
0.0900	−0.9655	−0.9687	−0.9687	−0.9676	−0.2173	0.1140	0.1122
0.0950	−0.6999	−0.7017	−0.7017	−0.6974	0.3496	0.6071	0.6093
0.1000	−0.2404	−0.2415	−0.2415	−0.2387	0.7006	1.1716	1.1717

method has excellent accuracy and convergence characteristics. Compared with other numerical approaches that use step-by-step time integration, the present method has a unique advantage of being capable of producing results with very good and stable accuracy at a long time interval because the error accumulation is avoided due to the use of the analytical time series.

References

[1] S. Woinowsky-Krieger, "The effect of an axial force on the vibration of hinged bars," *Journal of Applied Mechanics ASME*, vol. 17, no. 1, pp. 35–36, 1950.

[2] R. Lewandowski, "Application of the Ritz method to the analysis of non-linear free vibrations of beams," *Journal of Sound and Vibration*, vol. 114, no. 1, pp. 91–101, 1987.

[3] M. Sathyamoorthy, *Nonlinear Analysis of Structures*, CRC Press, Boca Raton, Fla, USA, 1997.

[4] K. Y. Sze, S. H. Chen, and J. L. Huang, "The incremental harmonic balance method for nonlinear vibration of axially moving beams," *Journal of Sound and Vibration*, vol. 281, no. 3–5, pp. 611–626, 2005.

[5] M. M. Gadagi and H. Benaroya, "Dynamic response of an axially loaded tendon of a tension leg platform," *Journal of Sound and Vibration*, vol. 293, no. 1-2, pp. 38–58, 2006.

[6] R. A. Ibrahim and R. J. Somnay, "Nonlinear dynamic analysis of an elastic beam isolator sliding on frictional supports," *Journal of Sound and Vibration*, vol. 308, no. 3–5, pp. 735–757, 2007.

[7] E. Ozkaya and A. Tekin, "Non linear vibrations of stepped beam system under different boundary conditions," *Structural Engineering and Mechanics*, vol. 27, no. 3, pp. 333–345, 2007.

[8] S. H. Chen, J. L. Huang, and K. Y. Sze, "Multidimensional Lindstedt-Poincaré method for nonlinear vibration of axially moving beams," *Journal of Sound and Vibration*, vol. 306, no. 1-2, pp. 1–11, 2007.

[9] L. Azrar, R. Benamar, and R. G. White, "A semi-analytical approach to the non-linear dynamic response problem of S-S and C-C beams at large vibration amplitudes part I: general theory and application to the single mode approach to free and forced vibration analysis," *Journal of Sound and Vibration*, vol. 224, no. 2, pp. 183–207, 1999.

[10] L. Azrar, R. Benamar, and R. G. White, "A semi-analytical approach to the non-linear dynamic response problem of beams at large vibration amplitudes, part I: multimode approach to the steady state forced periodic response," *Journal of Sound and Vibration*, vol. 255, no. 1, pp. 1–41, 2002.

[11] A. Y. T. Leung and S. G. Mao, "Symplectic integration of an accurate beam finite element in non-linear vibration," *Computers and Structures*, vol. 54, no. 6, pp. 1135–1147, 1995.

[12] A. Y. T. Leung and S. G. Mao, "A symplectic Galerkin method for non-linear vibration of beams and plates," *Journal of Sound and Vibration*, vol. 183, no. 3, pp. 475–491, 1995.

[13] A. Y. T. Leung and T. Ge, "Normal multi-modes of non-linear euler beams," *Journal of Sound and Vibration*, vol. 202, no. 2, pp. 145–160, 1997.
[14] R. Lewandowski, "Computational formulation for periodic vibration of geometrically nonlinear structures—part 1: theoretical background," *International Journal of Solids and Structures*, vol. 34, no. 15, pp. 1925–1947, 1997.
[15] R. Lewandowski, "Computational formulation for periodic vibration of geometrically nonlinear structures—part 2: numerical strategy and examples," *International Journal of Solids and Structures*, vol. 34, no. 15, pp. 1949–1964, 1997.
[16] M. I. Younis and A. H. Nayfeh, "A study of the nonlinear response of a resonant microbeam to an electric actuation," *Nonlinear Dynamics*, vol. 31, no. 1, pp. 91–117, 2003.
[17] S. A. Emam and A. H. Nayfeh, "On the nonlinear dynamics of a buckled beam subjected to a primary-resonance excitation," *Nonlinear Dynamics*, vol. 35, no. 1, pp. 1–17, 2004.
[18] S. A. Emam and A. H. Nayfeh, "Nonlinear responses of buckled beams to subharmonic-resonance excitations," *Nonlinear Dynamics*, vol. 35, no. 2, pp. 105–122, 2004.
[19] P. Ribeiro, "Hierarchical finite element analyses of geometrically non-linear vibration of beams and plane frames," *Journal of Sound and Vibration*, vol. 246, no. 2, pp. 225–244, 2001.
[20] R. Bellman, B. G. Kashef, and J. Casti, "Differential quadrature: a technique for the rapid solution of nonlinear partial differential equations," *Journal of Computational Physics*, vol. 10, pp. 40–52, 1972.
[21] CH. W. Bert, S. K. Jang, and A. G. Striz, "Nonlinear bending analysis of orthotropic rectangular plates by the method of differential quadrature," *Computational Mechanics*, vol. 5, no. 2-3, pp. 217–226, 1989.
[22] H. Zhong and Q. Guo, "Nonlinear vibration analysis of Timoshenko beams using the differential quadrature method," *Nonlinear Dynamics*, vol. 32, no. 3, pp. 223–234, 2003.
[23] J. Yang, S. Kitipornchai, and K. M. Liew, "Large amplitude vibration of thermo-electro-mechanically stressed FGM laminated plates," *Computer Methods in Applied Mechanics and Engineering*, vol. 192, no. 35-36, pp. 3861–3885, 2003.
[24] J. Yang, S. Kitipornchai, and K. M. Liew, "Non-linear analysis of the thermo-electro-mechanical behaviour of shear deformable FGM plates with piezoelectric actuators," *International Journal for Numerical Methods in Engineering*, vol. 59, no. 12, pp. 1605–1632, 2004.
[25] E. Manoach and P. Ribeiro, "Coupled, thermoelastic, large amplitude vibrations of Timoshenko beams," *International Journal of Mechanical Sciences*, vol. 46, no. 11, pp. 1589–1606, 2004.
[26] M.-H. Hsu, "Mechanical analysis of non-uniform beams resting on nonlinear elastic foundation by the differential quadrature method," *Structural Engineering and Mechanics*, vol. 22, no. 3, pp. 279–292, 2006.
[27] S. Tomasiello, "A DQ based approach to simulate the vibrations of buckled beams," *Nonlinear Dynamics*, vol. 50, no. 1-2, pp. 37–48, 2007.
[28] C. Mei, "Finite element displacement method for large amplitude free flexural vibrations of beams and plates," *Computers and Structures*, vol. 3, no. 1, pp. 163–174, 1973.

Hindawi Publishing Corporation
Mathematical Problems in Engineering
Volume 2010, Article ID 650247, 11 pages
doi:10.1155/2010/650247

Research Article

Sensitivity with Respect to the Path Parameters and Nonlinear Stiffness of Vibration Transfer Path Systems

Yimin Zhang and Xianzhen Huang

School of Mechanical Engineering and Automation, Northeastern University, Shenyang 110004, China

Correspondence should be addressed to Yimin Zhang, neu831109@yahoo.com.cn

Received 17 December 2009; Accepted 6 April 2010

Academic Editor: Carlo Cattani

Generally speaking, a vibration system consists of three parts: vibration resource, vibration transfer path, and vibration receiver. Based on the dynamic sensitivity technique, this paper proposes a method for evaluating the contribution of each vibration transfer path to the dynamic response of the vibration receiver. Nonlinear stiffness is an important factor in causing the nonlinearity of vibration systems. Taking sensitivity as the evaluation criteria, we present an effective approach for estimating the influence of nonlinear stiffness in vibration transfer paths on the dynamic response of the vibration receiver. Using the proposed method, the sensitivity of the vibration system with multiple and/or multidimensional transfer paths could be determined in the time domain.

1. Introduction

The level of vibration and noise relates to the quality of mechanical products and equipments. That is to say mechanical products with proper vibration and noise characteristics are prone to be favored by customers and are prone to make more profits for the enterprise. Therefore, the study of the transfer of vibration and noise in vibration systems with multiple and/or multi-dimensional transfer paths is of significant value. As well known, the technology of vibration and noise control plays an important role both in the improvement of the comprehensive property and technical index of mechanical products and in the advancement of the scientific and technical grade of mechanical equipments. The conventional conception of vibration and noise control in practical engineering projects is to cut off the transfer path of vibration and noise so as to reduce vibration and noise disturbance. However, in practical applications, it is out of the question to completely cut off the vibration transfer path. And an engineer can only try to minimize the energy transfer in vibration

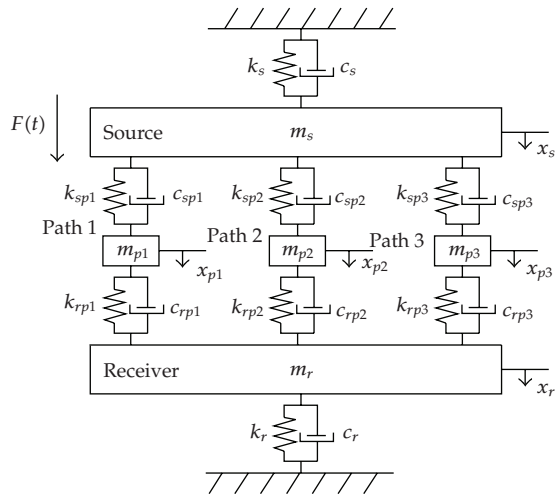

Figure 1: The model of 5-DOF vibration transfer path systems.

transfer paths while the vibration transfer paths in vibration systems are precisely identified. Therefore, the researches on the interaction of the vibration source, vibration transfer path, and vibration receiver are mainly focused on energy transfer techniques and physical experiments. The methods based on energy (or power) transfer and dynamic tests have been widely used to investigate the dynamic characteristics of vibration transfer path systems [1–5].

When conducting a dynamic design or modification, a designer always needs to know which parameters have more significant effects on the dynamic performance of the system. Therefore, dynamic sensitivity analysis has turned to be a powerful and multipurpose design tool in optimum structural design, structural parameter identification, system dynamic control, and so forth. Generally speaking, vibration tests are needed in dynamic design of a practical engineering project. Once the design scheme is changed, the whole process of the vibration test should be performed once again, which wastes great expenditures of resources, both human and material. In this case, a designer relies largely upon his experiences and past works, which is blind to some extent. Therefore, we need to study the sensitivity of vibration systems with respect to path parameters. In this way, the performance variation of the dynamic system following the change of path parameters can be figured out.

On the basis of the basic conception of vibration theories, this paper presents a method to quantify the contribution of each vibration transfer path to the dynamic response of the vibration transfer path system by employing the dynamic sensitivity as an evaluation index. Especially, a method for sensitivity analysis of nonlinear vibration transfer path systems with respect to different kinds of non-linear stiffness is also explored in the time domain. In view of the above studies, the designer can figure out which kind of non-liner stiffness has more significant influence on the dynamic response of the vibration transfer path system. Then precautionary measures can be taken to reduce the energy transfer of vibration and noise by modifying the structural parameter and topology or by changing components in the significant transfer paths.

2. Vibration Transfer Path Systems

Generally speaking, every vibration engineering problem can be rationalized into three parts: vibration source (i.e., what is the dynamic loading), vibration path (i.e., what is the structural mass, stiffness, and damping), and vibration response and its effects on the "receiver" (typically, the receiver is humans, occupying the structure but could also be vibration sensitive equipment). As shown in Figure 1, a five-degree-of-freedom (5-DOF) vibration transfer path system with non-linear stiffness is subjected to a dynamic excitation. Newton's law can be applied to obtain the vibration differential equations of the 5-DOF vibration transfer path system as follows:

$$\mathbf{M}\ddot{\mathbf{x}} + \mathbf{C}\dot{\mathbf{x}} + \mathbf{K}(\mathbf{x})\mathbf{x} = \mathbf{F}(t), \tag{2.1}$$

where

$$\begin{gathered}
\mathbf{M} = \operatorname{diag}\left[m_s \quad m_{p1} \quad m_{p2} \quad m_{p3} \quad m_r\right], \\
\mathbf{C} = \begin{bmatrix} c_s + c_{sp1} + c_{sp2} + c_{sp3} & -c_{sp1} & -c_{sp2} & -c_{sp3} & 0 \\ -c_{sp1} & c_{sp1} + c_{rp1} & 0 & 0 & -c_{rp1} \\ -c_{sp2} & 0 & c_{sp2} + c_{rp2} & 0 & -c_{rp2} \\ -c_{sp3} & 0 & 0 & c_{sp3} + c_{rp3} & -c_{rp3} \\ 0 & -c_{rp1} & -c_{rp2} & -c_{rp3} & c_r + c_{rp1} + c_{rp2} + c_{rp3} \end{bmatrix}, \\
\mathbf{K} = \begin{bmatrix} k_s + k_{sp1} + k_{sp2} + k_{sp3} & -k_{sp1} & -k_{sp2} & -k_{sp3} & 0 \\ -k_{sp1} & k_{sp1} + k_{rp1} & 0 & 0 & -k_{rp1} \\ -k_{sp2} & 0 & k_{sp2} + k_{rp2} & 0 & -k_{rp2} \\ -k_{sp3} & 0 & 0 & k_{sp3} + k_{rp3} & -k_{rp3} \\ 0 & -k_{rp1} & -k_{rp2} & -k_{rp3} & k_r + k_{rp1} + k_{rp2} + k_{rp3} \end{bmatrix}, \\
\mathbf{F}(t) = \{F_0 \sin(\omega t) 0000\}^T, \qquad \mathbf{x}(t) = \left\{x_s x_{p1} x_{p2} x_{p3} x_r\right\}^T.
\end{gathered} \tag{2.2}$$

In this paper, k_{sp1} is supposed to be non-linear stiffness. In general, there are two kinds of non-linear elastic forces, which are called the material non-linear force and the piecewise linear force. $k_{sp1}^{e(i)}$ $(i = 1, 2)$ is used to denote the equivalent linear stiffness of the above mentioned two kinds of non-linear stiffness. In engineering practice, the non-linear stiffness is usually approximately described by equivalent linear stiffness as

$$\mathbf{K}^e = \frac{\partial \mathbf{F}(\mathbf{x})}{\partial \mathbf{x}^T} = \frac{\partial[\mathbf{K}(\mathbf{x})\mathbf{x}]}{\partial \mathbf{x}^T} = \mathbf{K}(\mathbf{x}) + \frac{\partial \mathbf{K}(\mathbf{x})}{\partial \mathbf{x}^T}(\mathbf{I}_n \otimes \mathbf{x}), \tag{2.3}$$

where $\mathbf{F}(\mathbf{x}) = \mathbf{K}(\mathbf{x})\mathbf{x}$ denotes the non-linear elastic force, $\mathbf{I}_n$ is a identity matrix with $n \times n$ dimensions, and the symbol $\otimes$ represents Kronecker product, which can be defined as

$$\mathbf{A}_{\mathbf{p}\times\mathbf{q}} \otimes \mathbf{B}_{\mathbf{s}\times\mathbf{t}} = \begin{bmatrix} \mathbf{a}_{11}\mathbf{B} & \mathbf{a}_{12}\mathbf{B} & \cdots & \mathbf{a}_{1\mathbf{q}}\mathbf{B} \\ \mathbf{a}_{21}\mathbf{B} & \mathbf{a}_{22}\mathbf{B} & \cdots & \mathbf{a}_{2\mathbf{q}}\mathbf{B} \\ \vdots & \vdots & \ddots & \vdots \\ \mathbf{a}_{\mathbf{p}1}\mathbf{B} & \mathbf{a}_{\mathbf{p}2}\mathbf{B} & \cdots & \mathbf{a}_{\mathbf{pq}}\mathbf{B} \end{bmatrix}_{\mathbf{ps}\times\mathbf{qt}}. \tag{2.4}$$

3. Nonlinear Stiffness in Vibration Transfer Path Systems

In most cases, the elastic force is non-linear. When dealing with a specific problem, based on experiments, the non-linear elastic force can always be expressed as a function of motion parameters after some simplifications. This approach is often an important step in dealing with vibration engineering problems with non-linear stiffness.

3.1. Material Non-Linear Stiffness

In actual engineering materials, the stress-strain relation is nonlinear and follows Hook's law only up to a certain deformation (displacement of one end with respect to the other). Beyond the deformation, the stress exceeds the yield point of the material and the stress-strain relation becomes nonlinear. This kind of non-linear stiffness is usually called material non-linear stiffness, which can be roughly divided into two types. (1) If the slope of the force-deflection curve increases with the increase of the deformation, the spring element is said to be hardening or hard. (2) If the slope of the force-deflection curve decreases with the increase of the deformation, the spring element is softening or soft. In many practical applications, the non-linear elastic force can be approximately denoted as

$$F_{sp1}^{(1)}(\mathbf{x}) = k_{sp1}^{1(1)}\left(x_{p1} - x_s\right) \pm k_{sp1}^{2(1)}\left(x_{p1} - x_s\right)^3, \tag{3.1}$$

where $k_{sp1}^{1(1)} > 0$, $k_{sp1}^{2(1)} > 0$ and $x_{p1} - x_s$ is the displacement of the spring from its free length, $k_{sp1}^{1(1)}(x_{p1} - x_s)$ denotes the linear elastic force, $k_{sp1}^{2(1)}(x_{p1} - x_s)^3$ denotes the non-linear elastic force, and the non-linear elastic force is often much smaller than the linear elastic force. Therefore the non-linear elastic force can be regarded as a correction term. Sign "±" indicates the character of stiffness, which is "+" or "−" depending on whether the character of the stiffness is hard or soft. Consequently, the coefficient of the equivalent linear stiffness, $k_{sp1}^{e(1)}$, of material non-linear stiffness can be represented as

$$k_{sp1}^{e(1)} = k_{sp1}^{1(1)} \pm 3k_{sp1}^{2(1)}\left(x_{p1} - x_s\right)^2. \tag{3.2}$$

As shown in (3.2), a nonlinear spring element does not have a single stiffness value because its slope is variable. For a hard spring, its slop and thus its stiffness increase with deflection. The stiffness of a soft spring decreases with deflection.

3.2. Piecewise Linear Stiffness

Sometimes a nonlinear model is unavoidable. This is the case when a system is designed to utilize two or more spring elements to achieve a spring constant that varies with the applied load. Even if each spring element is linear, the combined system will be nonlinear. An example of such a system is the vehicle suspension with a main spring and an auxiliary spring. Furthermore, some vibrating machineries, such as the vibrating screen and the oscillating conveyer, use the spring set to get the desired dynamic characteristics. As for this kind of non-linear elastic model, under certain circumstances, two or more groups of springs work together in the form of parallel or series to increase or decrease the stiffness of the system. From statics, we know that the non-linear restoring force of the piecewise linear stiffness vibration system can be represented as

$$F_{sp1}^{(2)}(\mathbf{x}) = \begin{cases} k_{sp1}^{2(2)}(x_{p1}-x_s) - \left(k_{sp1}^{1(2)}-k_{sp1}^{2(2)}\right)(x_{p1}-x_s)_0, & -(x_{p1}-x_s)_0 \geq (x_{p1}-x_s), \\ k_{sp1}^{1(2)}(x_{p1}-x_s), & -(x_{p1}-x_s)_0 \leq (x_{p1}-x_s) \leq (x_{p1}-x_s)_0, \\ k_{sp1}^{2(2)}(x_{p1}-x_s) + \left(k_{sp1}^{1(2)}-k_{sp1}^{2(2)}\right)(x_{p1}-x_s)_0, & (x_{p1}-x_s)_0 \leq (x_{p1}-x_s). \end{cases} \tag{3.3}$$

Therefore, for the non-linear stiffness of piecewise linearity, the equivalent stiffness $k_{sp1}^{e(2)}$ of k_{sp1} is

$$k_{sp1}^{e(2)} = \begin{cases} k_{sp1}^{1(2)}, & -(x_{p1}-x_s)_0 \leq (x_{p1}-x_s) \leq (x_{p1}-x_s)_0. \\ k_{sp1}^{2(2)}, & \text{otherwise.} \end{cases} \tag{3.4}$$

To investigate the influences of different kinds of non-linear stiffness on the dynamic response of the vibration transfer path system, we present a method for sensitivity analysis of the dynamic response of the vibration receiver with respect to the equivalent linear stiffness coefficients ($k_{sp1}^{e(1)}$ and $k_{sp1}^{e(2)}$) of material non-linear stiffness and piecewise linear stiffness. In this way, which kind of nonlinear stiffness has more significant influence on the dynamic responses of vibration transfer path systems can be accurately judged.

4. Sensitivity with Respect to Path Parameters and Non-Linear Stiffness

Sensitivity analysis plays an important role in optimization design and dynamic modification. Based on design sensitivity results, an engineer can decide on the direction and amount of design change needed to improve the performance measures. In addition, design sensitivity information can provide answers to "what if" questions by predicting performance measure perturbations when the perturbations of design variables are provided. The dynamic sensitivity analysis provides a theoretical basis for identifying the parameter contribution of each transfer path to the dynamic response of vibration transfer path systems.

Based on Kronecker algebra and matrix calculus, we can obtain general sensitivity equations through partial differential vector calculus of (2.1):

$$\mathbf{M}\frac{D\ddot{\mathbf{x}}}{D\mathbf{V}^T}+\mathbf{C}\frac{D\dot{\mathbf{x}}}{D\mathbf{V}^T}+\mathbf{K}\frac{D\mathbf{x}}{D\mathbf{V}^T}=\frac{\mathbf{F}(\mathbf{t})}{\partial\mathbf{V}^T}-\frac{\partial\mathbf{M}}{\partial\mathbf{V}^T}(\mathbf{I}_s\otimes\ddot{\mathbf{x}})-\frac{\partial\mathbf{C}}{\partial\mathbf{V}^T}(\mathbf{I}_s\otimes\dot{\mathbf{x}})-\frac{\partial\mathbf{K}}{\partial\mathbf{V}^T}(\mathbf{I}_s\otimes\mathbf{x}), \tag{4.1}$$

where $\mathbf{I}_s$ is a identity matrix with $s\times s$ dimensions, signal "$\otimes$" is the Kronecker product, $\mathbf{V}=(m_{p1}\ m_{p2}\ m_{p3}\ c_{sp1}\ c_{sp2}\ c_{sp3}\ c_{rp1}\ c_{rp2}\ c_{rp3}\ k_{sp1}\ k_{sp2}\ k_{sp3}\ k_{rp1}\ k_{rp2}\ k_{rp3})^T$, and $D\mathbf{x}/D\mathbf{V}^T$, $D\dot{\mathbf{x}}/D\mathbf{V}^T$, $D\ddot{\mathbf{x}}/D\mathbf{V}^T$ are Jacobian matrices, namely, the parameter sensitivity matrices. And the parameter sensitivity matrices can be obtained by substituting the solutions of (2.1), $\mathbf{x}$, $\dot{\mathbf{x}}$, $\ddot{\mathbf{x}}$ into (4.1). Then the sensitivity of dynamic response of the vibration transfer path system with respect to each path parameter can be solved as follows:

$$\frac{D\mathbf{x}}{Dm_p}=\frac{\partial\mathbf{x}}{\partial m_{p1}}+\frac{\partial\mathbf{x}}{\partial m_{p2}}+\frac{\partial\mathbf{x}}{\partial m_{p3}}, \tag{4.2a}$$

$$\frac{D\mathbf{x}}{Dc_{sp}}=\frac{\partial\mathbf{x}}{\partial c_{sp1}}+\frac{\partial\mathbf{x}}{\partial c_{sp2}}+\frac{\partial\mathbf{x}}{\partial c_{sp3}}, \tag{4.2b}$$

$$\frac{D\mathbf{x}}{Dc_{rp}}=\frac{\partial\mathbf{x}}{\partial c_{rp1}}+\frac{\partial\mathbf{x}}{\partial c_{rp2}}+\frac{\partial\mathbf{x}}{\partial c_{rp3}}, \tag{4.2c}$$

$$\frac{D\mathbf{x}}{Dk_{sp}}=\frac{\partial\mathbf{x}}{\partial k_{sp1}}+\frac{\partial\mathbf{x}}{\partial k_{sp2}}+\frac{\partial\mathbf{x}}{\partial k_{sp3}}, \tag{4.2d}$$

$$\frac{\mathrm{D}\mathbf{x}}{\mathrm{D}k_{rp}}=\frac{\partial\mathbf{x}}{\partial k_{rp1}}+\frac{\partial\mathbf{x}}{\partial k_{rp2}}+\frac{\partial\mathbf{x}}{\partial k_{rp3}}, \tag{4.2e}$$

where $D\mathbf{x}/Dm_p$, $D\mathbf{x}/Dc_{sp}$, $D\mathbf{x}/Dc_{rp}$, $D\mathbf{x}/Dk_{sp}$, and $D\mathbf{x}/Dk_{rp}$ are the sensitivity of the dynamic response of the vibration receiver with respect to the mass, damping and stiffness of the vibration transfer path system, respectively. These sensitivity matrices can be used to judge the contribution of each path parameter to the dynamic response of the vibration receiver. The sign of sensitivity can be positive or negative. When a sensitivity coefficient is positive, an increase in the model parameter leads to an increase in the corresponding state variable, and when it is negative, the opposite is true. Moreover, the larger the absolute value of sensitivity is, the more significant is the factor for the response of the vibration transfer path system.

Sensitivity analysis of a vibration transfer path system with respect to non-linear path stiffness provides a theoretical basis for identifying the parameter contribution of each kind of non-linear stiffness to the dynamic response of the vibration receiver. Through the differential of (2.1) with respect to $k_{sp1}^{e(i)}$, we get the following sensitivity function:

$$\mathbf{M}\frac{\mathrm{d}\ddot{\mathbf{x}}}{\mathrm{d}k_{sp1}^{e(i)}}+\mathbf{C}\frac{\mathrm{d}\dot{\mathbf{x}}}{\mathrm{d}k_{sp1}^{e(i)}}+\mathbf{K}\frac{\mathrm{d}\mathbf{x}}{\mathrm{d}k_{sp1}^{e(i)}}=-\frac{\mathrm{d}\mathbf{K}}{\mathrm{d}k_{sp1}^{e(i)}}\mathbf{x}\quad(i=1,2), \tag{4.3}$$

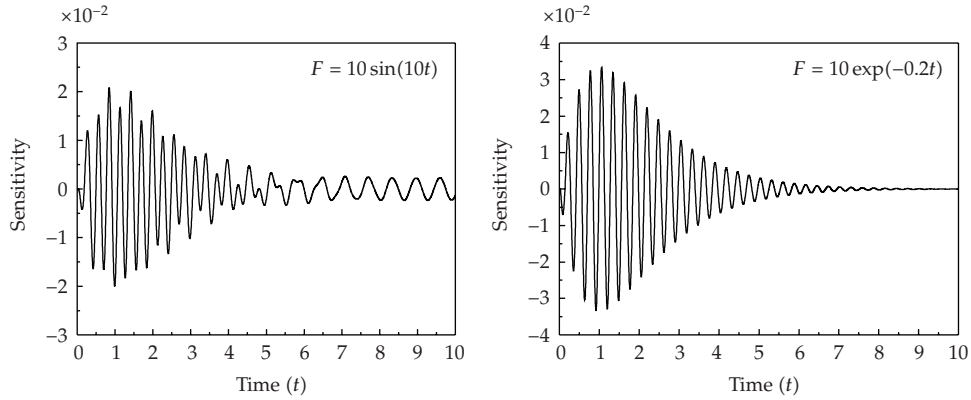

Figure 2: Sensitivity with respect to mass.

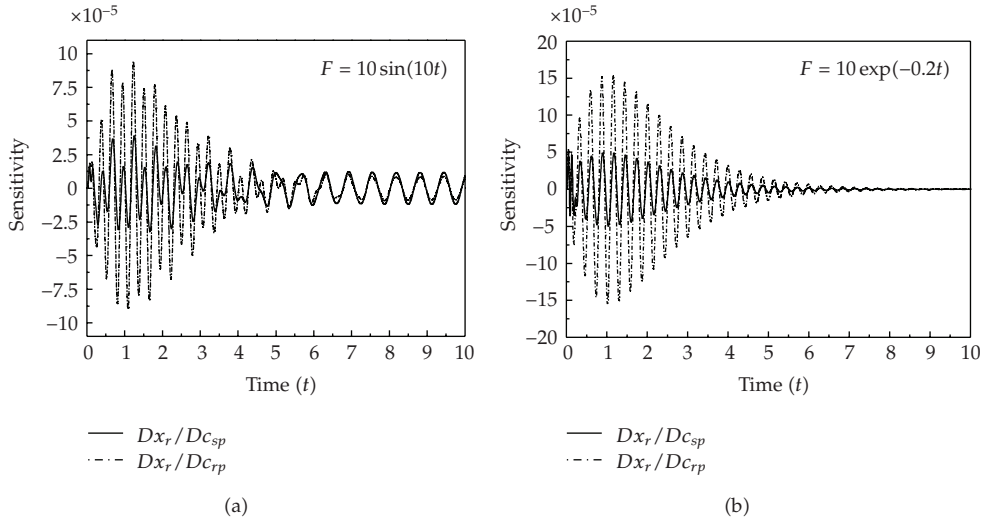

Figure 3: Sensitivity with respect to damping.

where $\mathrm{d}\mathbf{x}/\mathrm{d}k_{sp1}^{e(i)}$, $\mathrm{d}\dot{\mathbf{x}}/\mathrm{d}k_{sp1}^{e(i)}$, and $\mathrm{d}\ddot{\mathbf{x}}/\mathrm{d}k_{sp1}^{e(i)}$ are sensitivity matrices of the dynamic response of the vibration receiver with respect to the coefficient of non-linear path stiffness. In order to identify the contribution of different kinds of non-linear stiffness in transfer paths, we present a sensitivity analysis model by which the sensitivity of the vibration transfer path system with respect to the coefficients of different kinds of non-linear stiffness, $\mathbf{V} = (k_{sp1}^{2(1)} k_{sp1}^{2(2)})^T$, can be obtained. Obviously, we can get the dynamic response of the vibration transfer path system, $\mathbf{x}$, $\dot{\mathbf{x}}$, and $\ddot{\mathbf{x}}$, from (2.1). Then, substituting the results of (2.1) into (4.1) and (4.3), we can get the sensitivity of the vibration transfer path system with respect to linear equivalent stiffness coefficients $k_{sp1}^{2(1)}$ and $k_{sp1}^{2(2)}$ to evaluate the effects of the non-linear stiffness on the dynamic response of the vibration receiver.

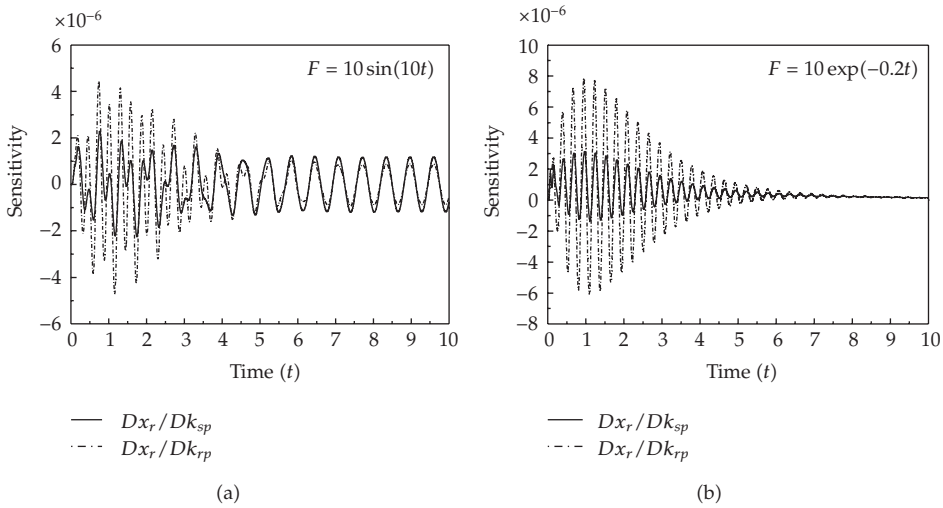

Figure 4: The curve of the sensitivity with respect to stiffness.

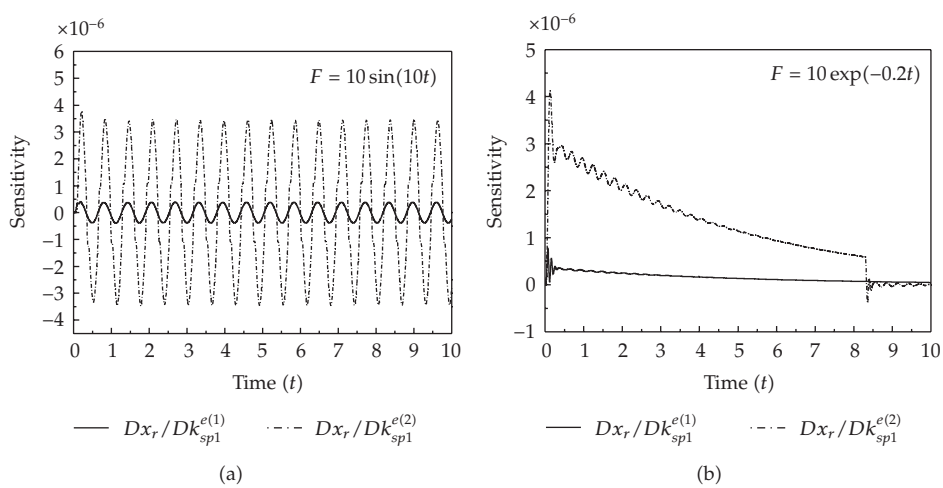

Figure 5: Sensitivity with respect to equivalent stiffness.

5. Numerical Examples

As the 5-DOF vibration transfer path system shown in Figure 1, the mass of the vibration resource is $m_s = 0.5\,\text{kg}$, the damping coefficient of the vibration resource system is $c_s = 1\,\text{N}\cdot\text{s/m}$, and the stiffness coefficient of the vibration resource system is $k_s = 500\,\text{N/m}$, the mass of the vibration receiver is $m_r = 0.5\,\text{kg}$, the damping coefficient of the vibration receiver system is $c_r = 1.0\,\text{N}\cdot\text{s/m}$, the stiffness of the vibration receiver system is $k_r = 1000\,\text{N/m}$. In the three transfer paths, the masses and the coefficients of the damping and stiffness are $m_{p1} = 0.4\,\text{kg}$, $m_{p2} = 0.5\,\text{kg}$, $m_{p3} = 0.6\,\text{kg}$, $c_{sp1} = c_{rp1} = 6\,\text{N}\cdot\text{s/m}$, $c_{sp2} = c_{rp2} = 4\,\text{N}\cdot\text{s/m}$, $c_{sp3} = c_{rp3} = 8\,\text{N}\cdot\text{s/m}$, $k_{sp1} = k_{rp1} = 800\,\text{N/m}$, $k_{sp2} = k_{rp2} = 600\,\text{N/m}$, and $k_{sp3} = k_{rp3} = 400\,\text{N/m}$, respectively. Try to figure out the sensitivity of the vibration transfer path system with respect to each path parameter when subjected to dynamic excitation, $F = 10\,\sin(10t)$ or $F = 10\,\exp(-0.2t)$.

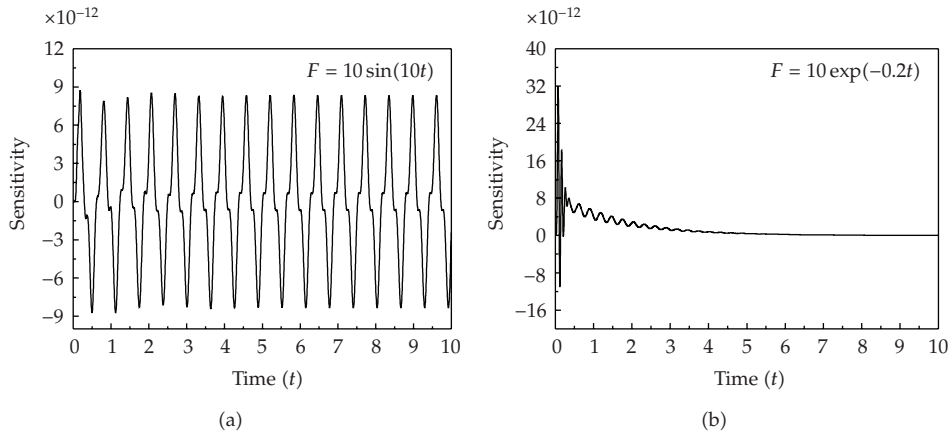

Figure 6: Sensitivity with respect to the material non-linear coefficient $k_{sp1}^{2(2)}$.

The sensitivity of the vibration transfer path system with respect to the mass, damping and stiffness of the vibration transfer path system can be depicted in Figures 2–4. From the results of sensitivity analysis, we can draw the conclusion that under the same excitation, the mass has the strongest influence on the vibration transfer path system, followed by the damping, and the stiffness. Besides, the damping and stiffness near the vibration receiver have stronger effect on the dynamic response of the vibration receiver at the transient vibration stage. Therefore, while modifying structural parameters or replacing components, the mass, damping and stiffness of the 5-DOF vibration transfer path system need to be sequentially considered, so that the transfer of vibration and noise in vibration transfer path systems can be decreased efficiently.

In the above mentioned 5-DOF vibration transfer path system, k_{sp1} is non-linear stiffness, and the liner parts of the non-linear stiffness are $k_{sp1}^{1(1)} = k_{sp1}^{1(2)} = 800\,\mathrm{N/m}$. The turning point of the piecewise linear stiffness is $(x_{p1} - x_s)_0 = 1.5 \times 10^{-3}\,\mathrm{m}$, and $k_{sp1}^{2(1)} = 80\,\mathrm{N/m^3}$. The nonlinear correction term of the non-linear material stiffness is $k_{sp1}^{2(2)} = 8\,\mathrm{N/m}$. Try to figure out the sensitivity of the dynamic response of the 5-DOF vibration transfer path system with respect to each kind of non-linear stiffness.

(1) The sensitivity of the dynamic response of the vibration receiver in the 5-DOF vibration transfer path system with respect to the linear equivalent stiffness coefficient of the non-linear stiffness $k_{sp1}^{e(i)}$ $(i = 1, 2)$ is depicted in Figure 5:

From Figure 5, we can draw the conclusion that although the linear parts of non-linear stiffness are equal, the sensitivity with respect to the linear equivalent stiffness of material nonlinear stiffness and piecewise linear stiffness is different. The reason is that the dependency relationship between the non-linear part of different kinds of non-linear stiffness and the dynamic response of the vibration transfer path system is different. In comparison, the sensitivity with respect to the equivalent linear stiffness of the piecewise linear stiffness is bigger than that of the material non-linear stiffness.

(2) The sensitivity of the dynamic response of the vibration receiver in the 5-DOF vibration transfer path system with respect to the coefficients of the non-linear part of the material non-linear stiffness and piecewise stiffness, $k_{sp1}^{2(1)}$ and $k_{sp1}^{2(2)}$, is depicted in Figures 6 and 7.

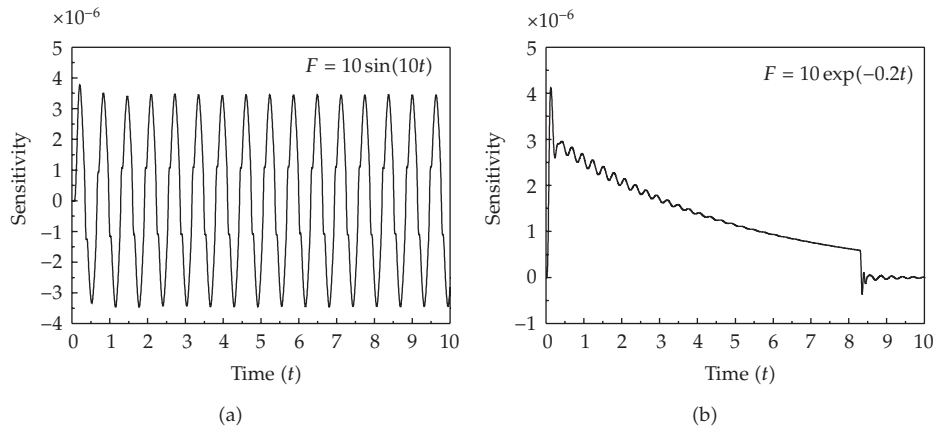

Figure 7: Sensitivity with respect to the piecewise linear coefficient $k_{sp1}^{2(2)}$.

From the results shown in Figures 6 and 7, we can draw the conclusion that in the above mentioned 5-DOF vibration transfer path system, the non-linear part of the piecewise stiffness, $k_{sp1}^{2(2)}$, is more sensitive to the dynamic responses of the vibration transfer path system than that of the material non-linear stiffness, $k_{sp1}^{2(1)}$. However these two non-linear stiffness parameters have different units; the results drawn above can only be used as a reference to decrease the transfer of vibration or noise in the vibration transfer path system.

6. Conclusion

The effects of non-linear stiffness parameters on vibration transfer path systems are discussed in this paper. Based on the sensitivity technology, sensitivity scheduling of dynamic responses of vibration transfer path systems with respect to path parameters and non-linear stiffness is provided in the time-domain. The units of mass and the coefficients of different kinds of non-linear stiffness are different; therefore the results drawn in this paper can only be used as a reference to decrease the transfer of vibration and noise in vibration transfer path systems. However, without a doubt, this paper provides an effective way to analyze the sensitivity of non-linear vibration transfer path systems with respect to path parameters and non-linear stiffness.

Acknowledgments

The authors would like to express their appreciation to Program for Changjiang Scholars and Innovative Research Team in university, Key National Science & Technology Special Project on "High-Grade CNC Machine Tools and Basic Manufacturing Equipment" (2010ZX04014-014), Chinese National Natural Science Foundation (50875039), and Fundamental Research Funds for the Central Universities (N090603002). Thanks to Professor R. Singh of The Ohio State University for providing the vibration path model (Figure 1) during the first author's visiting as a scholar.

References

[1] L. Cremer and M. Heckle, *Structure-Borne Sound: Structural Vibrations and Sound Radiation at Audio Frequencies*, Springer, New York, NY, USA, 1973.

[2] R. H. Lyon and R. G. Dejong, *Theory and Application of Statistical Energy Analysis*, Butterworth-Heinemann, Boston, Mass, USA, 1995.

[3] J. C. Wohlever and R. J. Bernhard, "Mechanical energy flow models of rods and beams," *Journal of Sound and Vibration*, vol. 153, no. 1, pp. 1–19, 1992.

[4] S. Kim and R. Singh, "Vibration transmission through an isolator modelled by continuous system theory," *Journal of Sound and Vibration*, vol. 248, no. 5, pp. 925–953, 2001.

[5] R. Singh and S. Kim, "Examination of multi-dimensional vibration isolation measures and their correlation to sound radiation over a broad frequency range," *Journal of Sound and Vibration*, vol. 262, no. 3, pp. 419–455, 2003.

Hindawi Publishing Corporation
Mathematical Problems in Engineering
Volume 2010, Article ID 653215, 7 pages
doi:10.1155/2010/653215

Research Article

The Well-Posedness of the Dirichlet Problem in the Cylindric Domain for the Multidimensional Wave Equation

Serik A. Aldashev

Aktobe State University, AGU, Br. Zhubanov Str 263, Aktobe 030000, Kazakhstan

Correspondence should be addressed to Serik A. Aldashev, aldashevg@yahoo.com

Received 26 October 2009; Accepted 29 April 2010

Academic Editor: Carlo Cattani

In the theory of hyperbolic PDEs, the boundary-value problems with conditions on the entire boundary of the domain serve typically as the examples of the ill-posedness. The paper shows the unique solvability of the Dirichlet problem in the cylindric domain for the multidimensional wave equation. We also establish the criterion for the unique solvability of the equation.

One of the fundamental problems of mathematical physics—the analysis of the behavior of the vibrating string—has been shown to be ill-posed when the boundary-value conditions are defined on the entire boundary ([1]). Furthermore, this problem (known as Dirichlet problem) has been shown to be ill-posed not only for the wave equation but for hyperbolic PDEs more generally (see [2, 3]). Some progress was done in [4] which showed that for some rectangles the solution of this problem existed under sufficient differentiability conditions. Further analyses of this problem reverted to functional analysis methods (see, e.g., [5]), which has the serious shortcoming of making the applications of such results in physics and engineering highly difficult. Moreover, most studies have concentrated so far on the 2D wave equation.

This paper studies the Dirichlet problem, using the classical methods, in the cylindric domain for the multidimensional wave equation. We show that the problem is well-posed. We also establish the criterion for the unique solvability of the problem.

Let Ω_α be the cylindric domain of the Euclidean space E_{m+1} of points $(x_1, \ldots, x_m, t)$, bounded by the cylinder $\Gamma = \{(x,t) : |x| = 1\}$, the planes $t = \alpha > 0$ and $t = 0$, where $|x|$ is the length of the vector $x = (x_1, \ldots, x_m)$.

Let us denote, respectively, with Γ_α, S_α, and S_0 the parts of these surfaces that form the boundary $\partial\Omega_\alpha$ of the domain Ω_α.

We study, in the domain Ω_α, the multidimensional wave equation

$$\Delta_x u - u_{tt} = 0, \tag{1}$$

where Δ_x is the Laplace operator on the variables $x_1, \ldots, x_m,\ m \geq 2$.

Hereafter, it is useful to move from the Cartesian coordinates $x_1, \ldots, x_m, t$ to the spherical ones $r, \theta_1, \ldots, \theta_m,\ t, r \geq 0,\ \ 0 \leq \theta_1 < 2\pi,\ 0 \leq \theta_i \leq \pi,\ i = 2, 3, \ldots, m-1$.

Problem 1 (Dirichlet). Find the solution of (1) in the domain Ω_α, in the class $C(\overline{\Omega}_\alpha) \cap C^2(\Omega_\alpha)$, that satisfies the following boundary-value conditions:

$$u|_{S_\alpha} = \varphi(r,\theta), \qquad u|_{\Gamma_\alpha} = \psi(t,\theta), \qquad u|_{S_0} = \tau(r,\theta). \tag{2}$$

Let $\{Y_{n,m}^k(\theta)\}$ be a system of linearly independent spherical functions of order $n,\ 1 \leq k \leq k_n, (m-2)!n!k_n = (n+m-3)!(2n+m-2)$, and let $W_2^l(S_0), l = 0, 1, \ldots$ be Sobolev spaces.

The following lemmata hold ([6]).

Lemma 1. *Let $f(r,\theta) \in W_2^l(S_0)$. If $l \geq m-1$, then the series*

$$f(r,\theta) = \sum_{n=0}^{\infty} \sum_{k=1}^{k_n} f_n^k(r) Y_{n,m}^k(\theta), \tag{3}$$

as well as the series obtained through its differentiation of order $p \leq l - m + 1$, converge absolutely and uniformly.

Lemma 2. *For $f(r,\theta) \in W_2^l(S_0)$, it is necessary and sufficient that the coefficients of the series* (3) *satisfy the inequalities*

$$\left| f_0^1(r) \right| \leq c_1, \quad \sum_{n=0}^{\infty} \sum_{k=1}^{k_n} n^{2l} \left| f_n^k(r) \right|^2 \leq c_2, \quad c_1, c_2 = \text{const}. \tag{4}$$

Let's denote as $\overline{\varphi}_n^k(r),\ \psi_n^k(t)$, and $\overline{\tau}_n^k(r)$ the coefficients of the series (3), respectively, of the functions $\varphi(r,\theta), \psi(t,\theta)$, and $\tau(r,\theta)$.

Theorem 3. *If $\varphi(r,\theta) \in W_2^l(S_\alpha),\ \psi(t,\theta) \in W_2^l(\Gamma_\alpha),\ \tau(r,\theta) \in W_2^l(S_0),\ l > 3m/2$, and*

$$\sin \mu_s \alpha \neq 0, \quad s = 1, 2, \ldots, \tag{5}$$

then Problem 1 is uniquely solvable, where μ_s are the positive nulls of the Bessel function of first type $J_{n+(m-2)/2}(z)$.

Theorem 4. *The solution of Problem 1 is unique if and only if condition* (5) *is satisfied.*

Proof of Theorem 3. In the spherical coordinates, (1) takes the form

$$u_{rr} + \frac{m-1}{r}u_r - \frac{1}{r^2}\delta u - u_{tt} = 0,$$
$$\delta \equiv -\sum_{j=1}^{m-1}\frac{1}{g_j \sin^{m-j-1}\theta_j}\frac{\partial}{\partial\theta_j}\left(\sin^{m-j-1}\theta_j\frac{\partial}{\partial\theta_j}\right), \quad g_1 = 1,\ g_j = \left(\sin\theta_1\cdots\sin\theta_{j-1}\right)^2,\ j > 1. \tag{6}$$

It is known (see [6]) that the spectrum of the operator δ consists of eigenvalues $\lambda_n = n(n+m-2)$, $n = 0,1,\ldots$, to each of which correspond k_n orthonormalized eigenfunctions $Y_{n,m}^k(\theta)$.

Given that solution of the problem that we are looking for belongs to the class $C(\overline{\Omega}_\alpha)\cap C^2(\Omega_\alpha)$, we can look for it in the form of the series

$$u(r,\theta,t) = \sum_{n=0}^{\infty}\sum_{k=1}^{k_n}\overline{u}_n^k(r,t)Y_{n,m}^k(\theta), \tag{7}$$

where $\overline{u}_n^k(r,t)$ are the functions to be determined.

Substituting (7) into (6) and using the orthogonality of the spherical functions $Y_{n,m}^k(\theta)$ ([6]), we get

$$\overline{u}_{nrr}^k + \frac{m-1}{r}\overline{u}_{nr}^k - \overline{u}_{ntt}^k - \frac{\lambda_n}{r^2}\overline{u}_n^k = 0, \quad k = \overline{1,k_n},\ n = 0,1,\ldots, \tag{8}$$

and given this, the boundary-value conditions (2), taking into account Lemma 1, will take the form

$$\overline{u}_n^k(r,0) = \overline{\tau}_n^k(r), \qquad \overline{u}_n^k(r,\alpha) = \overline{\varphi}_n^k(r), \qquad \overline{u}_n^k(1,t) = \psi_n^k(t), \quad k = \overline{1,k_n},\ n = 0,1,\ldots. \tag{9}$$

In (8) and (9), making the substitution of variables

$$\overline{\vartheta}_n^k(r,t) = \overline{u}_n^k(r,t) - \psi_n^k(t), \tag{10}$$

we get

$$\overline{\vartheta}_{nrr}^k + \frac{m-1}{r}\overline{\vartheta}_{nr}^k - \overline{\vartheta}_{ntt}^k - \frac{\lambda_n}{r^2}\overline{\vartheta}_n^k = \overline{f}_n^k(r,t),$$
$$\overline{\vartheta}_n^k(r,0) = \overline{\tau}_n^k(r), \quad \overline{\vartheta}_n^k(r,\alpha) = \varphi_n^k(r), \quad \overline{\vartheta}_n^k(1,t) = 0, \quad k = \overline{1,k_n},\ n = 0,1,\ldots, \tag{11}$$
$$\overline{f}_n^k(r,t) = \psi_{ntt}^k + \frac{\lambda_n}{r^2}\psi_n^k, \qquad \tau_n^k(r) = \overline{\tau}_n^k(r) - \psi_n^k(0), \qquad \varphi_n^k(r) = \overline{\varphi}_n^k(r) - \psi_n^k(\alpha).$$

Making the substitution of the variable $\overline{\vartheta}_n^k(r,t) = r^{(1-m)/2}\vartheta_n^k(r,t)$, we can reduce the problem (11) to the following problem

$$\begin{gathered} L\vartheta_n^k \equiv \vartheta_{nrr}^k - \vartheta_{ntt}^k + \frac{\overline{\lambda}_n}{r^2}\vartheta_n^k = f_n^k(r,t), \\ \vartheta_n^k(r,0) = \tilde{\tau}_n^k(r), \qquad \vartheta_n^k(r,\alpha) = \tilde{\varphi}_n^k(r), \qquad \vartheta_n^k(1,t) = 0, \\ \overline{\lambda}_n = \frac{(m-1)(3-m)-4\lambda_n}{4}, \qquad f_n^k(r,t) = r^{(1-m)/2}\overline{f}_n^k(r,t), \\ \tilde{\tau}_n^k(r) = r^{(1-m)/2}\tau_n^k(r), \qquad \tilde{\varphi}_n^k(r) = r^{(1-m)/2}\varphi_n^k(r). \end{gathered} \tag{12}$$

We look for the solution of the problem (12) in the form $\vartheta_n^k(r,t) = \vartheta_{1n}^k(r,t) + \vartheta_{2n}^k(r,t)$, where $\vartheta_{1n}^k(r,t)$ is the solution of the problem

$$\begin{gathered} L\vartheta_{1n}^k = f_n^k(r,t), \\ \vartheta_{1n}^k(r,0) = 0, \qquad \vartheta_{1n}^k(r,\alpha) = 0, \qquad \vartheta_{1n}^k(1,t) = 0 \end{gathered} \tag{13}$$

whereas $\vartheta_{2n}^k(r,t)$ is the solution of the problem

$$\begin{gathered} L\vartheta_{2n}^k = 0, \\ \vartheta_{2n}^k(r,0) = \tilde{\tau}_n^k(r), \qquad \vartheta_{2n}^k(r,\alpha) = \tilde{\varphi}_n^k(r), \qquad \vartheta_{2n}^k(1,t) = 0. \end{gathered} \tag{14}$$

We analyze the solutions of the above problems, analogously to [7], in the form

$$\vartheta_n^k(r,t) = \sum_{s=1}^{\infty} R_s(r)T_s(t); \tag{15}$$

moreover, let

$$f_n^k(r,t) = \sum_{s=1}^{\infty} a_s(t)R_s(r), \qquad \tilde{\tau}_n^k(r) = \sum_{s=1}^{\infty} b_s R_s(r), \qquad \tilde{\varphi}_n^k(r) = \sum_{s=1}^{\infty} d_s R_s(r). \tag{16}$$

Substituting (15) into (13) and taking into account (16), we get

$$R_{srr} + \frac{\overline{\lambda}_n}{r^2}R_s + \mu R_s = 0, \quad 0 < r < 1, \tag{17}$$

$$R_s(1) = 0, \qquad |R_s(0)| < \infty, \tag{18}$$

$$T_{stt} + \mu T_s = -a_s(t), \quad 0 < t < \alpha, \tag{19}$$

$$T_s(0) = T_s(\alpha) = 0. \tag{20}$$

The bounded solution of the problems (17) and (18) is (see [8])

$$R_s(r) = \sqrt{r} J_\upsilon(\mu_s r), \tag{21}$$

where $\upsilon = n + (m-2)/2$, $\mu = \mu_s^2$.

The general solution of (19) can be represented in the form (see [8])

$$T_s(t) = c_{1s}\cos\mu_s t + c_{2s}\sin\mu_s t + \frac{\cos\mu_s t}{\mu_s}\int_0^t a_s(\xi)\sin\mu_s\xi\, d\xi - \frac{\sin\mu_s t}{\mu_s}\int_0^t a_s(\xi)\cos\mu_s\xi\, d\xi, \tag{22}$$

where c_{1s} and c_{2s} are arbitrary constants; satisfying the condition (20), we will get

$$\begin{gathered} c_{1s} = 0, \\ c_{2s}\mu_s \sin\mu\alpha = -\cos\mu_s\alpha\int_0^\alpha a_s(\xi)\sin\mu_s\xi\, d\xi - \sin\mu_s\alpha\int_0^\alpha a_s(\xi)\cos\mu_s\xi\, d\xi. \end{gathered} \tag{23}$$

Substituting (21) into (16), we get

$$\begin{gathered} r^{-1/2} f_n^k(r,t) = \sum_{s=1}^\infty a_s(t) J_\upsilon(\mu_s r), \qquad r^{-1/2}\tilde{\tau}_n^k(r) = \sum_{s=1}^\infty b_s J_\upsilon(\mu_s r), \\ r^{-1/2}\tilde{\varphi}_n^k(r) = \sum_{s=1}^\infty d_s J_\upsilon(\mu_s r), \quad 0 < r < 1. \end{gathered} \tag{24}$$

Series (24) are the decompositions into the Fourier-Bessel series (see [9]), if

$$a_s(t) = \frac{2}{\left[J_{\upsilon+1}(\mu_s)\right]^2}\int_0^1 \sqrt{\xi} f_n^k(\xi,t) J_\upsilon(\mu_s\xi)\, d\xi, \tag{25}$$

$$b_s = \frac{2}{\left[J_{\upsilon+1}(\mu_s)\right]^2}\int_0^1 \sqrt{\xi}\tilde{\tau}_n^k(\xi) J_\upsilon(\mu_s\xi)\, d\xi, \qquad d_s = \frac{2}{\left[J_{\upsilon+1}(\mu_s)\right]^2}\int_0^1 \sqrt{\xi}\tilde{\varphi}_n^k(\xi) J_\upsilon(\mu_s\xi)\, d\xi, \tag{26}$$

μ_s, $s = 1, 2, \ldots$ are positive nulls of the Bessel functions, set in the increasing order.

From (21)–(23) we get the solution of the problem (13):

$$\begin{aligned} \vartheta_{1n}^k(r,t) = \sum_{s=1}^\infty \frac{\sqrt{r}}{\mu_s}\Bigg\{ &\left[\int_0^\alpha a_s(\xi)\cos\mu_s\xi d\xi - \cot\mu_s\alpha\int_0^\alpha a_s(\xi)\sin\mu_s d\xi\right]\sin\mu_s t \\ &+ \cos\mu_s t\int_0^t a_s(\xi)\sin\mu_s\xi d\xi - \sin\mu_s t\int_0^t a_s(\xi)\cos\mu_s d\xi\Bigg\} J_\upsilon(\mu_s r), \end{aligned} \tag{27}$$

where $a_s(t)$ is determined from (25).

Next, substituting (15) into (14) and taking into account (16), we will get

$$T_{stt} + \mu_s^2 T_s = 0, \quad 0 < t < \alpha, \tag{28}$$

$$T_s(0) = b_s, \qquad T_s(\alpha) = d_s. \tag{29}$$

The general solution of (28) will become

$$T_s(t) = c'_{1s} \cos \mu_s t + c'_{2s} \sin \mu_s t; \tag{30}$$

satisfying the condition (29), we will get

$$\begin{gathered} c'_{1s} = b_s, \\ c'_{2s} = \frac{d_s}{\sin \mu_s \alpha} - b_s \cot \mu_s \alpha. \end{gathered} \tag{31}$$

From (21), (30), and (31) we find the solution of the problem (14):

$$\vartheta_{2n}^k(r,t) = \sum_{s=1}^{\infty} \sqrt{r} \left[b_s \cos \mu_s t - \left(\frac{d_s}{\sin \mu_s \alpha} - b_s \cot \mu_s \alpha \right) \sin \mu_s t \right] J_\upsilon(\mu_s r), \tag{32}$$

where b_s and d_s are found from (26).

Thus, the unique solution of Problem 1 is the function

$$u(r,\theta,t) = \sum_{n=0}^{\infty} \sum_{k=1}^{k_n} \left\{ \varphi_n^k(t) + r^{(1-m)/2} \left[\vartheta_{1n}^k(r,t) + \vartheta_{2n}^k(r,t) \right] \right\} \Upsilon_{n,m}^k(\theta), \quad t > 0, \tag{33}$$

where $\vartheta_{1n}^k(r,t)$ and $\vartheta_{2n}^k(r,t)$ are determined from (27) and (32).

Taking into account the formula (see [9]) $J'_\upsilon(z) = J_{\upsilon-1}(z) + J_{\upsilon+1}(z)$, the estimates (see [6, 9])

$$\begin{gathered} |J_\upsilon(z)| \le \frac{1}{\Gamma(1+\upsilon)} \left(\frac{z}{2} \right)^\upsilon, \qquad k_n \le c_1 n^{m-2}, \\ \left| \frac{\partial^q}{\partial \theta_j^q} \Upsilon_{n,m}^k(\theta) \right| \le c_2 n^{m/2-1+q}, \qquad j = \overline{1, m-1}, \ q = 0, 1, \ldots, \end{gathered} \tag{34}$$

where $\Gamma(z)$ is the gamma-function, the lemmata, and the bounds on the given functions $\varphi(r,\theta), \psi(t,\theta)$, and $\tau(r,\theta)$, we can show that the obtained solution (33) belongs to the class $C(\overline{\Omega}_\alpha) \cap C^2(\Omega_\alpha)$.

Theorem 3 is proven. □

Proof of Theorem 4. If condition (5) is satisfied, then from Theorem 3, it follows that the solution of Problem 1 is unique.

Now, suppose condition (5) does not hold, at least for one $s = 1$.

Then, if we look for the solution of the homogeneous problem, corresponding to Problem 1, in the form (7), then we get to the problem

$$L\vartheta_n^k = 0,$$
$$\vartheta_n^k(r,0) = 0, \qquad \vartheta_n^k(r,\alpha) = 0, \qquad \vartheta_n^k(1,t) = 0, \quad k = \overline{1,k_n},\ n = 0,1,\ldots, \tag{35}$$

the solution of which is the function

$$\vartheta_n^k(r,t) = \sqrt{r}\sin\mu_l t J_{n+(m-2)/2}(\mu_l r). \tag{36}$$

Therefore, the nontrivial solution of homogeneous Problem 1 is written as

$$u(r,\theta,t) = \sum_{n=2}^{\infty}\sum_{k=1}^{k_n} n^{-l} r^{(2-m)/2}\sin\mu_l t J_{n+(m-2)/2}(\mu_l r)\Upsilon_{n,m}^k(\theta). \tag{37}$$

From estimates (34) it follows that $u \in C(\overline{\Omega}_\alpha) \cap C^2(\Omega_\alpha)$, if $l > 3m/2$. □

References

[1] J. Hadamard, "Sur les problèmes aux dérivées partielles et leur signification physique," *Princeton University Bulletin*, vol. 13, pp. 49–52, 1902.

[2] A. V. Bitsadze, *The Equations of Mixed Type*, Izd-vo AN SSSR, Moscow, Russia, 1959.

[3] A. M. Nakhushev, *Problems with a Shift for Partial Differential Equations*, Nauka, Moscow, Russia, 2006.

[4] D. G. Bourgin and R. Duffin, "The Dirichlet problem for the virbrating string equation," *Bulletin of the American Mathematical Society*, vol. 45, pp. 851–858, 1939.

[5] D. W. Fox and C. Pucci, "The Dirichlet problem for the wave equation," *Annali di Matematica Pura ed Applicata*, vol. 46, no. 1, pp. 155–182, 1958.

[6] S. G. Mikhlin, *Multi-Dimensional Singular Integrals and Integral Equations*, Fizmatgiz, Moscow, Russia, 1962.

[7] A. N. Tikhonov and A. A. Samarskii, *Equations of Mathematical Physics*, Nauka, Moscow, Russia, 1977.

[8] E. Kamke, *Handbook of Ordinary Differential Equations*, Nauka, Moscow, Russia, 1965.

[9] G. Bateman and A. Erdelyi, *Higher Transcendental Functions. Vol. 2*, Nauka, Moscow, Russia, 1974.

Hindawi Publishing Corporation
Mathematical Problems in Engineering
Volume 2010, Article ID 738648, 12 pages
doi:10.1155/2010/738648

Research Article

Nonlinear Dynamic Response of Functionally Graded Rectangular Plates under Different Internal Resonances

Y. X. Hao,[1] W. Zhang,[2] and X. L. Ji[3]

[1] *College of Mechanical Engineering, Beijing Information Science and Technology University, Beijing 100192, China*
[2] *College of Mechanical Engineering, Beijing University of Technology, Beijing 100142, China*
[3] *National Key Laboratory of Mechatronics Engineering and Control, Beijing Institute of Technology, Beijing 100081, China*

Correspondence should be addressed to X. L. Ji, xiulingji0127@bit.edu.cn

Received 17 November 2009; Revised 29 April 2010; Accepted 1 May 2010

Academic Editor: Carlo Cattani

The nonlinear dynamic response of functionally graded rectangular plates under combined transverse and in-plane excitations is investigated under the conditions of 1 : 1, 1 : 2 and 1 : 3 internal resonance. The material properties are assumed to be temperature-dependent and vary along the thickness direction. The thermal effect due to one-dimensional temperature gradient is included in the analysis. The governing equations of motion for FGM rectangular plates are derived by using Reddy's third-order plate theory and Hamilton's principle. Galerkin's approach is utilized to reduce the governing differential equations to a two-degree-of-freedom nonlinear system including quadratic and cubic nonlinear terms, which are then solved numerically by using 4th-order Runge-Kutta algorithm. The effects of in-plane excitations on the internal resonance relationship and nonlinear dynamic response of FGM plates are studied.

1. Introduction

Functionally graded materials (FGMs) are new engineering materials. Due to their advantages of being able to withstand severe high-temperature gradient while maintaining structural integrity, FGMs are considered to be advanced composite materials in high temperature and vibration environments [1, 2].

With the increasing use of FGMs, it is important to understand the nonlinear vibration behavior of FGM structures. Quite a few studies in this area have been conducted. Praveen and Reddy [3] analyzed the nonlinear static and dynamic response of functionally graded ceramic-metal plates in a steady temperature field based on the first-order shear deformation

plate theory.Sundararajan et al. [4] carried out finite element analysis of nonlinear-free vibration of both rectangular and skew FGM plates. Yang et al. [5] investigated the large amplitude vibration of pre-stressed FGM plates composed of a functionally graded layer and two surface-mounted piezoelectric actuator layers.

A semi analytical method and Galerkin technique were employed to predict the nonlinear vibration behavior of FGM-laminated plates. The parametric resonance of functionally graded rectangular plates under harmonic in-plane loading was investigated by Ng et al. [6]. Using a higher-order shear and normal deformable plate theory (HOSNDPT) and a meshless local Petrov-Galerkin (MLPG) method, Qian et al. [7] analyzed the static deformation, and free and forced vibrations of a thick rectangular functionally graded plate.Vel and Batra [8] gave a three-dimensional exact solution for the linear free and forced vibration of simply supported FGM rectangular plates. Woo and Meguid [9] studied the nonlinear deflection of FGM plates and shells under transverse mechanical loads and a temperature field. Hao et al. [10] reported a nonlinear dynamic analysis of a simply supported FGM rectangular plate subjected to transversal and in-plane excitations. The resonant case considered in their work is 1 : 1 internal resonance and principal parametric resonance. The asymptotic perturbation method is used to obtain four-dimensional nonlinear averaged equation. It was found that periodic, and quasiperiodic solutions and chaotic motions occur under some conditions. It is known that for a two-degree-of-freedom nonlinear vibration system, different internal resonance between two modes, such as 1 : 1, 1 : 2, and 1 : 3 internal resonances, can exist in some cases. To the best of the authors' knowledge, there is still no literature concerning nonlinear dynamic behavior of FGM plates with different cases of internal resonances.

The present work aims to investigate the nonlinear dynamic response of a simply supported FGM rectangular plate subjected to transversal and in-plane excitations in a thermal environment. The cases considered in this paper include 1 : 1, 1 : 2, and 1 : 3 internal resonances and principal parametric resonance-1/2 subharmonic resonance. It is assumed that the material properties of the plate are graded in the thickness direction according to a power-law distribution. The analysis is based on the nonlinear dynamic governing equations derived in our previous work [10]. The influences of the in-plane excitations on the internal resonance relationship and nonlinear dynamic response of the FGM plate are studied in numerical examples.

2. Theoretical Formulation

2.1. Material Properties

It is assumed that the bottom surface of the plate is metal rich, whereas the top surface is ceramic rich. The material properties P, such as Young's modulus E, the coefficient of thermal expansion α, thermal conductivity κ, and mass density ρ, can be expressed as a function of temperature as [11]

$$P_i = P_0\left(P_{-1}T^{-1} + 1 + P_1T + P_2T^2 + P_3T^3\right), \tag{2.1}$$

where P_0, P_{-1}, P_1, P_2, and P_3 are temperature coefficients.

The effective material properties P of the FGM plate can be expressed as

$$P = P_t V_c + P_b V_m, \tag{2.2}$$

where subscripts "t" and "b" represent the top and bottom surfaces of the FGMs plate, respectively, and V_c and V_m are the volume fraction of ceramic and metal which add to unity

$$V_c + V_m = 1. \tag{2.3}$$

The metal volume fraction V_m is defined as

$$V_m(z) = \left(\frac{2z + h}{2h}\right)^N, \tag{2.4}$$

where exponent N is a real number that characterizes the material profile along plate thickness.

From (2.2)–(2.4), the effective values of E, α, ρ, and κ at an arbitrary point of the plate can be expressed as

$$\begin{aligned} E &= (E_b - E_t)\ V_m + E_t, \\ \alpha &= (\alpha_b - \alpha_t)\ V_m + \alpha_t, \\ \rho &= (\rho_b - \rho_t)\ V_m + \rho_t, \\ \kappa &= (\kappa_b - \kappa_t)\ V_m + \kappa_t. \end{aligned} \tag{2.5}$$

It is also assumed that the plate is initially stress free at T_0 and is subjected to a uniform temperature variation $\Delta T = T - T_0$ that is constant in the xy plane of the plate while varies in the thickness direction only. In this case, the temperature distribution along plate thickness can be obtained from a steady-state heat transfer equation:

$$-\frac{d}{dz}\left[\kappa(z)\frac{dT}{dz}\right] = 0. \tag{2.6}$$

This equation is solved by imposing boundary condition of $T = T_b$ at $z = h/2$ and $T = T_t$ at $z = -h/2$. As a special case, the solution of (2.6) for isotropic homogeneous material, may be expressed as

$$T(z) = \frac{T_t + T_b}{2} + \frac{T_b - T_t}{h} z. \tag{2.7}$$

2.2. Equations of Motion

A simply supported four-edges FGMs rectangular plate of length a, width b and thickness h, which is subjected to the in-plane and transversal excitations is considered, as shown in

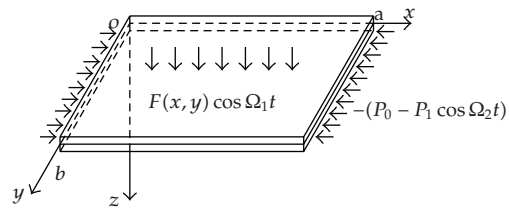

Figure 1: The model of a FGMs rectangular plate and the coordinate system.

Figure 1. The in-plane excitation of the FGMs plate is distributed along the y direction at $x = 0$ and $x = a$ and is of the form $p_0 - p_1 \cos\Omega_2 t$. The transversal excitation subject to the FGMs plate is represented by $F(x,y)\cos\Omega_1 t$. Here the Ω_1 and Ω_2 are the frequencies of the transversal excitation and the in-plane excitation, respectively.

As usual, the coordinate $Oxyz$ has its origin at the corner of the plate on the middle plane. Assume that (u,v,w) and (u_0,v_0,w_0) represent the displacements of an arbitrary point and a point in the middle surface of the FGMs rectangular plate in the x, y and z directions, respectively. It is also assumed that ϕ_x and ϕ_y, respectively, represent the mid-plane rotations of two transverse normals about the x and y axes. With Reddy's third-order shear deformation plate theory [12], the displacements of the FGM plate can be expressed as follows:

$$\begin{gathered} u(x,y,t) = u_0(x,y,t) + z\phi_x(x,y,t) - z^3\frac{4}{3h^2}\left(\phi_x + \frac{\partial w_0}{\partial x}\right), \\ v(x,y,t) = v_0(x,y,t) + z\phi_y(x,y,t) - z^3\frac{4}{3h^2}\left(\phi_y + \frac{\partial w_0}{\partial y}\right), \\ w(x,y,t) = w_0(x,y,t) \end{gathered} \tag{2.8}$$

Based on the nonlinear strains-displacement relation and the above displacement field, we obtain

$$\begin{gathered} \varepsilon_{xx} = \frac{\partial u}{\partial x} + \frac{1}{2}\left(\frac{\partial w}{\partial x}\right)^2, \quad \varepsilon_{yy} = \frac{\partial v}{\partial y} + \frac{1}{2}\left(\frac{\partial w}{\partial y}\right)^2, \\ \gamma_{xy} = \frac{1}{2}\left(\frac{\partial u}{\partial x} + \frac{\partial v}{\partial y} + \frac{\partial w}{\partial x}\frac{\partial w}{\partial y}\right), \\ \gamma_{yz} = \frac{1}{2}\left(\frac{\partial v}{\partial z} + \frac{\partial w}{\partial y}\right), \quad \gamma_{zx} = \frac{1}{2}\left(\frac{\partial u}{\partial z} + \frac{\partial w}{\partial x}\right), \end{gathered} \tag{2.9}$$

$$\begin{gathered} \begin{Bmatrix} \varepsilon_{xx} \\ \varepsilon_{yy} \\ \gamma_{xy} \end{Bmatrix} = \begin{Bmatrix} \varepsilon_{xx}^{(0)} \\ \varepsilon_{yy}^{(0)} \\ \gamma_{xy}^{(0)} \end{Bmatrix} + z\begin{Bmatrix} \varepsilon_{xx}^{(1)} \\ \varepsilon_{yy}^{(1)} \\ \gamma_{xy}^{(1)} \end{Bmatrix} + z^3\begin{Bmatrix} \varepsilon_{xx}^{(3)} \\ \varepsilon_{yy}^{(3)} \\ \gamma_{xy}^{(3)} \end{Bmatrix}, \\ \begin{Bmatrix} \gamma_{yz} \\ \gamma_{zx} \end{Bmatrix} = \begin{Bmatrix} \gamma_{yz}^{(0)} \\ \gamma_{zx}^{(0)} \end{Bmatrix} + z^2\begin{Bmatrix} \gamma_{yz}^{(2)} \\ \gamma_{zx}^{(2)} \end{Bmatrix}, \end{gathered} \tag{2.10}$$

where

$$\begin{Bmatrix} \gamma_{yz}^{(0)} \\ \gamma_{zx}^{(0)} \end{Bmatrix} = \begin{Bmatrix} \phi_y + \dfrac{\partial w_0}{\partial y} \\ \phi_x + \dfrac{\partial w_0}{\partial x} \end{Bmatrix}, \qquad \begin{Bmatrix} \gamma_{yz}^{(2)} \\ \gamma_{zx}^{(2)} \end{Bmatrix} = -c_2 \begin{Bmatrix} \phi_y + \dfrac{\partial w_0}{\partial y} \\ \phi_x + \dfrac{\partial w_0}{\partial x} \end{Bmatrix},$$

$$\begin{Bmatrix} \varepsilon_{xx}^{(0)} \\ \varepsilon_{yy}^{(0)} \\ \gamma_{xy}^{(0)} \end{Bmatrix} = \begin{Bmatrix} \dfrac{\partial u_0}{\partial x} + \dfrac{1}{2}\left(\dfrac{\partial w_0}{\partial x}\right)^2 \\ \dfrac{\partial v_0}{\partial y} + \dfrac{1}{2}\left(\dfrac{\partial w_0}{\partial y}\right)^2 \\ \dfrac{\partial u_0}{\partial y} + \dfrac{\partial v_0}{\partial x} + \dfrac{\partial w_0}{\partial x}\dfrac{\partial w_0}{\partial y} \end{Bmatrix}, \qquad \begin{Bmatrix} \varepsilon_{xx}^{(1)} \\ \varepsilon_{yy}^{(1)} \\ \gamma_{xy}^{(1)} \end{Bmatrix} = -c_1 \begin{Bmatrix} \dfrac{\partial \phi_x}{\partial x} \\ \dfrac{\partial \phi_y}{\partial y} \\ \dfrac{\partial \phi_x}{\partial y} + \dfrac{\partial \phi_y}{\partial x} \end{Bmatrix},$$

$$\begin{Bmatrix} \varepsilon_{xx}^{(3)} \\ \varepsilon_{yy}^{(3)} \\ \gamma_{xy}^{(3)} \end{Bmatrix} = -c_1 \begin{Bmatrix} \dfrac{\partial \phi_x}{\partial x} + \dfrac{\partial^2 w_0}{\partial x^2} \\ \dfrac{\partial \phi_y}{\partial y} + \dfrac{\partial^2 w_0}{\partial y^2} \\ \dfrac{\partial \phi_x}{\partial y} + \dfrac{\partial \phi_y}{\partial x} + 2\dfrac{\partial^2 w_0}{\partial x \partial y} \end{Bmatrix},$$

$$c_2 = 3c_1, \qquad c_1 = \frac{4}{3}h^2. \tag{2.11}$$

Taking into account the thermal effects, the linear stress-strain constitutive relationship is

$$\begin{Bmatrix} \sigma_{xx} \\ \sigma_{yy} \\ \sigma_{yz} \\ \sigma_{zx} \\ \sigma_{xy} \end{Bmatrix} = \begin{Bmatrix} Q_{11} & Q_{12} & 0 & 0 & 0 \\ Q_{21} & Q_{22} & 0 & 0 & 0 \\ 0 & 0 & Q_{44} & 0 & 0 \\ 0 & 0 & 0 & Q_{55} & 0 \\ 0 & 0 & 0 & 0 & Q_{66} \end{Bmatrix} \left\{ \begin{Bmatrix} \varepsilon_{xx} \\ \varepsilon_{yy} \\ \gamma_{yz} \\ \gamma_{zx} \\ \gamma_{xy} \end{Bmatrix} - \begin{Bmatrix} \alpha_{xx} \\ \alpha_{yy} \\ 0 \\ 0 \\ 2\alpha_{xy} \end{Bmatrix} \Delta T \right\}, \tag{2.12}$$

where Q are elastic stiffness elements [12].

According to Reddy's third-order shear deformation theory and Hamilton's principle, the nonlinear governing equations of motion for the FGM rectangular plate are given as [10]

$$N_{xx,\,x} + N_{xy,\,y} = I_0 \ddot{u}_0 + (I_1 - c_1 I_3)\ddot{\phi}_x - c_1 I_3 \frac{\partial \ddot{w}_0}{\partial x},$$

$$N_{yy,\,y} + N_{xy,x} = I_0 \ddot{v}_0 + (I_1 - c_1 I_3)\ddot{\phi}_y - c_1 I_3 \frac{\partial \ddot{w}_0}{\partial y},$$

$$
\begin{aligned}
&N_{yy,\,y}\frac{\partial w_0}{\partial y}+N_{yy}\frac{\partial^2 w_0}{\partial y^2}+N_{xy,\,x}\frac{\partial w_0}{\partial y}+N_{xy,\,y}\frac{\partial w_0}{\partial x}+2N_{xy}\frac{\partial^2 w_0}{\partial y\partial x}\\
&\qquad+N_{xx,\,x}\frac{\partial w_0}{\partial x}+N_{xx}\frac{\partial^2 w_0}{\partial x^2}+c_1\left(P_{xx,\,xx}+2P_{xy,xy}+P_{yy,\,yy}\right)\\
&\qquad+\left(Q_{x,\,x}-c_2R_{x,\,x}\right)+\left(Q_{y,\,y}-c_2R_{y,\,y}\right)+F-\gamma\dot{w}_0\\
&\quad=I_0\ddot{w}_0+c_1I_3\left(\frac{\partial\ddot{u}_0}{\partial x}+\frac{\partial\ddot{v}_0}{\partial x}\right)+c_1(I_4-c_1I_6)\left(\frac{\partial\ddot{\phi}_x}{\partial x}+\frac{\partial\ddot{\phi}_y}{\partial y}\right),\\
&M_{xx,\,x}+M_{xy,\,y}-c_1P_{xx,\,x}-c_1P_{xy,\,y}-\left(Q_x-c_2R_x\right)\\
&\quad=(I_1-c_1I_3)\ddot{u}_0+\left(I_2-2c_1I_4+c_1^2I_6\right)\ddot{\phi}_x-c_1(I_4-c_1I_6)\frac{\partial\ddot{w}_0}{\partial x},\\
&M_{yy,\,y}+M_{xy,\,x}-c_1P_{yy,\,y}-c_1P_{xy,\,x}-\left(Q_y-c_2R_y\right)\\
&\quad=(I_1-c_1I_3)\ddot{v}_0+\left(I_2-2c_1I_4+c_1^2I_6\right)\ddot{\phi}_y-c_1(I_4-c_1I_6)\frac{\partial\ddot{w}_0}{\partial y},
\end{aligned}
\tag{2.13}
$$

where γ is the damping coefficient, a comma denotes the partial differentiation with respect to a specified coordinate, and a super dot implies the partial differentiation with respect to time.

All kinds of inertias in (2.13) are calculated by

$$
I_i=\int_{-h/2}^{h/2}z^i p(z)dz,\quad (i=0,\ 1,\ 2,\ 3,\ 4,\ 6). \tag{2.14}
$$

the stress resultants are represented as follows

$$
\begin{gathered}
\begin{Bmatrix}\mathbf{N}\\ \mathbf{M}\\ \mathbf{P}\end{Bmatrix}=\begin{Bmatrix}\mathbf{A} & \mathbf{B} & \mathbf{E}\\ \mathbf{B} & \mathbf{D} & \mathbf{F}\\ \mathbf{E} & \mathbf{F} & \mathbf{H}\end{Bmatrix}\begin{Bmatrix}\boldsymbol{\varepsilon}^{(0)}\\ \boldsymbol{\varepsilon}^{(1)}\\ \boldsymbol{\varepsilon}^{(3)}\end{Bmatrix}+\begin{Bmatrix}\mathbf{N}^T\\ \mathbf{M}^T\\ \mathbf{P}^T\end{Bmatrix},\\
\begin{Bmatrix}\mathbf{Q}\\ \mathbf{R}\end{Bmatrix}=\begin{Bmatrix}\mathbf{A} & \mathbf{D}\\ \mathbf{D} & \mathbf{F}\end{Bmatrix}\begin{Bmatrix}\gamma^{(0)}\\ \gamma^{(2)}\end{Bmatrix},
\end{gathered}
\tag{2.15}
$$

where the membrane stress resultants, moments, higher-order moments, transverse shear stress resultants, and their higher-order counterparts are represented as follows:

$$
\begin{gathered}
\mathbf{N}=\left[N_{xx},N_{yy},N_{xy}\right]^{\mathbf{T}},\qquad \mathbf{M}=\left[M_{xx},M_{yy},M_{xy}\right]^{\mathbf{T}},\\
\mathbf{P}=\left[P_{xx},P_{yy},P_{xy}\right]^{\mathbf{T}},\quad \mathbf{Q}=\left[Q_{yy},Q_{xx}\right]^{\mathbf{T}},\quad \mathbf{R}=\left[R_{yy},R_{xx}\right]^{\mathbf{T}}.
\end{gathered}
\tag{2.16}
$$

The stiffness elements of the FGMs plate are denoted by

$$\begin{gathered}(A_{ij}, B_{ij}, D_{ij}, E_{ij}, F_{ij}, H_{ij}) = \int_{-h/2}^{h/2} Q_{ij}\left(1,\ z,\ z^2,\ z^3,\ z^4,\ z^6\right)dz, \quad (\ i,j = 1,\ 2,\ 6), \\ (A_{ij}, D_{ij}, F_{ij}) = \int_{-h/2}^{h/2} Q_{ij}\left(1,\ z^2,\ z^4\right)dz, \quad (i,j = 4,\ 5).\end{gathered} \tag{2.17}$$

And the thermal stress resultants in (2.16) can be represented as

$$\left\{\mathbf{N}^T, \mathbf{M}^T, \mathbf{P}^T\right\} = \begin{Bmatrix} N_{xx}^T & M_{xx}^T & P_{xx}^T \\ N_{yy}^T & M_{yy}^T & P_{yy}^T \\ N_{xy}^T & M_{xy}^T & P_{xy}^T \end{Bmatrix} = \int_{-h/2}^{h/2} \left[A_{xx}, A_{yy}, A_{xy}\right]^{\mathbf{T}} \left(1,\ z^2,\ z^3\right)\ \Delta T\, dz, \tag{2.18}$$

where

$$\begin{Bmatrix} A_{xx} \\ A_{yy} \\ A_{xy} \end{Bmatrix} = -\begin{bmatrix} Q_{11} & Q_{12} & 0 \\ Q_{21} & Q_{22} & 0 \\ 0 & 0 & Q_{66} \end{bmatrix} \begin{bmatrix} 1 & 0 \\ 0 & 1 \\ 0 & 0 \end{bmatrix} \begin{bmatrix} \alpha \\ \alpha \end{bmatrix}. \tag{2.19}$$

The nonlinear governing equations of motion for the FGM rectangular plate can be expressed in ters of displacements $(u_0,\ v_0,\ w_0, \phi_x, \phi_y)$ by substituting for the force and moments resultants. The equations of motion are very complicate nonlinear partial differential equations that can be seen in the conference [10].

The boundary conditions for the simply supported FGM plate requires that

at $x = 0$ and $x = a$,

$$w = \phi_y = M_{xx} = P_{xx} = N_{xy} = 0, \tag{2.20}$$

at $y = 0$ and $y = b$,

$$\begin{gathered} w = \phi_x = M_{yy} = P_{yy} = N_{xy} = 0, \qquad N_{yy}\big|_{y=0,b} = 0, \\ \int_0^b N_{xx}|_{x=0,a}\, dy = -\int_0^b (p_0 - p_1 \cos \Omega_2 t)\, dy. \end{gathered} \tag{2.21}$$

The present study focuses on the nonlinear transverse oscillations of FGM plates in the first two modes. It is then reasonable to construct deflection functions as a combination of the first two vibration mode shapes as follows:

$$w(x, y, t) = w_1(t) \sin \frac{\pi x}{a} \sin \frac{3\pi y}{b} + w_2(t) \sin \frac{3\pi x}{a} \sin \frac{\pi y}{b}, \tag{2.22}$$

where w_1 and w_2 are the amplitudes of two modes, respectively.

The transverse excitation can be represented as

$$F(x,y,t) = F_1(t)\sin\frac{\pi x}{a}\sin\frac{3\pi y}{b} + F_2(t)\sin\frac{3\pi x}{a}\sin\frac{\pi y}{b}, \tag{2.23}$$

where F_1 and F_2 represent the amplitudes of the transverse forcing excitation corresponding to the two nonlinear modes.

Based on research given in [13, 14], neglecting all inertia terms on u, v, ϕ_x, and ϕ_y in (2.13), we can obtain the displacements u, v, ϕ_x, and ϕ_y with respect to w. Then by the Galerkin procedure, the governing differential equations of transverse motion of the FGMs rectangular plate are obtained

$$\begin{aligned}
&\ddot{w}_1 + \omega_1^2 w_1 + a_1\dot{w}_1 + a_2 w_1\cos\Omega_2 t + a_3 w_1^2 + a_4 w_2^2 + a_5 w_1 w_2^2 \\
&\quad + a_6 w_1^3 + a_7 w_1 w_2 = f_1\cos\Omega_1 t, \\
&\ddot{w}_2 + \omega_2^2 w_2 + b_1\dot{w}_2 + b_2 w_2\cos\Omega_2 t + b_3 w_1 w_2 + b_4 w_1^2 + b_5 w_2^2 \\
&\quad + b_6 w_2 w_1^2 + b_7 w_2^3 = f_2\cos\Omega_1 t,
\end{aligned} \tag{2.24}$$

where w_1 and w_2 are the vibration amplitudes of the first two modes, respectively. f_1 and f_2 are the amplitudes of the transverse excitation force corresponding to the two nonlinear modes. The lengthy expressions of constants $a_1 - a_7$, $b_1 - b_7$ and the transverse excitation force f_1 and f_2 are not given here for brevity.

The present study focuses on the transverse nonlinear oscillations of a simply supported FGM rectangular plate in the first two modes.

The first two linear frequencies of this nonlinear dynamic system can be rewritten as

$$\begin{aligned}
\omega_1^2 &= -\frac{m_{007} + p_0 m_{008}}{m_{001}}, \\
\omega_2^2 &= -\frac{n_{007} + P_0 n_{008}}{n_{002}},
\end{aligned} \tag{2.25}$$

where p_0 is the static component in the in-plane excitation. The other coefficients in (2.13) are functions of geometric and physical parameters, in-plane excitations, and temperature field. That means that under different conditions, the system can have different internal resonance and exhibit different dynamic response.

It is seen that the in-plane stationary excitation p_0 can change the type of internal resonance.

When ω_1 is close to ω_2, the one-to-one internal resonance occurs and p_0 is as follows:

$$p_{01} = \frac{m_{007}n_{002} - m_{001}n_{007}}{m_{001}n_{008} - m_{008}n_{002}}. \tag{2.26}$$

When $\omega_2 \approx 2\omega_1$ or $\omega_2 \approx 3\omega_1$, the one-to-two or one-to-three internal resonance occurs.

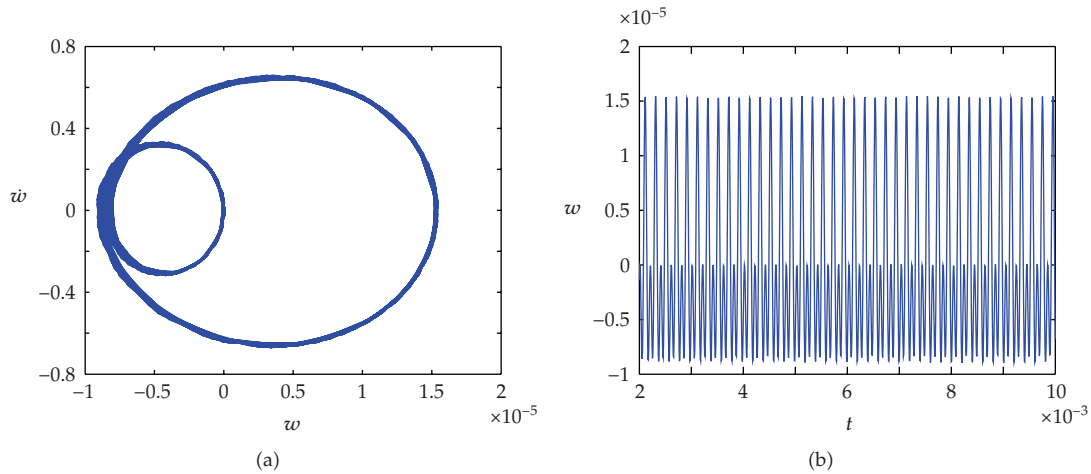

Figure 2: Effect of in-plane excitation on the dynamic response of the FGM plate with $1:1$ internal resonance.

The in-plane forces in these cases are given by (2.27)

$$p_{02} = \frac{m_{007}n_{002} - 4m_{001}n_{007}}{4m_{001}n_{008} - m_{008}n_{002}},$$
$$p_{03} = \frac{m_{007}n_{002} - 9m_{001}n_{007}}{9m_{001}n_{008} - m_{008}n_{002}}. \tag{2.27}$$

3. Numerical Results

The influence of in-plane stationary excitation on internal resonance is studied. The fourth-order Runge-Kutta algorithm is employed to numerically solve (2.11) and (2.12) to obtain the nonlinear dynamic response of the FGM rectangular plate subjected to thermal and mechanical loads with various internal resonance and primary parametric resonance.

Aluminum oxide and Ti-6Al-4V are chosen to be the constituent materials of the plate ($a = b = 1\,\mathrm{m}$, $h = a/20$). The volume fraction exponent is $n = 0.2$. The transverse load amplitude is $-10^6\,\mathrm{N/m^2}$. In addition, the plate is subjected to a temperature field where the aluminum oxide rich top surface is held at 900 K and the Ti-6Al-4V rich bottom surface is held at 300 K. Their temperature-dependent material properties evaluated at $T_0 = 300\,\mathrm{K}$ are as follows.

Ti-6Al-4V:

$$E = 105.7\,\mathrm{GPa}, \qquad \nu = 0.2981, \qquad \rho = 4429\,\frac{\mathrm{kg}}{\mathrm{m}^3}. \tag{3.1}$$

Aluminum oxide:

$$E = 320.24\,\mathrm{GPa}, \qquad \nu = 0.2600, \qquad \rho = 3750\,\frac{\mathrm{kg}}{\mathrm{m}^3}. \tag{3.2}$$

Figures 2–4 depict, respectively, nonlinear dynamic response of FGM plates. The plots of phase portrait for the cases of $1:1$, $1:2$ and $1:3$ internal resonance with different in-plane

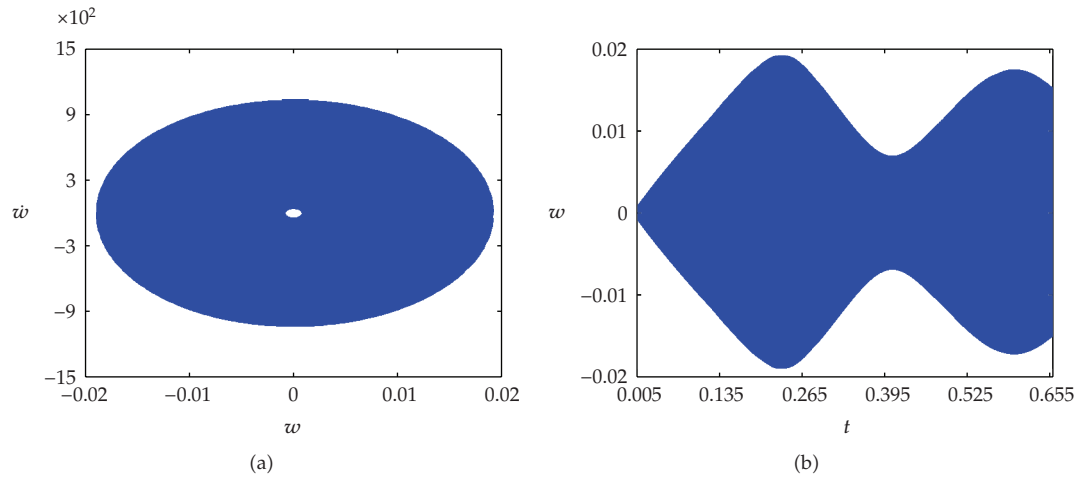

Figure 3: Effect of in-plane excitation on the dynamic response of the FGM plate with 1 : 2 internal resonance.

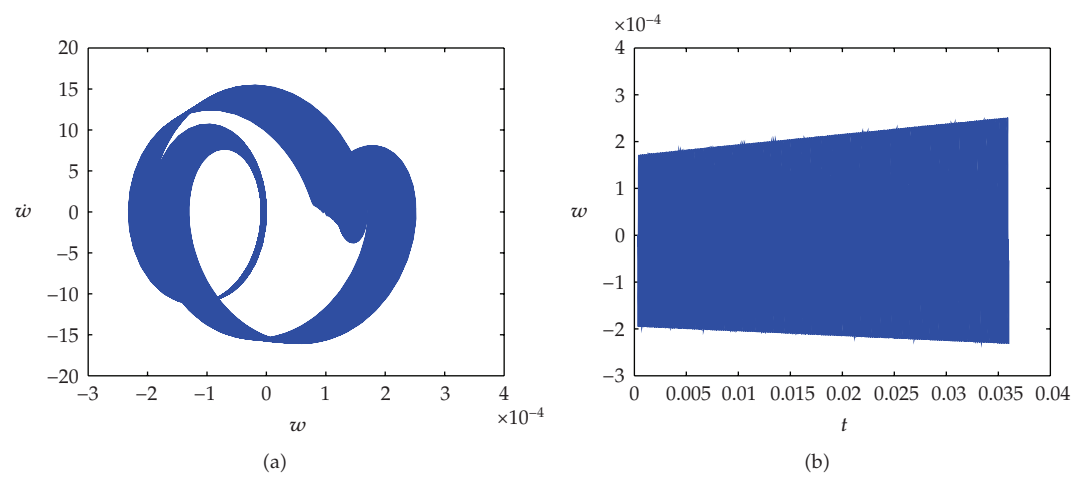

Figure 4: Effect of in-plane excitation on the dynamic response of the FGM plate with 1 : 3 internal resonance.

stationary loading are shown in Figures 2(a), 3(a), and 4(a) and the central deflection versus time curve is displayed in Figures 2(b), 3(b), and 4(b). The combinational resonance of the additive type is

$$\omega_1 = \frac{\Omega_1}{2}, \qquad \Omega_2 = \Omega_1. \tag{3.3}$$

It is observed that the central deflections are reduced by increasing the ratio of the two frequencies. In the case of 1 : 2 internal resonance the amplitude of the central deflection is larger than the one at other two frequency ratios. The case of internal resonance can be controlled by changing the in-plane excitation force, indicating that in the different case of internal resonance there is a different fundamental frequency.

Obviously, Figure 2 illustrates that the periodic response of the FGM rectangular plate occurs at 1 : 1 internal resonance when the p_0 is as 7.33×10^9 N/m. Figures 3 and 4 show that the beat vibration and quasiperiod dynamic response take place at 1 : 2 internal resonance when p_0 is as 6.24×10^{10} N/m and 1 : 3 internal resonance when p_0 is as 1.11×10^{11} N/m, respectively.

4. Conclusions

The nonlinear dynamics response of FGM rectangular plates under combined transverse and in-plane excitations is investigated in the cases of 1 : 1, 1 : 2 and 1 : 3 internal resonance. The material properties are assumed to be temperature-dependent. Based on Reddy's third-order shear deformation plate theory, the governing equations of motion for the FGMs rectangular plate are derived using Hamilton's principle. Galerkin's approach is used to reduce the governing equations of motion to a two-degree-of-freedom nonlinear system including the quadratic and cubic nonlinear terms. 1 : 1, 1 : 2 and 1 : 3 internal resonance and principal parametric resonance-1/2 subharmonic resonance are considered and solutions are obtained by using fourth-order Runge-Kutta method.

Numerical results show that plate geometry parameter, in-plane excitation and temperature field play important role in the internal resonance relationship and the nonlinear dynamic behavior of the FGM plate. In the case of 1 : 2 internal resonance and principal parametric resonance-1/2 subharmonic resonance, the vibration amplitude at the plate center is much greater than the one at other two cases of internal resonance. So in the actual condition, it is necessary to analyze what kinds of internal resonance may occur and how to control them.

Acknowledgments

The authors gratefully acknowledge the support of the National Natural Science Foundation of China (NNSFC) through Grant nos. 10732020 and 10972026 and the Science Foundation of Beijing Municipal Education Commission through Grant nos. KM200910772004 and KM201010772003.

References

[1] J. Yang and X.-L. Huang, "Nonlinear transient response of functionally graded plates with general imperfections in thermal environments," *Computer Methods in Applied Mechanics and Engineering*, vol. 196, no. 25–28, pp. 2619–2630, 2007.

[2] C.-S. Chen and A.-H. Tan, "Imperfection sensitivity in the nonlinear vibration of initially stresses functionally graded plates," *Composite Structures*, vol. 78, no. 4, pp. 529–536, 2007.

[3] G. N. Praveen and J. N. Reddy, "Nonlinear transient thermoelastic analysis of functionally graded ceramic-metal plates," *International Journal of Solids and Structures*, vol. 35, no. 33, pp. 4457–4476, 1998.

[4] N. Sundararajan, T. Prakash, and M. Ganapathi, "Nonlinear free flexural vibrations of functionally graded rectangular and skew plates under thermal environments," *Finite Elements in Analysis and Design*, vol. 42, no. 2, pp. 152–168, 2005.

[5] J. Yang, S. Kitipornchai, and K. M. Liew, "Large amplitude vibration of thermo-electro-mechanically stressed FGM laminated plates," *Computer Methods in Applied Mechanics and Engineering*, vol. 192, no. 35-36, pp. 3861–3885, 2003.

[6] T. Y. Ng, K. Y. Lam, and K. M. Liew, "Effects of FGM materials on the parametric resonance of plate structures," *Computer Methods in Applied Mechanics and Engineering*, vol. 190, no. 8–10, pp. 953–962, 2000.

[7] L. F. Qian, R. C. Batra, and L. M. Chen, "Static and dynamic deformations of thick functionally graded elastic plates by using higher-order shear and normal deformable plate theory and meshless local Petrov-Galerkin method," *Composites Part B*, vol. 35, no. 6–8, pp. 685–697, 2004.

[8] S. S. Vel and R. C. Batra, "Three-dimensional exact solution for the vibration of functionally graded rectangular plates," *Journal of Sound and Vibration*, vol. 272, no. 3–5, pp. 703–730, 2004.

[9] J. Woo and S. A. Meguid, "Nonlinear analysis of functionally graded plates and shallow shells," *International Journal of Solids and Structures*, vol. 38, no. 42-43, pp. 7409–7421, 2001.

[10] Y. X. Hao, L. H. Chen, W. Zhang, and J. G. Lei, "Nonlinear oscillations, bifurcations and chaos of functionally graded materials plate," *Journal of Sound and Vibration*, vol. 312, no. 4-5, pp. 862–892, 2008.

[11] S. C. Pradhan, C. T. Loy, K. Y. Lam, and J. N. Reddy, "Vibration characteristics of functionally graded cylindrical shells under various boundary conditions," *Applied Acoustics*, vol. 61, no. 1, pp. 111–129, 2000.

[12] J. N. Reddy, "A refined nonlinear theory of plates with transverse shear deformation," *International Journal of Solids and Structures*, vol. 20, no. 9-10, pp. 881–896, 1984.

[13] A. Bhimaraddi, "Large amplitude vibrations of imperfect antisymmetric angle-ply laminated plates," *Journal of Sound and Vibration*, vol. 162, no. 3, pp. 457–470, 1993.

[14] A. Nosier and J. N. Reddy, "A study of non-linear dynamic equations of higher-order shear deformation plate theories," *International Journal of Non-Linear Mechanics*, vol. 26, no. 2, pp. 233–249, 1991.

Hindawi Publishing Corporation
Mathematical Problems in Engineering
Volume 2010, Article ID 802720, 14 pages
doi:10.1155/2010/802720

Research Article

Vehicle Vibration Analysis in Changeable Speeds Solved by Pseudoexcitation Method

Li-Xin Guo and Li-Ping Zhang

School of Mechanical Engineering and Automation, Northeastern University, Shenyang 110004, China

Correspondence should be addressed to Li-Xin Guo, lxguo@mail.neu.edu.cn

Received 31 December 2009; Revised 20 February 2010; Accepted 28 August 2010

Academic Editor: Carlo Cattani

The vehicle driving comfort has become one of the important factors of vehicle quality and receives increasing attention. In this paper, the mechanical and mathematical models of the half-car, five degrees of freedom (DOF) of a vehicle were established, as well as the pseudoexcitation model of road conditions for the front wheel and the rear wheel. By the pseudoexcitation method, the equations of transient response and power spectrum density were established. After numerical simulation to vehicle vibration response of changeable driving, the results show that the pseudoexcitation method is more convenient than the traditional method and effectively solves the smoothness computation problems of vehicles while the pseudoexcitation method is used to analyze vehicle vibration under nonstationary random vibration environments.

1. Introduction

The mechanical and mathematical model of vehicle systems is usually simplified as a multiple-mass, complicated vibration system. Due to road excitation, vehicles may come into complicated vibration, which is disadvantageous to passenger health and goods protection [1, 2]. Therefore, it is important and necessary to control the vehicle's vibration within a limited and comfortable grade in order to ensure safety steering and physical health of drivers and passengers, as well as the operating stability of man-vehicle-road system. In the process of automobile moving, the random and changeable road surface is the main factor to induce vehicle vibration. Therefore, investigation of vehicle's stochastic vibration [3, 4] induced by road excitation has been a significant problem of vehicle design and its performance simulation.

At present, for this kind of problems, the Fourier transform analysis is used to investigate the dynamic characteristics of constant driving problems of automobiles based on stationary random vibration theory. After finishing vibration model of vehicles, it is important to derive the frequency characteristic of vehicle vibration responses and to

establish power spectrum density function of road excitation and vehicle vibration responses [5]. Then it can be used to analyze the influence of vehicle structural parameters and road excitation on vehicle random vibration [6]. Although this method was relatively simple, its derivation process is too complicated, that is, this method needs not only to derive the frequency response characteristics of vehicle vibration system, but also to derive the frequency response characteristics of vehicle vibration response values.

However, in some circumstances, vehicles are running in changeable speeds, such as in accelerating starting period and decelerating stopping period. In these cases, the road excitation and the vehicle dynamic response in time domain are nonstationary [7, 8]. The stochastic vibration analysis method based on Fourier transform and its inverse transform has been used to study the changeable speed response of vehicles in unevenness roads, but its computation work is enormous. The pseudoexcitation method was used to analyze the stochastic vibration of structural systems [9–11]. By pseudoexcitation method, stochastic vibration analysis was carried on a two-DOF system vibration of a quarter-vehicle model [12–14], in which the vibration response of a constant speed moving vehicle was investigated to a stationary random road excitation. The changeable speed vehicle vibration response was also conducted under one-point road excitation [15]. In addition, some last investigations [16, 17] have dealt with a quarter-car model with a harmonic excitation while the study [18] considers the additional stochastic component in the road surface roughness. In this study, the time-space frequency relationship of vehicle vibration under changeable speed moving was derived by pseudoexcitation method, and then the equation of transient power spectrum density of vehicle vibration response under nonstationary random road excitation input was obtained. At the end, we also conducted the numerical simulations to the vibration responses of a half-car, five-DOF vehicle system under changeable speed moving conditions.

2. Theory of Pseudoexcitation Method

When a linear system is randomly excited by self-spectrum density $S_{xx}(w)$, the self-power spectrum of its response y is

$$S_{yy}(w) = |H(w)|^2 S_{xx}(w), \tag{2.1}$$

where $H(w)$ is the frequency response function, and its meaning is shown in Figure 1 [19], that is, the corresponding harmonic response is $y = H(w)e^{iwt}$ when the random excitation is replaced by harmonic excitation e^{iwt}. From Figure 1, it can be seen that if it multiplies a constant $\sqrt{S_{xx}}$ before the excitation e^{iwt}, it can create a pseudoexcitation,

$$\tilde{x}(t) = \sqrt{S_{xx}}e^{iwt}. \tag{2.2}$$

After multiplying a same constant to its response value, it can give the following equations:

$$\begin{gathered}
\tilde{y}^*\tilde{y} = \left|\tilde{y}\right|^2 S_{xx} = S_{yy}, \\
\tilde{x}^*\tilde{y} = \sqrt{S_{xx}}e^{-iwt} \cdot \sqrt{S_{xx}}e^{iwt} = S_{xx}H = S_{xy}, \\
\tilde{y}^*\tilde{x} = \sqrt{S_{xx}}e^{-iwt} \cdot \sqrt{S_{xx}}He^{iwt} = S_{xx}H = S_{sy}.
\end{gathered} \tag{2.3}$$

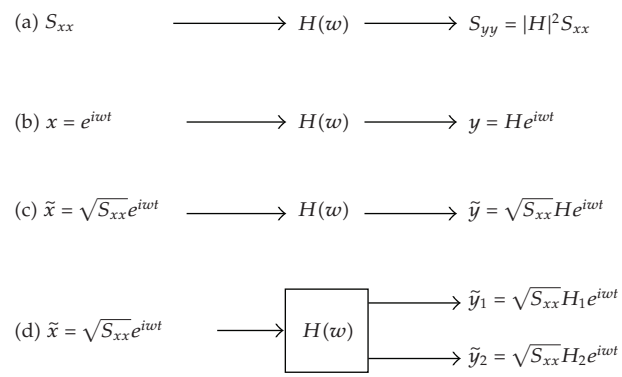

Figure 1: The principle of pseudoexcitation method.

The last formula in the above 3 equations is the conventional expressions of self-spectrum density or mutual spectrum density.

If the pseudoresponse values $\tilde{y}_1$ and $\tilde{y}_2$ are considered in the above system, the following equations can be validated:

$$\begin{gathered}\tilde{y}_1^*\tilde{y}_2 = H_1{}^*\sqrt{S_{xx}}e^{-iwt}\cdot H_2\sqrt{S_{xx}}e^{iwt} = H_1{}^*S_{xx}H_2 = S_{y1y2},\\ \tilde{y}_2^*\tilde{y}_1 = H_2{}^*S_{xx}H_1 = S_{y2y1}.\end{gathered} \tag{2.4}$$

Then the matrixes of power spectrum density are as follows:

$$\begin{aligned}[S_{yy}] &= \{\tilde{y}\}^*\cdot\{\tilde{y}\}^T,\\ [S_{xy}] &= \{\tilde{x}\}^*\cdot\{\tilde{y}\}^T,\\ [S_{yx}] &= \{\tilde{y}\}^*\cdot\{\tilde{x}\}^T.\end{aligned} \tag{2.5}$$

If the pseudoexcitation of a random process is $\tilde{x}(t) = \sqrt{S_{xx}}e^{iwt}$, then it can give

$$\dot{\tilde{x}} = iw\sqrt{S_{xx}}e^{iwt}, \qquad \ddot{\tilde{x}} = -w^2\sqrt{S_{xx}}e^{iwt}, \tag{2.6}$$

$$S_{\ddot{x}\ddot{x}} = w^4S_{xx}. \tag{2.7}$$

That is the power spectrum density of accelerations, and in the same way, we can obtain the following equations:

$$S_{\ddot{\tilde{y}}\ddot{\tilde{y}}} = \{\ddot{\tilde{y}}\}^*\cdot\{\ddot{\tilde{y}}\}^T, \tag{2.8}$$

$$S_{\ddot{\tilde{y}}_1\ddot{\tilde{y}}_2} = \{\ddot{\tilde{y}}_1\}^*\cdot\{\ddot{\tilde{y}}_2\}^T, \tag{2.9}$$

where $*$ is a complex conjugate, and T is a matrix transfer.

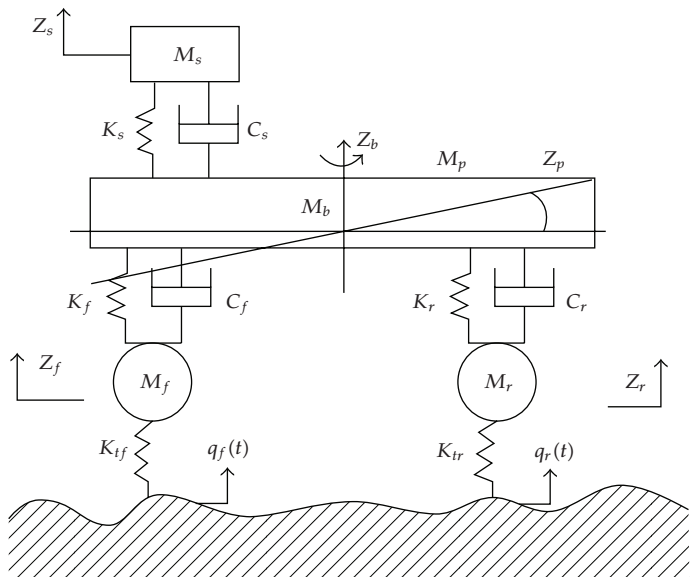

Figure 2: The mechanical model of a half-car, five-DOF automobile system.

After computing the vibration response of the system in the case of the pseudo harmonic excitation, all the power spectrum densities of them can be solved according to (2.5)–(2.9). Then the self-spectrum density and mutual spectrum density of them can also be obtained.

3. Vibration Analysis of the Half-Car, Five-DOF Vehicle System in Changeable Speeds

3.1. Mechanical and Mathematical Models of the System

For analyzing automobile vibration, it is important to establish its mechanical and mathematical model of the automobile structural system, so that the vibration characteristic response value of the mathematical model of vehicle vibration can be solved and obtained. For the mechanical modeling of automobiles, a seven-DOF mechanical model [20] has been developed to investigate the influence of active and semiactive suspension to automobile dynamic performance. In addition, the moving smartness and operating stability of automobiles were also investigated by spatial mechanical models of automobiles [21]. In this study, a half-car, five-DOF linear mechanical model [22] of an automobile system was developed as shown in Figure 2.

In Figure 2, m_s is the mass of driver and chair and m_b is the mass of automobile structure. m_f, m_r are the nonspring supported mass of front and rear suspensions, respectively. k_s and c_s are the rigidity coefficient and damping coefficient of the chair, respectively. k_f, k_r are the rigidity coefficient of front and rear suspensions, respectively. k_{tf}, k_{tr} are the rigidity coefficient of front and rear wheels, respectively. q_f, q_r are the road excitation forces at front and rear wheels, respectively. l_1 is the distance between chair and vehicle mass center. l_2, l_3 are the distances from the vehicle mass center to front and rear wheel axles, respectively.

By Lagrange equations, the mathematical model of the vehicle mechanical model in Figure 2 is as follows:

$$[M]\{\ddot{Z}\} + [C]\{\dot{Z}\} + [K]\{Z\} = [F]\{Q\}, \tag{3.1}$$

where

$$M = \begin{bmatrix} m_s & 0 & 0 & 0 & 0 \\ 0 & m_b & 0 & 0 & 0 \\ 0 & 0 & m_p & 0 & 0 \\ 0 & 0 & 0 & m_f & 0 \\ 0 & 0 & 0 & 0 & m_r \end{bmatrix},$$

$$C = \begin{bmatrix} c_s & -c_s & c_s l_1 & 0 & 0 \\ -c_s & c_s + c_f + c_r & -c_s l_1 - c_f l_2 + c_r l_3 & -c_f & -c_r \\ c_s l_1 & -c_s l_1 - c_f l_2 + Crl_3 & c_s l_1^2 + c_f l_2^2 + c_r l_3^2 & c_f l_2 & -Crl_3 \\ 0 & -c_f & c_f l_1 & c_f & 0 \\ 0 & -c_r & -c_r l_3 & 0 & c_r \end{bmatrix},$$

$$K = \begin{bmatrix} k_s & -k_s & k_s l_1 & 0 & 0 \\ -k_s & k_s + k_f + k_r & -k_s l_1 - k_f l_2 + k_r l_3 & -k_f & -k_r \\ k_s & -k_s l_1 - k_f l_2 + k_r l_3 & k_s l_1^2 + k_f l_2^2 + k_r l_3^2 & k_f l_2 & -k_r l_3 \\ 0 & -k_f & k_f l_2 & k_f + k_{tf} & 0 \\ 0 & -k_r & -k_r l_3 & 0 & k_r + k_{tr} \end{bmatrix}, \tag{3.2}$$

$$F = \begin{bmatrix} 0 & 0 \\ 0 & 0 \\ 0 & 0 \\ k_{tf} & 0 \\ 0 & k_{tr} \end{bmatrix}, \qquad \{Z\} = \{z_s \;\; z_b \;\; z_p \;\; z_f \;\; z_r\}^T, \qquad \{Q\} = \{q_f \;\; q_r\}^T.$$

3.2. Road Excitation

The unevenness degree of road profile can be generally described by power spectrum density. The international GB7031 recommends that the power spectrum density of road profile is described by

$$S_q(n) = S_q(n_0)\left(\frac{n}{n_0}\right)^{-w}, \tag{3.3}$$

where $S_q(n_0)$ is the unevenness coefficient of road profile. n_0 is the referenced spatial frequency, $n_0 = 0.1\,(m^{-1})$. n is the spatial frequency (m^{-1}). w is the frequency exponent of the graded road spectrum and generally chosen as 2. In this study, $S_q(n_0)$ is set as $S_q(n_0) = 64 \times 10^{-6}\,(m^2/m^{-1})$, that is, Grade B road condition.

When automobiles move in changeable speeds, the excitations of automobile systems are different in time domain and space domain. It is not stationary in space domain but in time domain. However, the automobile's mechanical responses are all nonstationary. By the inherent characteristics of frequency response function $H(w)$ of vehicle system in time domain and the relation of time frequency w and space frequency n, the transient frequency response function $H(s,n)$ can be obtained, then we can solve the stochastic vibration of the vehicle system in changeable speed moving [11, 23].

The unevenness degree of roads in time domain is shown as follows [24]:

$$q(t) = h_0 e^{jwt}, \tag{3.4}$$

where h_0 is the amplitude of unevenness degree of roads. The expression of unevenness degree of roads in space domain is as follows:

$$q = h_0 e^{j\Omega s}, \tag{3.5}$$

$$wt = \Omega v, \tag{3.6}$$

where Ω is the spatial angular frequency.

When the automobile is moving in a constant speed, $s = vt$, it has the following relation, $w = \Omega s$ or $f = nv$.

When the automobile is moving in a changeable speed, it has

$$s = v_0 + \frac{at^2}{2}, \tag{3.7}$$

where v_0 is the initial velocity of the automobile and a is its acceleration. Then (3.6) can be rewritten as

$$\begin{gathered} wdt = \Omega ds, \\ w = \Omega \frac{ds}{dt} = 2n\pi(v_0 + at) = 2n\pi\left(2as + {v_0}^2\right)^{1/2}. \end{gathered} \tag{3.8}$$

Equation (3.8) reflects the time-space frequency relation of automobiles in an accelerated moving.

3.3. Pseudoexcitation of Random Road at Front and Rear Wheels

By the time-frequency expression of unevenness degree of roads, a pseudoexcitation of road $\tilde{q}(t)$ can be built which is corresponding with the road excitation $q(t)$, as follows:

$$\tilde{q}(t) = \sqrt{S_q(n)}e^{iwt}. \tag{3.9}$$

Hypothesize that the road excitations on four wheels of the automobile are the same and the delay relation [14] between front wheel excitation $q_f(t)$ and rear wheel excitation $q_r(t)$ is as follows:

$$q_r(t) = q_f(t-\tau), \tag{3.10}$$

where $\tau = l/v$, l is the distance between two wheel axles, then it has

$$\begin{gathered} \tilde{q}_f(t) = \sqrt{S_q(n)}e^{iwt}, \\ \tilde{q}_r(t) = \tilde{q}_f(t-\tau) = \sqrt{S_q(n)}e^{iw(t-\tau)} = e^{-iwt\tau}\tilde{q}(t). \end{gathered} \tag{3.11}$$

Therefore, the excitation input is written as follows:

$$\{\tilde{q}(t)\} = \begin{bmatrix} \tilde{q}_f(t) \\ \tilde{q}_r(t) \end{bmatrix} = \begin{bmatrix} 1 \\ e^{-iw\tau} \end{bmatrix} \tilde{q}(t) = \{H_q(w)\}\tilde{q}(t). \tag{3.12}$$

The road excitations from front wheel and rear wheel can be simplified as an excitation input $\{\tilde{q}(t)\}$, and its frequency response characteristic is $\{H_q(w)\}$. Thus, the two-point excitations are simplified as one-point excitation.

3.4. Formulation of System Response

For a multiple degrees-of-freedom system, its frequency response characteristic is the complex number ratio of response vector and excitation vector. For the half-car, five-DOF vehicle system in this study, if we supposed that its frequency response is $[H(w)]$, then the relation of pseudoresponse and pseudoexcitation is

$$\{\tilde{z}(t)\} = [H(w)]\{\tilde{q}(t)\}. \tag{3.13}$$

Substituting (3.12) into (3.13) gives

$$\{\tilde{z}(t)\} = [H(w)]\{H_q(w)\}\tilde{q}(t) = \{h_g(w)\}\tilde{q}(t). \tag{3.14}$$

Since $\{h_g(w)\} = [H(w)]\{H_q(w)\}$, then

$$\{\dot{\tilde{z}}(t)\} = \{h_g(w)\}\dot{\tilde{q}}(t) = iw\{h_g(w)\}\tilde{q}(t), \tag{3.15}$$

$$\{\ddot{\tilde{z}}(t)\} = -w^2\{h_g(w)\}\tilde{q}(t). \tag{3.16}$$

Substitute (3.15) and (3.16) into the system equation, then the system frequency response function can be obtained as follows:

$$[H(w)] = \Big[[K] - w^2[M] + iw[C]\Big]^{-1} F, \tag{3.17}$$

where

$$[H(w)]_{5\times 2} = \begin{bmatrix} H(w)_s \\ H(w)_b \\ H(w)_p \\ H(w)_f \\ H(w)_r \end{bmatrix}. \tag{3.18}$$

The frequency response functions of the relative displacement of suspension and the dynamic loads of tires are as follows, respectively:

$$\begin{aligned} H_{rd}(w) &= \frac{z_b(w) - l_2 z_p(w) - z_f(w)}{q_f(w)}, \\ H_{tf}(w) &= \frac{z_f(w) - z_r(w)}{q_f(w)} k_{tf}. \end{aligned} \tag{3.19}$$

By substituting (3.13) into (3.19), it gives the frequency response functions of the relative displacement of suspension and the dynamic loads of tires as follows:

$$\begin{aligned} H_{rd}(w) &= H_b(w) - l_2 H_p(w) - H_f(w), \\ H_{tf}(w) &= \left[H_f(w) - H_r(w)\right] k_{tf}. \end{aligned} \tag{3.20}$$

It can be found that the system response result by pseudoexcitation method is the same as the result obtained by Fourier transform analysis. After obtaining the automobile structural parameters and the road excitation parameters, the pseudoexcitation responses $\{\tilde{z}(t)\}$ and $\{\ddot{\tilde{z}}(t)\}$ can be solved in accordance with (3.14) and (3.16). The response power spectrum can be achieved according to (2.5) and (2.6).

The power spectrum matrix of vertical acceleration of the system is

$$\begin{aligned} \{S_{\ddot{z}\ddot{z}}(w)\} &= \{\ddot{\tilde{z}}(t)\}^* \cdot \{\ddot{\tilde{z}}(t)\}^T = w^4 \{h_g(w)\} \sqrt{S_q(n)} e^{-iwt} \{h_g(w)\}^T \sqrt{S_q(n)} e^{iwt} \\ &= w^4 \{h_g(w)\} \{h_g(w)\}^T S_q(n) \\ &= w^4 [H(w)] \{H_q(w)\} \{H_q(w)\}^T [H(w)]^T S_q(n). \end{aligned} \tag{3.21}$$

By substituting $w = 2n\pi(2as + v_0{}^2)^{1/2}$ into (3.21), the spatial acceleration power spectrum density of system responses can be obtained as follows:

$$\{S_{\ddot{z}\ddot{z}}(s,n)\} = (2\pi n)^4 \left(2as + v_0{}^2\right)^2 [H(s,n)] \{H_q(s,n)\} \{H_q(s,n)\}^T [H(s,n)]^T S_q(n), \tag{3.22}$$

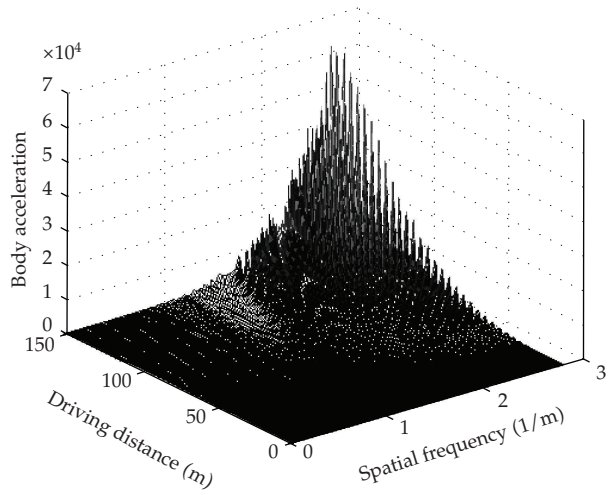

Figure 3: 3D spectrum of body acceleration.

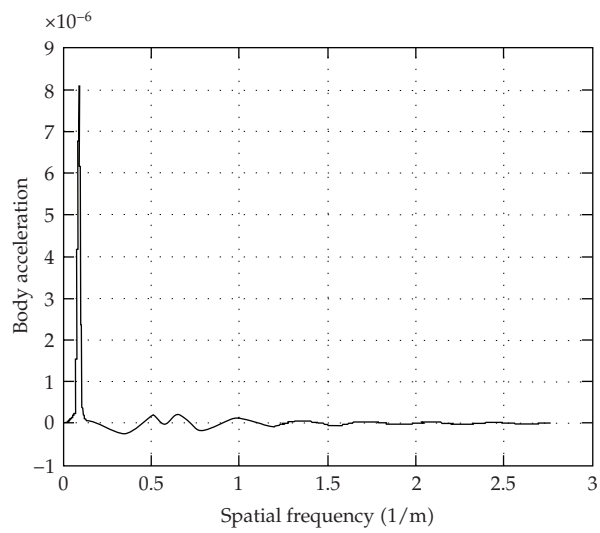

Figure 4: 2D spectrum of body acceleration.

where

$$H(s,n) = \left[[K] - 4n^2\pi^2\left(2as + v_0{}^2\right)[M] + i\left(2n\pi\sqrt{2as + v_0{}^2}[C]\right)\right]^{-1} F,$$
$$\{H_q(s,n)\} = \begin{bmatrix} 1 \\ e^{-i(2n\pi\sqrt{2as+v_0{}^2}\tau)} \end{bmatrix} \sqrt{S_q(n)}\, e^{-i(2n\pi\sqrt{2as+v_0{}^2}t)}. \tag{3.23}$$

In the same way, according to the frequency response function of relative displacement of suspensions and dynamic loads of tires, we can obtain the transient spatial power spectrum

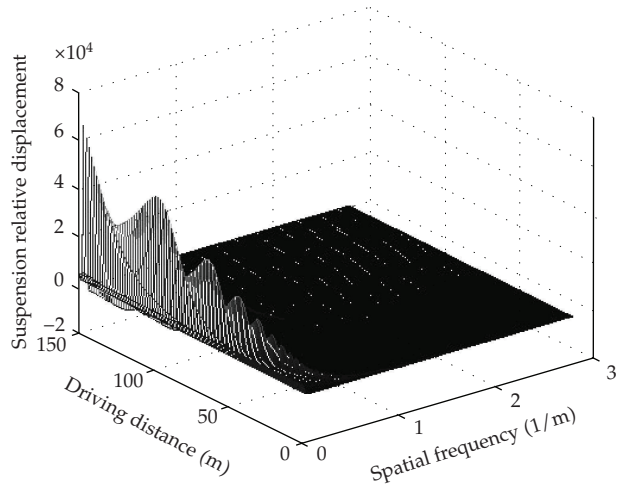

Figure 5: 3D spectrum of relative displacement of vehicle suspension.

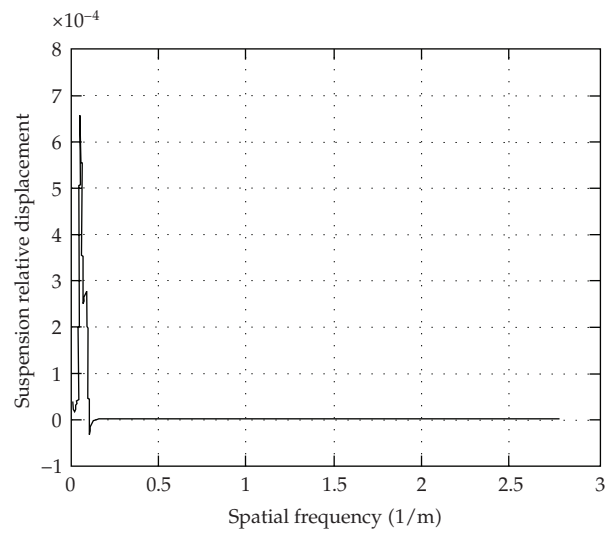

Figure 6: 2D spectrum of relative displacement of vehicle suspension.

density functions. It is important to substitute $w = 2n\pi(2as + v_0{}^2)^{1/2}$ into them to get the corresponding power spectrum density as follows:

$$\begin{aligned} S_{rd}(s,n) &= H_{rd}(s,n)S_q(n)\left[H_{rd}(s,n)\right]^T, \\ S_{tf}(s,n) &= H_{tf}(s,n)S_q(n)\left[H_{tf}(s,n)\right]^T. \end{aligned} \tag{3.24}$$

By means of computing $\{S_{\ddot{z}\ddot{z}}(s,n)\}$, $S_{rd}(s,n)$, and $S_{tf}(s,n)$, we can obtain the dynamic characteristics of vehicles and driving comfort of vehicles.

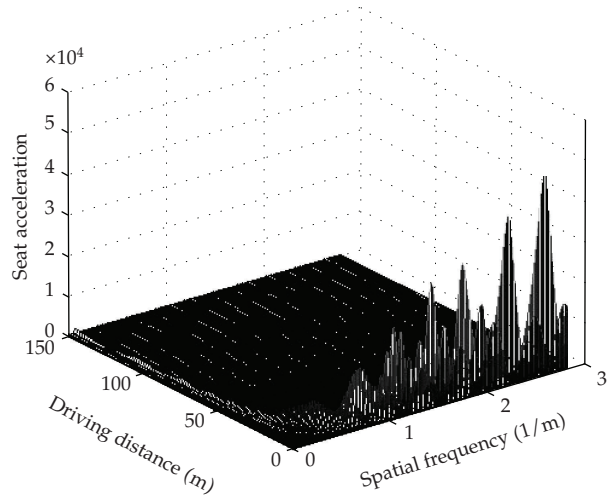

Figure 7: 3D spectrum of seat acceleration.

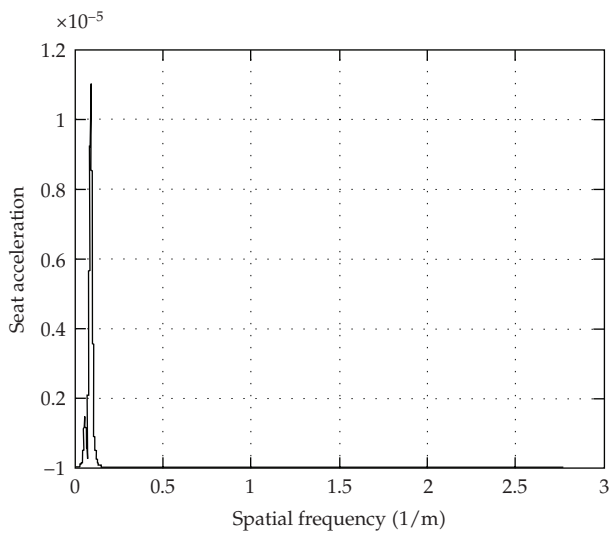

Figure 8: 2D spectrum of seat acceleration.

4. Computing Case

In order to check the validation of the above mathematical models of transient response analysis of the half-car, five-DOF automobile system based on pseudoexcitation, we carried out the simulations as follows. To mimic an accelerating process of the automobile, set the acceleration as $a = 1.0\,\text{ms}$ and the running distance as $s = 150\,\text{m}$, respectively. The other mechanical model parameters of the five-DOF automobile system are shown in Table 1.

Figures 3 and 4 show the 3D (three-dimensional) and 2D (two-dimensional) spectrums of body acceleration, respectively. Figures 5 and 6 show the 3D and 2D spectrums of relative displacement of vehicle suspension, respectively. Figures 7 and 8 show the 3D and 2D spectrums of seat acceleration, respectively. Figures 9 and 10 show the 3D and

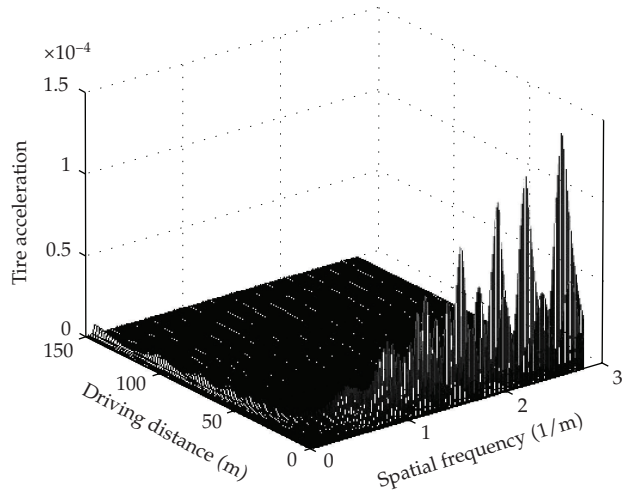

Figure 9: 3D spectrum of tire acceleration.

Table 1: Mechanical model parameters of the five-DOF automobile system.

Items	m_s(kg)	m_b(kg)	m_p(kg.m^2)	m_f(kg)	m_r(kg)
Values	70	2100	3500	140	210
Items	k_s	k_f	k_r	k_{tf}	k_{tr}
Values	12200	74000	120000	520000	520000
Items	c_s	c_f	c_r		
Values	550	1800	1200		

2D spectrums of tire acceleration, respectively. Figure 11 shows the 2D spectrum of tire dynamic load. The nonstationary response spectrum analysis of the vehicle system shows that the low-spatial frequency ingredient has a main role with vehicle speed increasing when the vehicle moves in a constant acceleration. With the speed increasing, the peak values of power spectrum of seat and body acceleration, as well as the low frequency values of power spectrum of dynamic tire loads, are not monotonously increasing, and some local values are decreasing. The changing of relative displacement of vehicle suspensions is not large. The nonlinearity of the vehicle suspension is not included in the current study, this is the limitation of this vehicle dynamic model, and it will be considered in the coming study.

5. Conclusion

By pseudoexcitation method, the vibration response characteristics of the half-car, five-DOF automobile system were obtained. The results show that the pseudoexcitation method is more convenient than the traditional method and effectively solves the smoothness computation of vehicles while the pseudoexcitation method is used to analyze vehicle vibration under nonstationary random vibration.

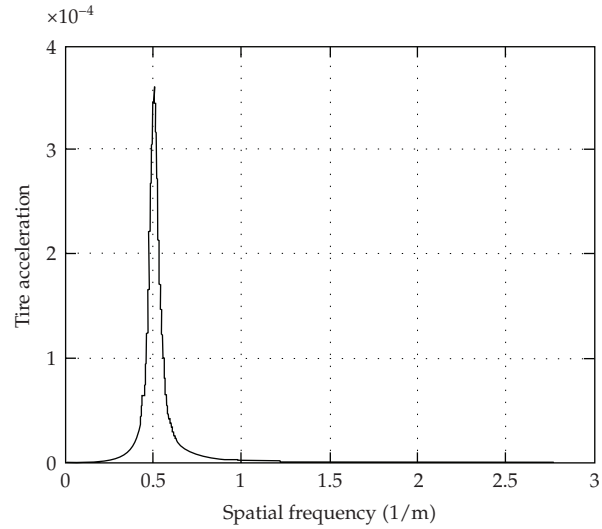

Figure 10: 2D spectrum of tire acceleration.

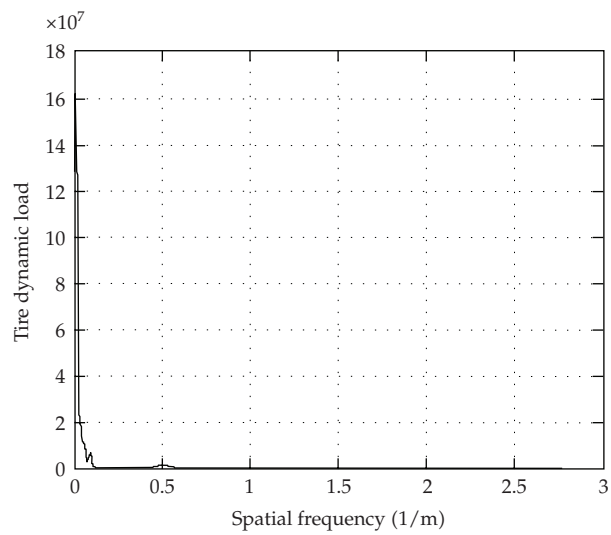

Figure 11: 2D spectrum of tire dynamic load.

Acknowledgments

The authors are grateful for the research Grants from the Program for New Century Excellent Talents in University (no. NCET-08-0103), the Scientific Research Foundation of China Postdoctor (nos. 20070420203 and 200801391), the Natural Science Foundation of China (no. 50875041), National 973 Program (2007CB210305-2), Basic Research Expense of National Universities (no. N090503001), Program for Changjiang Scholars and Innovative Research Team in University, and a research fund from Northeastern University, China.

References

[1] J.-D. Wu and R.-J. Chen, "Application of an active controller for reducing small-amplitude vertical vibration in a vehicle seat," *Journal of Sound and Vibration*, vol. 274, no. 3–5, pp. 939–951, 2004.

[2] Z. S. Yu, *Automobile Theory*, Mechanical Industry Press, Beijing, China, 1992.

[3] P. Cacciola, N. Maugeri, and G. Muscolino, "A modal correction method for non-stationary random vibrations of linear systems," *Probabilistic Engineering Mechanics*, vol. 22, no. 2, pp. 170–180, 2007.

[4] H. E. M. Hunt, "Stochastic modelling of traffic-induced ground vibration," *Journal of Sound and Vibration*, vol. 144, no. 1, pp. 53–70, 1991.

[5] W. Gao, N. Zhang, and J. Dai, "A stochastic quarter-car model for dynamic analysis of vehicles with uncertain parameters," *Vehicle System Dynamics*, vol. 46, no. 12, pp. 1159–1169, 2008.

[6] A. M. A. Soliman, "Effect of road roughness on the vehicle ride comfort and rolling resistance," Tech. Rep. SAE paper no. 2006-01-1297, 2006.

[7] E. M. ElBeheiry, "Effects of small travel speed variations on active vibration control in modern vehicles," *Journal of Sound and Vibration*, vol. 232, no. 5, pp. 857–875, 2000.

[8] V. Rouillard and M. A. Sek, "Simulation of non-stationary vehicle vibrations," *Proceedings of the Institution of Mechanical Engineers. Part D. Journal of Automobile Engineering*, vol. 215, no. 10, pp. 1069–1075, 2001.

[9] J. Lin, W. Zhang, and J. Li, "Structural responses to arbitrarily coherent stationary random excitations," *Computers and Structures*, vol. 50, no. 5, pp. 629–633, 1994.

[10] F. Lu, Q. Gao, J. H. Lin, and F. W. Williams, "Non-stationary random ground vibration due to loads moving along a railway track," *Journal of Sound and Vibration*, vol. 298, no. 1-2, pp. 30–42, 2006.

[11] F. Lu, J. H. Lin, D. Kennedy, and F. W. Williams, "An algorithm to study non-stationary random vibrations of vehicle-bridge systems," *Computers and Structures*, vol. 87, no. 3-4, pp. 177–185, 2009.

[12] C. Papalukopoulos and S. Natsiavas, "Nonlinear biodynamics of passengers coupled with quarter car models," *Journal of Sound and Vibration*, vol. 304, no. 1-2, pp. 50–71, 2007.

[13] S. S. Parthasarathy and Y. G. Srinivasa, "Design of an active suspension system for a quarter-car road vehicle model using model reference control," *Proceedings of the Institution of Mechanical Engineers. Part I. Journal of Systems and Control Engineering*, vol. 220, no. 2, pp. 91–108, 2006.

[14] J. Li, Y. Y. Qin, Q. Zhao, and W. Zhang, "A pseudo excitation method for automotive vibration analysis," *Mechanical Science and Technology*, vol. 28, no. 3, pp. 281–285, 2009.

[15] X. Peng, X.-H. Liu, and G.-L. Wen, "Vibration analysis of vehicle at uneven speed with pseudo-excitation method," *Journal of Hunan University Natural Sciences*, vol. 34, no. 11, pp. 37–41, 2007.

[16] G. Litak, M. Borowiec, M. I. Friswell, and K. Szabelski, "Chaotic vibration of a quarter-car model excited by the road surface profile," *Communications in Nonlinear Science and Numerical Simulation*, vol. 13, no. 7, pp. 1373–1383, 2008.

[17] R. D. Naik and P. M. Singru, "Establishing the limiting conditions of operation of magneto-rheological fluid dampers in vehicle suspension systems," *Mechanics Research Communications*, vol. 36, no. 8, pp. 957–962, 2009.

[18] G. Litak, M. Borowiec, M. I. Friswell, and W. Przystupa, "Chaotic response of a quarter car model forced by a road profile with a stochastic component," *Chaos, Solitons and Fractals*, vol. 39, no. 5, pp. 2448–2456, 2009.

[19] J. H. Lin and Y. H. Zhang, *Pseudo Excitation Method of Random Vibration*, Science Press, Beijing, China, 2004.

[20] H. Y. Zhou, *Development and control of an automotive smart suspension system*, Ph.D. thesis, University of Toronto, Ontario, Canada, 2002.

[21] D. E. Williams and W. M. Haddad, "Active suspension control to improve vehicle ride and handling," *Vehicle System Dynamics*, vol. 28, no. 1, pp. 1–24, 1997.

[22] J. B. Hoyle, "Modelling the static stiffness and dynamic frequency response characteristics of a leaf spring truck suspension," *Proceedings of the Institution of Mechanical Engineers. Part D. Journal of Automobile Engineering*, vol. 218, no. 3, pp. 259–278, 2004.

[23] M. Mitschke, *Vehicle Dynamics*, China Communications Press, Beijing, China, 1994.

[24] L. Sun and B. S. Greenberg, "Dynamic response of linear systems to moving stochastic sources," *Journal of Sound and Vibration*, vol. 229, no. 4, pp. 957–972, 2000.

Hindawi Publishing Corporation
Mathematical Problems in Engineering
Volume 2010, Article ID 806475, 15 pages
doi:10.1155/2010/806475

Research Article

Flow-Induced Vibration Analysis of Supported Pipes Conveying Pulsating Fluid Using Precise Integration Method

Long Liu[1] and Fuzhen Xuan[2]

[1] *Logistics Engineering College, Shanghai Maritime University, Shanghai 201306, China*
[2] *School of Mechanical and Power Engineering, East China University of Science and Technology, Shanghai 200237, China*

Correspondence should be addressed to Long Liu, liu.long@gmail.com

Received 1 January 2010; Revised 6 May 2010; Accepted 19 August 2010

Academic Editor: Carlo Cattani

Dynamic analysis of supported pipes conveying pulsating fluid is investigated in Hamiltonian system using precise integration method (PIM). First, symplectic canonical equations of supported pipes are deduced with state variable vectors composed of displacement and momentum. Then, PIM with linear interpolation formula is proposed to solve these equations. Finally, this approach's precision is testified by several numerical examples of pinned-pinned pipes with different fluid velocities and frequencies. The results show that PIM is an efficient and rapid approach for flow-induced dynamic analysis o f supported pipes.

1. Introduction

As the pipes are widely used in many industrial fields, flow-induced vibration analysis of pipes conveying fluid has been one of the attractive subjects in structural dynamics. It is well known that pipeline systems may undergo divergence and flutter types of instabilities generated by fluid-structure interaction. Over the last sixty years, extensive studies have been carried out on dynamic analysis of pipeline systems subject to different boundary conditions and loadings. Notable contributions in this area include the works of Chen [1] and Paidoussis [2, 3]. At present, most of the research is concentrated on nonlinear dynamic analysis of pipes conveying pulsating fluid. A recent survey on bifurcations for supported pipes can be found in [4]. Folley and Bajaj [5] considered nonlinear spatial dynamic characteristics of cantilever pipes conveying fluid.

In most cases, the corresponding ordinary differential motion equations of fluid-conveyed pipes are deduced using Galerkin's method in Lagrange system. Then many

numerical methods, such as transfer matrix method, finite element method, perturbation method, Runge-Kutta method, and differential quadrature method, are applied to solve these equations.

For example, Jensen [6] analyzed dynamic behaviors of vibrating pipe containing fluid subject to lateral resonant base excitation using the perturbation method of multiple scales. Yang et al. [7] investigated the effect of fluid viscosity and mass ratio on instability regions of a Kelvin-type viscoelastic pipe conveying harmonically pulsating fluid using multiple scales method. Wang et al. [8] studied the nonlinear dynamics of curved fluid conveying pipe with differential quadrature method.

Jeong et al. [9] proposed a finite element model of pipes conveying periodically pulsating fluid and analyzed the influence of fluid velocities on pipe's stability. Stangl et al. [10] solved the extended version of Lagrange nonlinear equations for cantilevered pipes using implicit Runge-Kutta solver HOTINT. Wang [11] explored numerically the effect of the nonlinear motion constraints on dynamics of simply supported pipes conveying pulsating fluid via the fourth-order Runge-Kutta scheme.

Nikolić and Rajković [12] used Lyapunov-Schmidt reduction and singularity theory to investigate the behaviors of extensive fluid-conveying pipe supported at both ends around the neighborhood of the bifurcation points. Furthermore, Modarres-Sadeghi and Païdoussis [13] studied the possible postdivergence flutter instabilities of this complete nonlinear supported pipe's model with Houbolt's finite difference method [14] and AUTO Software package. Xu et al. [15] proposed the analytical expression of natural frequencies of fluid-conveying pipes with the help of homotopy perturbation method. Those calculated frequencies were in good agreement with experiment results.

Considering the effect of the internal and external fluids, the three-dimensional nonlinear differential equations of a fluid-conveying pipe undergoing overall motions were derived based on Kane's equation and the Ritz method [16]. Moreover, the time histories for the displacements were obtained using the incremental harmonic balance method. Based on Timoshenko beam model, Shen et al. [17] studied the band gap properties of the flexural vibration for periodic pipe system conveying fluid using the transfer matrix method. These methods have proved to be effective in analyzing flow-induced vibration of certain pipes.

It is well known that analysis of pipe dynamics could be conducted based on the energy-based approach according to Hamiltonian principle [18, 19]. However, these approximation methods mentioned above are not ideal for Hamiltonian systems [20], because they are not structurally stable, which means that the Hamiltonian system will become dissipative.

Recently, many numerical algorithms, which can inherit the symplectic structure of Hamiltonian system, have been studied. Especially, Zhong and Williams [21] have proposed the precise integration method, which can give the highly precise numerical integration result and approach the full computer precision for these homogeneous equations. Moreover, this approach has been applied to solving complicated inhomogeneous problems with nonlinear time-variant item, for example, Floquet transition matrix, control problems, and so on [22–25].

In this paper, a Hamiltonian model of nonlinear flow-induced dynamics of supported pipes is analyzed numerically using precise integration method. Firstly, nonlinear equations of supported pipes conveying harmonically fluctuating fluid are deduced to two-order ordinary differential equations using the Galerkin's method. Then the equations are transformed into symplectic canonical equations composed of displacement and momentum. Moreover, PIM with linear interpolation formula is proposed. Finally, several numerical

examples of pinned-pinned pipe conveying pulsating fluid are used to testify the precision of this approach. The results are compared with those using traditional Runge-Kutta method. The influence of different fluid parameters on nonlinear behaviors of supported pipes is also discussed.

2. Formulation of Problem in Hamiltonian System

In this section, typical governing equations of supported pipe conveying fluid are deduced in Hamiltonian system.

2.1. Equation of Motion

We consider a straight supported pipe conveying the harmonically pulsating flow (Figure 1). It is assumed that the motion is planar, and the pipe is nominally horizontal. The cross-sectional area of the flow is assumed constant. The effects of gravity and external tension are ignored. Moreover, the pipe behaves like an Euler-Bernoulli beam in transverse vibration and the fluid is assumed to be incompressible.

The transverse motion equation of the pipe is given by Païdoussis and Issid [26],

$$\frac{\partial^2 M}{\partial x^2} + m_1(L-x)\frac{\partial u}{\partial t}\frac{\partial^2 y}{\partial x^2} + \left(m_1 u^2 + pA\right)\frac{\partial^2 y}{\partial x^2} + 2m_1 u\frac{\partial^2 y}{\partial x \partial t} + (m_1+m_2)\frac{\partial^2 y}{\partial t^2} = 0, \tag{2.1}$$

where x is the longitudinal coordinate, y the transverse deflection, M the moment of flexure of the pipe, L the pipe length, m_1 the mass of the fluid conveyed per unit length, m_2 pipe mass per unit length, u the fluid velocity, p the fluid pressure, and A the cross-sectional area of the flow.

Then the viscoelastic Kelvin-Voigt damping model is introduced,

$$M = \left(E + \eta\frac{\partial}{\partial t}\right) I y'', \tag{2.2}$$

where EI is the flexural stiffness of the pipe material, and η is the coefficient of Kelvin-Voigt viscoelastic damping.

Moreover, the velocity $u(t)$ of pulsating fluid is assumed to be harmonically fluctuating, and has the following form:

$$\begin{aligned} u(t) &= u_0\left(1 + \mu\cos\overline{\omega}t\right), \\ u^2(t) &\approx u_0^2\left(1 + 2\mu\cos\overline{\omega}t\right), \end{aligned} \tag{2.3}$$

where u_0 is the mean flow velocity, μ the amplitude of the harmonic fluctuation (assumed small), and $\overline{\omega}$ the fluid pulsating frequency. This fluctuating flow velocity appears as parametric excitation term in the equation of motion and may lead to parametric instabilities.

Substituting (2.2) and (2.3) into (2.1) yields that

$$\left(E+\eta\frac{\partial}{\partial t}\right)I\frac{\partial^4 y}{\partial x^4}+\left[-m_1u_0(L-x)\mu\overline{\omega}\sin\overline{\omega}t+m_1u_0^2(1+2\mu\cos\overline{\omega}t)+pA\right]\frac{\partial^2 y}{\partial x^2}$$
$$+2m_1u_0(1+\mu\cos\overline{\omega}t)\frac{\partial^2 y}{\partial x\partial t}+(m_1+m_2)\frac{\partial^2 y}{\partial t^2}=0. \tag{2.4}$$

Incorporate the following dimensionless quantities:

$$\xi=\frac{x}{L},\qquad W=\frac{y}{L},\qquad \tau=\frac{t}{L^2}\left(\frac{EI}{m_1+m_2}\right)^{0.5},\qquad v=u_0L\left(\frac{m_1}{EI}\right)^{0.5},\qquad T=pA\frac{L^2}{EI},$$
$$\beta=\frac{m_1}{m_1+m_2},\qquad H=\frac{\eta}{L^2}\left(\frac{I}{E(m_1+m_2)}\right)^{0.5},\qquad \omega=\overline{\omega}L^2\left(\frac{m_1+m_2}{EI}\right)^{0.5}. \tag{2.5}$$

Then the equation of motion can be nondimensionalized as

$$H\frac{\partial^5 W}{\partial\xi^4\partial\tau}+\frac{\partial^4 W}{\partial\xi^4}+\left[v^2(1+\mu\cos\omega\tau)^2-v\beta^{0.5}(1-\xi)\mu\omega\sin\omega t+T\right]\frac{\partial^2 W}{\partial\xi^2}$$
$$+2v\beta^{0.5}(1+\mu\cos\omega\tau)\frac{\partial^2 W}{\partial\xi\partial\tau}+\frac{\partial^2 W}{\partial\tau^2}=0. \tag{2.6}$$

The motion equation above is inhomogeneous, as the derivative coefficients of W are explicit functions of ξ and τ.

Then we discretize (2.6) using the Galerkin's method. Let

$$W(\xi,\tau)=\sum_{r=1}^{n}\phi_r(\xi)q_r(\tau), \tag{2.7}$$

where $q_i(\tau)$ $(i=1,2,\ldots,n)$ are generalized coordinates of the discretized pipe and $\phi_i(\xi)$ are eigenfunctions of the beam with the same boundary conditions.

It has been pointed out that instability boundaries for supported pipes could be determined with adequate precision using the two-mode expansion [2]. So the two-mode expansion of (2.7) is used in the analytical model for simplicity to investigate qualitative behaviors of supported pipes conveying fluid.

Substitute (2.7) with $n=2$ into (2.6). Then according to the orthogonal property of modal modes, the partial differential equation could be transformed into the second-order

ordinary differential equation

$$\begin{aligned}\ddot{q} + \left(H\Lambda + 2\beta^{0.5}vB\right)\dot{q} + \left[\Lambda + \left(v^2 + T\right)C\right]q \\ = -\left(2\beta^{0.5}v\mu\cos\omega\tau B\right)\dot{q} - \left[v^2 2\mu\cos\omega\tau\right)C + \beta^{0.5}v\mu\sin\omega\tau(D - C)\Big]q,\end{aligned} \tag{2.8}$$

$$\ddot{q} + G\dot{q} + Kq = f_1(\tau)\dot{q} + f_2(\tau)q, \tag{2.9}$$

where

$$\begin{gathered}G = H\Lambda + 2\beta^{0.5}vB, \qquad K = \Lambda + \left(v^2 + T\right)C, \\ f_1(\tau) = -2\beta^{0.5}v\mu\cos\omega\tau B, \\ f_2(\tau) = -2v^2\mu\cos\omega\tau C - \beta^{0.5}v\mu\omega\sin\omega\tau(D - C).\end{gathered} \tag{2.10}$$

In (2.9), G and K denote the structural damping matrix and stiffness matrix, respectively. These two matrices are associated with systematic parameters, such as dimensionless flow velocity v and mass ratio β. λ_i $(i = 1, 2)$ are the ith eigenvalues of the supported pipe and Λ is the diagonal matrix with elements λ_i^4.

Moreover, B, C, and D are matrices with elements b_{sr}, c_{sr}, and d_{sr} $(s, r = 1, 2)$, respectively. They are defined as

$$b_{sr} = \int_0^1 \phi_s\phi_r \mathrm{d}\xi, \qquad c_{sr} = \int_0^1 \phi_s\phi_r'' \mathrm{d}\xi, \qquad d_{sr} = \int_0^1 \phi_s\xi\phi\eta_r'' \mathrm{d}\xi. \tag{2.11}$$

Different value should be taken for those three parameters depending on different boundary conditions of the pipe. For the pinned-pinned pipe, we have

$$\begin{aligned}b_{sr} &= \begin{cases}\dfrac{2\lambda_r\lambda_s}{\lambda_r^2 - \lambda_s^2}\left\{(-1)^{r+s} - 1\right\} & s \neq r, \\ 0 & s = r,\end{cases} \\ c_{sr} &= \begin{cases}0 & s \neq r, \\ -\lambda_r^2 & s = r,\end{cases} \\ d_{sr} &= \begin{cases}\dfrac{4\lambda_r^3\lambda_s}{\left(\lambda_r^2 - \lambda_s^2\right)^2}\left\{1 - (-1)^{r+s}\right\} & s \neq r, \\ \dfrac{1}{2}c_{rr} & s = r.\end{cases}\end{aligned} \tag{2.12}$$

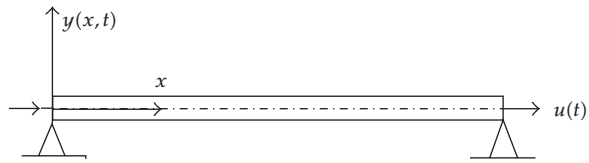

Figure 1: The simply supported pipe conveying fluid.

2.2. Symplectic Canonical Equation

According to Hamiltonian principle, the nonlinear equation of supported pipe conveying pulsating fluid can be transformed into symplectic canonical equation with state variable vectors composed of displacement Q and corresponding momentum P,

$$\dot{V} = HV + F, \tag{2.13}$$

where

$$\begin{aligned} V &= \{Q \;\; P\}^T, \\ Q &= \{q_1 \;\; q_2\}^T, \qquad P = \{p_1 \;\; p_2\}^T = \dot{Q} + \frac{GQ}{2}, \\ H &= \begin{bmatrix} -\dfrac{G}{2} & I \\ -K - \dfrac{G^T G}{4} & \left(\dfrac{G}{2}\right)^T \end{bmatrix}, \\ F &= \{0 \;\; 0 \;\; f_1 P + (f_2 - f_1 G)Q\}^T. \end{aligned} \tag{2.14}$$

So, we can see that H is a 4×4 Hamiltonian symplectic matrix and F is a time-variant matrix related to state variable vectors.

3. Precise Integration Method with Linear Interpolation Approximation

In this section, the principle of precise integration method is briefly introduced. For a more detailed explanation, it is suggested that [21, 22] are consulted.

The precise integration method for homogeneous equations with initial value is fundamental, so it is described in the next subsection firstly.

3.1. Integration of Homogeneous Equation

The general solution of homogeneous equation $\dot{V} = HV$ $(V_0 = V(0))$ can be expressed as

$$V(t) = e^{Ht} \cdot V_0. \tag{3.1}$$

Suppose that the time step is $\tau = t_{k+1} - t_k$, and then we have the following recursive steps:

$$V_1 = TV_0, \qquad V_2 = TV_1, \ldots, V_{k+1} = TV_k, \tag{3.2}$$

where $T = e^{H\tau}$. It is seen that how to compute the exponential matrix T is essential for the integration precision.

Then split the time interval τ into a smaller one. Define $\Delta t = \tau/m$ and $m = 2^N$. For example, $m = 1048576$ when $N = 20$. As τ is small, Δt is an extremely small time interval.

Assume that $T_a = (H\Delta t)(I + H\Delta t)/2$, execute the cycle

$$\text{For } (i = 0;\ i < N;\ i++) \quad \{T_a = 2T_a + T_a \times T_a\}, \tag{3.3}$$

where I is the identity matrix.

So T_a is no longer a very small matrix. It could be computed by the following function:

$$T = I + T_a. \tag{3.4}$$

The algorithm given above is called precise integration method. It has no serious numerical round-off error and could approach full computer precision [20].

3.2. Integration of Inhomogeneous Equation

In this subsection, PIM with linear interpolation formula would be proposed to solve inhomogeneous equations.

With the solution of homogeneous equation, (2.13) could been written as

$$\dot{V}(t) = HV(t) + F(V,t). \tag{3.5}$$

Then its solution could be given by the Duhamel's integration as

$$V(t) = e^{Ht}V_0 + \int_0^t e^{H(t-\tau)}F(V,\tau)d\tau. \tag{3.6}$$

Similarly, the duration of structural dynamic response is also divided into small time intervals. The response between (t_k, t_{k+1}) can be written as

$$V(t_{k+1}) = TV_k + \int_{t_k}^{t_{k+1}} e^{H(t_k-\tau)}F(V,\tau)d\tau. \tag{3.7}$$

To solve this inhomogeneous equation, the analytical expression of the time-variant item $F(V,t)$ is required. But it is not always available.

In this study, the linear interpolation formula is used to approximate this nonlinear item.

Assume that

$$F_{k+1} = F_k + (t - t_k)\dot{F}_k, \tag{3.8}$$

where

$$F_k = F(V, t_k), \qquad \dot{F}_k = \left(\frac{\partial F}{\partial t} + \sum_n \frac{\partial F}{\partial V_i} \frac{\partial V_i}{\partial t} \right)_{t=t_k}. \tag{3.9}$$

Substituting (3.8) into (3.7) gives the linear interpolation expression

$$V(t_{k+1}) = T\left[V_k + H^{-1}\left(F_k + H^{-1}\dot{F}_k\right)\right] - H^{-1}\left[F_k + H^{-1}\dot{F}_k + \tau\dot{F}_k\right]. \tag{3.10}$$

Thus, we have the numerical expression of symplectic canonical equation using PIM with linear interpolation formula.

In the next section, this method would be used to investigate the motion of supported pipes conveying pulsating fluid under different conditions.

4. Numerical Examples

In this section, several numerical examples of pinned-pinned pipes are used to testify the effectiveness of precise integration method.

4.1. Dynamic Response of Pipes Conveying Stable Fluid

In this subsection, this approach is used to analyze the dynamic response of stable fluid-conveying pipes, especially for their computation stability after a long period. In this case, the pipe's dynamic function is a homogeneous equation. The results are compared with those using traditional forth-order Runge-Kutta method.

Consider that the dimensionless mean flow velocity v is 2.0, the mass ratio $\boldsymbol{\beta}$ is 0.32 and the fluid pressure $T = 1$. The initial conditions are chosen to be $[q_1 \;\; q_2 \;\; \dot{q}_1 \;\; \dot{q}_2]^T = [-0.1 \;\; 0.2 \;\; 0.1 \;\; 0.4]^T$. Time increases from 0 to 1000 s and the time step Δt is selected as 0.2 s.

Figure 2 illustrates time history of four state variables ($q_1 \;\; q_2 \;\; p_1 \; p_2$) of pipe's middle point using the Runge-Kutta method, while Figure 3 shows the results calculated by precise integration method.

It can be found that there are evident differences for four state variables' amplitudes using two methods. The amplitudes in Figure 2 decrease gradually with time. When the simulation time is long enough, state variables may converge to zero. However, those in Figure 3 still keep constant with time, which are almost unaffected by the time step.

So we can conclude that there is the energy dissipation using traditional Runge-Kutta method, which cannot get the accurate numerical results. However, precise integration method is an energy conservative method and could maintain the stability of the numerical simulation in the long period of time.

Table 1: Computation time needed using two methods.

Method	$\Delta t = 0.2$ s	$\Delta t = 0.5$ s
Runge-Kutta Method	90 s	80 s
Precise Integration Method	5 s	4 s

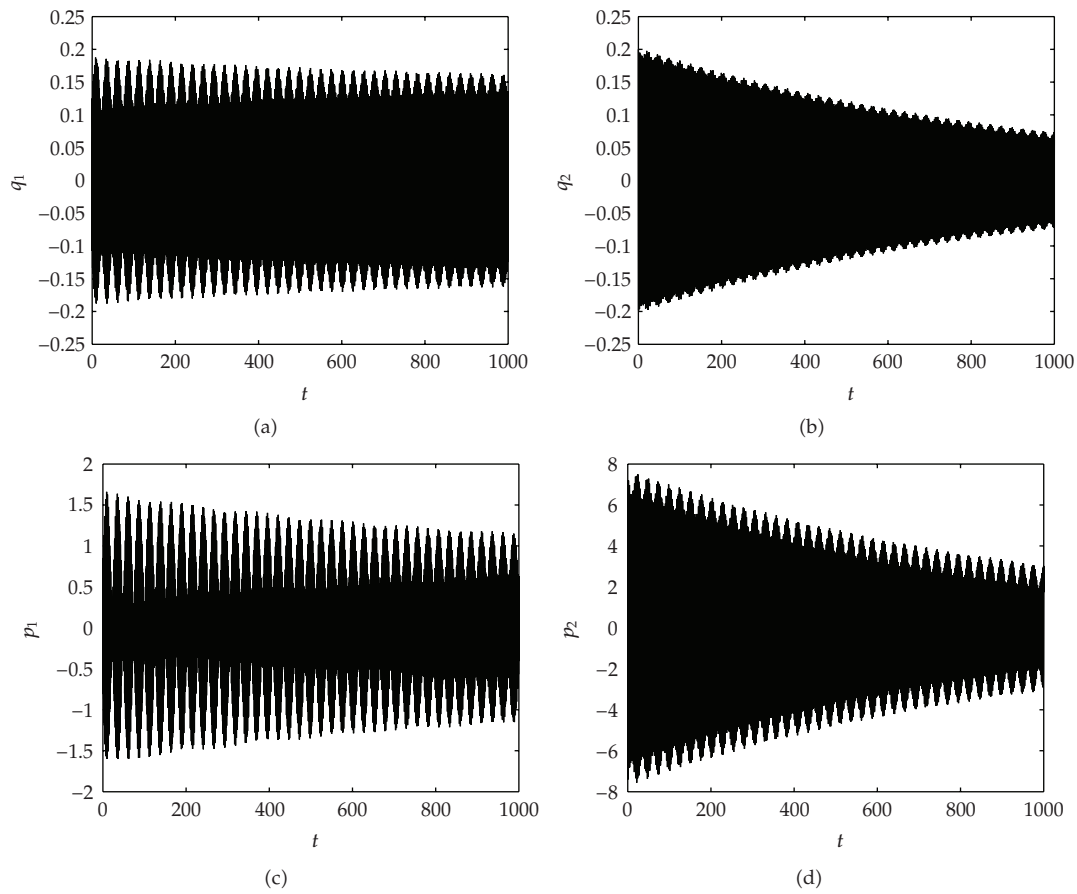

Figure 2: Time history of four state variables using Runge-Kutta method.

Table 1 lists the computation time needed for two methods, as two different time intervals are selected. It can be noted that precise integration method needs much less computing time than Runge-Kutta method.

4.2. Dynamic Response of Pipes Conveying Pulsating Fluid

In this subsection, PIM with linear approximation is used to analyze the dynamic response of supported pipes conveying harmonically pulsating fluid. Similarly, the results are compared with those using forth-order Runge-Kutta method.

Consider the dimensionless mean flow velocity v is 1, the amplitude $\mu = 0.4$, the frequency $\omega = 2.5$, the mass ratio $\boldsymbol{\beta} = 0.32$, and the fluid pressure $T = 1$. The initial conditions

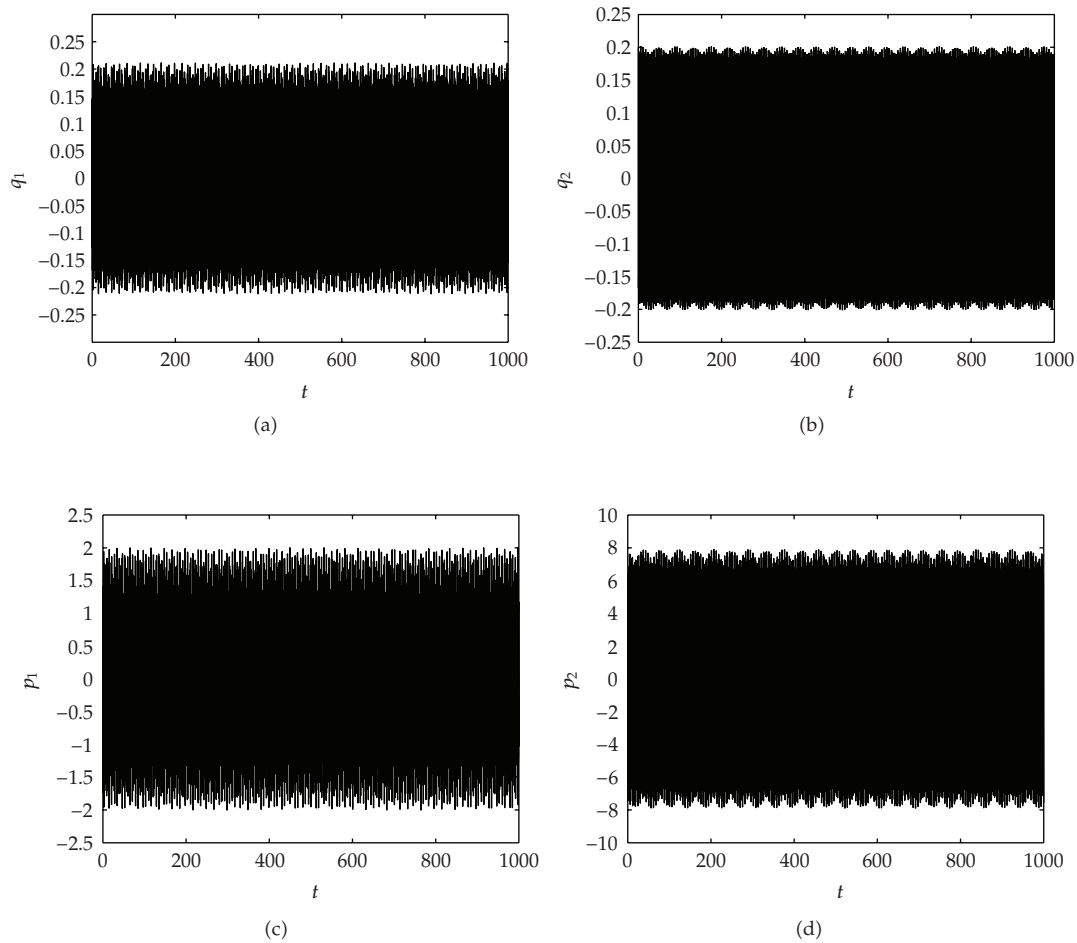

Figure 3: Time history of four state variables using precise integration method.

are chosen to be $[q_1 \;\; q_2 \;\; \dot{q}_1 \;\; \dot{q}_2]^T = [-0.001 \;\; 0.001 \;\; 0 \;\; 0]^T$. Time increases from 0 to 100 s, and two time steps involved in this example are selected as $\Delta t = 0.01$ s and 0.05 s, respectively. By the way, the relative stable dynamic response after 20 s is considered.

Figure 4 illustrates time history of displacement response and phase planes of pipe's middle point using the forth-order Runge-Kutta method, while Figure 5 shows the results calculated by PIM, when the time step is 0.01 s. Figures 6 and 7 show the results with time step 0.05 s using two methods, respectively.

These figures show that phrase planes of two modes would shrink gradually with time and converge to a point if time is long enough. The precise integration method shows nearly the same precision during calculating the dynamic response of supported pipes conveying pulsating fluid.

Furthermore, Table 2 lists the computation time needed for two methods. Similarly, PIM with linear interpolation formula need much less computing time than Runge-Kutta method. This approach is very quick to obtain dynamic response because of running a number of cycles during the computation, which is shown in (3.3). So it is suitable for long-term dynamic analysis of fluid-conveyed pipes.

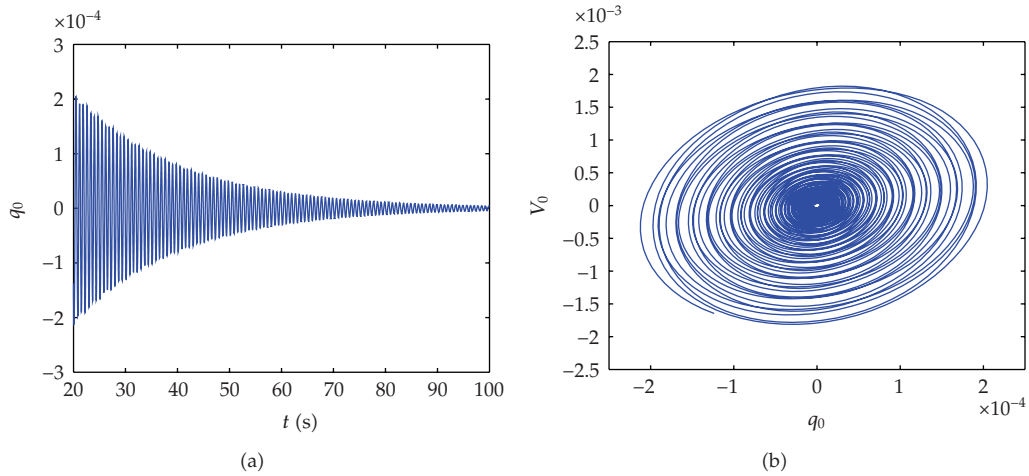

Figure 4: Displacement response and phase diagram of pipe's middle point using Runge-Kutta ($\Delta t = 0.01$).

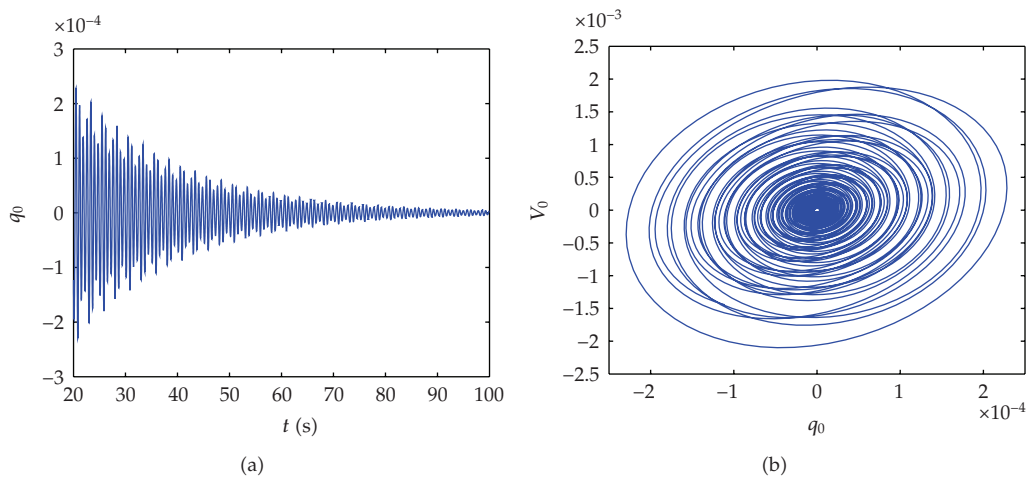

Figure 5: Displacement response and phase diagram of pipe's middle point using PIM ($\Delta t = 0.01$).

Table 2: Computation time needed using two methods.

Method	$\Delta t = 0.01$	$\Delta t = 0.05$
Runge-Kutta Method	16 s	12 s
Precise Integration Method	2 s	0.9 s

4.3. Stability Analysis of Pipes under Different Fluid Velocities and Frequencies

In this subsection, the influence of different fluid parameters on nonlinear behaviors of pinned-pinned pipes is discussed using PIM with linear interpolation formula.

The dimensionless fluid frequency ω increases from 0 to 70, and three fluid velocities in this example are selected as $v = 1.0$, 1.5, and 2.0. The fluid frequency step and the time step

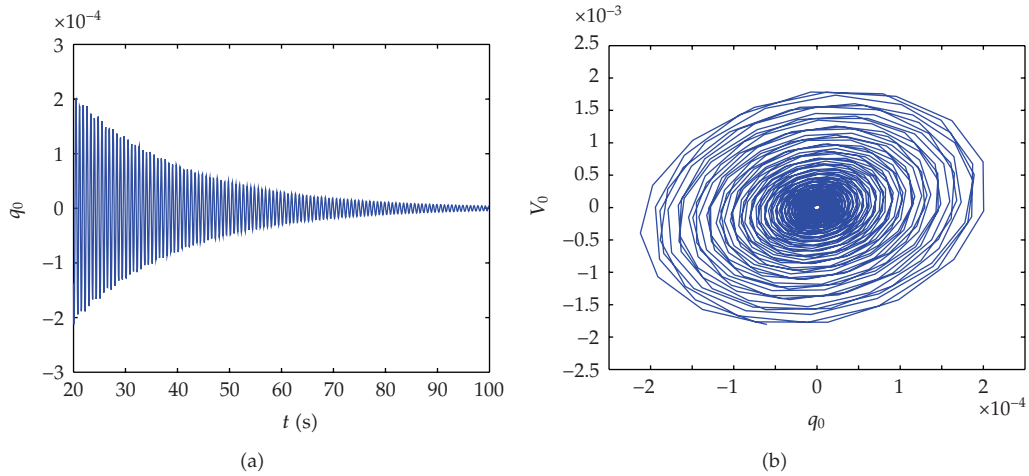

Figure 6: Displacement response and phase diagram of pipe's middle point using Runge-Kutta ($\Delta t = 0.05$).

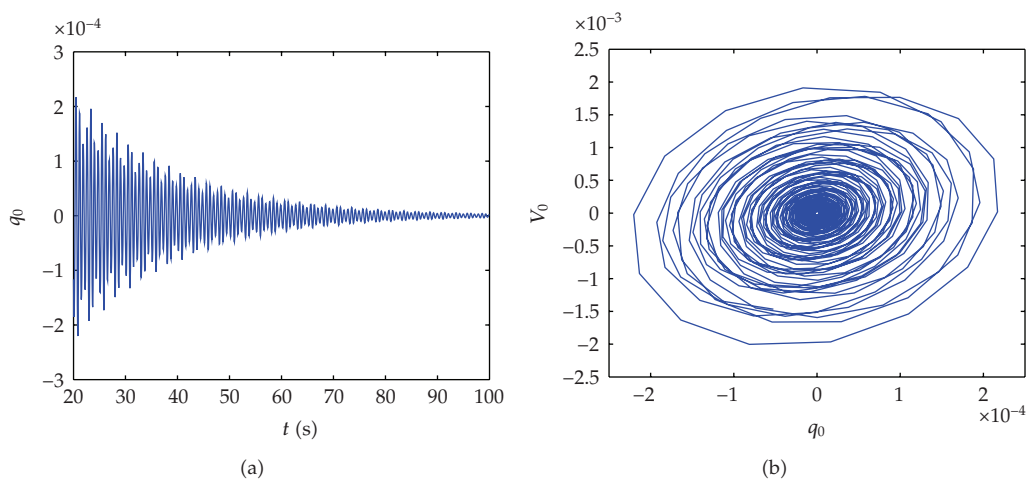

Figure 7: Displacement response and phase diagram of pipe's middle point using PIM ($\Delta t = 0.05$).

are selected as $\Delta\omega = 0.4$ and $\Delta t = 0.01$ s, respectively. Others parameters are the same with the preceding Section 4.2.

The displacement response q_0 of the pipe's middle point under different fluid parameters is calculated. Figure 8 shows the displacement responses of the middle point versus the pulsating fluid frequency. It can be seen that the pipe keeps stable at most frequencies domain. For example, as $\omega = 5$, the pipe behaves stable on the limit loop condition, which is shown as Figure 9(a). However, when the frequencies lie between $(16, 18)$ and $(46, 49)$, the pipes are unstable. For example, the pipe will be divergent as Figure 9(b) shows when $\omega = 17$. So, it is very dangerous for pipes' operating safety.

Figures 10 and 11 show the displacement response variations of the middle point versus the pulsating fluid frequency as $v = 1.5$ and 2.0, respectively. It can be shown that the instable zone is changing with fluid frequencies. As $v = 1.5$, the instable zones are at

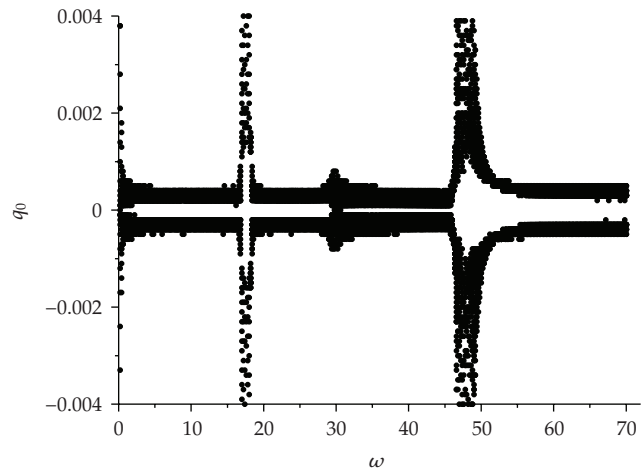

Figure 8: Displacement response of pipe's middle point as the function of the dimensionless pulsating fluid frequency ($v = 1.0$).

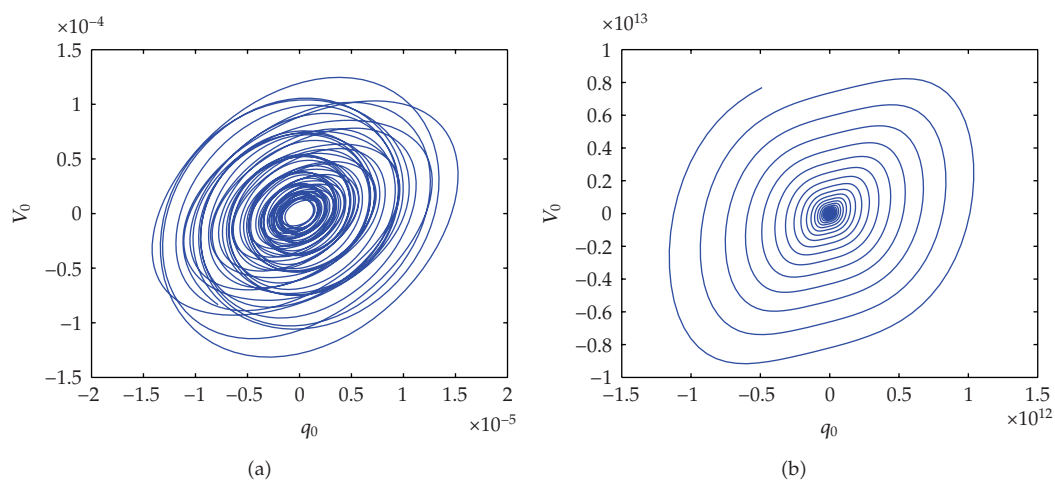

Figure 9: Phase diagram of pipe's middle point as $v = 1.0$. (a) $\omega = 5$; (b) $\omega = 17$.

$(14, 18)$, $(44, 51)$, and $(68, 70)$. As $v = 2.0$, the instable zones lie at $(6, 7)$, $(11, 16)$, $(42, 50)$, and $(65, 70)$.

It can be seen that with the increasing of fluid velocity, the critical fluid frequency gets smaller and the pipe shows complicated nonlinear vibration.

5. Conclusion

In this study, PIM with linear interpolation formula is presented to analyze nonlinear dynamics of Hamiltonian model of supported straight pipe conveying pulsating fluid. Several numerical examples are used to testify the effectiveness of this approach. The results show this approach could keep stable even for long period of time, and is much more rapid

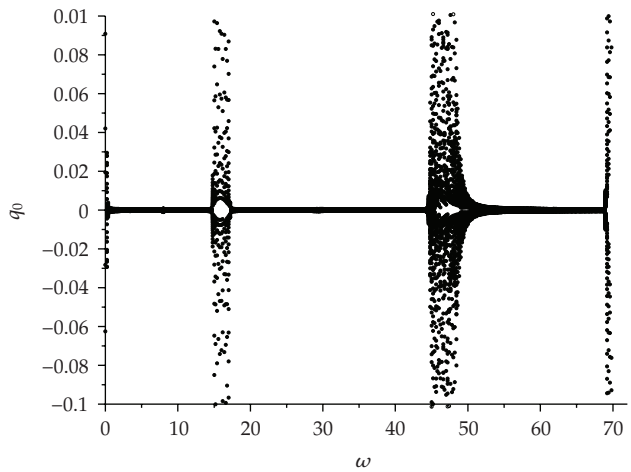

Figure 10: Displacement response of pipe's middle point as the function of the dimensionless pulsating fluid frequency (v = 1.5).

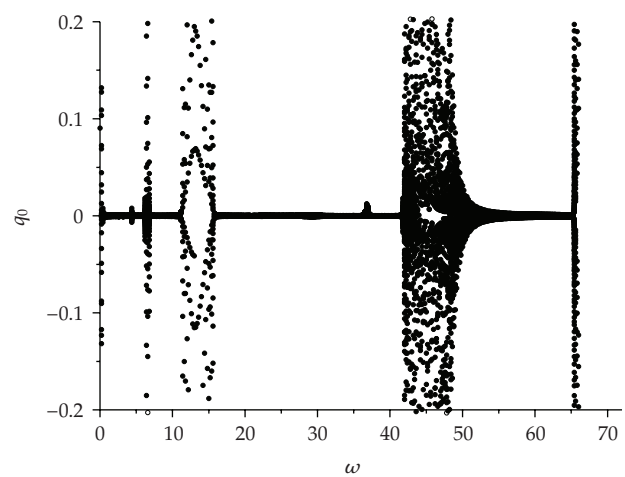

Figure 11: Displacement response of pipe's middle point as the function of the dimensionless pulsating fluid frequency (v = 2.0).

than traditional Runge-Kutta method. Moreover, the pipe's nonlinear behaviors under the condition of different fluid parameters are discussed.

The work presented here provides an alternative approach for investigating the nonlinear dynamic response of the pipes conveying fluid. However, it should be pointed out that linear interpolation formula is a rough approximation method, and more accurate methods should be studied to analyze nonlinear flow-induced dynamics in Hamiltonian system.

References

[1] S. S. Chen, "Dynamic stability of tube conveying fluid," *Journal of Engineering Mechanical Division*, vol. 97, pp. 1469–1485, 1971.

[2] M. P. Paidoussis, *Fluid-Structure Interactions: Slender Structures and Axial Flow V1*, Academic Press, Amsterdam, The Netherlands, 1998.

[3] M. P. Paidoussis, *Fluid-Structure Interactions: Slender Structures and Axial Flow V2*, Academic Press, Amsterdam, The Netherlands, 2004.

[4] M. Nikolić and M. Rajković, "Bifurcations in nonlinear models of fluid-conveying pipes supported at both ends," *Journal of Fluids and Structures*, vol. 22, no. 2, pp. 173–195, 2006.

[5] C. N. Folley and A. K. Bajaj, "Spatial nonlinear dynamics near principal parametric resonance for a fluid-conveying cantilever pipe," *Journal of Fluids and Structures*, vol. 21, no. 5-7, pp. 459–484, 2005.

[6] J. S. Jensen, "Fluid transport due to nonlinear fluid-structure interaction," *Journal of Fluids and Structures*, vol. 11, no. 3, pp. 327–344, 1997.

[7] X. Yang, T. Yang, and J. Jin, "Dynamic stability of a beam-model viscoelastic pipe for conveying pulsative fluid," *Acta Mechanica Solida Sinica*, vol. 20, no. 4, pp. 350–356, 2007.

[8] L. Wang, Q. Ni, and Y.-Y. Huang, "Hopf bifurcation of a nonlinear restrained curved fluid conveying pipe by differential quadrature method," *Acta Mechanica Solida Sinica*, vol. 16, no. 4, pp. 345–352, 2003.

[9] W. B. Jeong, Y. S. Seo, S. H. Jeong, S. H. Lee, and W. S. Yoo, "Stability analysis of a pipe conveying periodically pulsating fluid using finite element method," *Mechanical Systems Machine Elements and Manufacturing*, vol. 49, no. 4, pp. 1116–1122, 2007.

[10] M. Stangl, J. Gerstmayr, and H. Irschik, "An alternative approach for the analysis of nonlinear vibrations of pipes conveying fluid," *Journal of Sound and Vibration*, vol. 310, no. 3, pp. 493–511, 2008.

[11] L. Wang, "A further study on the non-linear dynamics of simply supported pipes conveying pulsating fluid," *International Journal of Non-Linear Mechanics*, vol. 44, no. 1, pp. 115–121, 2009.

[12] M. Nikolić and M. Rajković, "Bifurcations in nonlinear models of fluid-conveying pipes supported at both ends," *Journal of Fluids and Structures*, vol. 22, no. 2, pp. 173–195, 2006.

[13] Y. Modarres-Sadeghi and M. P. Païdoussis, "Nonlinear dynamics of extensible fluid-conveying pipes, supported at both ends," *Journal of Fluids and Structures*, vol. 25, no. 3, pp. 535–543, 2009.

[14] C. Semler, W. C. Gentleman, and M. P. Païdoussis, "Numerical solutions of second order implicit non-linear ordinary differential equations," *Journal of Sound and Vibration*, vol. 195, no. 4, pp. 553–574, 1996.

[15] M.-R. Xu, S.-P. Xu, and H.-Y. Guo, "Determination of natural frequencies of fluid-conveying pipes using homotopy perturbation method," *Computers and Mathematics with Applications*, vol. 60, pp. 520–527, 2010.

[16] D. Meng, H. Y. Guo, and S. P. Xu, "Nonlinear dynamic model of a fluid-conveying pipe undergoing overall motions," *Applied Mathematical Modelling*, vol. 35, no. 2, pp. 781–796, 2011.

[17] H.-J. Shen, J.-H. Wen, D.-L. Yu, and X.-S. Wen, "Flexural vibration property of periodic pipe system conveying fluid based on Timoshenko beam equation," *Acta Physica Sinica*, vol. 58, no. 12, pp. 8357–8363, 2009.

[18] M. Stangl, N. A. Beliaev, and A. K. Belyaev, "Applying Lagrange equations and Hamilton's principle to vibrations of fluid conveying pipes," in *Proceedings of the 33th Summer School on Advanced Problems in Mechanics (APM '05)*, pp. 269–275, St. Petersburg, Russia, 2005.

[19] M. Stangl and H. Irschik, "Dynamics of an Euler elastic pipe with internal flow of fluid," *Proceedings of Applied Mathematics and Mechanics*, vol. 6, pp. 335–336, 2006.

[20] K. Feng and M. Z. Qin, "Hamiltonian algorithms for Hamiltonian dynamical systems," *Progress in Natural Science*, vol. 1, no. 2, pp. 105–116, 1991.

[21] W. X. Zhong and F. W. Williams, "A precise time step integration method," *Journal of Mechanical Engineering Science*, vol. 208, no. 6, pp. 427–430, 1994.

[22] W. X. Zhong, "On precise integration method," *Journal of Computational and Applied Mathematics*, vol. 163, no. 1, pp. 59–78, 2004.

[23] J. Lin, W. Shen, and F. W. Williams, "A high precision direct integration scheme for structures subjected to transient dynamic loading," *Computers and Structures*, vol. 56, no. 1, pp. 113–120, 1995.

[24] G. Zhou, Y. X. Wang et al., "A homogenized high precise direct integration based on Taylor serials," *Journal of Shanghai Jiaotong University*, vol. 35, no. 12, pp. 1916–1919, 2001.

[25] T. C. Fung, "Construction of higher-order accurate time-step integration algorithms by equal-order polynomial projection," *Journal of Vibration and Control*, vol. 11, no. 1, pp. 19–49, 2005.

[26] M. P. Païdoussis and N. T. Issid, "Dynamic stability of pipes conveying fluid," *Journal of Sound and Vibration*, vol. 33, no. 3, pp. 267–294, 1974.

Hindawi Publishing Corporation
Mathematical Problems in Engineering
Volume 2010, Article ID 587317, 20 pages
doi:10.1155/2010/587317

Research Article

Seismic Response of Power Transmission Tower-Line System Subjected to Spatially Varying Ground Motions

Li Tian,[1,2] Hongnan Li,[2] and Guohuan Liu[2]

[1] *Faculty of Infrastructure Engineering, Dalian University of Technology, No.2 Linggong Road, Ganjingzi District, Dalian, Liaoning 116024, China*
[2] *State Key Laboratory of Coastal and Offshore Engineering, Dalian University of Technology, Dalian 116024, China*

Correspondence should be addressed to Li Tian, tianli1225@yahoo.com.cn

Received 10 March 2010; Revised 18 May 2010; Accepted 21 June 2010

Academic Editor: Carlo Cattani

The behavior of power transmission tower-line system subjected to spatially varying base excitations is studied in this paper. The transmission towers are modeled by beam elements while the transmission lines are modeled by cable elements that account for the nonlinear geometry of the cables. The real multistation data from SMART-1 are used to analyze the system response subjected to spatially varying ground motions. The seismic input waves for vertical and horizontal ground motions are also generated based on the Code for Design of Seismic of Electrical Installations. Both the incoherency of seismic waves and wave travel effects are accounted for. The nonlinear time history analytical method is used in the analysis. The effects of boundary conditions, ground motion spatial variations, the incident angle of the seismic wave, coherency loss, and wave travel on the system are investigated. The results show that the uniform ground motion at all supports of system does not provide the most critical case for the response calculations.

1. Introduction

In China, the west-to-east power transmission project will play an important role in changing the uneven distribution of our country's energy resources. Transmission projects extend thousands of kilometers and cost billions of dollars to construct and maintain, and most of them will cross high-intensity earthquake zones. However, most of research attentions on it have been paid on the actions of static load, impulsive load, equivalent static wind load and so forth. There are no code provisions for earthquake design of transmission tower-line system. It is unrealistic to assume that the transmission towers and lines are safe to go through

(a) (b) (c)

Figure 1: Transmission tower-line system of Sichuan electric network damaged by the Wenchuan earthquake.

earthquakes without adequate analysis. There are several recent cases of damage to power lines during earthquakes. In the 1999 CHI-CHI earthquake, transmission towers and lines was damaged most severely, and a lot of lines were broken and some towers collapsed [1]. Sichuan electric network were damaged by the Wenchuan earthquake in China, and some pictures are shown in Figure 1. Therefore, earthquake forces may govern the design in high-intensity earthquake zones.

In the past one or two decades, researchers have done some earthquake dynamic analysis on the transmission tower-line system. Noteworthy contributions to the related study of transmission towers include some work that has developed effective approaches to deal with the actual problems. Li et al. [2–4] have completed a number of investigations on seismic problems of coupled system of long-span transmission towers. Ghobarah et al. [5] investigated the effect of multisupport excitations on the lateral responses of overhead power transmission lines. Transmission towers were modeled by space truss elements and the cables were modeled by straight two-node elements. In all these studies, longitudinal and transverse response under uniform excitation and lateral response under multiple-support excitations are obtained.

A major problem that arises in the analysis of the long span structures such as transmission tower-line system is the difference among the ground motion components affecting various support points of the structure. The system response using uniform support excitation is compared with the response using multiple support excitations which is a more realistic assumption. In this paper, spatially varying ground motions of real data from the dense digital arrays of strong motion seismographs in SMART-1 are selected. The seismic input waves for vertical and horizontal ground motions are also generated based on Code for Design of Seismic of Electrical Installations [6]. Both the incoherency of seismic waves and wave travel effects are accounted for. Three-dimensional finite tower-line system models are considered in studying the response of this system. The transmission towers are modeled by beam elements while the transmission line is modeled by cable elements that account for the nonlinear geometry of the cable. The primary differences between the present work and previous work include the following: (1) the effect of the boundary condition is studied by three towers and two-span line and three towers and four-span line; (2) the effects of spatially varying ground motions which are obtained from real data are considered in this study; (3) the effect of incident angle of the seismic wave is considered in this paper; (4) the effects of coherency loss and wave travel are also investigated, respectively, in this paper. It should

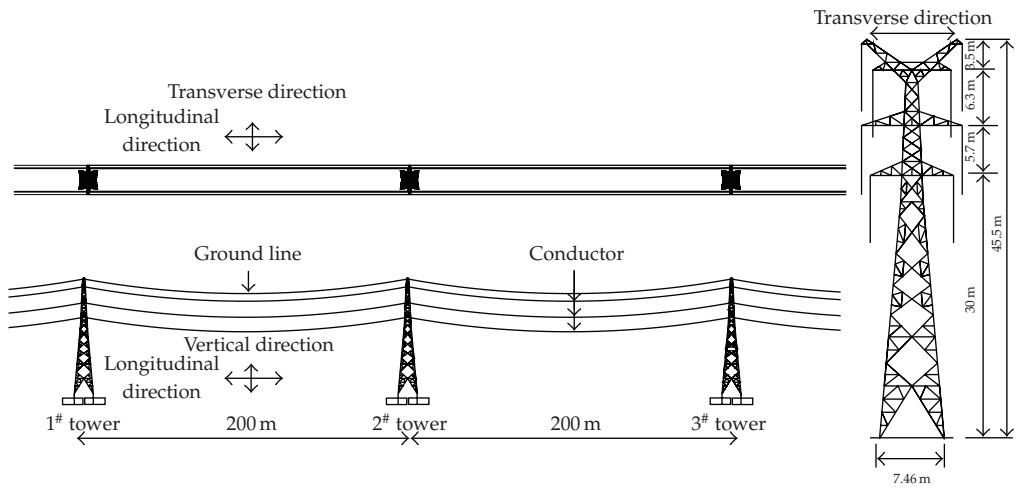

Figure 2: Finite element model of three towers and four-span lines coupled system.

be noted that geometric nonlinear responses are considered but material nonlinear is not included.

2. Power Transmission Tower-Line System Model and Geometric Stiffness Matrix of Cable Element

2.1. Power Transmission Tower-Line System Model

Three-dimension finite element tower-line system according to practical project is established. A finite-element computer program SAP2000 is selected to establish the model. As shown in Figure 2, the power transmission tower-line system includes three towers ($1^{\#}$, $2^{\#}$, and $3^{\#}$) and four-span line. The tower is 45.5 m high, and its weight is approximately 9.2 t. The structural members of the tower are made of angle steel with the elastic modulus of 206 GPa. The tower is modeled by 1369 space beam members and 107 nodes, and the connections of members are rigid. The transmission line is modeled by 200 two-node isoparametric cable elements with three translational DOFs at each node. The upper 8 cables are ground lines and lower 24 cables are single bundled conductor. The spans to adjacent towers are all 200 m. The base points of the transmission tower are fixed on the ground, and the connections between transmission towers and lines are hinged, and the side spans of the lines are hinged at the same height of middle tower.

The initial axial force and large deformation effect of cable are taken into consideration. Under self weight, the cable spatial configuration is a catenary. Based on the coordinate system illustrated in Figure 3, the mathematical expression used to define the initial geometry of the cable profile is given in the following form [7]:

$$z = \frac{H}{q}\left|\cosh(\alpha) - \cosh\left|\frac{2\beta x}{l} - \alpha\right|\right|, \tag{2.1}$$

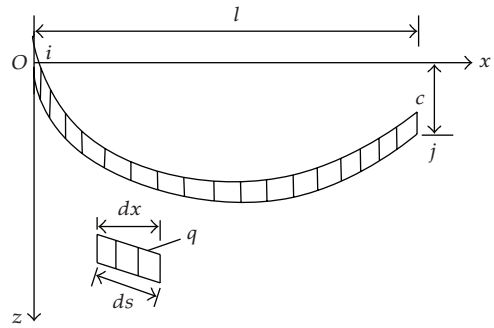

Figure 3: Coordinates of a single cable under self weight.

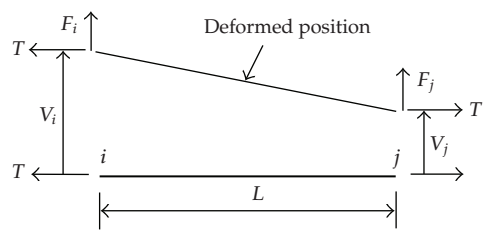

Figure 4: Force acting on a cable element.

where $\alpha = \sinh^{-1}|\beta(c/l)/\sin(\beta)| + \beta$, $\beta = ql/2H$, in which H represents initial horizontal tension which can be obtained from a preliminary static analysis, and q denotes uniformly distributed gravity loads along the transmission line.

2.2. Geometric Stiffness Matrix of Cable Element

The fundamental equation for geometric stiffness for a cable is very simple to drive. Consider the horizontal cable shown in Figure 4 of length L with an initial tension T. If the cable is subjected to lateral displacements, V_i and V_j, at both ends, as shown, then additional forces, F_i and F_j, must be developed for the cable element to be in equilibrium in its displaced position. Note that we have assumed that all forces and displacements are positive in the up direction. We have also made the assumption that the displacements are small and do not change the tension in the cable. The lateral forces can be expressed in terms of the lateral displacements by the following matrix equation [8]:

$$\begin{bmatrix} F_i \\ F_j \end{bmatrix} = \frac{T}{L}\begin{bmatrix} 1 & -1 \\ -1 & 1 \end{bmatrix}\begin{bmatrix} v_i \\ v_j \end{bmatrix} = k_g \begin{bmatrix} v_i \\ v_j \end{bmatrix}. \tag{2.2}$$

Note that the 2-by-2 geometric stiffness matrix, k_g, is not a function of the mechanical properties of the cable and is only a function of the element's length and the force in the element. The cables have geometric nonlinearity because large displacement of the cable changes its stiffness and its frequencies of free vibration [5]. Therefore, transmission lines should be treated as nonlinear structures.

3. Simulation of Spatially Varying Ground Motions

Spatially varying ground motions can be available directly from the seismometer arrays data if the distance between the supports of the structure under investigation is equal to that between the stations of the array considered [9]. Otherwise, when the properties of the ground motion have to be known at each point of the field, the simulation of the excitation, as a nonstationary random process, is needed [10].

3.1. SMART-1 Array, Taiwan

The SMART-1 array was the first large array of digital accelerometers specially designed to investigate the near-field properties of earthquake ground motion. It was located in the northeast corner of Taiwan near city of Lotung on the Lanyang plain. The array consists of 12 triaxial strong-motion accelerometers located in each of three concentric circular rings having radius of 200 m, 1000 m, and 2000 m and one triaxial accelerometer located at the center of the array. Figure 5 shows the location map of SMART-1, Taiwan [11].

This paper will use the data from the largest event recorded that had an epicenter within close proximity to the array, event 45, the earthquake of 14 November 1986 [12]. Its epicentral direction almost coincided with the diameter from I06 to I12, that is, close to the N-S direction. Here, only data from the inner ring are considered. Figure 6 shows the event 45 of SMART-1 array.

Results are presented in the following for the application of the proposed approach to data recorded at the centre station C00, two inner stations (I06 and I12). Figure 7 shows the displacement time-history of each station at a distance of 200 meters under earthquake event 45. The records include one vertical and two horizontal ground motions. The three stations are set in line, 200 meters apart from each other. Distinct differences can be found among the 3 records, in terms of the shape of the curve, the value of peak ground displacement, as well as the arrival time of the ground motion.

3.2. Simulation of Spatially Varying Ground Motions

The variation in seismic ground motion affecting different supports of a long-span structure is influenced by three main factors. The first factor is the wave travel effect that results from the finite speed of seismic waves. The second factor is the coherency effect that results from the reflection and refraction of seismic waves. The third factor is the site effect. The first two factors are accounted for in this simulation while the site specific effects are beyond the scope of this study.

To account for the variation in seismic ground motion, a seismological approach based on the seismic wave propagation from the epicenter to the supporting structure may be used. Alternatively, a stochastic approach based on random vibration analysis may be adopted. The ground motion cross-power spectral density function of spatial ground motions at point i and j on ground surface can be written as

$$S_{ij}(\omega) = S_g(\omega)\gamma_{ij}(\omega, d_{ij}), \tag{3.1}$$

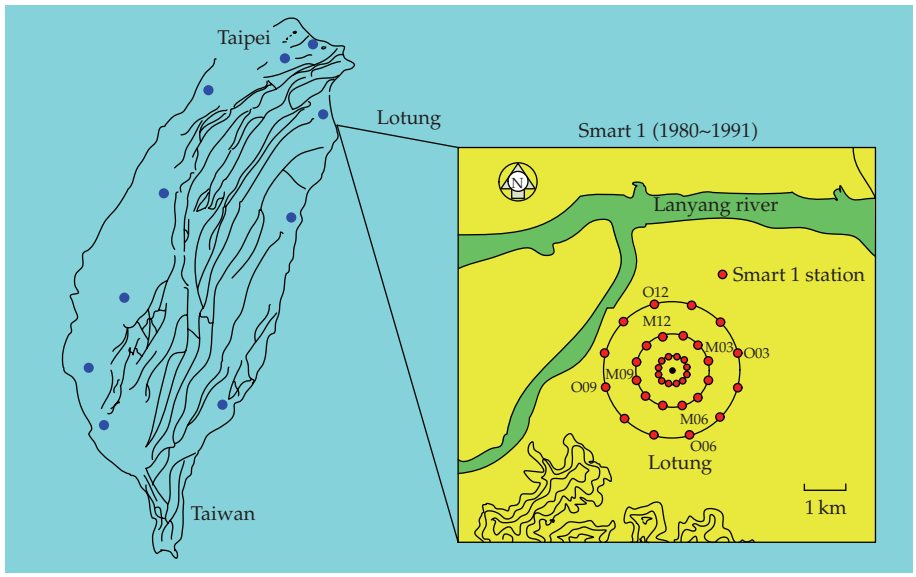

Figure 5: The location map of SMART-1, Taiwan.

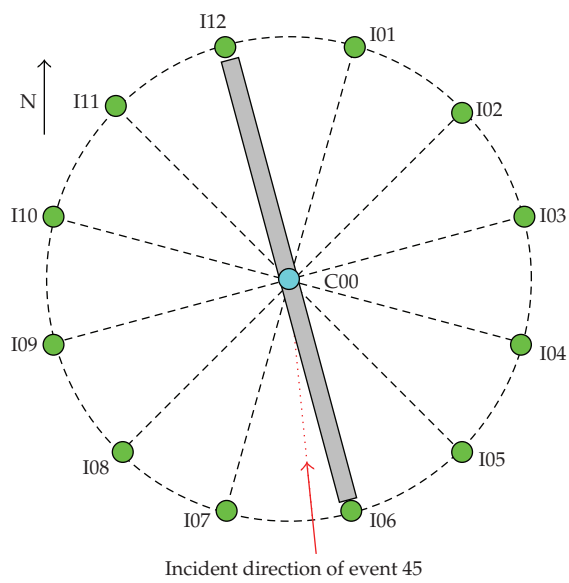

Figure 6: Event 45 of SMART-1, Taiwan.

where

$$S_g(\omega) = \frac{\omega_g^4 + 4\xi_g^2\omega_g^2\omega^2}{\left(\omega_g^2 - \omega^2\right)^2 + 4\xi_g^2\omega_g^2\omega^2} \cdot \frac{\omega^4}{\left(\omega_f^2 - \omega^2\right)^2 + 4\xi_f^2\omega_f^2\omega^2} S_0 \tag{3.2}$$

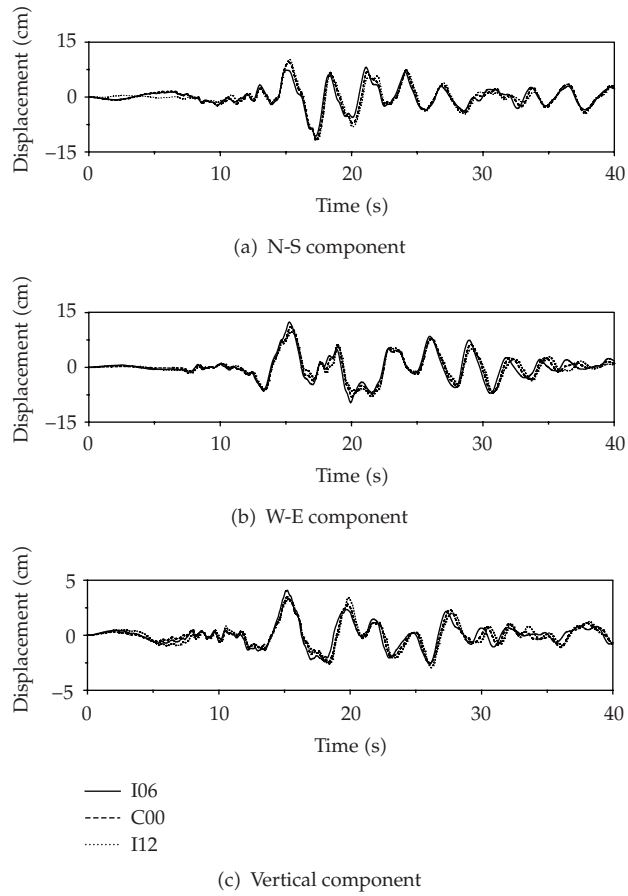

Figure 7: Displacement time-history of each station at a distance of 200 meters under event 45.

is a filtered Tajimi-Kanai power spectral density function [13], in which S_0 is a scale factor depending on the ground motion intensity, ω_g and ξ_g are the predominant frequency and damping ratio of the first filter, ω_f and ξ_f are those of the second filter, and

$$\gamma_{ij}(\omega, d_{ij}) = \left|\gamma_{ij}(\omega, d_{ij})\right| e^{-i\omega d_{ij}/v} \tag{3.3}$$

is an empirical coherency function. In the present paper, the coherency loss function at points i and j was derived from SMART-1 array data by Hao et al. [12] and is modeled in the following form:

$$\left|\gamma_{ij}(\omega, d_{ij})\right| = \exp-(\beta d_{ij}) \cdot \exp\left\{-a(\omega)\sqrt{d_{ij}}\left(\frac{\omega}{2\pi}\right)^2\right\} \tag{3.4}$$

in which d_{ij} is the projected distance in the wave propagation direction between points i and j on ground surface, β is a constant, and $\alpha(\omega)$ is a function with the following form:

$$a(\omega) = \begin{cases} \dfrac{2\pi a}{\omega} + \dfrac{b\omega}{2\pi} + c, & 0.314\,\text{rad/s} \le \omega \le 62.83\,\text{rad/s}, \\ 0.1a + 10b + c, & \omega \ge 62.83\,\text{rad/s}, \end{cases} \tag{3.5}$$

where the constants a, b, c, and β can be obtained by least-squares fitting the coherency function of recorded motions. Here, the apparent velocity $v = 800\,\text{m/s}$ is assumed [14]. The constants in coherency function are $a = 3.583 \times 10^{-3}$, $b = -1.811 \times 10^{-5}$, $c = 1.177 \times 10^{-4}$, and $\beta = 1.019 \times 10^{-4}$, which were obtained by processing recorded motions during event 45 at the SMART-1 array.

According to Penzien and Watabe's research [15], the three components of ground motions along a set of principal axes are uncorrelated. These components, directed along the principal axes, are usually such that the major principal axis is directed towards the expected epicenter, the moderate principal axis is directed perpendicular to it, and the minor principal axis is directed vertically. In this study, the three components of the ground motion are assumed to be directed along the principal axes.

In this study, the transmission tower-line system is assumed to locate in the Chinese Seismic Intensity Zone 8 with peak longitudinal ground acceleration 0.2 g and locate in the medium firm soil. The intensity of the transverse component and vertical component, as stated in the code, is 0.85 and 0.65 times of the longitudinal component. Figure 8 shows the corresponding 2% damped longitudinal, transverse, and vertical code response spectrums for medium firm soil condition defined in the Code for design of seismic of electrical installations.

The generated ground displacements considering both incoherency and wave travel effects are shown in Figure 9. It is seen from the figure that the three generated records, 200 m apart, are well correlated at $v = 800\,\text{m/s}$. The coherency loss between tower $1^{\#}$ and tower $2^{\#}$ is also calculated and compared to the model coherence loss function in Figure 10; it is seen from the figure that the simulated result is well. The response of a typical set of longitudinal, transverse, and vertical simulated ground motions and the corresponding response spectrum specified in the design code are shown in Figure 11. It can be seen from the figure that the simulated ground motions are compatible with the target response spectrum.

4. Analytical Method

Most of the commonly available computer programs for the seismic analysis of structures do not allow the introduction of multiple acceleration time histories. The use of the displacement time history of the ground motion instead of the acceleration time history may be appropriate for long-span structures [5]. The equations of motion for the structure due to the multiple support excitations are derived. The n-degree-of-freedom linear system subjected to m support motions can be written in the matrix form [13]:

$$\begin{bmatrix} \mathbf{M}_{aa} & \mathbf{M}_{ab} \\ \mathbf{M}_{ba} & \mathbf{M}_{bb} \end{bmatrix} \begin{Bmatrix} \ddot{x}_a \\ \ddot{x}_b \end{Bmatrix} + \begin{bmatrix} \mathbf{C}_{aa} & \mathbf{C}_{ab} \\ \mathbf{C}_{ba} & \mathbf{C}_{bb} \end{bmatrix} \begin{Bmatrix} \dot{x}_a \\ \dot{x}_b \end{Bmatrix} + \begin{bmatrix} \mathbf{K}_{aa} & \mathbf{K}_{ab} \\ \mathbf{K}_{ba} & \mathbf{K}_{bb} \end{bmatrix} \begin{Bmatrix} x_a \\ x_b \end{Bmatrix} = \begin{Bmatrix} 0 \\ \mathbf{P}_b(t) \end{Bmatrix}, \tag{4.1}$$

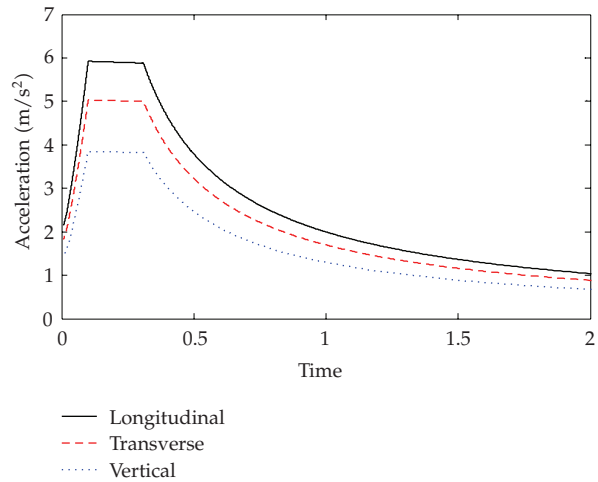

Figure 8: Code response spectrums with 2% damping for Chinese Seismic Intensity Zone 8.

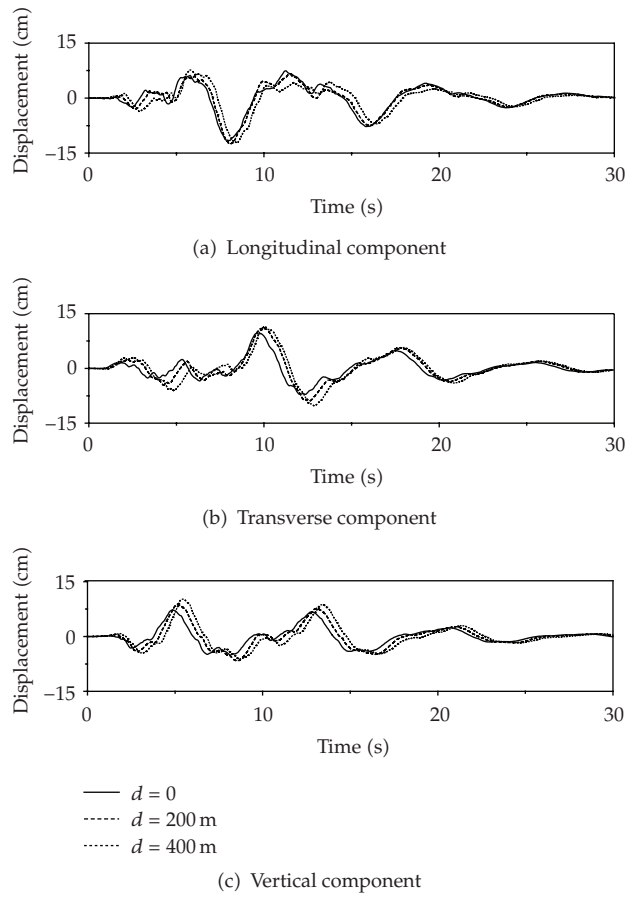

Figure 9: Generated ground displacement considering both wave travel and incoherency effects.

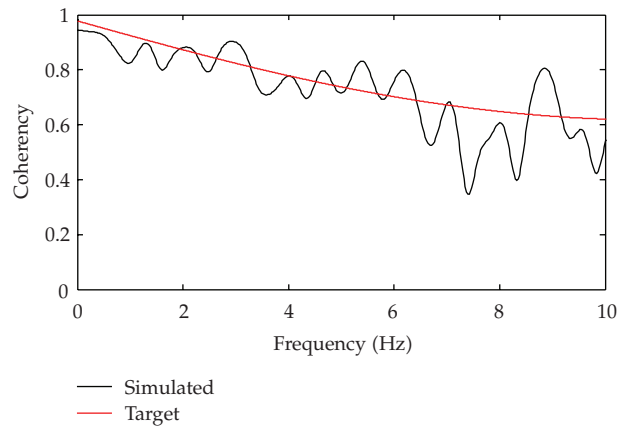

Figure 10: Coherency function of the generated ground motion comparison with model.

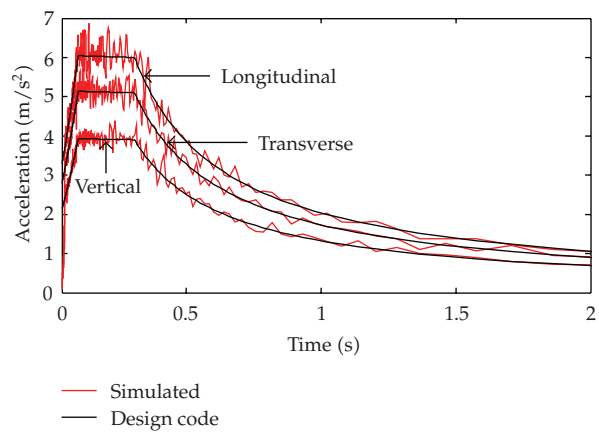

Figure 11: Code response spectrum and the response spectrum of typical simulated ground motions.

where $x_a = [x_{a1}, \ldots, x_{an}]^{\mathrm{T}}$ denotes the n-vector of displacements at the unconstrained degrees of freedom; $x_b = [x_{b1}, \ldots, x_{bn}]^{\mathrm{T}}$ means the m-vector of prescribed support displacements; $\mathbf{M}_{aa}$, $\mathbf{C}_{aa}$, and $\mathbf{K}_{aa}$ are the $n \times n$ mass, damping, and stiffness matrices associated with the unconstrained degrees of freedom, respectively; $\mathbf{M}_{bb}$, $\mathbf{C}_{bb}$, and $\mathbf{K}_{bb}$ are the $m \times m$ matrices associated with the supported degrees of freedom; $\mathbf{M}_{ab}$, $\mathbf{C}_{ab}$, and $\mathbf{K}_{ab}$ are the $n \times m$ coupling matrices associated with the both sets of degrees of freedom; $\mathbf{P}_b(t)$ is the m-vector of the reacting forces at the support degrees of freedom.

The equation defining the response degrees of freedom "a" is given by

$$\mathbf{M}_{aa}\ddot{x}_a + \mathbf{C}_{aa}\dot{x}_a + \mathbf{K}_{aa}x_a = -\mathbf{M}_{ab}\ddot{x}_b - \mathbf{C}_{ab}\dot{x}_b - \mathbf{K}_{ab}x_b. \tag{4.2}$$

The solution of (4.2) depends on how the earthquake motion is defined in the right-hand side of the equation.

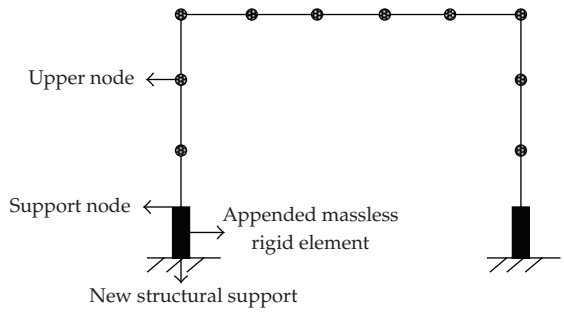

Figure 12: Model sketch massless rigid element method.

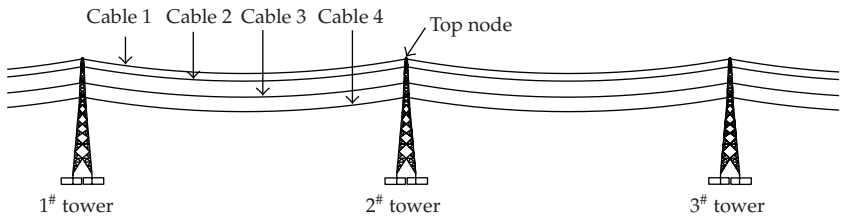

Figure 13: The numbers of cables and top node of tower.

Assuming that the mass matrix is diagonal and $\mathbf{C}_{ab}$ is neglected, (4.2) is reduced to

$$\mathbf{M}_{aa}\ddot{x}_a + \mathbf{C}_{aa}\dot{x}_a + \mathbf{K}_{aa}x_a = \mathbf{K}_{ab}x_b. \tag{4.3}$$

Equation (4.3) can be extended to three components:

$$\mathbf{M}_{aa}\ddot{u}_a + \mathbf{C}_{aa}\dot{u}_a + \mathbf{K}_{aa}u_a = \mathbf{K}_{ab}\left(x_b + y_b + z_b\right), \tag{4.4}$$

where x_b, y_b, and z_b are the input ground motion displacements in two horizontal and one vertical directions, respectively. According to [16], the problem of current input displacement model cannot be ignored. Thus, the appended massless rigid element method is adopted here, which was put forward by Liu et al. [17]. Owing to the space limitations, the appended massless rigid element method is described by Figure 12.

The current versions of SAP2000 can accommodate multiple excitation analysis only if excitations are defined as displacements and not accelerations. Furthermore, if displacement is applied to a node which is part of an integrated system such as a set of interconnected plate elements representing the mat foundation, only the node excited would move and the other nodes connected to it are not displaced. The two horizontal and one vertical ground displacement histories are applied to the bottom end of these rigid pedestals and the supports of every tower are subjected to different displacements.

5. Numerical Results and Discussions

To analyze the response of transmission lines to spatial ground motion, the model shown in Figure 2 for the transmission tower-line system is used in the analysis. The system is subjected

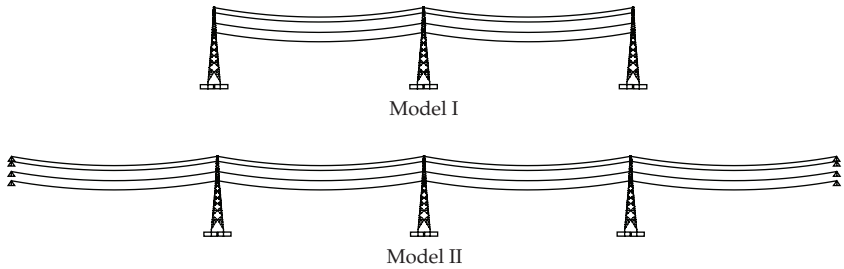

Figure 14: Finite element model of transmission tower-line coupled system.

Table 1: Maximum response of Model I and Model II.

Tower	Model I	Model II	Cable	Model I	Model II
Axial force (N)	85776	66643	Cable 1 (N)	4938	5238
Moment (N·m)	1661	1134	Cable 2 (N)	9342	9646
Shear force (N)	948	668	Cable 3 (N)	9499	9613
Displacement (cm)	6.33	4.63	Cable 4 (N)	9612	9849

to the real data from arrays in SMART-1 and the artificially generated ground motions. The supports of tower $1^{\#}$ are subjected to the generated ground displacement at 0 m, the supports of tower $2^{\#}$ are subjected to the generated ground displacement at 200 m, and the supports of tower $3^{\#}$ are subjected to the generated ground displacement at 400 m.

The dynamic performance is analyzed in terms of axial force, shear force, and moment at the tower bases as well as the displacement of tower and cables. The first, second, third, and forth layers of cables are called cable 1, cable 2, cable 3, and cable 4, respectively. The numbers of cables and top node of tower are shown in Figure 13. The current work mainly concentrates on the effect of the boundary condition, spatially varying ground motions, incident angle of the seismic wave, coherency loss, and wave travel.

5.1. Effect of Boundary Condition

Currently, most researchers established three towers and two-span model and focused on the response of middle tower. Here, comparisons for the model of three towers and two spans (Model I) with the model of three towers and four spans (Model II) are done. Figure 14 shows the finite element models of Model I and Model II. In Model II, the side spans of the lines are hinged at the same height of middle tower.

In order to study the effect of the boundary condition, I06-C00-I12 of event 45 is selected. Table 1 gives the maximum responses of Model I and Model II. It can be seen from the table that the tower's results of Model I are larger than Model II's while the cable's results of Model I are smaller than Model II's. The results in Table 1 also show that the force and displacement differences in tower using Model I and Model II are obvious.

Figure 15 shows longitudinal displacement of top node of transmission tower. The reasons for the response differences between two models are due to the effect of boundary condition. In order to obtain accurate results, three towers and four-span model (Model II) must be considered.

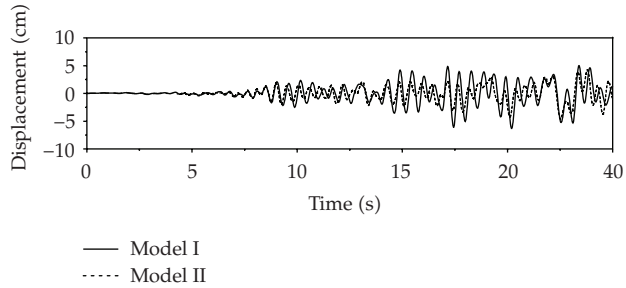

Figure 15: Longitudinal displacement of top node of transmission tower.

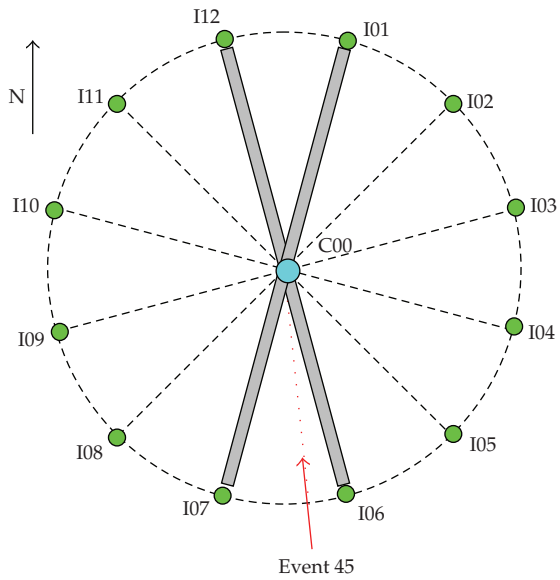

Figure 16: I06-C00-I12 and I07-C00-I01 of Event 45.

5.2. Effect of Spatially Varying Ground Motions

In order to study the effect of the spatially varying ground motions, I06-C00-I12 and I07-C00-I01 of event 45 are selected. Figure 16 shows the map of I06-C00-I12 and I07-C00-I01 of event 45.

The results in Table 2 show the maximum responses of towers under I06-C00-I12 and I07-C00-I01 excitations. The results in Table 3 show the maximum responses of cables under I06-C00-I12 and I07-C00-I01 excitations. It is evident from these tables that for two cases of input ground motions considered, the assumption of uniform ground motion at all supports does not represent the most critical case for the responses of tower and cable. For example, the magnification in tower's axial force is larger for this case; that is, the response increases from 40.58 kN for the uniform ground motion to 70.02 kN for the multiple support excitations. The maximum force in the cable is 86.51 kN for the uniform ground motion while for the multiple support excitations the response is 98.61 kN.

Figure 17 shows the longitudinal displacement of the top node of transmission tower. The effect of spatially varying ground motions is very important. The uniform ground motion

Table 2: Maximum response of tower under I06-C00-I12 and I07-C00-I01 excitations.

Tower	I06-C00-I12		I07-C00-I01	
	Uniform	Multiple	Uniform	Multiple
Axial force (N)	48073	66643	40580	70020
Moment (N · m)	858	1134	786	1091
Shear force (N)	491	668	465	628
Displacement (cm)	3.14	4.63	3.14	4.59

Table 3: Maximum response of cable under I06-C00-I12 and I07-C00-I01 excitations.

Cable	I06-C00-I12		I07-C00-I01	
	Uniform	Multiple	Uniform	Multiple
Cable 1 (N)	4679	5238	4598	5162
Cable 2 (N)	8888	9646	8745	9642
Cable 3 (N)	8692	9613	8661	9579
Cable 4 (N)	8704	9849	8651	9861

assumption cannot give the critical response. This observation indicates that the influence of ground motion spatial variation is significant in the considered transmission tower-line system example.

5.3. Effect of Incident Angle of the Seismic Wave

The angle of incidence of the seismic wave is investigated by varying the direction of wave propagation with respect to the longitudinal direction of the system as shown in Figure 18. The longitudinal direction of system is assumed to coincide with the array direction. Five different cases are considered in the study, namely, (I) I06-C00-I12, (II) I07-C00-I01, (III) I05-C00-I11, (IV) I08-C00-I02, and (V) I09-C00-I03. Figure 18 shows the various angle directions of earthquake wave of event 45.

Table 4 shows the maximum responses of tower under various angle excitations. Table 5 shows the maximum responses of cables under various angle excitations. It is seen from the table that the variation of the incident angle of seismic wave has a slight effect on the responses, especially for the tower axial force. Assuming that the longitudinal direction of the ground motion and the direction of the wave propagation coincide with the longitudinal direction of the system could not obtain the maximum responses of the system.

The above analyses demonstrated the importance of boundary conditions, ground motion spatial variation, and the incident angle of seismic wave on the transmission tower-line system responses. As discussed above, ground motion spatial variation is induced by wave passage and coherency loss. In the following, these two effects on ground motion spatial variations are investigated separately in detail to examine their influence on the transmission tower-line system.

5.4. Effect of Coherency Loss

To investigate the influence of spatially varying ground motions on the middle tower, highly, intermediately, weakly correlated, and uncorrelated ground motions are considered.

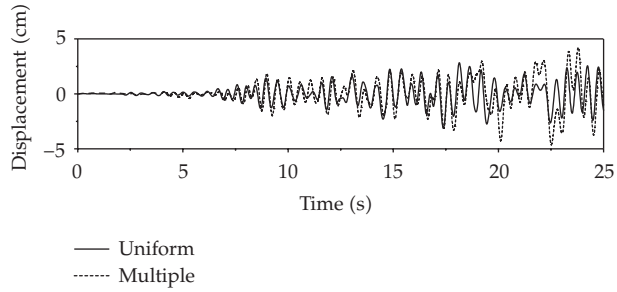

Figure 17: Longitudinal displacement of top node of transmission tower.

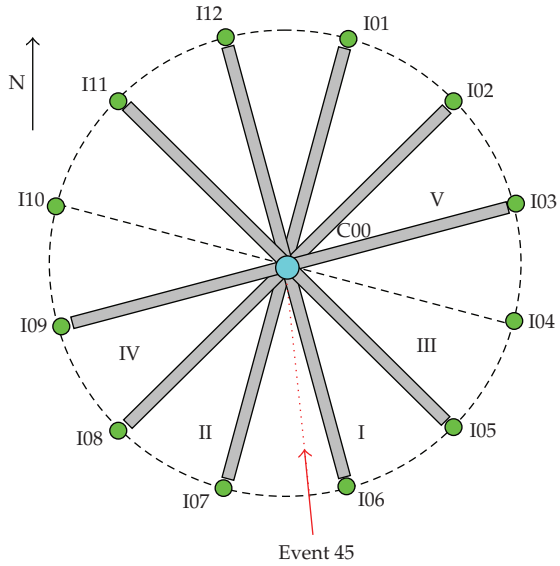

Figure 18: Various angle earthquake wave of Event 45.

Table 4: Maximum response of tower under various angle excitations.

Number	Degree	Axial force (N)	Moment (N · m)	Shear force (N)	Displacement (cm)
I	9°	66643	1134	668	4.63
II	21°	70020	1091	628	4.59
III	39°	58945	1100	641	4.28
IV	51°	66532	1159	666	4.65
V	81°	58065	966	552	3.64

Table 5: Maximum response of cable under various angle excitations.

Number	Degree	Cable 1 (N)	Cable 2 (N)	Cable 3 (N)	Cable 4 (N)
I	9°	5238	9646	9613	9849
II	21°	5162	9642	9579	9861
III	39°	5830	10416	9915	9816
IV	51°	5644	10667	9603	10105
V	81°	5219	9665	9326	10218

Table 6: Parameters for coherency loss functions.

Coherency loss	β	a	b	c
Highly	1.109×10^{-4}	3.583×10^{-3}	-1.811×10^{-5}	1.177×10^{-4}
Intermediately	3.697×10^{-4}	1.194×10^{-2}	-1.811×10^{-5}	1.177×10^{-4}
Weakly	1.109×10^{-3}	3.583×10^{-2}	-1.811×10^{-5}	1.177×10^{-4}

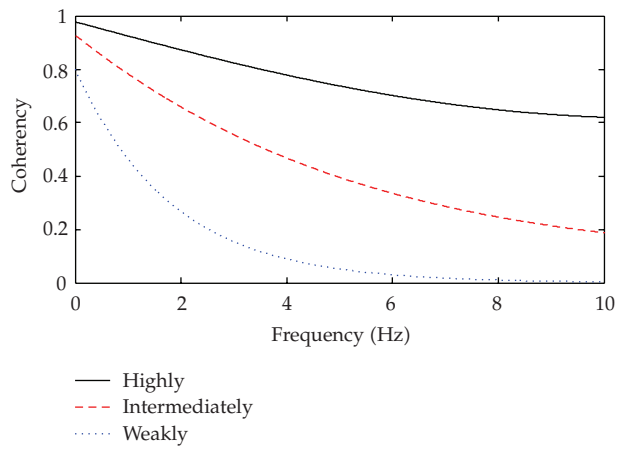

Figure 19: Coherency functions of the simulated spatially varying ground motions.

It should be noted that the correlation as low as uncorrelated does not usually occur at short distances, unless there are considerable changes in the local geology from one support to the other. The parameters are given in Table 6 [18]. The coherency functions for three cases are shown in Figure 19. The Uniform ground motion is also considered and $v = 800\,\mathrm{m/s}$ is used in this section. It should be noted that ground motions are generated with the same apparent velocity. Therefore the only differences are cross correlations between the spatial ground motions.

The maximum response of tower under various degrees of coherency is shown in Table 7. Figure 20 shows the cable displacement ratios. Cable displacement ratio is defined as ratio between multiple excitation and uniform excitation. It is noted from the table and figure that for the case of uncorrelated ground motion the responses are higher than those for the case of intermediately, weakly, or highly correlated ground motion. For the uniform ground motion, the responses are the lowest of all cases. Various degrees of coherency used to generate the ground motion may have a significant influence on the response of system. For example, the maximum axial force in the tower is 23.7 kN for the uniform ground motion while for the uncorrelated case of multiple support excitations the response is 83.3 kN. The reasons for these are attributed to the contribution of the quasistatic part of the response.

In order to obtain a representative analysis, various degrees of coherency of spatial ground motions should be considered. Neglecting loss of coherency between spatial ground motions may result in substantial underestimations of system responses.

Table 7: Maximum response of tower under various degrees of coherency.

Coherency	Axial force (N)	Moment (N · m)	Shear force (N)	Displacement (cm)
Uniform	23704	562	318	2.44
Highly	34578	929	515	3.75
Intermediately	46670	1170	656	5.18
Weakly	69875	1415	813	6.86
Uncorrelated	83342	2037	1157	9.41

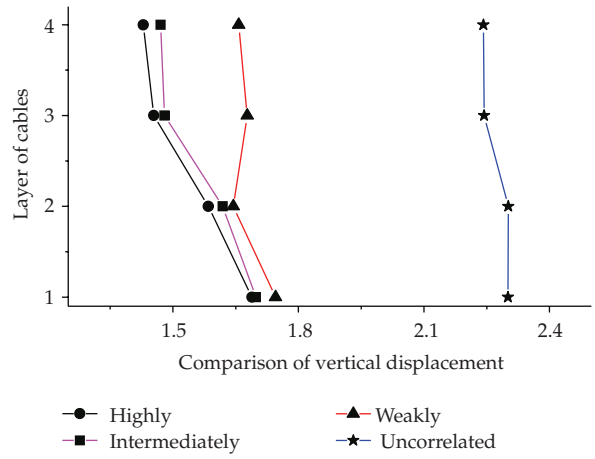

Figure 20: Cable's displacement ratio.

5.5. Effect of Wave Travel

Wave propagation will cause a phase delay between spatial ground motions. The phase delay depends on the separation distance and the wave propagation apparent velocity. Previous study revealed that wave propagation apparent velocity is quite irregular [10]. There is no general consent yet on how the apparent velocities should be modeled. In most studies of ground motion spatial variations, constant apparent velocities are often assumed [19, 20]. In this study, constant apparent velocities are also assumed. To study the effect of wave travel, four different velocities of wave propagation are considered in the analysis, 200, 400, 800, and 1600 m/s, to cover the range of practical propagation velocities in the engineering. The case of uniform ground motion at all supports corresponds to a wave propagating with infinite velocity. In all these cases, the ground motion is also assumed to be highly correlated.

Maximum response of tower under different wave travel excitations is shown in Table 8. As can be seen, increasing the spatial ground motion phase delay, that is, reducing the seismic wave apparent velocity from uniform to 1600 m/s, 800 m/s, 400 m/s, and to 200 m/s increases the response of transmission tower, indicating that the structure is sensitive to earthquake ground motion phase delay. In general, the more significant is the phase delay between spatial ground motions, the larger is the structural response. Figure 21 shows cable axial force ratios. Cable axial force ratio is defined as ratio between multiple excitation and uniform excitation. The figure indicates that as the velocity of propagation increases, the responses become close to the case of uniform excitation. When the apparent velocity is 1600 m/s, the spatial ground motion has smaller ratio than other cases.

Table 8: Maximum response of tower under different wave travel excitations.

Apparent velocity	Axial force (N)	Moment (N · m)	Shear force (N)	Displacement (cm)
Uniform	23704	562	318	2.44
200 m/s	90550	2969	1716	12.3
400 m/s	68679	2185	1262	8.39
800 m/s	34578	929	515	3.75
1600 m/s	27173	667	381	2.46

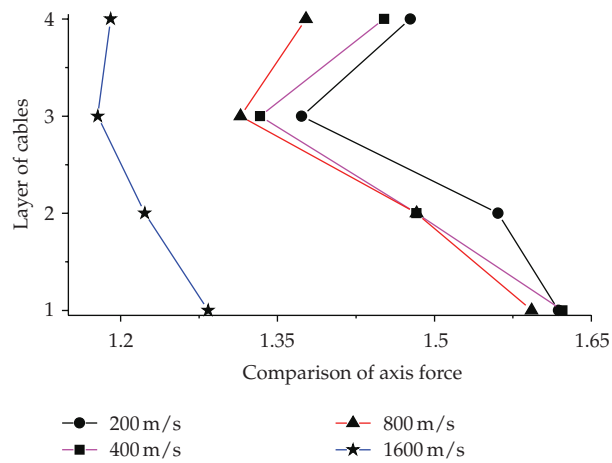

Figure 21: Cable's axial force ratio.

The above results demonstrate that the spatial ground motion phase difference has a significant effect on the structural responses. Neglecting spatial ground motion phase difference may lead to erroneous estimation of system responses. As shown in Table 8, the maximum axial force in the tower in the case of uniform ground motion is 23.7 kN. It is evident from the table that considering multiple support excitation increases the response in the tower for all cases. The maximum increase is about 3.8 times for wave propagation velocity of 200 m/s. Therefore, in order to obtain a reliable seismic response analysis of transmission tower-line system, spatial ground motion phase difference should not be neglected. These conclusions, particularly to the numerical example selected for the study, may vary with the tower dimensions, cable geometry, and generated ground motion.

6. Conclusions

The effect of the spatial variation of earthquake ground motion on the response of the transmission tower-line system has been investigated in this paper. The members of transmission tower are modeled by beam elements and the nonlinear dynamic behavior of cables is taken into account. The input of ground motion is taken as displacement time histories. The real data from the close digital arrays of strong motion seismographs in SMART-1 are selected. Artificial ground displacement records are also developed and used in the analysis. The nonlinear time history analytical method is used in the analysis. The influence of the boundary condition, spatially varying ground excitations, incident angle

of the seismic wave, coherency, and wave travel on the system are considered. Following conclusions can be obtained based on the above studies.

(1) The boundary condition has an obvious effect on the response of the system. In order to obtain accurate results, three towers and four-spans model must be taken in the analysis.

(2) The case of uniform support excitation does not produce the maximum response in the system. The multiple support excitations, which is a more realistic assumption, can result in larger response. The effect of spatially varying ground motions cannot be neglected.

(3) The incident angle of the seismic wave has a slight effect on the responses of system. Assuming that the longitudinal of the ground motion and the direction of the wave propagation coincide with the longitudinal direction of the system could not obtain the maximum responses of the system.

(4) The coherency loss has a significant effect on the response of the system. The uncorrelated ground motion gives bigger responses than other cases. In order to obtain a representative analysis, the various degrees of coherency should be considered.

(5) The assumed velocity of propagation of seismic waves has a significant effect on the response of system to seismic ground motion. In order to obtain a representative analysis of the system, an accurate estimation of the wave velocity is required.

Based on the obtained results, uncorrelated ground motion and the apparent velocity of 200 m/s provide the most critical case for the response calculations. It should be noted that many studies have been reported on the ground motion spatial variation effect on bridges, viaducts, pipelines, and dams; very limited study on transmission tower-line system can be found in the literature. This study demonstrates that the ground motion spatial variation effect is very important to transmission tower-line system. As many cat head type towers, cup towers, and guyed towers are of transmission systems, more studies are deemed necessary to further investigate the ground motion spatial variation effects on responses of these systems.

Acknowledgments

This work is supported by the National Natural Science Foundation of China under Grant no. 50638010 and the Foundation of Ministry of Education for Innovation Group under Grant no. IRT0518. This support is greatly appreciated.

References

[1] R.-H. Yin, D.-L. Li, G.-L. Liu, and T. Zhai, "Seismic damage and analysis of power transmissions towers," *World Information on Earthquake Engineering*, vol. 21, no. 1, pp. 51–54, 2005 (Chinese).

[2] H.-N. Li, W. L. Shi, and L.-G. Jia, "Simplified aseicmic calculation method considering effects of line on transmission tower," *Journal of Vibration Engineering*, vol. 16, no. 2, pp. 233–237, 2003 (Chinese).

[3] H. Li, W. Shi, and L. Jia, "Limitations of effects of lines on in-plane vibration of transmission towers and simplified seismic calculation method," *Journal of Vibration and Shock*, vol. 23, no. 2, pp. 1–7, 2004 (Chinese).

[4] H.-N. Li, W.-L. Shi, G.-X. Wang, and L.-G. Jia, "Simplified models and experimental verification for coupled transmission tower-line system to seismic excitations," *Journal of Sound and Vibration*, vol. 286, no. 3, pp. 569–585, 2005.

[5] A. Ghobarah, T. S. Aziz, and M. El-Attar, "Response of transmission lines to multiple support excitation," *Engineering Structures*, vol. 18, no. 12, pp. 936–946, 1996.
[6] GB 50260-96, *Code for Seismic Design of Electrical Facilities*, China Plan Press, Beijing, China, 1996.
[7] S. Z. Shen, C. B. Xu, and C. Zhao, *Design of Suspension Structure*, China Architecture and Building Press, Beijing, China, 1997.
[8] E. L. Wilson, *Three Dimensional Statics and Dynamic Analysis of Structures: A Physical Approach with Emphasis on Earthquake Engineering*, Computer and Structures, Inc, Berkley, Calif, USA, 2002.
[9] A. M. Abdel-Ghaffar and L. I. Rubin, "Suspension bridge response to multiple-support excitations," *Journal of Engineering Mechanics, ASCE*, vol. 108, no. 2, pp. 419–435, 1982.
[10] H. Hao, "Effects of spatial variation of ground motions on large multiply-supported structures," Tech. Rep. UCB/EERC-89/06, July 1989.
[11] Institute of Earth Science, "SMART-1 Array data repository," Tawain, 1980–1991, http://www.earth.sinica.edu.tw/~smdmc/.
[12] H. Hao, C. S. Oliveira, and J. Penzien, "Multiple-station ground motion processing and simulation based on smart-1 array data," *Nuclear Engineering and Design*, vol. 111, no. 3, pp. 293–310, 1989.
[13] R. W. Clough and J. Penzien, "Dynamics of Structures," McGraw-Hill, New York, NY, USA, 1975.
[14] GB 50011, *Code for Seismic Design of Buildings*, National standard of the People's Republic of China, Beijing, China, 2001.
[15] J. Penzien and M. Watabe, "Characteristics of 3-dimensional earthquake ground motions," *Earthquake Engineering and Structural Dynamics*, vol. 3, no. 4, pp. 365–373, 1975.
[16] G. H. Liu, H.-N. Li, and H. Lin, "Comparison and evaluation of models for structural seismic responses analysis," *Engineering Mechanics*, vol. 26, no. 2, pp. 10–15, 2009 (Chinese).
[17] G.-H. Liu, H.-N. Li, W. Guo, and L. Tian, "A new method for solving problem of current displacement input model for calculating structural seismic responses" (Chinese), *Engineering Mechanics*. In press.
[18] K. Bi, H. Hao, and N. Chouw, "Required separation distance between decks and at abutments of a bridge crossing a canyon site to avoid seismic pounding," *Earthquake Engineering and Structural Dynamics*, vol. 39, no. 3, pp. 303–323, 2009.
[19] H. Hao, "Torsional response of building structures to spatial random ground excitations," *Engineering Structures*, vol. 19, no. 2, pp. 105–112, 1997.
[20] H. Hao and S.-R. Zhang, "Spatial ground motion effect on relative displacement of adjacent building structures," *Earthquake Engineering and Structural Dynamics*, vol. 28, no. 4, pp. 333–349, 1999.

Hindawi Publishing Corporation
Mathematical Problems in Engineering
Volume 2010, Article ID 570136, 8 pages
doi:10.1155/2010/570136

Research Article

Application of Periodized Harmonic Wavelets towards Solution of Eigenvalue Problems for Integral Equations

Carlo Cattani[1] and Aleksey Kudreyko[2]

[1] *diFarma, University of Salerno, Via Ponte Don Melillo, 84084 Fisciano, Italy*
[2] *Department of Mathematics and Computer Science, University of Salerno, Via Ponte Don Melillo, 84084 Fisciano, Italy*

Correspondence should be addressed to Aleksey Kudreyko, akudreyko@unisa.it

Received 12 October 2009; Accepted 19 November 2009

Academic Editor: Alexander P. Seyranian

This article deals with the application of the periodized harmonic wavelets for solution of integral equations and eigenvalue problems. The solution is searched as a series of products of wavelet coefficients and wavelets. The absolute error for a general case of the wavelet approximation was analytically estimated.

1. Introduction

Mathematical models describe a variety of physical and engineering problems and processes which can be represented by integral equations (IEs). The homogeneous Fredholm IE is written as follows:

$$\lambda f(x) - \int_a^b K(x,t) f(t) dt = 0, \tag{1.1}$$

where a and b are finite numbers, the kernel $K(x,t)$ is known function, and λ and $f(x)$ are the unknown eigenvalue and associated eigenfunction. Equation (1.1) has a nontrivial solution only for some values of λ.

There exist two different methods to solve IEs numerically. The first one is to expand the equation by the appropriate set of basis functions, such as the classical orthogonal polynomials [1] or wavelets (e.g. [2, 3]), and to reduce the equation to simultaneous

equations with respect to the expansion coefficients. The second method is to use the trapezoidal formula for integration [4]. Since we are interested in application of periodic harmonic wavelets (PHWs) as basis functions, we will focus our attention on the first approach.

These methods have their own advantages and disadvantages. The main advantage of our approach over the existing wavelet methods is that the wavelet expansion coefficients can be computed analytically. In addition, it will be shown that the computational cost of our approach is low and the accuracy is high. It is worth to be mentioned that the application of wavelets takes a special place in the modern computational methods thanks to quick convergence of a series of wavelets and the possibility to find the solution with a low approximation error.

The pioneering contribution into the wavelet approach for solution of IEs belongs to Beylkin et al. [5]. There were many other approaches by, for example, [2, 6, 7] towards this problem. The interest in the wavelet approach for solution of IEs is popular nowadays [8].

The most part of the existing research programs is devoted to solution of the Fredholm and Volterra-type IEs. The Galerkin and collocation methods are mainly used in such papers [2, 6, 7, 9], where besides the well-known Daubechies wavelets many other wavelets have been used, such as the Haar wavelets [2, 8, 9], CAS-wavelets [3], and so forth.

In our opinion, the attention to the PHW and its application for solution of IEs have not been sufficiently paid, although there were attempts to use this basis for solution of partial differential equations (e.g., [10–12]). The advantage of our choice is that PHWs are continuous and differentiable functions everywhere.

It is known that the wavelet approach offers an alternative route for a signal and function decomposition in the time-frequency domain. Recent applications of the wavelet transform to engineering and applied problems can be found in several studies [13]. In order to analyze some applied engineering problems, Newland proposed [13, 14] wavelets whose spectrum is confined exactly to an octave band. It was suggested that the "level" of a signal's multiresolution would be interchangeable with its frequency band and the interpretation of the frequency content would be easier for engineers.

In addition, for the convenience of the further analysis it would be better to operate with such functions, whose Fourier transform was compact and which could, if possible, be constructed from simple functions. The wavelets considered in our paper are called PHW and they possess all mentioned properties and constitute a specific but a representative example of wavelets in general.

The main purpose of the present work is to propose for numerical solution of IEs a simple approach based on periodized harmonic wavelets. This technique is also applicable with minor changes to the Fredholm, Volterra, and integro-differential equations. In Section 2 of the paper we show that PHWs satisfy the axioms of the multiresolution analysis and can be used as basis functions in solution of IEs. An illustrative example is presented in Section 3. The generalized error estimation is given in Section 4 and it shows that the accuracy of computations is very high even when the approximation level is small.

2. Periodized Harmonic Wavelets

It is known [13–15] that PHWs are defined as follows:

$$\psi\left(2^j x - k\right) = 2^{-j} \sum_{m=2^j}^{2^{j+1}-1} e^{2\pi i m(x-(k/2^j))}, \tag{2.1}$$

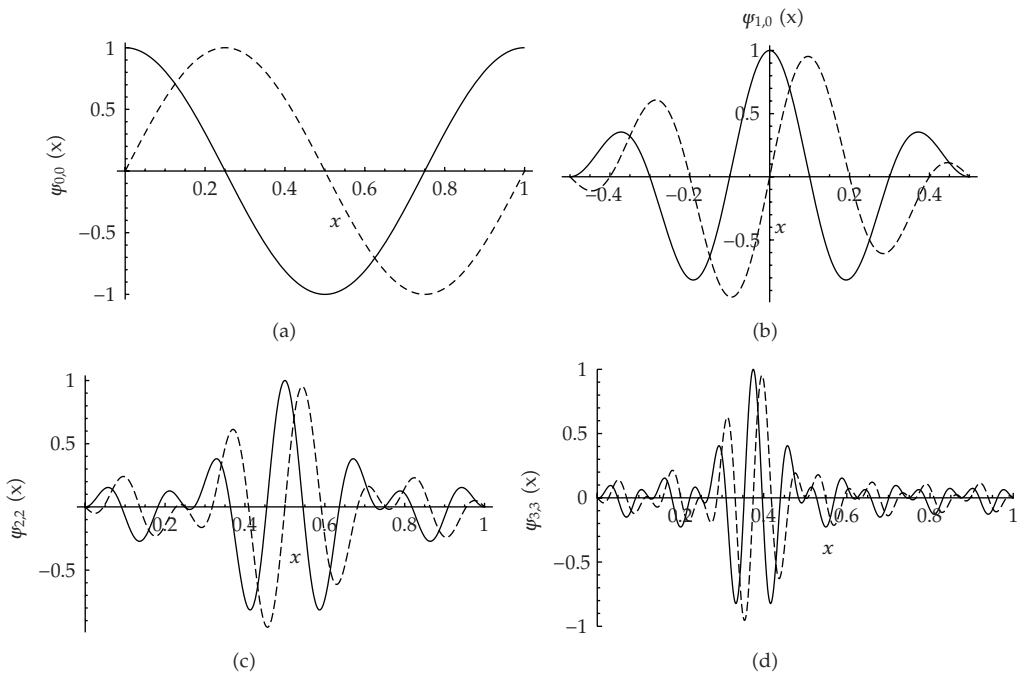

Figure 1: Real (solid line) and imaginary (dashed line) parts of the periodic harmonic wavelets $\psi_{0,0}(x)$, $\psi_{1,0}(x)$, $\psi_{2,2}(x)$, and $\psi_{3,3}(x)$.

where the scaling parameter $k = 0, \ldots, 2^j - 1$ and the dilation parameter $j = 0, \ldots, N - 1$. The 1-periodicity of function (2.1) can be demonstrated as follows:

$$\psi\left(2^j(x+1) - k\right) = 2^{-j} \sum_{m=2^j}^{2^{j+1}-1} e^{2\pi i m\left((x+1) - \frac{k}{2^j}\right)} = \psi\left(2^j x - k\right). \tag{2.2}$$

The plots for several values of the scaling parameter j are shown on Figure 1 for selected positions k.

According to [14, 16], PHWs construct basis for 1-periodic functions from $L^2([0;1])$. The orthogonal projection of the function $f(x)$ onto the space of wavelets V_N of the level N is written as follows:

$$\mathcal{P}_{V_N} f(x) = a_0 \varphi(x) + \sum_{j=0}^{N-1} \sum_{k=0}^{2^j-1} \left\{ a_{j,k} \psi_{j,k}(x) + \tilde{a}_{j,k} \psi_{j,k}^*(x) \right\}, \tag{2.3}$$

where the harmonic scaling function is $\varphi(x) = 1$ [14] and the "$*$" over $\psi_{j,k}$ stands for its complex conjugate. If $N \to \infty$, then $\lim_{N\to\infty} \mathcal{P}_{V_N} f(x) = f(x)$ and expansion (2.3) becomes

$$f(x) = a_0 \varphi(x) + \sum_{j=0}^{\infty} \sum_{k=0}^{\infty} \left\{ a_{j,k} \psi_{j,k}(x) + \tilde{a}_{j,k} \psi_{j,k}^*(x) \right\}. \tag{2.4}$$

Thus, we have a set of functions, which form basis for the $L^2([0;1])$ functions. It means that we can substitute the expansion (2.3) into (1.1) and reduce it to a system of equations with respect to wavelet coefficients.

3. Eigenvalues and Eigenfunctions

Let us consider the homogeneous Fredholm integral equation

$$\widehat{f}(\widehat{x}) - \lambda \int_0^{\pi} \cos\left(\widehat{x} + \widehat{t}\right) \widehat{f}\left(\widehat{t}\right) d\widehat{t} = 0. \tag{3.1}$$

In order to deal with 1-periodic functions, it is convenient to introduce new variables as follows: $\widehat{x} = 2\pi x$ and $\widehat{t} = 2\pi t$. And we get the new equation

$$f(x) - 2\pi\lambda \int_0^{0.5} \cos[2\pi(x+t)] f(t) dt = 0, \tag{3.2}$$

which we will solve by the collocation method. Denote the collocation points by

$$a \le x_1 < x_2 < \cdots < x_l < \cdots \le b. \tag{3.3}$$

Recalling the decomposition of a real periodic function (2.3) on the space of PHW, we have

$$p_{V_1} f(x) = a_0 + \varphi_{0,0}(x) + \widetilde{a}_{0,0} \varphi^*_{0,0}(x), \tag{3.4}$$

for $N = 1$. Also, $a_{0,0} = \widetilde{a}_{0,0}$ for a real function. The corresponding choice of the collocation points $\{x_l\}$ leads us to a system of linear algebraic equations with the parameter λ and unknowns $\{a_0; a_{0,0}; \widetilde{a}_{0,0}\}$ as

$$a_0 + a_{0,0} e^{2\pi i x_l} + \widetilde{a}_{0,0} e^{-2\pi i x_l} - 2\pi\lambda \int_0^{1/2} \cos[2\pi(x_l + t)] \left(a_0 + a_{0,0} e^{2\pi i t} + \widetilde{a}_{0,0} e^{-2\pi i t}\right) dt = 0. \tag{3.5}$$

The solution of this system of equations gives us two pairs of coefficients $\{0; 0.5; 0.5\}$ and $\{0; -i/2; i/2\}$. Thus, we can find parameters $\lambda_1 = 2/\pi, \lambda_2 = -2/\pi$ and the eigenfunctions $\widehat{f}_1(\widehat{x}) = \cos\widehat{x}$, $\widehat{f}_2(\widehat{x}) = \sin\widehat{x}$.

We obtained the projection of the solution of the unknown eigenfunctions f_1, f_2 on the first level of approximation. Note that the obtained projection for $N = 1$ coincides with the analytical solution. If we have continued to search for the solution on the other levels of approximation, the connection coefficients $\{a_{j,k}\}$ would be zeros.

4. Approximation Properties of Multiresolution Spaces

Let us now consider the approximation error for the periodic wavelets. Let $f(x) \in L^2([0;1])$ and assume that its periodic expansion (2.4) is P times differentiable everywhere. Denote the approximation error as follows:

$$e_N^{\text{per}}(x) = f(x) - \mathcal{P}_{V_N} f(x), \quad x \in [0;1], \tag{4.1}$$

where $\mathcal{P}_{V_N} f(x)$ is the orthogonal projection of $f(x)$ onto the space of PHW. The symbol "per" over e_N assumes that the error is a periodic function. The derivation of the value of $e_N^{\text{per}}(x)$ is presented in the following theorem.

Theorem 4.1. *The approximation error* (4.1) *is bounded by the exponential decay* $|e_N^{per}(x)| = \mathcal{O}(2^{-NP})$.

Proof. Using the wavelet periodic expansion (2.4), we find that

$$\mathcal{P}_{V_N} f(x) = \sum_{k=0}^{\infty} a_{\varphi,k}\varphi(x-k) + \sum_{j=0}^{N-1}\sum_{k=0}^{2^j-1} a_{j,k}\psi_{j,k}(x). \tag{4.2}$$

At any given scale, the projection of the function on the subspace of wavelets of the certain scale approaches to the function as the number of zero wavelet moments P tends to infinity, that is, $N \to \infty$ and we get $f(x)$ itself:

$$f(x) = \sum_{k=0}^{\infty} a_{\varphi,k}\varphi(x-k) + \sum_{j=0}^{\infty}\sum_{k=0}^{\infty} a_{j,k}\psi_{j,k}(x). \tag{4.3}$$

Then, by subtracting (4.2) from (4.3), we obtain an expression for the error e_N^{per} in terms of the wavelets at scales $j \geq N$:

$$e_N^{\text{per}}(x) = \sum_{j=N}^{\infty}\sum_{k=0}^{2^j-1} a_{j,k}\psi_{j,k}(x). \tag{4.4}$$

Define

$$C_\psi = \max_{x\in I_{j,k}}\left|\psi\left(2^j x - k\right)\right| = \max_{y\in[0,D-1]}|\psi(y)|. \tag{4.5}$$

Since $\max_{x\in I_{j,k}}|\psi_{j,k}(x)| = 2^{j/2}C_\psi$ and according to the Theorem of decay of wavelet coefficients [17], it is

$$\left|a_{j,k}\psi_{j,k}(x)\right| \leq C_P 2^{-jP}\max_{\xi\in I_{j,k}}\left|f^{(P)}(\xi)\right|C_\psi. \tag{4.6}$$

Recall that

$$\operatorname{supp}(\psi_{j,k}) = I_{j,k} = \left[\frac{k}{2^j}; \frac{k+D-1}{2^j}\right]. \tag{4.7}$$

Hence, there are at most $D-1$ intervals $I_{j,k}$ containing a given value of x. Thus, for any x only $D-1$ terms in the inner summation in (4.4) are nonzero. Let I_j be a union of all these intervals, that is,

$$I_j(x) = \bigcup_{\{l: x \in I_{j,l}\}} I_{j,l}, \tag{4.8}$$

and let

$$\mu_j^P(x) = \max_{\xi \in I_j(x)} \left| f^P(\xi) \right|. \tag{4.9}$$

Then we can find a common bound for all terms in the inner sum:

$$\sum_{k=-\infty}^{\infty} \left| a_{j,k} \psi_{j,k} \right| \le C_\psi C_P 2^{-jP} (D-1) \mu_j^P(x). \tag{4.10}$$

The outer sum over j can be evaluated using the fact that

$$\mu_N^P(x) \ge \mu_{N+1}^P(x) \ge \mu_{N+2}^P(x) \ge \ldots, \tag{4.11}$$

and we establish the bound

$$\begin{aligned} \left| e_N^{\text{per}}(x) \right| &\le C_\psi C_P (D-1) \mu_N^P(x) \sum_{j=N}^{\infty} 2^{-jP} \\ &= C_\psi C_P (D-1) \mu_N^P(x) \frac{2^{-NP}}{1-2^{-P}}. \end{aligned} \tag{4.12}$$

Thus, we see that for an arbitrary, but fixed x, the approximation error will be bounded as follows:

$$\left| e_N^{\text{per}}(x) \right| = \mathcal{O}\left(2^{-NP}\right), \tag{4.13}$$

where $\mathcal{O}$ only denotes an upper bound. This is an exponential decay with respect to the resolution N. Furthermore the greater number of vanishing moments P of a periodic wavelet increases the rate of the decay. □

Let us compare the approximation error of wavelets with the error of the Fourier approximation for N terms. In order to do this, we need to introduce a smooth function of the order q.

Definition 4.2. A smooth function is a function that has continuous derivatives up to some desired order q over some domain. A function can, therefore, be said to be smooth over a restricted interval such as $[a;b]$.

According to [18], we can find that the approximation error of the Fourier series is

$$\left|e^{F}(q,N)\right| = \max_{a\le x\le b}\left|F(N,x)-f(x)\right| = \mathcal{O}\left(N^{-q-0.5}\right). \tag{4.14}$$

This is also an exponential decay with respect to the number of terms in the series and the level of smoothness of a function. In order to give a more detailed comparison of these two methods, it is necessary to consider specific examples.

5. Concluding Remarks

In this work we have proposed PHWs as basis functions for solution of IEs. The approach was verified by solving a test problem and its approximation error was analytically estimated for periodized wavelets. The assumption of 1-periodicity of solution does not restrict the generality of the problem, since we can always make the substitutional change of variables.

There are several important facts to remember about the wavelet approximation.

(1) The goal of the wavelet expansion of a function or signal is to obtain the coefficients of the expansion $a_{j,k}$.

(2) The second goal is to have the most zero coefficients or very small. This is called a sparse representation and it is very important in applications for statistical estimation and detection, data compression, noise reduction, and fast algorithms.

(3) The fact that the error is restricted to a small neighborhood of the discontinuity is the result of the "locality" of wavelets. The behavior of $f(x)$ at one location affects only the coefficients of wavelets close to that location.

(4) Most of the linear part of $f(x)$ is represented exactly.

We can infer from the example that the present approach is applicable to a large class of problems, where the expected solution is a periodic function. It should be also mentioned that any differential equation can be transformed into an integral equation. It means that it might be solved a large class of eigenvalue equations derived by differential equations.

Acknowledgment

The work of A. Kudreyko is supported by the Istituto Nazionale di Alta Matematica Francesco Severi (Rome-IT) under scholarship U 2008/000564, 21/11/2008.

References

[1] C. M. Bender and E. Ben-Naim, "Nonlinear-integral-equation construction of orthogonal polynomials," *Journal of Nonlinear Mathematical Physics*, vol. 15, supplement 3, pp. 73–80, 2008.

[2] U. Lepik and E. Tamme, "Application of the Haar wavelets for solution of linear integral equations," in *Proceedings of the Dynamical Systems and Applications*, vol. 510, pp. 494–507, Antalya, Turkey, July 2004.
[3] S. Yousefi and A. Banifatemi, "Numerical solution of Fredholm integral equations by using CAS wavelets," *Applied Mathematics and Computation*, vol. 183, no. 1, pp. 458–463, 2006.
[4] Y.-p. Liu and L. Tao, "Mechanical quadrature methods and their extrapolation for solving first kind Abel integral equations," *Journal of Computational and Applied Mathematics*, vol. 201, no. 1, pp. 300–313, 2007.
[5] G. Beylkin, R. Coifman, and V. Rokhlin, "Fast wavelet transforms and numerical algorithms I," *Communications on Pure and Applied Mathematics*, vol. 44, no. 2, pp. 141–183, 2006.
[6] Y. Mahmoudi, "Wavelet Galerkin method for numerical solution of nonlinear integral equation," *Applied Mathematics and Computation*, vol. 167, no. 2, pp. 1119–1129, 2005.
[7] J.-Y. Xiao, L.-H. Wen, and D. Zhang, "Solving second kind Fredholm integral equations by periodic wavelet Galerkin method," *Applied Mathematics and Computation*, vol. 175, no. 1, pp. 508–518, 2006.
[8] U. Lepik, "Solving fractional integral equations by the Haar wavelet method," *Applied Mathematics and Computation*, vol. 214, no. 2, pp. 468–478, 2009.
[9] U. Lepik, "Numerical solution of evolution equations by the Haar wavelet method," *Applied Mathematics and Computation*, vol. 185, no. 1, pp. 695–704, 2007.
[10] C. Cattani, "Harmonic wavelets towards the solution of nonlinear PDE," *Computers and Mathematics with Applications*, vol. 50, no. 8-9, pp. 1191–1210, 2005.
[11] C. Cattani and A. Kudreyko, "On the discrete harmonic wavelet transform," *Mathematical Problems in Engineering*, vol. 2008, Article ID 687318, 7 pages, 2008.
[12] S. V. Muniandy and I. M. Moroz, "Galerkin modeling of the Burgers equation using harmonic wavelets," *Physics Letters A*, vol. 235, pp. 352–356, 1997.
[13] D. E. Newland, *An Introduction to Random Vibrations, Spectral & Wavelet Analysis*, Longman Scientific & Technical, Essex, UK, 3rd edition, 1993.
[14] D. E. Newland, "Harmonic wavelet analysis," *The Royal Society*, vol. 443, pp. 203–225, 1993.
[15] D. E. Newland, "Harmonic wavelets in vibrations and acoustics," *Philosophical Transactions of the Royal Society A*, vol. 357, no. 1760, pp. 2607–2625, 1999.
[16] T. Morita, "Expansion in Harmonic wavelets of a periodic function," *Interdisciplinary Information Sciences*, vol. 3, no. 1, pp. 5–12, 1997.
[17] S. Mallat, *A Wavelet Tour of Signal Processing*, École Polytechnique, Paris, France, 2nd edition, 1990.
[18] G. P. Miroshnichenko and A. G. Petrashen, "Numerical methods," Saint-Petersburg, p. 120, 2008.

Hindawi Publishing Corporation
Mathematical Problems in Engineering
Volume 2010, Article ID 829484, 14 pages
doi:10.1155/2010/829484

Research Article

Effects of Time Delay and Noise on Asymptotic Stability in Human Quiet Standing Model

Caihong Wang and Jian Xu

School of Aerospace Engineering and Applied Mechanics, Tongji University, Shanghai 200092, China

Correspondence should be addressed to Jian Xu, xujian@mail.tongji.edu.cn

Received 25 December 2009; Revised 12 May 2010; Accepted 2 September 2010

Academic Editor: Carlo Cattani

A human quiet standing stability is discussed in this paper. The model under consideration is proposed to be a delayed differential equation (DDE) with multiplicative white noise perturbation. The method of the center manifold is generalized to reduce a delayed differential equation to a two-dimensional ordinary differential equation, to study delay-induced instability or Hopf bifurcation. Then, the stochastic average method is employed to obtain the Itô equation. Thus, the top Lyapunov exponent is calculated and the necessary and sufficient condition of the asymptotic stability in views of probability one is obtained. The results show that the exponent is related to not only the strength of noise but also the delay, namely, the reaction speed of brain. The effect of the strength of noise on the human quiet standing losing stability is weak for a small delay. With the delay increasing, such effect becomes stronger and stronger. A small change in the strength of noise may destabilize the quiet standing for a large delay. It implies that a person with slow reaction is easy to lose the stability of his/her quiet standing.

1. Introduction

The human quiet standing model is complex neuromuscular control biological system with time delay. The time delay reflects finite transmission related to the transport or processing of matter, energy, and signals through the systems [1, 2]. Noise is an immanent property in biological systems, and such stochasticity may arise from muscle contractions as well as imperfections, and nervous system operates under the very noisy environment in the balance control system. Previous experimental studies have shown that the movement of the pressure center during quiet standing is stochastic and obeys a correlated random walk [3, 4]. For healthy people, balancing body stability is an easy task. However, older people or some patients often find walking difficult and need to put more effort in quiet standing. To help these groups, the principles making quiet standing must be discovered firstly. As the gravitational force destabilizes the inverted-pendulum-like skeletal system,

the study of human balance stability is extremely essential. However, serious difficulties will be encountered because of the combination of delay and stochastic processes when the qualitative stochastic differential delay system is investigated in human quiet standing.

In recent years, many researchers have studied the postural control system in quiet standing [5–21]. Experimentally, human quiet standing has most often been investigated in terms of the center of pressure (COP) trajectories [3, 10]. The time-delayed model is studied by the measurements of the transfer function which is based on statistical quantities such as the root mean square of the COP trajectory [9, 11]. In 2004, Verdaasdonk et al. [12] have computed the branches of fold and Hopf bifurcation by numerical bifurcation analysis of the inverted pendulum human model indicated that the period of the stable limit cycles, emerging beyond the Hopf branch, will increase with increasing time delay. Bottaro et al. [13] have indicated that the control in postural sway during quiet standing is intermittent, but not continuous. The effects of delay for the human reaction during balancing system without stochastic perturbation have been studied in [5–7]. In 2002, based on the investigation of a delayed random walk with an unstable fixed point, it has been observed that the random walker with delay moves away from the unstable fixed point more slowly than with the absence of delay [15]. The deterministic Hopf bifurcation has been qualitatively discussed with the help of stochastic delayed differential equations (DDEs) by Yao et al., but the stochastic effect was only made by numerical analysis [18]. In [19], a novel modeling approach to such two-feedback posture control has been proposed using a system of stochastic delay differential equations with two delays and noise as well as a drifting fixed point meant to represent the slower fluctuation of the COM. Effects of time delay on the dynamics behavior of the human quiet standing systems are a subject of many experimental studies, while the study on simultaneous consideration of time delay and stochastic excitation is very limited. Most of researches about the time-delay human standing model still with stochastic perturbation are studied by numerical simulation.

In this paper, we consider the single inverted pendulum model proposed by Eurich et al. [9, 11, 18, 19]. The single inverted pendulum with an antagonistic muscle pair represents a person who tries to maintain an upright position by flexing and extending the ankles. Influence of delay and noise on the Hopf bifurcation and asymptotic stability will be analyzed theoretically. However, it becomes infinite-dimensional problem due to considering the time delay in quiet standing system, which increases work difficulty. In stochastic systems, theoretically studied methods about bifurcation and stability are rare. Existing research methods are limited, such as the stability of a linearly controlled system with time delay subjected to Gaussian white noise which has been investigated using the top Lyapunov exponent calculated from Monte Carlo simulation by Grigoriu [22]. The asymptotic Lyapunov stability with probability one for quasi-integrable and nonresonant Hamiltonian systems with time-delayed feedback control has been studied in terms of the stochastic average method [23]. Asymptotic techniques, such as Taylor series expansion, integral averaging method, Fourier series, and perturbation methods, are often used under the assumption of small delays. However, these methods will be invalid for a large delay. Therefore, we will reduce a stochastic DDE to a stochastic ordinary differential equation (ODE) on the center manifold by adopting the center manifold method which has been proved by Arnold and Boxler [24]. The existence of the stochastic center manifold has been also proved in [24–26]. If a stochastic DDE is reduced to a stochastic ODE, then this ODE on the centre manifold may be converted into amplitude and phase relations and corresponding scalar bifurcation equations of amplitude may be obtained in terms of the integral averaging method [27].

The paper is organized as follows. In Section 2, the human quiet standing model is introduced and the conditions of Hopf bifurcation are computed in order to obtain regions of stability and instability. Section 3 is devoted to effects of time delay and noise on the asymptotic stability of the human dynamics with stochastic perturbation. Section 4 analyzes the application to balance. Finally, we draw conclusions.

2. The Model and Linearized Analysis

In this paper, we use a simplified single inverted pendulum model for the human in quiet standing with stochastic perturbation [6, 8, 16] :

$$I\ddot{\theta} + \gamma\dot{\theta} - mgL\sin\theta = \tilde{f}(\theta(t-\tau)) + \tilde{c}\eta(t)\theta(t), \tag{2.1}$$

where I represents the moment of inertia of human body around the ankle, θ the tilt angle, g the gravity acceleration, m the body mass, L the distance from the ankle joint to the body COM (Center of Mass), γ the damping coefficient, $f(x(t))$ the postural sway feedback function, τ the time delay, and $\eta(t)$ a stochastic process of zero mean value Gauss white noise.

Let $q = L\sin\theta$, where x is the transverse displacement of the gravity center. Then (2.1) can be rewritten as follows:

$$\ddot{q} = \frac{mgL}{I}q - \frac{r}{I}\dot{q} + f + \tilde{\tilde{b}}\eta(t)q(t). \tag{2.2}$$

Then (2.2) can be written as

$$\dot{x}(t) = ax(t) + bf(x(t-\tau)) + c\eta(t)x(t), \tag{2.3}$$

where

$$x(t) = q + d\dot{q}, \qquad a = \frac{mgL}{I}\left(\frac{r}{I} + \sqrt{\frac{r^2}{I^2} + 4\frac{mgL}{I}}\right) > 0, \qquad d = \frac{r}{I} + \sqrt{\frac{r^2}{I^2} + 4\frac{mgL}{I}}, \tag{2.4}$$

and $b < 0$ is the feedback coefficient. The feedback function $f(x(t))$ should be in the form of a smoothed on-off switch at some delayed time τ_0 for proprioception at the ankles, so we take $f(x(t-\tau)) = \tanh[x(t-\tau)]$ in this paper. Since $\tanh[x(t)] = x(t) - (1/3)x^3(t) + o(x^4)$ by the Taylor expansion, then (2.2) becomes

$$\dot{x}(t) = ax(t) + bx(t-\tau) - \frac{b}{3}x^3(t-\tau) + c\eta(t)x(t) + o\left(x^4\right). \tag{2.5}$$

The linear part of (2.2) is given by

$$\dot{x}(t) = ax(t) + bx(t-\tau). \tag{2.6}$$

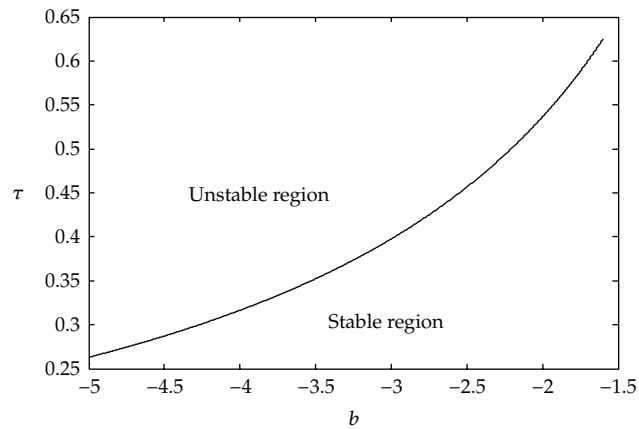

Figure 1: The critical values of τ_0 under Hopf bifurcation.

Trial exponential solutions of the form $x(t) = e^{\lambda t}$, $x(t-\tau) = e^{\lambda}(t-\tau)$ yield the transcendental characteristic equation

$$\Delta(\lambda, \tau) = a + be^{-\lambda\tau} - \lambda = 0. \tag{2.7}$$

The stability of system (2.3) depends on the real parts sign of the roots in (2.5). Let $\lambda = v + iw$ be a root of the characteristic equation (2.7), where v and w take real values. Substituting this expression into (2.7), and equating the real and imaginary parts to zero, we have a pair of algebraic equations

$$v = a + be^{-v\tau}\cos w\tau, \qquad w = -be^{-v\tau}\sin\, w\tau. \tag{2.8}$$

The transversality condition by the implicit function theorem is

$$\mathrm{Re}\left(\frac{dv}{d\tau}\right) = be^{-v\tau}\left(-\frac{\partial v}{\partial \tau}\tau - v\right)\cos w\tau - wbe^{-v\tau}\sin w\tau \neq 0. \tag{2.9}$$

As a necessary condition for Hopf bifurcation, we have to put $v = 0$ in (2.8). The following algebraic equations are obtained:

$$w = \pm\sqrt{b^2 - a^2}, \qquad a + b\cos\tau\sqrt{b^2 - a^2} = 0. \tag{2.10}$$

Varying the coefficient a and keeping $a = 1.6$, one can draw the parametric place (b, τ) as Figure 1, namely, stability region diagram.

3. Stability of the Hopf Bifurcation

We have obtained the conditions that system (2.3) undergoes a Hopf bifurcation at the equilibrium point $(0, 0)$ when bifurcation parameter τ passes through the critical value.

In this section, the bifurcating stability of system (2.3) at τ_0 will be presented by employing the central manifold reduction and stochastic average method.

3.1. The Stochastic ODE

In this section, we derive the center manifold of the nonlinear stochastic ODEs which reduce the DDE with infinite dimension to ODE with two dimension. To this end, let $t = \tau s$, $u(t) = x(t\tau)$. By rescaling the time to normalize the delay, system (2.5) is equivalent to the following equation

$$\dot{u}(t) = \tau\left(au(t) + bu(t-1) - \frac{b}{3}u^3(t-1) + cu(t)\eta(t)\right) + o\left(u^4(t-1)\right). \tag{3.1}$$

We choose the delay τ as bifurcation parameter, which is subject to a small change $\varepsilon\mu$ from its critical value τ_0, namely, $\tau = \tau_0 + \varepsilon\mu$. The values of u, c have been rescaled, and we obtain $u \to \varepsilon^{1/2}u$, $c \to \varepsilon^{1/2}c$, $0 < \varepsilon \ll 1$. Then (3.1) can be rewritten as follows:

$$\dot{u}_t(0) = \tau_0(au_t(0) + bu_t(-1)) + \varepsilon\mu(au_t(0) + bu_t(-1)) + g\left(\mu, u_t(-1)\right), \tag{3.2}$$

where $u_t(\theta) = u(t+\theta)$, $\theta \in [-\tau, 0]$.

The linear part of (3.2) is given by

$$\dot{u}(t) = \tau_0(au(t) + bu(t-1)) + \varepsilon\mu(au(t) + bu(t-1)). \tag{3.3}$$

Since $0 < \varepsilon \ll 1$, the nonlinear part is given by

$$g\left(\mu, u_t\right) = -\frac{b}{3}\tau u_t^3(-1) + \varepsilon^{-1/2}\tau c\eta(t)u_t(0). \tag{3.4}$$

Let $L_\mu : C[-1,0] \to R$, which is a one-parameter family of bounded continuous linear operator. Then

$$L(0)u_t = \tau_0(au_t(0) + bu_t(-1)), \qquad L(\mu)u_t = \mu(au_t(0) + bu_t(-1)). \tag{3.5}$$

By Riesz representation theorem, there exists a bounded function $\zeta(\theta, \mu)$ in $[-1,0] \to R$ for any $\phi \in C[-1,0]$, such that

$$L(0)\phi = \int_{-1}^{0} [d\zeta(\theta)]\phi(\theta), \qquad L(\mu)\phi = \int_{-1}^{0} \left[d\zeta(\theta,\mu)\right]\phi(\theta), \tag{3.6}$$

where

$$\zeta(\theta,\mu) = \tau_0(a\delta(\theta) + b\delta(\theta+1)) \quad (\delta(\theta) \text{ is Dirac function}),$$

$$A(0)\phi = \begin{cases} \dfrac{d\phi(\theta)}{d\theta} & \text{for } \theta \in [-1,0), \\ L(0)\phi & \text{for } \theta = 0, \end{cases}$$

$$A(\mu)\phi = \begin{cases} \dfrac{d\phi(\theta)}{d\theta} & \text{for } \theta \in [-1,0), \\ L(\mu)\phi & \text{for } \theta = 0, \end{cases} \tag{3.7}$$

$$D\phi = \begin{cases} 0 & \text{for } \theta \in [-1,0), \\ g(t,\phi) & \text{for } \theta = 0. \end{cases}$$

In order to study Hopf bifurcation problem conveniently, we can rewrite (3.2) as a function differential equation (FDE)

$$\dot{u}_t = A(0)u_t + \varepsilon A(\mu)u_t + \varepsilon D u_t. \tag{3.8}$$

The adjoint equation of (3.3) is given by

$$\dot{w}\left(\hat{t}\right) = -\tau_0\left(aw\left(\hat{t}\right) + bw\left(\hat{t}+1\right)\right) \quad \hat{C} := ([0,1], R). \tag{3.9}$$

The corresponding operator A^* of A is defined by

$$A^*(\mu)\psi = \begin{cases} -\dfrac{d\psi(s)}{ds}, & s \in (0,1], \\ \displaystyle\int_{-1}^{0} \left[d\zeta^T(s,\mu)\right]\psi(-s), & s = 0, \end{cases} \tag{3.10}$$

and the bilinear relation

$$\begin{gathered} (\psi_j(s), \phi_k(\theta)) = (\psi_j(0), \phi_k(0)) + \tau_0 b \int_{-1}^{0} \psi_j(\xi+1)\phi_k(\xi)d\xi, \\ \psi_j(s) \in \hat{C}, \quad \phi_k(\theta) \in C, \quad j,k = 1,2, \end{gathered} \tag{3.11}$$

where $\hat{C}$ is the dual space of C, $\Phi \in C, \Psi \in \hat{C}$. Hale and his colleagues have shown that there exist two disjoint subspaces P, Q as $C = P \oplus Q$. From the Hopf bifurcation conditions given in the previous section, we know the subspace P is the eigenspace corresponding to the eigenvalues $\pm wi$ of $\Delta(\lambda,\tau) = 0$ at Hopf bifurcation, and Q is the infinite-dimensional complementary subspace associated with the remaining eigenvalues $\Delta(\lambda,\tau) = 0$. For the particular eigenvalues $\lambda_{1,2} = \pm wi$, we have $\phi(\theta) = \Phi(\theta)\beta \in C$ $(-1 \le \theta \le 0)$ and $\psi(s) = \Psi(s)\hat{\beta} \in \hat{C}$ $(0 \le s \le 1)$, where the values $\Phi(\theta) = [\phi_1(\theta), \phi_2(\theta)]$ and $\Psi(s) = [\psi_1(s), \psi_2(s)]^{\mathrm{T}}$.

We define the elements of the initial continuous function $\phi(\theta) \in C$, projections $\phi^P(\theta), \phi^Q(\theta)$ onto the center, and stable subspaces $P, Q \in C$. Through the initial function $\phi(\theta) \in C$, suppose $x_t(\phi(\theta), \mu, \varepsilon) \in C$ be the unique solution of (2.1). Then we have the representations

$$u_t(\phi(\theta), \mu, \varepsilon) = u_t^P(\phi(\theta), \mu, \varepsilon) + u_t^Q(\phi(\theta), \mu, \varepsilon), \tag{3.12}$$

and $\phi(\theta) = \phi^P(\theta) + \phi^Q(\theta)$, where $x_t^P(\phi(\theta), \mu, \varepsilon)$, $\phi^P(\theta) \in P$ and $x_t^Q(\phi(\theta), \mu, \varepsilon)$, $\phi^Q(\theta) \in Q$. Making a change of variables $x_t^P(\theta) = \Phi(\theta)y(t) + x_t^Q(\theta)$ with $y(t) = (\overline{\Psi}(s), \phi(\theta)) \in R^2$, then the center manifold stochastic ODEs of the generalized eigenspace $P \in C$ can be obtained:

$$\dot{y}(t) = By(t) + \varepsilon\overline{\Psi}(0)g(\mu, y(t)), \tag{3.13}$$

where the values B and $\overline{\Psi}(0)$ are obtained in Appendix A.

We obtain

$$\begin{aligned}
\dot{y}_1(t) &= -wy_2 - \varepsilon p_1\Big(a\mu y_1(t) + b\mu\big(y_1(t)\cos w\theta + y_2(t)\sin w\theta\big) \\
&\qquad -\frac{1}{3}b\tau\big(y_1(t)\cos w\theta - y_2(t)\sin w\theta\big)^3 + \varepsilon^{-1/2}\tau c\eta(t)y_1(t)\Big), \\
\dot{y}_2(t) &= wy_1 - \varepsilon p_2\Big(a\mu y_1 + b\mu\big(y_1(t)\cos w\theta + y_2(t)\sin w\theta\big) \\
&\qquad -\frac{1}{3}b\tau\big(y_1(t)\cos w\theta + y_2(t)\sin w\theta\big)^3 + \varepsilon^{-1/2}\tau c\eta(t)y_1(t)\Big),
\end{aligned} \tag{3.14}$$

where

$$p_1 = \frac{-\varphi_{22}}{\varphi_{11}\varphi_{22} - \varphi_{12}^2}, \qquad p_2 = \frac{\varphi_{12}}{\varphi_{11}\varphi_{22} - \varphi_{12}^2}. \tag{3.15}$$

Carrying out a change of variables from (y_1, y_2) to (z_1, z_2), namely,

$$z_1 = y_1 - \frac{p_1}{p_2}y_2, \qquad z_2 = y_2 - \frac{p_1}{p_2}wy_1. \tag{3.16}$$

we obtain expressions for (y_1, y_2)

$$\begin{aligned}
y_1 &= \frac{p_2^2}{p_2^2 + p_1^2w^2}\left(z_1 + \frac{p_1}{p_2}wz_2\right), \\
y_2 &= \frac{p_2^2}{p_2^2 + p_1^2w^2}\left(z_2 - \frac{p_1}{p_2}wz_1\right).
\end{aligned} \tag{3.17}$$

Then the centre manifold stochastic ODEs (3.14) become

$$\begin{aligned}
\dot{z}_1(t) &= -wz_2,\\
\dot{z}_2(t) &= wz_1 - \varepsilon\frac{p_2^2+p_1^2w}{p_2}\Big(-\frac{1}{3}b\tau\big(p_{11}z_1(t)+p_{12}z_2(t)\big)^3\\
&\qquad + \mu\big(q_{11}z_1(t)+q_{12}z_2(t)\big) + \varepsilon^{-1/2}\tau c\eta(t)\big(g_{11}z_1(t)+g_{12}z_2(t)\big)\Big),
\end{aligned} \tag{3.18}$$

where

$$\begin{aligned}
p_{11} &= \frac{p_2^2}{p_2^2+p_1^2w^2}\Big(\cos w - \frac{p_1}{p_2}w\sin w\Big), \qquad p_{12} = \frac{p_2^2}{p_2^2+p_1^2w^2}\Big(\sin w + \frac{p_1}{p_2}w\cos w\Big),\\
q_{11} &= \frac{p_2^2}{p_2^2+p_1^2w^2}\Big(a + b\cos w - \frac{bp_1}{p_2}w\sin w\Big), \qquad g_{11} = \frac{p_2^2}{p_2^2+p_1^2w^2},\\
q_{12} &= \frac{p_2^2}{p_2^2+p_1^2w^2}\Big(\frac{p_1}{p_2}(a+bw\cos w) + \sin w\Big), \qquad g_{12} = \frac{p_2p_1w}{p_2^2+p_1^2w^2}.
\end{aligned} \tag{3.19}$$

Then, using the relations $z_1 = \beta(t)\sin\Theta$, $z_2 = -\beta(t)\sin\Theta$, and $\Theta = wt + \varphi(t)$, (3.18) is transformed to the following system with polar coordinates:

$$\begin{aligned}
\dot{\beta}(t) &= \varepsilon\frac{p_2^2+p_1^2w}{p_2^2}\beta\Big(-\frac{1}{3}b\beta^2\tau\big(p_{11}\sin\Theta - p_{12}\cos\Theta\big)^3\\
&\qquad + \mu\big(q_{11}\sin\Theta - q_{12}\cos\Theta\big) + \varepsilon^{-1/2}\tau c\eta(t)\big(g_{11}\sin\Theta - g_{12}\cos\Theta\big)\Big)\cos\Theta,\\
\dot{\varphi}(t) &= -\varepsilon\frac{p_2^2+p_1^2w}{p_2^2}\Big(-\frac{1}{3}b\tau\beta^2\big(p_{11}\sin\Theta - p_{12}\cos\Theta\big)^3\\
&\qquad + \mu\big(q_{11}\sin\Theta - q_{12}\cos\Theta\big) + \varepsilon^{-1/2}\tau c\eta(t)\big(g_{11}\sin\Theta - g_{12}\cos\Theta\big)\Big)\sin\Theta.
\end{aligned} \tag{3.20}$$

3.2. The Maximum Lyapunov Exponent

In the above subsection, we reduce the system to a two-dimensional ordinary differential equation (3.20). According to the Khasminskii limit theorem, we obtain the averaging Itô stochastic equations of (3.20) as follows:

$$\begin{aligned}
d\beta(t) &= \frac{p_2^2+p_1^2w}{p_2^2}\varepsilon\beta\Big(\frac{1}{8}b\tau\big(p_{11}^2p_{12}+p_{12}^3\big)\beta^2 - \frac{1}{2}q_{12}\mu + \frac{p_2^2+p_1^2w}{4p_2^2}\tau^2\big(g_{11}^2+g_{12}^2\big)c^2\Big)dt\\
&\quad + \varepsilon^{1/2}\frac{\sqrt{2\big(g_{11}^2+3g_{12}^2\big)}\big(p_2^2+p_1^2w\big)}{4p_2^2}\tau\beta c\,dw_1,
\end{aligned} \tag{3.21a}$$

$$d\varphi(t) = \varepsilon \frac{p_2^2 + p_1^2 w}{p_2^2}\left(\frac{1}{8} b\tau\left(p_{11}^3 + p_{11}p_{12}^2\right)\beta^2 - \frac{1}{2} q_{11}\mu\right)dt + \varepsilon^{1/2}\frac{\sqrt{2(3g_{11}^2 + g_{12}^2)}(p_2^2 + p_1^2 w)}{4p_2^2}\tau c dw_2, \tag{3.21b}$$

where w_1, w_2 are independent standard Wiener processes. The averaged amplitude and phase of (3.21a) and (3.21b) are uncoupled, so we study stability using the averaged amplitude equation (3.21a). To examine the stability of $\beta_0(t)$, let $\beta(t) = \beta_0(t) + r(t)$ and $\rho(t) = \ln r(t)$, where $r(t)$ represents a small variation around the stationary solution $\beta_0(t)$ when $d\beta(t) = 0$, and using the stochastic differential rule to Itô, we will obtain the linearized Itô equation governing $r(t)$ and $\rho(t)$, namely,

$$\begin{aligned} dr(t) &= \frac{p_2^2 + p_1^2 w}{p_2^2}\varepsilon r\left(\frac{3}{8} b\tau\left(p_{11}^2 p_{12} + p_{12}^3\right)\beta_0^2 - \frac{1}{2} q_{12}\mu + \frac{p_2^2 + p_1^2 w}{4p_2^2}\tau^2\left(g_{11}^2 + g_{12}^2\right)c^2\right)dt \\ &\quad + \varepsilon\frac{1}{2}\frac{\sqrt{2(g_{11}^2 + 3g_{12}^2)}(p_2^2 + p_1^2 w)}{4p_2^2}\tau r c dw_1, \\ d\rho(\mathrm{t}) &= \frac{p_2^2 + p_1^2 w}{p_2^2}\varepsilon\left(\frac{3}{8} b\tau\left(p_{11}^2 p_{12} + p_{12}^3\right)\beta_0^2 - \frac{1}{2} q_{12}\mu + \frac{p_2^2 + p_1^2 w}{4p_2^2}\tau^2\left(g_{11}^2 + g_{12}^2\right)c^2\right)dt \\ &\quad + \varepsilon^{1/2}\frac{\sqrt{2(g_{11}^2 + 3g_{12}^2)}(p_2^2 + p_1^2 w)}{4p_2^2}\tau c dw_1. \end{aligned} \tag{3.22}$$

Sample stability of the stochastic dynamical system is determined by the qualitative evaluation of the Lyapunov exponents. According to the multiplicative ergodic theorem [28], the top Lyapunov exponent λ of the amplitude process is obtained as

$$\lambda = \frac{p_2^2 + p_1^2 w}{p_2^2}\varepsilon\left[\frac{3}{8} b\tau\left(p_{11}^2 p_{12} + p_{12}^3\right)E\left[\beta_0^2\right] - \frac{1}{2} q_{12}\mu + \frac{p_2^2 + p_1^2 w}{4p_2^2}\tau^2\left(g_{11}^2 + g_{12}^2\right)c^2\right], \tag{3.23}$$

where $E[\beta_0^2]$ denotes the expected value of β_0^2. For the trivial solution $\beta_0^2 = 0$, (3.23) gives $\lambda = -(1/2)q_{12}\mu + ((p_2^2 + p_1^2 w)/4p_2^2)\tau^2(g_{11}^2 + g_{12}^2)c^2 = 0$. Thus, the trivial solution is asymptotically stable with probability one (w.p.1) if $\lambda < 0$, that is, $\mu < (g_{11}^2 + g_{12}^2)\tau^2 c^2((p_2^2 + p_1^2 w)/2p_2^2 q_{12})$ and $q_{12} > 0$ and unstable when $q_{12} < 0$.

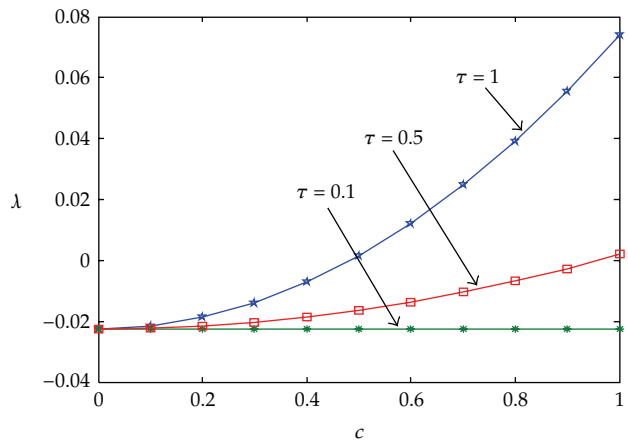

Figure 2: The top Lyapunov exponent λ max of system (2.1) versus noise intensity for different values of time delay, $\tau \cdot a = 1, \quad b = -2, \quad \varepsilon = 0.1, \quad \mu = 0.1$.

From Figure 2, we can observe that the top Lyapunov exponent λ increases as the excitation intensity c or time delay τ increases. The original system is stable if $\lambda < 0$ and unstable if $\lambda > 0$. When $\tau = 1.0$, the system (2.1) becomes unstable at $c = 0.447214$. The effect of the strength of noise on the human quiet standing losing stability is weak when time delay $\tau = 0.10$. Obviously, the systems (2.1) is easily unstable if time delay τ is larger for the fixed excitation intensity c. A small change in the strength of noise may destabilize the quiet standing for a large delay.

4. Conclusions

The primary purpose of this paper is to study effects of delay and noise on asymptotic stability of the human quiet standing system with stochastic excitation. For the deterministic quiet standing system, its stable conditions, namely, the Hopf bifurcation, are presented and the regions of stability and instability are discussed. On one hand, by using proper variable transform, the second model for the human standing is changed into a first one. The given relation expressions between coefficients and physical quantities are practically significant too. On the other hand, the method of the center manifold reduction is generalized to investigate the asymptotic stability when the quiet standing system is subjected to a stochastic perturbation or the white noise. Compared to numerical methods, this analytical method permits some general conclusions for the classes of feedback functions. The necessary and sufficient conditions of the stability are obtained approximately by computing the largest Lyapunov exponent of the linearized stochastic ordinary differential system. The relation among the delay, the strength of noise, and the top Lyapunov exponent is represented in the parameter figure. The results show that the exponent is related not only to the strength of noise but also to the delay, namely, the reaction speed of brain, but such relation is not linear. In fact, the effect of the strength of noise on the human quiet standing losing stability is weak for a small delay. With the delay increasing, such effect becomes stronger and stronger. A small change in the strength of noise may destabilize the quiet standing for a large delay. It implies that a person with slow reaction easily lose the stability of his/her quiet standing. This conclusion is in agreement with observation in the real life.

This may be of great help in diagnosing and treating some disease in this paper. However, noise is not always bad for cognitive performance, and moderate noise is beneficial for cognitive performance. Recently, it has been shown that noise can enhance human body balance via a mechanism known as stochastic resonance (SR) [29–31]. In the future, we will demonstrate the facilitating effects of SR by qualitative mathematical method.

Appendix

A. The Computation of the B and $\overline{\Psi}(0)$

The values of the basis $\Phi(\theta) \in \mathrm{C}$ for P is given by

$$\begin{aligned}\phi(\theta) = \Phi(\theta)\beta = \left[\phi_1(\theta), \phi_2(\theta)\right] &= \alpha_1 e^{iw\theta} + \alpha_2 e^{-iw\theta} \\ &= \left[(\alpha_1 + \alpha_2)\cos w\theta, i(\alpha_1 - \alpha_2)\sin w\theta\right] = \left[\cos w\theta, -\sin w\theta\right]\begin{bmatrix}\beta_1 \\ \beta_2\end{bmatrix},\end{aligned} \tag{A.1}$$

where

$$\alpha_1 = p + iq, \quad \alpha_2 = p - iq, \quad \alpha_1 + \alpha_2 = 2p = \beta_1, \quad i(\alpha_1 - \alpha_2) = -2q = \beta_2. \tag{A.2}$$

Similarly, the basis $\psi(s) \in \widehat{C}$ for $\widehat{P}$ is of the form

$$\Psi(s) = \begin{pmatrix}\psi_1(s) \\ \psi_2(s)\end{pmatrix} = \begin{pmatrix}\cos ws \\ -\sin ws\end{pmatrix}, \quad 0 \le s \le 1. \tag{A.3}$$

The inner product matrix $(\psi(s), \phi(\theta)) = (\psi_j(s), \phi_k(\theta)), \quad i, j = 1, 2$ is given by

$$\left(\psi(s), \phi(\theta)\right) = \begin{pmatrix}\cos ws \cos w\theta & -\cos ws \sin\ w\theta \\ \sin ws \cos w\theta & \sin ws \sin\ w\theta\end{pmatrix}. \tag{A.4}$$

The elements $(\psi_j(s), \phi_k(\theta))$ substitute into the bilinear relation (3.11), which gives the nonsingular matrix

$$(\Psi, \Phi)_{nsg} = \begin{pmatrix}\psi_{11} & \psi_{12} \\ \psi_{21} & \psi_{22}\end{pmatrix}, \tag{A.5}$$

where

$$\begin{aligned}
\psi_{11} &= 1 + b\tau_0 \int_{-1}^{0} \cos w(\xi+1)\cos w\xi d\xi = 1 + \frac{b\tau_0}{2}\left(\frac{1}{w}\sin w + \cos w\right),\\
\psi_{12} &= -b\tau_0 \int_{-1}^{0} \cos w(\xi+1)(\sin w\xi) d\xi = \frac{b\tau_0}{2}\sin w,\\
\psi_{21} &= -b\tau_0 \int_{-1}^{0} \sin w(\xi+\tau)\cos w\xi d\xi = -\frac{b}{2}\sin w,\\
\psi_{22} &= b\tau_0 \int_{-1}^{0} \sin w(\xi+1)\sin w\xi d\xi = \frac{b\tau_0}{2}\left(-\frac{1}{w}\sin w + \cos w\right).
\end{aligned} \tag{A.6}$$

Then, the basis $\Psi(s) \in \widehat{P}$ in $\widehat{C}$ of the adjoint (3.9) is normalized to $\overline{\Psi}(s) = [\overline{\varphi}_1(s), \overline{\varphi}_2(s)]^T \in \widehat{C}$. By computing

$$(\Psi,\Phi)_{nsg}^{-1} = \frac{1}{\det(\Psi,\Phi)_{nsg}}\begin{pmatrix} \psi_{22} & -\psi_{21} \\ -\psi_{12} & \psi_{11} \end{pmatrix} = \frac{1}{\psi_{11}\psi_{22} - \psi_{12}^2}\begin{pmatrix} \psi_{22} & -\psi_{21} \\ -\psi_{12} & \psi_{11} \end{pmatrix}, \tag{A.7}$$

we obtain

$$\overline{\Psi}(s) = (\Psi,\Phi)_{nsg}^{-1}\Psi(s) = \frac{1}{\psi_{11}\psi_{22} - \psi_{12}^2}\begin{pmatrix} \psi_{22} & -\psi_{21} \\ -\psi_{12} & \psi_{11} \end{pmatrix}\begin{pmatrix} \psi_1(s) \\ \psi_2(s) \end{pmatrix} = \begin{pmatrix} \overline{\varphi}_1(s) \\ \overline{\varphi}_2(s) \end{pmatrix}, \tag{A.8}$$

where

$$\begin{aligned}
\overline{\varphi}_1(s) &= \frac{1}{\psi_{11}\psi_{22} - \psi_{12}^2}\left(\psi_{22}\cos ws - \psi_{21}\sin ws\right),\\
\overline{\varphi}_2(s) &= \frac{1}{\psi_{11}\psi_{22} - \psi_{12}^2}\left(-\psi_{12}\cos ws - \psi_{11}\sin ws\right).
\end{aligned} \tag{A.9}$$

Then, we have

$$\overline{\Psi}(0) = \frac{1}{\psi_{11}\psi_{22} - \psi_{12}^2}\begin{pmatrix} \psi_{22} \\ -\psi_{12} \end{pmatrix}. \tag{A.10}$$

The substitution of the elements $(\overline{\varphi}_j(s), \phi_k(\theta))$, $j,k = 1,2$ into the bilinear relation (3.11) will yield the 2×2 identity matrix, namely,

$$(\Psi,\Phi)_{id} = \frac{1}{\psi_{11}\psi_{22} - \psi_{12}^2}\begin{pmatrix} \psi_{11}\psi_{22} - \psi_{12}^2 & 0 \\ 0 & \psi_{11}\psi_{22} - \psi_{12}^2 \end{pmatrix} = \begin{pmatrix} 1 & 0 \\ 0 & 1 \end{pmatrix}. \tag{A.11}$$

Defining the constant matrix $B \in C, \widehat{B} \in \widehat{C}$, the elements of B, $\widehat{B}$ at Hopf bifurcation are $B \equiv \widehat{B} = \left(\begin{smallmatrix} 0 & -w \\ w & 0 \end{smallmatrix}\right)$, which satisfy $A(\mu)\Phi(\theta) = \Phi(\theta)B$, $\widehat{A}(\mu)\Psi(s) = \Psi(s)\widehat{B}$. On the basis of algebraic simplifications

$$e^{B\theta} = I + B\theta + \frac{(B\theta)^2}{2!} + \frac{(B\theta)^3}{3!} + \cdots = \begin{pmatrix} \cos w\theta & -\sin w\theta \\ \sin w\theta & \cos w\theta \end{pmatrix}, \tag{A.12}$$

the following formulas can be easily obtained

$$\begin{aligned} \Phi(\theta) &= \Phi(0)e^{B\theta} = \begin{pmatrix} \cos w\theta & -\sin w\theta \end{pmatrix}, \quad -1 \le \theta \le 0, \\ \Psi(s) &= \Psi(0)e^{-\widehat{B}S} = \begin{pmatrix} \cos w\theta & -\sin w\theta \end{pmatrix}^{\mathrm{T}}, \quad 0 \le s \le 1. \end{aligned} \tag{A.13}$$

Acknowledgment

This paper is supported by the State Key Program of National Natural Science of China under Grant no. 11032009 and the National Science Foundation for Distinguished Young Scholars of China under Grant no. 10625211.

References

[1] U. an der Heiden, "Delays in physiological systems," *Journal of Mathematical Biology*, vol. 8, no. 4, pp. 345–364, 1979.
[2] G. Stepan, "Delay effects in brain dynamics," *Philosophical Transactions of the Royal Society A: Mathematical, Physical and Engineering Sciences*, vol. 367, no. 1891, pp. 1059–1062, 2009.
[3] J. J. Collins and C. J. de Luca, "Open-loop and closed-loop control of posture: a random-walk analysis of center-of-pressure trajectories," *Experimental Brain Research*, vol. 95, no. 2, pp. 308–318, 1993.
[4] J. L. Cabrera and J. G. Milton, "On-off intermittency in a human balancing task," *Physical Review Letters*, vol. 89, no. 15, Article ID 158702, 4 pages, 2002.
[5] G. Haller and G. Stépán, "Micro-chaos in digital control," *Journal of Nonlinear Science*, vol. 6, no. 5, pp. 415–448, 1996.
[6] E. Enikov and G. Stépán, "Microchaotic motion of digitally controlled machines," *Journal of Vibration and Control*, vol. 4, no. 4, pp. 427–443, 1998.
[7] G. Stépán and L. Kollár, "Balancing with reflex delay," *Mathematical and Computer Modelling*, vol. 31, no. 4-5, pp. 199–205, 2000.
[8] A. J. van Soest and L. A. Rozendaal, "The inverted pendulum model of bipedal standing cannot be stabilized through direct feedback of force and contractile element length and velocity at realistic series elastic element stiffness," *Biological Cybernetics*, vol. 99, no. 1, pp. 29–41, 2008.
[9] C. W. Eurich and J. G. Milton, "Noise-induced transitions in human postural sway," *Physical Review E*, vol. 54, no. 6, pp. 6681–6684, 1996.
[10] H. Nakata and K. Yabe, "Automatic postural response systems in individuals with congenital total blindness," *Gait and Posture*, vol. 14, no. 1, pp. 36–43, 2001.
[11] J. Milton, J. L. Cabrera, T. Ohira et al., "The time-delayed inverted pendulum: implications for human balance control," *Chaos*, vol. 19, no. 2, Article ID 026110, 12 pages, 2009.
[12] B. W. Verdaasdonk, H. F. J. M. Koopman, S. A. van Gils, and F. C. T. van der Helm, "Bifurcation and stability analysis in musculoskeletal systems: a study in human stance," *Biological Cybernetics*, vol. 91, no. 1, pp. 48–62, 2004.
[13] A. Bottaro, Y. Yasutake, T. Nomura, M. Casadio, and P. Morasso, "Bounded stability of the quiet standing posture: an intermittent control model," *Human Movement Science*, vol. 27, no. 3, pp. 473–495, 2008.
[14] F. Moss and J. G. Milton, "Medical technology: balancing the unbalanced," *Nature*, vol. 425, no. 6961, pp. 911–912, 2003.

[15] T. Hosaka, T. Ohira, C. Luciani, J. L. Cabrera, and J. G. Milton, "Balancing with noise and delay," *Progress of Theoretical Physics Supplement*, vol. 161, pp. 314–319, 2006.
[16] K. Masani, A. H. Vette, N. Kawashima, and M. R. Popovic, "Neuromusculoskeletal torque-generation process has a large destabilizing effect on the control mechanism of quiet standing," *Journal of Neurophysiology*, vol. 100, no. 3, pp. 1465–1475, 2008.
[17] Y. Asai, Y. Tasaka, K. Nomura, T. Nomura, M. Casadio, and P. Morasso, "A model of postural control in quiet standing: robust compensation of delay-induced instability using intermittent activation of feedback control," *PLoS ONE*, vol. 4, no. 7, article e6169, 2009.
[18] W. Yao, P. Yu, and C. Essex, "Delayed stochastic differential model for quiet standing," *Physical Review E*, vol. 63, no. 2, Article ID 021902, 8 pages, 2001.
[19] J. Boulet, R. Balasubramaniam, A. Daffertshofer, and A. Longtin, "Stochastic two-delay differential model of delayed visual feedback effects on postural dynamics," *Philosophical Transactions of the Royal Society A: Mathematical, Physical and Engineering Sciences*, vol. 368, no. 1911, pp. 423–438, 2010.
[20] J. Milton, J. L. Townsend, M. A. King, and T. Ohira, "Balancing with positive feedback: the case for discontinuous control," *Philosophical Transactions of the Royal Society A: Mathematical, Physical and Engineering Sciences*, vol. 367, no. 1891, pp. 1181–1193, 2009.
[21] G. Stepan, "Delay effects in the human sensory system during balancing," *Philosophical Transactions of the Royal Society A: Mathematical, Physical and Engineering Sciences*, vol. 367, no. 1891, pp. 1195–1212, 2009.
[22] M. Grigoriu, "Control of time delay linear systems with Gaussian white noise," *Probabilistic Engineering Mechanics*, vol. 12, no. 2, pp. 89–96, 1997.
[23] Z. H. Liu and W. Q. Zhu, "Asymptotic Lyapunov stability with probability one of quasi-integrable Hamiltonian systems with delayed feedback control," *Automatica*, vol. 44, no. 7, pp. 1923–1928, 2008.
[24] L. Arnold and P. Boxler, "Eigenvalues, bifurcation, and center manifolds in the presence of noise," in *Differential Equations (Xanthi, 1987)*, C. M. Dafermos, G. Ladas, and G. Papanicolaou, Eds., vol. 118 of *Lecture Notes in Pure and Applied Mathematics*, pp. 33–48, Dekker, New York, NY, USA, 1989.
[25] J. Hale, *Theory of Functional Differential Equations*, Springer, New York, NY, USA, 2nd edition, 1977.
[26] G. Stepan, *Retarded Dynamical Systems*, Longman, Harlow, UK, 1989.
[27] R. L. Stratonovich, "On stochastic processes defined by differential equations with small parameter," *Theoretical Probability*, pp. 390–406, 1966.
[28] Y. I. Oseledec, "A multiplicative ergodic theorem: Lyapunov characteristic number for dynamical systems," *Transactions of the Moscow Mathematical Society*, vol. 19, pp. 197–231, 1968.
[29] S. Guillouzic, I. L'Heureux, and A. Longtin, "Small delay approximation of stochastic delay differential equations," *Physical Review E*, vol. 59, no. 4, pp. 3970–3982, 1999.
[30] D. C. Gravelle, C. A. Laughton, N. T. Dhruv et al., "Noise-enhanced balance control in older adults," *NeuroReport*, vol. 13, no. 15, pp. 1853–1856, 2002.
[31] A. A. Priplata, B. L. Patritti, J. B. Niemi et al., "Noise-enhanced balance control in patients with diabetes and patients with stroke," *Annals of Neurology*, vol. 59, no. 1, pp. 4–12, 2006.

Hindawi Publishing Corporation
Mathematical Problems in Engineering
Volume 2010, Article ID 853679, 16 pages
doi:10.1155/2010/853679

Research Article

Getting a Suitable Terminal Cost and Maximizing the Terminal Region for MPC

Wang Ya-feng,[1,2] Sun Fu-chun,[2] Zhang You-an,[1] Liu Hua-ping,[2] and Min Haibo[2]

[1] *Department of Control Engineering, Naval Aeronautical and Astronautical University, Yantai 264001, China*
[2] *Department of Computer Science and Technology, Tsinghua University, Beijing 100084, China*

Correspondence should be addressed to Wang Ya-feng, wyfyxy@sina.com

Received 23 November 2009; Revised 25 February 2010; Accepted 30 August 2010

Academic Editor: Irina N. Trendafilova

The model predictive control (MPC) subject to control and state constraint is studied. Given a terminal cost, a terminal region is obtained through iterative estimation by using support vector machine (SVM). It is proved that the obtained terminal region is the largest terminal region when the terminal cost is given. The relationships between terminal cost and terminal region and between terminal cost and total cost are discussed, respectively. Based on these relationships, a simple method to get a suitable terminal cost is proposed and it can be adjusted according to our need. Finally, some experiment results are presented.

1. Introduction

Model predictive control also known as receding horizon control has become quite popular recently. The key advantage is its ability to handle control and state constraints. It was pointed out in [1] that what MPC solves is the standard optimal control (SOC) problem except that it uses the finite-horizon optimization (some paper used quasi-infinite horizon optimization, such as [2, 3]) to replace the infinite-horizon optimization of SOC and the control is computed online.

Generally, to say that an MPC is good or bad, it is contrasted with SOC from two aspects: the domain of attraction and the total cost (the wasted performance index from initial time to infinity). If an MPC has a larger domain of attraction and for any initial state point the total cost is fewer than those of another MPC, it is considered as a better MPC. In MPC, there are three factors playing important roles in its performances on the two aspects as just mentioned: the prediction horizon, the terminal region, and the terminal cost. As known to all, lengthening the prediction horizon, the domain of attraction will be enlarged and the

total cost will decrease, but the computation burden of online optimization will increase. Recently, many attentions have concentrated on the latter two factors: (I) how to get a large terminal region? (II) and how to get a suitable terminal cost? Here, only some typical papers are listed. Chen and Allgöwer [2] presented a terminal cost by using SOC method based on the linearized model of system and took an ellipsoidal set in which the state can be drived to the equilibrium point by linear feedback control as the terminal region. Cannon et al. [4] used a polytopic set to replace the ellipsoidal set. De Doná et al. [5] took the stabilizable region of using saturated control as the terminal region. Ong et al. [6] got a very large stabilizable region and a terminal cost of using linear feedback control via support vector machine. Limon et al. [7] proved that, for MPC without terminal state constraint in its on-line optimization, the terminal region will be enlarged by weighting the terminal cost. Most of these papers have a common shortage; the terminal region is computed under a precondition; some explicit controller was given in advance, like linear feedback controller and saturated controller. So, the computed terminal region is somewhat conservative, in other words, it is not the largest one.

In this paper, a novel method is proposed to get a terminal state region. Given a terminal cost, a set sequence is obtained by using one-step set contraction iteratively. It is proved that, when the iteration time goes to infinity, this set sequence will converge to the maximal terminal region. In this sequence, each set is estimated by using support vector machine (SVM, see [7, 8] for details). Next, the relationships between terminal cost and terminal region and between terminal cost and total cost are discussed, respectively. Then, a simple method to get a suitable terminal cost according to our need is given. Finally, some experiment results are presented.

2. The Relationship between SOC and MPC

As mentioned, MPC is an approximation to SOC, and SOC is the counterpoint to evaluate MPC. Here, the study on MPC begins with the comprehension of SOC. Consider the discrete-time system as follows:

$$x_{k+1} = f(x_k, u_k), \tag{2.1}$$

where $x_k \in R^n$, $u_k \in R^m$ are the state and the input of the system at sampling time $t = k$, respectively. $x_{k+1} \in R^n$ is the successor state and the mapping $f : R^{n+m} \mapsto R^n$ with $f(\mathbf{0}, \mathbf{0}) = \mathbf{0}$ is known. The system is subject to constraints on both state and control action, and they are given by $x_k \in X, u_k \in U$, where X is a closed set and U a compact set, both of them containing the origin. The control objective is usually to steer the state to the origin.

The optimization problem $P_\infty(x_0)$ of SOC at the initial state x_0 can be stated as follows:

$$\begin{gathered}\min_{u(i,x_0)\in U} J_\infty(\mathbf{u}, x_0) = \sum_{i=0}^{\infty} q(x(i,x_0), u(i,x_0)),\\ \text{s.t. } x(i+1,x_0) = f(x(i,x_0), u(i,x_0)),\\ x(i+1,x_0) \in X, \quad u(i,x_0) \in U,\end{gathered} \tag{2.2}$$

where $x(0, x_0) = x_0$, $q(x, u)$ is the stage cost and its form is chosen as $q(x, u) = x^T Q x + u^T R u$ in which Q, R are positive definites.

It is well known that the stability is guaranteed if $P_\infty(x_0)$ has feasible solution. Here, assume that the solution of $P_\infty(x_0)$ is known if it has the following. $J^*_\infty(x_0)$ is defined as the solution, $u^*_\infty(i,x_0)$, $i = 1,2,\ldots,\infty$, the optimal control trajectory and $x^*_\infty(i,x_0)$, the corresponding state trajectory. As is well known, $J^*_\infty(x_0)$ is the total cost of using $u^*_\infty(i,x_0)$ to drive x_0 to 0.

But solving $P_\infty(x_0)$ is not an easy job, especially when f is nonlinear. To avoid this problem, the infinite-horizon optimization of SOC can be approximated by the finite-horizon optimization of MPC (As mentioned, quasi-infinite horizon optimization was used in [2, 3]. For convenience, we consider it to belong to the frame of finite-horizon optimization).

Similarly, the optimization problem $P_N(x_0)$ of MPC at the initial state x_0 can be stated as

$$\begin{gathered}\min_{u(i,x_0)\in U} J_N(\mathbf{u},x_0) = \sum_{i=0}^{N-1} q(x(i,x_0),u(i,x_0)) + F(x(N,x_0)),\\ \text{s.t. } x(i+1,x_0) = f(x(i,x_0),u(i,x_0)),\\ x(i+1,x_0)\in X,\quad u(i,x_0)\in U,\quad x(N,x_0)\in X_f,\end{gathered} \tag{2.3}$$

where N is prediction horizon, X_f is terminal region, and F is terminal cost satisfying $F(\mathbf{0}) = 0$ and $F(x) \geq \alpha(\|x\|)$, (the mapping $\alpha : R_+ \mapsto R_+$ satisfying $\alpha(0) = 0$ is continuous and strictly increasing, where $R_+ = \{x \in R \mid x > 0\}$).

There exist many optimization algorithms to compute the solution of $P_N(x_0)$. Let $J^*_N(x_0)$ be the solution, $\mathbf{u}^*_N(x_0)=\{u^*_N(0,x_0),\ldots,u^*_N(N-1,x_0)\}$, $\mathbf{x}^*_N(x_0)=\{x^*_N(0,x_0),\ldots,x^*_N(N-1,x_0)\}$ be the optimal control trajectory and corresponding predicted state trajectory of $P_N(x_0)$, respectively.

At sampling time $t = 0$, $u^*_N(0,x_0)$ is inputted to the system. At the next sampling time $t = 1$, $x_1 = f(x_0,u^*_N(0,x_0))$ is outputted, and the control input $u^*_N(0,x_1)$ can be computed by solving the optimization problem $P_N(x_1)$. By repeating this procedure, two trajectories can be obtained: $\mathbf{u}_{\mathrm{RH}}(x_0)=\{u^*_N(0,x_0),u^*_N(0,x_1),\ldots\}$, $\mathbf{x}_{\mathrm{RH}}(x_0)=\{x_0,x_1,\ldots\}$. Here, for convenience, they are called as the receding horizon control trajectory and the receding horizon state trajectory of MPC with $P_N(x_0)$, respectively.

The introduction of X_f and F in (2.3) is to guarantee the closed loop stability of system.

Lemma 2.1. *Define $\Gamma_N := \{x_0 \in X \mid x^*_N(N,x_0) \in X_f\}$. For any $x_0 \in \Gamma_N$ if X_f and F satisfy two conditions as follows:*

(C1) *F being a Lyapunov function, more strictly, for any $x \in X_f$, there exists*

$$F(x) \geq \min_{u\in U}\{q(x,u) + F(f(x,u))\}, \tag{2.4}$$

(C2) *X_f being an invariant set. In other words, one has $f(x,u) \in X_f$. Here, u is the control in (C1).*

It is guaranteed that, x will be led to 0 by using $\mathbf{u}_{\mathrm{RH}}(x_0)$. Γ_N is called the domain of attraction.

The proof can be found in [1].

Obviously, the optimal choice of $F(x(N,x_0))$ is $J_\infty(x(N,x_0))$. The total cost with this choice is $J_\infty(x_0)$, namely it is the least one. But, as mentioned, J_∞ can not be obtained generally, so other ways should be found to get F. Certainly, the closer it approaches to J_∞, the better it is. When F is given, X_f can be found to satisfy the conditions (C1) and (C2). There are many X_f satisfying the conditions and different X_f will be obtained by different methods. But, to make the domain of attraction the largest, it is wished that the largest X_f can be obtained. Here, define $X_{f,\max}$ as the largest terminal region when F is given, and in the next section, a novel method to get $X_{f,\max}$ will be proposed.

3. Maximizing the Terminal Region for MPC

Until now, there exist many methods to construct X_f. As mentioned, these methods have a common basic idea: some controller like linear feedback controller or saturation controller is given in advance, then a stabilizable domain of using this controller is computed and works as the terminal region of MPC. It is obvious that this kind of construction is somewhat conservative and the X_f computed by using this method does not approximate to $X_{f,\max}$ to the largest extent.

In this paper, a novel method is proposed in which X_f is constructed directly from conditions (C1) and (C2).

3.1. Approximating the Largest Terminal Region Asymptotically

Define X_f as

$$X_f := \left\{ x \in X \mid F(x) \geq F^*_{X_f}(x) \right\}, \tag{3.1}$$

where $F^*_{X_f}(x) = \min F_{X_f}(x)$ is the solution of the following optimization problem:

$$\begin{gathered} \min_{u \in U} F_{X_f}(x) = q(x,u) + F\big(f(x,u)\big), \\ \text{s.t. } f(x,u) \in X_f. \end{gathered} \tag{3.2}$$

Obviously, for an $x \in X$, it cannot be decided whether x belongs to X_f from (3.1) and (3.2) when X_f is unknown. The difficulty is that the state constraint in the optimization (3.2) uses the X_f itself. To avoid it, the method of asymptotic approximation is adopted. Firstly, an initial set X_f^0 which can be obtained by the following discriminant is given:

$$X_f^0 := \left\{ x \in X \mid F(x) \geq F^*_{X_f^0}(x) \right\}, \tag{3.3}$$

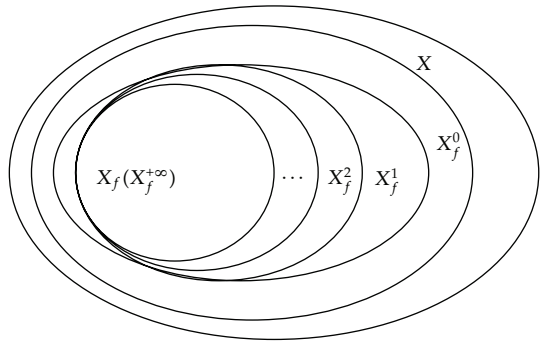

Figure 1: The approximation of $X_{f,\max}$.

where $F^*_{X_f^0}(x)$ is the solution of

$$\min_{u\in U} F_{X_f^0}(x) = q(x,u) + F\big(f(x,u)\big),$$
$$\text{s.t. } f(x,u) \in X. \tag{3.4}$$

Then, using X_f^0 instead of X in the state constraint in optimization of (3.4), X_f^1 can be obtained. One by one, $X_f^2 X_f^3, \ldots$ will be obtained. The whole procedure can be pictured as in Figure 1.

In Figure 1, X_f^1 is defined as

$$X_f^1 := \left\{ x \in X_f^0 \mid F(x) \geq F^*_{X_f^1}(x) \right\}, \tag{3.5}$$

where $F^*_{X_f^1}(x)$ is the solution of

$$\min_{u\in U} F_{X_f^1}(x) = q(x,u) + F\big(f(x,u)\big),$$
$$\text{s.t. } f(x,u) \in X_f^0. \tag{3.6}$$

Similarly, X_f^j can be defined as?

$$X_f^j := \left\{ x \in X_f^{j-1} \mid F(x) \geq F^*_{X_f^j}(x) \right\}, \tag{3.7}$$

and $F^*_{X_f^j}(x)$ is the solution of

$$\min_{u\in U} F_{X_f^j}(x) = q(x,u) + F\big(f(x,u)\big),$$
$$\text{s.t. } f(x,u) \in X_f^{j-1}. \tag{3.8}$$

Obviously, as Figure 1 shows, there exists $X_f^0 \supseteq X_f^1 \supseteq \cdots \supseteq X_f^j \supseteq X_f$. As j increases, X_f^j will converge to a set denoted by $X_f^{+\infty}$. But, whether is $X_f^{+\infty}$ the terminal region we want? Theorem 3.1 provides the answer to this question.

Theorem 3.1. *For X_f^j defined in* (3.7), *when j goes to infinity, X_f^j will converge to $X_{f,\max}$, namely, as $j \to +\infty$, one has $X_f^j \to X_{f,\max}$.*

This theorem is proved by contradiction.

Proof. (A) Assume that there exists X_{spo} which satisfies $X_{\text{spo}} \supset X_{f,\max}$ and $X_f^j \to X_{\text{spo}}$, as $j \to +\infty$ then for any $x \in X_{\text{spo}}$, we have $F(x) \geq \min_{u\in U}\{q(x,u) + F(f(x,u))\}$ and $f(x,u) \in X_{\text{spo}}$. Obviously this is contradicted with $X_{f,\max}$ being the largest one satisfying (C1) and (C2).

(B) Similarly, assume that there exists X_{spo} which satisfies $X_{\text{spo}} \subset X_{f,\max}$ and $X_f^j \to X_{\text{spo}}$, as $j \to +\infty$, then there exists N with $0 \leq N < +\infty$ satisfying $X_f^N \supseteq X_{f,\max}$ and $X_{f,\max} \setminus X_f^{N+1} \neq \Phi$, where Φ denotes the empty set. Choose any $x \in X_{f,\max} \setminus X_f^{N+1}$, it is obviouse that, x satisfies $F(x) \geq \min_{u\in U}\{q(x,u) + F(f(x,u))\}$ and $f(x,u) \in X_{f,\max} \subseteq X_f^N$. On the other hand, we know that $x \in X_f^N$, so x meets the conditions in the definition of X_f^{N+1} and we have $x \in X_f^{N+1}$. This is contradicted with $x \in X_{f,\max} \setminus X_f^{N+1}$. □

Remark 3.2. Generally, in the computation of $X_{f,\max}$, it is impossible to keep computation until $j \to +\infty$. So, when the iteration goes to $j = N$, if X_f^N is equal to X_f^{N-1} in principle, X_f^N can be taken as the terminal region we want.

Remark 3.3. The terminal region computed through the method in Remark 3.2 is not $X_{f,\max}$ itself, but its enclosing set. Then, the corresponding domain of attraction may include some points which should not be in the real domain of attraction. To avoid this problem, the outspread skill from smaller region to larger one can be used to turn¡?ehlt?¿ the contraction skill from larger region to smaller one in this paper. The concrete algorithm is not presented here, just the general idea is stated; giving a known subset of $X_{f,\max}$, denoted by $X_{f,0}$ in advance and using $X_{f,0}$ to serve as the state constraint in (3.4), then a larger region $X_{f,1}$ will be computed. By the same procedure as presented in Section 3.1, a terminal region which is a subset of $X_{f,\max}$ will be gotten.

To obtain X_f^j is not an easy job. The only tool is statistical learning method. Here, the SVM is used.

3.2. Support Vector Machine

SVM (see [8, 9]) is the youngest part of statistical learning theory. It is an effective approach for pattern recognition. In SVM approach, the main aim of an SVM classifier is obtaining a function, which determines the decision boundary or hyperplane. This hyperplane optimally separates two classes of input data points.

Take the example of separating X into A and $X \setminus A$. For each $x_i \in A$, an additional variable $y_i = +1$ is introduced. Similarly, for each $x_i \in X \setminus A$, $y_i = -1$ is introduced. Define

$I^+ := \{i : y_i = +1\}$, $I^- := \{i : y_i = -1\}$. SVM is used to find a separating hyperplane $O(x) := w \cdot \phi(x_i) + b = 0$, between A and $X \setminus A$. Then, we obtain an estimated set of A, $\widehat{A} = \{x \in X \mid O(x) \geq 0\}$. $O(x)$ can be obtained by solving the following problem:

$$\begin{gathered}\min_{\alpha} \frac{1}{2}\sum_i\sum_j \alpha_i\alpha_j y_i y_j \ker(x_i, x_j) - \sum_i \alpha_i, \\ \text{s.t.} \sum_i \alpha_i y_i = 0, \\ 0 \leq \alpha_i \leq C, \quad \forall i \in I^+, \quad \alpha_i \geq 0, \quad \forall i \in I^-,\end{gathered} \tag{3.9}$$

where ker denotes the kernel function.

In this paper, the following Gaussian kernel is used:

$$\ker(x, x_i) = \exp\left(-\frac{\|x - x_i\|^2}{2\sigma^2}\right), \tag{3.10}$$

with σ being the positive Gaussian kernel width.

There are many software packages of SVM available on internet. They can be downloaded and used directly. By using SVM, the support vectors are extracted from $\{x_i\}$ and their relevant weights are exported. Denote P_s as the number of support vectors and X_s as the support vectors set, the optimal hyperplane is described as follows:

$$O(x) = \sum_{i=1}^{P_s} w_i \cdot \ker(x_i, x) + b, \tag{3.11}$$

where $x_i \in X_s$ is a support vector, and $w_i = \alpha_i y_i$ satifying $\sum_{i=1}^{P_s} w_i = 0$ is the relevant weight.

3.3. Estimating the Largest Terminal Region

In SVM classifier, the training data is inputted and the hyperplane will be outputted. To us, the training of data is the only job.

Take the separation of X_f^0 from X as an example. Firstly, choose arbitrary points $x_i \in X$, $i = 1, 2, \ldots, N_p$ (N_p is the number of training points) then decide the value of y_i corresponding to x_i by using the following procedure

If $F(x_i) \geq F^*_{X_f^0}(x_i)$,

$y_i = +1$; else $y_i = -1$

endif.

When all the y_i for all the x_i are gotten, they can be packed to constitute the training data. Then, by inputting the training data into SVM classifier, an optimal hyperplane $O^0(x) = 0$ and an estimated set of X_f^0, $\widehat{X}_f^0 = \{x \in X \mid O^0(x) \geq 0\}$ will be obtained.

When $\widehat{X}_f^0$ is known, the training data for separating X_f^1 from X_f^0 can be known by the similar procedure. By inputting them into SVM classifier, a hyperplane $O^1(x) = 0$ and an estimated set of X_f^1, $\widehat{X}_f^1 = \{x \in X \mid O^1(x) \geq 0\}$ will be gotten.

Repeatedly, a hyperplane series $O^j(x) = 0$, $j = 1, 2, \ldots$ will be obtained. When $j = N$ if it is satisfied that, for $x_i \in X_{\sup,N-1}$, $i = 1, 2, \ldots, N_{\sup,N-1}$, there exists

$$\sum_{i=1}^{N_{\sup,N-1}} \left\| O^N(x_i) - O^{N-1}(x_i) \right\| \leq \varepsilon N_{\sup,N-1}, \tag{3.12}$$

it is deemed that $\widehat{X}_f^N$ is equal to $\widehat{X}_f^{N-1}$ in principle and $\widehat{X}_f^N$ is taken as the final estimation of $X_{f,\max}$. Where $X_{\sup,N-1}$ is the support vectors set at $j = N - 1$, $N_{\sup,N-1}$ is the number of support vectors and ε is a tunable threshold. The smaller it is, the higher the precision of $\widehat{X}_f^N$ approximating to $X_{f,\max}$ is.

Remark 3.4. Here, we used the information that, in SVM classifier, the hyperplanes are decided just on the support vectors.

4. Choosing an Appropriate Terminal Cost

In the previous chapter, a method to maximize the terminal region was proposed, but the method has a premise: the terminal cost is given in advance. In this chapter, how to get a terminal cost will be shown. Before this, some properties of terminal cost will be analyzed.

4.1. Weighting Terminal Cost, the Domain of Attraction Will Be Enlarged

From conditions (C1) and (C2), it is known that the terminal region is based on the choice of the terminal cost. We want to know what the relationship between them is and this relationship will give us what messages when we choose terminal cost. Theorem 4.1 will give us the answer.

Denote $X_{f,\max}$, $X_{\lambda,\max}$ as the terminal regions of $P_N(x_0)$ and $P_{N,\lambda}(x_0)$ with a weighted terminal cost λF, $\lambda \geq 1$, respectively. Limon et al. [7] proved that the terminal region will be enlarged by weighting the terminal cost for MPC without terminal constraint in its on-line optimization. Here, we will show that, this property will also hold water in our case.

Theorem 4.1. *Consider F and $X_{f,\max}$ satisfying conditions (C1) and (C2). When a weighted terminal cost λF, $\lambda \geq 1$ is used, the corresponding terminal region $X_{\lambda,\max}$ is larger than $X_{f,\max}$, namely, $X_{f,\max} \subseteq X_{\lambda,\max}$.*

Proof. For any $x_0 \in X_{f,\max}$, the conditions of (C1) and (C2) are equivalent to the fact that there exists a control trajectory $\mathbf{u} = \{u_0, u_1, u_2, \ldots\}$ to make the following inequalities stand up:

$$F(x_i) \geq q(x_i, u_i) + F(x_{i+1}), \quad i = 0, 1, 2, \ldots, \tag{4.1}$$

where $x_{i+1} = f(x_i, u_i)$.

It is obvious that, when the terminal cost is λF, these inequalities also stand up using the same control trajectory

$$\lambda F(x_i) \geq q(x_i, u_i) + \lambda F(x_{i+1}). \tag{4.2}$$

So, we can see that $x_0 \in X_{\lambda,\max}$, namely, $X_{f,\max} \subseteq X_{\lambda,\max}$. □

Remark 4.2. When the prediction horizon is given, the larger the terminal region is, the larger the domain of attraction is. So Theorem 4.1 shows that, giving the prediction horizon, by weighting terminal cost, the domain of attraction will be enlarged.

4.2. Weighting Terminal Cost, the Total Cost Will Increase

It is known from the last section that, when the terminal cost is weighted, the terminal region is enlarged. So, can we weight the terminal cost arbitrarily? The answer is no. This section will tell us the reason the total cost will be increased by weighting the terminal cost.

Let $J^*_{N,\lambda}(x_0)$ be the solution of $P_{N,\lambda}(x_0)$, $\mathbf{u}^*_{N,\lambda}(x_0) = \{u^*_{N,\lambda}(0,x_0),\ldots,u^*_{N,\lambda}(N,x_0)\}$, $\mathbf{x}^*_{N,\lambda}(x_0) = \{x^*_{N,\lambda}(0,x_0),\ldots,x^*_{N,\lambda}(N,x_0)\}$ be the optimal control trajectory and corresponding state trajectory, respectively, and let $\mathbf{u}_{\mathrm{RH},\lambda}(x_0) = \{u^*_N(0,x_0),u^*_N(0,x_{1,\lambda}),\ldots\}$, $\mathbf{x}_{\mathrm{RH},\lambda}(x_0) = \{x_0,x_{1,\lambda},x_{2,\lambda},\ldots\}$ be the receding horizon control trajectory and receding horizon state trajectory of using MPC with $P_{N,\lambda}(x_0)$, respectively. Define $J_{\mathrm{RH},\lambda}(x_0)$, $J_{\mathrm{RH}}(x_0)$ as the total costs of using MPC with $P_{N,\lambda}(x_0)$ and with $P_N(x_0)$, respectively.

For convenience, consider an assumption.

Assumption 1. For any $x_0 \in \Gamma_N$, where Γ_N is the domain of attraction of MPC with $P_N(x_0)$, the terminal state by solving $P_{N,\lambda}(x_0)$ belongs to $X_{f,\max}$, that is to say $x^*_{N,\lambda}(N,x_0) \in X_{f,\max}$.

Remark 4.3. Assumption 1 means, for any $x_0 \in \Gamma_N$, that the solution of $P_{N,\lambda}(x_0)$ with $X_{\lambda,\max}$ as its terminal region is equal to that with $X_{f,\max}$ as its terminal region. A few points in Γ_N may not satisfy this assumption, for convenience, their influence is neglected. Under this assumption, it is obviouse that $J^*_{N,\lambda}(x_0) \geq J^*_N(x_0)$ and the following lemma holds water.

Lemma 4.4. *For any $x_0 \in \Gamma_N$, there exists*

$$\left(J^*_{N-1,\lambda} - J^*_{N-1}\right)\left(x^*_N(1,x_0)\right) \geq \left(J^*_{N-1,\lambda} - J^*_{N-1}\right)\left(x^*_{N,\lambda}(1,x_0)\right). \tag{4.3}$$

Proof. From the view of optimality, $J^*_N(x_0)$ can be expressed as

$$J^*_N(x_0) = q\left(x_0,u^*_N(0,x_0)\right) + J^*_{N-1}\left(x^*_N(1,x_0)\right). \tag{4.4}$$

Considering Assumption 1 and by optimality, there exists

$$J^*_N(x_0) \leq q\left(x_0,u^*_{N,\lambda}(0,x_0)\right) + J^*_{N-1}\left(x^*_{N,\lambda}(1,x_0)\right). \tag{4.5}$$

Similarly, $J^*_{N,\lambda}(x_0)$ can be expressed as

$$J^*_{N,\lambda}(x_0) = q\left(x_0,u^*_{N,\lambda}(0,x_0)\right) + J^*_{N-1,\lambda}\left(x^*_{N,\lambda}(1,x_0)\right). \tag{4.6}$$

And by optimality, there exists

$$J^*_{N,\lambda}(x_0) \leq q\left(x_0,u^*_N(0,x_0)\right) + J^*_{N-1,\lambda}\left(x^*_N(1,x_0)\right). \tag{4.7}$$

Obviously, the result of subtracting $J_N^*(x_0)$ from the right hand of (4.7) is bigger than the result of subtracting the right hand of (4.5) from $J_{N,\lambda}^*(x_0)$, in other words,

$$\begin{aligned}&\left(q\left(x_0, u_N^*(0,x_0)\right) + J_{N-1,\lambda}^*\left(x_N^*(1,x_0)\right)\right) - J_N^*(x_0)\\&\quad \geq J_{N,\lambda}^*(x_0) - \left(q\left(x_0, u_{N,\lambda}^*(0,x_0)\right) + J_{N-1}^*\left(x_{N,\lambda}^*(1,x_0)\right)\right).\end{aligned} \tag{4.8}$$

Finally, the following result can be obtained:

$$\left(J_{N-1,\lambda}^* - J_{N-1}^*\right)\left(x_N^*(1,x_0)\right) \geq \left(J_{N-1,\lambda}^* - J_{N-1}^*\right)\left(x_{N,\lambda}^*(1,x_0)\right). \tag{4.9}$$

□

Define $F_{\mathcal{K}}$ as a kind of $\mathcal{K}$ functions satisfying the following: for any $F_1, F_2 \in F_{\mathcal{K}}$, and $x_1, x_2 \in X$, there exists the following: if $F_1(x_1) \geq F_1(x_2)$, the inequality $F_2(x_1) \geq F_2(x_2)$ stands up.

To continue discussion, another assumption is needed.

Assumption 2. All of the positive cost functions used in this paper like J_{N-1}^*, J_N^*, $J_{N-1,\lambda}^*$, and $J_{N,\lambda}^*$ and the results of the addition or subtraction between them like $J_{N-1,\lambda}^* - J_{N-1}^*$, $J_{N-1,\lambda}^* + J_N^*$ belong to $F_{\mathcal{K}}$.

Based on Assumption 2 and Lemma 4.4, it is known that, for any $x_0 \in \Gamma_N$ and $F_{\mathcal{K}}$, there exists

$$F_{\mathcal{K}}\left(x_N^*(1,x_0)\right) \geq F_{\mathcal{K}}\left(x_{N,\lambda}^*(1,x_0)\right). \tag{4.10}$$

Then, by using (4.10) and Assumptions 1 and 2, another lemma which is a key for our study on this issue can be gotten.

Lemma 4.5. *Under Assumptions 1 and 2, for any $x_0 \in \Gamma_N$ and any positive cost function $F_{\text{tra}} \in F_{\mathcal{K}}$ satisfying $F_{\text{tra}} \leq J_{N-1}^*$, there exists*

$$q\left(x_0, u_N^*(0,x_0)\right) + F_{\text{tra}}(x_1) \leq q\left(x_0, u_{N,\lambda}^*(0,x_0)\right) + F_{\text{tra}}(x_{1,\lambda}). \tag{4.11}$$

Proof. Here, x_1 means $x_N^*(1,x_0)$ and $x_{1,\lambda}$ means $x_{N,\lambda}^*(1,x_0)$. From Assumption 2, it is known that $(J_{N-1}^* - F_{\text{tra}}) \in F_{\mathcal{K}}$, so there exists

$$\begin{aligned}&q\left(x_0, u_N^*(0,x_0)\right) + F_{\text{tra}}(x_1)\\&\quad = q\left(x_0, u_N^*(0,x_0)\right) + J_{N-1}^*(x_1) - \left(J_{N-1}^* - F_{\text{tra}}\right)(x_1)\\&\quad \leq q\left(x_0, u_{N,\lambda}^*(0,x_0)\right) + J_{N-1}^*(x_{1,\lambda}) - \left(J_{N-1}^* - F_{\text{tra}}\right)(x_{1,\lambda})\\&\quad = q\left(x_0, u_{N,\lambda}^*(0,x_0)\right) + F_{\text{tra}}(x_{1,\lambda}).\end{aligned} \tag{4.12}$$

Here, we used the fact that $J_N^*(x_0) \leq J_{N,\lambda}^*(x_0)$ and $(J_{N-1}^* - F_{\text{tra}})(x_1) \geq (J_{N-1}^* - F_{\text{tra}})(x_{1,\lambda})$.

□

Then, the reason why we cannot weight the terminal cost arbitrarily can be presented.

Theorem 4.6. *Under Assumptions 1 and 2, for any $x_0 \in \Gamma_N$, the following inequality stands up:*

$$J_{\mathrm{RH}}(x_0) \leq J_{\mathrm{RH},\lambda}(x_0). \tag{4.13}$$

Proof. It is obvious that J_N^* meets the condition in Lemma 4.5 because of $J_N^* \leq J_{N-1}^*$. Choose $F_{\mathrm{tra}} = J_N^*$ in Lemma 4.5. There exists

$$q(x_0, u_N^*(0, x_0)) + J_N^*(x_1) \leq q\left(x_0, u_{N,\lambda}^*(0, x_0)\right) + J_N^*(x_{1,\lambda}). \tag{4.14}$$

Similarly, for any $x \in \Gamma_N$, the following result can be obtained:

$$\begin{aligned} &q(x, u_N^*(0, x)) + J_N^*(x_N^*(1, x)) \\ &\quad \leq q(x, u_N^*(0, x)) + J_{N-1}^*(x_N^*(1, x)) = J_N^*(x) \leq J_{N-1}^*(x). \end{aligned} \tag{4.15}$$

So, choose

$$F_{\mathrm{tra}}(x) = q(x, u_N^*(0, x)) + J_N^*(x_N^*(1, x)). \tag{4.16}$$

By using x_1, $x_{1,\lambda}$ to replace x, respectively, there exists

$$\begin{aligned} &q(x_0, u_N^*(0, x_0)) + q(x_1, u_N^*(0, x_1)) + J_N^*(x_2) \\ &\quad = q(x_0, u_N^*(0, x_0)) + F_{\mathrm{tra}}(x_1) \\ &\quad \leq q\left(x_0, u_{N,\lambda}^*(0, x_0)\right) + F_{\mathrm{tra}}(x_{1,\lambda}) \\ &\quad = q\left(x_0, u_{N,\lambda}^*(0, x_0)\right) + q(x_{1,\lambda}, u_N^*(0, x_{1,\lambda})) + J_N^*(x_N^*(1, x_{1,\lambda})). \end{aligned} \tag{4.17}$$

From Assumption 1, it is known that, for $x_0 \in \Gamma_N$, there exists $x_{1,\lambda} \in \Gamma_N$. Replacing x_0 with $x_{1,\lambda}$ in (4.14), the following inequality can be gotten:

$$q(x_{1,\lambda}, u_N^*(0, x_{1,\lambda})) + J_N^*(x_N^*(1, x_{1,\lambda})) \leq q\left(x_{1,\lambda}, u_{N,\lambda}^*(0, x_{1,\lambda})\right) + J_N^*(x_{2,\lambda}). \tag{4.18}$$

So, there exists

$$\begin{aligned} &q(x_0, u_N^*(0, x_0)) + q(x_1, u_N^*(0, x_1)) + J_N^*(x_2) \\ &\quad \leq q\left(x_0, u_{N,\lambda}^*(0, x_0)\right) + q\left(x_{1,\lambda}, u_{N,\lambda}^*(0, x_{1,\lambda})\right) + J_N^*(x_{2,\lambda}) \\ &\quad \leq q\left(x_0, u_{N,\lambda}^*(0, x_0)\right) + q\left(x_{1,\lambda}, u_{N,\lambda}^*(0, x_{1,\lambda})\right) + J_{N,\lambda}^*((x_{2,\lambda})). \end{aligned} \tag{4.19}$$

Repeating this procedure, there exists

$$\begin{aligned} &q(x_0, u_N^*(0,x_0)) + \cdots + q(x_j, u_N^*(0,x_j)) + J_N^*(x_{j+1}) \\ &\quad \le q\left(x_0, u_{N,\lambda}^*(0,x_0)\right) + \cdots + q\left(x_{j,\lambda}, u_{N,\lambda}^*(0,x_{j,\lambda})\right) + J_{N,\lambda}^*((x_{j+1,\lambda})). \end{aligned} \tag{4.20}$$

Let $j \to +\infty$, the final result can be obtained as follows:

$$J_{\mathrm{RH}}(x_0) \le J_{\mathrm{RH},\lambda}(x_0). \tag{4.21}$$

□

Theorem 4.6 shows that, weighting the terminal cost, the total cost will be increased. So, when choosing a terminal cost, people should not only take into account the need of enlarging the terminal region.

4.3. Getting an Appropriate Terminal Cost

It was pointed out from Theorems 4.1 and 4.6 that the terminal cost is a double-edged sword. On its choice, two factors, the terminal region and the total cost, must be considered. With different emphasis, different terminal cost should be chosen.

Here, a simple method to get a terminal cost is presented, whose basic idea is getting an initial terminal cost in advance then adjusting it according to our need.

As mentioned, a good terminal cost should approximate to J_∞^* as close as possible. People can only achieve it in a small neighborhood around the origin by using SOC method, see [2] for continuous-time system.

Consider the linearization of the system (2.1) at the origin

$$x_{k+1} = Ax_k + Bu_k, \tag{4.22}$$

with $A = (\partial f/\partial x)(0,0)$ and $B = (\partial f/\partial u)(0,0)$.

Here, assume that (4.22) is stabilizable, then a terminal cost which serves as an initial candidate can be found through the following procedure.

Step 1. Solving the Riccati equation to get a preparatory G_0,

$$G_0 = A^T G_0 A - \left(A^T G_0 B\right)\left(B^T G_0 B + R\right)^{-1}\left(B^T G_0 A\right) + Q. \tag{4.23}$$

Step 2. Getting a locally stabilizing linear state feedback gain K,

$$K = -\left(B^T G_0 B + R\right)^{-1}\left(B^T G_0 A\right). \tag{4.24}$$

Step 3. Computing G_K by solving the following Riccati equation:

$$(\alpha A_K)^T G_K (\alpha A_K) - G_K = -Q_K, \tag{4.25}$$

where $A_K = A + BK$, $Q_K = Q + K^T RK$, and $\alpha \in [1, +\infty)$ is an adjustable parameter satisfying $\alpha|\lambda_{\max}(A_K)| < 1$.

Then, $F(x) = x^T G_K x$ can serve as an initial terminal cost. According to our need and the properties of terminal cost, the initial one can be adjusted to get an appropriate one, $F(x) = x^T(\lambda G_K)x$, $\lambda > 0$. For example, if a larger terminal region is wanted and the total cost is not cared, λ can be set to be a larger number; otherwise, if a lower total cost is demanded and the domain of attraction already covers the operating region of system, a small one can be used.

5. Simulation Experiment

The model is an approximate discrete-time realization from a continuous-time system used in [2] as follows:

$$\begin{bmatrix} x_1(k+1) \\ x_2(k+1) \end{bmatrix} = \begin{bmatrix} 1 & T \\ T & 1 \end{bmatrix} \begin{bmatrix} x_1(k) \\ x_2(k) \end{bmatrix} + \begin{bmatrix} T\mu \\ T\mu \end{bmatrix} u_k + \begin{bmatrix} T(1-\mu) & 0 \\ 0 & -4T(1-\mu) \end{bmatrix} \begin{bmatrix} x_1(k) \\ x_2(k) \end{bmatrix} u_k, \tag{5.1}$$

where $\mu = 0.5$, $T = 0.1$ s, and the state constraint and control constraint are $X = \{x \mid \|x\|_1 \le 4\}$, $U = \{u \mid |u| \le 2\}$, respectively.

The stage cost is chosen as $q(x, u) = x^T Qx + u^T Ru$ with $Q = 0.5I$ and $R = 1$. By using SOC method, the locally linear feedback gain is adopted as $K = -[2.0107 \;\; 2.0107]$ and $|\lambda_{\max}(A_K)| = 0.9000$ is obtained. Then, choose $\alpha = 1.11$ and get the terminal cost as $F(x) = x^T Gx$ with $G = [1107.356 \;\; 857.231; 857.231 \;\; 1107.356]$.

To estimate each X_f^j, 4000 training points are generated. Set $\varepsilon = 1$, when $j = 15$, there exists

$$\sum_{i=1}^{N_{\sup,14}} \left\| O^{15}(x_i) - O^{14}(x_i) \right\| \le \varepsilon N_{\sup,14}, \tag{5.2}$$

where $x_i \in X_{\sup,14}$, $X_{\sup,14}$ is the support vectors set at $j = 14$, and $N_{\sup,14}$ is the number of support vectors. Then, it is deemed that $\widehat{X}_f^{15}$ is equal to $\widehat{X}_f^{14}$ in principle and $\widehat{X}_f^{15}$ can be taken as the final estimation of $X_{f,\max}$. Figure 2 shows the approximation process of $X_{f,\max}$. The blue line is the hyperplane at $j = 1$, the black dot line is that at $j = 15$, and the red lines between them are those at $j = 2, 3, \ldots, 14$. Let the prediction horizon be $N = 3$. Figure 3 shows the closed-loop trajectories of some points chosen from the domain of attraction arbitrarily.

When the terminal cost is enlarged to $F(x) = x^T(10G)x$, a new terminal region larger than the old one can be obtained. Figure 4 shows it. The red line is the new hyperplane and the black dot line is the old one.

For convenience, let (A) denote the MPC using $x^T Gx$ as its terminal cost and (B) the MPC using $x^T(10G)x$. For some points chosen from Γ_3 of (A) arbitrarily, Figure 5 shows their

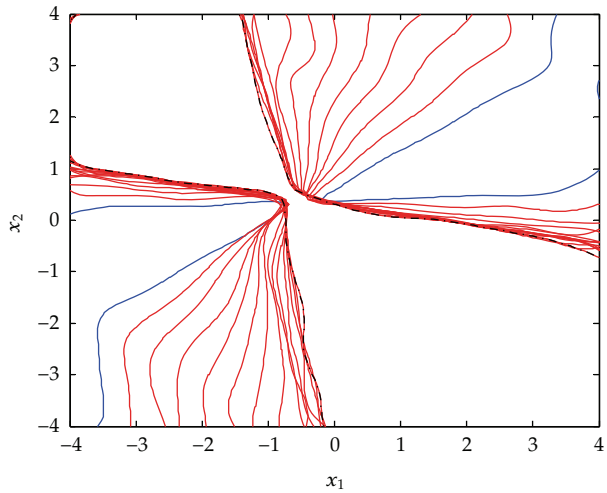

Figure 2: The approximation process of terminal region.

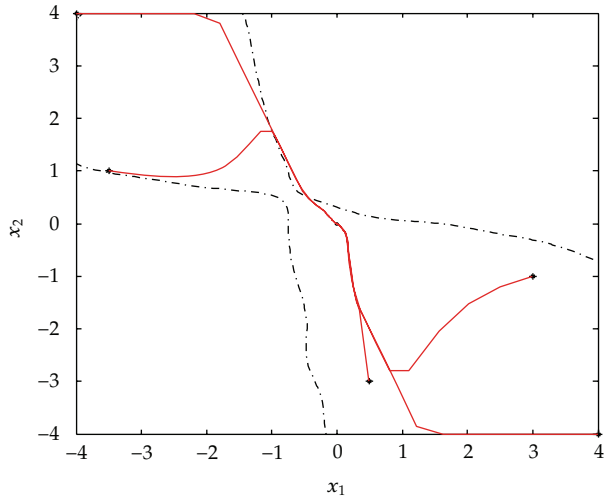

Figure 3: The closed-loop trajectories of points in Γ_3.

Table 1: Comparison of the total costs.

Initial points	$\begin{bmatrix} 2 \\ -1 \end{bmatrix}$	$\begin{bmatrix} 1 \\ -2 \end{bmatrix}$	$\begin{bmatrix} -1 \\ 2 \end{bmatrix}$	$\begin{bmatrix} -1 \\ 1 \end{bmatrix}$
(A)	34.7915	18.2460	16.4528	7.9936
(B)	37.0120	20.6714	23.2854	23.8467

closed-loop trajectories of using (A) and (B), respectively, where red lines denote the results of using (A), and blue dash-dotted lines denote the results of using (B). Table 1 shows the comparison of the total costs. Obviously, for the same point, the total cost of using (A) is smaller than that of using (B).

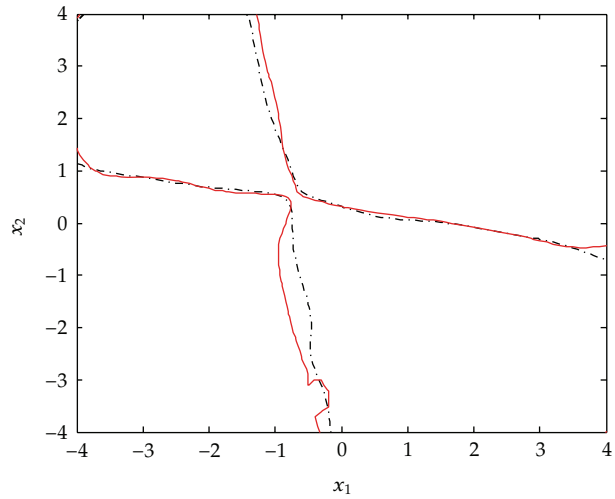

Figure 4: Comparison of the terminal regions.

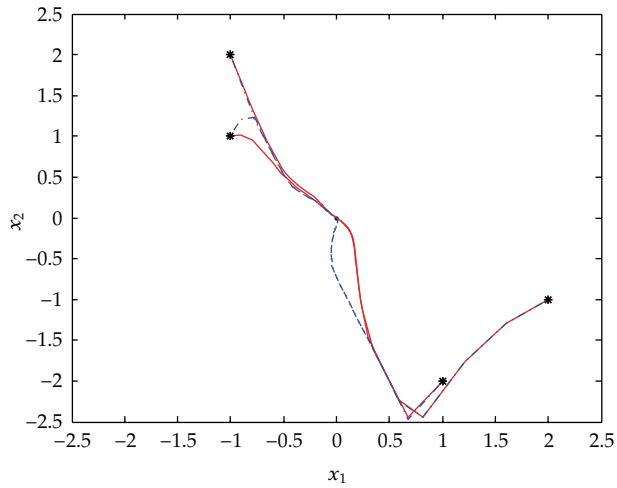

Figure 5: Comparison of the closed-loop trajectories.

6. Conclusion

This paper discussed the relationships between terminal cost and terminal region and between terminal cost and total cost, respectively. It showed that, by enlarging the terminal cost, terminal region will be enlarged, but the total cost will be increased too. A simple method to get a suitable terminal cost was proposed, it can be adjusted according to our need. For example, to get a larger terminal region, it can be weighted; to reduce the total cost, it can be unweighted. When a terminal cost was given, a novel method was proposed to receive a maximal terminal region by using SVM. With the same prediction horizon, its corresponding domain of attraction is the largest one.

References

[1] D. Q. Mayne, J. B. Rawlings, C. V. Rao, and P. O. M. Scokaert, "Constrained model predictive control: stability and optimality," *Automatica*, vol. 36, no. 6, pp. 789–814, 2000.
[2] H. Chen and F. Allgöwer, "A quasi-infinite horizon nonlinear model predictive control scheme with guaranteed stability," *Automatica*, vol. 34, no. 10, pp. 1205–1217, 1998.
[3] V. T. Minh and N. Afzulpurkar, "A comparative study on computational schemes for nonlinear model predictive control," *Asian Journal of Control*, vol. 8, no. 4, pp. 324–331, 2006.
[4] M. Cannon, V. Deshmukh, and B. Kouvaritakis, "Nonlinear model predictive control with polytopic invariant sets," *Automatica*, vol. 39, no. 8, pp. 1487–1494, 2003.
[5] J. A. De Doná, M. M. Seron, D. Q. Mayne, and G. C. Goodwin, "Enlarged terminal sets guaranteeing stability of receding horizon control," *Systems & Control Letters*, vol. 47, no. 1, pp. 57–63, 2002.
[6] C. J. Ong, D. Sui, and E. G. Gilbert, "Enlarging the terminal region of nonlinear model predictive control using the support vector machine method," *Automatica*, vol. 42, no. 6, pp. 1011–1016, 2006.
[7] D. Limon, T. Alamo, F. Salas, and E. F. Camacho, "On the stability of constrained MPC without terminal constraint," *IEEE Transactions on Automatic Control*, vol. 51, no. 5, pp. 832–836, 2006.
[8] C. C. Burges, "A tutorial on support vector machines for pattern recognition," *Data Mining and Knowledge Discovery*, vol. 2, no. 2, pp. 121–167, 1998.
[9] V. N. Vapnik, *The Nature of Statistical Learning Theory*, Springer, New York, NY, USA, 1995.

Hindawi Publishing Corporation
Mathematical Problems in Engineering
Volume 2010, Article ID 808019, 18 pages
doi:10.1155/2010/808019

Research Article

Nonlinear Filtering of Oscillatory Measurements in Cardiovascular Applications

Ranjan Vepa

School of Engineering and Materials Science, Queen Mary, University of London, London E14NS, UK

Correspondence should be addressed to Ranjan Vepa, r.vepa@qmul.ac.uk

Received 5 November 2009; Revised 4 February 2010; Accepted 13 March 2010

Academic Editor: Carlo Cattani

An array of nonidentical and locally connected chaotic biological neurons is modelled by a single representative chaotic neuron model based on an extension of the Hindmarsh-Rose neuron. This model is then employed in conjunction with the unscented Kalman filter to study the associated state estimation problem. The archetypal system, which was deliberately chosen to be chaotic, was corrupted with noise. The influence of noise seemed to annihilate the chaotic behaviour. Consequently it was observed that the filter performs quite well in reconstructing the states of the system although the introduction of relatively low noise had a profound effect on the system. Neither the noise-corrupted process model nor the filter gave any indications of chaos. We believe that this behaviour can be generalised and expect that unscented Kalman filtering of the states of a biological neuron is completely feasible even when the uncorrupted process model exhibits chaos. Finally the methodology of the unscented Kalman filter is applied to filter a typical simulated ECG signal using a synthetic model-based approach.

1. Introduction

Oscillatory signals in the cardiovascular region either originate directly from the sinoatrial node or one of the neurons as an action potential traverses to the ventricle myocytes. Alternatively they are functions or weighted sums of action potentials arising at spatially distributed points. To consider a range of oscillatory measurements in the cardiovascular region, it is important to consider the output of typical neuronal cell.

Neural information is mainly encoded in various firing patterns of a neuron, such as periodic spiking (or bursting) and chaotic spiking (or bursting), travelling among coupled neurons within a physiological domain of neurons such as the heart. The "action potential" is a spontaneously and rhythmically produced electrical impulse in a membrane of neuron cell that occurs during the firing of the neuron due to an exchange of charged ions inside

and outside a neural cell. Although not a definition, a dynamic system may be considered chaotic if it exhibits (i) sensitive dependence on the initial conditions and (ii) a number of dense orbits with a multiplicity of periods for a range of parameters. Two nonlinear dynamic systems with chaotic responses can sometimes exhibit the phenomenon of synchronization when the responses of the two lock in and seem to drive each other with a common feature such as the phase, phase-lag, amplitude, and envelope or even some generalised property that can be described in terms of a functional of the features of the response. Physiological observations have confirmed the existence of synchronous motion of neurons in different areas of the heart (Elson et al. [1], Pinto et al. [2], and Szucs et al. [3]). Synchronization of neurons is possible when a single neuron faithfully encodes the timing of successive peaks, burst, or spikes and a group of neurons can respond collectively to a common synaptic current. Moreover, a group of interacting coupled neurons can display various synchronous cardio-vascular rhythms. Several types of synchronization of coupled neurons have been studied under the influence of parameter changes and it is observed that when the coupling strength is above a critical value, certain synchronization mechanisms between neurons can be achieved. This applies both to bursting neurons as well as to neurons exhibiting periodic spikes. The presence of noise can have a profound effect and can enhance synchronization between neurons under certain conditions. Thus it was felt that one could employ a nonlinear filter such as the unscented Kalman filter (UKF) to estimate the states and parameters of an archetypal neuron.

In this paper the state and parameter estimation of an array of nonidentical, locally connected chaotic biological neuronal models is considered. It is known that, under certain conditions, even a single biological neuron can exhibit chaotic behaviour. Chaos may be achieved by introducing the nonlinear effects of the chemical and electrical synapses. Alternately, the chaotic behaviour of the single biological neuron is achieved by driving it with periodic excitations. The global behaviour of an array of biological neurons may then be investigated by considering a spatial distribution of identical neurons, where spatiotemporal chaos emerges, as well as in presence of spatial diversity, generated by a distribution law which could be stochastic or chaotic. In the latter case, it has been observed that the introduction of spatial disorder enhances the self-organization or synchronisation capability. In particular, in agreement with the results presented in the works of Elson et al. [1], Pinto et al. [2], and Szucs et al. [3], the introduction of spatial diversity generated by such a distribution leads to an improvement in synchronization. While the phenomenon of synchronization in dynamics has been observed over a long time, two or more chaotic systems can be synchronized by linking them with mutual coupling or with a common signal or signals. Ideal synchronisation could be induced by mutually coupling a pair of identical chaotic systems when all trajectories converge to the same value and remain in step with each other during further evolution. Linking chaotic systems given by identical differential-dynamic models but with different system parameters can lead to practical synchronization involving phase synchronization. Initially unexcited biological neural models, subsequently externally excited by periodic oscillators, can synchronize both in chaotic and periodic regimes. Provided the amplitudes and frequencies of certain modes are within certain limits, it has been observed that a number of independent neurons can exhibit periodic or chaotic behaviour and achieve a regime of complete synchronization including phase synchronization.

In this paper, we consider a typical extended four-state Hindmarsh-Rose (HR) model (Hindmarsh and Rose, [4]) as a representation of an ensemble of biological neurons. This is preferred over the two-dimensional map model of Rulkov [5] and Shilnikov and Rulkov

[6] although the map may be easier to implement in a filter. The neuron model was subjected to the same type of periodic forcing as the biological neurons. The autonomous periodic bursting pattern of the four-dimensional neuron model was observed to be similar to a biological neuron. The fact that HR model represents an ensemble of biological models is accounted for by introducing low-level process noise. Thus both the process and measurement were assumed to be corrupted by the introduction of very low levels of white noise. The noise had a profound effect on the response of the model as it seemed to annihilate the chaos. The unscented Kalman filtering method was applied to estimate the states of the model. It was observed that the filter performs quite well in reconstructing the states the system, which was deliberately chosen to be chaotic. Neither the filter nor the noise corrupted process model gave any indications of chaos.

Finally the methodology is applied to the Electro-cardiogram (ECG) measurements which are modelled as oscillatory signals using a synthetic model first proposed by McSharry et al. [7]. Like the Hindmarsh-Rose model, it exhibits limit cycle oscillations and chaos and can represent the primary characteristic (P, Q, R, S, T) points in an ECG. The methodology of the UKF is used to filter and reconstruct a measured ECG signal and validated by simulation.

2. Chaotic Model of a Neuron

The analysis of biological neurons had that shown they could be modelled with only three or four states, we chose initially to use a familiar simplified model put forward by Hindmarsh and Rose [4]. The general form of this model contains three terms:

$$\begin{bmatrix} \dot{x} \\ \dot{y} \\ \dot{z} \end{bmatrix} = \begin{bmatrix} ax^2 - x^3 + y - z \\ bx^2 + y_0 - y \\ \mu(S(x + x_0) - z) \end{bmatrix} + \begin{bmatrix} I_0 + I_{\sin}(t) \\ 0 \\ 0 \end{bmatrix}. \tag{2.1}$$

It is hard to establish a one-to-one correspondence between the states of the HR neuron and the states of a biological neuron. Yet the HR neuron model seems to reproduce the overall behaviour of the action potential fairly accurately. After appropriate scaling, the output of the HR neuron model can be made to lie within the same nominal limits as a biological neuron, $-65\,\text{mV} < V < 20\,\text{mV}$. Furthermore the other principal states of the HR neuron show the same behaviour as the principal compartmental currents and gating variables that can be established by considering the diffusion of ionic charge carriers from one compartment to the other. The net result of this type of diffusion is the generation of a potential difference, across the two compartments which can be described by the Nernst equation. For this reason the HR neuron may be employed as a representative model for constructing reduced order observers of the neuron dynamics. The three equations in (2.1) represent the original HR model where $x(t)$ corresponds to membrane voltage, $y(t)$ represents a "fast" current and by making $\mu \ll 1$, $z(t)$ a "slow" current. These three equations (the 3-state model) can produce several modes of spiking-bursting activity including a regime of chaos that appears similar to that seen in biological neurons. However, the parameter space for the chaotic behaviour is much more

restricted than that we observe in real neurons. Following Szucs et al. [3], the chaotic regime is greatly expanded by incorporation of the fourth term into the model:

$$\begin{bmatrix} \dot{x} \\ \dot{y} \\ \dot{z} \\ \dot{w} \end{bmatrix} = \begin{bmatrix} 3x^2 - x^3 + y - z \\ 1.8 + 7x^2 - y - w/80 \\ 0.0021(4(x + 1.56) - z) \\ \nu(-w + 0.88(y - 0.9)) \end{bmatrix} + \begin{bmatrix} I_0 + I_{\sin}(t) \\ 0 \\ 0 \\ 0 \end{bmatrix}, \tag{2.2}$$

where, $I_{\sin}(t) = A\sin(2ft)$ and $\nu = 0.0004$.

Adding the term $w(t)$ to introduce an even slower process ($\nu < \mu \ll 1$) is intended to represent the dynamics of intracellular Calcium^{2+} (Ca^{2+}) ions. To couple the additional equation to the original three-state HR model, a $-g^{*}w(t)$ term is included in the second equation. When this term is taken into account, the model produces simulations of intracellular activity that are even more similar to the biological observations. However it is not known yet if the $w(t)$ term actually represents Ca^{2+} ion kinetics in sinoatrial node (SAN) and ventricular neurons and numerical simulations are currently under way to compare Ca^{2+} transients in HR neurons using realistic biological models. Because of its relative simplicity, the extended HR model was extremely useful in constructing a simulation model that could perform the computations necessary to emulate SAN neurons in real-time. A similar model has been employed by Mayer et al. [8] to model thalamocortical circuits. Although this simplified model is difficult to compare with biological neurons which are made up of a multitude of individual conductance and compartments, we expect the model to provide us with the experience in estimating the states of a real biological model. Since the estimation of these states and parameters is crucial in establishing physiological mechanisms, we also developed several multicompartmental type models that provide a more biologically realistic representation of the nonlinear voltage-current relations than that of Hindmarsh and Rose. Röbenack and Goel [9], and Goel and Röbenack [10] demonstrated that it was possible to reconstruct the currents and gate dynamics from measurements of the action potential by using a "reduced order observer." An observer is an electronic circuit that is expected to reconstruct the internal dynamics of a system, whatever the nature of the dynamics may be, solely from the measurements, in such way that the error between the actual signal and its reconstruction is asymptotically stable. Goel and Röbenack employed a four- and a six-state model to construct their observer. While in this work the HR neuron model has been employed to demonstrate the viability of successfully observing the state of a neuron, the application of the methodology to a multicompartmental biologically inspired model will presumably facilitate the reconstruction of the internal dynamics within the cell using measurements of the action potential. We accordingly employed a modified Hodgkin and Huxley type (Hodgkin and Huxley, [11]) seven-state model to reconstruct all the states of the system. When this model, as well as several other biologically inspired models, was used to construct UKF-based state estimators from a biological neural measurement in our first attempt, all of these models exhibited filter instability. Further analysis indicated that this could be due to one of three reasons: (i) the chaotic nature of the dynamics (ii) unobservability due to inadequate measurements, and (iii) the nonlinear functions arising from the Nernst equations for the compartmental currents due to the ionic concentrations and the sigmoid-like functions associated with the gate time constants and final values, which must lie within the prescribed final values. The question of unobservability was

dealt with by including a range of simulated measurements. It was essential to identify which of the remaining reasons was the predominant cause for the filter instability. So it was decided to first eliminate the possibility of the chaotic dynamics being the primary factor in causing the filter instability. For this reason before employing these models it was decided to apply the UKF to the simplified extended HR model. In this context we note that observers and the extended Kalman filtering have been applied in the past to construct neural estimators by Cruz and Nijmeijer [12]. The reconstruction of the neural dynamics has been considered by Steur et al. [13] and Tyukin et al. [14] have considered the application of adaptive observers to neural systems. However, our objective is to reconstruct the action potential and its features such as the duration, particularly of a group of spatially distributed neurons, over an extended time frame, and to ultimately extend the application to complex multicompartmental models of biological neurons. An adaptive nonlinear observer wherein the gain of the observer is continually modified in accordance with the magnitude of the measurements and noise statistics by an appropriate adaption law would be more suitable in this case than a conventional nonlinear observer like the UKF.

The neuron model described by (2.2), which represents a typical nonlinear oscillator, is described in the parameter plane with the coordinates as the amplitude and frequency of the forcing (Glass and Mackey [15]). A study of the response characteristics of this model reveals subharmonic and superharmonic synchronization or chaotic behaviour, depending on the amplitude and frequency of the forcing. In some cases the chaos occurs after a period-doubling bifurcation. For the parameter set considered in (2.2), the response is chaotic. However, the addition of a relatively small level of noise to the initial conditions seemed to completely annihilate the chaos. A typical response of the model is shown in Figure 1(a) and the magnified plot in Figure 1(b), and it illustrates the fact that the response is chaotic. In Figure 1(a) the second state is scaled down by 400 to plot it on the same figure. This can be demonstrated by a one-dimensional Poincaré plot (Abarbanel [16]). The Poincaré map corresponding to Figure 1(b) shows that the system is chaotic, and it is shown in Figure 1(c).

3. The Unscented Kalman Filter

Most dynamic models employed for purposes of estimation neural action potential signals are generally not linear. To extend and overcome the limitations of linear models, a number of approaches such as the extended Kalman filter (EKF) have been proposed in the literature for nonlinear estimation using a variety of approaches. Unlike the Kalman filter, the EKF may diverge, if the consecutive linearizations are not a good approximation of the linear model over the entire uncertainty domain. Yet the EKF provides a simple and practical approach to dealing with essential nonlinear dynamics.

The main difficulty in applying the EKF algorithm to problems related to the estimation of a neural action potential signal is in determining the proper Jacobian matrices. The UKF is a feasible alternative that has been proposed to overcome this difficulty, by Julier et al. [17] as an effective way of applying the Kalman filter to nonlinear systems. It is based on the intuitive concept that it is easier to approximate a probability distribution than to approximate an arbitrary nonlinear function or transformation of a random variable.

The UKF gets its name from the unscented transformation, which is a method of calculating the mean and covariance of a random variable undergoing nonlinear

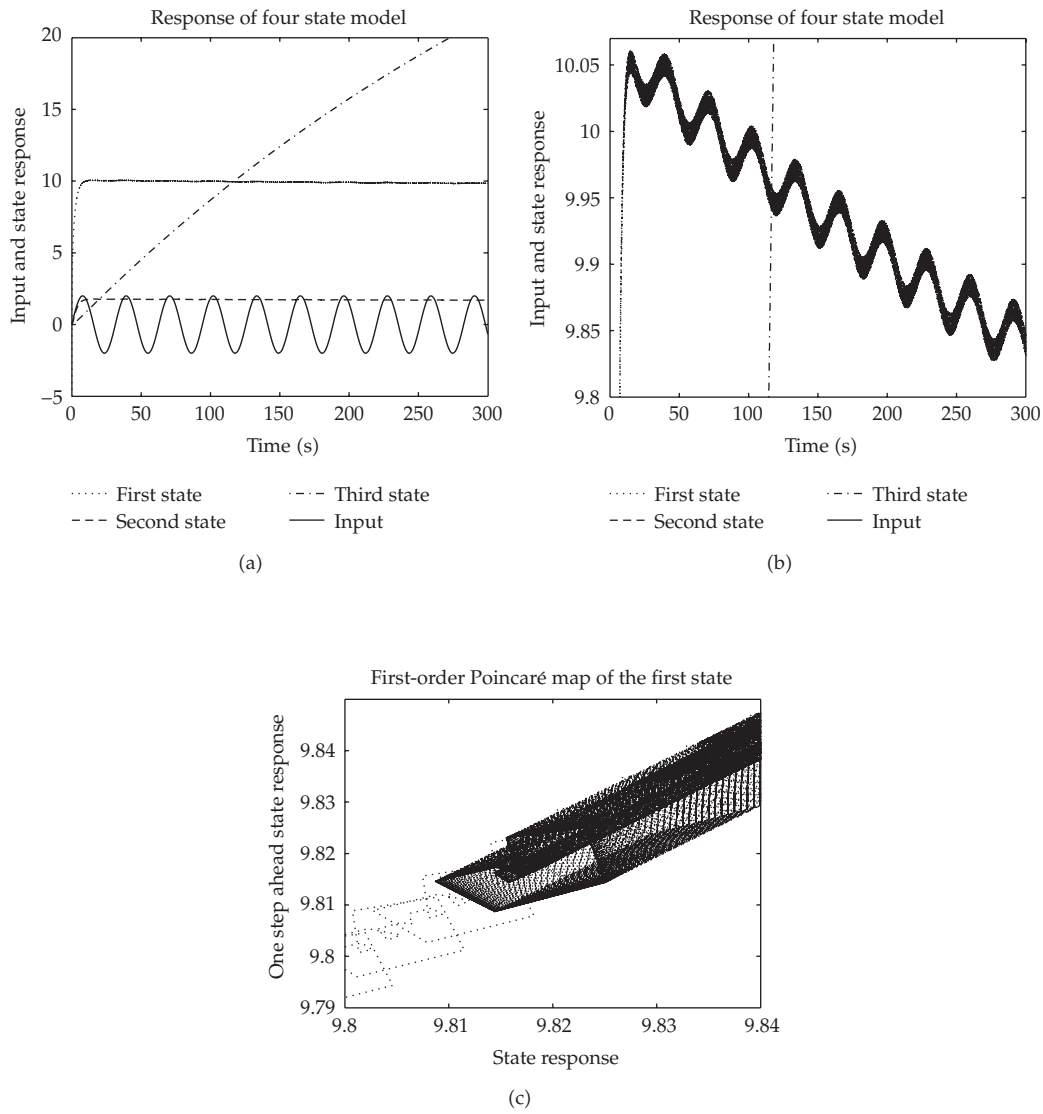

Figure 1: (a) Extended HR neuron: state-response plot comparing response of three states to input. (b) Extended HR neuron: close-up of state-response plot of the first two states illustrating chaos. (c) Extended HR neuron: close-up of the Poincaré map of the chaotic first state corresponding to Figure 1(b).

transformation $\mathbf{y} = \mathbf{f}(\mathbf{w})$. Although it is a derivative-free approach, it does not really address the divergence problem. In essence, the method constructs a set of *sigma vectors* and propagates them through the same nonlinear function. The mean and covariance of the transformed vector are approximated as a weighted sum of the transformed *sigma vectors* and their covariance matrices.

Consider a random variable $\mathbf{w}$ with dimension L which is going through the nonlinear transformation $\mathbf{y} = \mathbf{f}(\mathbf{w})$. The initial conditions are that $\mathbf{w}$ has a mean $\overline{\mathbf{w}}$ and a covariance $\mathbf{P}_{ww}$. To calculate the statistics of $\mathbf{y}$, a matrix χ of $2L+1$ sigma vectors is formed. Sigma vector

points are calculated according to the following equations:

$$\begin{aligned} \chi_0 &= \overline{\mathbf{w}}, \\ \chi_{\mathrm{i}} &= \overline{\mathbf{w}} + \left(\sqrt{(L+\lambda_{\mathrm{us}})\mathbf{P}_{ww}}\right)_i, \quad i = 1,2,\ldots,L, \\ \chi_{\mathrm{i}} &= \overline{\mathbf{w}} - \left(\sqrt{(L+\lambda_{\mathrm{us}})\mathbf{P}_{ww}}\right)_i, \quad i = L+1, L+2,\ldots,2L, \end{aligned} \tag{3.1}$$

where $\lambda_{\mathrm{us}} = \alpha_{\mathrm{us}}^2(L+\kappa) - L$, α_{us} is a scaling parameter between 0 and 1 and κ is a secondary scaling parameter. $(\sqrt{(L+\lambda_{\mathrm{us}})\mathbf{P}_{ww}})_i$ is the ith column of the matrix square root. This matrix square root can be obtained by Cholesky factorization. The weights associated with the sigma vectors are calculated from the following [18]:

$$\begin{aligned} W_0^{(m)} &= \frac{\lambda_{\mathrm{us}}}{L+\lambda_{\mathrm{us}}}, \\ W_0^{(c)} &= \left(\frac{\lambda_{\mathrm{us}}}{L+\lambda_{\mathrm{us}}}\right) + 1 - \alpha_{\mathrm{us}}^2 + \beta, \\ W_i^{(m)} = W_i^{(c)} &= \frac{1}{2(L+\lambda_{\mathrm{us}})}, \quad i = 1,2,\ldots,2L, \end{aligned} \tag{3.2}$$

where β is chosen as 2 for Gaussian distributed variables. We have chosen to use the scaled unscented transformation proposed by Julier [18], as this transformation gives one the added flexibility of scaling the sigma points to ensure that the covariance matrices are always positive definite. The mean, covariance, and cross-covariance of $\mathbf{y}$ calculated using the unscented transformation are given by

$$\begin{aligned} \mathbf{y}_i &= \mathbf{f}(\chi_i), \\ \overline{\mathbf{y}} &\approx \sum_{i=0}^{2L} W_i^{(m)} \mathbf{y}_i, \\ \mathbf{P}_{yy} &\approx \sum_{i=0}^{2L} W_i^{(c)} (\mathbf{y}_i - \overline{\mathbf{y}})(\mathbf{y}_i - \overline{\mathbf{y}})^T, \\ \mathbf{P}_{wy} &\approx \sum_{i=0}^{2L} W_i^{(c)} (\chi_i - \overline{\chi})(\mathbf{y}_i - \overline{\mathbf{y}})^T, \end{aligned} \tag{3.3}$$

where $W_i^{(m)}$ and $W_i^{(c)}$ are the set of weights defined in a manner so approximations of the mean and covariance are accurate up to the third order for Gaussian inputs for all nonlinearities, and to at least the second order for non-Gaussian inputs. The sigma

points in the sigma vectors are updated using the nonlinear model equations without any linearization.

Given a general discrete nonlinear dynamic system in the form

$$\mathbf{x}_{k+1} = \mathbf{f}_k(\mathbf{x}_k, \mathbf{u}_k) + \mathbf{w}_k, \qquad \mathbf{y}_k = \mathbf{h}_k(\mathbf{x}_k) + \mathbf{v}_k, \tag{3.4}$$

where $\mathbf{x}_k \in R^n$ is the state vector, $\mathbf{u}_k \in R^r$ is the known input vector, and $\mathbf{y}_k \in R^m$ is the output vector at time k, $\mathbf{w}_k$ and $\mathbf{v}_k$ are, respectively, the disturbance or process noise and sensor noise vectors, which are assumed to be Gaussian white noise with zero mean. Furthermore $\mathbf{Q}_k$ and $\mathbf{R}_k$ are assumed to be the covariance matrices of the process noise sequence, $\mathbf{w}_k$ and the measurement noise sequence $\mathbf{v}_k$, respectively. The unscented transformations of the states are denoted as

$$\mathbf{f}_k^{\mathrm{UT}} = \mathbf{f}_k^{\mathrm{UT}}(\mathbf{x}_k, \mathbf{u}_k), \qquad \mathbf{h}_k^{\mathrm{UT}} = \mathbf{h}_k^{\mathrm{UT}}(\mathbf{x}_k) \tag{3.5}$$

while the transformed covariance matrices and cross-covariance are, respectively, denoted as

$$\begin{aligned} \mathbf{P}_k^{ff} &= \mathbf{P}_k^{ff}(\widehat{\mathbf{x}}_k, \mathbf{u}_k), \\ \mathbf{P}_k^{hh-} &= \mathbf{P}_k^{hh}(\widehat{\mathbf{x}}_k^-), \\ \mathbf{P}_k^{xh-} &= \mathbf{P}_k^{xh-}(\widehat{\mathbf{x}}_k^-, \mathbf{u}_k). \end{aligned} \tag{3.6}$$

The UKF estimator can then be expressed in a compact form. The state time-update equation, the propagated covariance, the Kalman gain, the state estimate, and the updated covariance are, respectively, given by,

$$\begin{aligned} \widehat{\mathbf{x}}_k^- &= \mathbf{f}_{k-1}^{\mathrm{UT}}(\widehat{\mathbf{x}}_{k-1}), \\ \widehat{\mathbf{P}}_k^- &= \mathbf{P}_{k-1}^{ff} + \mathbf{Q}_{k-1}, \\ \mathbf{K}_k &= \widehat{\mathbf{P}}_k^{xh-}\left(\widehat{\mathbf{P}}_k^{hh-} + \mathbf{R}_k\right)^{-1}, \\ \widehat{\mathbf{x}}_k &= \widehat{\mathbf{x}}_k^- + \mathbf{K}_k\left[\mathbf{y}_k - \mathbf{h}_k^{\mathrm{UT}}(\widehat{\mathbf{x}}_k^-)\right], \\ \widehat{\mathbf{P}}_k &= \widehat{\mathbf{P}}_k^- - \mathbf{K}_k\left(\widehat{\mathbf{P}}_k^{hh-} + \mathbf{R}_k\right)^{-1}\mathbf{K}_k^T. \end{aligned} \tag{3.7}$$

Equations (3.7) in the same form as the traditional Kalman filter and the EKF. Thus higher order nonlinear models capturing significant aspects of the dynamics may be employed to ensure that the Kalman filter algorithm can be implemented to effectively estimate the states in practice. For our purposes we adopt the UKF approach to estimate the neuron states in the process model.

The UKF is based on approximating the probability distribution function than on approximating a nonlinear function as in the case of EKF. The state distributions are

approximated by a Gaussian probability density, which is represented by a set of deterministically chosen sample points. The nonlinear filtering using the Gaussian representation of the posterior probability density via a set of deterministically chosen sample points is the basis for the UKF. It is based on statistical linearization of the state dynamics rather than analytical linearization (as in the EKF). The statistical linearization is performed by employing linear regression using a set of regression (sample) points. The sigma points are chosen as the regression points. The mean and covariance at the sigma points then represent the true mean and covariance of the random variable with the particular Gaussian probability density. Thus when transformed to the nonlinear systems, they represent the true mean and covariance accurately only to the second order of the nonlinearity. Thus this can be a severe limitation of the UKF unless the nonlinearities can be limited to the first and second order in the process model.

4. UKF Estimation Applied to a Neuron Model

The success of the application of the UKF depends largely on the approximation to the covariance which is estimated as a weighted linear sum of the covariance at the sigma points. When this approximation is such that the covariance is not positive definite, the UKF algorithm fails as the Cholesky decomposition is not possible. To ensure that this covariance is essential, adjust the scaling parameter α_{us}, if and when necessary. In the example illustrated, α_{us} was chosen to be very small positive number. First, to see the need for the UKF, the traditional extended Kalman filter (EKF) is also applied to the same responses and the two sets of results are compared. These comparisons are shown in Figure 2. Figure 2 also illustrates the simulated neuron model states plotted to the same scale. While the state estimates obtained by the UKF and EKF are almost the same in the case of the first state (which was measured), the EKF estimates of all the other states tend to zero. Although in the case of the third state z, the EKF seems to perform better than the UKF, the state estimate in this case as well tends to zero in steady state. This may be due to the inadequacy of the number of measurements but it is natural to assume that the internal states cannot be measured. Given that only the first state can be measured, the UKF definitely tends to perform better than the traditional EKF.

Figure 3 shows the corresponding errors in the simulated states and UKF estimated states over the same time frame. Figure 4 shows the simulated measurement error of a typical sensor. Finally it must be said that the filter was run over a much longer time frame and the performance of the filter did not deteriorate in spite of this long-term operation. Thus the implementation of an UKF-based state estimator for the HR neuron is successfully demonstrated over a relatively long time frame.

In particular we observe the relatively large error in the third state, z. We also note that this error does not significantly influence the error in the estimate of the first state. The addition of a relatively small level of noise to the initial conditions seems to have the effect of generating a response that completely shrouds and annihilates the chaotic behaviour and this appears to be a consequence of the sensitive dependence of the initial conditions as well. What appears to be noise in the response may well be a combination of both noise and chaos, but it is not possible to distinguish between the two. This significant change in the response of z in the estimator, which can be recognized by comparing Figures 1 and 2, explains the reason for the chaos to be annihilated as this state plays a key role in the appearance of the chaotic response in the first state. In fact it acts like a switch or gate and the addition of noise

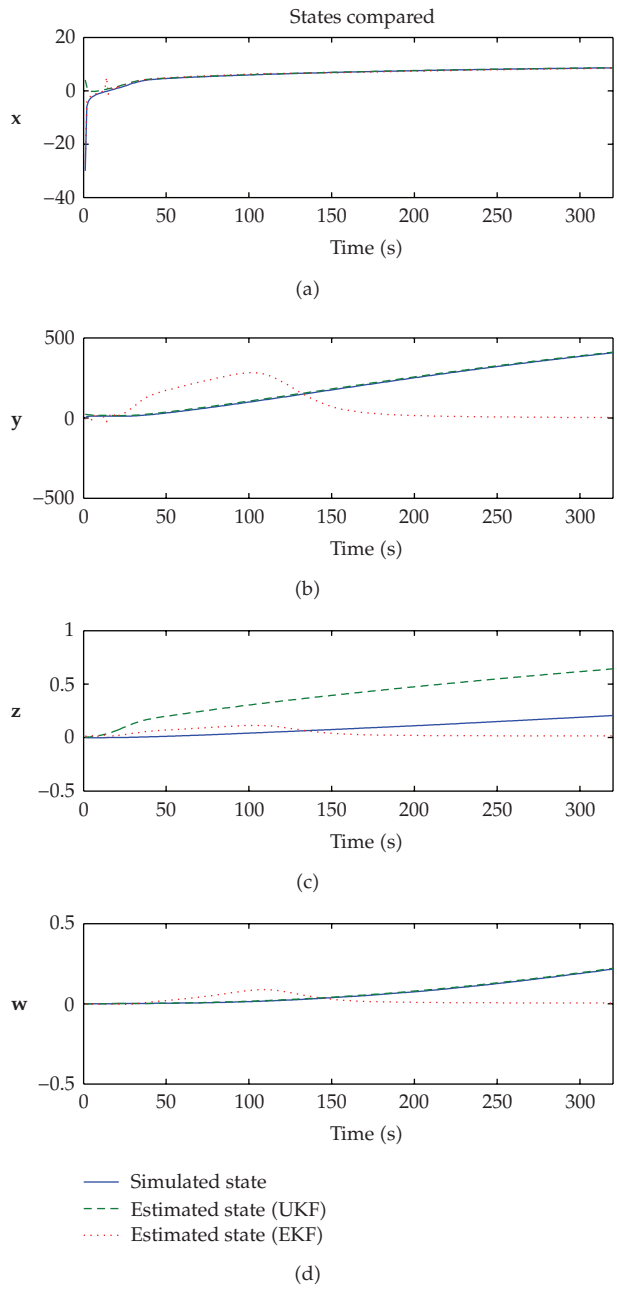

Figure 2: Neuron model states: plots of the simulated and estimated states on the same scale versus the time in seconds.

to the equation for z changes the dynamics of its mean value quite significantly which in turn is responsible for switching off the chaos. However, we also observe that this is not a feature of the estimator but a result of the addition of noise to the Hiindmarsh-Rose model of the dynamics of the neuron. We had also observed that when no chaos was present and z was already well behaved, the introduction of noise was not so significant.

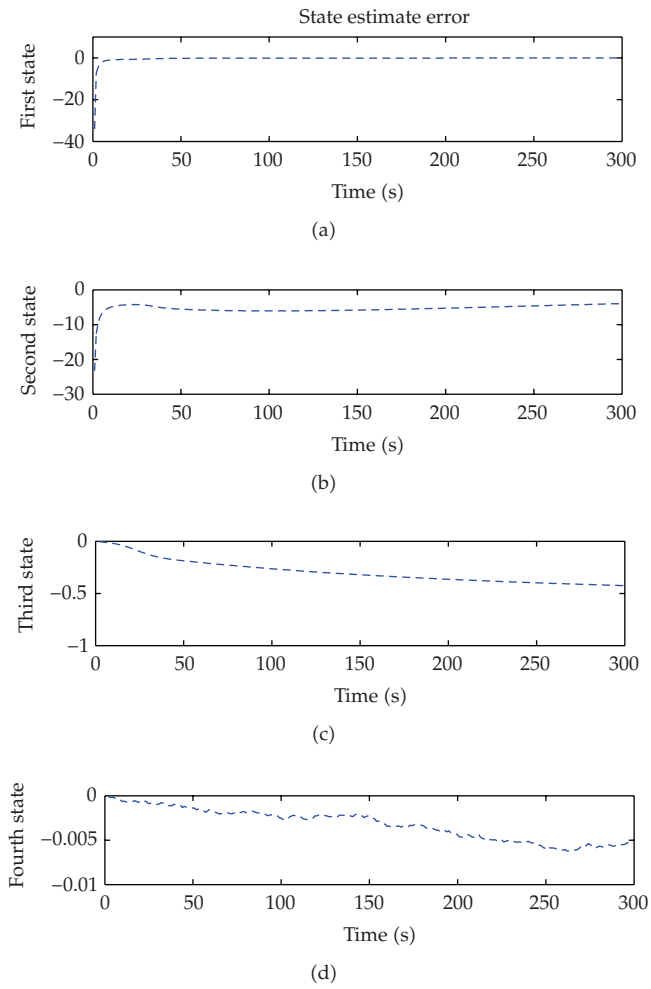

Figure 3: Neuron model states: plots of the UKF estimate errors in the state variables versus the time in seconds.

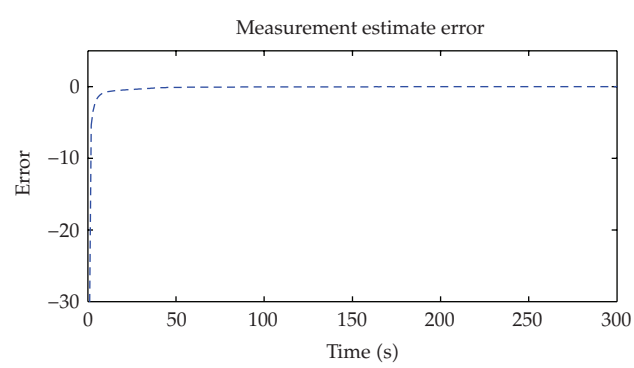

Figure 4: Neuron model states: plot of the evolution of estimated measurement error versus the time in seconds.

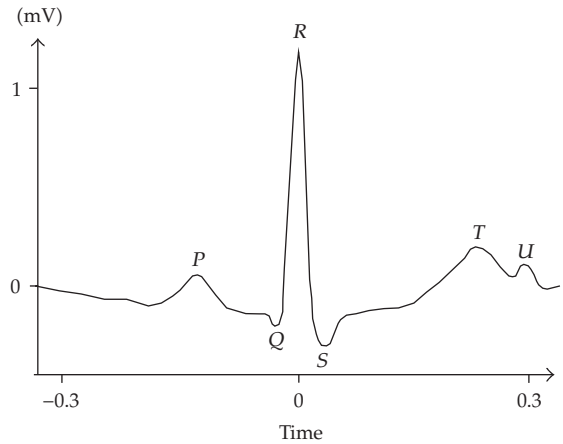

Figure 5: A typical *R-R* ECG signal.

5. Application to ECG Estimation

McSharry et al. [7] have proposed a theoretical nonlinear dynamic model that is capable of emulating an ECG, which is characterised by several parameters that are adaptable to many measured ECG signals. A typical ECG signal, shown in Figure 5, is characterised by six important points labelled as P, Q, R, S, T, or U. These points define the "fiducial" points which are the landmarks on the ECG signal such as the isoelectric line (PQ junction), the onset of individual waves such as QRS complex and the P and T waves, and the PQ, QT, and ST time intervals. The ECG signal is periodic and the period is the elapsed time between two R-R peaks. The circular radian frequency $\omega = 2\pi/T_{R\text{-}R}$ is related to the *Heart Rate*. The heart rate is by no means steady as several rhythmic variations are known to influence it. Coupling between the heart rate and the respiratory cycle causes oscillations in the heart rate at about 0.25 Hz and is termed as the respiratory sinus arrhythmia. *Heart Rate Variability* (HRV) influences the fiducial points and is controlled by the baroreflex regulatory feedback. The baroreflex feedback mechanism is modelled by a nonlinear delay-differential equation by McSharry et al. [19] based on a model by Fowler and McGuinness [20] to capture and to describe the interactions between the heart rate and blood pressure. The model gives rise to the oscillations in the blood pressure known as *Mayer waves* with a time period ranging from 10 to 25 seconds, due to the presence of a time delay. The model maintains an intrinsically stable heart rate in the absence of nervous control and features baroreflex influence on both heart rate and peripheral resistance. Irregularities in the baroreflex feedback which can create disturbances in the blood pressure such as the *Mayer waves* manifest themselves in some form in the ECG signal. The *Mayer waves* and the heart rate variability modelling have also been studied by Seydnejad and Kitney [21]. Analysis of Heart rate variability is also the basis for the assessment of the sympathetic and parasympathetic responses of the autonomic nervous system, with the sympathetic tone influencing the low-frequency spectrum only while both the sympathetic and parasympathetic responses influence the high frequency component of the ECG spectrum. Consequently the heart rate estimation generally involves both ECG and additional measurements of the arterial blood pressure and/or features associated with the respiratory system. For this reason, in this paper, the heart rate is assumed to be either known or independently estimated.

The original model proposed by McSharry et al. [7] generates a trajectory in a three-dimensional state space with coordinates (x, y, and z). The ECG is plot of the z coordinate with respect to time. An observation of the responses shows that they exhibit a limit-cycle behaviour and that it is not sinusoidal. The dynamical equations of motion are given by a set of three ordinary differential equations

$$\dot{x} = (1 - r)x - \omega_1 y, \tag{5.1a}$$

$$\dot{y} = (1 - r)y + \omega_1 x, \tag{5.1b}$$

$$\dot{z} = -\sum_{1=1}^{5} a_i \Delta\theta_i \exp\left(\frac{-\Delta\theta_i^2}{2b_i^2}\right) - (z - z_0), \tag{5.1c}$$

where $r = \sqrt{x^2 + y^2}$, $\Delta\theta_i = (\theta - \theta_i) \bmod 2\pi$, $\theta = \operatorname{atan}2(y, x)$ is the four-quadrant inverse tangent (arctangent) given the sine (y) and cosine (x) of the angle θ defined in the range $-\pi < \theta \leq \pi$, and ω_1 is the angular velocity of the trajectory as it moves around the limit cycle which is assumed to be either measured or estimated adaptively and hence is treated as a known parameter. The baseline value of z_0 in (5.1c) is assumed to be driven by the respiratory circular frequency ω_2 according to

$$z_0(t) = A_0 \sin(\omega_2 t), \tag{5.2}$$

where the constant $A_0 = 0.15\,\text{mV}$. These equations of motion may be integrated numerically using the MATLAB built-in *m*-file *ode*45.*m* which is based on an explicit Dormand-Prince Runge-Kutta ((3.2), (3.3)) pair of formulae over each fixed time step $\Delta t = 1/f_s$ where f_s is the sampling frequency. Equation (5.1c) may be expressed as

$$\dot{z} = -\sum_{i=1}^{5} a_i \Delta\theta_i \exp\left(-\gamma_i \Delta\theta_i^2\right) - (z - z_0), \quad \gamma_i = \frac{1}{(2b_i^2)}. \tag{5.3}$$

The parameters of the modified representation of the (5.1c) given by (5.3) are defined in Table 1.

As rightly pointed by Sameni et al. [22], the first two equations (5.1a) and (5.1b) could be transformed two other dynamic equations in terms of

$$\begin{aligned} r &= \sqrt{x^2 + y^2}, \\ \theta &= \operatorname{atan}2(y, x). \end{aligned} \tag{5.4}$$

Table 1: Parameters of the ECG model given by (2.1).

Index (i)	1 (P)	2 (Q)	3 (R)	4 (S)	5 (T)
Time (secs)	−0.2	−0.05	0	0.05	0.3
θ_i (radians)	$-\frac{1}{3}\pi$	$-\frac{1}{12}\pi$	0	$\frac{1}{12}\pi$	$\frac{1}{2}\pi$
a_i	1.2	−5.0	30.0	−7.5	0.75
γ_i	8.000	50.00	50.00	50.0	3.125

Table 2: Typical initial conditions for the states in (3.3).

θ	1.5π	a_1	1.2	γ_1	50.0
Z	−0.0110	a_2	−5.0	γ_2	34.7222
ϕ_1	0	a_3	15.0	γ_3	55.4017
		a_4	−7.5	γ_4	78.1250
		a_5	0.75	γ_5	8.0

The r-dynamics take the form $\dot{r} = f(r)$ and are essentially unobservable. Consequently (5.1a) and (5.1b) may be replaced by $\dot{\theta} = \omega_1$. Thus (5.1a), (5.1b), and (5.3) may now be augmented by additional state equations and expressed as

$$\dot{\theta} = \omega_1, \tag{5.5a}$$

$$\dot{z} = -\sum_{i=1}^{5} a_i \Delta\theta_i \exp\left(-\gamma_i \Delta\theta_i^2\right) - \left(z - A_0 \sin\phi_2\right), \tag{5.5b}$$

$$\dot{a}_i = 0, \quad \dot{\gamma}_i = 0, \quad i = 1, 2, \ldots, 5, \quad \dot{\phi}_2 = \omega_2. \tag{5.5c}$$

Equations (5.5a) and (5.5b) represent a classic pair of the first-order equations that exhibit both limit cycle and chaotic behaviour. The complete set of 13 equations characterised by eight parameters θ_i, $i = 1, 2, \ldots, 5$, ω_1, ω_2, and A_0 represents a dynamic model of the ECG with typical initial conditions as illustrated in Table 2. In addition one could assume that the state space dynamics include a number of disturbances. The state space equations including the random white noise disturbances are given by (5.6) as

$$\begin{gathered}
\dot{\theta} = \omega_1 + w_1, \\
\dot{z} = -\sum_{i=1}^{5} a_i \Delta\theta_i \exp\left(-\gamma_i \Delta\theta_i^2\right) - \left(z - A_0 \sin\phi_2\right) + w_2, \\
\dot{\phi}_2 = \omega_2 + w_3, \qquad \dot{a}_i = w_{i+3}, \quad \dot{\gamma}_i = w_{i+8}, \quad i = 1, 2, \ldots, 5,
\end{gathered} \tag{5.6}$$

with the set w_j $i = 1, 2, \ldots, 13$ being zero mean white noise process disturbances with a known covariance matrix.

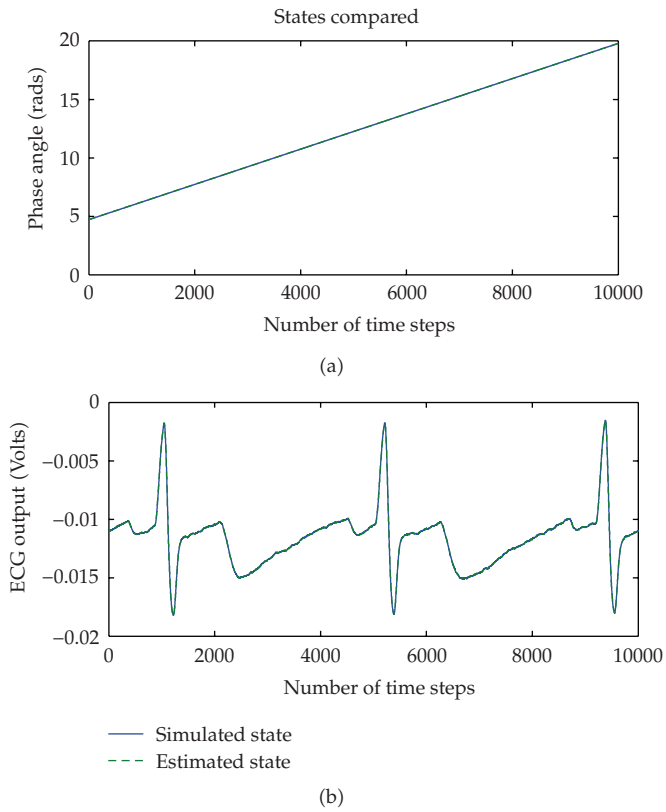

Figure 6: Comparison of simulated and estimated responses of the states θ, z plotted against the number of time steps.

Given a set of continuously sampled ECG measurements, the measurements may be expressed by the equation

$$z_m = z + v \tag{5.7}$$

with v being a zero mean white noise measurement disturbance with a known covariance. The UKF may be employed to estimate the states θ, z and the augmented states ϕ_1, a_i, γ_i, $i = 1, 2, \ldots, 5$.

In Figure 6 a typical set of simulated and estimated responses of the states θ, z is compared. In Figure 7 the errors in the estimate over 10 000 time steps, $\Delta t = 0.0002\,\mathrm{s}$ are shown.

In Figure 8 a typical estimated error in the measurement is shown. Thus the UKF is capable of performing extremely well given the measurements with well-behaved covariance characteristics. When the noise covariance matrices are unknown, it is possible to estimate the states adaptively. The filter is currently undergoing extensive tests with actual measured ECG data and in this case the adaptive estimation appears not only to be more appropriate but also performs better than the nonadaptive UKF. A complete discussion of the application of the adaptive UKF to ECG measurements, where the process and measurement noise covariance

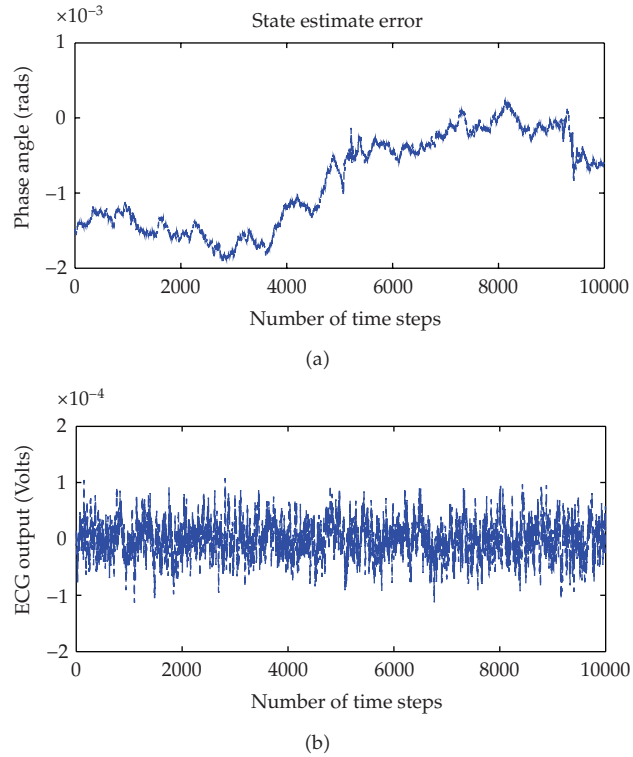

Figure 7: Errors in the estimated responses of the states θ, z, plotted against the number of time steps.

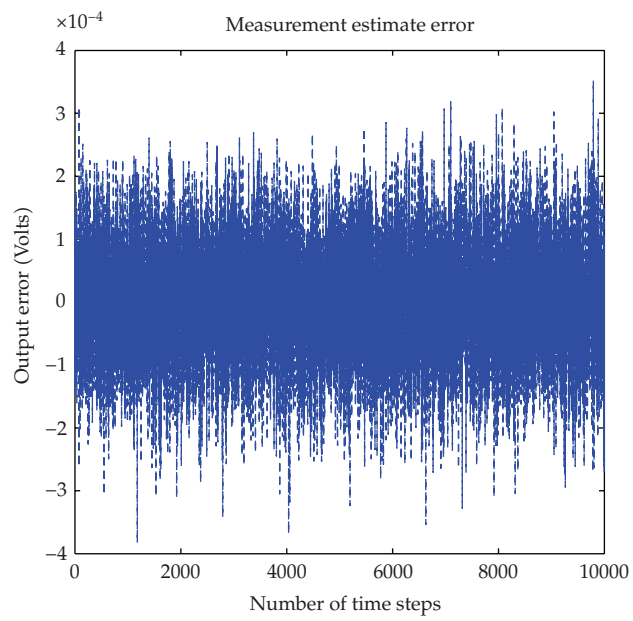

Figure 8: Measurement estimate error, plotted against the number of time steps.

matrices are recursively updated, is beyond the scope of this paper and will be presented elsewhere.

6. Conclusions and Discussion

The unscented Kalman filtering method was applied to estimate the states of an HR-like neuron model which in the absence of noise were deliberately chosen to be chaotic. The process and measurement was then corrupted by the introduction of very low levels of white noise. The noise had a profound effect on the response of the model as it seemed to annihilate the chaos. It was observed that the filter performs quite well in reconstructing the states of the system. Neither the filter nor the noise corrupted process model gave any indications of chaos. Moreover, the exercise gave us valuable experience in applying the UKF to a biological neuron. Preliminary studies of the application of the UKF to a Hodgkin-Huxley type model indicated that the successful application of the unscented approach to an ensemble of biological neurons was feasible, provided the sigma points were scaled according to certain scaling laws related to the gate constants. Finally the methodology of the unscented Kalman filter is successfully applied to filter a typical simulated ECG signal using a synthetic model-based approach.

References

[1] R. C. Elson, A. I. Selverston, R. Huerta, N. F. Rulkov, M. I. Rabinovich, and H. D. I. Abarbanel, "Synchronous behavior of two coupled biological neurons," *Physical Review Letters*, vol. 81, no. 25, pp. 5692–5695, 1998.

[2] R. D. Pinto, P. Varona, A. R. Volkovskii, A. Szücs, H. D.I. Abarbanel, and M. I. Rabinovich, "Synchronous behavior of two coupled electronic neurons," *Physical Review E*, vol. 62, no. 2, pp. 2644–2656, 2000.

[3] A. Szucs, R. C. Elson, M. I. Rabinovich, H. D. I. Abarbanel, and A. I. Selverston, "Nonlinear behavior of sinusoidally forced pyloric pacemaker neurons," *Journal of Neurophysiology*, vol. 85, no. 4, pp. 1623–1638, 2001.

[4] J. L. Hindmarsh and R. M. Rose, "A model of neuronal bursting using three coupled first order differential equations," *Proceedings of the Royal Society of London B*, vol. 221, no. 1222, pp. 87–102, 1984.

[5] N. F. Rulkov, "Modeling of spiking-bursting neural behavior using two-dimensional map," *Physical Review E*, vol. 65, no. 4, Article ID 041922, 9 pages, 2002.

[6] A. L. Shilnikov and N. F. Rulkov, "Subthreshold oscillations in a map-based neuron model," *Physics Letters A*, vol. 328, no. 2-3, pp. 177–184, 2004.

[7] P. E. McSharry, G. D. Clifford, L. Tarassenko, and L. A. Smith, "A dynamical model for generating synthetic electrocardiogram signals," *IEEE Transactions on Biomedical Engineering*, vol. 50, no. 3, pp. 289–294, 2003.

[8] J. Mayer, H. G. Schuster, and J. C. Claussen, "Role of inhibitory feedback for information processing in thalamocortical circuits," *Physical Review E*, vol. 73, no. 3, Article ID 031908, 15 pages, 2006.

[9] K. Röbenack and P. Goel, "Observer based measurement of the input current of a neuron," *Mediterranean Journal of Measurement and Control*, vol. 3, no. 1, pp. 22–29, 2007.

[10] P. Goel and K. Röbenack, "Observing the current input in neurons," Tech. Rep. 38, Mathematical Biosciences Institute, The Ohio State University, 2005.

[11] A. L. Hodgkin and A. F. Huxley, "A quantitative description of membrane current and its application to conduction and excitation in nerve," *The Journal of Physiology*, vol. 117, no. 4, pp. 500–544, 1952.

[12] C. Cruz and H. Nijmeijer, "Synchronization through extended Kalman filtering," in *New Directions in Nonlinear Observer Design*, H. Nijmeijer and T. I. Fossen, Eds., vol. 244 of *Lecture Notes in Control and Information Sciences*, pp. 469–490, Springer, London, UK, 1999.

[13] E. Steur, I. Yu. Tyukin, H. Nijmeijer, and C. van Leeuwen, "Reconstructing dynamics of spiking neurons from input-output measurements in vitro," in *Proceedings of the 3rd IEEE Conference on Physics and Control*, Potsdam, Germany, 2007, Paper no. 3-7.

[14] I. Yu. Tyukin, E. Steur, H. Nijmeijer, and C. van Leeuwen, "State and parameter estimation for systems in non-canonical adaptive observer form," in *Proceedings of the 17th IFAC World Congress on Automation Control*, vol. 17, Seoul, Korea, 2008, Paper no. 6-1.

[15] L. Glass and M. C. Mackey, Eds., *From Clocks to Chaos: The Rhythms of Life*, Princeton University Press, Princeton, NJ, USA, 1988.

[16] H. D. I. Abarbanel, *Analysis of Observed Chaotic Data*, Institute for Nonlinear Science, Springer, New York, NY, USA, 1996.

[17] S. Julier, J. Uhlmann, and H. F. Durrant-Whyte, "A new method for the nonlinear transformation of means and covariances in filters and estimators," *IEEE Transactions on Automatic Control*, vol. 45, no. 3, pp. 477–482, 2000.

[18] S. J. Julier, "The scaled unscented transformation," in *Proceedings of the American Control Conference*, vol. 6, pp. 4555–4559, 2002.

[19] P. E. McSharry, M. J. McGuinness, and A. C. Fowler, "Confronting a cardiovascular system model with heart rate and blood pressure data," *Computers in Cardiology*, vol. 32, pp. 587–590, 2005.

[20] A. C. Fowler and M. J. McGuinness, "A delay recruitment model of the cardiovascular control system," *Journal of Mathematical Biology*, vol. 51, no. 5, pp. 508–526, 2005.

[21] S. R. Seydnejad and R. I. Kitney, "Modeling of mayer waves generation mechanisms: determining the origin of the low- and very low frequency components of BPV and HRV," *IEEE Engineering in Medicine and Biology Magazine*, vol. 20, no. 2, pp. 92–100, 2001.

[22] R. Sameni, M. B. Shamsollahi, C. Jutten, and M. Babaie-Zadeh, "Filtering noisy ECG signals using the extended Kalman filter based on a modified dynamic ECG model," *Computers in Cardiology*, vol. 32, pp. 1017–1020, 2005.

Hindawi Publishing Corporation
Mathematical Problems in Engineering
Volume 2010, Article ID 972873, 23 pages
doi:10.1155/2010/972873

Research Article

A Model of Gear Transmission: Fractional Order System Dynamics

Katica (Stevanović) Hedrih[1,2] and Vera Nikolić-Stanojević[3,4]

[1] *Mathematical Institute SANU, Belgrade, Serbia*
[2] *Faculty of Mechanical Engineering, University of Niš, Yu-18 000, ul. Vojvode Tankosića 3/22, Niš, Serbia*
[3] *State University of Novi Pazar, Novi Pazar, Serbia*
[4] *Faculty of Mechanical Engineering, University of Kragujevac, Kragujevac, Serbia*

Correspondence should be addressed to Katica (Stevanović) Hedrih, khedrih@eunet.rs

Received 24 January 2010; Revised 2 March 2010; Accepted 6 May 2010

Academic Editor: Alexander P. Seyranian

A theoretical model of multistep gear transmission dynamics is presented. This model is based on the assumption that the connection between the teeth of the gears is with properties within the range from ideal clasic to viscoelastic so that a new model of connection between the teeth was expressed by means of derivative of fractional order. For this model a two-step gear transmision with three degrees of freedom of motion has been used. The obtained solutions are in the analytic form of the expansion according to time. As boundary cases this model gives results for the case of ideally elastic connection of the gear teeth and for the case of viscoelastic connection of the gear teeth, as well. Eigen fractional modes are obtained and a vizualization is done.

1. Introduction

Gear transmissions have a long history dating back since the time of the first engineering systems. Their practical usage in the present day modern engineering systems is enormous. In accordance with contemporary development of mechanical engineering technics ever growing requirements have been imposed concerning characteristics and working specifications. The machines which utilize high-power duty gear transmissions (excavating machines, crushing mashines, rolling machines, ships, etc.) operate under nonstationary conditions so that the loads of the elements of these gear transmissions are variable. For example, abrupt accelerations and abrupt decelerations of machine parts, that is, masses of the gear transmissions cause inertial forces which, in addition to the conditions of operation, influence the magnitude of actual leads of the elements of gear transmissions. All this, together with the changes of the torque of drive and operating machine, the forces induced by dynamic

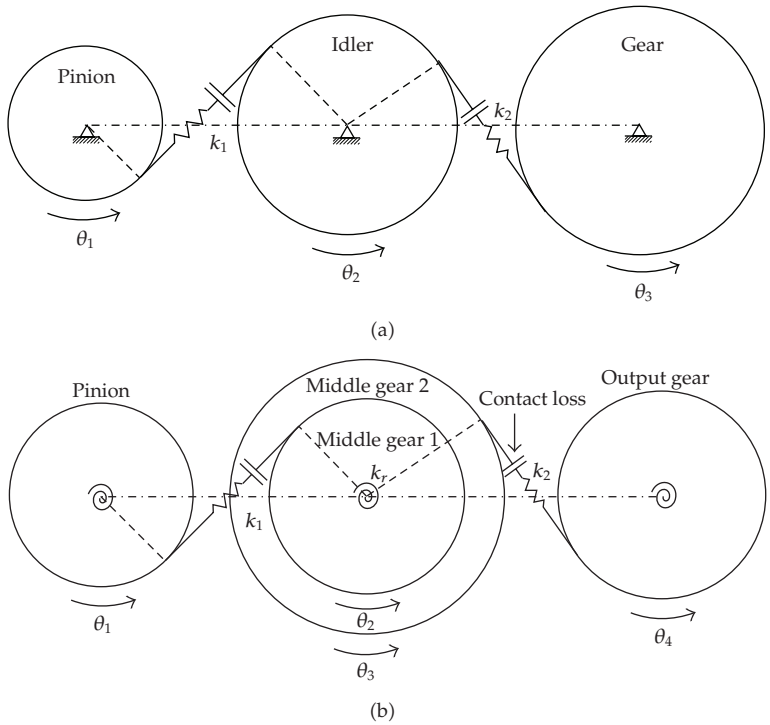

Figure 1: Two models of the gear power transmission with visco-elastic fractional order tooth coupling.

behaviours of the complete system, and so forth, lead to the simulation where the stresses in the gears are higher than critical stresses; after certain time this may result in breakage of the teeth.

1.1. Introduction into Nonlinear Dynamics of the Rotors

Dynamics of coupled rotors (see Figure 1) and of gyrorotors are very old engineering problems with many different research results and discoveries of new nonlinear phenomena, and of stationary and no stationary vibrations regimes with different kinetic parameters of the dynamical system (see [1–14]). However, even nowadays many researchers pay attention to this problem again.

Chaotic clock models, as well as original ideas on a paradigm for noise in machines were presented by Moon (see [15]): "All machines exhibit a greater or lesser amount of noise. The question arises as to whether a certain level of noise is natural or inevitable in a complex assembly of mechanical or electromechanical devices?" In the cited paper, the nature of noise or chaos in a specific class of complex multibody machines, namely the clock was examined. For examining natural clocks of reductors (power transmission), as well as source of nonlinear vibrations and noise in its dynamics, it is necessary to investigate properties of nonlinear dynamics, and phase portraits, as well as structures of homoclinic orbits, layering and sensitivity of this layering of homoclinic orbits and bifurcation of homoclinic points, as it is presented in [6, 9–11].

Following up the idea of Mossera that the distance between trajectories be measured maintaining different time scales or "clock" with which time is measured along each motion, Leela (see [16]) defines the new concepts of orbital stability in terms of given topology of the function space. Leela's paper pointed out the different kind of clock. Perfect clock corresponds to stable system dynamics, entire clock space corresponds to the chaotic topology and chaotic-like dynamics of the system.

By using examples of the rotor system which rotates about two axes with section or without section, we applied the vector method of the kinetic parameters analysis of the rotors with many axes which is done in [12, 13, 17–28]. In the previous listed papers, the expressions for the corresponding linear momentum and angular momentum, as well as their derivatives in time for the rotors with coupled rotation are used in the vector form. By these expressions, the vector equations of the gyrorotor system dynamics are derived, as well as the expression for the kinetic pressures on the gyro rotor system bearings. The mass moment vectors introduced and defined by first author (see [6, 7, 17, 18, 29–36]), are used to present a vector method for the analysis of kinetic parameter of coupled rigid rotors dynamics with deviational mass properties of rotor, as well as of the dynamics of rotor with changeable mass distribution (see [32, 32]).

By using vector equations (see [21, 22, 24, 25]), two scalar differential equations of the heavy rotor system nonlinear dynamic for the case that disc is skewly eccentrically positioned on the own polhode shaft axis (gyrodisk-rotor) is studied. For the case when one rotation about axis is controlled by constant angular velocity, the nonlinear dynamics of the rotation about other axis is studied. Non-linear gyrodisc-rotor system dynamics is presented by phase portrait in the phase plane, with trigger of the coupled singularities, as well as with homoclinic orbits and homoclinic points of the no stable type saddle. For the case of gyrodisc-rotor system dynamics under the action of the perturbed couple the sensitive dependence in the vicinity of the equilibrium no stable position which corresponds to homoclinic point of the type no stable saddle, the possibility of the chaotic character behavior is pointed out.

Expressions of the kinetic pressures of shaft bearing are determined.

The analogy between motions of heavy material point: on the circle in vertical plane which rotates around vertical axis in the plane (see [37, 38]) and corresponding motions case of the heavy rotor around two axes with cross section, as well as of the gyrodisc-rotor which rotates around two axes is pointed out (see [5, 21, 24, 25, 39, 40]).

Dynamics of disc on the one, or more, shaft is a classical engineering problem. This problem attracts attention of many researchers and permanently takes place in world scientific and engineering professional literature (see [3, 41, 42]). Some of these problems are classical and can be found in university text books of mechanics (see [42]). As we can see, these problems are in the nonlinear dynamics described by nonlinear differential equations without analytical solutions. In present time these problems were conditionally and approximately solved by approximate solutions or by linearizations (first by Simes, Stodola, Rubanik and others [38, 43]). Problem of dynamics of the eccentric, skewly positioned disc on one-shaft rotation is classical problem with gyroscopic effect (see classical text books [17, 38, 43, 44]) which takes place in all text books of Dynamics and Theory of Oscillations with applications in engineering, but their presentations are finished only by nonlinear differential equations without their solutions and expression for kinetic pressures. Nowadays, numerous new published papers containing different approximations of the solutions of different classes of the mathematical descriptions of rotor dynamics are not enough to take are into account all real influential factors to describe real system dynamics. This is inspiration for new research in this area.

By using knowledge of nonlinear mechanics (see [37, 45]), as well as by using introduced mass moments vectors and vector rotators in the series of the published papers [8, 19, 23–25, 34, 36, 46–49] phase portrait of gyrorotor dynamics with analysis of static and dynamical equilibrium positions depending on system kinetic parameters are presented in new light and new approach.

Using new knowledge in the nonlinear mechanics, theory of chaos and dynamical systems published in [19, 50, 51], the sensitive dependence of the initial conditions and of the forced motion—oscillation/rotation/stochasticlike-chaoticlike motion of the heavy rotor with vibrating axis as well as gyrorotor in the "vicinity" of the homoclinic point and orbit are analyzed. We followed the ideas of Holmes from [52] on the example pendulum excited by one frequency force, and which showed us that Poincare maps contain the Smale horseshoe map as well as global analysis processes of the dynamical systems which posses on the homoclinic orbit is suitable for applying to study of the rotor dynamic. By using ideas of Holmes from [52], it is easy to prove that forced dynamic of the heavy gyrorotor has in the vicinity of homoclinic point sensitive dependence of initial conditions.

In the paper [6] the motion of a heavy body around a stationary axis in the field with turbulent damping [53] is investigated and kinetic pressures on bearings are expressed by mass moment vectors for the pole in the stationary bearing and for the axis of the body rotation. The motion equations of a variable mass object rotating around a fixed axis are expressed by mass moment vector for the pole and the axis and presented in [20].

A trigger of coupled singularities, on an example of coupled rotors with deviational material particles are presented in [54]. Non-linear phenomena in rotor dynamics were investigated in the series of [6].

From time to time it is useful to pay attention again to classical models of dynamics of mechanical systems and evaluate possibilities for new approaches to these classical results by using other than the methods usually used in the classical literature.

The interest in the study of vector and tensor methods with applications in the *Dynamics* especially in *Kinetics* of rigid and solid body rotational motions and deformation displacements as a new qualitative approach to the optimization of the time for study process grew exponentially over the last few years because theoretical challenges involved in the study of technical sciences need such optimization of university systems study. Short time for fundamental knowledge transfer during one term (semester) courses with high level of apparent study results requires the optimization of the time for introducing new basic high level scientific ideas (logic and philosophical) which are easy to understand to most of students in the study process and for engineering applications this is very important.

Also, we can conclude that the impact of different possibilities to establish the phenomenological analogy of different model dynamics expressed by vectors connected to the pole and the axis and the influence of such possibilities to applications allows professors, researchers and scientists to obtain larger views within their specialization fields.

This is the reason to introduce mass moment vectors to presentation of the kinetic parameters of the rotor dynamics and multistep gear transmission. On the basis of this approach we built the first model presented in this paper.

In industry there is an increased need for detailed investigation of the toothed coupling through models that involute the coupling of more than two teeth and for more than two, the systems which give high revolution numbers and others. Relatively new models (see [1–4, 14, 15, 26–28, 41, 55, 56]) have been established to study numerous problems in the gear transmission dynamics.

1.2. Introduction into Fractional Order Dynamics of the Rotors

In use, gear transmissions are very often exposed to action of forces that change with time (dynamic load). There are also internal dynamic forces present. The internal dynamic forces in gear teeth meshing, are the consequence of elastic deformation of the teeth and defects in manufacture such as pitch differences of meshed gears and deviation of shape of tooth profile. Deformation of teeth results in the so-called collision of teeth which is intensified at greater difference in the pitch of meshed gears. Occurrence of internal dynamic forces results in vibration of gears so that the meshed gears behave as an oscillatory system. This model consists of reduced masses of the gear with elastic and damping connections (see [2, 4, 55]). By applying the basic principles of mechanics and taking into consideration initial and boundary conditions, the system of equation is established which describes physicality of the gear meshing process. On the other hand, extremely cyclic loads (dynamic forces) can result in breakage of teeth, thus causing failure of the mechanism or system.

Primary dependences between geometrical and physical quantities in the mechanics of continuum (and with gear transmissions as well) include mainly establishing the constitutive relation between the stress state and deformation state of the tooth's material in the two teeth in contact for each particular case.

Thus, solving this task, it is necessary to reduce numerous kinetic parameters to minimal numbers and obtain a simple abstract model describing main properties for investigation of corresponding dynamical influences. Analytic methods include determination of mathematical functions which detemine the solution in closed form. They are based on the constitutive laws and relations of the stress-strain states in gear's materials, and they can give solutions for a very small number of boundary tasks. But, always each aproach needs certain assumotions-approximations concerning description of real contours, properties of teeth is contacts and initial conditions. For this reason numerous researchers resort to application of numeric method in solving differential equation of the gear transmission motion. The basic characteristic of the numeric methods is that the fundamental equations of the Elasticity theory, including the boundary conditions, are solved by approximative numeric methods. The solutions obtained are approximate.

Based on previous analysis at starting this part, we take into account that contact between two teeth is possible to be constructed by standard light element with constitutive stress—strain state relations which can be expressed by fractional order derivatives.

For that Reason, Let us make a short survey of the present results published in the literatute.

The monographs [57, 58] contain a basic mathematical description of fractional calculus and some solutions of the fractional order differential equations necessary for applications of the corresponding mathematical description of a model of gear transmission based on the teeths coupling by standard light fractional order element.

In series of the papers (see [59–62]) and in the monograph [63] analytical mechanics of discrete hereditary systems is constructed and based on the standard light hereditary elements in the form of neglected mass and with viscoelastic properties with corresponding constitutive relations between forces and element deformations. Special case are constitutive relations expressed by fractional order derivatices.

In [61] discrete continuum method was presented by use of the system of the material particles coupled viscoelastically or creeping mass less standard light elements with different stress-strain constitutive relations expressed by corresponding mathematical relations.

Standard light element with constitutive stress-strain relation expressed by members with fractional order derivatives are also used.

In the series of [45, 64–69] a series of the mixed discrete-continuum or continuum mechanical systems with fractional order creep properties are mathematically described by members contained in fractional order derivatives and analytically solved. These examples with mathematical descriptions and solutions are basic for new model of the gear transmission with fractional order properties.

2. Model of the Gear Transmission of the Fractional Order Tooth Coupling

2.1. Description of the Gear Transmission Model of the Fractional Order Tooth Coupling

Let us consider a model who is based on the three-step coupled rigid rotors but couplings between gear teeth are realized by standard light elements fractional order constitutive stress-strain relations, Figure 1(a). The second model of gear transmissions dynamics consists of three rigid disks coupled by two standard light fractional order elements, as it is presented in Figure 1(b). (see Appendix B).

2.2. Standard Light Fractional Order Element

Basic elements of multistep gear transmission system are

(i) gears in the form of disks with mass axial inertia moments $\mathbf{J_k}$, $\mathbf{k} = 1, 2, 3$,

(ii) *standard light coupling elements* of negligible mass in the form of axially stressed rod without bending, and which has the ability to resist deformation under static and dynamic conditions; Constitutive stress-strain relation between restitution force $\mathbf{P}$ and element elongation x can be written in the general form $f_{\mathrm{psr}}(\mathbf{P}, \dot{\mathbf{P}}, x, \dot{x}, x_t^{\alpha}, \mathfrak{D}, \mathfrak{D}_t^{\alpha}, \mathcal{J}, n, c, \tilde{c}, \mu, \alpha, c_{\alpha}, T, U, \ldots) = 0$, where $\mathfrak{D}$, $\mathfrak{D}_t^{\alpha}$ and $\mathcal{J}$ are differential, fractional order and integral operators (for detail see monographs [45, 58–67, 70, 71]) which find their justification in experimental verifications of material behavior, while $n, c, \tilde{c}, \mu, c_{\alpha}, \alpha, \ldots$ are material constants, which are also determined experimentally.

For each single standard coupling light element of negligible mass, we shall define a particular stress-strain constitutive relation-law of material properties. This means that we will define stress-strain constitutive relation as description relation between forces and deformations of two gears teeth in contact determined and constrained by rotation angles of the gear model in the form of disk and with changes of distances in time, with accuracy up to constants which depend on the accuracy of their determination through experiment.

The accuracy of those constants laws and with them the relation between forces and elongations will depend not only on knowing the nature of object, but also on our having the knowledge necessary for dealing with very complex stress-strain relations in the coupling gears teeth (for details see [2, 4, 55]). In this paper we shall use three types of such light

standard constraint elements: *light standard creep constraint element* for which the stress-strain relation for the restitution force in the function of element elongation is given by fractional order derivatives (see [62]) in the form

$$P(t) = -\left\{c_0 x(t) + c_\alpha \mathfrak{D}_\alpha^t[x(t)]\right\}, \tag{2.1}$$

where $\mathfrak{D}_t^\alpha[\cdot]$ is fractional order differential operator of the αth derivative with respect to time t in the following form:

$$\mathfrak{D}_\alpha^t[x(t)] = \frac{d^\alpha x(t)}{dt^\alpha} = x^{(\alpha)}(t) = \frac{1}{\Gamma(1-\alpha)}\frac{d}{dt}\int_0^t \frac{x(\tau)}{(t-\tau)^\alpha}d\tau, \tag{2.2}$$

where c, c_α are rigidity coefficients is momentary and prolonged one, and α a rational number between 0 and 1, $0 < \alpha < 1$.

2.3. Governing Equations of the Two-Step Gear Transmission with Fractional Order Tooth Coupling

For defined model of the two-step gear transmission fractional order system vibrations, we use three generalized coordinates—angle of gear disks rotation ϑ_i, $i = 1, 2, 3$, and we take into account that defined system poses three degrees of freedom.

Kinetic energy of the of the two-step gear transmission fractional order system vibrations is in the form

$$\mathbf{E_k} = \frac{1}{2}\sum_{k=1}^{k=2} \mathbf{J}_k \dot{\vartheta}_k^2 + \frac{1}{2}\mathbf{J}_3\dot{\vartheta}_2^2 + \frac{1}{2}\mathbf{J}_4\dot{\vartheta}_3^2. \tag{2.3}$$

The first standard light fractional order coupling element is between first gear disk and second and is strained for $x_1 = R_1((R_2/R_1)\vartheta_2 - \vartheta_1)$, and the second standard light fractional order coupling element is between the third gear disk and fourth and is strained for $x_2 = R_3((R_4/R_3)\vartheta_3 - \vartheta_2)$. On the basis of the previous constitutive stress-strain relation of the first and second standard light fractional order coupling elements between geared disks in the two-step gear power transmission are

$$\begin{aligned} P_1 &= -cx_1 - c_\alpha \mathfrak{D}_\alpha^t[x_1] = -cR_1\left(\frac{R_2}{R_1}\vartheta_2 - \vartheta_1\right) - c_\alpha \mathfrak{D}_\alpha^t\left[R_1\left(\frac{R_2}{R_1}\vartheta_2 - \vartheta_1\right)\right], \\ P_2 &= -cx_2 - c_\alpha \mathfrak{D}_\alpha^t[x_2] = -cR_3\left(\frac{R_4}{R_3}\vartheta_3 - \vartheta_2\right) - c_\alpha \mathfrak{D}_\alpha^t\left[R_3\left(\frac{R_4}{R_3}\vartheta_3 - \vartheta_2\right)\right]. \end{aligned} \tag{2.4}$$

Governing system of the double gear transmission fractional order differential equations is in the following form:

$$\begin{aligned}
\mathbf{J}_1\ddot{\vartheta}_1 &= -P_1 = cR_1\left(\frac{R_2}{R_1}\vartheta_2 - \vartheta_1\right) + c_\alpha \mathfrak{D}_\alpha^t\left[R_1\left(\frac{R_2}{R_1}\vartheta_2 - \vartheta_1\right)\right],\\
(\mathbf{J}_2 + \mathbf{J}_3)\ddot{\vartheta}_2 &= P_1 - P_2 = -cR_1\left(\frac{R_2}{R_1}\vartheta_2 - \vartheta_1\right) - c_\alpha \mathfrak{D}_\alpha^t\left[R_1\left(\frac{R_2}{R_1}\vartheta_2 - \vartheta_1\right)\right]\\
&\quad + cR_3\left(\frac{R_4}{R_3}\vartheta_3 - \vartheta_2\right) + c_\alpha \mathfrak{D}_\alpha^t\left[R_3\left(\frac{R_4}{R_3}\vartheta_3 - \vartheta_2\right)\right],\\
\mathbf{J}_4\ddot{\vartheta}_3 &= P_2 = -cR_3\left(\frac{R_4}{R_3}\vartheta_3 - \vartheta_2\right) - c_\alpha \mathfrak{D}_\alpha^t\left[R_3\left(\frac{R_4}{R_3}\vartheta_3 - \vartheta_2\right)\right].
\end{aligned} \tag{2.5}$$

After introducing the following notations:

$$\omega_0^2 = \frac{c}{\mathbf{J}_1}R_1, \quad \omega_{0\alpha}^2 = \frac{c_\alpha}{\mathbf{J}_1}R_1, \quad k_{21} = \frac{R_2}{R_1}, \quad k_{31} = \frac{R_3}{R_1}, \quad k_{41} = \frac{R_4}{R_1}, \quad \lambda_{23,1} = \frac{(\mathbf{J}_2 + \mathbf{J}_3)}{\mathbf{J}_1}, \quad \lambda_{4,1} = \frac{\mathbf{J}_4}{\mathbf{J}_1} \tag{2.6}$$

governing system of the l fractional order differential equations is possible to write in the following form:

$$\begin{aligned}
&\ddot{\vartheta}_1 - \omega_0^2 k_{21}\vartheta_2 + \omega_0^2\vartheta_1 = \omega_{0\alpha 1}^2 \mathfrak{D}_\alpha^t[(k_{21}\vartheta_2 - \vartheta_1)],\\
&\ddot{\vartheta}_2 - \omega_0^2\lambda_{23,1}\vartheta_1 + \omega_0^2\lambda_{23,1}(k_{21} + k_{31})\vartheta_2 - \omega_0^2\lambda_{23,1}k_{41}\vartheta_3 = \omega_{0\alpha}^2\lambda_{23,1}\mathfrak{D}_\alpha^t[\vartheta_1 + (k_{21} + k_{31})\vartheta_2 - k_{41}\vartheta_3],\\
&\ddot{\vartheta}_3 + \omega_0^2\lambda_{413}(k_{41}\vartheta_3 - k_{31}\vartheta_2) = -\omega_{0\alpha}^2\lambda_{4,1}\mathfrak{D}_\alpha^t[(k_{41}\vartheta_3 - k_{31}\vartheta_2)].
\end{aligned} \tag{2.7}$$

2.4. Solutions of the Governing System of Differential Equations of Two-Step Gear Transmission Dynamics, with Fractional Order Tooth Coupling

Now, for beginning let us consider corresponding basic systems of the differential equations in linear form:

$$\begin{aligned}
&\ddot{\vartheta}_1 - \omega_0^2 k_{21}\vartheta_2 + \omega_0^2\vartheta_1 = 0,\\
&\ddot{\vartheta}_2 - \omega_0^2\lambda_{23,1}\vartheta_1 + \omega_0^2\lambda_{23,1}(k_{21} + k_{31})\vartheta_2 - \omega_0^2\lambda_{23,1}k_{41}\vartheta_3 = 0,\\
&\ddot{\vartheta}_3 + \omega_0^2\lambda_{413}(k_{41}\vartheta_3 - k_{31}\vartheta_2) = 0,
\end{aligned} \tag{2.8}$$

and with proposed solutions in the following form:

$$\vartheta_k(t) = A_k\cos(\omega t + \alpha), \tag{2.9}$$

and taking the following notation $u = \omega^2/\omega_0^2$, we can write the following systems of algebra of algebra equations with respect to unknown amplitudes A_k in the matrix form

$$\begin{pmatrix} (1-u) & -k_{21} & 0 \\ -\lambda_{23,1} & [\lambda_{23,1}(k_{21}+k_{31})-u] & -\lambda_{23,1}k_{41} \\ 0 & -\lambda_{413}k_{31} & (\lambda_{413}k_{41}-u) \end{pmatrix} \begin{Bmatrix} A_1 \\ A_2 \\ A_3 \end{Bmatrix} = \{0\}, \tag{2.10}$$

and corresponding frequency equation in the developed form

$$\begin{aligned} f(u) = {} & (1-u)[\lambda_{23,1}(k_{21}+k_{31})-u](\lambda_{413}k_{41}-u) \\ & - k_{21}\lambda_{23,1}(\lambda_{413}k_{41}-u) - \lambda_{413}k_{31}\lambda_{23,1}k_{41}(1-u) = 0. \end{aligned} \tag{2.11}$$

From the previous frequency equation, we can obtain the following three roots u_s, $s = 1,2,3$ and corresponding eigen circular frequencies: $\omega_s^2 = u_s\omega_0^2$, $s = 1,2,3$, and corresponding cofactors are: $K_{31}^{(s)} = -k_{21}(\lambda_{413}k_{41} - u_s)$; $K_{32}^{(s)} = -\lambda_{23,1}k_{41}(1-u)$; $K_{33}^{(s)} = -k_{21}\lambda_{23,1}k_{41}$. Then, solution of the basic linear differential equations is

$$\vartheta_k(t) = \sum_{s=1}^{s=3} \vartheta_k^{(s)}(t) = \sum_{s=1}^{s=3} A_k^{(s)} \cos(\omega_s t + \alpha_s) = \sum_{s=1}^{s=3} K_{3k}^{(s)} C_s \cos(\omega_s t + \alpha_s) = \sum_{s=1}^{s=3} K_{3k}^{(s)} \xi_s, \tag{2.12}$$

where $\xi_s = C_s \cos(\omega_s t + \alpha_s)$, $s = 1,2,3$ are main coordinates of the linear system.

By using the expression for generalized coordinates ϑ_i, $i = 1,2,3$ by normal coordinates of the linear system, the governing system of the fractional differential equations (2.12) is possible to be transform as in the following form:

$$\ddot{\xi}_s + \omega_s^2 \xi_s = -\omega_{\alpha s}^2 D_\alpha^t[\xi_s], \quad s = 1,2,3, \tag{2.13}$$

where

$$\omega_s^2 = \frac{\sum_{i=1}^{i=3}\sum_{j=1}^{j=3} c_{ij} K_{3i}^{(s)} K_{3j}^{(s)}}{\sum_{i=1}^{i=3}\sum_{j=1}^{j=3} a_{ij} K_{3i}^{(s)} K_{3j}^{(s)}}, \quad s = 1,2,3, \qquad \omega_{\alpha s}^2 = \frac{\sum_{i=1}^{i=3}\sum_{j=1}^{j=3} c_{\alpha ij} K_{3i}^{(s)} K_{3j}^{(s)}}{\sum_{i=1}^{i=3}\sum_{j=1}^{j=3} a_{ij} K_{3i}^{(s)} K_{3j}^{(s)}}, \quad s = 1,2,3. \tag{2.14}$$

Obtained system of the three fractional order differential equations (2.14) present three uncoupled fractional order differential equations independent along normal coordinates ξ_s, $s = 1,2,3$ of the considered fractional order model of the gear transmission dynamics. All three fractional order differential equations are of the same type and each presents one mode of the fractional order mode vibrations. Analytical solution is easy to obtain by using one of [58] or [42] or [69] or [62]. Solutions of here fractional order differential equation is possible to solve by using the approach presented in the Appendix A. (It is possible to solve these fractional order differential equation by using the approach presented in the Appendix A).

Then, for the solutions of the each fractional order differential equations (2.13), we can write the following expressions:

$$\begin{aligned}\xi_s(t) &= \xi_{0s}\sum_{k=0}^{\infty}(-1)^k\omega_{\alpha s}^{2k}t^{2k}\sum_{j=0}^{k}\binom{k}{j}\frac{(\mp 1)^j\omega_{\alpha s}^{2j}t^{-\alpha j}}{\omega_s^{2j}\Gamma(2k+1-\alpha j)}\\ &\quad+\dot{\xi}_{0s}\sum_{k=0}^{\infty}(-1)^k\omega_{\alpha s}^{2k}t^{2k+1}\sum_{j=0}^{k}\binom{k}{j}\frac{(\mp 1)^j\omega_{\alpha s}^{-2j}t^{-\alpha j}}{\omega_s^{2j}\Gamma(2k+2-\alpha j)},\quad s=1,2,3,\end{aligned}\tag{2.15}$$

where $\xi_s(0)=\xi_{0s}$ and $\dot{\xi}_s(0)=\dot{\xi}_{0s}$ are initial values of these main coordinates defined by initial conditions. Expressions (2.15) for main system coordinates present fractional order models like one frequency vibration modes.

Now, we can separate three sets of the two fractional order time components $\eta_s(t)$ and $\zeta_s(t)$, $s=1,2,3$ and in the expression of the solutions along normal coordinates of the governing system of fractional differential equations describing our second model of the gear transmission fractional order dynamics we can write in the following forms:

$$\eta_s(t)=\sum_{k=0}^{\infty}(-1)^k\omega_{\alpha s}^{2k}t^{2k}\sum_{j=0}^{k}\binom{k}{j}\frac{(\mp 1)^j\omega_{\alpha s}^{2j}t^{-\alpha j}}{\omega_s^{2j}\Gamma(2k+1-\alpha j)},\quad s=1,2,3,\tag{2.16}$$

$$\zeta_s(t)=\sum_{k=0}^{\infty}(-1)^k\omega_{\alpha s}^{2k}t^{2k+1}\sum_{j=0}^{k}\binom{k}{j}\frac{(\mp 1)^j\omega_{\alpha s}^{-2j}t^{-\alpha j}}{\omega_s^{2j}\Gamma(2k+2-\alpha j)},\quad s=1,2,3.\tag{2.17}$$

These three series of the two fractional order time components $\eta_s(t)$ and $\zeta_s(t)$, $s=1,2,3$ present series of the six fractional order modes like one frequency modified cos as well as sin vibration mode components.

Then the solution of the basic system of the fractional order differential equations (2.7) along generalized coordinates ϑ_i, $i=1,2,3$ contain sixth time functions in the forms (2.16) and (2.17). Finally for the solution of the basic system of the fractional order differential equations (2.7) describing dynamics of the fractional order two-step gear transmission it is possible to express in the following form:

$$\begin{aligned}\vartheta_k(t) &= \sum_{s=1}^{s=3}K_{3k}^{(s)}\xi_s(t)=\sum_{s=1}^{s=3}K_{3k}^{(s)}\xi_{0s}\sum_{k=0}^{\infty}(-1)^k\omega_{\alpha s}^{2k}t^{2k}\sum_{j=0}^{k}\binom{k}{j}\frac{(\mp 1)^j\omega_{\alpha s}^{2j}t^{-\alpha j}}{\omega_s^{2j}\Gamma(2k+1-\alpha j)}\\ &\quad+\sum_{s=1}^{s=3}K_{3k}^{(s)}\dot{\xi}_{0s}\sum_{k=0}^{\infty}(-1)^k\omega_{\alpha s}^{2k}t^{2k+1}\sum_{j=0}^{k}\binom{k}{j}\frac{(\mp 1)^j\omega_{\alpha s}^{-2j}t^{-\alpha j}}{\omega_s^{2j}\Gamma(2k+2-\alpha j)},\quad k=1,2,3.\end{aligned}\tag{2.18}$$

2.5. Numerical Analysis of the Solutions of the Governing System of Fractional Order Differential Equations of Two-Step Gear Transmission Dynamics, with Fractional Order Tooth Coupling

We can see that for fractional order model of the double gear transmission vibrations was transformed by eigen normal coordinates ξ_s, $s=1,2,3$ of the corresponding linear system

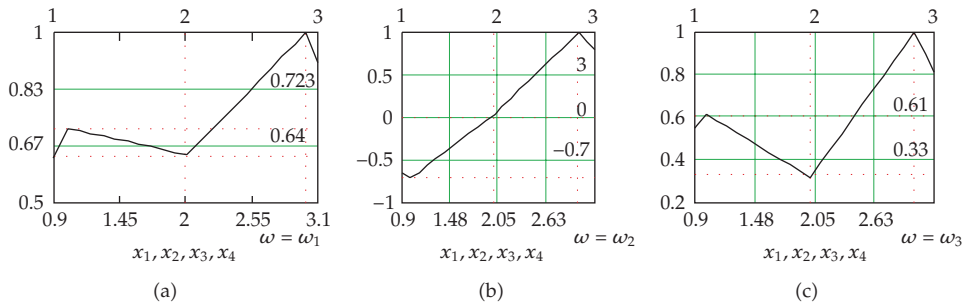

Figure 2: Relations between eigen amplitudes of eigen main normal modes of corresponding system of the basic linear differential equations (2.12), (a) for first, (b) for second, and (c) for third mode.

into three separate independent fractional order oscillators, each with one degree of freedom, and each fractional order differential equation contain only one main coordinate of the system dynamics.

Relations between eigen amplitudes of eigen main normal modes of corresponding system of the basic linear differential equations (2.8) are given on Figure 2(a) for first, 2(b) for second and 2(c) for third mode.

By using different numerical values of the kinetic and geometrical parameters of the two-step gear transmission model, the series of the graphical presentation of the three sets of the two-time components $\eta_s(t)$ and $\zeta_s(t)$, $s = 1, 2, 3$ of the solutions, by using expressions (2.15) and (2.16), are obtained. In the series Figures 3–7 are presented characteristic modes for different values of the α coefficient of the fractional order of the used standard light fractional order element for describing teeth coupling between gears (see Appendix B).

In Figure 3, first eigen fractional order time components $\eta_1(t)$ and $\zeta_1(t)$ for different system kinetic and geometric parameter values are presented.

In Figure 4, first eigen fractional order mode $\xi_1(t)$ with corresponding first eigen fractional order time components $\eta_1(t)$ and $\zeta_1(t)$ for different system kinetic and geometric parameter values are presented. First eigen fractional order mode is like one frequency vibration mode similar to first single frequency eigen mode of the corresponding linear system.

In Figure 5, second eigen fractional mode $\xi_2(t)$ with corresponding second fractional order time components $\eta_2(t)$ and $\zeta_2(t)$ for different system kinetic and geometric parameter values, are presented. Second eigen fractional order mode is like one frequency vibration mode similar to second single frequency eigen mode of the corresponding linear system.

In Figure 6, third eigen fractional mode $\xi_3(t)$ with corresponding third fractional order time components $\eta_3(t)$ and $\zeta_3(t)$ for different system kinetic and geometric parameter values are presented. Third eigen fractional order mode is like one frequency vibration mode similar to third single frequency eigen mode of the corresponding linear system.

In Figure 7, first and second eigen fractional modes, $\xi_1(\alpha, t)$ and $\xi_2(\alpha, t)$ are presented by surfaces with corresponding first and second fractional order time components, $\eta_1(\alpha, t)$—surfaces in left column and $\eta_2(\alpha, t)$—surfaces in right column for same system kinetic and geometric parameter values are presented.

The third eigen fractional mode $\xi_3(\alpha, t)$ is not presented by surfaces with corresponding third fractional order time components $\eta_3(\alpha, t)$ by the reason that corresponding surfaces qe similar as two previous first and second eigen fractional modes, $\xi_1(\alpha, t)$ and $\xi_2(\alpha, t)$

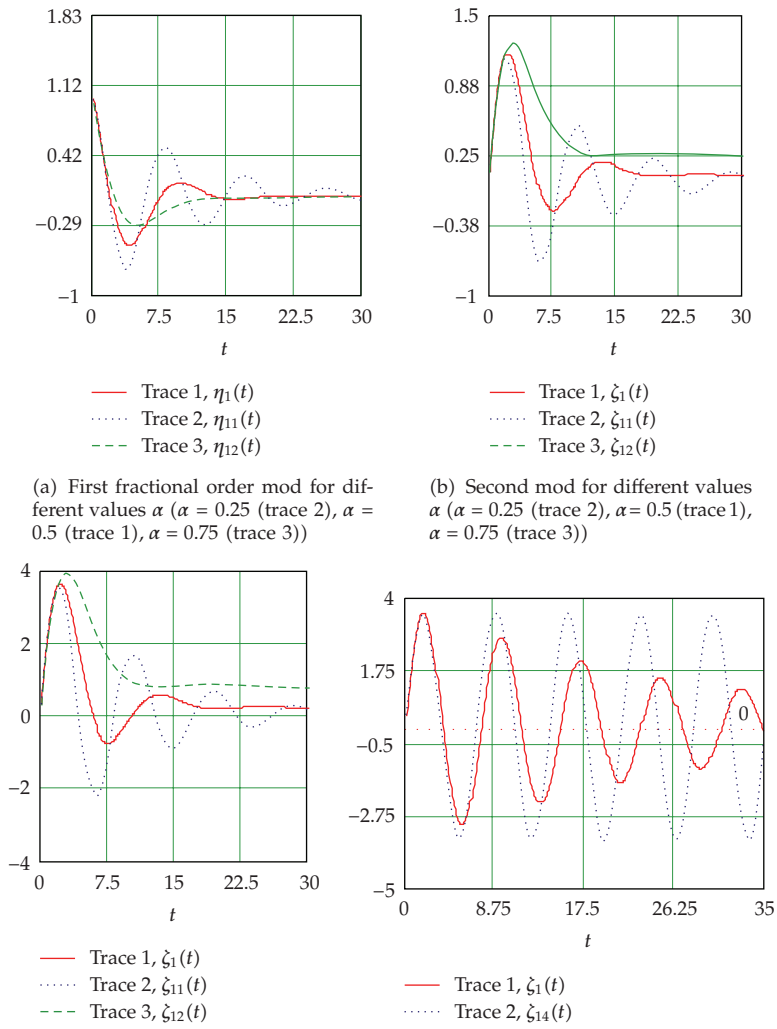

(a) First fractional order mod for different values α ($\alpha = 0.25$ (trace 2), $\alpha = 0.5$ (trace 1), $\alpha = 0.75$ (trace 3))

(b) Second mod for different values α ($\alpha = 0.25$ (trace 2), $\alpha = 0.5$ (trace 1), $\alpha = 0.75$ (trace 3))

(c) The first coordinate for diferent values α ($\alpha = 0.25$ (trace 2), $\alpha = 0.5$ (trace 1), $\alpha = 0.75$ (trace 3))

(d) The first coordinate for diferent values α ($\alpha = 0$ (trace 2) and $\alpha = 0.2$ (trace 1))

Figure 3: First eigen fractional order time components $\eta_1(t)$ and $\zeta_1(t)$ for different system kinetic and geometric parameter values.

presented in Figure 7, and some characteristic properties are visible in the graph presented in Figure 6.

3. Concluding Remarks

Two approaches to the models of the gear transmission system dynamics with possibility of investigate different properties of the very complex dynamics of the corresponding real gear transmission system are possible.

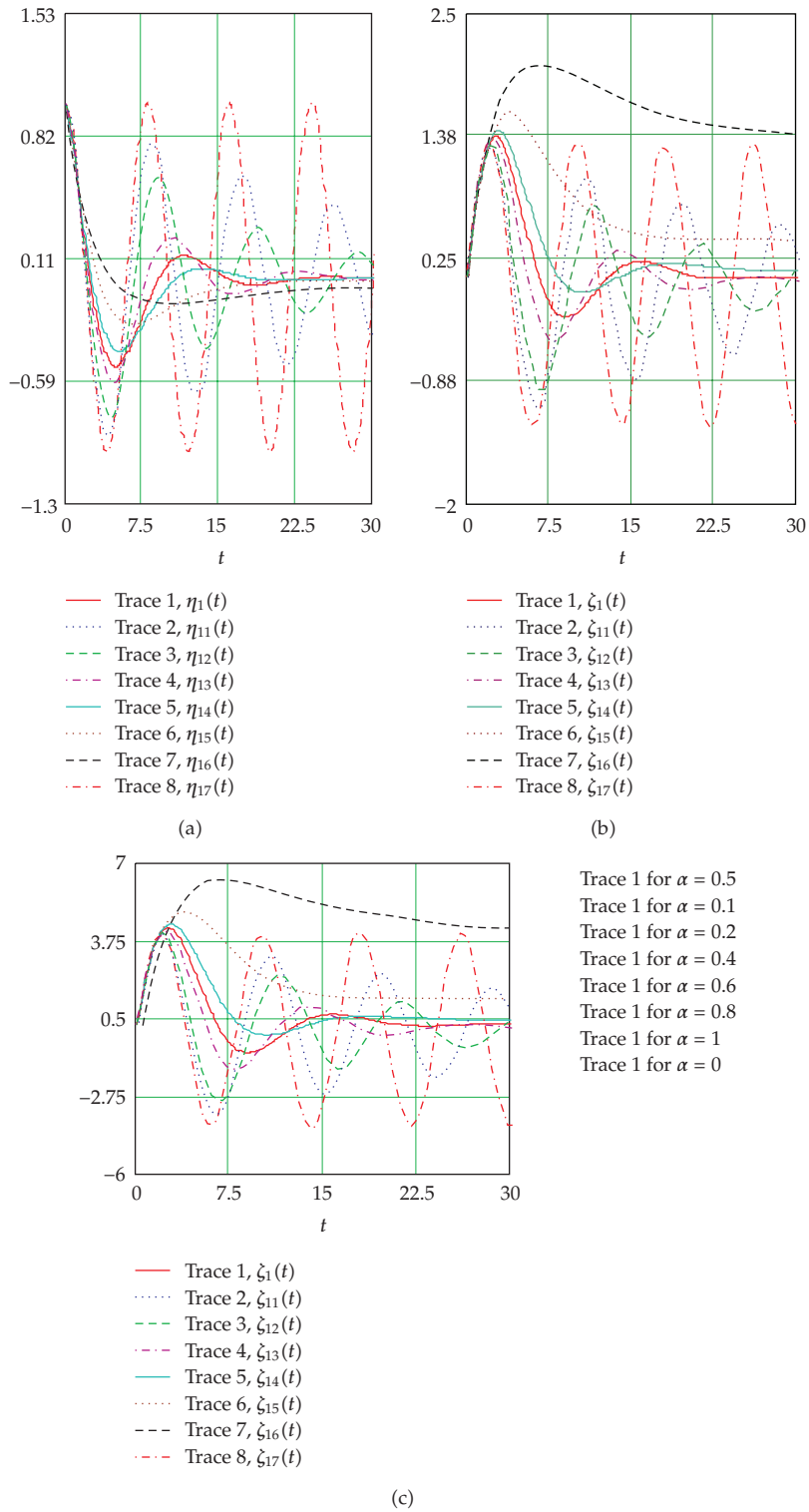

Figure 4: First eigen fractional mode $\xi_1(t)$ with corresponding first fractional order time components $\eta_1(t)$ and $\zeta_1(t)$ for different system kinetic and geometric parameter values. Eigen fractional order mode is like one frequency vibration mode similar to first single frequency eigen mode of the corresponding linear system.

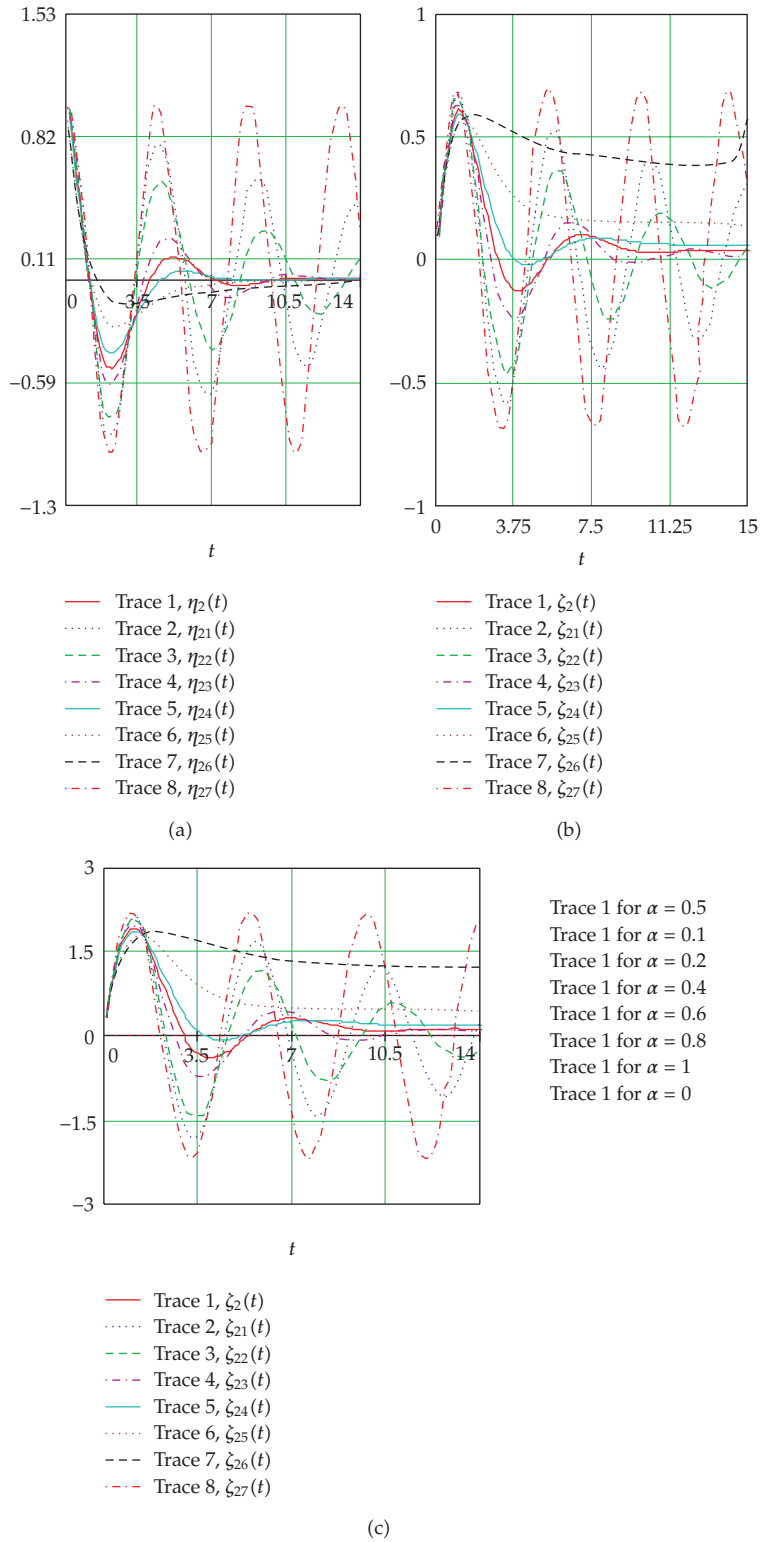

Figure 5: Second eigen fractional mode $\xi_2(t)$ with corresponding second fractional order time components $\eta_2(t)$ and $\zeta_2(t)$ for different system kinetic and geometric parameter values. Eigen fractional order mode is like one frequency vibration mode similar to second single frequency eigen mode of the corresponding linear system.

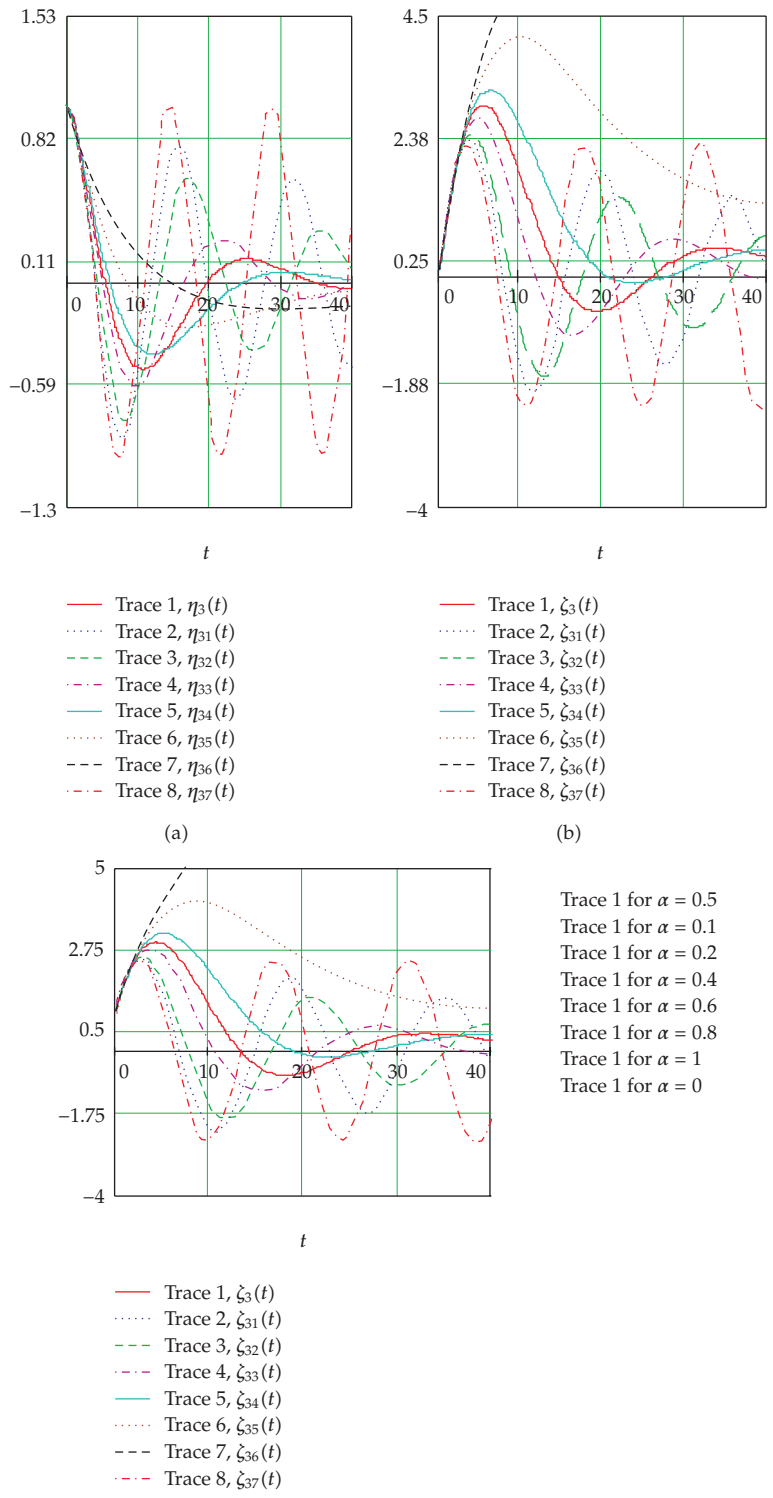

Figure 6: Third eigen fractional mode $\xi_3(t)$ with corresponding third fractional order time components $\eta_3(t)$ and $\zeta_3(t)$ for different system kinetic and geometric parameter values. Eigen fractional order mode is like one frequency vibration mode similar to third single frequency eigen mode of the corresponding linear system.

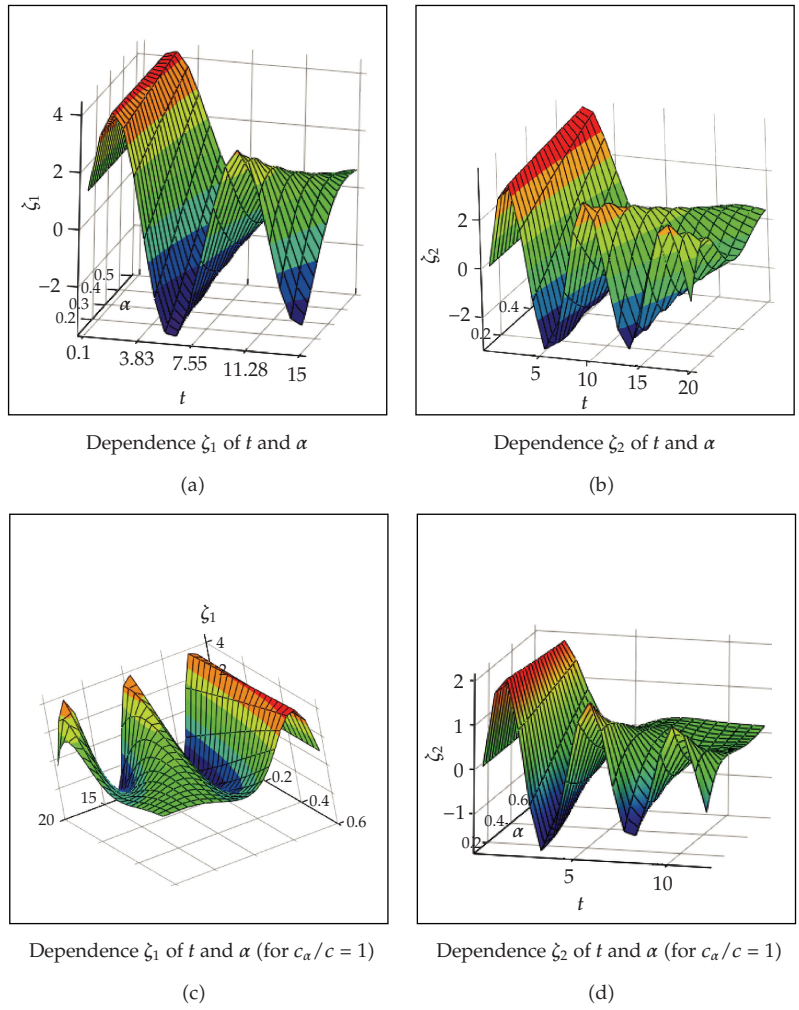

Dependence ζ_1 of t and α

(a)

Dependence ζ_2 of t and α

(b)

Dependence ζ_1 of t and α (for $c_\alpha/c = 1$)

(c)

Dependence ζ_2 of t and α (for $c_\alpha/c = 1$)

(d)

Figure 7: First and second eigen fractional modes, $\xi_1(\alpha, t)$ and $\xi_2(\alpha, t)$ presented by surfaces with corresponding first and second fractional order time components $\eta_1(\alpha, t)$—surfaces in left column and $\eta_2(\alpha, t)$—surfaces in right column for same system kinetic and geometric parameter values.

First approach give a model based on the rigid rotors coupled with rigid gear teeth, with mass distributions not balanced and in the form of the mass particles as the series of the mass debalances of the gears in multistep gear transmission. By very simple model is possible and useful investigation of the nonlinear dynamics of the multistep gear transmission and nonlinear phenomena in free and forced dynamics. This model is suitable to explain source of vibrations and big noise, as well as no stability in gear transmission dynamics. Layering of the homoclinic orbits in phase plane is source of a sensitive dependence nonlinear type of regime of gear transmission system dynamics.

Second approach give a model based on the two-step gear transmission taking into account deformation and creeping and also visco-elastic teeth gears coupling. Our investigation was focused to a new model of the fractional order dynamics of the gear transmissiont. For this model we obtain analytical expressions for the corresponding

fractional order modes like one frequency eigen vibrational modes. Generalization of this model to the similar model of the multistep gear transmission is very easy.

Appendices

A. Solution of a Fractional Order Differential Equation of a Fractional Order Creep Oscillator with Single Degree of Freedom

The fractional order differential equations from all three (79) obtained and considered cases of eigen fractional order partial-particular oscillators of the hybrid fractional order gear transmission system are in mathematical analogy same type of fractional order differential equation with corresponding unknown time-function, $\xi_s(t)$, $s = 1,2,3$. For all these time functions $\xi_s(t)$, $s = 1,2,3$, we can use notation $T(t)$ and all previous derived fractional order differential equations (79) of eigen fractional order partial oscillators with one degree of freedom, correspond to the fractional order model dynamics of the gear transmission system dynamics with three degree of freedom, we can rewrite it in the following form:

$$\ddot{T}(t) \pm \omega_\alpha^2 T^{(\alpha)}(t) + \omega_0^2 T(t) = 0. \tag{A.1}$$

This fractional order differential equation (A.1) on unknown time-function $T(t)$, can be solved by applying Laplace transforms (see [42, 58] or [67, 69]). Upon that fact Laplace transform of solution is in the form

$$\mathcal{T}(p) = \mathcal{L}[T(t)] \frac{pT(0) + \dot{T}(0)}{p^2 + \omega_0^2 \left[1 \pm \left(\omega_\alpha^2/\omega_0^2\right)\mathbf{R}(p)\right]}, \tag{A.2}$$

where $\mathcal{L}[\mathfrak{D}_\alpha^t[T(t)]] = \mathbf{R}(p)\mathcal{L}[T(t)]$ is Laplace transform of a fractional derivative $d^\alpha T(t)/dt^\alpha$ for $0 \le \alpha \le 1$. For creep rheological material those Laplace transforms are of the form:

$$\mathcal{L}\left[\mathfrak{D}_\alpha^t[T(t)]\right] = \mathbf{R}(p)\mathcal{L}[T(t)] - \frac{d^{\alpha-1}}{dt^{\alpha-1}}T(0) = p^\alpha \mathcal{L}[T(t)] - \frac{d^{\alpha-1}}{dt^{\alpha-1}}T(0) \tag{A.3}$$

where the initial value are

$$\left.\frac{d^{\alpha-1}T(t)}{dt^{\alpha-1}}\right|_{t=0} = 0, \tag{A.4}$$

so, in that case Laplace transform of time-function is given by the following expression:

$$\mathcal{L}\{T(t)\} = \frac{pT_0 + \dot{T}_0}{\left[p^2 \pm \omega_\alpha^2 p^\alpha + \omega_0^2\right]}. \tag{A.5}$$

Table 1: The datas of gear box.

	Pinion	Middle 1	Middle 2	Output gear
Number of the teeth	51	72	19	73
Modulus, mm	1,405	1,405	2,2175	2,2175
Face whith, mm	22,5	29	20	20
Inertias	0 01837	0 03837	0 00071	0 1740
Contact ratio	1,60		1,7	
Mean stiffness	$4,24 \times 10^9$		$3,45 \times 10^9$	
Mesh Phasing	0 257			
Torque T, Nm	100	0	0	258,4

For boundary cases, when material parameters α take the following values: $\alpha = 0$ and $\alpha = 1$ we have the two special simple cases, whose corresponding fractional-differential equations and solutions are known. In these cases fractional-differential equations are:

$$(1^*) \quad \ddot{T}(t) \pm \tilde{\omega}_{0\alpha}^2 T^{(0)}(t) + \omega_0^2 T(t) = 0 \quad \text{for } \alpha = 0, \tag{A.6}$$

where $T^{(0)}(t) = T(t)$, and

$$(2^*) \quad \dddot{T}(t) \pm \omega_{1\alpha}^2 T^{(1)}(t) + \omega_0^2 T(t) = 0 \quad \text{for } \alpha = 1, \tag{A.7}$$

where $T^{(1)}(t) = \dot{T}(t)$.

The solutions to equations (C.6) and (C.7) are

$$(1^*) \quad T(t) = T_0 \cos t\sqrt{\omega_0^2 \pm \tilde{\omega}_{0\alpha}^2} + \frac{\dot{T}_0}{\sqrt{\omega_0^2 \pm \tilde{\omega}_{0\alpha}^2}} \sin t\sqrt{\omega_0^2 \pm \tilde{\omega}_{0\alpha}^2} \tag{A.8}$$

for $\alpha = 0$.

$$\left(2^{*(a)}\right) \quad T(t) = e^{\mp(\omega_1^2/2)t}\left\{T_0 \cos t\sqrt{\omega_0^2 - \frac{\omega_{1\alpha}^4}{4}} + \frac{\dot{T}_0}{\sqrt{\omega_0^2 - \omega_{1\alpha}^4/4}} \sin t\sqrt{\omega_0^2 - \frac{\omega_{1\alpha}^4}{4}}\right\} \tag{A.9}$$

for $\alpha = 1$ and for $\omega_0 > (1/2)\omega_{1\alpha}^2$, (for soft creep) or for strong creep:

$$\left(2^{*(b)}\right) \quad T(t) = e^{\mp(\omega_{1\alpha}^2/2)t}\left\{T_0 Ch\, t\sqrt{\frac{\omega_{1\alpha}^4}{4} - \omega_0^2} + \frac{\dot{T}_0}{\sqrt{\omega_{1\alpha}^4/4 - \omega_0^2}} Sh\, t\sqrt{\frac{\omega_{1\alpha}^4}{4} - \omega_0^2}\right\} \tag{A.10}$$

for $\alpha = 1$ and for $\omega_0 < (1/2)\omega_{1\alpha}^2$.

For kritical case

$$\left(2^{*(c)}\right) \quad T(t) = e^{\mp(\omega_{1\alpha}^2/2)t}\left\{T_0 + \frac{2\dot{T}_0}{\omega_{1\alpha}^2} t\right\} \text{za } \alpha = 1, \quad \text{za} \quad \omega_0 = \frac{1}{2}\omega_{1\alpha}^2. \tag{A.11}$$

Fractional-differential equation (A.1) for the general case, when α is real number from interval $0 < \alpha < 1$ can be solved by using Laplace's transformation. By using that is

$$\mathcal{L}\left\{\frac{d^{\alpha}T(t)}{dt^{\alpha}}\right\} = p^{\alpha}\mathcal{L}\{T(t)\} - \left.\frac{d^{\alpha-1}T(t)}{dt^{\alpha-1}}\right|_{t=0} = p^{\alpha}\mathcal{L}\{T(t)\}, \tag{A.12}$$

and by introducing for initial conditions of fractional derivatives in the form (A.3), and after taking Laplace's transform of (A.1) we obtain the equation (A.2) with respect to the Laplace transform of solution, or in the following form:

$$\mathcal{L}\{T(t)\} = \frac{pT_{0i} + \dot{T}_{0i}}{2\left(p^2 \pm \omega_{\alpha}^2 p^{\alpha} + \omega_0^2\right)}. \tag{A.13}$$

For the case when $\omega_0^2 \neq 0$, the Laplace transform of the solution can be developed into series by following way:

$$\begin{aligned}\mathcal{L}\{T(t)\} &= \frac{pT_0 + \dot{T}_0}{p^2\left[1 + \left(\omega_{\alpha}^2/p^2\right)\left(\pm p^{\alpha} + \omega_0^2/\omega_{\alpha}^2\right)\right]} \\ &= \left(T_0 + \frac{\dot{T}_0}{p}\right)\frac{1}{p}\frac{1}{1 + \left(\omega_{\alpha}^2/p^2\right)\left(\pm p^{\alpha} + \omega_0^2/\omega_{\alpha}^2\right)},\end{aligned} \tag{A.14}$$

$$\begin{aligned}\mathcal{L}\{T(t)\} &= \left(T_0 + \frac{\dot{T}_0}{p}\right)\frac{1}{p}\sum_{k=0}^{\infty}\frac{(-1)^k\omega_{\alpha}^{2k}}{p^{2k}}\left(\pm p^{\alpha} + \frac{\omega_0^2}{\omega_{\alpha}^2}\right)^k, \\ \mathcal{L}\{T(t)\} &= \left(T_0 + \frac{\dot{T}_0}{p}\right)\frac{1}{p}\sum_{k=0}^{\infty}\frac{(-1)^k\omega_{\alpha}^{2k}}{p^{2k}}\sum_{j=0}^{k}\binom{k}{j}\frac{(\mp 1)^j p^{\alpha j}\omega_{\alpha}^{2(j-k)}}{\omega_o^{2j}}.\end{aligned} \tag{A.15}$$

In writing (A.15) it is assumed that expansion leads to convergent series. The inverse Laplace transform of previous Laplace transform of solution (A.15) in term-by-term steps is based on known theorems, and yield the following solution of differential equation (A.1) of time function in the following form of time series:

$$\begin{aligned}T(t) = \mathcal{L}^{-1}\mathcal{L}\{T(t)\} &= T_0\sum_{k=0}^{\infty}(-1)^k\omega_{\alpha}^{2k}t^{2k}\sum_{j=0}^{k}\binom{k}{j}\frac{(\mp 1)^j\omega_{\alpha}^{2j}t^{-\alpha j}}{\omega_o^{2j}\Gamma(2k+1-\alpha j)} \\ &+ \dot{T}_0\sum_{k=0}^{\infty}(-1)^k\omega_{\alpha}^{2k}t^{2k+1}\sum_{j=0}^{k}\binom{k}{j}\frac{(\mp 1)^j\omega_{\alpha}^{-2j}t^{-\alpha j}}{\omega_o^{2j}\Gamma(2k+2-\alpha j)}.\end{aligned} \tag{A.16}$$

B. Example of Numerical Experiment

See Table 1.

Acknowledgments

Parts of this research were supported by the Ministry of Sciences of Republic Serbia through Mathematical Institute SANU Belgrade Grants no. ON144002 Theoretical and Applied Mechanics of the Rigid and Solid Body. Mechanics of Materials, and also through the Faculty of Mechanical Engineering University of Niš and State University of Novi Pazar.

References

[1] M. Benton and A. Seireg, "Influecing instability and resonances in geared systems," *Journal of Mechanical Design*, vol. 103, no. 2, pp. 372–378, 1981.

[2] M. Blagojević, V. Nikolić-Stanojević, N. Marjanović, and L. J. Veljović, "Analysis of cycloid drive dynamic behavior," *Scientific Technical Rewiew*, no. 1, pp. 52–56, 2009.

[3] J. G. Bollinger and R. J. Harker, "Instability potencijal of high speed gearing," *Journal of the Industrial Mathematics*, vol. 17, pp. 35–39, 1967.

[4] D. Dimitrijevic and V. Nikolić, "Eigenfreuqency analysis of the spur gear pair with moving excentric masses on the body of one of the gears," *FME Transactions*, vol. 35, no. 3, pp. 157–163, 2007.

[5] K. Hedrih (Stevanović), "Interpretation of the motion of a heavy body around a stationary axis and kinetic pressures on bearing by means of the mass moment vectors for the pole and the axis," *Theoretical and Applied Mechanics*, no. 20, pp. 69–88, 1994.

[6] K. Hedrih (Stevanović), "Comments to the fundamental theorem and extension of the rotation tensor of the deformable body," *Tensor*, vol. 61, no. 3, pp. 290–303, 1999.

[7] K. Hedrih (Stevanović), "Leonhard Euler (1707–1783) and rigid body dynamics," *Scientific Technical Review*, vol. 57, no. 3-4, pp. 3–12, 2008.

[8] K. Hedrih (Stevanović), "Contribution to the coupled rotor nonlinear dynamics," in *Advances in Nonlinear Sciences*, Monograph, pp. 229–259, Academy of Nonlinear Sciences, Belgrade, Serbia, 2004.

[9] K. Hedrih (Stevanović), "Homoclinic orbits layering in the coupled rotor nonlinear dynamics and 2chatic clock models: a paradigm for vibrations and noise in machines," in *Proceedings of the 21st International Congress of Theoretical and Applied Mechanics (ICTAM '04)*, p. 320, Warsaw, Poland, August 2004.

[10] K. Hedrih (Stevanović), "Phase portraits and homoclinic orbits visualization of nonlinear dynamics of multiple step reductor/multiplier," in *Proceedings of the 11th World Congress in Mechanism and Machine Sciences (IFToMM '04)*, vol. 2, pp. 1508–1512, China Machine Press, Tianjin, China, April 2004.

[11] K. Hedrih (Stevanović), "Homoclinic orbits layering in the coupled rotor nonlinear dynamics and chaotic clock models," in *Proceedings of the 21st International Congress of Theoretical and Applied Mechanics (ICTAM '04)*, W. Gutkowski and T. A. Kowalewski, Eds., vol. 2, p. 421, Springer, Warsaw, Poland, August 2004.

[12] K. Hedrih (Stevanović), R. Knežević, and R. Cvetković, "Dynamics of planetary reductoe with turbulent damping," *International Journal of Nonlinear Sciences and Numerical Simulation*, vol. 2, no. 3, pp. 265–277, 2001.

[13] K. Hedrih (Stevanović) and R. Knežević, "Structural stability of the planetary reductor nonlinear dynamics phase portrait," *Facta Universitatis, Series Mechanical Engineering*, vol. 1, no. 7, pp. 911–923, 2000.

[14] H. Vinayak and R. Singh, "Multi-body dynamics and modal analysis of compliant gear bodies," *Journal of Sound and Vibration*, vol. 210, no. 2, pp. 171–212, 1998.

[15] F. C. Moon, "Chaotic clock models: a paradigm for noise in machines," in *Proceedings of the IUTAM Symposium on Chaotic Dynamics and Control of Systems and Processes in Mechanics*, vol. 39, pp. 41–44, Dipartimento di Ingegneria Strutturale e Geotecnica, Università di Roma " La Sapienza", Roma, Italy, 2003.

[16] S. Leela, "A new unified concept of stability," *Facta Universitates, Series Mechanics, Automatic Control and Robotics*, vol. 4, no. 16, pp. 33–42, 2004.

[17] K. Hedrih (Stevanović), *Vector Method of the Heavy Rotor Kinetic Parameter Analysis and Nonlinear Dynamics*, Monograph, University of Niš, 2001.

[18] K. Hedrih (Stevanović), "The analogy between the stress state model, the strain state model and the mass inertia moment state model," *Facta Universitatis, Series Mechanics, Automatic Control and Robotics*, vol. 1, no. 1, pp. 105–120, 1991.

[19] K. Hedrih (Stevanović), "Nonlinear dynamics of a gyrorotor and sensitive dependence on initial conditions of a heavy gyrorotor forced vibration/rotation motion," in *Proceednings of the 2nd International Conference on Control of Oscillations and Chaos (COC '00)*, F. L. Chernousko and A. I. Fradkov, Eds., vol. 2, pp. 259–266, IEEE, CSS, IUTAM, SPICS, St. Petersburg, Institute for Problems of mechanical Engineering of Russian Academy of Sciences and St. Petersburg State University, 2000, Semi-Plenary Invited Lecture.

[20] K. Hedrih (Stevanović), "Nonlinear dynamics of a gyrorotor with turbulent damping," *Nauka Tehnika Bezbednost*, vol. 1, pp. 109–127, 2001, Serbian.

[21] K. Hedrih (Stevanović), "Axoids (cones) in the nonlinear dynamics of the heavy rotors with many axes of the rotation (gyrorotors)," in *Proceedings of the International Congress of Nonlinear Analysis and It's Applications*, p. 130, Moscow, Russia, September 1998.

[22] K. Hedrih (Stevanović) and G.. Janevski, "Nonlinear dynamics of a gyro-disc-rotor and structural dependence of a phase portrait on the initial conditions," in *Proceedings of Dynamics of Machine*, pp. 81–88, Institute of Thermomechanics, Czech Committee of the European Mechanics Society, Prague, Czech Republic, 2000.

[23] K. Hedrih (Stevanović) and L. Simonović, "Phase portraits and homoclinic orbits: visualization of nonlinear dynamics of reductor," *Journal of Politechnica University Timisoara, Romonia, Transaction on Mechanical Engineering*, vol. 47, no. 61, pp. 76–86, 2008.

[24] K. Hedrih (Stevanović) and L. Veljović, "Nonlinear dynamics of the heavy gyro-rotor with two skew rotating axes," *Journal of Physics: Conference Series*, vol. 96, no. 1, Article ID 012221, 2008.

[25] K. Hedrih (Stevanović) and L. Veljović, "Nonlinear dynamic of heavy gyro- rotor with two rotating axes," *Facta Universitates Series Mechanics, Automatic Control and Robotics*, vol. 14, no. 16, pp. 55–68, 2004.

[26] J. Lin and R. G. Parker, "Analatical characterization od the unique properties of planetarly gear free vibration," *Journal of Vibrattion and Acoustics*, vol. 121, pp. 316–321, 1999.

[27] S. Y.T. Lang, "Graph-theoretic modelling of epicyclic gear systems," *Mechanism and Machine Theory*, vol. 40, no. 5, pp. 511–529, 2005.

[28] T. Sun and H. Hu, "Nonlinear dynamics of a planetary gear system with multiple clearances," *Mechanism and Machine Theory*, vol. 38, no. 12, pp. 1371–1390, 2003.

[29] K. Hedrih (Stevanović), "WEB Presentation of the Lectures on Mechanics III—Dynamics," 2006-2007, http://www.hm.co.yu/mehanika/.

[30] K. Hedrih (Stevanović), "Vectors of the body mass moments: topics from mathematics and mechanics," *Zbornik radova*, vol. 8, no. 16, pp. 45–104, 1998.

[31] K. Hedrih (Stevanović), "The mass moment vectors at n-dimensional coordinate system," *Tensor*, vol. 54, pp. 83–87, 1993.

[32] K. Hedrih (Stevanović), "Derivatives of the mass moment vectors at the dimensional coordinate system N," *Facta Universitatis. Series: Mathematics and Informatics*, vol. 13, no. 1, pp. 139–150, 2001.

[33] K. Hedrih (Stevanović), "Derivatives of the mass moments vectors with applications," in *Proceedings of the 5th National Congress on Mechanics*, pp. 694–705, Ioannina, Greece, 1998, invited lecture.

[34] K. Hedrih (Stevanović), "Vector method of the kinetic parameters analysis of the rotor with many axes and nonlinear dynamics," in *Proceedings of the 3rd International Conference on Nonlinear Mechanics (ICNM '98)*, pp. 42–47, Shanghai, China, August 1998, Parallel General Lecture.

[35] K. Hedrih (Stevanović), "On some interpretations of the rigid bodies kinetic parameters," in *Proceedings of the 18th International Congress of Theoretical and Applied Mechanics (ICTAM '92)*, pp. 73–74, Haifa, Israel, August 1992.

[36] K. Hedrih (Stevanović), "For optimal time of study: vector and tensor methods in classical mechanics," *Nonlinear Dynamics*, pp. 98–107, 2008.

[37] A. A. Andronov, A. A Vitt, and S. E. Haykin, *Teoriya Kolebaniy*, Nauka, Moscow, Russia, 1981.

[38] D. Rašković and K. Hedrih (Stevanović), "Ubrzanje drugog reda (trzaj) pri obrtanju tela oko nepomične tačke," *Zbornik radova Tehničkog fakulteta, Niš*, pp. 93–100, 1966-1967.

[39] K. Hedrih (Stevanović), "Dynamics of coupled systems," *Nonlinear Analysis: Hybrid Systems*, vol. 2, no. 2, pp. 310–334, 2008.

[40] K. Hedrih (Stevanović), "Vectorial method of the kinetic parameters analysis of the rotor with two rotation axes and nonlinear dynamics in the field of the turbulent damping," in *Proceedings of the 3rd International Symposium on Classical and Celestial Mechanics*, p. 163, Velikiye Luki, Russia, 1998.

[41] M. Ajmi and P. Velex, "A model for simulating the quasi-static and dynamic behaviour of solid wide-faced spur and helical gears," *Mechanism and Machine Theory*, vol. 40, no. 2, pp. 173–190, 2005.
[42] B. S. Bačlić and T. M. Atanacković, "Stability and creep of a fractional derivative order viscoelastic rod," *Bulletin, Classe des Sciences Mathématiques et Natturalles Sciences Mathématiques*, no. 25, pp. 115–131, 2000.
[43] D. Rašković, *Theory of Vibrations*, Naučna knjiga, Beograd, Serbia, 1965.
[44] D. Rašković, *Mehanika III, Dinamika*, Naučna knjiga, Beograd, Serbia, 1972.
[45] K. Hedrih (Stevanović), "Partial fractional order differential equations of transversal vibrations of creep-connected double plate systems," in *Fractional Differentiation and Its Applications*, A. Le Mahaute, J. A. Tenreiro Machado, J. C. Trigeassou, and J. Sabatier, Eds., vol. 2 of *Monograph*, pp. 289–302, 2005.
[46] K. Hedrih (Stevanović), "Interpretation of the motion of a heavy body around a stationary axis in the field with turbulent damping and kinetic pressures on bearing by means of the mass moment vector for the pole and the axis," *Facta Universitatis, Series Mechanics, Automatic Control and Robotics*, vol. 1, no. 4, pp. 519–538, 1994.
[47] K. Hedrih (Stevanović), "Some interpretations of the rigid body kinetic parameters," *Tehnika, Mašinstvo*, vol. 45, pp. M8–M13, 1996.
[48] K. Hedrih (Stevanović), "Vector method and phase plane method, approach for the analysis of kinetic parameters and hmoclinic orbits of coupled rotor dynamics," in *Proceedings of the International Symposium on Analysis, Manifolds and Mechanics*, Calcutta, India, 2003, in Honor of Professor M. C. Chaki's 90th Birth Anniversary.
[49] K. Hedrih (Stevanović), "Nonlinear dynamics of rotor with a vibrating axis and sensitive dependence on initial conditions of forced vibration/rotation/stochasticlikechaoticlike motion of a heavy rotor," in *Proceedings of the 3rd Bogoliubov Readings: Asymptotic and Qualitative Methods of Nonlinear Mechanics (ASYM '97)*, pp. 73–74, Tezi dopovidey, Mezhdunarodnaya konferenciya, Inst. Math. NANU, Kiev, Russia, September 1997.
[50] K. Hedrih (Stevanović), "Nonlinear dynamics of a rotor with a vibrating axis, and sensitive dependence on the initial conditions of the forced vibration of a heavy rotor," *Nelīnĭnī Kolivannya* , vol. 3, no. 1, pp. 129–145, 2000.
[51] K. Hedrih (Stevanović), "Nonlinear Dynamics of a Rotor with a vibrating axis, and sensitive dependence on the initial conditions of the forced vibration of a heavy rotor," *International Journal Nonlinear Oscillations*, vol. 3, no. 1, pp. 129–145, 2000.
[52] Ph. Holmes, "Nonlinear oscillations and the smale horseshoe map," in *Proceedings of Symposium in Applied Mathematics*, vol. 39, pp. 81–88, American Mathematical Society, Providence, RI, USA, 1989.
[53] J. J. Stoker, *Nonlinear Vibrations*, Interscience, New York, NY, USA, 1950.
[54] K. Hedrih (Stevanović), "Homoclinic Orbits of Nonlinear Dynamics of Multi-step Reductor," *Nauka Tehnika Bezbednost*, vol. 12, no. 1, pp. 45–65, 2002.
[55] V. Nikolić, *Mechanical Analysis of the Gear Transmission*, Monograph, Mašinski fakultet u Kragujevcu, 1999.
[56] J. Posa and S. Wojciech, "Dynamics of systems with changing configuration and with flexible beam-like links," *Mechanism and Machine Theory*, vol. 35, no. 11, pp. 1515–1534, 2000.
[57] M. Enelund, *Fractional Calculus and Linear Viscoelasticity in Structural Dynamics*, Division of Solid Mechanics, Chalmers Tekniska Hogskola, Goteborg, Sweden, 1996.
[58] R. Gorenflo and F. Mainardi, "Fractional calculus, integral and differential equations of fractional order," in *Fractals and Fractional Calculus in Continuum Mechanics (Udine, 1996)*, vol. 378 of *CISM Courses and Lectures*, pp. 223–276, Springer, Vienna, Austria, 1997.
[59] O. A Goroško and K. Hedrih (Stevanović), "Construction of the Lagrange's mechanics of the hereditary systems," *Facta Universitatis, Series Mechanics, Automatic Control and Robotics*, vol. 6, no. 1, pp. 1–22, 2007.
[60] O. A. Goroško and K. Hedrih (Stevanović), "Advances in development of the analytical dynamics of the hereditary discrete systems," *Journal of Physics: Conference Series*, vol. 96, no. 1, Article ID 012143, 2008.
[61] K. Hedrih (Stevanović), "Discrete continuum method," in *Proceedings of the 6th World Congress on Computational Mechanics (WCCM VI) in Conjunction with the 2nd Asian-Pacific Congress on Computational Mechanics (APCOM '04)*, vol. 1, pp. 1–11, Tsinghua University Press & Springer, Beijing, China, September 2004.
[62] K. Hedrih (Stevanović), "Modes of the homogeneous chain dynamics," *Signal Processing*, vol. 86, no. 10, pp. 2678–2702, 2006.

[63] O. A Goroško and K. Hedrih (Stevanović), *Analytical Dynamics (Mechanics) of Discrete Hereditary Systems*, Monograph, University of Niš, 2001.

[64] K. Hedrih (Stevanović), "Creep vibrations of a fractional derivative order constititive relation deformable bodies," in *Proceedings of the 8th American Congress of Applied Mechanics (PACAM '04)*, vol. 10 of *Applied Mechanics in Americas*, pp. 548–551, La Habana, Cuba, 2004.

[65] K. Hedrih (Stevanović), "Transversal creep vibrations of a beam with fractional derivative constitutive relation order, first part: partial fractional-differential equation . part second: stochastic stability of the beam dynamic shape, under axial bounded noise excitation," in *Proceedings of 4th International Conference on Nonlinear Mechanics (ICNM '04)*, W. Z. Chien, Ed., vol. 10 of *Applied Mechanics in Americas*, pp. 584–595, Shanghai, China, August 2002.

[66] K. Hedrih (Stevanović), "The transversal creeping vibrations of a fractional derivative order constitutive relation of nonhomogeneous beam," *Mathematical Problems in Engineering*, vol. 2006, no. 5, Article ID 46236, 18 pages, 2006.

[67] K. Hedrih (Stevanović), "Partial fractional order differential equations of transversal vibrations of creep connected double plates systems," in *Proceedings of 1st IFAC Workshop on Fractional Differentiation and Its Application (FDA ' 04)*, vol. 10, pp. 299–304, Bordeaux, France, July 2004.

[68] K. Hedrih (Stevanović), "The longitudinal and transversal creep vibrations of a fractional order constitutive relation beams," *Scientific Bulletin of the Politehnica, University of Timisoara, Transaction on Mechanics*, vol. 48, no. 62, pp. 5–12, 13–22, 2003.

[69] K. Hedrih (Stevanović) and A. Filipovski, "Longitudinal vibration of a fractional derivative order rheological rod with variable cross section," *Facta Universitatis, Series Mechanics, Automatic Control and Robotics*, vol. 3, no. 12, pp. 327–350, 2000.

[70] K. Hedrih (Stevanović), "Dynamics of multipendulum systems with fractional order creep elements," *Journal of Theoretical and Applied Mechanics*, vol. 46, no. 3, pp. 483–509, 2008.

[71] K. Hedrih (Stevanović), "Hybrid systems and hybrid dynamics: theory and applications," in *Proceedings of the 8th HSTAM International Congress on Mechanics*, N. Bazwos, D. L. Karabalis, D. Polyzos, D. E. Beskos, and J. T. Katsikadelis, Eds., vol. 1, pp. 77–86, Patras, Greece, July 2007, invited plernary lecture.

Hindawi Publishing Corporation
Mathematical Problems in Engineering
Volume 2010, Article ID 261826, 14 pages
doi:10.1155/2010/261826

Research Article

Research on Ossicular Chain Mechanics Model

Wen-juan Yao,[1,2] Hua-cong Zhou,[1] Bao-lin Hu,[2] Xin-sheng Huang,[3] and Xiao-qing Li[1]

[1] *Department of Civil Engineering, Shanghai University, Shanghai 200072, China*
[2] *Shanghai Institute of Applied Mathematics and Mechanics, Shanghai 200072, China*
[3] *ENT Department, Zhongshan Hospital, Fudan University, Shanghai 200032, China*

Correspondence should be addressed to Wen-juan Yao, wenjuan@mail.shu.edu.cn and Xin-sheng Huang, huangxinsh@hotmail.com

Received 30 November 2009; Revised 12 March 2010; Accepted 28 March 2010

Academic Editor: Carlo Cattani

On account of the complex structure of the middle ear and that it is more difficult to carry out experiments to test the nature of the mechanical components, the relevant data is hard to obtain, which has become an obstacle restricting analysis of the middle ear mechanic. Based on spatial structure and mechanical properties of ossicular chain, the paper has established functional relationship between load and members displacement with elastic principles and variation principles, in order that experimental results will be reflected in mechanical model. In the process of solving equations, we use the experimental data of a known special point or the various components function of statistical regression method and then combine them with the time shift function, so that the analytical solution of the various components will be achieved. The correctness of equation derived in this paper is verified by comparing the experimental data. So the model has provided a convenient way to obtain date in the future research analysis.

1. Introduction

Recently, with the rapid development of biological science, there is a growing concern about the research on human organs. So the research on middle ear structure and function has started in the ascendant. From different views, many scholars have been studying on middle-ear and sound conduction with different methods [1–20]. Abel et al. have obtained the geometry of ossicular in order to establish the finite element model in magnetic resonance microimaging [21]. Sun et al. have created middle ear FEM by a cross-calibration technique, and applied it to predicate stapes footplate displacement and the ossicular mechanics character of the human middle ear [22]. In the same year, in Takuji Koike's study, a three-dimensional FEM of the human middle ear has been established, including features of the middle ear which were not considered in the previous model, that is, the ligaments,

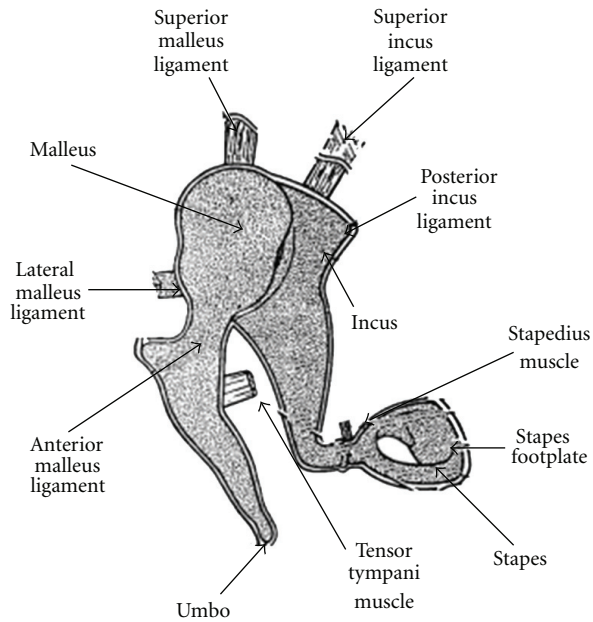

Figure 1: Spatial structure of ossicular chain [25].

tendons, I–S joint, loading of the cochlea, external auditory meatus, middle-ear cavities, and so forth. The validity of this model was confirmed by comparing the motion of the tympanic membrane and ossicular obtained by this model with the measurement data [23]. In Gan et al. study, they proposed a three-dimensional finite element model of the human ear. This model was constructed based on a complete set of histological section images of a left ear temporal bone. The FEM of the human ear was used to simulate ossicular joint to sound conduction affect [24].

Although these achievements are of great significant, the question of research process can not be ignored. For example, early research results were almost done on the cadaveric head or living animal; only observation experiment of some part in middle ear was done on normal human and lacked measurement of the whole member motion. Therefore, the quantity of measurement data was less than numerical simulation requirement. This limits the development numerical simulation method which was applied on middle ear research. In order to solve the problem, we have established mechanical model of ossicular and given its mathematical expression. The model can be used to test numerical simulation results.

2. Spatial Structure of Ossicular Chain

The ossicular chain is the smallest group of bones in human body, three bones together, they are the hammer (malleus), the anvil (incus), and the stirrup (stapes). These bones are connected and composition of a tiny link chain; see Figure 1. The ossicular chain comprises incudomalleolar joint and incudostapedial joint. Incudomalleolar joint is comprised of malleus and incus. Incudostapedial joint is comprised of incus and stapes. In general conditions, incudomalleolar joint and incudostapedial joint are immovable. Only in high sound pressure, the relative motion could occur. The ossicular chain is fixed the middle

Table 1: Parameters.

Name	Length	Area	Displacement	Elastic modulus
Anterior malleus ligament	l_1	s_{l1}	w_1	k_{l1}
Lateral malleus ligament	l_2	s_{l2}	w_2	k_{l2}
Superior malleus ligament	l_3	s_{l3}	w_3	k_{l3}
Tensor tympani muscle	l_4	s_{l4}	w_4	k_{l4}
Superior incus ligament	l_5	s_{l5}	w_5	k_{l5}
Posterior incus ligament	l_6	s_{l6}	w_6	k_{l6}
Stapedius muscle	l_7	s_{l7}	w_7	k_{l7}

Table 2: Parameters.

Name	Area	Displacement	Elastic modulus	Density
Stapes footplate	s_{l8}	w_{10}	k_{st}	—
Malleus	—	w_8	—	ρ_{ma}
Incus	—	w_9	—	ρ_{in}
Stapes	—	w_{10}	—	ρ_{st}
Load on malleus	$w_{8\mid x=q}$		frequency	ϖ

ear cavity depending on ligaments and tendons. Fixed malleus ligaments include superior, anterior and lateral ligament. Another tensor tympani muscle can help ligament fix malleus. Fixed incus ligaments include superior and posterior ligament. Fixed stapes include annular ligament and stapedius muscle. These ligaments and muscles can determine spatial position of ossicular chain in the middle ear cavity and affect motion states of ossicular chain under external dynamic loads.

3. Establishing Mechanics Model of Ossicular Chain

The length axis of ligament and muscle was defined to parallel coordinated axis in order to be simplified to derive formula. Tables 1 and 2 gave displacement and physics property of ligament, muscle, and ossicular chain.

Energy expressions of ossicular chain, ligament, and muscle be follows.

Malleus Kinetic Energy:

$$T_{\mathrm{ma}} = \iiint_{\Omega} \frac{1}{2}\rho_{\mathrm{ma}}\varpi^2 w_8^2 d\Omega. \tag{3.1}$$

Incus Kinetic Energy:

$$T_{\mathrm{in}} = \iiint_{\Omega} \frac{1}{2}\rho_{\mathrm{in}}\varpi^2 w_9^2 d\Omega. \tag{3.2}$$

Stapes Kinetic Energy:

$$T_{\mathrm{st}} = \iiint_{\Omega} \frac{1}{2}\rho_{\mathrm{st}}\varpi^2 w_{10}^2 d\Omega. \tag{3.3}$$

Elastic potential energy of anterior malleus ligament:

$$E_{l1} = \frac{1}{2}\iiint_{\Omega} k_{l1}\left[\left(\frac{\partial w_1}{\partial x}\right)^2 + \left(\frac{\partial w_1}{\partial y}\right)^2 + \left(\frac{\partial w_1}{\partial z}\right)^2\right] + \frac{k_{l1}}{2(1+\mu)}\left[\left(\frac{\partial w_1}{\partial x} + \frac{\partial w_1}{\partial y}\right)^2 + \left(\frac{\partial w_1}{\partial y} + \frac{\partial w_1}{\partial z}\right)^2 + \left(\frac{\partial w_1}{\partial x} + \frac{\partial w_1}{\partial z}\right)^2 d\Omega\right]. \tag{3.4}$$

Elastic potential energy of lateral malleus ligament:

$$E_{l2} = \frac{1}{2}\iiint_{\Omega} k_{l2}\left[\left(\frac{\partial w_2}{\partial x}\right)^2 + \left(\frac{\partial w_2}{\partial y}\right)^2 + \left(\frac{\partial w_2}{\partial z}\right)^2\right] + \frac{k_{l2}}{2(1+\mu)}\left[\left(\frac{\partial w_2}{\partial x} + \frac{\partial w_2}{\partial y}\right)^2 + \left(\frac{\partial w_2}{\partial y} + \frac{\partial w_2}{\partial z}\right)^2 + \left(\frac{\partial w_2}{\partial x} + \frac{\partial w_2}{\partial z}\right)^2 d\Omega\right]. \tag{3.5}$$

Elastic potential energy of superior malleus ligament:

$$E_{l3} = \frac{1}{2}\iiint_{\Omega} k_{l3}\left[\left(\frac{\partial w_3}{\partial x}\right)^2 + \left(\frac{\partial w_3}{\partial y}\right)^2 + \left(\frac{\partial w_3}{\partial z}\right)^2\right] + \frac{k_{l3}}{2(1+\mu)}\left[\left(\frac{\partial w_3}{\partial x} + \frac{\partial w_3}{\partial y}\right)^2 + \left(\frac{\partial w_3}{\partial y} + \frac{\partial w_3}{\partial z}\right)^2 + \left(\frac{\partial w_3}{\partial x} + \frac{\partial w_3}{\partial z}\right)^2 d\Omega\right]. \tag{3.6}$$

Elastic potential energy of tensor tympani muscle:

$$E_{l4} = \frac{1}{2}\iiint_{\Omega} k_{l4}\left[\left(\frac{\partial w_4}{\partial x}\right)^2 + \left(\frac{\partial w_4}{\partial y}\right)^2 + \left(\frac{\partial w_4}{\partial z}\right)^2\right] + \frac{k_{l4}}{2(1+\mu)}\left[\left(\frac{\partial w_4}{\partial x} + \frac{\partial w_4}{\partial y}\right)^2 + \left(\frac{\partial w_4}{\partial y} + \frac{\partial w_4}{\partial z}\right)^2 + \left(\frac{\partial w_4}{\partial x} + \frac{\partial w_4}{\partial z}\right)^2 d\Omega\right]. \tag{3.7}$$

Elastic potential energy of superior incus ligament

$$E_{l5} = \frac{1}{2}\iiint_{\Omega} k_{l5}\left[\left(\frac{\partial w_5}{\partial x}\right)^2 + \left(\frac{\partial w_5}{\partial y}\right)^2 + \left(\frac{\partial w_5}{\partial z}\right)^2\right] + \frac{k_{l5}}{2(1+\mu)}\left[\left(\frac{\partial w_5}{\partial x} + \frac{\partial w_5}{\partial y}\right)^2 + \left(\frac{\partial w_5}{\partial y} + \frac{\partial w_5}{\partial z}\right)^2 + \left(\frac{\partial w_5}{\partial x} + \frac{\partial w_5}{\partial z}\right)^2 d\Omega\right]. \tag{3.8}$$

Elastic potential energy of posterior incus ligament:

$$E_{l6} = \frac{1}{2}\iiint_{\Omega} k_{l6}\left[\left(\frac{\partial w_6}{\partial x}\right)^2 + \left(\frac{\partial w_6}{\partial y}\right)^2 + \left(\frac{\partial w_6}{\partial z}\right)^2\right] + \frac{k_{l6}}{2(1+\mu)}\left[\left(\frac{\partial w_6}{\partial x} + \frac{\partial w_6}{\partial y}\right)^2 + \left(\frac{\partial w_6}{\partial y} + \frac{\partial w_6}{\partial z}\right)^2 + \left(\frac{\partial w_6}{\partial x} + \frac{\partial w_6}{\partial z}\right)^2 d\Omega\right]. \tag{3.9}$$

Elastic potential energy of stapedius muscle:

$$E_{l7} = \frac{1}{2}\iiint_{\Omega} k_{l7}\left[\left(\frac{\partial w_7}{\partial x}\right)^2 + \left(\frac{\partial w_7}{\partial y}\right)^2 + \left(\frac{\partial w_7}{\partial z}\right)^2\right] + \frac{k_{l7}}{2(1+\mu)}\left[\left(\frac{\partial w_7}{\partial x} + \frac{\partial w_7}{\partial y}\right)^2 + \left(\frac{\partial w_7}{\partial y} + \frac{\partial w_7}{\partial z}\right)^2 + \left(\frac{\partial w_7}{\partial x} + \frac{\partial w_7}{\partial z}\right)^2 d\Omega\right]. \tag{3.10}$$

Elastic potential energy of stapes footplate:

$$E_{\mathrm{st}} = \frac{1}{2}\iint_{s} k_{\mathrm{st}} w_{10}^2 ds \tag{3.11}$$

External loads do work:

$$W = \frac{1}{2} P w_8 \Big|_{x=q}. \tag{3.12}$$

Structure strain energy:

$$V = E_{l1} + E_{l2} + E_{l3} + E_{l4} + E_{l5} + E_{l6} + E_{l7} + E_{\mathrm{st}} - W. \tag{3.13}$$

Potential energy of structure:

$$U = V - T = E_{l1} + E_{l2} + E_{l3} + E_{l4} + E_{l5} + E_{l6} + E_{l7} + E_{\mathrm{st}} - W - T_{\mathrm{ma}} - T_{\mathrm{in}} - T_{\mathrm{st}}. \tag{3.14}$$

When the load was applied on ossicular chain, all members were together moving. Moreover displacement direction was the same in interface of two members. So displacement relationship in members is as follows.

Displacement Relationship between anterior malleus ligament and malleus:

$$w_8 - w_1 \mid s_1 = 0. \tag{3.15}$$

Displacement Relationship between lateral malleus ligament and malleus:

$$w_8 - w_2 \mid s_2 = 0. \tag{3.16}$$

Displacement Relationship between superior malleus ligament and malleus:

$$w_8 - w_3 \mid s_3 = 0. \tag{3.17}$$

Displacement Relationship between tensor tympani muscle and malleus:

$$w_8 - w_4 \mid s_4 = 0. \tag{3.18}$$

Displacement Relationship between superior incus ligament and incus:

$$w_9 - w_5 \mid s_5 = 0. \tag{3.19}$$

Displacement Relationship between posterior incus ligament and incus:

$$w_9 - w_6 \mid s_6 = 0. \tag{3.20}$$

Displacement Relationship between stapedius muscle and stapes:

$$w_{10} - w_7 \mid s_7 = 0. \tag{3.21}$$

Displacement Relationship between malleus and incus:

$$w_9 - w_8 \mid s_8 = 0. \tag{3.22}$$

Displacement Relationship between incus and stapes:

$$w_{10} - w_9 \mid s_9 = 0, \tag{3.23}$$

where $s_1 \cdots s_9$ is the area of interface.

Boundary Constraint

Displacement of the fixed end in anterior malleus ligament:

$$w_1 \mid s_{10} = 0. \tag{3.24}$$

Displacement of the fixed end in lateral malleus ligament:

$$w_2 \mid s_{11} = 0. \tag{3.25}$$

Displacement of the fixed end in superior malleus ligament:

$$w_3 \mid s_{12} = 0. \tag{3.26}$$

Displacement of the fixed end in tensor tympani muscle:

$$w_4 \mid s_{13} = 0. \tag{3.27}$$

Displacement of the fixed end in superior incus ligament:

$$w_5 \mid s_{14} = 0. \tag{3.28}$$

Displacement of the fixed end in posterior incus ligament:

$$w_6 \mid s_{15} = 0. \tag{3.29}$$

Displacement of the fixed end in stapedius muscle:

$$w_7 \mid s_{16} = 0, \tag{3.30}$$

where $s_{10} \cdots s_{16}$ is the area of the fixed end in ligament and muscle.

Because elastic modulus of bone is ten thousand times than soft tissue, bone strain is less than soft tissue under loads and can be ignored. So bone displacement can be seen as rigid displacement caused by soft tissue motion. According to the published literature, when soft tissue strain is in elastic range, load and displacement will show linear relationship in terms of mechanical principle [26, 27]. Therefore, the whole structure displacement will show in linear relationship in the low stress conditions.

Based on the above analysis, the paper makes the two following assumptions:

(a) when load is fixed, the relationship between member displacement and spatial coordinate will be linear;

(b) when point is chosen, the point displacement will relate to load.

Based on the assumption, the composition of member displacement is coordinate and load. Moreover, the displacement of coordinate and load is independent. Member displacement expression:

Displacement of anterior malleus ligament

$$w_1 = \left(a_{11}x + b_{11}y + c_{11}z + d_{11}\right) \cdot f. \tag{3.31}$$

Displacement lateral malleus ligament:

$$w_2 = \left(a_{21}x + b_{21}y + c_{21}z + d_{21}\right) \cdot f. \tag{3.32}$$

Displacement of superior malleus ligament:

$$w_3 = \left(a_{31}x + b_{31}y + c_{31}z + d_{31}\right) \cdot f. \tag{3.33}$$

Displacement of tensor tympani muscle:

$$w_4 = \left(a_{41}x + b_{41}y + c_{41}z + d_{41}\right) \cdot f. \tag{3.34}$$

Displacement of superior incus ligament:

$$w_5 = \left(a_{51}x + b_{51}y + c_{51}z + d_{51}\right) \cdot f. \tag{3.35}$$

Displacement of posterior incus ligament:

$$w_6 = \left(a_{61}x + b_{61}y + c_{61}z + d_{61}\right) \cdot f. \tag{3.36}$$

Displacement of stapedius muscle:

$$w_7 = \left(a_{71}x + b_{71}y + c_{71}z + d_{71}\right) \cdot f. \tag{3.37}$$

Malleus displacement:

$$w_8 = \begin{cases} \left(a_{81}x + b_{81}y + c_{81}z + d_{81}\right) \cdot f & x < x_1, \\ \left(a_{82}x + b_{82}y + c_{82}z + d_{82}\right) \cdot f & x > x_1. \end{cases} \tag{3.38}$$

Incus displacement:

$$w_8 = \begin{cases} \left(a_{91}x + b_{91}y + c_{91}z + d_{91}\right) \cdot f & x < x_2, \\ \left(a_{92}x + b_{92}y + c_{92}z + d_{92}\right) \cdot f & x > x_2. \end{cases} \tag{3.39}$$

Stapes displacement:

$$w_{10} = \left(a_{101}x + b_{101}y + c_{101}z + d_{101}\right) \cdot f, \tag{3.40}$$

where x_1, x_2 is the interface of variable malleus section or variable incus section. a, b, c, d are coefficient and they have subscript. f is a function to relate with load.

$w_1, w_2 \cdots w_7$, expression including f is solved by knowing boundary conditions and testing results of key points. And then based on relationship of ossicular and ligament, w_8, w_9, w_{10} expression including f is solved. Finally all expressions are substituted to potential energy of structure U. Applying on variation principles to f, getting $\delta U = 0$, f is solved and is substituted to displacement expression of members (ossicular, ligament and muscle).

Another method is that displacement function expressions of member were obtained by linear regression based on similar results. The geometrical size of finite element model based on the images of CT in healthy human by Zhongshan Hospital affiliated to Fudan University. All patients were scanned with a 64-slice multiple spiral CT scanner (GE lightspeed VCT) using the following parameters: 0.625 mm collimation, 0.42 second per

Table 3: Material properties of ossicular chain [22].

Name	Density (kg/m^3)	Elastic modulus (Pa)
malleus		
for head	2.55e3	1.41e10
for neck	4.53e3	1.41e10
for handle	3.7e3	1.41e10
for body	2.36e3	1.41e10
Superior ligament	2.5e3	4.9e4
lateral ligament	2.5e3	6.7e4
anterior ligament	2.5e3	2.1e6
incus		
for short process	2.26e3	1.41e10
for long process	5.08e3	1.41e10
superior ligament	2.5e3	4.9e4
posterior ligament	2.5e3	6.5e5
Stapes	2.2e3	1.41e10
tympani muscle	2.5e3	2.6e6
stapedius muscle	2.5e3	5.2e5
cochlea impedance	—	60

wrap, 0.625 mm reconstruction slice thickness, and 0.5–0.625 mm reconstruction increment. The scan images were managed with self-edit program to form a geometric model. The model was reconstructed for optimizing meshes, setting boundary conditions and material properties in ANSYS. Finally, the 3D fluid-solid coupling finite element model of ossicular chain was established successfully; see Figure 2. Finite element model of ossicular chain referred to Zhai et al.'s results [28]. Ligament dimension in ossicular chain referred to Lemmerling et al.'s results [29]. The dimension of stapedius muscle and tensor tympani muscle referred to Beer et al.'s data [30]. Table 3 gave material properties of ossicular chain, which referred to Sun et al.'s data [22].

Figure 3 gave the simulation result of the displacement in different sound pressure levels: 50 dB, 70 dB, 90 dB, 105 dB, and 120 dB. The conclusions were obtained from similar results. Members were together moving, and moving direction was shown in Figure 3. Displacement direction was the same in interface of members in Figure 3; The result tested the hypothesis of theoretical derivation to be valid. Coordinate function of member displacement of linear regression by similar data was done.

Then the function was multiplied by f function. Expression is as follows.

Displacement of anterior malleus ligament:

$$w_1 = \left(0.001351x - 0.000685y + 0.002547z - 0.00000044\right) \cdot f. \tag{3.41}$$

Displacement of lateral malleus ligament:

$$w_2 = \left(-0.002916x + 0.001829y + 0.000761z + 0.0000134\right) \cdot f. \tag{3.42}$$

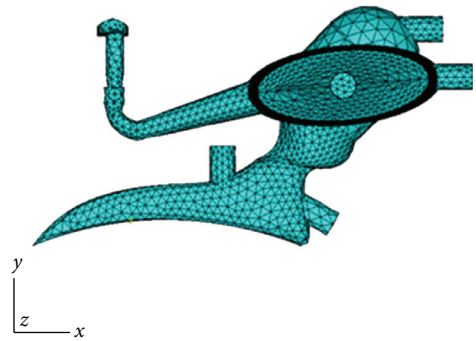

Figure 2: Finite element model of ossicular chain.

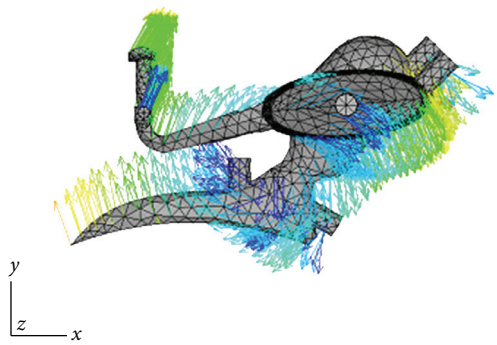

Figure 3: Moving direction of ossicular chain.

Displacement of superior malleus ligament:

$$w_3 = \left(-0.008318x - 0.007172y - 0.0025405z + 0.0000997\right) \cdot f. \tag{3.43}$$

Displacement of tensor tympani muscle:

$$w_4 = \left(-0.000432x - 0.001813y + 0.000575z + 0.00000506\right) \cdot f. \tag{3.44}$$

Displacement of superior incus ligament:

$$w_5 = \left(-0.006154x - 0.005452y + 0.000487z + 0.0000736\right) \cdot f. \tag{3.45}$$

Displacement of posterior incus ligament:

$$w_6 = \left(0.000493x + 0.001017y - 0.003073z + 0.0000159\right) \cdot f. \tag{3.46}$$

Displacement of stapedius muscle:

$$w_7 = \left(-0.000633x - 0.00299y - 0.007289z + 0.0000131\right) \cdot f. \tag{3.47}$$

Malleus displacement:

$$w_8 = \begin{cases} (-0.001699x - 0.000251y + 0.000848z + 0.0000572) \cdot f & x < 0.00267 \\ (0.001409x + 0.000777y - 0.000617z - 0.00000392) \cdot f & x > 0.00267. \end{cases} \tag{3.48}$$

Incus displacement:

$$w_9 = \begin{cases} (-0.001567x + 0.001242y + 0.000268z + 0.00000207) \cdot f & x < 0.00256 \\ (0.001020x + 0.001420y - 0.000488z - 0.000004510) \cdot f & x > 0.00256. \end{cases} \tag{3.49}$$

Stapes displacement:

$$w_{10} = (-0.000204x + 0.000541y - 0.002076z + 0.00000566) \cdot f. \tag{3.50}$$

Front displacements were substituted to energy equation. Finally energy equations were substituted to potential energy of structure U. Applying on variation principles to f, getting $\delta U = 0$, f was solved and was substituted to displacement expression of members (ossicular, ligament, and muscle).

4. Example

The curve that displacement of umbo and footplate centre was changed with frequency under 105 dB was computed. Load and displacement equations of linear regression by similar data were substituted to potential energy of structure U. Applying on variation principles to f, getting $\delta U = 0$, f was solved:

$$f = \frac{1.56 * 10^{-10}}{2 * 3.39 * 10^{-9} - 2 * 1.01 * 10^{-15}\varpi^2}, \tag{4.1}$$

f and relating to coordinate were substituted to displacement expression of umbo and footplate centre Expression is as follows.
Footplate centre displacement:

$$w_{10} = \frac{2.63 * 10^{-16}}{2 * 3.39 * 10^{-9} - 2 * 1.01 * 10^{-15}\varpi^2}. \tag{4.2}$$

Umbo displacement:

$$w_9 = \frac{3.83 * 10^{-16}}{2 * 3.39 * 10^{-9} - 2 * 1.01 * 10^{-15}\varpi^2}. \tag{4.3}$$

Computing results were compared with the data in published paper; see Figure 4 [31]. The curves of analytical solution were similar to those of experiment. This showed that analytical solution is valid. The difference of two curves was little in low and high frequency and big in 700–2000 Hz from Figure 4. It was caused by geometry size of model.

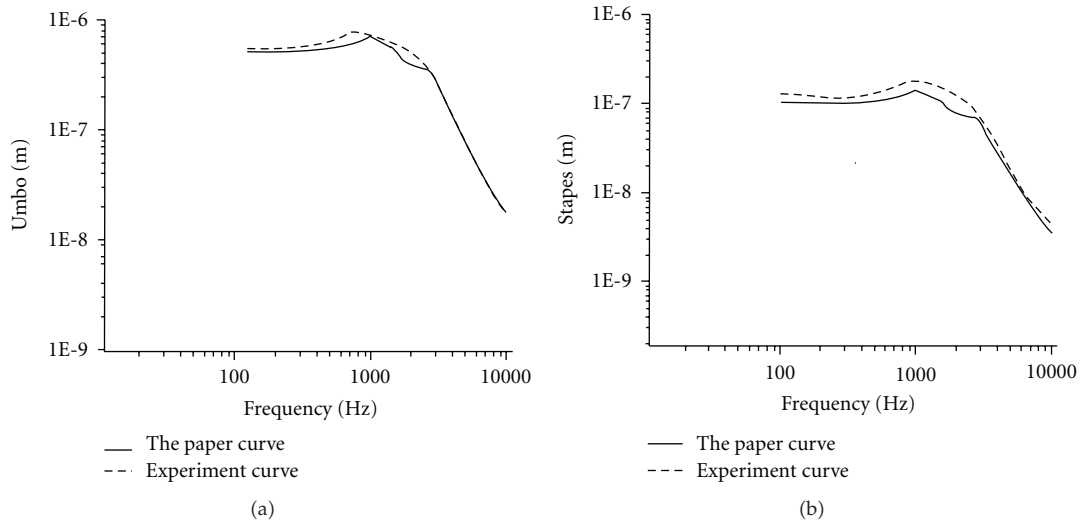

Figure 4: Comparing the amplitude of stapes and umbo under 105 dB (units: m)

5. Conclusion

The equation in the paper was one of the valid methods of obtaining experiment data. It could determinate function relationship based on experiment data of special point, and then experiment data of unknown point were computed according to the function relationship. This could get a large number of experiment data and solve difficulty of getting data. In addition, the model can analyze the effect which was caused by members' injury in motion or material changes to stapes displacement. For example, these problems were some lesions of middle ear, joint injury, ligament sclerosis, or tendon sclerosis.

Acknowledgment

The authors gratefully acknowledge the Major Project of Shanghai Scientific Committee for Fundamental Research (no. 08jc1404700).

References

[1] M. Kringlebotn, "Frequency characteristics of sound transmission in middle ears from Norwegian cattle, and the effect of static pressure differences across the tympanic membrane and the footplate," *The Journal of the Acoustical Society of America*, vol. 107, no. 3, pp. 1442–1450, 2000.

[2] M. Kringlebotn, "Acoustic impedances at the oval window, and sound pressure transformation of the middle ear in Norwegian cattle," *The Journal of the Acoustical Society of America*, vol. 108, no. 3, pp. 1094–1104, 2000.

[3] S. Puria, "Measurements of human middle ear forward and reverse acoustics: implications for otoacoustic emissions," *The Journal of the Acoustical Society of America*, vol. 113, no. 5, pp. 2773–2789, 2003.

[4] E. Hernandez-Torres and M. A. Sosa, "Theoretical study and computational simulation of the tympanic membrane," in *Proceedings of the 8th Mexican Symposium on Medical Physics*, pp. 182–185, 2004.

[5] H. M. Ladak, W. F. Decraemer, J. J. J. Dirckx, and W. R. J. Funnell, "Response of the cat eardrum to static pressures: mobile versus immobile malleus," *The Journal of the Acoustical Society of America*, vol. 116, no. 5, pp. 3008–3021, 2004.

[6] H. M. Ladak, W. R. J. Funnell, W. F. Decraemer, and J. J. J. Dirckx, "A geometrically nonlinear finite-element model of the cat eardrum," *The Journal of the Acoustical Society of America*, vol. 119, no. 5, pp. 2859–2868, 2006.

[7] S. E. Voss and C. A. Shera, "Simultaneous measurement of middle-ear input impedance and forward/reverse transmission in cat," *The Journal of the Acoustical Society of America*, vol. 116, no. 4, pp. 2187–2198, 2004.

[8] M. P. Feeney and C. A. Sanford, "Age effects in the human middle ear: wideband acoustical measures," *The Journal of the Acoustical Society of America*, vol. 116, no. 6, pp. 3546–3558, 2004.

[9] M. R. Stinson and G. A. Daigle, "Comparison of an analytic horn equation approach and a boundary element method for the calculation of sound fields in the human ear canal," *The Journal of the Acoustical Society of America*, vol. 118, no. 4, pp. 2405–2411, 2005.

[10] C. E. Stepp and S. E. Voss, "Acoustics of the human middle-ear air space," *The Journal of the Acoustical Society of America*, vol. 118, no. 2, pp. 861–871, 2005.

[11] H. M. Ladak, W. R. J. Funnell, W. F. Decraemer, and J. J. J. Dirckx, "A geometrically nonlinear finite-element model of the cat eardrum," *The Journal of the Acoustical Society of America*, vol. 119, no. 5, pp. 2859–2868, 2006.

[12] R. Z. Gan, C. Dai, and M. W. Wood, "Laser interferometry measurements of middle ear fluid and pressure effects on sound transmission," *The Journal of the Acoustical Society of America*, vol. 120, no. 6, pp. 3799–3810, 2006.

[13] S. Stenfelt, "Middle ear ossicles motion at hearing thresholds with air conduction and bone conduction stimulation," *The Journal of the Acoustical Society of America*, vol. 119, no. 5, pp. 2848–2858, 2006.

[14] P. Parent and J. B. Allen, "Wave model of the cat tympanic membrane," *The Journal of the Acoustical Society of America*, vol. 122, no. 2, pp. 918–931, 2007.

[15] X. Wang, T. Cheng, and R. Z. Gan, "Finite-element analysis of middle-ear pressure effects on static and dynamic behavior of human ear," *The Journal of the Acoustical Society of America*, vol. 122, no. 2, pp. 906–917, 2007.

[16] T. Cheng and R. Z. Gan, "Mechanical properties of stapedial tendon in human middle ear," *Journal of Biomechanical Engineering*, vol. 129, no. 6, pp. 913–918, 2007.

[17] W. F. Decraemer, O. de La Rochefoucauld, W. Dong, S. M. Khanna, J. J. J. Dirckx, and E. S. Olson, "Scala vestibuli pressure and three-dimensional stapes velocity measured in direct succession in gerbil," *The Journal of the Acoustical Society of America*, vol. 121, no. 5, pp. 2774–2791, 2007.

[18] R. Z. Gan and X. Wang, "Multifield coupled finite element analysis for sound transmission in otitis media with effusion," *The Journal of the Acoustical Society of America*, vol. 122, no. 6, pp. 3527–3538, 2007.

[19] S. E. Voss, J. J. Rosowski, S. N. Merchant, and W. T. Peake, "Non-ossicular signal transmission in human middle ears: experimental assessment of the "acoustic route" with perforated tympanic membranes," *The Journal of the Acoustical Society of America*, vol. 122, no. 4, pp. 2135–2153, 2007.

[20] M. E. Ravicz, E. S. Olson, and J. J. Rosowski, "Sound pressure distribution and power flow within the gerbil ear canal from 100 Hz to 80 kHz," *The Journal of the Acoustical Society of America*, vol. 122, no. 4, pp. 2154–2173, 2007.

[21] E. W. Abel, R. M. Lord, and R. P. Mills, "Magnetic resonance microimaging in the measurement of the ossicular chain for finite element modelling," in *Proceedings of the 20th Annual International Conference of the IEEE Engineering in Medicine and Biology Society*, pp. 3170–3172, Hong Kong, 1998.

[22] Q. Sun, R. Z. Gan, K.-H. Chang, and K. J. Dormer, "Computer-integrated finite element modeling of human middle ear," *Biomechanics and Modeling in Mechanobiology*, vol. 1, pp. 109–122, 2002.

[23] T. Koike, H. Wada, and T. Kobayashi, "Modeling of the human middle ear using the finite-element method," *The Journal of the Acoustical Society of America*, vol. 111, no. 3, pp. 1306–1317, 2002.

[24] R. Z. Gan, B. Feng, and Q. Sun, "Three-dimensional finite element modeling of human ear for sound transmission," *Annals of Biomedical Engineering*, vol. 32, no. 6, pp. 847–859, 2004.

[25] P. Ferris and P. J. Prendergast, "Middle-ear dynamics before and after ossicular replacement," *Journal of Biomechanics*, vol. 33, no. 5, pp. 581–590, 2000.

[26] T. Cheng and R. Z. Gan, "Experimental measurement and modeling analysis on mechanical properties of tensor tympani tendon," *Medical Engineering & Physics*, vol. 30, no. 3, pp. 358–366, 2008.

[27] T. Cheng and R. Z. Gan, "Mechanical properties of anterior malleolar ligament from experimental measurement and material modeling analysis," *Biomechanics and Modeling in Mechanobiology*, vol. 7, no. 5, pp. 387–394, 2008.

[28] Z. Zhai, X. Zhang, and X. Huang, "Application of multislice CT to measure the three-dimension anatomic structures of auditional ossicle," *Chinese Computed Medical Imaging*, vol. 12, no. 3, pp. 166–169, 2006.

[29] M. M. Lemmerling, H. E. Stambuk, A. A. Mancuso, P. J. Antonelli, and P. S. Kubilis, "CT of the normal suspensory ligaments of the ossicular in the middle ear," *American Journal of Neuroradiology*, vol. 18, no. 3, pp. 471–477, 1997.

[30] H. J. Beer, M. Bomitz, J. Drescher, et al., "Finite element modelling of the human eardrum and application," in *Proceedings of the Intenational Workshop on Middle Ear Mechanics*, pp. 40–47, University of Technology, Dresden, Germany, September 1996.

[31] R. Z. Gan, M. W. Wood, and K. J. Dormer, "Human middle ear transfer function measured by double laser interferometry system," *Otology and Neurotology*, vol. 25, no. 4, pp. 423–435, 2004.

Hindawi Publishing Corporation
Mathematical Problems in Engineering
Volume 2010, Article ID 385742, 17 pages
doi:10.1155/2010/385742

Research Article

Stability Analysis and Investigation of a Magnetoelastic Beam Subjected to Axial Compressive Load and Transverse Magnetic Field

Mei-Feng Liu[1] and Tai-Ping Chang[2]

[1] *Department of Applied Mathematics, I-Shou University, Kaohsiung 840, Taiwan*
[2] *Department of Construction Engineering, National Kaohsiung First University of Science & Technology, Kaohsiung 824, Taiwan*

Correspondence should be addressed to Mei-Feng Liu, meifeng@isu.edu.tw

Received 22 December 2009; Revised 22 April 2010; Accepted 3 June 2010

Academic Editor: Carlo Cattani

The interactive behaviors between transverse magnetic fields and axial loads of a magnetoelastic (ME) beam subjected to general boundary conditions are investigated. In particular, the instability criterion for the magneto-mechanical buckling problem is intricately discussed based on the structure characteristics and the initial conditions. The equation of motion for the proposed physical model is introduced according to the Hamilton's principle, and the stability criterion is obtained by using the method of multiple scales implemented on both spatial and time domains. Eventually a so-called Schrodinger equation with cubic nonlinearity (NLS) can be generated by suitably changing the variables; as a result, the stable criterion for the magnetoelastic beam can be acquired after dissecting the nonlinear Schrodinger equation and requiring the imaginary part of the time domain solution to be vanished. Stability criterion curve for the dispersion equation of the ME beam is firstly depicted in order to reveal the magnificent influence of the structure characteristic itself, followed by the instability constraint due to the variation of initial conditions and the observation locations. The results indicate that the prior one actually denotes a parabola, whereas the latter one is sometimes a diamond-like or ellipse-like region spotting along the prior one.

1. Introductions

The electromagnetic phenomena which arose from electrical machinery, communicating equipments, and computer chips have addressed wide attention in the past years due its significant role on human's daily life. and diamagnetic structures such as beams, plates, and shells are extensively employed in the modern electromagnetic equipments, and accordingly

provide a real understanding for the mechanism of electricity and magnetism coexisting in the conventional elasticity.

Since the structures are often set in high magnetic fields, they are correspondingly subjected to strong magnetic forces resulting from the applied magnetic fields, however, the magnetic force not only causes the structural deformation but also respectively changes with the deformation itself. Therefore, when the induced magnetization is under consideration, the analysis of the magnetoelastic structures with multiphases coupling effects becomes more complicated, and indeed requires further examination either on the dynamical behavior or stability issues.

In this paper, the interactive behaviors between transverse magnetic fields and axial loads of a magnetoelastic beam subjected to general boundary conditions are investigated. In specific, the instability criterion for the magnetomechanical buckling problem is intricately discussed according to the structure characteristics as well as the initial conditions. The fundamental concepts and relations about the electro-magnetic theory are adopted in this paper based on the content written in [1], and some other systematic references for the theory of magnetoelastic solid mechanics found in [2] are also contained. Inspections on the behavior of interaction between magnetic field and mechanical deformation for the structures made of magnetoelastic materials have been conducted by many researchers and engineers. Some of them are briefly described in the next paragraph.

Moon and Pao [3] proposed a mathematical model for the buckling problem of a cantilever beam-plate in a transverse magnetic field with distributed magnetic forces and torques. Wallerstein and Peach [4] studied the magnetoelastic buckling of beams and plates with magnetically soft material. Miya et al. [5] investigated the magnetoelastic buckling of a cantilevered beam-plate by applying the experimental and finite element methods. Moon and Pao [6] presented the vibration and parametric instability of a cantilevered beam-plate in a transverse magnetic field and also provided the theoretical and experimental results. In Moon-Pao's theoretical analysis, the magnetic torque without axial load was considered; therefore, the axial load studied in this paper does not apply to their discussion. Kojima et al. [7] investigated the parameter nonlinear forced vibrations of a beam with a tip mass subjected to alternating electromagnetic forces acting on the tip mass. Shin et al. [8] have studied the transient vibrations of a simply supported beam with axial loads and transverse magnetic fields. Liu and Chang [9] performed the vibration analysis of a beam with general boundary conditions in a magnetic field subjected to axial load and external force by introducing the orthogonal characteristic polynomial. Wu [10] performed the analysis of dynamic instability and vibration motions of a pinned beam with transverse magnetic field and thermal loads. Pratiher and Dwivedy [11] studied the parametric instability of a cantilever beam with magnetic field and periodic axial load.

In view of the fact that the interactions among axial load, magnetic force, and magnetic couples are complicated, yet, important to the dynamical analysis of structural instability, a magnetoelastic (ME) beam system involving axial load, transverse magnetic field, and spring foundation is considered in the present paper. For simplicity, the axial force and transverse magnetic field are assumed to be static, that is, independent of time variable; however, this paper is aiming at finding out the stability criterions under which the magnetoelastic beam can be dynamically stabilized; therefore, it is suggested that neither the magnitude of axial force nor that of the transverse magnetic field should exceed the parameters restrained by the criterion even though they are set to be periodical or other else.

The equation of motion for the proposed physical model is introduced based on the authors' previous work, and some of the quantities related to magnetic field are evaluated

by adopting reasonable assumptions and approximations. The stability criterion for an ME beam subjected to both transverse magnetic field and axial load can be obtained by using the method of multiple scales implemented on both spatial and time variables. After collecting the small perturbed parameter ε with the same order, a set of relevant partial differential equations resulting from the perturbation process can thus be derived. Based on some assumptions dedicating to simplify the mathematical modeling of the whole system, the analytic solutions of the respective perturbed equations can be solved one by one successively. As a result of suitably changing the variables, a so-called Schrodinger equation with cubic nonlinearity (NLS) will be generated from the evaluation of perturbation equation for $O(\varepsilon^3)$. By sophisticated technique dissecting the above nonlinear Schrodinger equation, the criterion for stable condition to the whole system can be acquired by requiring the imaginary part of the time domain solution to be vanished.

2. Formulations

2.1. Statement of the Problem

In this paper, the physical model of a magnetoelastic (ME) beam system rested upon a Winkler-type foundation and subjected to axial applied force and transverse magnetic field as shown in Figure 1 is investigated. The beam is made of linearly magnetoelastic material with width d, thickness h, length L and is subjected to an applied axial force $\vec{P} = P_0\vec{i}$ in the x-direction and a transverse magnetic field $\vec{B} = B_0\vec{j}$, linear viscous damper in the y-direction, and attached by the linear springs with constant K. In order to simplify the analysis, the proposed beam is assumed as Euler-Bernoulli type.

2.2. Mathematical Modeling

Hamilton's principle [8] is adopted to derive the equation of motion of the beam as follows:

$$m\frac{\partial^2 w}{\partial t^2} + C_d\frac{\partial w}{\partial t} + YI\frac{\partial^4 w}{\partial x^4} + Kw + P\frac{\partial^2 w}{\partial x^2} = \frac{\partial c}{\partial x} + \frac{\partial}{\partial x}\left[\left(\int_0^x p\,d\xi\right)\frac{\partial w}{\partial x}\right], \tag{2.1}$$

where $w(x,t)$ denotes the transverse displacement of the middle plane, m is the mass per unit length, C_d is the damping coefficient, Y is the Young's modulus, I is the moment of inertia of the cross section, K is the constant of spring, P is the axial load per unit length along x direction, c represents the induced couple per unit length due to the existence of magnetic field, and p is the body force per unit length contributed by the magnetic force.

For the dia- and para-magnetoelastic material, the magnetization $\mathbf{M}$ of the medium due to the existence of auxiliary magnetic field $\mathbf{H}$ can be defined as $\mathbf{M} = \chi_m\mathbf{H}$ and $\mathbf{H}$ can be determined by the relation $\mathbf{B} = \mu_0\mathbf{H}$ with $\mathbf{B}$ being the externally applied magnetic field. Thus the induced couple or magnetic torque can be read as

$$\mathbf{c} = \int(\mathbf{M}\times\mathbf{B})\mathbf{dV}, \tag{2.2}$$

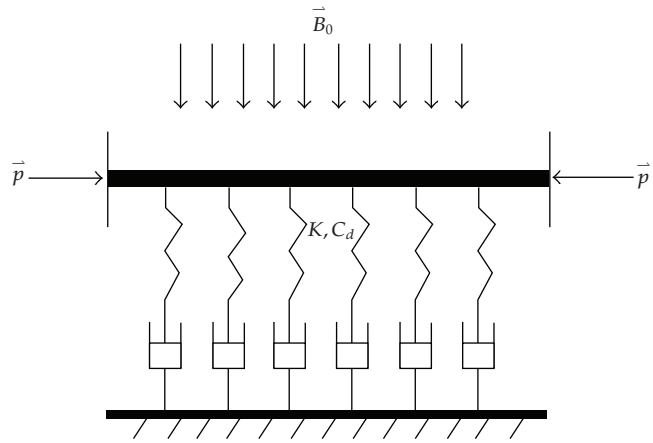

Figure 1: Physical model for a magnetoelastic (ME) beam subjected to axial load and magnetic field.

in which $\chi_m \equiv (\mu_0 - \mu)/\mu_0 = 1 - \mu_r$ is the magnetic susceptibility with μ being the material permeability and μ_0 the permeability of free space. The magnetization $\mathbf{M}$ can be rewritten as $\mathbf{M} = (\chi_m/\mu_0)\mathbf{B} = (\chi_m/\mu_0)|B_0|\vec{n}$ and is also called volume density of magnetic moment, meanwhile, the magnetic field $\mathbf{B}$ is sometimes called the magnetic displacement or the induced magnetic field.

According to the small deformation theory, it can be shown [9] that the velocity term, $\dot{x}$, for the magnetoelastic beam can be simplified into

$$\dot{x} \equiv \frac{dx}{dt} \approx -\int_0^x \frac{\partial w}{\partial \xi}\frac{\partial^2 w}{\partial t \partial \xi}\, d\xi. \tag{2.3}$$

As a result, the component of the body force contributed by the magnetic field $\mathbf{B}$ can be written as

$$p = \text{component} \int \sigma\left(\vec{\dot{r}} \times \vec{B}_0\right) \times \vec{B}_0\, dV = \sigma B_0^2 hd\frac{dx}{dt} = -\sigma B_0^2 hd \int_0^x \frac{\partial w}{\partial \xi}\frac{\partial^2 w}{\partial t \partial \xi}\, d\xi. \tag{2.4}$$

Mean while, the component of the magnetic couple induced by the applied magnetic field can be expressed as

$$c = \text{component} \int \vec{M} \times \vec{B}_0 dV = MB_0 hd \sin\theta \approx MB_0 hd\theta = MB_0 hd\frac{\partial w}{\partial x}, \tag{2.5}$$

in which σ is the electrical conductivity of the ME beam and h and d represent the thickness and the depth of the beam, respectively.

2.3. Perturbation and Multiscale Method

For the nonlinear differential system stated in (2.1), the solutions in a form of harmonic wave propagation are permitted, however, with the restriction that the bending wave is slowly

changed in spatial and time domain than the carrying wave [12]. Therefore, it is fairly feasible to practice the solution of (2.1) in the following form at the vicinity of the equilibrium state:

$$w = \varepsilon w_1 + \varepsilon^2 w_2 + \varepsilon^3 w_3 + \cdots, \tag{2.6}$$

in which the small perturbed parameter can be taken as $\varepsilon \equiv \lambda_c/\lambda_e \ll 1$ with λ_c and λ_e indicating the wave lengths of carrying and bending waves, respectively.

By adopting x and t as usual space and time variables for carrying wave, and performing the method of multiple scales, a set of "slow" time and space variables: $T_n = \varepsilon^n t$, $X_n = \varepsilon^n x$, are introduced in the present study. Due to the principle of chain rule, the operators of differentiation $\partial/\partial x$ and $\partial/\partial t$ in (2.1) should be accordingly modified in order to account for the dependence of "slow" variables T_n and X_n on regular x and t variables; therefore, these derivatives are transformed into the following operators:

$$\begin{aligned} \frac{\partial}{\partial x} &\equiv \frac{\partial}{\partial X_0} + \sum_{n=1} \varepsilon^n \frac{\partial}{\partial X_n}, \\ \frac{\partial}{\partial t} &\equiv \frac{\partial}{\partial T_0} + \sum_{n=1} \varepsilon^n \frac{\partial}{\partial T_n}. \end{aligned} \tag{2.7}$$

It should be noted that the variables $X_0 \equiv \varepsilon^0 x = x$, X_n, $T_0 \equiv \varepsilon^0 t = t$, and T_n stated above are all independent variables with respect to each other, and, for the sake of briefness, the variables T_0 and X_0 will be replaced by x and t correspondingly in the following derivations and for the rest of the paper.

Substituting (2.6) and (2.7) into (2.1) and equating the terms with the same order of ε, one can obtain

$$O(\varepsilon): \quad L_0 w_1 = 0, \qquad L_0 \equiv m\frac{\partial^2}{\partial t^2} + C_d \frac{\partial}{\partial t} + YI\frac{\partial^4}{\partial x^4} + K + (P - MB_0 hd)\frac{\partial^2}{\partial x^2}, \tag{2.8}$$

$$O\left(\varepsilon^2\right): \quad L_0 w_2 = -2m\frac{\partial^2 w_1}{\partial t \partial T_1} - C_d \frac{\partial w_1}{\partial T_1} - 4YI\frac{\partial^2 w_1}{\partial^3 x \partial X_1} - 2(P - MB_0 hd)\frac{\partial^2 w_1}{\partial x \partial X_1}, \tag{2.9}$$

$$\begin{aligned} O\left(\varepsilon^3\right): \quad L_0 w_3 = {} & -m\left(2\frac{\partial^2 w_1}{\partial t \partial T_2} + \frac{\partial^2 w_1}{\partial T_1^2} + 2\frac{\partial^2 w_2}{\partial t_0 \partial T_1}\right) - C_d\left(\frac{\partial w_2}{\partial T_1} + \frac{\partial w_1}{\partial T_2}\right) \\ & - YI\left[4\frac{\partial^4 w_1}{\partial x_0^3 \partial X_2} + 6\frac{\partial^4 w_1}{\partial x^2 \partial X_1^2} + 4\frac{\partial^4 w_2}{\partial x^3 \partial X_1}\right] \\ & - (P - MB_0 hd)\left(2\frac{\partial^2 w_1}{\partial x_0 \partial X_2} + \frac{\partial^2 w_1}{\partial X_1^2} + 2\frac{\partial^2 w_2}{\partial x \partial X_1}\right) \\ & - \left(\sigma B_0^2 hd\right)\left(\int_0^{x_0} \frac{\partial w_1}{\partial \xi}\frac{\partial^2 w_1}{\partial t \partial \xi} d\xi \cdot \frac{\partial w_1}{\partial x_0}\right) \\ & - \left(\sigma B_0^2 hd\right)\left(\int_0^{x_0}\int_0^{\xi} \frac{\partial w_1}{\partial \eta}\frac{\partial^2 w_1}{\partial t \partial \eta} d\eta\, d\xi \cdot \frac{\partial^2 w_1}{\partial x_0^2}\right). \end{aligned} \tag{2.10}$$

It is noticed that (2.8) is actually a homogenous version of the governing equation, say (2.1), and one can easily express the solution of (2.8) in the form of harmonic waves with the amplitude depending on slow variables, that is,

$$w_1 = A(X_1, T_1, X_2, T_2, \ldots)\exp(i\theta) + \text{c.c.},$$
$$\theta = kx - \omega t, \tag{2.11}$$

wherein c.c. stands for the complex conjugate and θ can be thought as the phase angle of the propagating wave. To assure that the net axial load appeared in (2.8), say $(P - MB_0hd)$, is of the compressive type, it is required that this term should be positive in the present study.

According to (2.8), the dispersion equation will have the following form:

$$m\omega^2 + iC_d\omega + \left[YIk^4 - (P - MB_0hd)k^2 + K\right] = 0, \tag{2.12}$$

and after imposing implicit differentiation with respect to k on the dispersion equation and suppose $\omega = \omega(k)$, the relation between ω and k can be expressed implicitly as

$$\frac{d\omega}{dk} = \frac{4YIk^3 - 2k(P - MB_0hd)}{2m\omega + iC_d}. \tag{2.13}$$

Substituting (2.11) into (2.9) gives

$$L_0w_2 = e^{i\theta}\left\{\frac{\partial A}{\partial T_1}[2m\omega i - C_d] + i\frac{\partial A}{\partial X_1}\left[4YIk^3 - 2(P - MB_0hd)k\right]\right\} + \text{c.c.} \tag{2.14}$$

The first term in (2.14) is secular term or sometimes called the small divisor term, and for the applicability of theory for excitation, we should demand the elimination of this term, that is,

$$\frac{\partial A}{\partial T_1}[2m\omega i - Cd] + i\frac{\partial A}{\partial X_1}\left[4YI\ k^3 - 2(P - MB_0hd)k\right] \equiv 0. \tag{2.15}$$

Since no other term left in (2.14) after imposing (2.15), there is no particular solution as a result, the general solution of (2.14) thus can be determined to be identical with the homogeneous solution, that is,

$$w_2 = A(X_1, T_1, X_2, T_2)e^{i\theta} = w_1. \tag{2.16}$$

By taking the same token, substituting (2.11) and (2.16) into (2.10) and demanding the vanish of secular terms will result in the following expression:

$$\begin{aligned}
&(2mi\omega - Cd)\frac{\partial A}{\partial T_2} + (-m)\frac{\partial^2 A}{\partial T_1^2} + \frac{\partial A}{\partial X_2}\left[-4YI(ik)^3 - 2(P - MB_0hd)(ik)\right] \\
&\quad + \frac{\partial^2 A}{\partial X_1^2}\left[-6YI(ik)^2 - (P - MB_0hd)\right] \\
&\quad - A|A|^2\left\{\left(\sigma B_0^2 hd\right)\left[(ik)^3(-i\omega)\frac{e^{2i\theta} - e^{-2i\omega t}}{2ik} + (ik)^4(-i\omega)\frac{1}{2ik}\left(\frac{e^{2i\theta} - e^{-2i\omega t}}{2ik} - \frac{x}{e^{2i\omega t}}\right)\right]\right\} \\
&= 0.
\end{aligned} \tag{2.17}$$

Meanwhile, by taking differentiation on (2.15) with respect to k, we have

$$\frac{\partial A}{\partial T_1}\left(mi\frac{d\omega}{dk}\right) + i\frac{\partial A}{\partial X_1}\left[6YIk^2 - (P - MB_0hd)\right] = 0; \tag{2.18}$$

furthermore, differentiating (2.18) with respect to T_1 gives

$$\frac{\partial^2 A}{\partial T_1^2}\left[-m\frac{d\omega}{dk}\right] - \frac{\partial^2 A}{\partial T_1 X_1}\left[6YIk^2 - (P - MB_0hd)\right] = 0; \tag{2.19}$$

similarly, differentiating (2.18) with respect to X_1 gives

$$\frac{\partial^2 A}{\partial X_1 \partial T_1}\left[mi\frac{d\omega}{dk}\right] + i\frac{\partial^2 A}{\partial X_1^2}\left[6YIk^2 - (P - MB_0hd)\right] = 0. \tag{2.20}$$

Adding the above two equations gets

$$\frac{\partial^2 A}{\partial T_1^2}(-m) + \frac{\partial^2 A}{\partial X_1^2}\left[6YIk^2 - (P - MB_0hd)\right] = \frac{\partial^2 A}{\partial T_1 \partial X_1}\left[\frac{6YIk^2 - (P - MB_0hd)}{d\omega/dk} - m\frac{d\omega}{dk}\right]; \tag{2.21}$$

also we have the following results after taking derivative with respect to X_1 on (2.15):

$$\frac{\partial^2 A}{\partial T_1 \partial X_1} = -\frac{\partial^2 A}{\partial X_1^2}\frac{4YIk^3 - 2(P - MB_0hd)k}{2m\omega + iCd} = -\frac{\partial^2 A}{\partial X_1^2}\frac{d\omega}{dk}; \tag{2.22}$$

thus (2.21) becomes

$$\frac{\partial^2 A}{\partial T_1^2}(-m) + \frac{\partial^2 A}{\partial X_1^2}\left[6YIk^2 - (P - MB_0hd)\right] = -\frac{\partial^2 A}{\partial X_1^2}\left[6YIk^2 - (P - MB_0hd) - m\left(\frac{d\omega}{dk}\right)^2\right]. \tag{2.23}$$

Therefore, (2.17) can be reduced into

$$\begin{aligned}(2mi\omega - Cd)\frac{\partial A}{\partial T_2} + \frac{\partial A}{\partial X_2}\left[-4YI(ik)^3 - 2(P - MB_0hd(ik))\right] \\ - \frac{\partial^2 A}{\partial X_1^2}\left[6YIk^2 - (P - MB_0hd) - m\left(\frac{d\omega}{dk}\right)^2\right] + A|A|^2\left[f(x,t)\right] = 0,\end{aligned} \tag{2.24}$$

where

$$f(x,t) \equiv -\left(\sigma B_0^2 hd\right)\left[(ik)^3(-i\omega)\frac{e^{2i\theta} - e^{-2i\omega t}}{2ik} + (ik)^4(-i\omega)\frac{1}{2ik}\left(\frac{e^{2i\theta} - e^{-2i\omega t}}{2ik} - \frac{x}{e^{2i\omega t}}\right)\right]. \tag{2.25}$$

In order to eliminate some variables, we now introduce a new variable $\overline{T}$ as

$$\overline{T} \equiv T_2 + \frac{dk}{d\omega}X_2, \tag{2.26}$$

which implies

$$\frac{\partial}{\partial \overline{T}} \equiv \frac{\partial}{\partial T_2}\frac{\partial T_2}{\partial \overline{T}} + \frac{\partial}{\partial X_2}\frac{\partial X_2}{\partial \overline{T}} = \frac{\partial}{\partial T_2} + \frac{d\omega}{dk}\frac{\partial}{\partial X_2}. \tag{2.27}$$

With the differential operator defined in (2.27), we can rewrite the first two terms in (2.24), say

$$(2mi\omega - Cd)\frac{\partial A}{\partial T_2} + \frac{\partial A}{\partial X_2}\left[4YIik^3 - 2ik(P - MB_0hd)\right], \tag{2.28}$$

into the following expression in term of $\overline{X}$:

$$(2mi\omega - Cd)\left[\frac{\partial A}{\partial T_2} + \frac{d\omega}{dk}\frac{\partial A}{\partial X_2}\right] = (2mi\omega - Cd)\frac{\partial A}{\partial \overline{T}}. \tag{2.29}$$

Therefore, the following Schrodinger-type equation can then by obtained as a result

$$i\frac{\partial A}{\partial \overline{T}} = \frac{6YIk^2 - (P - MB_0hd) - m(d\omega/dk)^2}{2m\omega + iCd}\frac{\partial^2 A}{\partial X_1^2} + \frac{[f(x,t)]}{2m\omega + iCd}A|A|^2, \tag{2.30}$$

which can be simplified as

$$i\frac{\partial A}{\partial \overline{T}} = \beta\frac{\partial^2 A}{\partial X_1^2} + \gamma A|A|^2, \tag{2.31}$$

where β and γ are complex, and can be expressed as follows:

$$\beta \equiv \frac{6YIk^2 - (P - MB_0hd) - m(d\omega/dk)^2}{2m\omega + iCd}, \tag{2.32}$$

$$\gamma \equiv \frac{-(\sigma B_0^2 hd)}{2m\omega + iCd}\left[(ik)^3(-i\omega)\frac{e^{2i\theta} - e^{-2i\omega t}}{2ik} + (ik)^4(-i\omega)\frac{1}{2ik}\left(\frac{e^{2i\theta} - e^{-2i\omega t}}{2ik} - \frac{x}{e^{2i\omega t}}\right)\right]. \tag{2.33}$$

By now we have the Schrodinger equation with complex coefficient as mentioned above; if the viscosity is neglected ($C_d = 0$), then the Schrodinger-type equation with real coefficients can then be obtained.

2.4. Stable Criterion for Schrodinger Equation

Equation (2.31) describes a behavior of modulated waves and is commonly referred to as the nonlinear Schrodinger (NLS) equation with cubic nonlinearity. Even though it has been proved that there is a solution for the NLS equation with real coefficient [13], however, the complex coefficients for NLS equation as stated in (2.31) make the analysis become more difficult, yet no related report can be found up to date.

In the following, an attempt to find the stable criterion for the NLS equation as stated in (2.31) is conducted; as a first step, we can express the solution for $A(X_1, \overline{T})$ in the following form:

$$A\left(X_1, \overline{T}\right) = A_0 \exp(i\Theta) = A_0 \exp\left[i\left(\kappa X_1 - \Omega\overline{T}\right)\right]. \tag{2.34}$$

Substituting it into (2.31) leads to

$$\Omega = -\beta\kappa^2 + \gamma A_0^2; \tag{2.35}$$

thus we can have

$$A\left(X_1, \overline{T}\right) = A_0 \exp\left\{i\left[\kappa X_1 + \left(\beta\kappa^2 - \gamma A_0^2\right)\overline{T}\right]\right\} = A_0 \exp(i\kappa X_1) \cdot \exp\left[i\left(\beta\kappa^2 - \gamma A_0^2\right)\overline{T}\right]. \tag{2.36}$$

For the above solution to be stable in the time domain, it is required that the imaginary part of the frequency should be greater than zero; therefore, the stability criterion would be given by the following inequality:

$$\mathrm{Im}\left(\beta\kappa^2 - \gamma A_0^2\right) > 0, \tag{2.37}$$

where A_0 can be indicated by the amplitude given in the initial conditions.

However, as we can detect from (2.32) and (2.33) that the value for β is purely real if damping coefficient C_d is neglected, and the value for γ is definitely complex with strong dependence on the slow variables, namely, x and t. This phenomenon suggests that the criterion for stability should be determined not only by the beam characteristics but also by the initial conditions it was provoked by, namely, the catching time t and the observation location x as well as the initial amplitude A_0. In the present study, the initial conditions ($t = 0$) at a specific location ($x = x_0$) will be accordingly imposed in order to see the spectacular influence caused by the value of γ, and by substituting related values into the inequality in (2.37), the diagrams for the stability region subjected to various beam characteristics can be depicted.

It should be noted that (2.37) shows how initial conditions can affect the stability of the wave propagation; nevertheless, the stable criterion for the whole system, say the differential equation, is actually dominated by the dispersion equation stated in (2.12). Therefore, as far as the stability problem is concerned, we should first examine the stability region for the dispersion equation with respect to different boundary conditions, and then carefully point out the instability criterions caused by the initial conditions as well as the observation location, which are expected to be some subdomains among the prior one or just on the border.

3. Numerical Examples

For the purpose of demonstration, a low-carbon steel is considered in this study, of which the material constants [9] are respectively $Y = 194\,\mathrm{GPa}$, $m = 0.03965\,\mathrm{kg/m}$, $L = 0.5\,\mathrm{m}$, $h = 0.005\,\mathrm{m}$, $d = 0.001\,\mathrm{m}$, $\mu_r = 1.00001$, $\mu_0 = 4\pi \times 10^{-7}\,\mathrm{Hm}^{-1}$, $\sigma = 10^7\,\mathrm{Sm}^{-1}$, and $K = 1.0\,\mathrm{N/m}$. To account for the effects of both initial conditions and boundary conditions on the stability criterion of the ME beam, several cases involving various combinations of these conditions have been examined. For the convenience of comparison, the catching time for all cases is set to be $t = 0$ whereas the magnitude of initial displacement is set to the same with the beam thickness, that is, $A_0 = h$ is chosen for all stability discussions in following examples.

Four kinds of commonly seen boundary conditions are implemented; they are, respectively, simply supported on both end (S-S), fixed at left and simply supported at right (C-S), cantilever beam (C-F), and fixed on both ends (C-C). The wave numbers with respect to the corresponding boundary conditions are stated is Table 1 as a reference despite the fact

Table 1: The first three wave numbers corresponding to various boundary conditions.

Boundary condition	Mode number $N = 1$	$N = 2$	$N = 3$
S-S	$\frac{\pi}{L}$	$\frac{2\pi}{L}$	$\frac{3\pi}{L}$
C-S	$\frac{3.926602}{L}$	$\frac{7.068583}{L}$	$\frac{10.210176}{L}$
C-F (Cantilever)	$\frac{1.875104}{L}$	$\frac{4.694091}{L}$	$\frac{7.854757}{L}$
C-C	$\frac{4.730041}{L}$	$\frac{7.853205}{L}$	$\frac{10.995607}{L}$

*S stands for Simply supported, C is for clamped, F is for free end

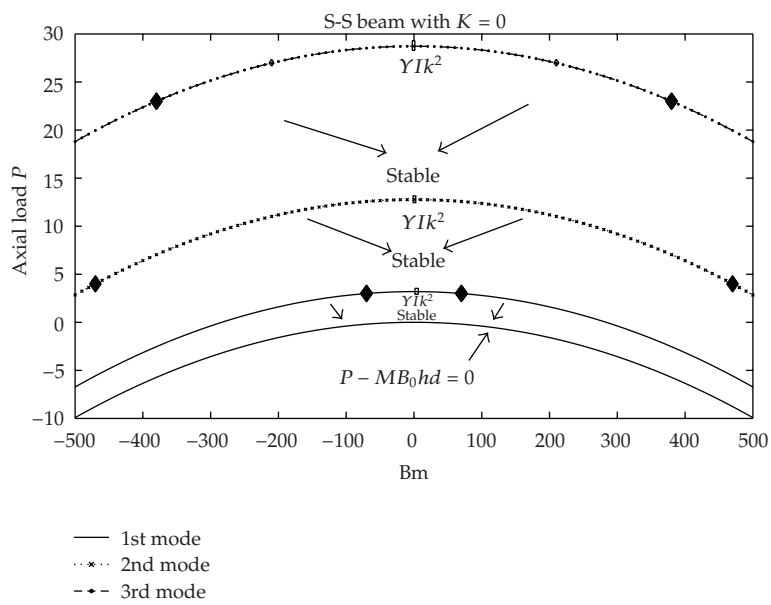

Figure 2: Stability Region for an ME beam with simply supported boundary conditions subjected to axial load and magnetic; with no spring support.

that they can still be found in any textbook related to the structure vibration problems. Due to the different beam characteristics with respect to different boundary conditions, the location for stable observation is properly pinpointed according to the imposed boundary conditions for each specific case. The observation location x_0 for the stability criterion of a cantilever beam is pinpointed at the right end ($x_0 = L$) of the ME beam; however, for the other cases, the location is fixed to be at the center point of the beam length, that is, $x_0 = L/2$.

Figure 2 presents the stability region for a magnetoelastic beam with S-S boundary conditions subjected to axial external force and transverse magnetic field; the effect of spring foundation is here neglected. Three modes of wave number are calculated; magnetic field is ranging from −500 Tesla to 500 Tesla whereas the axial external force is from −10 N to 30 N. The signs for magnetic fields and axial forces simply indicate the direction these forces are applying to, that is, positive axial force means compression while negative implies tension,

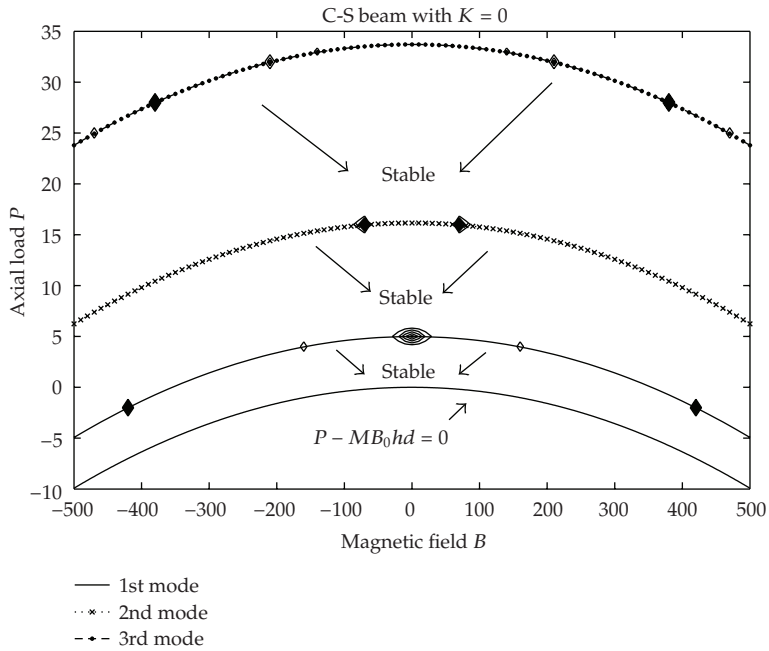

Figure 3: Stability Region for an ME beam with clamped-hinged boundary conditions subjected to axial load and magnetic field with no spring support.

positive magnetic field represents upward, and negative denotes downward. As it can be detected from Figure 2, the stability criterion curve for the dispersion equation, say (2.12), is indeed a parabola, and the instability constraint due to the initial condition, say (2.33), is presented in the shaded region, in which the parameters reside will incur imaginary parts of (2.37) to be negative. It should be noted that due to the numerical discreteness, the latter one looks like a shape of diamond; however, it is not necessarily a diamond and might be a circle or ellipse.

Figures 3–5 demonstrate the stability regions for a magnetoelastic beam with other boundary conditions subjected to the same setting as in Figure 2. Parabola for criterion curve can be observed again and the shaded regions are sometimes replaced by the lined regions, which indicate that the parameters for instability might not be compact on a bounded zone. By the fact that the strong instability due to the initial conditions and observation points makes the analysis become more complicated, a slight change in the number of shaded regions can be noticed, and a new added ellipse centered in the vicinity of zero magnetic field is detected. This incident reminds us that even though no external magnetic field is applied, that is, pure buckling problem for the ME beam is under consideration, yet we must be careful on examining the initial conditions in addition to the buckling criteria, so that accidentally invoking the instability of the system can be avoided. However, due to the distinct natures with respect to different boundary conditions, the aforementioned instability ellipses can be found to be centered along different modes of dispersion curves.

As it can be seen from Figure 3, the instability ellipse is center at the dispersion curve of the first mode for an ME beam with clamped-hinged boundary conditions. Also it is noticed that the instability diamonds become more frequently appeared along the curves than the simply supported case. Nevertheless, unlike the clamped-hinged case, the instability ellipses

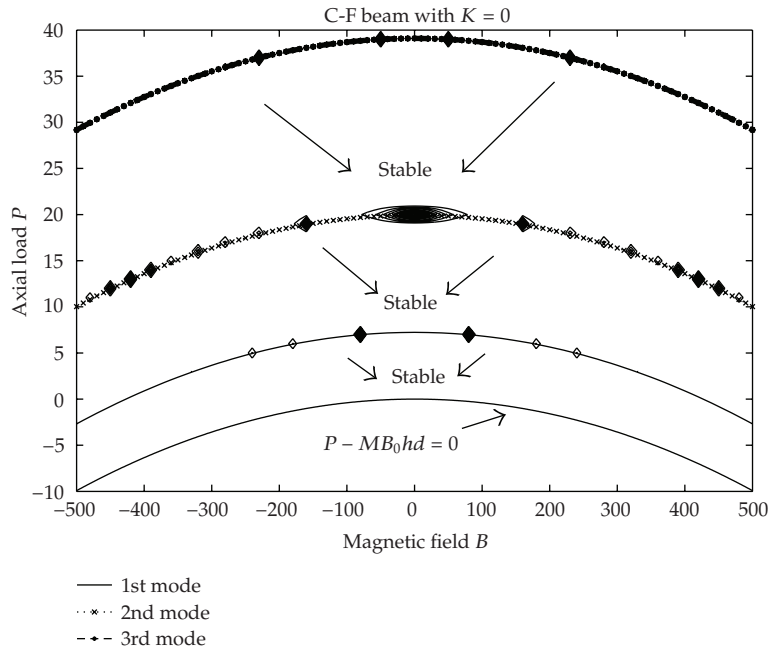

Figure 4: Stability Region for an ME beam with cantilever boundary conditions subjected to axial load and magnetic field with no spring support.

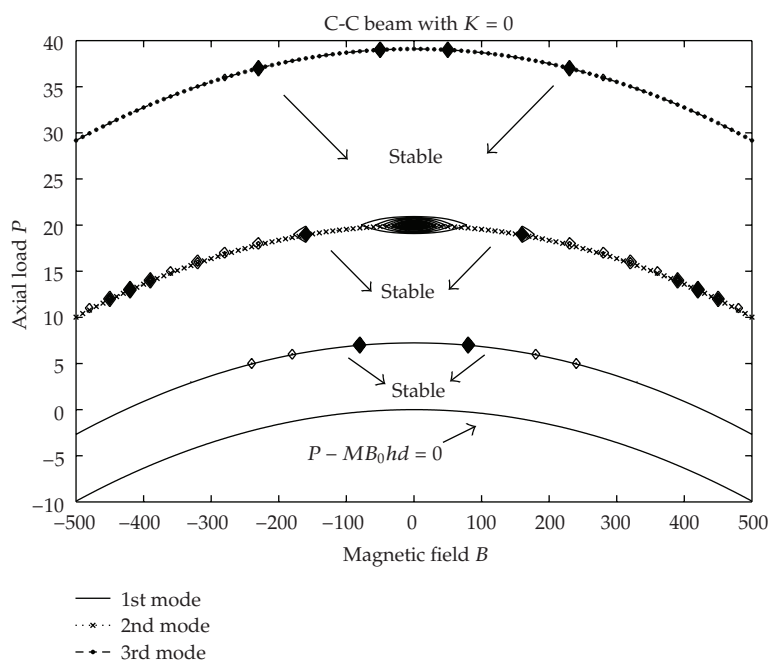

Figure 5: Stability Region for an ME beam with fixed-fixed boundary conditions subjected to axial load and magnetic field with no spring support.

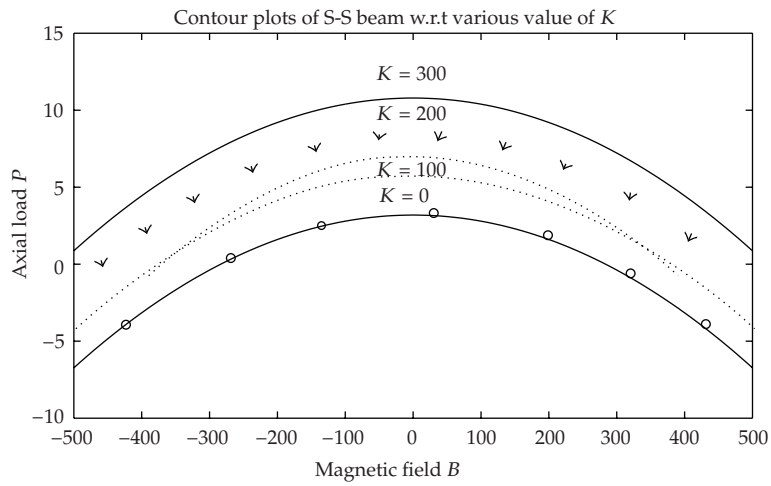

Figure 6: Stability Region for an ME beam with simply supported boundary conditions subjected to axial load and magnetic field with various spring constants.

for the cantilever ME beam, see Figure 4, can be found to seat on the dispersion curve of the third mode. In particular, the number of instability diamond is dramatically soaring so that almost every mode possesses at least 8 of the particular zones. Similar situation can also be observed in the case of fixed-fixed ME beam as shown in Figure 5, except that a remarkable instability ellipse resides on the dispersion curve of the second mode. It seems that on the curve of the second mode the instability restraints due to the initial conditions are compactly revealed, that is, we should put more attention when dealing with the instability problem for the second mode than the others.

Figure 6 demonstrates the dispersion curves of a simply supported ME beam subjected to external axial load and magnetic field with respect to various spring constant as foundation. As we expected, the larger value of spring constant results in the wider stability region to the ME beam system, that is, spring foundation plays a role in stabilizing the system, that is, if some certain axial load and magnetic field are necessarily imposed on the EM beam system, one way to promote the stability region, or to avoid instability, is to put the system on the Wrinkler-type foundation, thus system stability can still be retained.

At last, in order to verify the correctness of the results obtained by using the proposed method, the time responses of the system are presented for the stable and unstable regions individually. If we take simply supported ME beam as an example, adopting sinusoidal functions to be the mode shapes of the system, a set of temporal equations can be achieved after imposing Galerkin's procedure on (2.1); therefore, by performing Runge-Kutta method, the time responses of the system at middle point of the beam can be carried out for any desired modes.

Figure 7 depicts the ratio of displacement to beam thickness when the magnetic field and axial load are taken from the stable region as shown in Figure 2, while Figure 8 shows the results taken from the unstable region as a comparison. As it can be detected from Figure 7, when $B = 10$ Tesla and $P = 3.0\,\mathrm{N}$, the time responses of the system for the first, second, and third modes are plotted and the total deflection is calculated, all of which can be found to be of stable state. On the other hand, as $B = 10$ Tesla and $P = 4.0\,\mathrm{N}$ are chosen in Figure 8, the

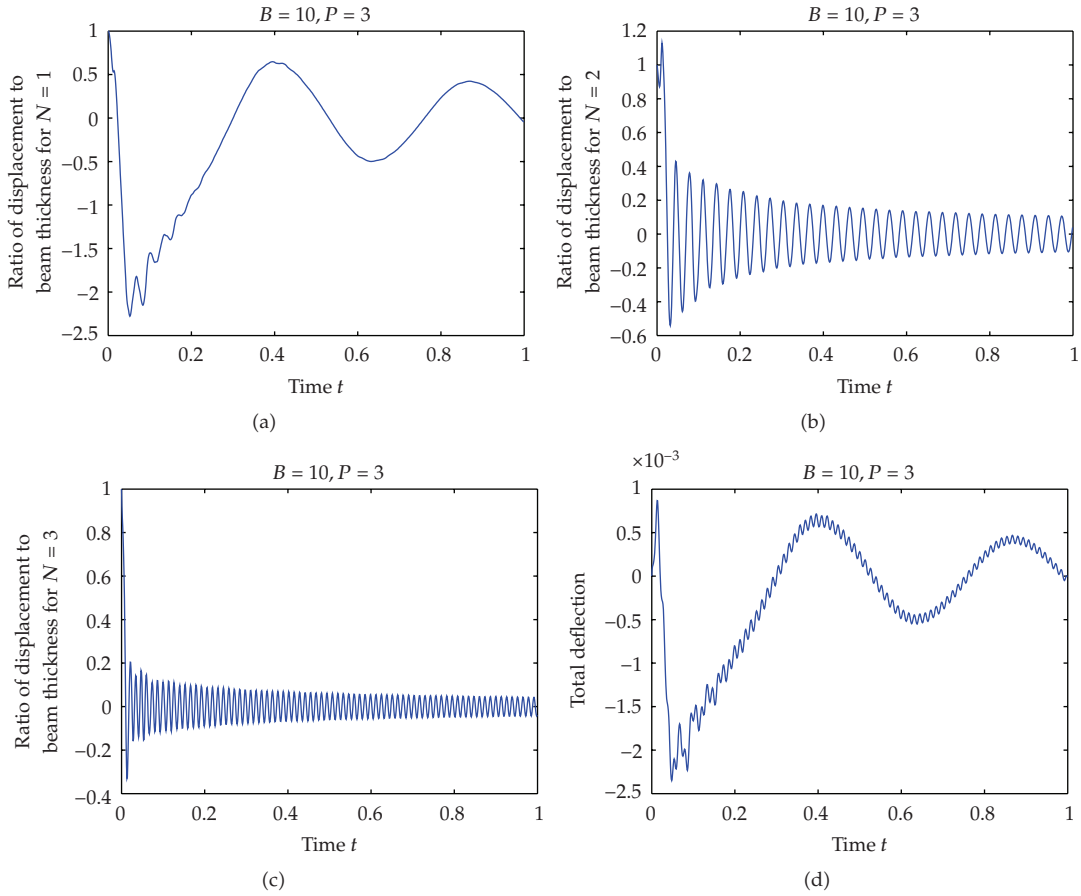

Figure 7: Transit response for an ME beam with simply supported boundary conditions subjected to axial load and magnetic field within stable region.

time response for the first mode is divergent, and those for the second and third modes are convergent; thus the total deflection is unstable as a result.

4. Conclusions

In this paper, the interactive behaviors between transverse magnetic fields and axial loads of a magnetoelastic (ME) beam subjected to general boundary conditions are investigated. In particular, the instability criterion for the magneto-mechanical buckling problem is intricately discussed according to the structure characteristics as well as the initial conditions. The equation of motion for the proposed physical model is introduced based on the Hamilton's principle, and the stability criterion is obtained by using the method of multiple scales implemented on both spatial and time domains. By performing the perturbation procedure, a set of relevant partial differential equations can thus be derived with respect to different collecting order; meanwhile the analytic solutions for the respective perturbed equations can be resolved order by order successively based on some simplifications. Eventually a so-called Schrodinger equation with cubic nonlinearity (NLS) can be generated by suitably changing

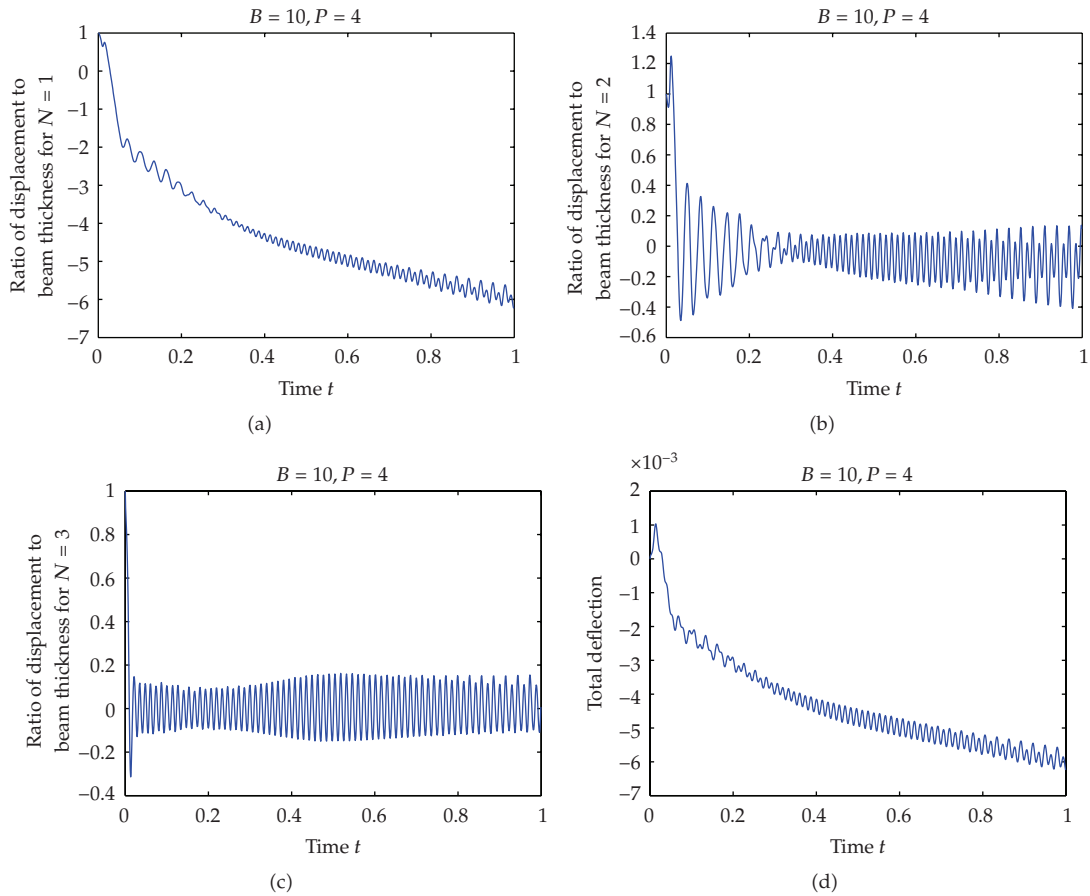

Figure 8: Divergent response for an ME beam with simply supported boundary conditions subjected to axial load and magnetic field outside the stable region.

the variables; as a result, the stable criteria for the magnetoelastic beam can be acquired after dissecting the nonlinear Schrodinger equation and requiring the imaginary part of the time domain solution to be vanished. Four kinds of boundary conditions are imposed to a low-carbon steel beam structure as examples in order to implement the proposed methodology, and the effects of both initial conditions and boundary conditions on the stability criterion of the ME beam are examined in detail. Stability criterion curve for the dispersion equation of the ME beam is firstly depicted in order to reveal the magnificent influence of the structure characteristic itself, followed by the instability constraint due to the variation of initial conditions and the observation locations. The prior one is actually denoting a parabola, whereas the latter one is sometimes a diamond-like or ellipse-like region spotting along the prior one. By the fact that the strong instability due to the initial conditions and observation points makes the analysis become more complicated, a slight change in the number of instability diamond can be noticed with respect to different boundary conditions, and an extra added instability ellipse centered in the vicinity of zero magnetic field is also detected for the cases other than simply supported beam. As we expected, the larger value of spring constant results in the wider stability region to the ME beam system, that is, spring foundation plays a role in stabilizing the system.

Acknowledgments

This work was partially supported by the National Science Council of the Republic of China under Grant NSC 95-2115-M-214-002 and by I-Shou University of the Republic of China under Grant ISU 94-02-22. The authors are grateful for these supports.

References

[1] J. R. Reitz, F. J. Milford, and R. W. Christy, *Foundations of Electromagnetic Theory*, Wesley, New York, NY, USA, 1992.
[2] F. C. Moon, *Magneto-Solid Mechanics*, Wiley, New York, NY, USA, 1984.
[3] F. C. Moon and Y. H. Pao, "Magneto-elastic buckling of a thin plate," *Journal of Applied Mechanics*, vol. 37, pp. 53–58, 1968.
[4] D. V. Wallerstein and M. O. Peach, "Magneto-elastic buckling of beams and thin plates of magnetically soft material," *Journal of Applied Mechanics*, vol. 39, pp. 451–455, 1972.
[5] K. Miya, K. Hara, and K. Someya, "Experimental and theoretical study on magneto-elastic buckling of ferro-elastic cantilevered beam-plate," *Journal of Applied Mechanics*, vol. 45, no. 2, pp. 355–360, 1978.
[6] F. C. Moon and Y. H. Pao, "Vibration and dynamic instability of a beam-plate in a transverse magnetic field," *Journal of Applied Mechanics*, vol. 36, pp. 92–100, 1969.
[7] H. Kojima, K. Nagaya, H. Shiraishi, and A. Yamashita, "Nonlinear vibration of a beam with a mass subjected to alternating electromagnetic force," *Bulletin of the JSME*, vol. 28, no. 237, pp. 468–474, 1985.
[8] Y.-S. Shih, G.-Y. Wu, and E. J. S. Chen, "Transient vibrations of a simply-supported beam with axial loads and transverse magnetic fields," *Mechanics of Structures and Machines*, vol. 26, no. 2, pp. 115–130, 1998.
[9] M.-F. Liu and T.-P. Chang, "Vibration analysis of a magneto-elastic beam with general boundary conditions subjected to axial load and external force," *Journal of Sound and Vibration*, vol. 288, no. 1-2, pp. 399–411, 2005.
[10] G. Y. Wu, "The analysis of dynamic instability and vibration motions of a pinned beam with transverse magnetic fields and thermal loads," *Journal of Sound and Vibration*, vol. 284, no. 1-2, pp. 343–360, 2005.
[11] B. Pratiher and S. K. Dwivedy, "Parametric instability of a cantilever beam with magnetic field and periodic axial load," *Journal of Sound and Vibration*, vol. 305, no. 4-5, pp. 904–917, 2007.
[12] D. J. Hasanyan, G. M. Khachaturyan, and G. T. Piliposyan, "Mathematical modeling and investigation of nonlinear vibration of perfectly conductive plates in an inclined magnetic field," *Thin-Walled Structures*, vol. 39, no. 1, pp. 111–123, 2001.
[13] C. Bu, "Generalized solutions to the cubic Schrödinger equation," *Nonlinear Analysis: Theory, Methods & Applications*, vol. 27, no. 7, pp. 769–774, 1996.

Hindawi Publishing Corporation
Mathematical Problems in Engineering
Volume 2010, Article ID 734340, 10 pages
doi:10.1155/2010/734340

Research Article

Stability Analysis of Interconnected Fuzzy Systems Using the Fuzzy Lyapunov Method

Ken Yeh[1] and Cheng-Wu Chen[2]

[1] *Department of Construction Science and Technology, De-Lin Institute of Technology, No.1, Lane 380, Qingyun Rd., Tucheng, Taipei 236, Taiwan*
[2] *Department of Logistics Management, Shu-Te University, 59 Hun Shan Road, Yen Chau, Kaohsiung 82445, Taiwan*

Correspondence should be addressed to Cheng-Wu Chen, cwchen@stu.edu.tw

Received 10 August 2009; Accepted 4 November 2009

Academic Editor: Carlo Cattani

The fuzzy Lyapunov method is investigated for use with a class of interconnected fuzzy systems. The interconnected fuzzy systems consist of J interconnected fuzzy subsystems, and the stability analysis is based on Lyapunov functions. Based on traditional Lyapunov stability theory, we further propose a fuzzy Lyapunov method for the stability analysis of interconnected fuzzy systems. The fuzzy Lyapunov function is defined in fuzzy blending quadratic Lyapunov functions. Some stability conditions are derived through the use of fuzzy Lyapunov functions to ensure that the interconnected fuzzy systems are asymptotically stable. Common solutions can be obtained by solving a set of linear matrix inequalities (LMIs) that are numerically feasible. Finally, simulations are performed in order to verify the effectiveness of the proposed stability conditions in this paper.

1. Introduction

In the recent years, a number of research activities have been conducted concerning stability analysis and the stabilization problems of large-scale systems, including electric power systems, nuclear reactors, aerospace systems, large electrical networks, economic systems, process control systems, chemical and petroleum industrial systems, different societal systems, ecological systems, and transportation systems. The interconnected models can be used to represent practical large-scale systems. Moreover, the field of interconnected systems is so broad as to cover the fundamental theory of modeling, optimization and control aspects, and such applications. Therefore, the methodologies used when dealing with interconnected models provide a viable technique whereby the manipulation of

system structure can be used to overcome the increasing size and complexity of the relevant mathematical models. Additionally, the fields of analysis, design, and control theory relating to interconnected systems have attained a considerable level of maturity and sophistication. They are currently receiving increasing attention from theorists and practitioners because they are methodologically interesting and have important real-life applications. Such systems comprise numerous interdependent subsystems which serve particular functions, share resources, and are governed by a set of interrelated goals and constraints. Recently, various approaches have been employed to elucidate the stability and stabilization of interconnected systems, as proposed in the literature and the references therein [1–3].

Since Zadeh [4] and Takagi and Sugeno [5] proposed a new concept for a fuzzy inference system which combines the flexibility of fuzzy logic theory and rigorous mathematical analysis tools into a unified framework, the application of fuzzy models has attracted great interest from the engineering and management community (e.g., see [6–20] and the references therein). This kind of fuzzy model suggests an efficient method to represent complex nonlinear systems via fuzzy reasoning. This has enabled the stability issues of fuzzy systems to be extensively applied in system analysis (see [21–26] and the references therein). Similarly, the stability criteria and stabilization problems have been discussed for fuzzy large-scale systems in Wang and Luoh [27], and Hsiao and Hwang [28], where the fuzzy large-scale system consists of J subsystems.

In the aforementioned results for T-S fuzzy models, most of the stability criteria and controller design have usually been derived based on the usage of a single Lyapunov function. However, the main drawback associated with this method is that the single Lyapunov function must work for all linear models of the fuzzy control systems, which in general leads to a conservative controller design [29]. Recently, in order to relax this conservatism, the fuzzy Lyapunov function approach has been proposed in [24, 29–33]. To the best of my knowledge, the stability analyses of interconnected systems based on fuzzy Lyapunov functions have not been discussed yet. Therefore, some novel sufficient conditions are derived from fuzzy Lyapunov functions for stability guarantees by fuzzy for interconnected fuzzy systems in this work.

The organization of the paper is presented as follows. First, the T-S fuzzy modeling is briefly reviewed and the interconnected scheme is used to construct a fuzzy dynamic model. Then, the stability conditions for the fuzzy Lyapunov functions are proposed which guarantee the stability of the interconnected fuzzy systems. In this section, the stability problems can be reformulated into a problem for solving a linear matrix inequality (LMI).

2. System Descriptions and Preliminaries

A fuzzy dynamic model was proposed in the pioneering work of Takagi and Sugeno [5] where complex nonlinear systems could be represented using local linear input/output relations. The main feature of this model is that each locally fuzzy implication (rule) is a linear system and the overall system model is achieved through linear fuzzy blending. This fuzzy dynamic model is described by fuzzy IF-THEN rules and are utilized in this study to deal with the stability analysis issue of an interconnected fuzzy system S that is composed of J subsystems Si $(j = 1, \ldots, J)$. The ith rule of the interconnected fuzzy model of the jth subsystem is proposed as having the following form.

Plant Rule i:

$$\begin{gathered}\text{IF } x_{1j}(t) \text{ is } M_{i1j}, \ldots, x_{gj}(t) \text{ is } M_{igj}, \\ \text{THEN } \dot{x}_j(t) = A_{ij}x_j(t) + \sum_{\substack{n=1 \\ n\neq j}}^{J} \widehat{A}_{inj}x_n(t), \quad i = 1, 2, \ldots, r_j,\end{gathered} \tag{2.1}$$

where r_j is the IF-THEN rule number; A_{ij} and $\widehat{A}_{inj}$ are constant matrices with appropriate dimensions; $x_j(t)$ is the state vector of the jth subsystem; $x_n(t)$ is the interconnection between the nth and jth subsystems; $M_{ipj}(p = 1, 2, \ldots, g)$ are the fuzzy sets; $x_{1j}(t) \sim x_{g\,j}(t)$ are the premise variables. Through the use of "fuzzy blending," the overall fuzzy model of the jth fuzzy subsystem can be inferred as follows [13]:

$$\dot{x}_j(t) = \frac{\sum_{i=1}^{r_j} w_{ij}(t)\left[A_{ij}x_j(t) + \sum_{n=1,n\neq j}^{J} \widehat{A}_{inj}x_n(t)\right]}{\sum_{i=1}^{r_j} w_{ij}(t)} = \sum_{i=1}^{r_j} h_{ij}(t)\left[A_{ij}x_j(t) + \sum_{\substack{n=1 \\ n\neq j}}^{J} \widehat{A}_{inj}x_n(t)\right], \tag{2.2}$$

with

$$w_{ij}(t) \equiv \prod_{p=1}^{g} M_{ipj}(x_{pj}(t)), \qquad h_{ij}(t) \equiv \frac{w_{ij}(t)}{\sum_{i=1}^{r_j} w_{ij}(t)}, \tag{2.3}$$

in which $M_{ipj}(x_{pj}(t))$ is the grade of membership of $x_{pj}(t)$ in M_{ipj}. In this study, it is assumed that $w_{ij}(t) \geq 0, i = 1, 2, \ldots, r_j$; $j = 1, 2, \ldots, J$. Therefore, the normalized membership function $h_{ij}(t)$ satisfies

$$h_{ij}(t) \geq 0, \quad \sum_{i=1}^{r_j} h_{ij}(t) = 1, \quad \forall t. \tag{2.4}$$

In the following, we state the lemmas which are useful to prove the stability of the interconnected fuzzy system **S** which consists of J closed-loop subsystems described in (2.1).

Lemma 2.1 (see [13]). *For any $A, B \in R^n$ and for any symmetric positive definite matrix $G \in R^{n\times n}$, one has*

$$2A^TB \leq A^TGA + B^TG^{-1}B. \tag{2.5}$$

Lemma 2.2 (see [34]). *(Schur complements) One has*

$$\text{The LMI } \begin{bmatrix} Q(x) & S(x) \\ S(x) & R(x) \end{bmatrix} > 0, \tag{2.6}$$

where $Q(x) = Q^T(x)$, $R(x) = R^T(x)$, and $S(x)$ depends on x that is equivalent to

$$R(x) > 0, \quad Q(x) - S(x)R^{-1}(x)S^T(x) > 0. \tag{2.7}$$

In other words, the set of nonlinear inequalities (2.7) *can be represented as the LMI* (2.6).

3. Stability Analysis by a Fuzzy Lyapunov Function

Here we define a fuzzy Lyapunov function and consider the stability conditions for the jth fuzzy subsystem (2.2).

Definition 3.1. Equation (3.1) is said to be a fuzzy Lyapunov function for the T-S fuzzy system (2.2) if the time derivative of $V(t)$ is always negative

$$V(t) = \sum_{j=1}^{J} v_j(t) = \sum_{j=1}^{J} \sum_{l=1}^{r_j} h_{lj}(t) x_j^T(t) P_{lj} x_j(t), \tag{3.1}$$

where P_{lj} is a positive definite matrix.

Because the fuzzy Lyapunov function shares the same membership functions with the T-S fuzzy model of a system, the time derivative of the fuzzy Lyapunov function contains the time derivative of the premise membership functions. Therefore, how to deal with the time derivative of the time derivative of the premise membership functions is an important consideration.

By taking the time derivative of (3.1), the following stability condition of open-loop system (2.7) will be obtained.

Theorem 3.2. *The fuzzy system* (2.7) *is stable in the large if there exist common positive definite matrices $P_1, P_2, \ldots, P_r$ such that the following inequality is satisfied:*

$$\sum_{\rho=1}^{r_j} \dot{h}_{\rho j}(t) P_{\rho j} + \sum_{l=1}^{r_j} \sum_{i=1}^{r_j} h_{lj}(t) h_{ij}(t) \left[A_{ij}^T P_{li} + P_{li} A_{ij} + \alpha(J-1) I + \sum_{n=1}^{J} \alpha^{-1} P_j \widehat{A}_{inj} \widehat{A}_{inj}^T P_j \right] < 0. \tag{3.2}$$

Proof. Consider the Lyapunov function candidate for the fuzzy system (2.2)

$$V(t) = \sum_{j=1}^{J} v_j(t) = \sum_{j=1}^{J} \sum_{l=1}^{r_j} h_{lj}(t) x_j^T(t) P_{lj} x_j(t). \tag{A1}$$

The time derivative of V is

$$\dot{V}(t) = \sum_{j=1}^{J}\sum_{\rho=1}^{r_j}\dot{h}_{\rho j}(t)x_j^T(t)P_{\rho j}x_j(t) + \sum_{j=1}^{J}\sum_{l=1}^{r_j}h_{lj}(t)\left\{\dot{x}_j^T(t)P_{lj}x_j(t) + x_j^T(t)P_{lj}\dot{x}_j(t)\right\} \tag{A2}$$

$$\begin{aligned}
&= \sum_{j=1}^{J}\sum_{\rho=1}^{r_j}\dot{h}_{\rho j}(t)x_j^T(t)P_{\rho j}x_j(t) \\
&\quad + \sum_{j=1}^{J}\sum_{l=1}^{r_j}h_{lj}(t)\left\{\left[\sum_{i=1}^{r_j}h_{ij}(t)\left(A_{ij}x_j(t) + \sum_{\substack{n=1\\ n\neq j}}^{J}\widehat{A}_{inj}x_n(t)\right)\right]^T P_{li}x_j(t)\right. \\
&\qquad \left. + x_j^T(t)P_{lj}\left[\sum_{i=1}^{r_j}h_{ij}(t)\left(A_{ij}x_j(t) + \sum_{\substack{n=1\\ n\neq j}}^{J}\widehat{A}_{inj}x_n(t)\right)\right]\right\}
\end{aligned} \tag{A3}$$

$$\begin{aligned}
&= \sum_{j=1}^{J}\sum_{\rho=1}^{r_j}\dot{h}_{\rho j}(t)x_j^T(t)P_{\rho j}x_j(t) + \sum_{j=1}^{J}\sum_{l=1}^{r_j}\sum_{i=1}^{r_j}h_{lj}(t)h_{ij}(t)x_j^T(t)\left[A_{ij}^TP_{li} + P_{li}A_{ij}\right]x_j(t) \\
&\quad + \sum_{j=1}^{J}\sum_{l=1}^{r_j}\sum_{i=1}^{r_j}\sum_{\substack{n=1\\ n\neq j}}^{J}h_{lj}(t)h_{ij}(t)\left[x_n^T(t)\widehat{A}_{inj}^TP_jx_j(t) + x_j^T(t)P_j\widehat{A}_{inj}x_n(t)\right].
\end{aligned} \tag{A4}$$

Based on Lemma 2.1, we have

$$\begin{aligned}
&\sum_{j=1}^{J}\sum_{l=1}^{r_j}\sum_{i=1}^{r_j}\sum_{\substack{n=1\\ n\neq j}}^{J}h_{lj}(t)h_{ij}(t)\left\{x_n^T(t)\widehat{A}_{inj}^TP_jx_j(t) + x_j^T(t)P_j\widehat{A}_{inj}x_n(t)\right\} \\
&\quad \leq \sum_{j=1}^{J}\sum_{l=1}^{r_j}\sum_{i=1}^{r_j}\sum_{\substack{n=1\\ n\neq j}}^{J}h_{lj}(t)h_{ij}(t)\left\{\alpha\left[x_n^T(t)x_n(t)\right] + \alpha^{-1}\left[x_j^T(t)P_j\widehat{A}_{inj}\widehat{A}_{inj}^TP_jx_j(t)\right]\right\}
\end{aligned} \tag{A5}$$

$$\begin{aligned}
&= \sum_{j=1}^{J}\sum_{l=1}^{r_j}\sum_{i=1}^{r_j}\sum_{n=1}^{J}h_{lj}(t)h_{ij}(t)\left\{\alpha\left[\left(1-\frac{1}{J}\right)x_j^T(t)x_j(t)\right]\right. \\
&\qquad \left. + \alpha^{-1}\left[x_j^T(t)P_j\widehat{A}_{inj}\widehat{A}_{inj}^TP_jx_j(t) - \frac{1}{J}x_j^T(t)P_j\widehat{A}_{ijj}\widehat{A}_{ijj}^TP_jx_j(t)\right]\right\}.
\end{aligned} \tag{A6}$$

(Based on the concept of interconnection, the matrix $\widehat{A}_{ijj}$ is equal to zero.) From (A4) and (A6), we obtain

$$\begin{aligned}\dot{V}(t) \leq & \sum_{j=1}^{J}\sum_{\rho=1}^{r_j}\dot{h}_{\rho j}(t)x_j^T(t)P_{\rho j}x_j(t) + \sum_{j=1}^{J}\sum_{l=1}^{r_j}\sum_{i=1}^{r_j}h_{lj}(t)h_{ij}(t)x_j^T(t) \\ & \times\left[A_{ij}^TP_{li} + P_{li}A_{ij} + \alpha(J-1)I + \sum_{n=1}^{J}\alpha^{-1}P_j\widehat{A}_{inj}\widehat{A}_{inj}^TP_j\right]x_j(t).\end{aligned} \tag{A7}$$

Therefore, $\dot{V}(t) < 0$ if (3.2) holds.However, condition (3.2) cannot be easily solved numerically because we need to consider the term of the time derivative $\dot{h}_{\rho j}(t)$. Eq. (3.2) is thus transformed into numerically feasible conditions described in Theorem 3.3 and upper bounds of the time derivative are used in place of the $h_\rho(t)$. □

Theorem 3.3. *The fuzzy system* (2.7) *is stable in the large if there exist common positive definite matrices* $P_{1j}, P_{2j}, \ldots, P_{rj}$ *such that inequality* $|\dot{h}_{\rho j}(t)| \leq \phi_{\rho j}$ *is satisfied and*

$$\sum_{\rho=1}^{r_j}\phi_{\rho j}P_{\rho j} + A_{ij}^TP_{li} + P_{li}A_{ij} + \alpha(J-1)I + \sum_{n=1}^{J}\alpha^{-1}P_j\widehat{A}_{inj}\widehat{A}_{inj}^TP_j. \tag{3.3}$$

Proof.

$$\begin{aligned}\dot{V}(t) \leq & \sum_{j=1}^{J}\sum_{\rho=1}^{r_j}\dot{h}_{\rho j}(t)x_j^T(t)P_{\rho j}x_j(t) \\ & + \sum_{j=1}^{J}\sum_{l=1}^{r_j}\sum_{i=1}^{r_j}h_{lj}(t)h_{ij}(t)x_j^T(t)\left[A_{ij}^TP_{li} + P_{li}A_{ij} + \alpha(J-1)I + \sum_{n=1}^{J}\alpha^{-1}P_j\widehat{A}_{inj}\widehat{A}_{inj}^TP_j\right]x_j(t) \\ \leq & \sum_{j=1}^{J}\sum_{l=1}^{r_j}\sum_{i=1}^{r_j}h_{lj}(t)h_{ij}(t)\left\{\sum_{\rho=1}^{r_j}x_j^T(t)\left[\phi_{\rho j}P_{\rho j}\right]x_j(t)\right\} \\ & + \sum_{j=1}^{J}\sum_{l=1}^{r_j}\sum_{i=1}^{r_j}h_{lj}(t)h_{ij}(t)x_j^T(t)\left[A_{ij}^TP_{li} + P_{li}A_{ij} + \alpha(J-1)I + \sum_{n=1}^{J}\alpha^{-1}P_j\widehat{A}_{inj}\widehat{A}_{inj}^TP_j\right]x_j(t) \\ = & \sum_{j=1}^{J}\sum_{l=1}^{r_j}\sum_{i=1}^{r_j}h_{lj}(t)h_{ij}(t)x_j^T(t)\left[\sum_{\rho=1}^{r_j}\phi_{\rho j}P_{\rho j} + A_{ij}^TP_{li} + P_{li}A_{ij} + \alpha(J-1)I\right. \\ & \left. + \sum_{n=1}^{J}\alpha^{-1}P_j\widehat{A}_{inj}\widehat{A}_{inj}^TP_j\right]x_j(t),\end{aligned} \tag{A8}$$

$\dot{V}(t) < 0$ if (3.3) holds. □

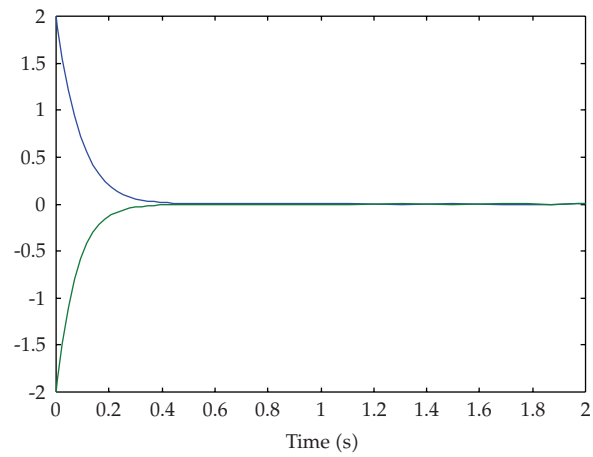

Figure 1: The state response of subsystem 1.

Remark 3.4. A special case of sufficient conditions without $\phi_{\rho j}$ is proposed to guarantee the asymptotically stability of fuzzy large-scale system **S**. If there exist symmetric positive definite matrices P_j which satisfy that each isolated subsystem is asymptotically stable as described in (3.4), the trajectories of the interconnected system are stable:

$$A_{ij}{}^T P_j + P_j A_{ij} + \sum_{n=1}^{J} \alpha^{-1} P_j \widehat{A}_{inj} \widehat{A}_{inj}^T P_j + \alpha(J-1)I < 0 \tag{3.4}$$

for $i = 1, 2, \ldots, r_j$; $j = 1, 2, \ldots, J$.

Remark 3.5. Equation (3.4) can be recast as an LMI problem based on Lemma 2.2. Therefore, new variables $W_j = P_j^{-1}$ and $\overline{\alpha} = \alpha^{-1}$ are introduced and (3.4) is rewritten as

$$\begin{bmatrix} W_j A_{ij}^T + A_{ij} W_j + \sum_{n=1}^{J} \overline{\alpha} \widehat{A}_{inj} \widehat{A}_{inj}^T & W_j \\ W_j & -\overline{\alpha}\left(\dfrac{1}{J-1}\right) I \end{bmatrix} < 0 \quad \text{for } i = 1, 2, \ldots, r_j. \tag{3.5}$$

4. A Numerical Example

Consider a interconnected fuzzy system **S** which consists of two fuzzy subsystems described by (2.2) with one rule.

Subsystem 1:

$\dot{x}_1\ (t) = h_{11}\ (t) \lfloor A_{11}\ x_1\ (t) + \widehat{A}_{121}\ x_2\ (t) \rfloor,$

Subsystem 2:

$\dot{x}_2(t) = h_{12}(t) \lfloor A_{12} x_2(t) + \widehat{A}_{112} x_1(t) \rfloor,$

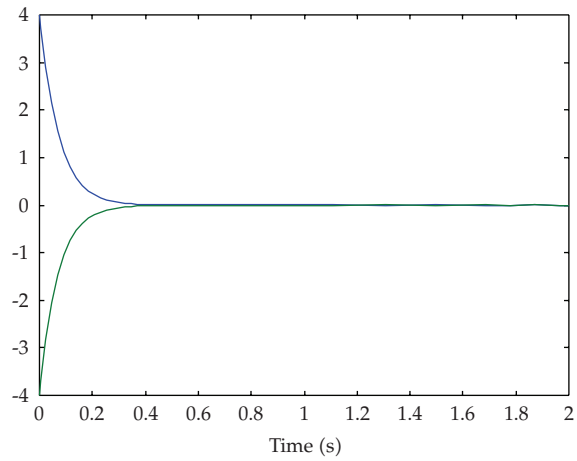

Figure 2: The state response of subsystem 2.

in which

$$x_1^T(t) = [x_{11}(t)x_{21}(t)], \quad x_2^T(t) = [x_{12}(t)x_{22}(t)], \quad A_{11} = \begin{bmatrix} -16.252 & -6.222 \\ -6.084 & -24.674 \end{bmatrix},$$
$$\widehat{A}_{121} = \begin{bmatrix} 0.3 & 0.2 \\ 0.1 & 0.4 \end{bmatrix}, \quad A_{12} = \begin{bmatrix} -21.800 & -7.710 \\ -7.150 & -23.210 \end{bmatrix}, \quad \widehat{A}_{112} = \begin{bmatrix} 0.3 & 0.3 \\ 0.3 & 0.3 \end{bmatrix}. \tag{4.1}$$

At first, based on (3.5), we can get the common solutions W_j and $\overline{\alpha}$ via the Matlab LMI optimization toolbox

$$W_1 = \begin{bmatrix} 0.811 & -0.2411 \\ -0.2411 & 0.342 \end{bmatrix}, \qquad W_2 = \begin{bmatrix} 2.9482 & 1.1952 \\ 1.1952 & 3.1873 \end{bmatrix}, \qquad \overline{\alpha} = 1. \tag{4.2}$$

Then, the following positive definite matrices $P_j (= W_j^{-1})$ and α can be obtained such that (3.4) is satisfied

$$P_1 = \begin{bmatrix} 1.5601 & 1.1002 \\ 1.1002 & 3.7001 \end{bmatrix}, \qquad P_2 = \begin{bmatrix} 0.4002 & -0.1511 \\ -0.1512 & 0.3703 \end{bmatrix}, \qquad \alpha = 1. \tag{4.3}$$

Therefore, based on the theorem, the interconnected fuzzy system **S** described in (4.1) is guaranteed to be asymptotically stable. From the simulation of Figures 1 and 2 and given the initial conditions, $x_{11}(0) = 2$, $x_{21}(0) = -2$, $x_{12}(0) = 4$, $x_{22}(0) = -4$, we observe that the interconnected fuzzy system **S** is asymptotically stable, because the trajectories of two subsystems starting from non-zero initial states both approach close to the origin.

5. Conclusions

For the class of continuous interconnected fuzzy system **S**, LMI-based stability conditions have been derived based on the new fuzzy Lyapunov function. Sufficient stability conditions were derived based on the asymptotically stability of the existence of a common positive definite matrix *Pi* which is able to satisfy the Lyapunov equation or the LMI for each subsystem *Si*. Finally, a numerical example was given to illustrate the effectiveness and ease of implementation of this approach.

Acknowledgment

This work was supported by the National Science Council of Republic of China under Grant nos. NSC 98-2221-E-237-009-, NSC 96-2628-E-366-004-MY2, and NSC 98-2221-E-366-006-MY2.

References

[1] C. W. Chen, W. L. Chiang, and F. H. Hsiao, "Stability analysis of T-S fuzzy models for nonlinear multiple time-delay interconnected systems," *Mathematics and Computers in Simulation*, vol. 66, no. 6, pp. 523–537, 2004.

[2] S. Tong, S. Tong, and Q. L. Zhang, "Robust stabilization of nonlinear time-delay interconnected systems via decentralized fuzzy control," *International Journal of Innovative Computing, Information and Control*, vol. 4, no. 7, pp. 1567–1582, 2008.

[3] S. Tong and Q. L. Zhang, "Decentralized output feedback fuzzy H infinity tracking control for nonlinear interconnected systems with time-delay," *International Journal of Innovative Computing, Information and Control*, vol. 4, pp. 3385–3398, 2008.

[4] L. Zadeh, "Outline of new approach to the analysis of complex systems and decision processes," *IEEE Transactions on Systems, Man, and Cybernetics*, vol. 3, pp. 28–44, 1973.

[5] T. Takagi and M. Sugeno, "Fuzzy identification of systems and its applications to modeling and control," *IEEE Transactions on Systems, Man, and Cybernetics*, vol. 15, no. 1, pp. 116–132, 1985.

[6] F. Amini and R. Vahdani, "Fuzzy optimal control of uncertain dynamic characteristics in tall buildings subjected to seismic excitation," *Journal of Vibration and Control*, vol. 14, no. 12, pp. 1843–1867, 2008.

[7] C. W. Chen, H. L. Wang, and J. W. Lin, "Managing target the cash balance in construction firms using a fuzzy regression approach," *International Journal of Uncertainty, Fuzziness and Knowledge-Based Systems*, vol. 17, no. 5, pp. 667–684, 2009.

[8] C. W. Chen, K. Yeh, and F. R. Liu, "Adaptive fuzzy sliding mode control for seismically excited bridges with lead rubber bearing isolation," *International Journal of Uncertainty, Fuzziness and Knowledge-Based Systems*, vol. 17, no. 5, pp. 705–727, 2009.

[9] C. Y. Chen, C. W. Shen, C. W. Chen, F. R. Liu, and M. J. Jeng, "A stability criterion for time-delay tension leg platform systems subjected to external force," *China Ocean Engineering*, vol. 23, no. 1, pp. 49–57, 2009.

[10] P. C. Chen, C. W. Chen, and W. L. Chiang, "GA-based modified adaptive fuzzy sliding mode controller for nonlinear systems," *Expert Systems with Applications*, vol. 36, no. 3, pp. 5872–5879, 2009.

[11] R. Guclu and M. Metin, "Fuzzy logic control of vibrations of a light rail transport vehicle in use in Istanbul traffic," *Journal of Vibration and Control*, vol. 15, no. 9, pp. 1423–1440, 2009.

[12] F. H. Hsiao, C. W. Chen, Y. W. Liang, S. D. Xu, and W. L. Chiang, "T-S fuzzy controllers for nonlinear interconnected systems with multiple time delays," *IEEE Transactions on Circuits and Systems I*, vol. 52, no. 9, pp. 1883–1893, 2005.

[13] F. H. Hsiao, W. L. Chiang, C. W. Chen, et al., "Application and robustness design of fuzzy controller for resonant and chaotic systems with external disturbance," *International Journal of Uncertainty, Fuzziness and Knowledge-Based Systems*, vol. 13, no. 3, pp. 281–295, 2005.

[14] T. Y. Hsieh, H. L. Wang, C. W. Chen, et al., "A new viewpoint of s-curve regression model and its application to construction management," *International Journal on Artificial Intelligence Tools*, vol. 15, no. 2, pp. 131–142, 2006.

[15] C. N. Ko and C. J. Wu, "A PSO-tuning method for design of fuzzy PID controllers," *Journal of Vibration and Control*, vol. 14, no. 3, pp. 375–395, 2008.
[16] M. L. Lin, C. W. Chen, Q. B. Wang, et al., "Fuzzy model-based assessment and monitoring of desertification using MODIS satellite imagery," *Engineering Computations*, vol. 26, no. 7, pp. 745–760, 2009.
[17] M. B. Trabia, J. M. Renno, and K. A. F. Moustafa, "Generalized design of an anti-swing fuzzy logic controller for an overhead crane with hoist," *Journal of Vibration and Control*, vol. 14, no. 3, pp. 319–346, 2008.
[18] C. H. Tsai, C. W. Chen, W. L. Chiang, and M. L. Lin, "Application of geographic information system to the allocation of disaster shelters via fuzzy models," *Engineering Computations*, vol. 25, no. 1, pp. 86–100, 2008.
[19] J. W. Tu, W. L. Qu, and J. Chen, "An experimental study on semi-active seismic response control of a large-span building on top of ship lift towers," *Journal of Vibration and Control*, vol. 14, no. 7, pp. 1055–1074, 2008.
[20] F. Zhao, J. Chen, L. Guo, and X. Li, "Neuro-fuzzy based condition prediction of bearing health," *Journal of Vibration and Control*, vol. 15, no. 7, pp. 1079–1091, 2009.
[21] C. W. Chen, "Modeling and control for nonlinear structural systems via a NN-based approach," *Expert Systems with Applications*, vol. 36, no. 3, pp. 4765–4772, 2009.
[22] C. W. Chen, "Stability conditions of fuzzy systems and its application to structural and mechanical systems," *Advances in Engineering Software*, vol. 37, no. 9, pp. 624–629, 2006.
[23] C. W. Chen, "The stability of an oceanic structure with T-S fuzzy models," *Mathematics and Computers in Simulation*, vol. 80, no. 2, pp. 402–426, 2009.
[24] C. W. Chen, C. L. Lin, C. H. Tsai, et al., "A novel delay-dependent criteria for time-delay T-S fuzzy systems using fuzzy Lyapunov method," *International Journal on Artificial Intelligence Tools*, vol. 16, no. 3, pp. 545–552, 2007.
[25] C. W. Chen, K. Yeh, W. L. Chiang, et al., "Modeling, H^∞ control and stability analysis for structural systems using Takagi-Sugeno fuzzy model," *Journal of Vibration and Control*, vol. 13, no. 11, pp. 1519–1534, 2007.
[26] C. W. Chen, "Modeling and fuzzy PDC control and its application to an oscillatory TLP structure," *Mathematical Problems in Engineering*, vol. 2010, 13 pages, 2010.
[27] W. Wang and L. Luoh, "Stability and stabilization of fuzzy large scale systems," *IEEE Transactions on Fuzzy Systems*, vol. 12, no. 3, pp. 309–315, 2004.
[28] F. H. Hsiao and J. D. Hwang, "Stability analysis of fuzzy large-scale systems," *IEEE Transactions on Systems, Man, and Cybernetics, Part B*, vol. 32, no. 1, pp. 122–126, 2002.
[29] H. N. Wu and H. Y. Zhang, "Reliable H-infinity fuzzy control for a class of discrete-time nonlinear systems using multiple fuzzy Lyapunov functions," *IEEE Transactions on Circuits and Systems I*, vol. 54, no. 4, pp. 357–361, 2007.
[30] K. Tanaka, T. Hori, and H. O. Wang, "A multiple Lyapunov function approach to stabilization of fuzzy control systems," *IEEE Transactions on Fuzzy Systems*, vol. 11, no. 4, pp. 582–589, 2003.
[31] K. Tanaka, H. Ohtake, and H. O. Wang, "A descriptor system approach to fuzzy control system design via fuzzy Lyapunov functions," *IEEE Transactions on Fuzzy Systems*, vol. 15, no. 3, pp. 333–341, 2007.
[32] K. Yeh, C. Y. Chen, and C. W. Chen, "Robustness design of time-delay fuzzy systems using fuzzy Lyapunov method," *Applied Mathematics and Computation*, vol. 205, no. 2, pp. 568–577, 2008.
[33] C. W. Chen, W. L. Chiang, C. H. Tsai, et al., "Fuzzy Lyapunov method for stability conditions of nonlinear systems," *International Journal on Artificial Intelligence Tools*, vol. 15, no. 2, pp. 163–171, 2006.
[34] S. Boyd, L. El Ghaoui, E. Feron, and V. Balakrishnan, *Linear Matrix Inequalities in System and Control Theory*, vol. 15 of *SIAM Studies in Applied Mathematics*, SIAM, Philadelphia, Pa, USA, 1994.

Hindawi Publishing Corporation
Mathematical Problems in Engineering
Volume 2010, Article ID 349489, 15 pages
doi:10.1155/2010/349489

Research Article

Influence of Control Valve Delay and Dead Zone on the Stability of a Simple Hydraulic Positioning System

Bálint Magyar,[1] Csaba Hős,[2] and Gábor Stépán[1]

[1] *Department of Applied Mechanics, Budapest University of Technology and Economics, Pf. 91, Budapest 1521, Hungary*
[2] *Department of Hydrodynamic Systems, Budapest University of Technology and Economics, Pf. 91, Budapest 1521, Hungary*

Correspondence should be addressed to Bálint Magyar, mabalint@email.arizona.edu

Received 4 March 2010; Accepted 17 June 2010

Academic Editor: Carlo Cattani

This paper deals with the PI control of a highly simplified dynamic model of a hydraulic cylinder. It is assumed that the hydraulic fluid is incompressible and that the pump provides constant flow rates, which results in the possibility of velocity control. Two types of anomalies are taken into account: (a) the time delay due to the controller computations and the internal pressure dynamics and (b) the dead zone of the controller valve. This results in a nonlinear system are described by a piecewise linear discontinuous map. Nonlinear behavior of the system is explored and the practically globally stable parameter domains are identified.

1. Introduction

Hydraulic systems are widely used in heavy-duty industrial applications, where the exertion of high forces with large stiffness is needed in a robust way. Although there is a considerable effort on developing advanced control strategies (see e.g., [1–4]), PID control still remains the most popular choice. However, it is well known that strong nonlinearities are present in these systems, such as pressure-flow rate relationship, dead zone of the control valves (see e.g., [1]), dry friction [3] or impact dynamics [5]. The discrete sampling time of the closed-loop control introduces additional complexity together with the response lag due to internal (mostly pressure) dynamics. Thus designing and tuning a PID controller of a hydraulic system is a highly challenging task mostly because the conventional ways are based on linear system theory. Moreover, some of the above-mentioned nonlinearities (e.g., dead zone or impact dynamics) cannot be coped with using linearization techniques.

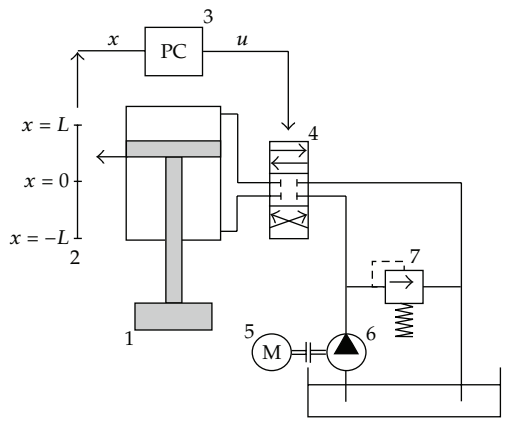

Figure 1: The hydraulic positioning system. 1: hydraulic cylinder, 2: position transducer, 3: PC on which the PI controller is implemented, 4: proportional directional valve, 5: electromotor, 6: gear pump, 7: pressure limiting valve.

The mathematical modelling of these systems often leads to equations with nonsmooth or even discontinuous right-hand side. Fortunately the progress in the theory of non-smooth dynamical systems (see e.g., [6] for an overview) provides a toolbox, albeit it is still far from being general. This is especially true for systems of higher dimensions (three, four, etc.) with several regions of different dynamics. For example, [7] gives a general theory on the existence of periodic and dense orbits for a bilinear one-dimensional map with a slight extension towards two-dimensional maps with delay and backlash. In [8], the authors study the border collision bifurcation in n-dimensional maps with two regions. Chaotic oscillations are also identified in these systems [9]. Based on numerical simulations, [10] describes an example on the effect of delay and backlash together.

This paper studies a highly simplified model of a hydraulic positioning system, which, despite its simplicity (from the engineering point of view) and linearity, poses interesting mathematical problems.

2. Mathematical Model

The subject of our investigation is a digitally controlled hydraulic system that consists of a differential hydraulic cylinder, a proportional directional valve, a linear potentiometer as position transducer, a gear pump, and a PC. The PC provides the PI (proportional-integral) controller. It receives the signal from the position transducer, calculates the error signal, and drives the hydraulic valve; see Figure 1. A typical characteristic of a directional proportional valve is shown in Figure 2.

The mass of the piston is neglected in this study, and the Newtonian dynamics of the system is further simplified by not considering frictional forces at the sealing of the piston rod. Clearly, the latter one has an essential influence on the nonlinear dynamics of the system due to small positive or even negative damping values. When we carry out the investigation with zero damping, we analyze the critical case which already presents an intricate dynamics due to the modeled delay, dead zone, and sampling.

The continuous physical process is sampled in time intervals t_s (sampling time), thus the position of the piston rod $x(t)$ is discretized in time as $x_n = x(nt_s)$. This position is fed into the PC which computes the error signal h. The time needed for this computation is denoted

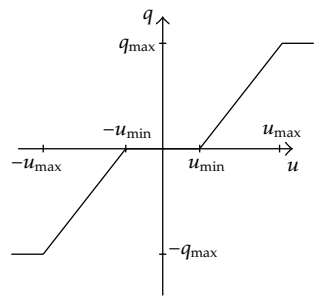

Figure 2: Dead zone in a typical flow rate/control signal characteristics of a directional proportional hydraulic valve. In the interval $(-u_{\min}, u_{\min})$ there is no fluid flow.

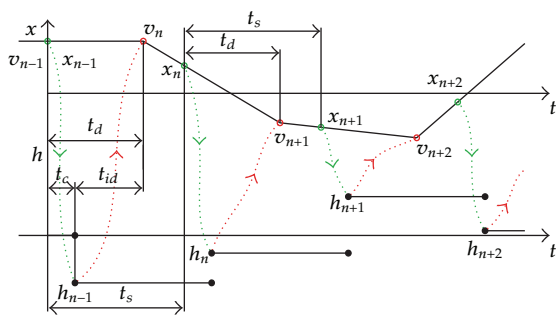

Figure 3: Scheme of the control. Instants signed with green circles represent the sampling; red circles show the moments of velocity actuations. For h_n, see equation (2.2); t_c stands for computational time, t_{id} represents the internal dynamics of the hydraulic system (see text for details), $t_d = t_c + t_{\mathrm{id}}$ is the overall delay, and t_s denotes sampling time.

by t_c. Due to the internal dynamics of the hydraulic system-(notably pressure dynamics), the variation of the velocity of the piston rod follows a second (or even higher) order lag system that is approximated by another delay denoted by t_{id}, with subscript referring to *i*nternal *d*ynamics. Thus, the overall delay between the previous sampling instant and its effect is $t_d = t_c + t_{\mathrm{id}}$. Note that the actual values and ratio of t_c and t_{id} are irrelevant. Since the Newtonian dynamics is neglected, the velocity of the piston is piecewise constant, and it can be discretized in the following way: $v_n(t) \equiv v((n-1)\ t_s + t_d)$, $t \in [(n-1)\ t_s + t_d, n\ t_s + t_d)$, accordingly, subscripts n refer to different time instants for positions and velocities as it is represented in the controlling scheme of Figure 3.

Assume the cases when we have $0 \leq t_d \leq t_s$. Integrating the piecewise constant velocities, we arrive at a relationship between two neighbouring sampled piston rod positions, which can be expressed as

$$x_{n+1} = x_n + v_n t_d + v_{n+1}(t_s - t_d). \tag{2.1}$$

Although this expression is similar to the Euler-discretization of the governing equations, this discrete form is the exact solution of the real physical system controlled digitally. Considering the proportional-integral controller, the error signal h_n is calculated in the following form:

$$h_n = P x_n + I y_n, \tag{2.2}$$

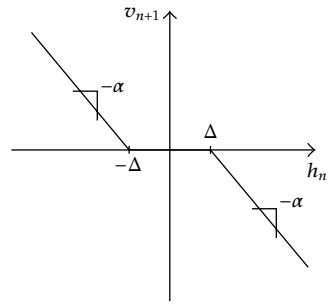

Figure 4: Simplified, saturation-free valve characteristics. In the interval $(-\Delta, \Delta)$ there is no fluid flow.

where P is the proportional gain I is the integral one, and

$$y_n = y_{n-1} + t_s x_{n-1} \tag{2.3}$$

is the discrete integral of the position function. The piston rod velocities v_{n+1} and v_n are calculated from h_n and h_{n-1}, respectively, according to the simplified characteristics of the proportional directional valve. Figure 4 represents this reduced, saturation-free characteristics. The interval of closure is $(-\Delta, \Delta)$ and the slope is characterized by $-\alpha$.

We introduce the dimensionless variables by means of

$$\widehat{x} = \frac{x}{L}, \qquad \widehat{v} = \frac{v}{L}, \qquad \widehat{y} = \frac{y}{L}, \qquad \delta = \frac{\alpha\Delta}{L}, \qquad \widehat{h}_n = \frac{\alpha h_n}{L}, \qquad \widehat{P} = \alpha P, \qquad \widehat{I} = \alpha I \tag{2.4}$$

and by abuse of the notation we drop the hats immediately. According to Figure 4, the velocity is a piecewise function of the error signal. With dimensionless quantities,

$$v_n = \begin{cases} \delta - h_{n-1}, & h_{n-1} > \delta, \\ 0 & \text{if } |h_{n-1}| \le \delta, \\ -\delta - h_{n-1}, & h_{n-1} < -\delta. \end{cases} \tag{2.5}$$

In the subsequent sections, we are going to construct a 4-dimensional linear mapping for the backlash-free system. In the presence of backlash, we derive a piecewise linear mapping which is compiled from 9 linear maps of dimension 4. If one also investigates the case $t_d > t_s$, then similar linear and piecewise linear mappings can be constructed, but their dimensions increase extremely. In order to represent the method in a compact mathematical form, we restrict the description to the basic case $0 \le t_d \le t_s$.

3. Stability Analysis of the Linear System

Eliminating the valve dead zone ($\delta = 0$), a linear valve characteristic means regarding to the piston rod velocity:

$$v_n = -\, h_{n-1}, \tag{3.1}$$

from equation (2.1):

$$x_{n+1} = x_n - h_{n-1}t_d - h_n(t_s - t_d). \tag{3.2}$$

Introducing $\mathbf{z}_n$, that consists of the actual and the previous piston positions, and integral values:

$$\mathbf{z}_n = \begin{pmatrix} x_n & x_{n-1} & y_n & y_{n-1} \end{pmatrix}^T, \tag{3.3}$$

with matrix formalism:

$$\mathbf{z}_{n+1} = \mathbf{A}\mathbf{z}_n, \tag{3.4}$$

$$\begin{pmatrix} x_{n+1} \\ x_n \\ y_{n+1} \\ y_n \end{pmatrix} = \underbrace{\begin{pmatrix} 1 - P(t_s - t_d) & -Pt_d & -I(t_s - t_d) & -It_d \\ 1 & 0 & 0 & 0 \\ t_s & 0 & 1 & 0 \\ 0 & 0 & 1 & 0 \end{pmatrix}}_{\mathbf{A}} \begin{pmatrix} x_n \\ x_{n-1} \\ y_n \\ y_{n-1} \end{pmatrix}. \tag{3.5}$$

The stability of the system depends on the eigenvalues of matrix $\mathbf{A}$, all of the absolute values of the eigenvalues have to be less than 1:

$$\begin{gathered} \det(-\mu\mathbf{I} + \mathbf{A}) = 0, \\ |\mu_i| < 1, \quad i = 1, \ldots, 4. \end{gathered} \tag{3.6}$$

The characteristic polynomial of matrix $\mathbf{A}$ is

$$\mu^4 + (P\ (t_s - t_d) - 2)\mu^3 + \left(1 + 2Pt_d - (P + It_d)t_s + It_s^2\right)\mu^2 + t_d(It_s - P)\mu = 0. \tag{3.7}$$

The polynomial has one root that equals to zero; therefore; it can be divided by $\mu \neq \mu_4 = 0$. Since the stability criteria of polynomials are determining the coefficients of polynomial so

that all of the roots should be on the left side of the complex plain, Moebius transformation has been applied:

$$\mu = \frac{1+\eta}{1-\eta}. \tag{3.8}$$

As a consequence of the transformation, the case of the absolute values of the eigenvalues of matrix $\mathbf{A}$ less than one is equal to the case of the roots of the transformed polynomial on the left side of the complex plain:

$$|\mu_i| < 1, \quad i = 1, \ldots, 4 \quad \Longleftrightarrow \operatorname{Re}(\eta_i) < 0, \quad i = 1, \ldots, 3. \tag{3.9}$$

The transformed characteristic polynomial is

$$a_3\eta^3 + a_2\eta^2 + a_1\eta + a_0 = 0 \tag{3.10}$$

and the coefficients are

$$\begin{aligned} a_3 &= 4 - (t_s - 2t_d)(2P - It_s), \\ a_2 &= 4(1 - Pt_d) + It_s(4t_d - t_s), \\ a_1 &= (2P - I(2t_d + t_s))t_s, \\ a_0 &= It_s^2. \end{aligned} \tag{3.11}$$

According to Routh-Hurwitz stability criterion, all of the polynomial coefficients (3.11) and the determinant of matrix $\mathbf{H}_2$ (3.13) should be positive:

$$\begin{gathered} a_i > 0, \quad i = 0, \ldots, 3, \\ \det(\mathbf{H}_2) > 0, \end{gathered} \tag{3.12}$$

where

$$\mathbf{H}_2 = \begin{pmatrix} a_2 & a_0 \\ a_3 & a_1 \end{pmatrix}. \tag{3.13}$$

Extracting the determinant,

$$a_1a_2 - a_0a_3 > 0. \tag{3.14}$$

Considering $0 < t_d < t_s$, $P > 0$ and $I > 0$, the necessary condition is:

$$0 < t_d\left(P(t_d + t_s) - 2It_st_d^2 - 1\right) - t_s + \sqrt{(Pt_d - 1)^2\left((t_s - t_d)^2 - \frac{4t_dt_s}{Pt_d - 1}\right)}, \tag{3.15}$$

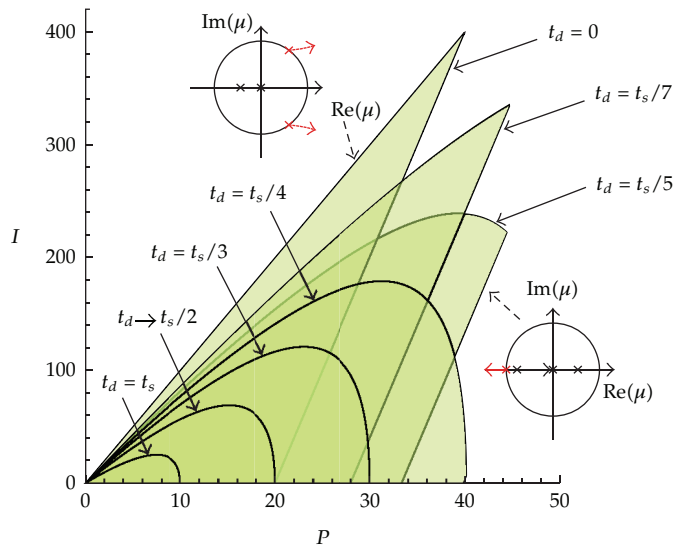

Figure 5: Linear stability chart at sampling time $t_s = 0.1\,\mathrm{s}$ and time delay $t_d = 0$, $t_d = t_s/7$, $t_d = t_s/5$, $t_d = t_s/4$, $t_d = t_s/3$, $t_d \to t_s/2$, $t_d = t_s$.

in addition, one of conditions (3.16)–(3.18) should be also satisfied for the stability:

$$4t_d = t_s, \qquad P < \frac{4(t_s - 3t_d)}{(t_s - 2t_d)^2}, \tag{3.16}$$

or

$$4t_d < t_s, \qquad P < \frac{4(t_s - 3t_d)}{(t_s - 2t_d)^2}, \qquad I < \frac{4 + 2P(2t_d - t_s)}{t_s(t_s - 2t_d)}, \tag{3.17}$$

or

$$4t_d > t_s, \qquad P < \frac{1}{t_d}. \tag{3.18}$$

In the above formulas, the continuous extension is to be used, when $t_d \to t_s/2$. Figure 5 shows parametric stability charts of the linear system at sampling time $t_s = 0.1\,\mathrm{s}$ and for various time delays in the range $t_d \in [0,\ t_s]$. It is easy to prove that the stability boundaries are straight lines when $t_d = 0$. On the left stability boundary, $|\mu_1| < 1$ and $|\mu_{2,3}| = 1$. It can also be shown that only this type of stability boundary exists when $t_d \geq t_s/4$. The rightmost stability boundary for $t_d < t_s/4$ is always a straight line, where $|\mu_1| < 1$, $|\mu_2| < 1$, and $|\mu_3| = 1$. As the system is overdetermined, $\mu_4 \equiv 0$.

4. Dynamics of the Piecewise Linear System

According to equation (2.1), the upcoming value of x_{n+1} depends on the actual v_{n+1} and the previous v_n values of velocities. Considering Equation (2.5), x_{n+1} is the piecewise linear

Table 1: Linear operator selection based on the error signals.

	$h_n > \delta$	$\lvert h_n\rvert \le \delta$	$h_n < -\delta$
$h_{n-1} > \delta$	F_1	F_4	F_7
$\lvert h_{n-1}\rvert \le \delta$	F_2	F_5	F_8
$h_{n-1} < -\delta$	F_3	F_6	F_9

function of two previous error signals h_n and h_{n-1}. Since each past value can fall into 3 cases, our system is described by 9 scalar equations:

$$x_{n+1} = \begin{cases} \begin{cases} x_n + (\delta - h_{n-1})\ t_d + (\delta - h_n)(t_s - t_d), & h_{n-1} > \delta, \\ x_n + (\delta - h_n)(t_s - t_d) & \text{if } \lvert h_{n-1}\rvert \le \delta,\ \ h_n > \delta, \\ x_n + (-\delta - h_{n-1})t_d + (\delta - h_n)(t_s - t_d), & h_{n-1} < -\delta, \end{cases} \\ \begin{cases} x_n + (\delta - h_{n-1})t_d, & h_{n-1} > \delta, \\ x_n & \text{if } \lvert h_{n-1}\rvert \le \delta,\ \ \lvert h_n\rvert \le \delta, \\ x_n + (-\delta - h_{n-1})t_d & h_{n-1} < -\delta, \end{cases} \\ \begin{cases} x_n + (\delta - h_{n-1})\ t_d + (-\delta - h_n)(t_s - t_d), & h_{n-1} > \delta, \\ x_n + (-\delta - h_n)(t_s - t_d) & \text{if } \lvert h_{n-1}\rvert \le \delta,\ \ h_n < -\delta, \\ x_n + (-\delta - h_{n-1})t_d + (-\delta - h_n)(t_s - t_d), & h_{n-1} < -\delta. \end{cases} \end{cases} \tag{4.1}$$

The piecewise system can be written in a compact form, where F_i is a linear operator, that shortens the matrix formalism:

$$\mathbf{z}_{n+1} = \mathbf{A}_{\mathrm{i}}\ \mathbf{z}_n + \mathbf{b}_i = F_i(\mathbf{z}_n), \quad i = 1, \ldots, 9. \tag{4.2}$$

In (4.2), the elements of $\mathbf{A}_i$ matrices and $\mathbf{b}_i$ vectors ($i = 1, \ldots, 9$) can be calculated as the coefficients of scalar equations listed in (4.1). See Appendix (A.1) for details. The appropriate F_i is selected according to the previous two error signals, shown in Table 1.

Extracting h_n according to (2.2), the 3 intervals of h_n result in 3 domains in the x-y plane:

$$\begin{gathered} Px_n + Iy_n < -\delta, \\ -\delta \le Px_n + Iy_n \le \delta, \\ \delta < Px_n + Iy_n, \end{gathered} \tag{4.3}$$

bordered by 2 lines:

$$y = -\frac{P}{I}x \pm \frac{\delta}{I}. \tag{4.4}$$

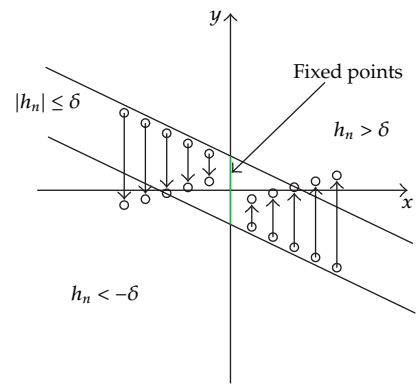

Figure 6: Three domains of the x-y plane, in the middle region the error signal is less then the threshold of the valve, there is no piston motion.

Figure 6 represents the x-y plane with the dead zone in the middle region. In the dead zone, x is constant, meaning that the piston rod is stopped, since the proportional directional valve is closed. Fixed points are on the y axis in the interval of $[-\delta/I, \delta/I]$. This invariant set corresponds to the trivial solution of the backlash-free linear system. From practical viewpoint, we are interested in the stability of the invariant set, since the actual value of y has no importance if we managed to reach the desired $x = 0$ position.

4.1. Periodic Orbits

Numerical simulations were carried out with sampling time $t_s = 0.1$ s, time delay $t_d = 0.04$ s, and dimensionless dead zone $\delta = 12$. By solving the system of algebraic equations shown in (4.8), starting the system from initial condition $\mathbf{z}_2 = (x_2\, x_1\, y_2\, y_1)^T = (1\,1\,1\,1)^T$, one finds that at the values of integral gain $I_{\text{cr}} = 24.982$ and proportional gain $P_{\text{cr}} = 3.5714$, a periodic orbit exists, and the invariant set is stable for $P_{\text{cr}} < P$ stable, and unstable for $P < P_{\text{cr}}$. This behavior is similar to a degenerate Hopf bifurcation, being neither sub- nor supercritical. Figure 7 represents the stable, unstable runs and one periodic orbit from those, which exist in the critical case.

According to the simulation results shown in Figure 8 for different modified dead zone sizes, the periodic orbit remains either periodic or it becomes a quasiperiodic dense orbit.

Figure 9 represents a periodic orbit in a general case. The numbering of the points starts from the first step outside the dead zone region; k is the number of steps in the upper region; j is half of the number of the steps inside the dead zone. Due to being a symmetric system, the examination of the half of the periodic orbit is satisfactory, with the end point subscript $k + j + 2$.

Initial conditions are arbitrarily chosen:

$$\mathbf{z}_2 = \begin{pmatrix} x_2 & x_1 & y_2 & y_1 \end{pmatrix}^T. \tag{4.5}$$

For a symmetric half-orbit, we have

$$\mathbf{z}_{k+j+2} = \begin{pmatrix} -x_2 & -x_1 & -y_2 & -y_1 \end{pmatrix}^T = -\mathbf{z}_2. \tag{4.6}$$

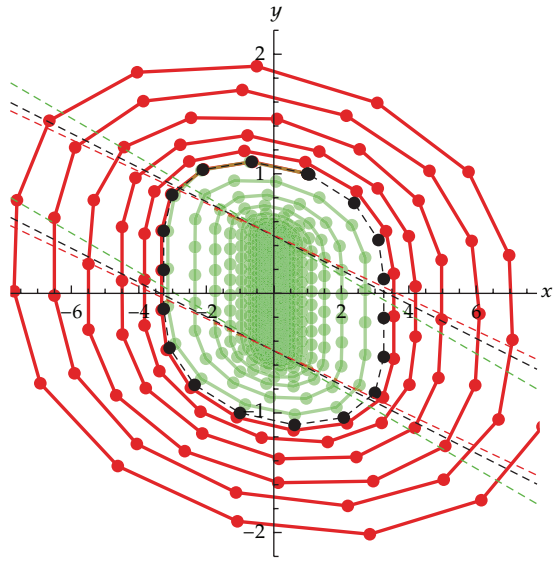

Figure 7: Three simulation results, both with initial conditions $\mathbf{z}_2 = (1\,1\,1\,1)^T$, $t_s = 0.1\,\mathrm{s}$, $t_\mathrm{d} = 0.04\,\mathrm{s}$, $\delta = 12$,and $I_\mathrm{cr} = 24.982$. Periodic orbit occurs at $P_\mathrm{cr} = 3.5714$ (black); the control is stable at $P = 4.1$ (green), unstable at $P = 3.3$ (red).

The first step is from point number 2 to number 3. In this case, both $h_2 > \delta$ and $h_1 > \delta$, therefore operator F_1 is used to calculate point number 3, just as on the next $k-1$ steps. As we reach the dead zone, according to Table 1, F_4 is applied on the border, and then F_5 $j-1$ times. The last step until the half-cycle is made with operator F_8. Therefore, the half-cycle is formed in general:

$$\mathbf{z}_{k+j+2} = F_8(F_5(\cdots(F_5(F_4(F_1(\cdots(F_1(\mathbf{z}_2))))))))) \xrightarrow{\text{def.}} F_8\left(F_5^{(j-1)}\left(F_4\left(F_1^{(k-1)}(\mathbf{z}_2)\right)\right)\right), \tag{4.7}$$

where $F_i^{(k)}$ means applying F_i operator k times. Extracting (4.7),

$$\mathbf{z}_{k+j+2} = -\mathbf{z}_2 = \mathbf{A}_8(\mathbf{A}_5(\cdots(\mathbf{A}_5(\mathbf{A}_4(\mathbf{A}_1(\cdots(\mathbf{A}_1\mathbf{z}_2 + \mathbf{b}_1) + \cdots) + \mathbf{b}_1) + \mathbf{b}_4) + \mathbf{b}_5) + \cdots) + \mathbf{b}_5) + \mathbf{b}_8. \tag{4.8}$$

Using (4.8), one can generate periodic orbits as follows. We fix t_d, t_s, and δ, furthermore, the initial condition x_1, y_1 and the "shape" of the orbit with k and j, then by solving the second and fourth components of (4.8) P and I can be calculated, with which x_2 and y_2 can be easily determined. In Figure 10, three optional periodic orbits are shown.

4.2. Stability of Periodic Orbits

We can reduce equation (4.8) to one single operation, introducing $\tilde{\mathbf{A}}$ and $\tilde{\mathbf{b}}$:

$$\mathbf{z}_{k+j+2} = \tilde{\mathbf{A}}\ \mathbf{z}_2 + \tilde{\mathbf{b}}, \tag{4.9}$$

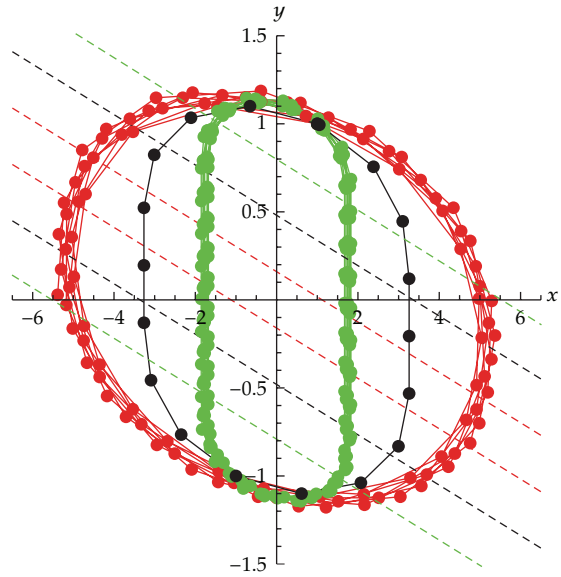

Figure 8: Three simulation results, both with initial conditions $\mathbf{z}_2 = (1\,1\,1\,1)^T$, $t_s = 0.1\,\mathrm{s}$, $t_d = 0.04\,\mathrm{s}$, $I_{\mathrm{cr}} = 24.982$ and $P_{\mathrm{cr}} = 3.5714$. Periodic orbit occurs at $\delta = 12$ (black), dense orbits with increased period length at different dead zone sizes, $\delta = 20$ (green) and $\delta = 4$ (red).

where

$$\begin{aligned}
\tilde{\mathbf{A}} &= \mathbf{A}_8\mathbf{A}_5^{j-1}\mathbf{A}_4\mathbf{A}_1^{k-1},\\
\tilde{\mathbf{b}} &= \mathbf{A}_8\mathbf{A}_5^{j-1}\mathbf{A}_4\mathbf{A}_1^{k-2}\mathbf{b}_1 + \mathbf{A}_8\mathbf{A}_5^{j-1}\mathbf{A}_4\mathbf{A}_1^{k-3}\mathbf{b}_1 + \cdots + \mathbf{A}_8\mathbf{A}_5^{j-1}\mathbf{A}_4\mathbf{b}_1\\
&\quad + \mathbf{A}_8\mathbf{A}_5^{j-1}\mathbf{b}_4 + \mathbf{A}_8\mathbf{A}_5^{j-2}\mathbf{b}_5 + \cdots + \mathbf{A}_8\mathbf{A}_5\mathbf{b}_5 + \mathbf{A}_8\mathbf{b}_5 + \mathbf{b}_8.
\end{aligned} \tag{4.10}$$

The stability of this reduced dynamical system shown in (4.9) depends on the eigenvalues of matrix $\tilde{\mathbf{A}}$. Since δ does not appear explicitly in $\tilde{\mathbf{A}}$, the stability boundary of the invariant set including the desired $x = 0$ position in the system with dead zone coincides with the stability boundary of the linear system with linear valve characteristics derived in Section 3. However, the structure of $\tilde{\mathbf{A}}$ could change if δ is large enough, and this way it can still affect the stability regions.

In the left panel of Figure 11, three pairs of those control parameters (P, I) are denoted at the limit of linear stability, where the periodic orbits exist as presented in Figure 10. Note that their numerical values were calculated with the previously described method (solving (4.8)).

Figure 12 shows the behavior of three periodic or dense orbits for three different values of P represented in the right panel of Figure 11. As it was shown above, the stability of the linear system is preserved by the invariant set including $x = 0$ in the system with dead zone. This means that all orbits will spiral outwards or inwards corresponding to the unstable or stable linear behavior independently whether the orbits are periodic or dense at the critical values of P. In other words, for each combination of the matrices $\mathbf{A}_i$ corresponding to any kinds of orbits, the eigenvalues of $\tilde{\mathbf{A}}$ behave similarly in terms of stability. In the phase space this means that the trajectories inside the dead zone are purely vertical and do not change

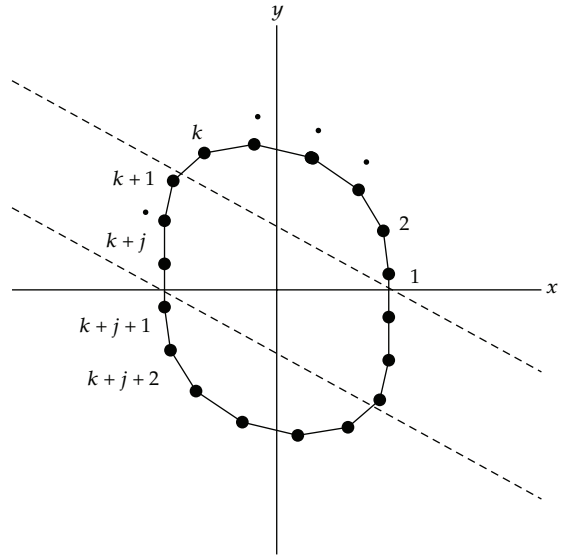

Figure 9: General periodic orbit, k is half of the number of steps outside the middle region, j is half of the number of steps inside the middle region.

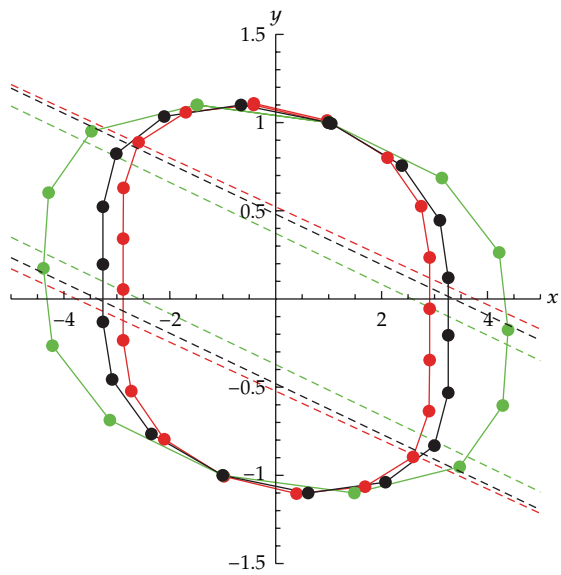

Figure 10: Three optional periodic orbits, both orbits step through $x_n = 1$ and $y_n = 1$, and have $t_s = 0.1$ s sampling time, $t_d = 0.04$ s time delay, and $\delta = 12$ dead zone width. Black colored orbit is produced with $P_{cr} = 3.5714$ and $I = 24.982$, red one is with parameters $P_{cr} = 3.1859$, $I = 22.968$, green one is with parameters $P_{cr} = 4.6586$ and $I = 32.259$.

the value of x—apart from the steps when the trajectory enters and leaves the dead zone. Roughly speaking, the dead zone only "cuts" and "extracts" an already existing orbit. This also explains why the orbits with dead zone behave similarly to the backlash-free case.

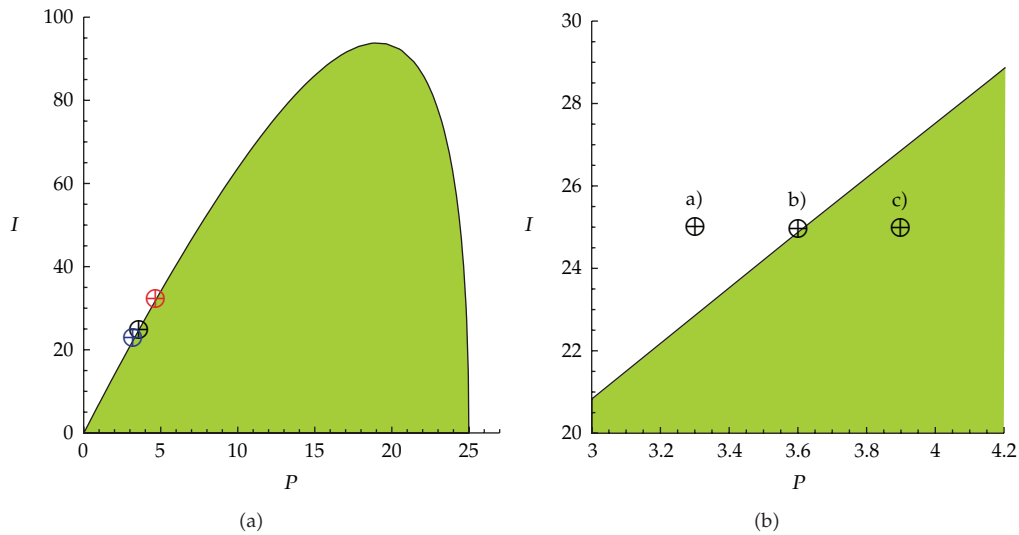

Figure 11: Left: linear stability chart at $t_s = 0.1$ s, $t_d = 0.04$ s. Black colored point shows $P_{cr} = 3.5714$ and $I = 24.982$; blue one shows parameters $P_{cr} = 3.1859$, $I = 22.968$; red one shows parameters $P_{cr} = 4.6586$ and $I = 32.259$, both with $\delta = 12$. Right: one point is picked on the boundary of linear stability, one inside the stable, one in the unstable region: (a) $P = 3.3$, $I = 24.982$, (b) $P = 3.5714$, $I = 24.982$, (c) $P = 3.9$, $I = 24.982$.

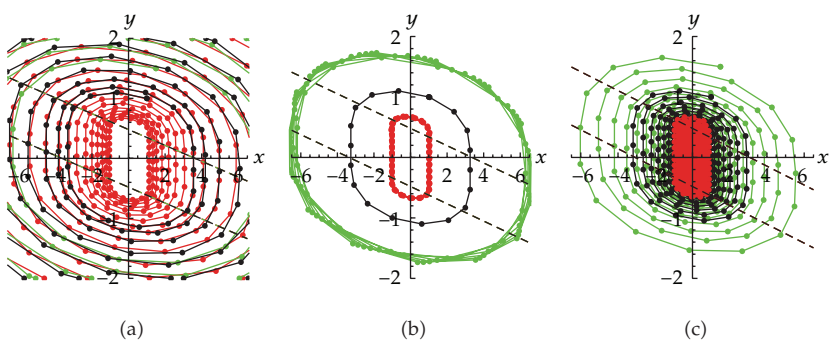

Figure 12: Simulation results with $\delta = 12$ corresponding to the parameters (a), (b), and (c) in Figure 11.

Further investigation is needed to study how these dynamical properties will change with slight perturbation caused by the damping. It is likely that the above structure of periodic and dense orbits will not survive, but some of them may exist either in the linearly stable or unstable domain, depending on whether the damping is slightly positive or negative.

5. Conclusions

In this paper, the PI control of a hydraulic positioning system with cylinder was studied with an emphasis on the interaction of digital sampling, time delay due to finite computational time and internal dynamics, and backlash due to valve characteristics affecting the global dynamics of the controlled system. The stability boundary of the backlash-free system was

computed analytically and represented on the (P, I) control parameter plane. Then, it was shown that the dynamics is described by a piecewise linear system with 9 possible states caused by the presence of backlash. It was shown that both periodic and dense orbits are present in the system when the parameters are tuned to the stability boundary of the backlash-free system.

An analytical method was presented which, for a given sequence of switchings, initial conditions, sampling and delay time, and dead zone width, allows the computation of the corresponding P and I parameters ensuring the existence of a periodic orbit. Moreover, it was shown that as the linear coefficient matrices of the piecewise linear system are independent of the dead zone width, so does the stability of the periodic or dense orbits. In other words, the stability boundary of the linear system provides a practical stability margin for the system with backlash, too.

Appendix

List of $\mathbf{A}_i$ matrices and $\mathbf{b}_i$ vectors.

$$\mathbf{A}_1 = \begin{pmatrix} 1 - P\ (t_s - t_d) & -Pt_d & -I\ (t_s - t_d) & -It_d \\ 1 & 0 & 0 & 0 \\ t_s & 0 & 1 & 0 \\ 0 & 0 & 1 & 0 \end{pmatrix}, \qquad \mathbf{b}_1 = \begin{pmatrix} \delta t_s & 0 & 0 & 0 \end{pmatrix}^T,$$

$$\mathbf{A}_2 = \begin{pmatrix} 1 - P\ (t_s - t_d) & 0 & -I(t_s - t_d) & 0 \\ 1 & 0 & 0 & 0 \\ t_s & 0 & 1 & 0 \\ 0 & 0 & 1 & 0 \end{pmatrix}, \qquad \mathbf{b}_2 = \begin{pmatrix} \delta(t_s - t_d) & 0 & 0 & 0 \end{pmatrix}^T,$$

$$\mathbf{A}_3 = \mathbf{A}_1, \qquad \mathbf{b}_3 = \begin{pmatrix} \delta\ (t_s - 2t_d) & 0 & 0 & 0 \end{pmatrix}^T,$$

$$\mathbf{A}_4 = \begin{pmatrix} 1 & -Pt_d & 0 & -It_d \\ 1 & 0 & 0 & 0 \\ t_s & 0 & 1 & 0 \\ 0 & 0 & 1 & 0 \end{pmatrix}, \qquad \mathbf{b}_4 = \begin{pmatrix} \delta t_d & 0 & 0 & 0 \end{pmatrix}^T, \tag{A.1}$$

$$\mathbf{A}_5 = \begin{pmatrix} 1 & 0 & 0 & 0 \\ 1 & 0 & 0 & 0 \\ t_s & 0 & 1 & 0 \\ 0 & 0 & 1 & 0 \end{pmatrix}, \qquad \mathbf{b}_5 = \mathbf{0},$$

$$\mathbf{A}_6 = \mathbf{A}_4, \qquad \mathbf{b}_6 = -\mathbf{b}_4,$$

$$\mathbf{A}_7 = \mathbf{A}_1, \qquad \mathbf{b}_7 = -\mathbf{b}_3,$$

$$\mathbf{A}_8 = \mathbf{A}_2, \qquad \mathbf{b}_8 = -\mathbf{b}_2,$$

$$\mathbf{A}_9 = \mathbf{A}_1, \qquad \mathbf{b}_9 = -\mathbf{b}_1,$$

References

[1] G. P. Liu and S. Daley, "Optimal-tuning nonlinear PID control of hydraulic systems," *Control Engineering Practice*, vol. 8, no. 9, pp. 1045–1053, 2000.

[2] P.-C. Chen and M.-C. Shih, "An experimental study on the position control of a hydraulic cylinder using a fuzzy logic controller," *JSME International Journal. Series III*, vol. 34, no. 4, pp. 481–489, 1991.

[3] M. A. Avila, A. G. Loukianov, and E. N. Sanchez, "Electro-hydraulic actuator trajectory tracking," in *Proceedings of the American Control Conference (AAC '04)*, pp. 2603–2608, Boston, Mass, USA, July 2004.

[4] M. De Volder, J. Coosemans, R. Puers, and D. Reynaerts, "Characterization and control of a pneumatic microactuator with an integrated inductive position sensor," *Sensors and Actuators A*, vol. 141, no. 1, pp. 192–200, 2008.

[5] G. Licskó, A. R. Champneys, and C. Hős, "Dynamical analysis of a Hydraulic pressure relief valve," in *Proceedings of the World Congress on Engineering*, vol. 2, 2009.

[6] M. di Bernardo, C. J. Budd, A. R. Champneys, and P. Kowalczyk, *Piecewise-Smooth Dynamical Systems: Theory and Applications*, Springer, London, UK, 2008.

[7] L. E. Kollár, G. Stépán, and J. Turi, "Dynamics of piecewise linear discontinuous maps," *International Journal of Bifurcation and Chaos in Applied Sciences and Engineering*, vol. 14, no. 7, pp. 2341–2351, 2004.

[8] P. S. Dutta, B. Routroy, S. Banerjee, and S. S. Alam, "On the existence of low-period orbits in n-dimensional piecewise linear discontinuous maps," *Nonlinear Dynamics*, vol. 53, no. 4, pp. 369–380, 2008.

[9] P. Glendinning and P. Kowalczyk, "Micro-chaotic dynamics due to digital sampling in hybrid systems of Filippov type," *Physica D*, vol. 239, no. 1-2, pp. 58–71, 2010.

[10] L. E. Kollár, G. Stépán, and S. J. Hogan, "Sampling delay and backlash in balancing systems," *Periodica Polytechnica, Mechanical Engineering*, vol. 44, no. 1, pp. 77–84, 2000.

Hindawi Publishing Corporation
Mathematical Problems in Engineering
Volume 2010, Article ID 314172, 21 pages
doi:10.1155/2010/314172

Research Article

Modelling and Quasilinear Control of Compressor Surge and Rotating Stall Vibrations

Ranjan Vepa

School of Engineering and Material Science, Queen Mary, University of London, E14NS London, UK

Correspondence should be addressed to Ranjan Vepa, r.vepa@qmul.ac.uk

Received 25 October 2009; Revised 23 February 2010; Accepted 9 April 2010

Academic Editor: Carlo Cattani

An unsteady nonlinear and extended version of the Moore-Greitzer model is developed to facilitate the synthesis of a quasilinear stall vibration controller. The controller is synthesised in two steps. The first step defines the equilibrium point and ensures that the desired equilibrium point is stable. In the second step, the margin of stability at the equilibrium point is tuned or increased by an appropriate feedback of change in the mass flow rate about the steady mass flow rate at the compressor exit. The relatively simple and systematic non-linear modelling and linear controller synthesis approach adopted in this paper clearly highlights the main features on the controller that is capable of inhibiting compressor surge and rotating stall vibrations. Moreover, the method can be adopted for any axial compressor provided its steady-state compressor and throttle maps are known.

1. Introduction

Compressor surge and rotating stall vibrations place fundamental limitations on aircraft engine performance and remain persistent problems in the development of axial compressor and fan stages. Compressor surge and rotating stall are purely fluid mechanic instabilities, while blade flutter, stall flutter, and surge flutter and their variants are aeroelastic instabilities involving both blade vibrations and fluid motion. Although both rotating stall flutter and rotating stall tend to occur when the blades of a compressor or fan are operating at high-incidence angles and/or speed, and unsteady viscous flow separation plays a key role in both of these phenomena, the various fluttering phenomena are precursors to compressor surge.

Surge is characterized by large amplitude fluctuations of the pressure in unsteady, circumferentially uniform, annulus-averaged mass flow. It is a one-dimensional instability that spreads through the compression system as a whole and culminates in a limit cycle

oscillation in the compressor map. In most situations surge is initiated in a compressor when the compressor mass flow is obstructed and throttled. The frequency of surge oscillations is relatively in a low-frequency band (<25–30 Hz) which could couple with the aeroelastic modes of vibration. The performance of the compressor in surge is characterised by a loss in efficiency leading to high-aeroelastic vibrations in the blade as well as influence the stress levels in the casing. In jet engines, surge can lead to the so-called flame-out of the combustor which could involve reverse flow and chaotic vibrations.

Based on the amplitude of mass flow and pressure fluctuations, surge was classified into four distinct categories: mild surge, classical surge, modified surge, and deep surge by de Jager [1]. This classification is now widely accepted and is used to differentiate between different forms of surge and rotating stall vibrations. During mild surge, the frequency of oscillations is around the Helmholtz frequency associated with the resonance within a cavity, that is, the resonance frequency of the compressor duct and the plenum volume connected to the compressor. This frequency is typically over an order of magnitude smaller than the maximal rotating stall frequency which is normally of the same order as the rotor frequency. Classical surge is a nonlinear phenomenon such as bifurcation and chaos with larger oscillations and at a lower frequency than mild surge, but the mass flow fluctuations remain positive. Modified surge is a mix of both classical surge and rotating stall. Deep surge, which is associated with reverse flow over part of the cycle, is associated with a frequency of oscillation well below the Helmholtz frequency and is induced by transient nonlinear processes within the plenum. Mild surge may be considered as the first stage of a complex nonlinear phenomenon which bifurcates into other types of surge by throttling the flow to compressor to lower mean mass flows. Mild surge is generally a relatively low-frequency phenomenon (≈5–10 Hz) while rotating stall is a relatively higher-frequency phenomenon (≈25–30 Hz).

There are two modes of stable control of a compressor, the first is based on surge avoidance which involves operating the compressor in a instability free domain (Epstein et al. [2], and Gu et al. [3]). Most control systems currently used in industry are based on this control strategy. In this simple strategy, a control point is defined in parameter space with a redefined stability margin from the conditions for instability defined in terms of stall point. This stability margin is defined by (i) typical uncertainties in the location of the stall point, (ii) typical disturbances including load variations, inlet distortions, and combustion noise, and (iii) a consideration of the available sensors and actuators and their limitations. Generally, a bleed valve or another form of bleeding or recycling of the flow is used to negate the effect of throttling the flow. The control is either the valve position or if one employs an on/off approach as in pulse width modulation, the relative full opening times of the bleed valve in a cycle. Such an approach achieves stability at the expense of performance and the approach is not particularly suitable when the flow is compressible. In short, the surge avoidance approach is not performance optimal. There are also problems associated with the detection of instability. The second mode of control involves continuous feedback control of the mass flow by introducing a control valve or an independently controlled fan. This method involves stability augmentation as the changes in the mass flow will effectively change the conditions for instability and thus increase the stability margin. Rather than operating away from the domain of instability, the domain is pushed further away from the operating point. Based on the experiments performed by a number of earlier researchers (see, e.g., Greitzer [4]), a 20% increase in mass flow is deemed achievable by this means of stability augmentation.

Several attempts have been made to incorporate the influence of blade dynamics into model for stall prediction. Compressor surge by itself places a fundamental limitation

on performance. Hence active control methods that tend to suppress the various forms of stall will allow the system to be effectively employed over the parameter space prior to the occurrence of surge. Moreover, it is important to consider the various forms of stall in a holistic and integrated fashion as it would be quite impossible to design individual control systems to eliminate each of the individual instabilities. To this end it is also important to develop a holistic and integrated dynamic model. The model developed by Moore and Greitzer [5] based on the assumptions that the system is incompressible except in a plenum which is assumed to enclose the compressor and turbine stages, and that radial variations are unimportant, represents the compressor surge as a Helmholtz-type hydrodynamic instability. In the original Moore and Greitzer model, an empirical, semiactuator disk representation of the compressor was used, incorporating Hawthorne and Horlock's [6] original actuator disc model of an axial compressor and it served as the basic model incorporating rotating stall. By introducing a semiempirical actuator disk theory into the model, Moore and Greitzer were able to predict rotating stall and surge. The advantage of the Moore and Greitzer model is the analyst ability to incorporate a host of hysteresis models into the compressor characteristics that permit the prediction of a variety of limit cycle response characteristics. Gravdahl and Egeland [7] extended the Moore and Greitzer model by including the spool dynamics and the input torque into the same framework as the original model, thus permitting the inclusion of the control inputs into the dynamics. The models may be derived by the application of finite volume type analysis and may also be extended to the case of rotating stall instability and rotating stall-induced flutter. In the Moore and Greitzer model, the downstream flow field is assumed to be a linearized flow with vorticity, so a solution of a form similar to the upstream solution can be found. The plenum chamber is assumed to be an isentropic compressible chamber in which the flow is negligibly small and perturbations are completely mixed and distributed. Thus the plenum acts merely as a "fluid spring". The throttle is modelled as a simple quasisteady device across which the drop in pressure is only a function of the mass flow rate. Flow variations across the compressor are subject to fluid-inertia lags in both the rotor and the stator, and these lags determine the rotation rate of rotating stall. Stability of rotating stall is determined by the slope of the compressor total-to-static pressure rise map. Greitzer [4] discussed the possibility of the active control of both stall and rotating stall by controlling the relevant Helmholtz cavity resonance frequencies which could be achieved by structural feedback.

Apart from the numerous methods of synthesizing control laws that have been proposed by the application of linear control law synthesis methods, which are only suitable for the guaranteed stabilisation of mild surge, a few nonlinear control law synthesis methods have also been proposed. In order to design an active feedback controller that can control deep surge, an inherently nonlinear surge-control model is essential. A number of nonlinear models have been proposed (Chen et al. [8], Krstic et al. [9], Nayfeh and Abed [10], Paduano et al. [11], and Young et al. [12]), and but almost all of these are oriented towards rotating stall control synthesis and include the dynamics of the amplitude of the leading circumferential mode. Many of these models (Gu et al. [13] and Hõs et al. [14]) have been employed to perform a bifurcation analysis to explore the behaviour of the postinstability dynamics.

In this paper, an unsteady nonlinear and extended version of the Moore-Greitzer model is developed to facilitate the synthesis of a surge and stall controller. The motivation is the need for a comprehensive and yet low-order model to describe the various forms of stall as well as the need to independently represent the transient disturbance and control inputs in the compressor pressure rise dynamics. Furthermore, the extended version of the Moore-Greitzer model is developed by reducing the number of independent model parameters to a

minimum. Our preliminary studies indicate that model can effectively capture the dynamics of the phenomenon of compressor surge and that its poststall instability behaviour is a well representative of the observed behaviours in real axial flow compressors. The controller is synthesised in two steps. In the first step, the desired equilibrium throttle position and the desired equilibrium value of the ratio of the nondimensional pressure rise at minimum flow to a quarter of the peak to peak variation of the pressure fluctuation at the compressor exit are established. This defines the equilibrium point and ensures that the desired equilibrium point is stable. In the second step, the margin of stability at the equilibrium point is tuned or increased by an appropriate feedback of change in the mass flow rate about the steady mass flow rate at the compressor exit. The first step may be considered to be an equilibrium point controller while the second corresponds to stability augmentation. Such a two-step process then ensures that both the desired equilibrium solution is reachable and that any perturbations about the equilibrium point are sufficiently stable.

2. Fundamental Model Equations

The unsteady and steady fluid mechanics of the flow upstream and downstream of the compressor is considered while the viscous effects are limited to within the actuator disc of the compressor which allows one to define nondimensional total to static pressure rise map. Compressibility is assumed to be confined to the plenum chamber downstream of the compressor where the compression is assumed to be uniform and isentropic. The throttle map sets the mass flow through the system and is a function of the plenum pressure and the throttle opening. It is essential in defining the flow characteristics of the compressor. The rate of change of the plenum pressure is determined from the one-dimensional continuity conditions and is a function of difference in the compressor flow averaged over the face of the compressor and the throttle flow. The second equation is defined by the one-dimensional rate of change of momentum which relates to the dynamic pressure. Two other equations complete the definition of the complete dynamics of the Moore-Greitzer model; the first relates to the rate of change of the throttle flow and the second defines the compressor dynamics and is based on an unsteady adaptation of the actuator disc model. These equations were first proposed by Greitzer [15] in 1976.

The dimensionless compressor mass flow is assumed to be ϕ_c and ψ is the dimensionless plenum pressure rise. Furthermore, $\Psi_{c,ss}$ is the dimensionless steady-state compressor pressure rise given in the compressor map, whereas Ψ_c is the dimensionless dynamic compressor pressure rise. The dimensionless throttle mass flow is ϕ_t and dimensionless pressure drop across the throttle is Ψ_t

$$\begin{aligned}
\frac{1}{B}\frac{d}{d\tau}\phi_c &= \Psi_c - \psi, \\
\frac{G}{B}\frac{d}{d\tau}\phi_t &= \psi - \Psi_t, \\
B\frac{d}{d\tau}\psi &= \phi_c - \phi_t, \\
\tau_c\frac{d}{d\tau}\Psi_c &= \Psi_{c,ss} - \Psi_c,
\end{aligned} \tag{2.1}$$

where $\phi_c = \dot{m}_c/(\rho_a A_c U_t)$, $\phi_t = \dot{m}_t/(\rho_a A_c U_t)$, $\Psi_c = 2\Delta p_c/(\rho_a U_t^2)$, $\Psi_t = 2\Delta p_t/(\rho_a U_t^2)$, B is the Greitzer parameter given by $B = U_t/2\omega_H L_c$, $\omega_H = a\sqrt{A_c/(V_p L_c)}$ is the Helmholtz cavity resonance frequency for the plenum, τ is the non-dimensional time defined in terms of the Helmholtz frequency and the time t, in seconds as, $\tau = \omega_H t$, G is the geometry ratio parameter of the throttle duct and control volume given by $G = (L_t/A_t)/(L_c/A_c)$, and τ_c is the time constant of the compression system that would be different for stall and for rotating stall. In the preceding definitions of the model parameters, $\dot{m}_c$ is the mass flow rate through the compressor, $\dot{m}_t$ is the mass flow rate through the throttle, Δp_c is the pressure rise across the compressor, Δp_t is the pressure drop across the throttle, ρ_a is the ambient air density, a is the speed of sound corresponding to ambient conditions, A_c is the cross-sectional area of the control volume, L_c is the length of the control volume, A_t is the cross-sectional area of the throttle duct, L_t is the length of the throttle duct, V_p is the volume of the plenum chamber, and U_t is the rotor tip speed.

The compressor map in steady flow is a plot of the non-dimensional pressure with the non-dimensional mass flow rate through the compressor for each rotation speed. However, the plots are self-similar and can be reduced to single plot by scaling the non-dimensional mass flow rate and the non-dimensional dynamic pressure rise. The compressor surge line is obtained simply by linking the maximum point on each compressor characteristic for a particular rotational speed. Representing the compressor characteristics in a non-dimensional manner for each rotation speed and appropriately scaling the axes simply reduces the "surge line" to a single point which is the maximum point on the characteristic. Following, Hõs et al. [14], the scaled compressor map in steady flow when $\phi_c = \phi_{cs}$ is assumed to be

$$\Psi_{c,ss}(\phi_{cs}) = \Psi_{c0} + \frac{H}{2}\left(2 + 3\left(\frac{\phi_{cs}}{F} - 1\right) - \left(\frac{\phi_{cs}}{F} - 1\right)^3\right). \tag{2.2}$$

In (2.2), H defines half the peak-to-peak variation of the pressure fluctuation at the compressor exit or the amplitude of the pressure fluctuation while F is half the change in the steady mass flow rate, ϕ_{cs} is required for the pressure to change from the minimum to the maximum. The definitions of the parameters H and F are illustrated in Figure 1.

The throttle map in steady flow when $\phi_t = \phi_{ts}$ is taken to be

$$\Psi_{t,ss} = \left(\frac{\phi_{ts}}{C_t \gamma}\right)^2, \tag{2.3}$$

where the dimensionless throttle parameter C_t is a coefficient defining the capacity of the fully opened throttle and γ is the dimensionless throttle position.

Following Gravdahl and Egeland [7], the input torque to the compressor may be included and the dynamics of the spool as another state equation is given by

$$I\left(\frac{d\omega}{dt}\right) = T_{\text{ext}} - T_c, \tag{2.4}$$

where I is the mass moment of inertia of the compressor rotor, ω the angular velocity which may be expressed in terms of the Greitzer parameter and tip radius as $\omega = U_t/R_t = 2\omega_H L_c B/R_t$, T_{ext} is the external torque input, and T_c is the torque necessary to drive the

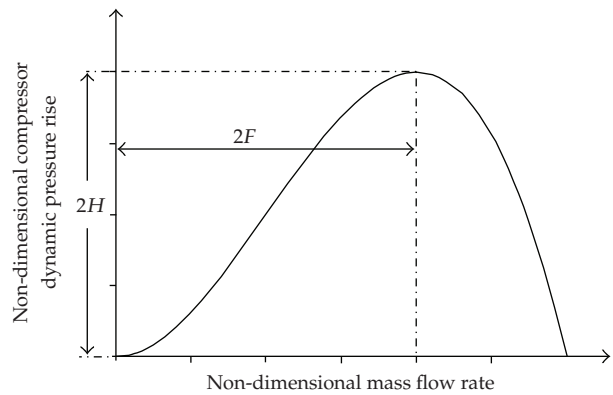

Figure 1: Definitions of the compressor characteristic parameters H and F.

compressor which may be expressed in terms of the slip ratio σ, as $T_c = \rho_a A_c U_t^2 R_t \phi_c \sigma$. The slip ratio σ can be defined as the ratio of the tangential velocity of the fluid at the compressor exit guide vanes and the tip speed. The external torque may be expressed in a non-dimensional form as, $\Gamma_{\text{ext}} = T_{\text{ext}}/\rho_a A_c U_t^2 R_t$. Hence (2.4) may be expressed in a non-dimensional form as

$$\frac{dB}{d\tau} = \frac{B^2(\Gamma_{\text{ext}} - \phi_c \sigma)}{\mu}, \tag{2.5}$$

where $\mu = I/2\rho_a R_t^2 A_c L_c$ is the non-dimensional inertia parameter, and Γ_{ext} is the non-dimensional torque input.

In this analysis all controls are initially assumed to be fixed as the uncontrolled dynamics is considered first. For this reason, any bleed valve that may have been included is closed and all control pressure perturbations are assumed to be equal to zero.

3. Steady Flow Analysis

Assuming the conditions of steady flow, the equations are

$$\frac{1}{B}\frac{d}{d\tau}\phi_c = \Psi_c - \psi = 0, \tag{3.1a}$$

$$\frac{G}{B}\frac{d}{d\tau}\phi_t = \psi - \Psi_t = 0, \tag{3.1b}$$

$$B\frac{d}{d\tau}\psi = \phi_c - \phi_t = 0, \tag{3.1c}$$

$$\tau_c \frac{d}{d\tau}\Psi_c = \Psi_{c,ss} - \Psi_c = 0, \tag{3.1d}$$

$$\frac{dB}{d\tau} = \frac{B^2}{\mu}(\Gamma_{\text{ext}} - \phi_c \sigma) = 0. \tag{3.1e}$$

From the third of the above equations, (3.1c), in steady flow, let

$$\phi_{cs} = \phi_{ts} = \phi_{s0}. \tag{3.2}$$

The steady flow conditions are obtained from the first two of the above equations, (3.1a) and (3.1b), and are given by $\Psi_{c,ss} = \Psi_{t,ss}$; that is,

$$\Psi_{c,ss}(\phi_{s0}) = \Psi_{c0} + \frac{H}{2}\left(2 + 3\left(\frac{\phi_{s0}}{F} - 1\right) - \left(\frac{\phi_{s0}}{F} - 1\right)^3\right) = \left(\frac{\phi_{s0}}{C_t\gamma}\right)^2. \tag{3.3}$$

A parameter p is defined as

$$p = \left(\frac{2}{H}\right)\left(\frac{F}{C_t\gamma_n}\right)^2, \tag{3.4}$$

where p is the throttle non-dimensional pressure rise at minimum flow and a parameter p_0

$$p_0 = \frac{2}{H}\Psi_{c0} + 2 \tag{3.5}$$

which is the ratio of the non-dimensional pressure rise at minimum flow to a quarter of the peak-to-peak variation of the pressure fluctuation at the compressor exit, then (3.3) reduces to

$$\Psi_{c,ss}(\phi_{s0}) = \frac{H}{2}\left(p_0 + 3x - x^3\right) = p\frac{H}{2}(1 + x)^2, \tag{3.6a}$$

where the variable x is

$$x = \left(\frac{\phi_{s0}}{F}\right) - 1. \tag{3.6b}$$

If one assumes that with the minimum flow through the compressor and the throttle, the flow is always steady, then with $\phi_{s0}/F = 1$, one obtains from (3.4),

$$p_0 = p. \tag{3.7}$$

Assuming that the position of the throttle γ is set to a nominal value $\gamma = \gamma_n$ when (3.6a)-(3.6b), and (3.7) are satisfied, (3.6a)-(3.6b) may be rearranged and written as

$$\Psi_{c0} = \frac{H}{2}(p - 2). \tag{3.8}$$

Eliminating Ψ_{c0}, the steady flow characteristic may be defined entirely in terms of the compressor and throttle map parameters, H, F and the product $\gamma_n C_t$ and is

$$3x - x^3 = px(x+2), \tag{3.9}$$

and (3.8) may be expressed as

$$x\left(x^2 + px + 2p - 3\right) = 0. \tag{3.10}$$

From the first factor of (3.10) the assumed solution, $\phi_{s0}/F = 1$, is recovered. Assuming $x \neq 0$ and solving for p

$$p = \frac{\left(3 - (\phi_{s0}/F - 1)^2\right)}{(\phi_{s0}/F + 1)}. \tag{3.11}$$

If one assumes that with the flow through the compressor and the throttle either minimum or below minimum, it is always steady, then $x = x_0$. Then it follows that,

$$\frac{H}{2}\left(p_0 + 3x_0 - x_0^3\right) = p\frac{H}{2}(1 + x_0)^2. \tag{3.12}$$

Eliminating p_0, one obtains

$$\left(3(x - x_0) - \left(x^3 - x_0^3\right)\right) = 2p(x - x_0) + p\left(x^2 - x_0^2\right). \tag{3.13}$$

Solving for p, one obtains

$$p = \frac{(3 - (x^2 + xx_0 + x_0^2))}{(x + x_0 + 2)}. \tag{3.14}$$

When $x_0 = 0$, (3.14) reduces to (3.11).

4. Unsteady NonLinear Extended Moore-Greitzer Model

Rather than combining the quasisteady and transient components of compressor pressure rise, the independent contributions from these two components of the pressure rise are separately identified. If one defines $\Delta\Psi_c = \Psi_c - \Psi_{c,qs}$ as the transient disturbance and control

pressure component of the compressor pressure rise, the first three unsteady equations may be expressed as

$$\frac{d\phi_c}{Bd\tau} = \Psi_{c,qs} - \psi + \Delta\Psi_c, \tag{4.1a}$$

$$\frac{Gd\phi_t}{Bd\tau} = \psi - \Psi_{t,qs}, \tag{4.1b}$$

$$\frac{Bd\psi}{d\tau} = \phi_c - \phi_t. \tag{4.1c}$$

The compressor transient disturbance and control dynamics, in the absence of a control pressure input, is defined entirely in terms of $\Delta\Psi_c$ as

$$\frac{\tau_c d\Delta\Psi_c}{d\tau} = -\Delta\Psi_c + \Psi_{c,ss} - \Psi_{c,qs}, \tag{4.2}$$

where the unsteady compressor characteristics, $\Psi_{c,qs}$, and the unsteady throttle map, $\Psi_{t,qs}$, are assumed to satisfy the quasisteady model equations given by

$$\Psi_{c,qs}(\phi_c) = \Psi_{c0} + \frac{H}{2}\left(2 + 3\left(\frac{\phi_c}{F} - 1\right) - \left(\frac{\phi_c}{F} - 1\right)^3\right), \tag{4.3a}$$

$$\Psi_{c0} = \frac{H}{2}(p-2), \qquad \Psi_{t,qs} = \left(\frac{\phi_t}{C_t\gamma}\right)^2. \tag{4.3b}$$

Furthermore

$$\Psi_{c,ss}(\phi_{s0}) = \frac{H}{2}\left(p + 3\left(\frac{\phi_{s0}}{F} - 1\right) - \left(\frac{\phi_{s0}}{F} - 1\right)^3\right). \tag{4.4}$$

Further from the definition of the parameter, p, one may write

$$C_t^2\gamma_n^2 = \frac{2F^2}{pH}. \tag{4.5}$$

In (4.5) one considers the throttle's non-dimensional nominal position, $\gamma = \gamma_n$, to be fixed and any perturbations to it must be considered as a deviation. If $\Delta\gamma$ is the deviation of the throttle position from the nominal position, $\gamma = \gamma_n$, then in the general case (4.5) may be written as

$$C_t^2\gamma^2 = \left(\sqrt{\frac{2F^2}{pH}} + C_t\Delta\gamma\right)^2. \tag{4.6}$$

Considering the last equation for the dynamics of the compressor spool, one assumes that that the non-dimensional torque input, Γ_{ext}, is provided by a non-dimensional power input and can be defined by $\Gamma_{\text{ext}} = \Pi_{\text{ext}}/B$. The equation for the spool dynamics is

$$\frac{dB}{d\tau} = \frac{B}{\mu}\left(\Pi_{\text{ext}} - B\phi_c\sigma\right), \tag{4.7}$$

where the non-dimensional power input is related to the real power, P_{ext}, by the equation

$$\Pi_{\text{ext}} = \frac{P_{\text{ext}}}{2\rho_a U_t^2} A_c \omega_H L_c. \tag{4.8}$$

In most practical situations involving jet engines, it is power that is delivered to a turbine driving the compressor by a combustor and this can be modelled independently.

Using (3.14) to (4.7), the complete unsteady nonlinear equations not including the control inputs may be expressed in terms of the five states ϕ_c, ϕ_t, ψ, $\Delta\Psi_c$, and B, as

$$\begin{aligned}
\frac{d\phi_c}{d\tau} &= B\Psi_{c,qs} + B\left(\Delta\Psi_c - \psi\right),\\
\frac{d}{d\tau}\phi_t &= -\frac{B}{G}\frac{\phi_t^2}{\left(\sqrt{2F^2/pH} + C_t\Delta\gamma\right)^2} + \frac{B\psi}{G},\\
\frac{d}{d\tau}\psi &= \frac{\left(\phi_c - \phi_t\right)}{B},\\
\frac{d\Delta\Psi_c}{d\tau} + \frac{\Delta\Psi_c}{\tau_c} &= \frac{\left(\Psi_{c,ss} - \Psi_{c,qs}\right)}{\tau_c},\\
\frac{dB}{d\tau} &= \frac{B}{\mu}\left(\Pi_{\text{ext}} - B\phi_c\sigma\right)
\end{aligned} \tag{4.9}$$

with

$$p = \frac{\left(3 - \left(\phi_{s0}/F - 1\right)^2\right)}{\left(\phi_{s0}/F + 1\right)}. \tag{4.10}$$

The eight model parameters are $\phi_{s0}/F, H, G, \tau_c, F, C_t\Delta\gamma, \mu$, and σ. The input to the model is defined by Π_{ext}, the non-dimensional power input to the compressor.

5. Application to Rotating Stall Vibrations

Equations (4.9) describe surge in our one-dimensional model but do not include rotating stall. The extension needed is derived and explained in detail by Moore and Greitzer [5] by Galerkin projection, and only the essence of the method is presented here. The Galerkin projection procedure represents the reduction of the differential equation by a set of basic or

coordinate functions to capture the behaviour in the circumferential direction with a finite set of modes. One-mode truncation via Galerkin projection results in an additional equation in terms of a new variable J that must be included with (4.9). The square of the new variable J represents the amplitude of the first Galerkin mode. Following Hõs et al. [14], the dynamics of J is described by

$$\tau_J \frac{dJ}{d\tau} = \frac{H}{F} J \left(1 - \left(\frac{\phi_c}{F} - 1 \right)^2 - \frac{1}{4} J \right), \tag{5.1}$$

where the time constant τ_J is related to the time constant of an N-stage compressor τ_c and the slope of the compressor duct flow parameter m, by the relations

$$\tau_J = \frac{\omega_H R(1 + ma)}{3aU_t}, \qquad \text{with } a = \frac{R}{\tau_c U_t}. \tag{5.2}$$

The presence of rotating stall influences the compressor characteristic (2.3), and following Hõs et al. [14], it is modified as

$$\Psi_{c,ss}(\phi_{cs}) = \Psi_{c0} + \frac{H}{2} \left(2 + 3 \left(\frac{\phi_{cs}}{F} - 1 \right) \left(1 - \frac{J}{2} \right) - \left(\frac{\phi_{cs}}{F} - 1 \right)^3 \right). \tag{5.3}$$

Conditions for steady flow now require additionally that either $J = J_s = 0$, corresponding to an equilibrium with no rotating stall disturbance, or $J = J_s = 4(1 - x^2)$, corresponding to an equilibrium with a rotating stall disturbance. Since J represents the amplitude of rotating stall amplitude, to avoid rotating stall J must tend to zero. If it tends to any other finite value the rotating stall amplitude is nonzero, implying that rotating stall exists. In the case when the rotating stall amplitude is nonzero, (3.4) and (3.5) are unchanged but (3.10) and (3.11) are, respectively, modified, in case J is given by the latter non-zero equilibrium point as

$$\begin{gathered} 5x^2 - xp - 3 - 2p = 0, \\ p = \frac{\left(5(\phi_{s0}/F - 1)^2 - 3\right)}{(\phi_{s0}/F + 1)}, \end{gathered} \tag{5.4}$$

where the definition of the parameter p is unchanged. In the model, it should be noted that the Greitzer parameter B is no longer a parameter but a slowly varying state. In this respect, our analysis is different from that of Moore and Greitzer [5] who treated it as a parameter and stated the conditions for surge in terms of this parameter. For control applications, particularly when the external control input is due to a control torque, it is most appropriate to allow the Greitzer parameter B to vary. However, when the Greitzer parameter B is assumed to be variable, it is essential that both the compressor steady characteristic parameters, H and F, are not constant but functions of B. Based on a set of typical characteristics, the parameters, H and F, are assumed to be linear functions of the Greitzer parameter B and given by

$$H = H_0 + H_B B, \qquad F = F_B B, \tag{5.5a}$$

where H_0, H_B, and F_B are assumed to be constants. Thus in steady state, when $B = B_0$, H and F are given by

$$H_s = H_0 + H_B B_0, \qquad F_s = F_B B_0. \tag{5.5b}$$

If one defines the change in J by $\Delta J = J - J_s$ in the unsteady case, (4.9) are now modified as

$$\frac{d\phi_c}{d\tau} = B\Psi_{c,qs} + B(\Delta\Psi_c - \psi), \tag{5.6a}$$

$$\frac{d}{d\tau}\phi_t = -\frac{B}{G}\frac{\phi_t^2}{\left(\sqrt{2F^2/pH} + C_t\Delta\gamma\right)^2} + \frac{B\psi}{G}, \tag{5.6b}$$

$$\frac{d}{d\tau}\psi = \frac{(\phi_c - \phi_t)}{B}, \tag{5.6c}$$

$$\frac{d\Delta\Psi_c}{d\tau} + \frac{\Delta\Psi_c}{\tau_c} = \frac{(\Psi_{c,ss} - \Psi_{c,qs})}{\tau_c}, \tag{5.6d}$$

$$\frac{dB}{d\tau} = \frac{B}{\mu}(\Pi_{\text{ext}} - B\phi_c\sigma), \tag{5.6e}$$

$$\tau_J\frac{d\Delta J}{d\tau} = \frac{H}{F}(J_s + \Delta J)\left(1 - \left(\frac{\phi_c}{F} - 1\right)^2 - \frac{1}{4}(J_s + \Delta J)\right) \tag{5.6f}$$

with

$$J_s = 0 \tag{5.7}$$

or

$$J_s = 4\left(\left(1 - \left(\frac{\phi_{s0}}{F}\right) - 1\right)^2\right), \tag{5.8}$$

where the parameter F is evaluated under steady conditions. Only the former is used and it also required the equilibrium point to be stable. Moreover, there is now an additional parameter τ_J, which may be related to τ_c as

$$\tau_J = \frac{\tau_c\omega_H(1 + mR\tau_c/U_t)}{3}, \tag{5.9}$$

but will be treated as an independent parameter. Equations (5.6a)–(5.6f) represent a six-state dynamic model of the dynamics of the compressor system.

Table 1: Typical parameter and initial state values for simulation.

Parameter	Primary value	State/input	Initial value
ϕ_{s0}	0.375	ϕ_c	0.4
F_B	0.625	ϕ_t	0.3
H_0	0.06	ψ	0.0
H_B	0.3	$\Delta\Psi_c$	1.0
G	2	B	0.4
σ	0.9	ΔJ	3.1 or 0.1
$C_t\Delta\gamma$	0.0	J_s	0
μ	40	Π_{ext}	0.17
τ_c	0.05	τ_J	0.5

6. Model Response and Instability

Although our primary interest is in establishing a nonlinear model for synthesizing an active surge controller, one needs to understand the dynamic response of the uncontrolled model not only in the vicinity of the domain of instability but also in the postinstability domains in the parameter space. For this reason, the dynamic response of the model proposed in the preceding section is considered, without including any controls which could include a bleed valve or a feedback controller that influences the transient dynamics of the compressor. The rotating stall dynamics is ignored in the first instance.

Table 1 lists the nominal typical values of the parameters, initial values of the states, and the inputs used in the simulation of the dynamic response, for which the system was stable. The parameter p is not shown in Table 1 as it is computed from the parameters in the table. It is however an important parameter as a high value represents greater levels of throttling and a reduced mass flow rate through the throttle. The system was not unstable unless either H was negative or $\gamma < \gamma_n$. A typical example of a stable response is shown in Figure 2.

The first case considered was with $C_t\Delta\gamma = 0$. In this case, no chaotic behaviour was observed although both stable and unstable behaviours were observed. When the compressor was stable, the behaviour was always lightly damped and oscillatory. Choosing the parameter $\gamma = \gamma_n$ represents a case of tuning or matching the throttle to the compressor. In most cases the instability could be eliminated by proper tuning of the parameters and no active stabilisation was deemed necessary.

When H is locally negative, it corresponds to the case of negative slope in the characteristic that was considered by Hõs et al. [14]. When H is negative and the parameter, $\gamma > \gamma_n$, the throttle mass flow is not matched to the compressor mass flow. Although the system was unstable, no chaos was observed. When H is negative and $\gamma < \gamma_n$, there was a clear incidence of chaos in the flow through the compressor, which was identified by a one-dimensional Poincaré map. The chaotic response with a negative H is significant as it represents the case of flame-out in jet-engines. However, this case is not of much practical importance for controller synthesis as the compressor becomes unstable before it becomes chaotic.

The responses of B and J, when H is negative and $\gamma > \gamma_n$ in the rotating stall case, are illustrated in Figure 3. Apparently the Greitzer "parameter" is itself stable in this case but the sustained response in J away from the trivial equilibrium solution ($J = 0$) represents the presence of rotating stall disturbances.

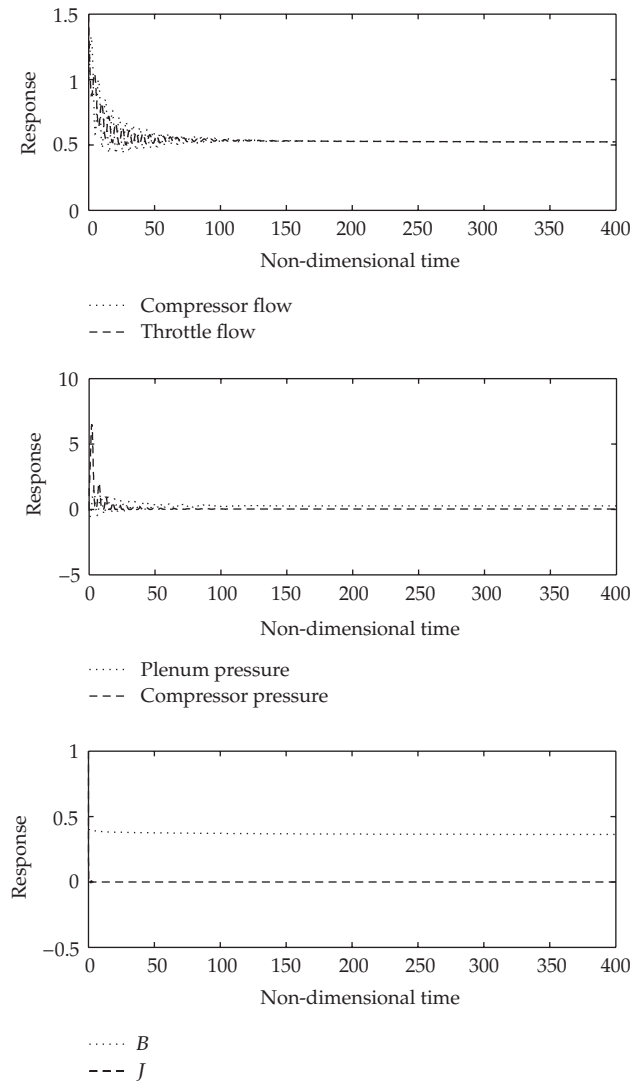

Figure 2: Stable responses of states to disturbance, for the nominal typical values of the parameters.

Considering the case of rotating stall with H positive and $C_t \Delta\gamma = 0$, the system always exhibited stability in the sense that the response converged to a steady state. With $\gamma \neq \gamma_n$ or $\gamma = \gamma_n$, H positive, and $\phi_{s0}/F < 2$, the equilibrium solution jumps from one with $J_s = 0$ to one with $J_s = 1$ and this is followed by the pressure in the plenum chamber falling to zero. The state responses in this case are illustrated in Figure 4(a). The corresponding unsteady compressor map and the operating point on the map are shown in Figure 4(b).

Although, when the compressor flow and throttle flow were matched, that is, with $\gamma = \gamma_n$, the system is stable; it is also important to maintain J at zero, as it represents the amplitude of the rotating stall disturbance amplitude. It can be concluded that open-loop stability is not enough to drive the operating point to $\gamma = \gamma_n$ and also suppress rotating stall disturbances, by using a controller such as an automatically controlled bleed valve. The bleed valve by itself is not always adequate to maintain J at zero and additional feedback is essential

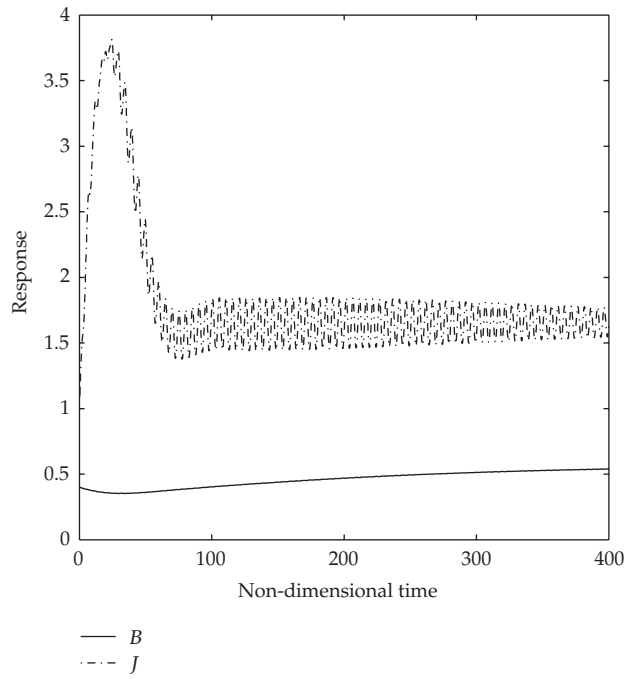

Figure 3: Typical responses of B and J when H is negative and $\gamma < \gamma_n$ in the rotating stall case.

to suppress the rotating stall disturbance by changing the operating equilibrium point. Some authors (Gu et al. [13]) have referred to this requirement as "bifurcation control".

7. Control Law for Throttle Setting

To design the throttle controller, one rewrites (5.6b) as

$$\frac{d}{d\tau}\phi_t = -\frac{B}{G}\frac{\phi_t^2}{\left(\sqrt{2F^2/p_d H} + C_t\Delta\gamma\right)^2} + \frac{B\psi}{G}, \tag{7.1}$$

where p_d is the desired set value for p. The first step in designing a controller is to choose an appropriate value for p_d. The next step is to gradually wash out $\Delta\gamma$ according to some dynamic law such as

$$\tau_u \frac{d\Delta\gamma}{d\tau} = -\Delta\gamma, \tag{7.2}$$

where τ_u is an appropriate time constant so the washout does not interfere with the plant dynamics.

If one further chooses $x > 1$, the equilibrium with $J = J_s = 0$ is stable. To establish the controller parameter p_d, a suitable choice may be made by first choosing x_0 and the operating point x and using (3.14). A typical choice could be $x_0 = 0$ and $x > 1$ giving a value for

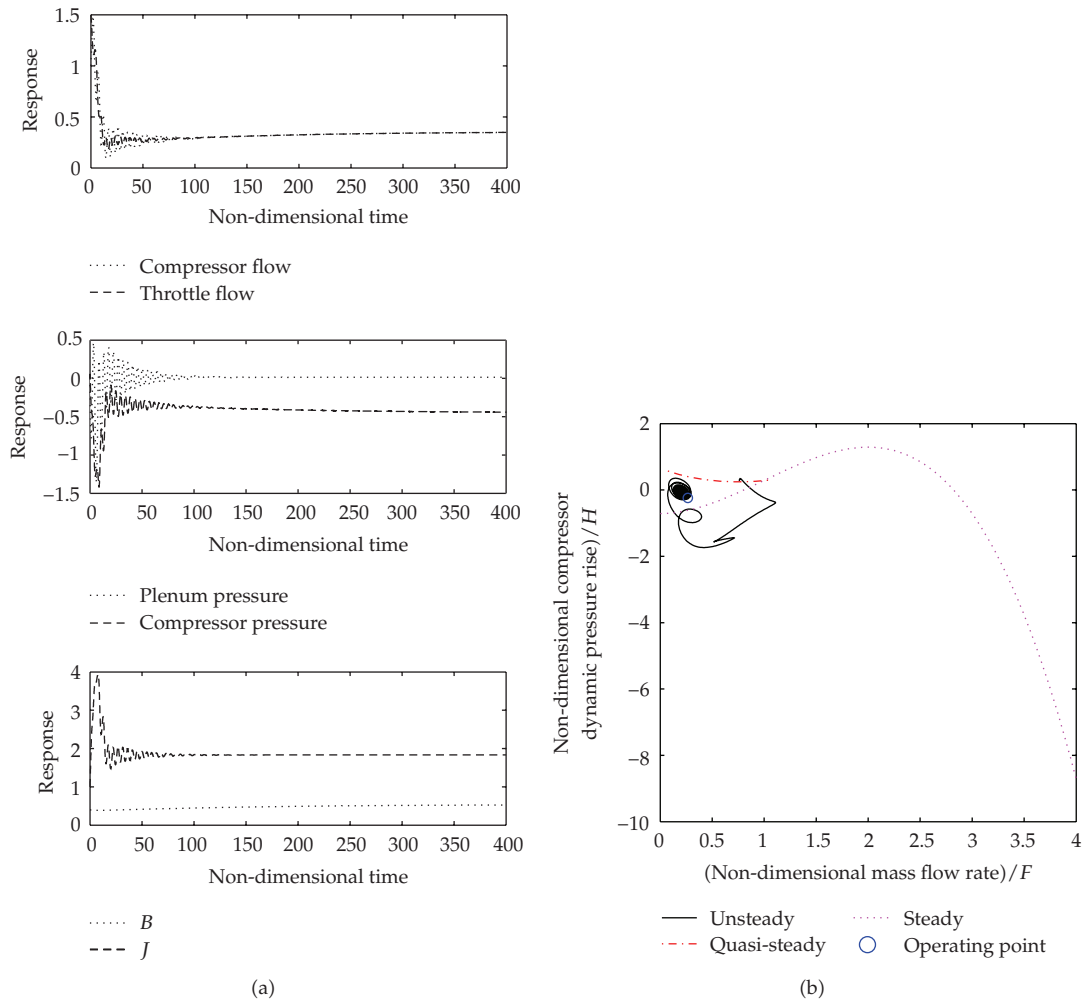

Figure 4: (a) Typical open-loop state responses when H is positive and $\phi_{s0}/F < 2$ in the rotating stall case. (b) Unsteady, quasisteady and steady characteristics of the compressor corresponding to (a).

$p_d < 0.666$. If the initial value of p is p_0 and is greater than this value, then the steady state value of $\Delta\Psi_c$ must be increased by

$$\Delta\Psi_{c,ss} = \frac{H}{2}(p_d - p_0) = \frac{H\Delta p}{2}. \tag{7.3}$$

The corresponding initial condition for $\Delta\gamma$ is then given by

$$\Delta\gamma(t)\big|_{t=0} = \gamma - \gamma_n = \gamma - \frac{\sqrt{2F^2/p_d H}}{C_t}. \tag{7.4}$$

8. Control of the Rotating Stall Vibration Amplitude

To increase the steady state value of $\Delta\Psi_c$, it is important to increase the steady flow delivered by the compressor. This can be done by increasing the input to the compressor. To incorporate such a feature in our model, one assumes a distribution of pressure sources at the inlet to the compressor and write the compressor unsteady pressure dynamics equation with a source control term included as

$$\frac{d\Delta\Psi_c}{d\tau} + \frac{\Delta\Psi_c}{\tau_c} = \frac{(\Psi_{c,ss} - \Psi_{c,qs})}{\tau_c} + \frac{\Delta u_0}{\tau_c}, \tag{8.1a}$$

where the control input is a distribution of pressure sources which are integrated over the inlet area of the compressor and chosen according to the control law

$$\Delta u_0 = \frac{H}{2}(p_d - p_0) + \Delta u = \frac{H\Delta p}{2} + \Delta u, \tag{8.1b}$$

where Δu is the control input perturbation to provide feedback. The complete model equations (5.6a)–(5.6f) including the controller may be expressed as

$$\frac{d\phi_c}{d\tau} = B\Psi_c(p_0, \phi_c) + B(\Delta\Psi_c - \psi), \tag{8.2a}$$

$$\frac{d}{d\tau}\phi_t = -\frac{B}{G}\frac{\phi_t^2}{\left(\sqrt{2F^2/p_d H} + C_t\Delta\gamma\right)^2} + \frac{B\psi}{G}, \tag{8.2b}$$

$$\frac{d}{d\tau}\psi = \frac{(\phi_c - \phi_t)}{B}, \tag{8.2c}$$

$$\frac{d\Delta\Psi_c}{d\tau} + \frac{\Delta\Psi_c}{\tau_c} = \frac{(\Psi_{c,ss}(p_0, \phi_{cs}) - \Psi_c(p_0, \phi_c))}{\tau_c} + \frac{\Delta u_0}{\tau_c}, \tag{8.2d}$$

$$\frac{dB}{d\tau} = \frac{B}{\mu}(\Pi_{\text{ext}} - B\phi_c\sigma), \tag{8.2e}$$

$$\tau_J\frac{d\Delta J}{d\tau} = \frac{H}{F}(J_s + \Delta J)\left(1 - \left(\frac{\phi_c}{F} - 1\right)^2 - \frac{1}{4}(J_s + \Delta J)\right), \tag{8.2f}$$

$$\tau_u\frac{dC_t\Delta\gamma}{d\tau} = -C_t\Delta\gamma, \tag{8.2g}$$

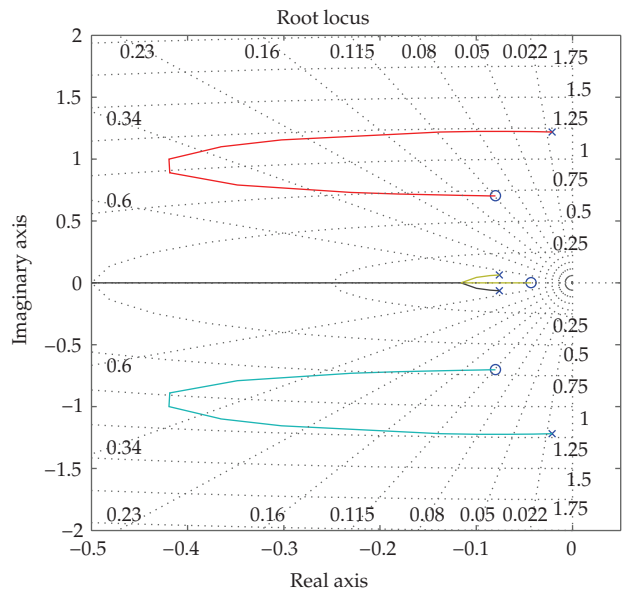

Figure 5: Root locus plot illustrating the effect of the negative feedback of $\Delta\phi_c$.

where

$$\begin{aligned}
\Psi_c(p_0,\phi_c) &= \frac{H}{2}\left(p_0 + \left(\frac{\phi_c}{F}-1\right)\left(1-\frac{J}{2}\right) - \left(\frac{\phi_c}{F}-1\right)^3\right),\\
\Psi_{c,ss}(p_0,\phi_{cs}) &= \Psi_c(p_0,\phi_c)\big|_{t\to\infty},\\
\Delta u_0 &= \frac{H}{2}(p_d - p_0) + \Delta u = \frac{H\Delta p}{2} + \Delta u.
\end{aligned} \tag{8.3}$$

To implement such a controller the parameter p_0 must be known. This parameter must therefore be identified offline *a priori* or adaptively, so the control input can be synthesised.

9. Stability of Controlled Equilibrium

An important step in the validation of the controller is the assessment of the stability of the closed loop equilibrium. To determine the stability of the controlled equilibrium, one first linearises (8.2a)–(8.2f), about the controlled equilibrium solution which is characterised by $p = p_d$ and $\phi_c = \phi_t = \phi_{sd}$. Perturbing the state vector and the control input and linearising (8.2a)–(8.2g) about the equilibrium states result in

$$\begin{aligned}
\frac{d\Delta\phi_c}{d\tau} &= \left(\Psi_c(p_d,\phi_{sd}) + B_0\frac{d\Psi_c(p_d,\phi_{sd})}{dB}\right)\Delta B\\
&\quad + B_0\left(\frac{d\Psi_c(p_d,\phi_{sd})}{d\phi_c}\Delta\phi_c + \frac{d\Psi_c(p_d,\phi_{sd})}{dJ}\Delta J + \Delta\Psi_c - \Delta\psi\right),
\end{aligned}$$

$$
\begin{aligned}
\frac{d\Delta\phi_t}{d\tau} &= \frac{B_0\Delta\psi}{G} \\
&\quad - \frac{B_0}{G}\frac{p_d H_s \phi_{sd}}{2F_s^2}\left(2\Delta\phi_t - \frac{2\phi_{sd}C_t\Delta\gamma}{\sqrt{2F_s^2/p_d H_s}} - \left(\frac{F_B}{F_s} - \frac{H_B}{2H_s}\right)\frac{\phi_{sd}}{\sqrt{2F_s^2/p_d H_s}}\Delta B\right), \\
\frac{d}{d\tau}\Delta\psi &= \frac{(\Delta\phi_c - \Delta\phi_t)}{B_0}, \\
\frac{d\Delta\Psi_c}{d\tau} + \frac{\Delta\Psi_c}{\tau_c} &= -\frac{1}{\tau_c}\left(\frac{d\Psi_c(p_d,\phi_{sd})}{d\phi_c}\Delta\phi_c + \frac{d\Psi_c(p_d,\phi_{sd})}{dJ}\Delta J + \frac{d\Psi_c(p_d,\phi_{sd})}{dB}\Delta B\right) + \frac{\Delta u}{\tau_c}, \\
&\quad \frac{d\Delta B}{d\tau} + \frac{\Delta B}{\mu}(2B_0\phi_{sd}\sigma - \Pi_{\text{ext}}) \\
&\quad = -\frac{B_0^2 F_s \sigma}{\mu}\frac{\Delta\phi_c}{F_s}, \\
\tau_J\frac{d\Delta J}{d\tau} &= -\frac{H_s}{F_s}\left(2J_s\left(\frac{\phi_{cs}}{F_s} - 1\right)\frac{\Delta\phi_c}{F_s}\right) \\
&\quad - \frac{H_s}{F_s}\left(\left(\left(\frac{\phi_{cs}}{F_s} - 1\right)^2 - 1 + \frac{J_s}{4}\right)J_s\left(\frac{H_B}{H_s} - \frac{F_B}{F_s}\right)\Delta B\right. \\
&\quad \left. + \left(\left(\frac{\phi_{cs}}{F_s} - 1\right)^2 - 1 + \frac{J_s}{2}\right)\Delta J,\right) \\
\tau_u\frac{dC_t\Delta\gamma}{d\tau} &= -C_t\Delta\gamma,
\end{aligned}
\tag{9.1}
$$

where Δu is the control input perturbation and $\Delta\phi_c$, $\Delta\phi_t$, $\Delta\psi$, $\Delta\Psi_c$, ΔJ, and ΔB are the perturbations to the corresponding states.

From (9.1) observe that the last three of the linearised perturbation equations are only weakly coupled with the first four. An analysis of the stability indicates that the controlled system is stable. Assume that the compressor perturbation mass flow ($\Delta\phi_c$) is measured; the root locus plot is obtained and shown in Figure 5. The two lightly damped poles correspond to modes associated primarily with $\Delta\phi_c$ and $\Delta\psi$. To increase the stability margins, one could include stability augmentation negative feedback (gain = 3.3) and this is implemented in calculating the closed loop response in the next section. The chosen value of the gain corresponds to the maximum stability margin based on root locus plot.

The controller can now be tested by simulating it and the complete nonlinear plant. The case of a compressor with the parameters as listed in Table 1 is considered. The desired compressor flow ratio is chosen to be $\phi_{sd}/F = 2.1$. The desired value of the parameter $p = p_d$ is then estimated from (3.14). The initial value for $\Delta\gamma$ is chosen to be -0.2. The results of the closed loop simulation including negative feedback are illustrated in Figure 6(a) which corresponds to the same case as the one shown in Figure 4(a) without feedback.

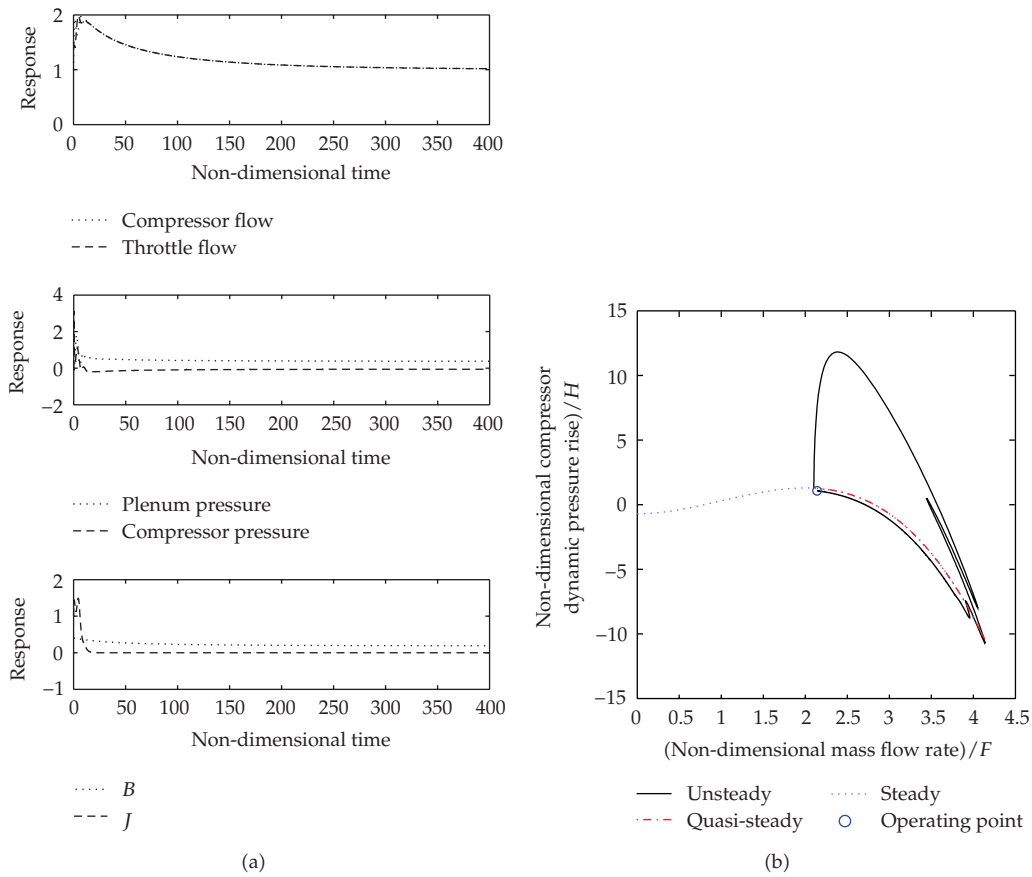

Figure 6: (a) Typical closed-loop state responses when H is positive and $\phi_{sd}/F > 2$ in the rotating stall case. (b) Unsteady, quasisteady and steady characteristics of the closed-loop compressor.

Figure 6(b) illustrates the unsteady characteristics of the closed-loop compressor which are compared with the steady-state characteristics. Also shown in the figure is the steady-state closed loop operating point. The results clearly indicate that the compressor now operates with the equilibrium $J = J_s = 0$ being stable. Thus the rotating stall disturbance is eliminated.

10. Conclusions

The dynamics of compressor stall has been reparameterised in a form that would facilitate the construction of a nonlinear control law for the active nonlinear control of compressor stall. The regions of stable performance in parameter space ($\gamma = \gamma_n$, $H > 0$, $J = J_s = 0$) and unstable performance ($\gamma \neq \gamma_n$ or $H < 0$, $J \neq 0$) were identified. This has led to the belief that a control law that maintains both $\gamma = \gamma_n$, $H > 0$ and $J = J_s = 0$ would actively stabilize the compressor. One observes that by merely setting the throttle at its optimum equilibrium position does not maintain, $J = J_s = 0$. An additional control input must aim to manipulate the transient and control pressure dynamics defined by (8.2d) which would involve control inputs to the compressors inlet guide vanes or some other means of feedback control. That in turn

points to a need for a better compressor pressure rise model incorporating the control input dynamics. Yet the relatively simple and systematic approach adopted in this paper clearly highlights the main features on the controller that is capable of inhibiting compressor surge and rotating stall. Moreover, the method can be adopted for any axial compressor provided its steady-state compressor and throttle maps are known. Furthermore, the linear perturbation controller synthesised in the previous section could be substituted by a nonlinear controller synthesised by applying the backstepping approach as demonstrated by Krstic et al. [9]. Preliminary implementations of such a controller have supported the view that there is a need for an improved, matching, nonlinear compressor pressure rise model including disturbance and uncertainty effects and the results of this latter study involving a robust complimentary nonlinear H_∞ optimal control law will be reported elsewhere. Coupled with the views expressed by Greitzer [4], the active structural control of surge and rotating stall could be effectively achieved by realistic low-order modelling of the compressor dynamics.

References

[1] B. de Jager, "Rotating stall and surge control: a survey," in *Proceedings of the 34th IEEE Conference on Decision and Control*, vol. 2, pp. 1857–1862, New Orleans, La, USA, 1995.

[2] A. H. Epstein, J. E. F. Williams, and E. M. Greitzer, "Active suppression of aerodynamic instabilities in turbomachines," *Journal of Propulsion and Power*, vol. 5, no. 2, pp. 204–211, 1989.

[3] G. Gu, S. Banda, and A. Sparks, "An overview of rotating stall and surge control for axial flow compressors," in *Proceedings of the IEEE Conference on Decision and Control*, pp. 2786–2791, Kobe, Japan, 1996.

[4] E. M. Greitzer, "Some aerodynamic problems of aircraft engines: fifty years after-the 2007 IGTI scholar lecture-," *Journal of Turbomachinery*, vol. 121, Article ID 031101, pp. 1–13, 2009.

[5] F. K. Moore and E. M. Greitzer, "A theory of post-stall transients in axial compressors—Part I. Development of the equations," *Journal of Engineering for Gas Turbines and Power*, vol. 108, no. 1, pp. 68–76, 1986.

[6] W. R. Hawthorne and J. H. Horlock, "Actuator disc theory of the Incompressible flow in axial compressor," *Proceedings of Institution of Mechanical Engineers, London*, vol. 196, no. 30, p. 798, 1962.

[7] J. T. Gravdahl and O. Egeland, "A Moore-Greitzer axial compressor model with spool dynamics," in *Proceedings of the 36th IEEE Conference on Decision and Control*, vol. 5, pp. 4714–4719, 1997.

[8] L. Chen, R. Smith, and G. Dullerud, "A linear perturbation model for a non-linear system linearized at an equilibrium neighbourhood," in *Proceedings of the 37th IEEE Conference on Decision and Control*, pp. 4105–4106, Tampa, Fla, USA, 1998.

[9] M. Krstic, J. M. Protz, J. D. Paduano, and P. V. Kokotovic, "Backstepping designs for jet engine stall and surge control," in *Proceedings of the IEEE Conference on Decision and Control*, vol. 3, pp. 3049–3055, 1995.

[10] M. A. Nayfeh and E. H. Abed, "High-gain feedback control of surge and rotating stall in axial flow compressors," in *Proceedings of the American Control Conference*, vol. 4, pp. 2663–2667, San Diego, Calif, USA, 1999.

[11] J. D. Paduano, A. H. Epstein, L. Valavani, J. P. Longley, E. M. Greitzer, and G. R. Guenette, "Active control of rotating stall in a low-speed axial compressor," *Journal of Turbomachinery*, vol. 115, no. 1, pp. 48–56, 1993.

[12] S. Young, Y. Wang, and R. M. Murray, "Evaluation of bleed valve rate requirements in non-linear control of rotating stall on axial flow compressors," Tech. Rep. CALTECH CDS TR 98-001, Division of Engineering and Applied Science, California Institute of Technology, Calif, USA, 1998.

[13] G. Gu, A. Sparks, and S. Banda, "Bifurcation based nonlinear feedback control for rotating stall in axial flow compressors," *International Journal of Control*, vol. 68, no. 6, pp. 1241–1257, 1997.

[14] C. Hős, A. Champneys, and L. Kullmann, "Bifurcation analysis of surge and rotating stall in the Moore-Greitzer compression system," *IMA Journal of Applied Mathematics*, vol. 68, no. 2, pp. 205–228, 2003.

[15] E. M. Greitzer, "Surge and rotating stall in axial flow compressors—part I, II," *Journal of Engineering for Power*, vol. 98, no. 2, pp. 190–217, 1976.

Hindawi Publishing Corporation
Mathematical Problems in Engineering
Volume 2010, Article ID 270646, 18 pages
doi:10.1155/2010/270646

Research Article

Chaos Control of a Fractional-Order Financial System

Mohammed Salah Abd-Elouahab,[1] Nasr-Eddine Hamri,[1] and Junwei Wang[2]

[1] *Department of Science and Technology, University Center of Mila, Mila 43000, Algeria*
[2] *Cisco School of Informatics, Guangdong University of Foreign Studies, Guangzhou 510006, China*

Correspondence should be addressed to Mohammed Salah Abd-elouahab, medsalah3@yahoo.fr

Received 4 November 2009; Revised 29 April 2010; Accepted 2 June 2010

Academic Editor: Carlo Cattani

Fractional-order financial system introduced by W.-C. Chen (2008) displays chaotic motions at order less than 3. In this paper we have extended the nonlinear feedback control in ODE systems to fractional-order systems, in order to eliminate the chaotic behavior. The results are proved analytically by applying the Lyapunov linearization method and stability condition for fractional system. Moreover numerical simulations are shown to verify the effectiveness of the proposed control scheme.

1. Introduction

Nonlinear chaotic systems have attracted more attention of researchers in various fields of natural sciences. This is because these systems are rich in dynamics, and possess great sensitivity to initial conditions. Since the chaotic phenomenon in economics was first found in 1985, great impact has been imposed on the prominent western economics at present, because the chaotic phenomenon's occurring in the economic system means that the macroeconomic operation has in itself the inherent indefiniteness. Although the government can adopt such macrocontrol measures as the financial policies or the monetary policies to interfere, the effectiveness of the interference is very limited. The instability and complexity make the precise economic prediction greatly limited, and the reasonable prediction behavior has become complicated as well. In the fields of finance, stocks, and social economics, because of the interaction between nonlinear factors, with all kinds of economic problems being more and more complicated and with the evolution process from low dimensions to high dimensions, the diversity and complexity have manifested themselves in the internal

structure of the system and there exists extremely complicated phenomenon and external characteristics in such a kind of system. So it has become more and more important to study the control of the complicated continuous economic system, and stabilize the instable periodic or stationary solutions, in order to make the precise economic prediction possible [1, 2].

Great interest has been paid to the application of fractional calculus in physics, engineering systems, and even financial analysis [3, 4]. The fact that financial variables possess long memories makes fractional modelling appropriate for dynamic behaviors in financial systems. Moreover, the control and synchronization of fractional-order dynamic systems is also performed by various researchers [5–10]. Fractional-order financial system proposed by Chen in [11] displays many interesting dynamic behaviors, such as fixed points, periodic motions, and chaotic motions. It has been found that chaos exists in this system with orders less than 3, period doubling, and intermittency routes to chaos were found. In this paper, we propose to eliminate the chaotic behaviors from this system, by extending the nonlinear feedback control in ODE systems to fractional-order systems. This paper is organized as follows. In Section 2, we present the financial system and its fractional version. In Section 3 general approach to feedback control scheme is given, and then we have extended this control scheme to fractional-order financial system, numerical results are shown. Finally, in Section 4 concluding comments are given.

2. Financial System

2.1. Integer-Order Financial System

Recently, the studies in [1, 2] have reported a dynamic model of finance, composed of three first-order differential equations. The model describes the time-variation of three state variables: the interest rate x, the investment demand y, and the price index z. The factors that influence the changes of x mainly come from two aspects: firstly, it is the contradiction from the investment market, (the surplus between investment and savings); secondly, it is the structure adjustment from goods prices. The changing rate of y is in proportion with the rate of investment, and in proportion by inversion with the cost of investment and the interest rate. The changes of z, on one hand, are controlled by the contradiction between supply and demand of the commercial market, and on the other hand, are influenced by the inflation rate. Here we suppose that the amount of supplies and demands of commercials is constant in a certain period of time, and that the amount of supplies and demands of commercials is in proportion by inversion with the prices. However, the changes of the inflation rate can in fact be represented by the changes of the real interest rate and the inflation rate equals the nominal interest rate subtracts the real interest rate. The original model has nine independent parameters to be adjusted, so it needs to be further simplified. Therefore, by choosing the appropriate coordinate system and setting an appropriate dimension to every state variable, we can get the following more simplified model with only three most important parameters:

$$\begin{aligned} \dot{x} &= z + (y - a)x, \\ \dot{y} &= 1 - by - x^2, \\ \dot{z} &= -x - cz, \end{aligned} \tag{2.1}$$

where $a \geq 0$ is the saving amount, $b \geq 0$ is the cost per investment, and $c \geq 0$ is the elasticity of demand of commercial markets. It is obvious that all three constants, a, b, and c, are nonnegative, For more detail about the study of the local topological structure and bifurcation of this system; see [1, 2]. We assume that a is control parameter and $b = 0.1$, $c = 1$.

2.1.1. Analysing the System

(i) If $a \geq 9$, system (2.1) has one fixed point:

$$p_1 = (0, 10, 0). \tag{2.2}$$

(ii) If $a < 9$, system (2.1) has three fixed points:

$$p_1 = (0, 10, 0), \qquad p_{2,3} = \left(\mp\sqrt{\frac{9-a}{10}}, a+1, \pm\sqrt{\frac{9-a}{10}} \right). \tag{2.3}$$

To study the stability of equilibrium points we apply the Lyapunov's first (indirect) method [12] so we have the following theorem.

Theorem 2.1. *Let $x = x^*$ be an equilibrium point of a nonlinear system:*

$$\dot{x} = f(x), \tag{2.4}$$

where $f : D \to \mathbb{R}^n$ is continuously differentiable and $D \subset \mathbb{R}^n$ is the neighborhood of the equilibrium point x^*. Let λ_i denote the eigenvalues of the Jacobian matrix $A = \partial f / \partial x|_{x^*}$ then the following are considered.

(i) *If $\operatorname{Re} \lambda_i < 0$ for all i, then $x = x^*$ is asymptotically stable.*

(ii) *If $\operatorname{Re} \lambda_i > 0$ for one or more i, then $x = x^*$ is unstable.*

(iii) *If $\operatorname{Re} \lambda_i \leq 0$ for all i and at least one $\operatorname{Re} \lambda_j = 0$, then $x = x^*$ may be either stable, asymptotically stable, or unstable.*

Since A is only defined at x^*, stability determined by the indirect method is restricted to infinitesimal neighborhoods of x^*.

To study the signs of the real parts of eigenvalues, we have the following famous criterion [13].

Criterion 1 (Routh-Hurwitz). Given the polynomial $P(\lambda) = \lambda^n + a_1\lambda^{n-1} + \cdots + a_{n-1}\lambda + a_n$, where the coefficients $a_i,\ i = 1, 2, \ldots, n$, are real constants, define the n Hurwitz matrices

$$\begin{aligned} H_1 &= (a_1), \\ H_2 &= \begin{pmatrix} a_1 & 1 \\ a_3 & a_2 \end{pmatrix} \\ &\vdots \\ H_n &= \begin{pmatrix} a_1 & 1 & 0 & 0 & \cdots & 0 \\ a_3 & a_2 & a_1 & 1 & \cdots & 0 \\ a_5 & a_4 & a_3 & a_2 & \cdots & 0 \\ \vdots & \vdots & \vdots & \vdots & \cdots & \vdots \\ 0 & 0 & 0 & 0 & \cdots & a_n \end{pmatrix}, \end{aligned} \tag{2.5}$$

where $a_i = 0$ if $i > n$.

All of roots of the polynomial have negative real part if and only if the determinants of all Hurwitz matrices are positive: $\det H_i > 0,\ i = 1, 2, \ldots, n$.

Routh-Hurwitz criteria for $n = 3$ are $a_1 > 0,\ a_3 > 0$ and $a_1a_2 - a_3 > 0$.

Stability of p_1

The Jacobian matrix of system (2.1) at the equilibrium point p_1 is

$$J_{p_1} = \begin{pmatrix} 10 - a & 0 & 1 \\ 0 & -\dfrac{1}{10} & 0 \\ -1 & 0 & -1 \end{pmatrix}, \tag{2.6}$$

its characteristic polynomial is

$$P(\lambda) = \lambda^3 + \left(a - \frac{89}{10}\right)\lambda^2 + \left(\frac{11a - 99}{10}\right)\lambda + \left(\frac{a - 9}{10}\right). \tag{2.7}$$

By applying the Routh-Hurwitz criterion we find that the real parts of these eigenvalues are all negative if and only if

$$\begin{gathered} a - \frac{89}{10} > 0, \\ a - 9 > 0, \\ \left(a - \frac{89}{10}\right)\left(\frac{11a - 99}{10}\right) - \left(\frac{a - 9}{10}\right) > 0. \end{gathered} \tag{2.8}$$

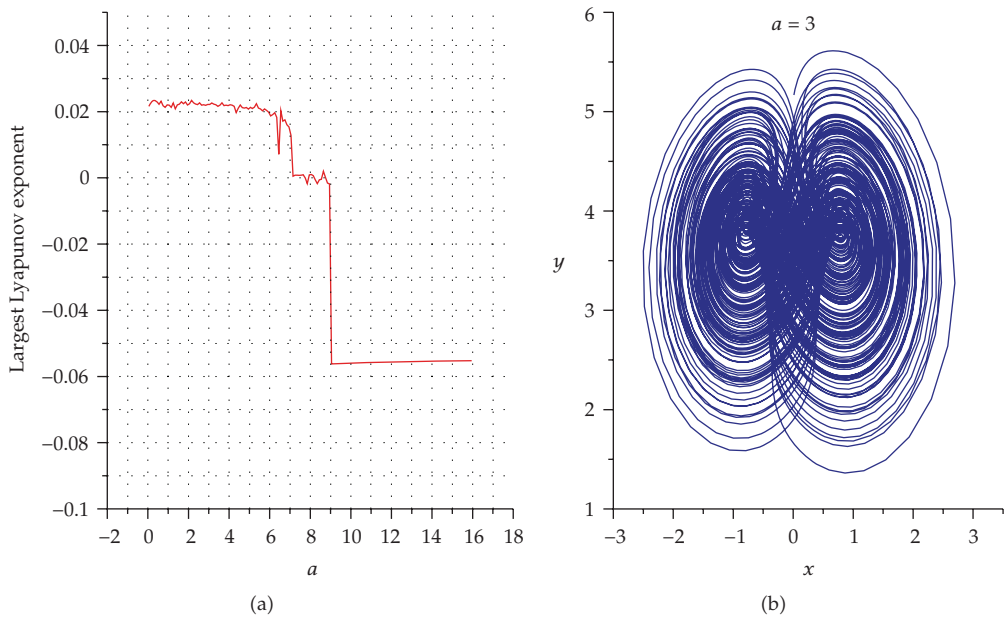

Figure 1: (a) Largest Lyapunov exponent according to a. (b) Chaotic attractor for $a = 3$.

Then it follows that $a > 9$, and thus p_1 is locally asymptotically stable if and only if $a > 9$.

Stability of $p_{2,3}$

The Jacobian matrix of system (2.1) at the equilibrium points $p_{2,3}$ is

$$J_{p_{2,3}} = \begin{pmatrix} 1 & \pm\sqrt{\dfrac{9-a}{10}} & 1 \\ \mp 2\sqrt{\dfrac{9-a}{10}} & -0.1 & 0 \\ -1 & 0 & -1 \end{pmatrix}, \tag{2.9}$$

and its characteristic polynomial is

$$\tilde{p}(\lambda) = \lambda^3 + \frac{1}{10}\lambda^2 + \left(-\frac{1}{5}a + \frac{18}{10}\right)\lambda + \left(-\frac{1}{5}a + \frac{18}{10}\right). \tag{2.10}$$

The real parts of these eigenvalues are all negative if and only if

$$\begin{gathered} -\frac{1}{5}a + \frac{18}{10} > 0, \\ \frac{1}{10}\left(-\frac{1}{5}a + \frac{18}{10}\right) - \left(-\frac{1}{5}a + \frac{18}{10}\right) > 0. \end{gathered} \tag{2.11}$$

Then it follows that

$$a < 9,$$
$$a > 9. \tag{2.12}$$

So $p_{2,3}$ are unstable for every value of a.

In order to detect the chaos we calculate the largest Lyapunov exponent $\lambda_{\max}$ using the scheme proposed by Wolf et al. [14]. The initial states are taken as $x(0) = 2$, $y(0) = 3$, $z(0) = 2$, Figure 1(a) displays the evolution of $\lambda_{\max}$ according to a and Figure 1(b) displays chaotic attractor for $a = 3$. System (2.1) displays chaotic behavior in the windows $0 < a < 7$ ($\lambda_{\max} > 0$), periodic behavior in $7 \leq a \leq 9$ ($\lambda_{\max} \approx 0$) and stationary behavior for $a > 9$ ($\lambda_{\max} < 0$).

2.2. Fractional-Order Financial System

Chen has introduced in [11] the generalization of system (2.1) for fractional incommensurate-order model which takes the form

$$\begin{aligned} D^{q_1} x &= z + (y - a)x, \\ D^{q_2} y &= 1 - by - x^2, \\ D^{q_3} z &= -x - cz. \end{aligned} \tag{2.13}$$

Fractional calculus is a generalization of ordinary differentiation and integration to arbitrary order but there are several definitions of fractional derivatives.

In this paper, we use the Caputo-type fractional derivative defined in [15] by:

$$\begin{aligned} D^q f(t) &= \frac{1}{\Gamma(n-q)} \int_0^t (t-\tau)^{n-q-1} f^{(n)}(\tau) d\tau \\ &= j^{n-q}\left(\frac{d^n}{dt^n} f(t)\right), \end{aligned} \tag{2.14}$$

where $n = [q]$ is the value of q rounded up to the nearest integer, Γ is the gamma function and j^α is the Riemann-Liouville integral operator defined by

$$j^\alpha f(t) = \frac{1}{\Gamma(\alpha)} \int_0^t (t-\tau)^{\alpha-1} f(\tau) d\tau. \tag{2.15}$$

For the numerical solutions of system (2.13) we use the Adams-Bashforth-Moulton predictor-corrector scheme [16].

We assume that q ($q_1 = q_2 = q_3 = q$) is the control parameter, and $c = 1$, $b = 0.1$, $a = 3$. Fractional system (2.13) has the same fixed points $p_{1,2,3}$ as integer system (2.1), but for the stability analysis we have this theorem introduced in [17, 18].

Theorem 2.2. *The fractional linear autonomous system*

$$\begin{aligned} D^{\alpha}X &= AX \\ X(0) &= X_0 \end{aligned} \quad X \in \mathbf{R}^n,\ 0 < \alpha < 2,\ A \in \mathbf{R}^n \times \mathbf{R}^n, \tag{2.16}$$

is locally asymptotically stable if and only if

$$\min_i \left|\arg(\lambda_i)\right| > \alpha\frac{\pi}{2}, \quad i = 1, 2, \ldots, n. \tag{2.17}$$

Proposition 2.3. *Let $x = x^*$ be an equilibrium point of a fractional nonlinear system*

$$D^{\alpha}x = f(x), \quad 0 < \alpha < 2. \tag{2.18}$$

If the eigenvalues of the Jacobian matrix $A = \partial f/\partial x|_{x^*}$ satisfy

$$\min_i \left|\arg(\lambda_i)\right| > \alpha\frac{\pi}{2}, \quad i = 1, 2, \ldots, n, \tag{2.19}$$

then the system is locally asymptotically stable at the equilibrium point x^*.

Proof. Let $x = x^* + \delta x$. Substituting in (2.18), we find

$$D^{\alpha}(x^* + \delta x) = f(x^* + \delta x). \tag{2.20}$$

so

$$D^{\alpha}(\delta x) = f(x^*) + A\delta x + \bigcirc\left(\|\delta x\|^2\right). \tag{2.21}$$

Since $f(x^*) = 0$ (x^* is the equilibrium point of system (2.18)) and $\lim_{\|\delta x\| \to 0}(\bigcirc(\|\delta x\|^2)/\|\delta x\|) = 0$, then

$$D^{\alpha}\delta x \approx A\delta x. \tag{2.22}$$

Taking into account Theorem 2.2, we deduce that If the eigenvalues of the matrix A satisfy

$$\min_i \left|\arg(\lambda_i)\right| > \alpha\frac{\pi}{2}, \quad i = 1, 2, \ldots, n, \tag{2.23}$$

then x^* is locally asymptotically stable.

This completes the proof. □

Stability of p_1

The Jacobian matrix of system (2.13) at the equilibrium point p_1 is

$$J_{p_1} = \begin{pmatrix} 7 & 0 & 1 \\ 0 & -\frac{1}{10} & 0 \\ -1 & 0 & -1 \end{pmatrix}, \tag{2.24}$$

and its characteristic polynomial is

$$P(\lambda) = \lambda^3 - \frac{59}{10}\lambda^2 - \frac{66}{10}\lambda - \frac{6}{10}. \tag{2.25}$$

its eigenvalues are $\lambda_1 \approx -0.87298$, $\lambda_2 = -1/10$, $\lambda_3 \approx 6.8730$, we note that λ_3 is real positive then $|\arg(\lambda_3)| = 0 < q(\pi/2)$, for all $q \in]0,2[$, so p_1 is unstable for all $q \in]0,2[$.

Stability of $p_{2,3}$

The Jacobian matrix of system (2.13) at the equilibrium point $p_{2,3}$ is

$$J_{p_{2,3}} = \begin{pmatrix} 1 & \pm\sqrt{\frac{3}{5}} & 1 \\ \mp 2\sqrt{\frac{3}{5}} & -\frac{1}{10} & 0 \\ -1 & 0 & -1 \end{pmatrix}, \tag{2.26}$$

its characteristic polynomial is

$$\tilde{p}(\lambda) = \lambda^3 + \frac{1}{10}\lambda^2 + \frac{6}{5}\lambda + \frac{6}{5}, \tag{2.27}$$

and its eigenvalues are $\lambda_1 \approx 0.31278 + 1.2474i$, $\lambda_2 \approx 0.31278 - 1.2474i$, and $\lambda_3 \approx -0.72556$, we have

$$\left|\arg(\lambda_{1,2})\right| \approx 1.3251, \qquad \left|\arg(\lambda_3)\right| = \pi, \tag{2.28}$$

so $\min_i |\arg(\lambda_i)| \approx 1.3251$, then the critical value of q is

$$q_c = \frac{2\min_i \left|\arg(\lambda_i)\right|}{\pi} \approx 0.8436, \tag{2.29}$$

(i) If $q < 0.8436$, then $p_{2,3}$ are locally asymptotically stable.

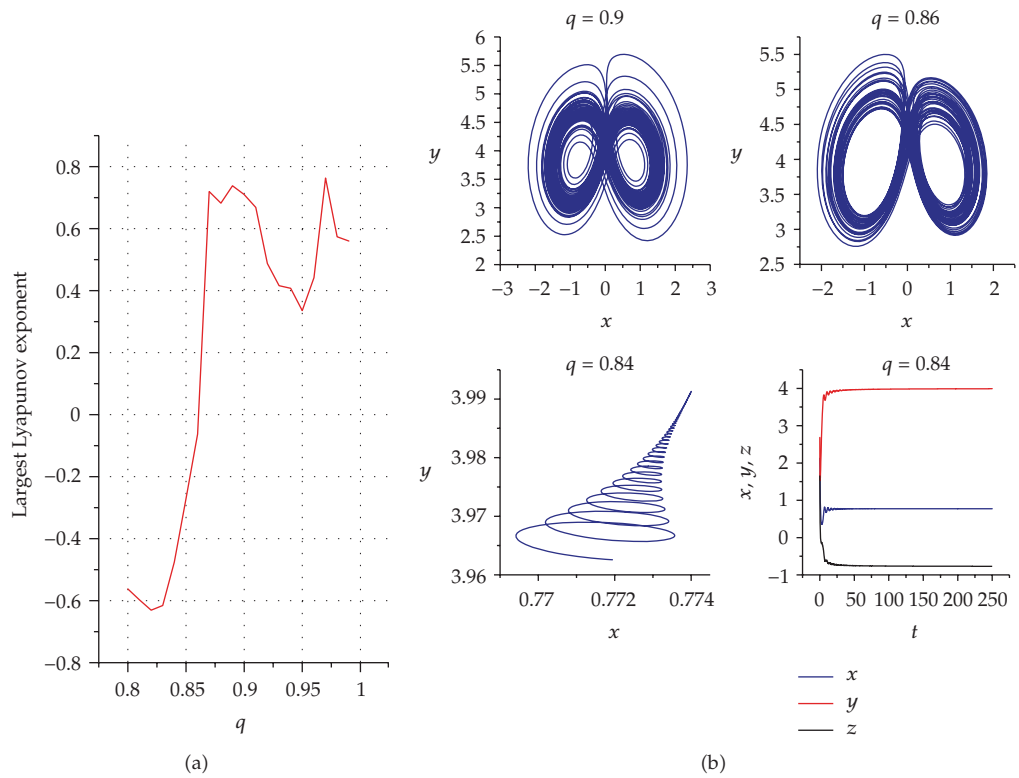

Figure 2: (a) Largest Lyapunov exponent according to q. (b) Phase diagram for some values of q.

(ii) If $q > 0.8436$, then $p_{2,3}$ are unstable.

In order to detect the chaos, we calculate the largest Lyapunov exponent $\lambda_{\max}$.

The initial states are taken as $x(0) = 2$, $y(0) = 3$, $z(0) = 2$, Figure 2(a) shows the evolution of $\lambda_{\max}$ according to q. System (2.13) exhibits chaotic behaviors for $q \geq 0.86$.

3. Feedback Control

3.1. Integer Case

A general approach to control a nonlinear dynamical system via feedback control can be formulated as follows:

$$\dot{x}(t) = f(x, u, t), \tag{3.1}$$

where $x(t)$ is the system state vector, and $u(t)$ the control input vector. Given a reference signal $\tilde{x}(t)$, the problem is to design a controller in the state feedback form:

$$u(t) = g(x, t), \tag{3.2}$$

where g is vector-valued function, so that the controlled system

$$\dot{x}(t) = f\big(x, g(x,t), t\big) \tag{3.3}$$

can be driven by the feedback control $g(x,t)$ to achieve the goal of target tracking so we must have

$$\lim_{t \to t_f} \|x(t) - \tilde{x}(t)\| = 0. \tag{3.4}$$

Proposition 3.1. *Let us consider the nonlinear system*

$$\dot{e} = F(e,t), \tag{3.5}$$

where $e = x - \tilde{x}$, $\tilde{x}(t)$ *is a periodic orbit (or fixed point) of the given system* (3.1) *with* $u = 0$, *and* $F(e,t) = f(x, g(x,t), t) - f(\tilde{x}, 0, t)$.

If 0 *is a fixed point of system* (3.5) *and all eigenvalues of the jacobian matrix* $A = \partial F/\partial x|_0$ *have negative real parts then the trajectory* $x(t)$ *of system* (3.3) *converge to* $\tilde{x}(t)$

Proof. Since $\tilde{x}(t)$ is a periodic orbit (or fixed point) of the given system (3.1) with $u = 0$, so it satisfies

$$\dot{\tilde{x}}(t) = f(\tilde{x}, 0, t), \tag{3.6}$$

a subtraction of (3.6) from (3.1) gives

$$\dot{x}(t) - \dot{\tilde{x}}(t) = f\big(x, g(x,t), t\big) - f(\tilde{x}, 0, t), \tag{3.7}$$

so

$$\dot{e} = F(e,t). \tag{3.8}$$

Since all eigenvalues of the jacobian matrix A have negative real parts, it follows from Theorem 2.1 that 0 is asymptotically stable, so we have $\lim_{t \to +\infty} \|e(t)\| = 0$ then $\lim_{t \to +\infty} \|x(t) - \tilde{x}(t)\| = 0$, finally $x(t) \underset{t \to t_f}{\longrightarrow} \tilde{x}(t)$. □

3.2. Fractional Case

Let us consider the fractional system

$$D^{\alpha} x(t) = f(x, u, t). \tag{3.9}$$

We proceed as in the integer case. the controlled system can be written as

$$D^{\alpha} x(t) = f\big(x, g(x,t), t\big). \tag{3.10}$$

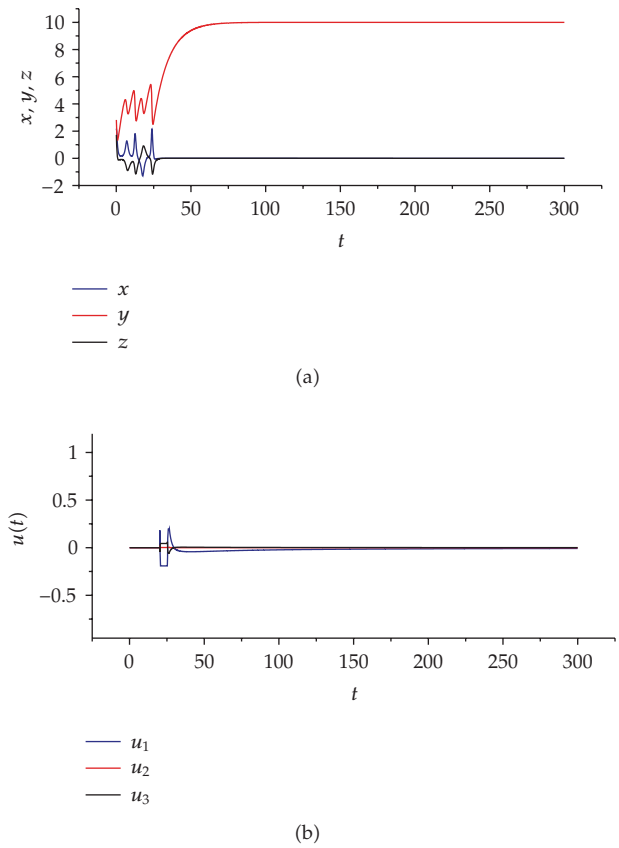

Figure 3: (a) Stabilizing the equilibrium point p_1 for $q = 0.9$. (b) Evolution of the perturbation $u(t)$.

Let $\tilde{x}(t)$ be a periodic orbit (or fixed point) of the given system (3.9) with $u = 0$, then we obtain the system error

$$D^{\alpha} e(t) = F(e, t) \tag{3.11}$$

Proposition 3.2. *If* 0 *is a fixed point of system* (3.11) *and the eigenvalues of the jacobian matrix* $A = \partial F / \partial x|_0$ *satisfies the condition*

$$\min_i \left| \arg(\lambda_i) \right| > \alpha \frac{\pi}{2}, \quad i = 1, 2, \ldots, n \tag{3.12}$$

then the trajectory $x(t)$ *of system* (3.10) *converge to* $\tilde{x}(t)$.

Proof. It follows directly from Proposition 2.3. □

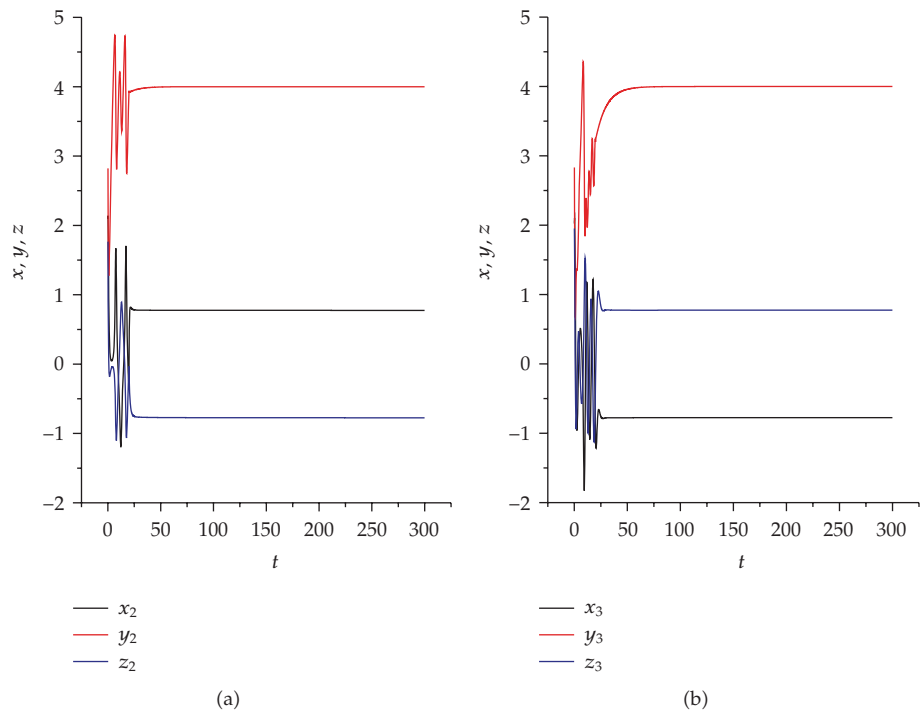

Figure 4: (a) Stabilizing the equilibrium point p_2 for $q = 0.95$. (b) Stabilizing the equilibrium point p_3 for $q = 1.4$.

3.3. Application to the Fractional Financial System

Let us consider the fractional financial system (2.13), we propose to stabilize unstable periodic orbit (or fixed point) $(\tilde{x}, \tilde{y}, \tilde{z})$, the controlled system is as follows:

$$\begin{aligned} D^{q_1} x &= z + (y - a)x + u_1(t), \\ D^{q_2} y &= 1 - by - x^2 + u_2(t), \\ D^{q_3} z &= -x - cz + u_3(t). \end{aligned} \tag{3.13}$$

Since $(\tilde{x}, \tilde{y}, \tilde{z})$ is solution of (2.13), then we have:

$$\begin{aligned} D^{q_1} \tilde{x} &= \tilde{z} + (\tilde{y} - a)\tilde{x}, \\ D^{q_2} \tilde{y} &= 1 - b\tilde{y} - \tilde{x}^2, \\ D^{q_3} \tilde{z} &= -\tilde{x} - c\tilde{z}. \end{aligned} \tag{3.14}$$

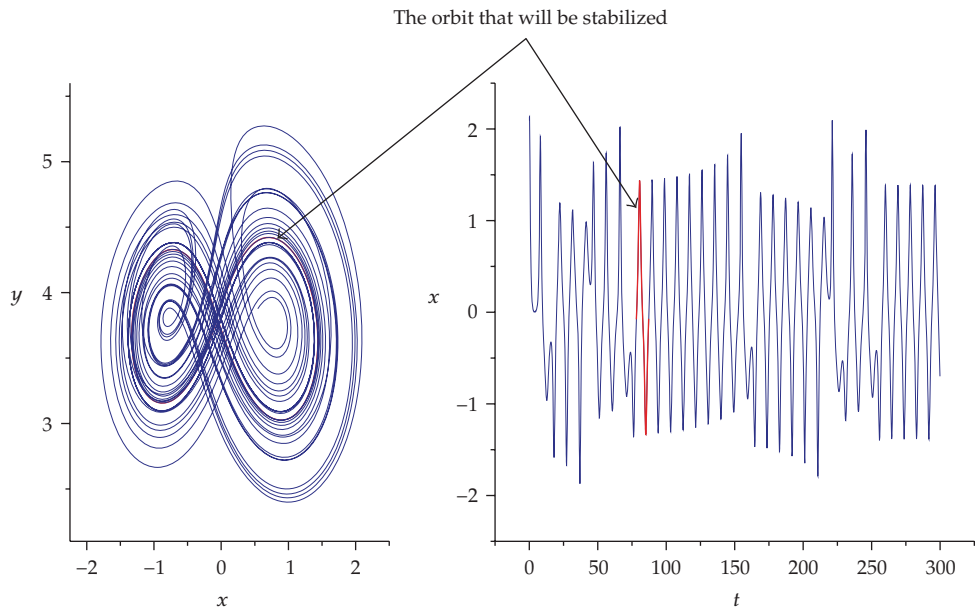

Figure 5: Selecting an unstable periodic orbit in the chaotic attractor of period $T = 9$ for $q = 0.97$.

Subtracting (3.14) from (3.13) with notation, $e_1 = x - \tilde{x},\ e_2 = y - \tilde{y},\ e_3 = z - \tilde{z}$, we obtain the system error:

$$\begin{aligned} D^{q_1} e_1 &= e_3 - a e_1 + xy - \tilde{x}\tilde{y} + u_1(t), \\ D^{q_2} e_2 &= -b e_2 - e_1(x + \tilde{x}) + u_2(t), \\ D^{q_3} e_3 &= -e_1 - c e_3 + u_3(t). \end{aligned} \tag{3.15}$$

We define the control functions as follow:

$$\begin{aligned} u_1(t) &= -(xy - \tilde{x}\tilde{y}), \\ u_2(t) &= e_1(x + \tilde{x}), \\ u_3(t) &= e_1. \end{aligned} \tag{3.16}$$

So the system error (3.15) becomes

$$\begin{aligned} D^{q_1} e_1 &= e_3 - a e_1, \\ D^{q_2} e_2 &= -b e_2, \\ D^{q_3} e_3 &= -c e_3. \end{aligned} \tag{3.17}$$

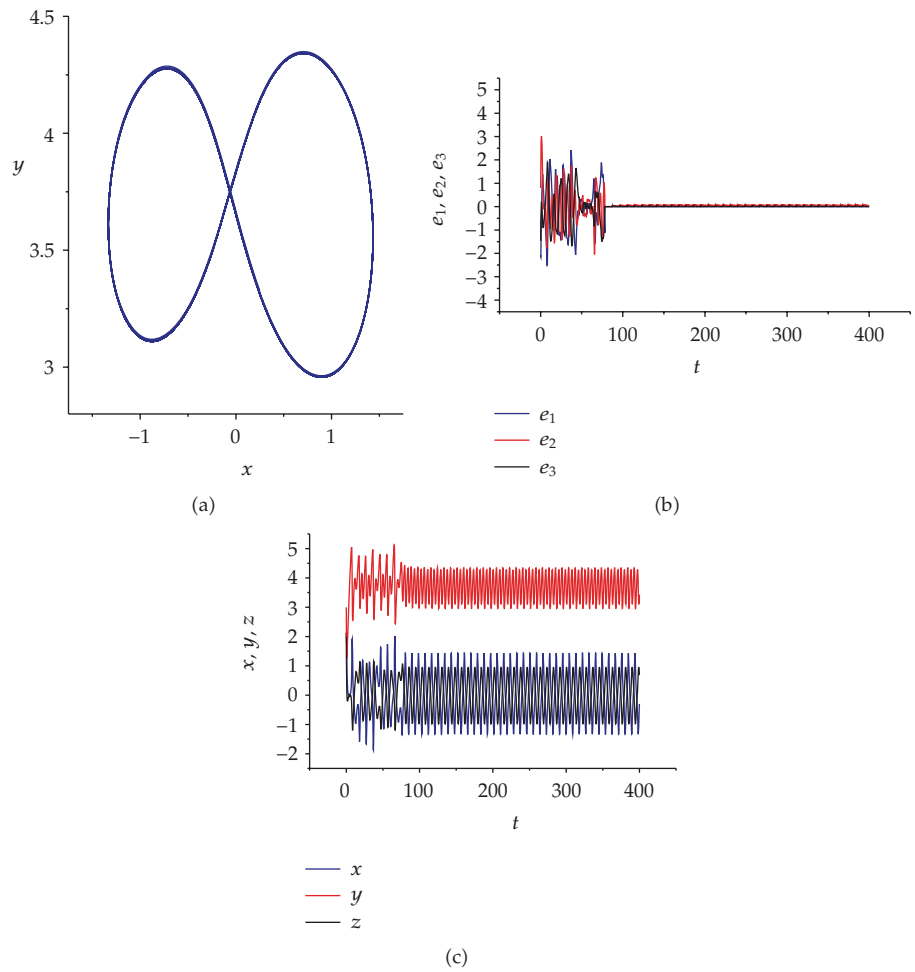

Figure 6: Stabilizing unstable periodic orbit of period $T = 9$ for $q = 0.97$.

The Jacobian matrix is $\begin{bmatrix} -a & 0 & 1 \\ 0 & -b & 0 \\ 0 & 0 & -c \end{bmatrix}$ and its characteristic polynomial is:

$$p(x) = x^3 + (a + b + c)x^2 + (ab + c(a + b))x + abc \tag{3.18}$$

so we have the eigenvalues $\lambda_1 = -a,\ \lambda_2 = -b,\ \lambda_3 = -c$. Since all eigenvalues are real negatives one has $\arg(\lambda_i) = \pi$, therefore $|\arg(\lambda_i)| > q(\pi/2)$, for all q satisfies $0 < q < 2$, it follows from Proposition 3.2 that the trajectory $x(t)$ of system (3.13) converges to $\tilde{x}(t)$ and the control is completed.

3.4. Simulation Results

In this section we give numerical results which prove the performance of the proposed scheme. As mentioned in Section 2.3 we have implemented the improved Adams-Bashforth-Moulton algorithm for numerical simulation.

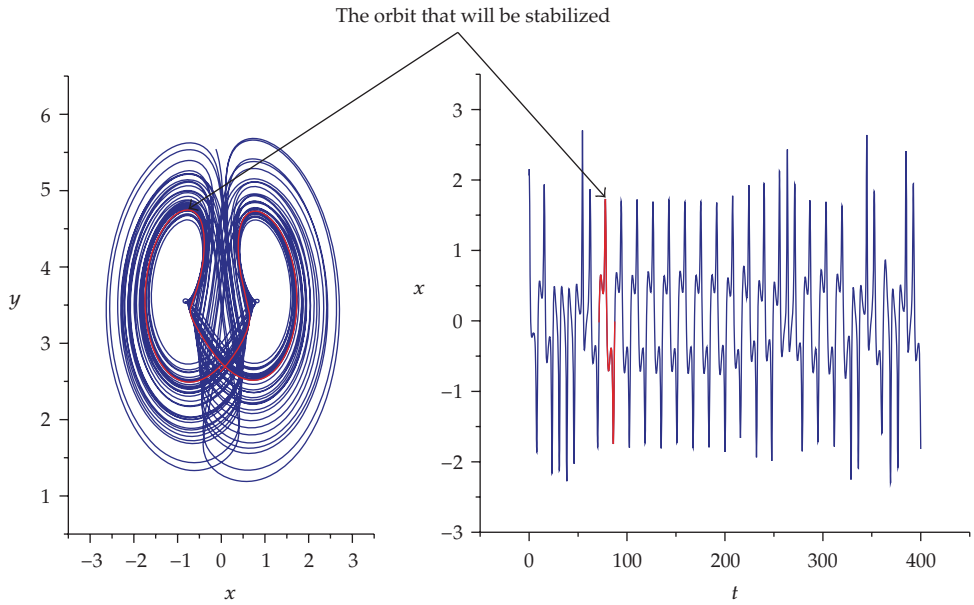

Figure 7: Selecting an unstable periodic orbit in the chaotic attractor of period $T = 16.05$ for $q = 1.1$.

The initial states are taken as $x(0) = 2,\ y(0) = 3,\ z(0) = 2$.

3.4.1. Stabilizing the Unstable Fixed Points

The control can be started at any time according to our needs, so we choose to activate the control when $t \geq 20$, in order to make a comparison between the behavior before activation of control and after it.

For $q = 0.9$ unstable point p_1 has been stabilized, as shown in Figure 3(a), note that $u_1(t) = -(x(t)y(t) - 0 \times 10) = -x(t)y(t)$, so the control is activated when $t \geq 20$ and $|x(t)y(t)| \leq 0.2$ (more precisely $t = 22.5$) in order to make the perturbation $u_1(t)$ smaller. firstly the evolution of $x(t), y(t), z(t)$ is chaotic, then when the control is started at $t = 22.5$ we see that p_1 is rapidly stabilized.

In Figure 3(b) we observe the evolution of the perturbation $u(t)$, when the control is started we see that $u_2(t)$ and $u_3(t)$ are very small but $u_1(t)$ is a bit larger, after that the perturbation $u(t)$ becomes close to zero rapidly.

For $q = 0.95$, the unstable point p_2 has been stabilized, as shown in Figure 4(a).

For $q = 1.4$ the fixed point p_3 was stabilized, Figure 4(b) shows the results of control.

When t is less than 20, there is a chaotic behavior, but when the control is activated at $t = 20$, the two points p_2 and p_3 are rapidly stabilized.

In the real world of finance if we want to have a good investment demand we can choose to stabilize p_1, and in this case the interest rate and price index will be near zero. During the recent financial crisis in 2009 many banks decided to reduce interest rates to nearly zero in order to control this situation.

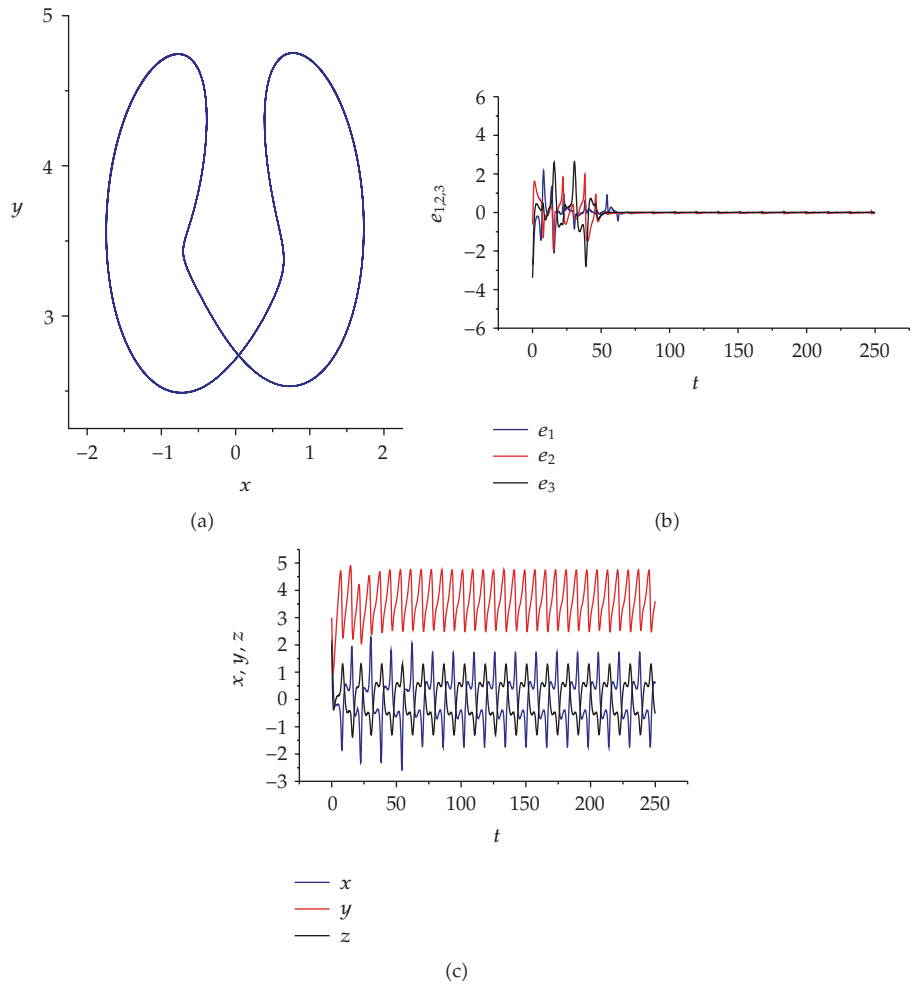

Figure 8: Stabilization an unstable periodic orbit of period $T = 16.05$ for $q = 1.1$.

3.4.2. Stabilizing Unstable Periodic Orbit

Although the unstable periodic orbits are dense in the chaotic attractor, we can choose one of them (which represent the performance of the system), by analyzing data experimental, after that we stabilize it. In this paper the close-return (CR) method [19] is used for the detection of UPO embedded in the attractor.

For $q = 0.97$ we choose an unstable periodic orbit with period $T = 9$, localized in the interval $[78.2, 87.2]$ as shown in Figure 5, then the control is started at $t = 87.2$, when the trajectory $x(t)$ begins to emerge from the unstable orbit, Figure 6 displays the results of control, if t is less then 78.2 there is chaotic behavior (the error $e(t)$ is large), after the activation of control, this chaotic behavior is replaced by a periodic behavior and we note that the error $e(t)$ becomes very close to zero.

For $q = 1.1$ we choose an unstable periodic orbit with period $T = 16.05$, localized in the interval $[71.45, 87.5]$ as shown in Figure 7, the control is started at $t = 20$, Figure 8 displays the results of control. Although the control is executing at $t = 20$, it does not give effect rapidly,

and the orbit is stabilized at $t = 63$, when the control is activated the error begins to diminish, and becomes close to zero after $t = 63$.

The stabilization of the periodic orbits is very important, because it permits, on the one hand to make some predictions, and secondly, it is more realistic than the stabilization of the stationary points in the financial circle, where one cannot generally fix the interest rate and the investment demand as well as the price index, for a long period.

4. Conclusions

Chaotic phenomenon makes prediction impossible in the financial world; then the deletion of this phenomenon from fractional financial system is very useful, the main contribution of this paper is to this end.

Nonlinear feedback control scheme has been extended to control fractional financial system. The results are proved analytically by applying the Lyapunov linearization method and stability condition for fractional system. Numerically the unstable fixed points $p_{1,2,3}$ have been successively stabilized for different values of q; moreover unstable periodic orbit has stabilized. This proves the performance of the proposed scheme.

References

[1] J. H. Ma and Y. S. Chen, "Study for the bifurcation topological structure and the global complicated character of a kind of nonlinear finance system. I," *Applied Mathematics and Mechanics*, vol. 22, no. 11, pp. 1240–1251, 2001.

[2] J. H. Ma and Y. S. Chen, "Study for the bifurcation topological structure and the global complicated character of a kind of nonlinear finance system. II," *Applied Mathematics and Mechanics*, vol. 22, no. 12, pp. 1375–1382, 2001.

[3] I. Podlubny, *Fractional Differential Equations: An Introduction to Fractional Derivatives, Fractional Differential Equations, to Methods of Their solution and Some of Their Application*, vol. 198 of *Mathematics in Science and Engineering*, Academic Press, San Diego, Calif, USA, 1999.

[4] R. Hilfer, Ed., *Applications of Fractional Calculus in Physics*, World Scientific, River Edge, NJ, USA, 2000.

[5] A. Oustaloup, J. Sabatier, and P. Lanusse, "From fractal robustness to the CRONE control," *Fractional Calculus & Applied Analysis*, vol. 2, no. 1, pp. 1–30, 1999.

[6] A. Oustaloup, F. Levron, B. Mathieu, and F. M. Nanot, "Frequency-band complex noninteger differentiator: characterization and synthesis," *IEEE Transactions on Circuits and Systems I*, vol. 47, no. 1, pp. 25–39, 2000.

[7] T. T. Hartley and C. F. Lorenzo, "Dynamics and control of initialized fractional-order systems," *Nonlinear Dynamics*, vol. 29, no. 1-4, pp. 201–233, 2002.

[8] J. Wang, X. Xiong, and Y. Zhang, "Extending synchronization scheme to chaotic fractional-order Chen systems," *Physica A*, vol. 370, no. 2, pp. 279–285, 2006.

[9] Z. M. Odibat, N. Corson, M. A. Aziz-Alaoui, and C. Bertelle, "Synchronization of chaotic fractional-order systems via linear control," *International Journal of Bifurcation and Chaos*, vol. 20, no. 1, pp. 81–97, 2010.

[10] X.-y. Wang, Y.-j. He, and M.-j. Wang, "Chaos control of a fractional order modified coupled dynamos system," *Nonlinear Analysis: Theory, Methods & Applications*, vol. 71, no. 12, pp. 6126–6134, 2009.

[11] W.-C. Chen, "Nonlinear dynamics and chaos in a fractional-order financial system," *Chaos, Solitons and Fractals*, vol. 36, no. 5, pp. 1305–1314, 2008.

[12] A. M. Lyapunov, *The General Problem of the Stability of Motion*, Taylor & Francis, London, UK, 1992.

[13] I. S. Gradshteyn and I. M. Ryzhik, *Table of Integrals, Series, and Products*, Translation edited and with a preface by A. Jeffrey and D. Zwillinger, Academic Press, San Diego, Calif, USA, 6th edition, 2000.

[14] A. Wolf, J. B. Swift, H. L. Swinney, and J. A. Vastano, "Determining Lyapunov exponents from a time series," *Physica D*, vol. 16, no. 3, pp. 285–317, 1985.

[15] M. Caputo, "Linear models of dissipation whose Q is almost frequency independent-II," *Geophysical Journal of the Royal Astronomical Society*, vol. 13, no. 5, pp. 529–539, 1967.

[16] K. Diethelm and A. D. Freed, "The FracPECE subroutine for the numerical solution of differential equations of fractional order," in *Forschung und wissenschaftliches Rechnen*, S. Heinzel and T. Plesser, Eds., pp. 57–71, Gesellschaft für Wisseschaftliche Datenverarbeitung, Gottingen, Germany, 1998.

[17] D. Matignon, "Stability properties for generalized fractional differential systems," in *Systèmes différentiels fractionnaires*, vol. 5 of *ESAIM Proc.*, pp. 145–158, Soc. Math. Appl. Indust., Paris, France, 1998.

[18] M. Moze and J. Sabatier, "LMI tools for stability analysis of fractional systems," in *Proceedings of ASME International Design Engineering Technical Conferences & Computers and Information in Engineering Conference*, pp. 1–9, Long Beach, Calif, USA, September 2005.

[19] D. Auerbach, P. Cvitanović, J.-P. Eckmann, G. Gunaratne, and I. Procaccia, "Exploring chaotic motion through periodic orbits," *Physical Review Letters*, vol. 58, no. 23, pp. 2387–2389, 1987.

Hindawi Publishing Corporation
Mathematical Problems in Engineering
Volume 2010, Article ID 986319, 15 pages
doi:10.1155/2010/986319

Research Article

Periodic and Chaotic Motions of a Two-Bar Linkage with OPCL Controller

Qingkai Han,[1] Xueyan Zhao,[1] Xiaoguang Yang,[2] and Bangchun Wen[1]

[1] *School of Mechanical Engineering and Automation, Northeastern University, Shenyang 110004, China*
[2] *School of Mechanical Engineering, University of Birmingham, Birmingham B15 2TT, UK*

Correspondence should be addressed to Qingkai Han, qhan@mail.neu.edu.cn

Received 16 December 2009; Accepted 25 June 2010

Academic Editor: Irina N. Trendafilova

A two-bar linkage, which is described in differential dynamical equations, can perform nonlinear behaviors due to system parameters or external input. As a basic component of robot system, the investigation of its behavior can improve robot performance, control strategy, and system parameters. An open-plus-close-loop (OPCL) control method therefore is developed and applied to reveal and classify the complicated behaviors of a two-bar linkage. In this paper, the conception and stability of OPCL are addressed firstly. Then it is applied to the dynamical equations of two-bar linkage. Different motions including single-periodic, multiple-periodic, quasiperiodic, and chaotic motions are unfolded by numerical simulations when changing the controller parameters. Furthermore, the obtained chaotic motions are sorted out for qualitative and quantificational study using Lyapunov exponents and hypothetic possibilities of surrogate data method.

1. Introduction

A two-bar linkage, as a basic component of mechanical system, can perform nonlinear motions, among which chaotic motion is the most typically complicated one. It is known that the performance of such a mechanism is influenced by system parameters such as mass and friction coefficient, the initial states, and external input such as driving torque controlled by specially designed controller. Conversely, study on these motions can provide a novel way to improve system's performance, optimize structure design, and develop new control strategy.

For a two-bar linkage, the motions of its two rotating links can be single periodic, multiple periodic, quasiperiodic, and chaotic. In the past decades, many control strategies were explored to obtain certain motions of a two-bar linkage mechanism. A neural controller was employed to achieve two typical synchronous motions, that is, giant rotating motion and

small swing motion as stated in [1, 2]. A PD feedback controller to obtain chaotic motions for a two-bar linkage was reported in [3, 4]. The bifurcation characteristics of motions of a two-bar linkage were presented in [5]. The transferring process of a two-bar linkage from period-doubling bifurcation to chaotic motions was studied by changing control variables in [6]. In recent research, it is known that the open-plus-close-loop (OPCL) control strategy is powerful for complicated dynamic systems, as stated in [7, 8], which has been used for chaotic control of chaotic systems [9] and synchronous systems [10, 11]. Besides, the parametric OPCL method [12] and the nonlinear OPCL method were also applied for motion control of some dynamic systems [13].

In this paper, an OPCL controller is proposed for a two-bar linkage to achieve different motions as stated above. The dynamics of the two-bar linkage is modeled with nonlinear differential equations, followed by the Lyapunov stability analysis of the controlled system. By changing the two coefficient matrices **A** and **B** of the OPCL controller, we obtain typical motions of the two-bar linkage in numerical simulations including single-periodic, multiple-periodic, quasiperiodic, as well as chaotic motions. These different motions are described in both qualitative and quantificational ways, such as phase-space portraits, frequency spectra, Lyapunov exponents, and the hypothetic possibilities of surrogate data.

2. Dynamical Equations of a Two-Bar Linkage with OPCL Controller

2.1. A Dynamical System with an OPCL Controller

Let a typical dynamical system be as follows:

$$\ddot{\boldsymbol{\theta}} = \mathbf{F}(\boldsymbol{\theta}, \dot{\boldsymbol{\theta}}, t), \tag{2.1}$$

where $\theta = \{\theta_1, \theta_2, \ldots, \theta_n\}^T$ is the state variable, and n is the number of DOF of the system.

The given motion goal of the system is

$$\mathbf{g} = \{g_1, g_2, \ldots, g_n\}^T. \tag{2.2}$$

Define a tracking error of the two-bar linkage as

$$\mathbf{e} = \boldsymbol{\theta} - \mathbf{g} = \{\theta_1 - g_1, \theta_2 - g_2, \ldots, \theta_n - g_n\}^T = \{e_1, e_2, \ldots, e_n\}^T. \tag{2.3}$$

Equation (2.1) is linearized and expanded in the neighborhood of the goal via Taylor series and it becomes

$$\begin{aligned}\ddot{\boldsymbol{\theta}} &= \mathbf{F}(\boldsymbol{\theta}, \dot{\boldsymbol{\theta}}, t) = \mathbf{F}(\mathbf{g}+\mathbf{e}, \dot{\mathbf{g}}+\dot{\mathbf{e}}, t) = \mathbf{F}(\mathbf{g}, \dot{\mathbf{g}}, t) + \left(\frac{\partial \mathbf{F}(\mathbf{g}, \dot{\mathbf{g}}, t)}{\partial \mathbf{g}}\right)\mathbf{e} + \left(\frac{\partial \mathbf{F}(\mathbf{g}, \dot{\mathbf{g}}, t)}{\partial \dot{\mathbf{g}}}\right)\dot{\mathbf{e}} + \mathbf{o}^2(\mathbf{g}, \dot{\mathbf{g}}) \\ &= \mathbf{F}(\mathbf{g}, \dot{\mathbf{g}}, t) + \mathbf{J}_{\mathbf{g}}\mathbf{e} + \mathbf{J}_{\dot{\mathbf{g}}}\dot{\mathbf{e}} + \mathbf{o}^2(\mathbf{g}, \dot{\mathbf{g}}),\end{aligned} \tag{2.4}$$

where $\mathbf{J}_{\mathbf{g}}$ and $\mathbf{J}_{\dot{\mathbf{g}}}$ are Jacobian matrices of $\mathbf{F}(\mathbf{g}, \dot{\mathbf{g}}, t)$ with respect to $\mathbf{g}$ and $\dot{\mathbf{g}}$, respectively.

An OPCL controller for the system is designed as [8]

$$\mathbf{U} = \ddot{\mathbf{g}} - \mathbf{F}(\mathbf{g}, \dot{\mathbf{g}}, t) - \mathbf{J}_{\mathbf{g}}\mathbf{e} - \mathbf{J}_{\dot{\mathbf{g}}}\dot{\mathbf{e}} + \mathbf{A}\dot{\mathbf{e}} + \mathbf{B}\mathbf{e}, \tag{2.5}$$

where the term of $\ddot{\mathbf{g}} - \mathbf{F}(\mathbf{g}, \dot{\mathbf{g}}, t)$ is the open-loop part, and the term of $-\mathbf{J}_{\mathbf{g}}\mathbf{e} - \mathbf{J}_{\dot{\mathbf{g}}}\dot{\mathbf{e}} + \mathbf{A}\dot{\mathbf{e}} + \mathbf{B}\mathbf{e}$ is the closed-loop part. In this controller, the coefficient matrices $\mathbf{A}$ and $\mathbf{B}$ are assumed to be diagonal.

The controlled system, that is, the dynamical system with its OPCL controller, is rewritten as follows:

$$\begin{aligned}
\ddot{\boldsymbol{\theta}} &= \mathbf{F}(\boldsymbol{\theta}, \dot{\boldsymbol{\theta}}, t) + \mathbf{U} \\
&= \mathbf{F}(\mathbf{g}, \dot{\mathbf{g}}, t) + \mathbf{J}_{\mathbf{g}}\mathbf{e} + \mathbf{J}_{\dot{\mathbf{g}}}\dot{\mathbf{e}} + \mathbf{o}^2(\mathbf{g}, \dot{\mathbf{g}}) + \ddot{\mathbf{g}} - \mathbf{F}(\mathbf{g}, \dot{\mathbf{g}}, t) - \mathbf{J}_{\mathbf{g}}\mathbf{e} - \mathbf{J}_{\dot{\mathbf{g}}}\dot{\mathbf{e}} + \mathbf{A}\dot{\mathbf{e}} + \mathbf{B}\mathbf{e} \\
&= \ddot{\mathbf{g}} + \mathbf{A}\dot{\mathbf{e}} + \mathbf{B}\mathbf{e} + \mathbf{o}^2(\mathbf{g}, \dot{\mathbf{g}}).
\end{aligned} \tag{2.6}$$

The tracking error equation defined as (2.3) can be deduced as follows with omitting higher-order term:

$$\ddot{\mathbf{e}} = \ddot{\boldsymbol{\theta}} - \ddot{\mathbf{g}} = \ddot{\mathbf{g}} + \mathbf{A}\dot{\mathbf{e}} + \mathbf{B}\mathbf{e} + \mathbf{o}^2(\mathbf{g}, \dot{\mathbf{g}}) - \ddot{\mathbf{g}} = \mathbf{A}\dot{\mathbf{e}} + \mathbf{B}\mathbf{e}. \tag{2.7}$$

It is noticed that, if the controlled system of (2.6) is asymptotically stable when coefficient matrices $\mathbf{A}$ and $\mathbf{B}$ are constant and with negative real parts of eigenvalues, that is, their elements a_{ii} and b_{ii} should be negative, (2.7) can be rewritten in an expanded form as

$$\begin{Bmatrix} \ddot{e}_1 \\ \ddot{e}_2 \\ \vdots \\ \ddot{e}_n \end{Bmatrix} = \operatorname{diag}(a_{11}, a_{22}, \ldots, a_{nn}) \begin{Bmatrix} \dot{e}_1 \\ \dot{e}_2 \\ \vdots \\ \dot{e}_n \end{Bmatrix} + \operatorname{diag}(b_{11}, b_{22}, \ldots, b_{nn}) \begin{Bmatrix} e_1 \\ e_2 \\ \vdots \\ e_n \end{Bmatrix} = \begin{Bmatrix} a_{11}\dot{e}_1 + b_{11}e_1 \\ a_{22}\dot{e}_2 + b_{22}e_2 \\ \vdots \\ a_{nn}\dot{e}_n + b_{nn}e_n \end{Bmatrix}. \tag{2.8}$$

Thus, if $\ddot{e}_i = a_{ii}\dot{e}_i + b_{ii}e_i$ $(i = 1, 2, \ldots, n)$ is asymptotically stable, the system is also stable. Therefore, the aforementioned assumption is true.

A Lyapunov function V is defined as

$$V(\dot{e}_i, e_i) = \frac{b_{ii}}{2a_{ii}}e_i^2 - \frac{1}{2a_{ii}}\dot{e}_i^2 > 0. \tag{2.9}$$

Then

$$\dot{V}(\dot{e}_i, e_i) = \frac{b_{ii}e_i\dot{e}_i - \dot{e}_i\ddot{e}_i}{a_{ii}} = \frac{b_{ii}e_i\dot{e}_i - \dot{e}_i(a_{ii}\dot{e}_i + b_{ii}e_i)}{a_{ii}} = -\dot{e}_i^2 < 0. \tag{2.10}$$

According to the Lyapunov stability theory, it is proved that the error equation of (2.7) is asymptotically stable if the real parts of the eigenvalues of the coefficient matrices **A** and **B** are negative. It can be found that such an OPCL controller is reliable enough to be applied on a two-bar linkage in order to get different motions as expected and these motions are asymptotically stable.

2.2. Dynamic Equations of Two-Bar Linkage

A two-bar linkage is shown in Figure 1. Its two joints can be driven, respectively, at o_1 and o_2, so that the upper link (Link 1) and the lower link (Link 2) can rotate, respectively, around their own joints of o_1 and o_2 within the range of $[-\pi,\pi]$. The upper joint o_1 is fixed on the ground.

In coordinate system O_1xy, as shown in Figure 1, θ_1 is the rotating angle of Link 1 with respect to y-axis, and θ_2 is the rotating angle of Link 2 with respect to the centerline of Link 1. The dynamical equations of the two-bar linkage are given as follows:

$$\begin{bmatrix} M_{11} & M_{12} \\ M_{21} & M_{22} \end{bmatrix} \begin{Bmatrix} \ddot{\theta}_1 \\ \ddot{\theta}_2 \end{Bmatrix} + \begin{Bmatrix} C_1(\theta_1,\theta_2,\dot{\theta}_1,\dot{\theta}_2) \\ C_2(\theta_1,\theta_2,\dot{\theta}_1,\dot{\theta}_2) \end{Bmatrix} + \begin{Bmatrix} K_1(\theta_1,\theta_2) \\ K_2(\theta_1,\theta_2) \end{Bmatrix} = \begin{Bmatrix} \tau_1 \\ \tau_2 \end{Bmatrix}, \tag{2.11}$$

where

$$\begin{aligned} M_{11} &= m_1 d_1^2 + m_2\left(l_1^2 + d_2^2 + 2l_1 d_2 \cos\theta_2\right) + I_1 + I_2, \\ M_{21} &= m_2\left(d_2^2 + l_1 d_2 \cos\theta_2\right) + I_2, \\ M_{12} &= m_2\left(d_2^2 + l_1 d_2 \cos\theta_2\right) + I_2, \\ M_{22} &= m_2 d_2^2 + I_2, \\ C_1(\theta_1,\theta_2,\dot{\theta}_1,\dot{\theta}_2) &= -m_2 l_1 d_2 \dot{\theta}_2^2 \sin\theta_2 - 2m_2 l_1 d_2 \dot{\theta}_1 \dot{\theta}_2 \sin\theta_2, \\ C_2(\theta_1,\theta_2,\dot{\theta}_1,\dot{\theta}_2) &= m_2 l_1 d_2 \dot{\theta}_1^2 \sin\theta_2, \\ K_1(\theta_1,\theta_2) &= (m_1 d_1 + m_2 l_1) g \sin\theta_1 + m_2 d_2 g \sin(\theta_1+\theta_2), \\ K_2(\theta_1,\theta_2) &= m_2 g d_2 \sin(\theta_1+\theta_2). \end{aligned} \tag{2.12}$$

In (2.11), m_i is the mass of Link i, $i = 1,2$; I_i is the moment of inertia of Link i with respect to its mass center, $i = 1,2$; d_i is the distance between Link i and joint i, $i = 1,2$; g is the acceleration of gravity; τ_i is driving moment in joint i, $i = 1,2$.

Equation (2.11) can be rewritten in the following form, which is also in the form of (2.1):

$$\begin{Bmatrix} \ddot{\theta}_1 \\ \ddot{\theta}_2 \end{Bmatrix} = \begin{bmatrix} H_{11} & H_{12} \\ H_{21} & H_{22} \end{bmatrix} \begin{Bmatrix} R_1 \\ R_2 \end{Bmatrix}, \tag{2.13}$$

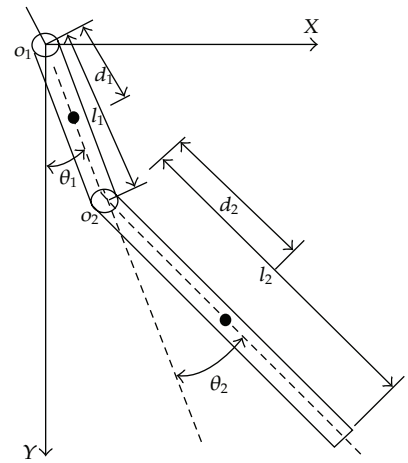

Figure 1: The schematic diagram of a two-bar linkage.

Table 1: The values of structural parameters of the two-bar linkage.

Parameter	m_1	m_2	I_1	I_2	l_{c1}	l_{c2}	l_1	l_2	g
Value	1	1	0.083	0.33	0.5	1	1	2	9.8

where

$$\begin{bmatrix} H_{11} & H_{12} \\ H_{21} & H_{22} \end{bmatrix} = \begin{bmatrix} M_{11} & M_{12} \\ M_{21} & M_{22} \end{bmatrix}^{-1}, \qquad \begin{Bmatrix} R_1 \\ R_2 \end{Bmatrix} = \begin{Bmatrix} \tau_1 - C_1(\theta_1, \theta_2, \dot{\theta}_1, \dot{\theta}_2) - K_1(\theta_1, \theta_2) \\ \tau_2 - C_2(\theta_1, \theta_2, \dot{\theta}_1, \dot{\theta}_2) - K_2(\theta_1, \theta_2) \end{Bmatrix}. \tag{2.14}$$

3. Simulations on Different Motions of Two-Bar Linkage

3.1. Conditions and Simulation Steps

In numerical simulations, the dimensionless structural parameters of the two-bar linkage are used and listed in Table 1.

The goal trajectories of the two rotating angles of the two links, θ_1 and θ_2, are designed as

$$\theta_1(t) = \sin(t), \qquad \theta_2(t) = \sin(t). \tag{3.1}$$

The simulation steps, mainly referring to the system of (2.6), are listed herein.

(1) Set the initial states and the structural parameter values of the two-bar linkage and the total number of simulation n.

(2) Set the control parameter matrices **A** and **B** of the OPCL controller of (2.5).

(3) Set the goal trajectory of (3.1).

(4) Calculate the joint angles based on (2.6) using the fourth-order Runge-Kutta method.

Table 2: The values of control parameters for different motions.

Control parameter **A**	Control parameter **B**	Motion patterns	Simulation results
$\mathbf{A} = \mathrm{diag}(-10, -10)$	$\mathbf{B} = \mathrm{diag}(-20, -20)$	Single-periodic motions	Section 3.2
$\mathbf{A} = \mathrm{diag}(-16, -16)$	$\mathbf{B} = \mathrm{diag}(-3, -9)$	Multiple-periodic motions	Section 3.3
$\mathbf{A} = \mathrm{diag}(-8, -8)$	$\mathbf{B} = \mathrm{diag}(-4, -8)$	Quasiperiodic motions	Section 3.4
$\mathbf{A} = \mathrm{diag}(-2.5, -2.5)$	$\mathbf{B} = \mathrm{diag}(-7, -7)$	Chaotic motions	Section 3.5

With different values of **A** and **B** of the OPCL controller, the two-bar linkage can achieve different motions including single-periodic, multiple-periodic, quasiperiodic, and chaotic motions. The typical parameter values of **A** and **B** and their corresponding motions are listed in Table 2. They are illustrated in the following sections, which are also listed in the fourth column of Table 2.

The obtained motions of link joints can be investigated qualitatively and quantificationally in different ways, including observation of frequency spectra and estimation of nonlinear parameters. Single- or multiamplitude lines in frequency spectra indicate a periodic motion or a multiple-periodic motion. Wide-range frequency distributions are often generated from quasiperiodic motion and chaotic motion. In Poincare mapping plots, one single point or some scattered points are often mapped by periodic motions whereas attractors with concentrated area and so-called strange attractors are mostly from either quasiperiodic or chaotic motions. In addition, for chaotic motions, there are also some critical methods to judge, for example, the well-known nonlinear parameter estimation of positive maximum Lyapunov exponent [14, 15] and the checking possibility of surrogate data method [16] which is powerful to distinguish a chaotic motion from a random one.

3.2. Single-Periodic Motions

Given $\mathbf{A} = \mathrm{diag}(-10, -10)$ and $\mathbf{B} = \mathrm{diag}(-20, -20)$, the two-bar linkage can achieve single-periodic motions. The simulated motions with initial conditions of $\theta_1 = 1$, $\dot{\theta}_1 = 0$, $\theta_2 = 1$, and $\dot{\theta}_2 = 0$ are shown in Figure 2.

In Figures 2(a) and 2(b), the motions of θ_1 and θ_2 are obviously periodic, that is, harmonic. The two phase plane portraits of θ_1 and θ_2, shown in Figures 2(c) and 2(d), are closed curves, which prove that the motions of the two-bar linkage are stable. Furthermore, the Poincare mapping portrait of each has only one isolated point, as shown in Figures 2(e) or 2(f). The frequency spectra of the two rotating angles show that there exists only single dominant frequency of about 0.16 Hz, as shown in Figures 2(g) and 2(h). The simulations can also show that periodic motions of the two-bar linkage are stable in this case.

3.3. Multiple-Periodic Motions

Given $\mathbf{A} = \mathrm{diag}(-16, -16)$ and $\mathbf{B} = \mathrm{diag}(-3, -9)$, the two-bar linkage can realize multiple-periodic motions. The typical simulated motions of the two rotating angles are shown in Figure 3 with initial conditions of $\theta_1 = 1$, $\dot{\theta}_1 = 0$, $\theta_2 = 1$, and $\dot{\theta}_2 = 0$.

In Figures 3(a) and 3(b), the motions of θ_1 and θ_2 are also periodical but with other harmonic components. The two phase plane portraits of θ_1 and θ_2, shown in Figures 3(c) and 3(d), are closed curves, which can indicate that the motions of the two-bar linkage are stable. Accordingly, the Poincare mapping portrait of each, shown in Figure 3(e) or 3(f), has some

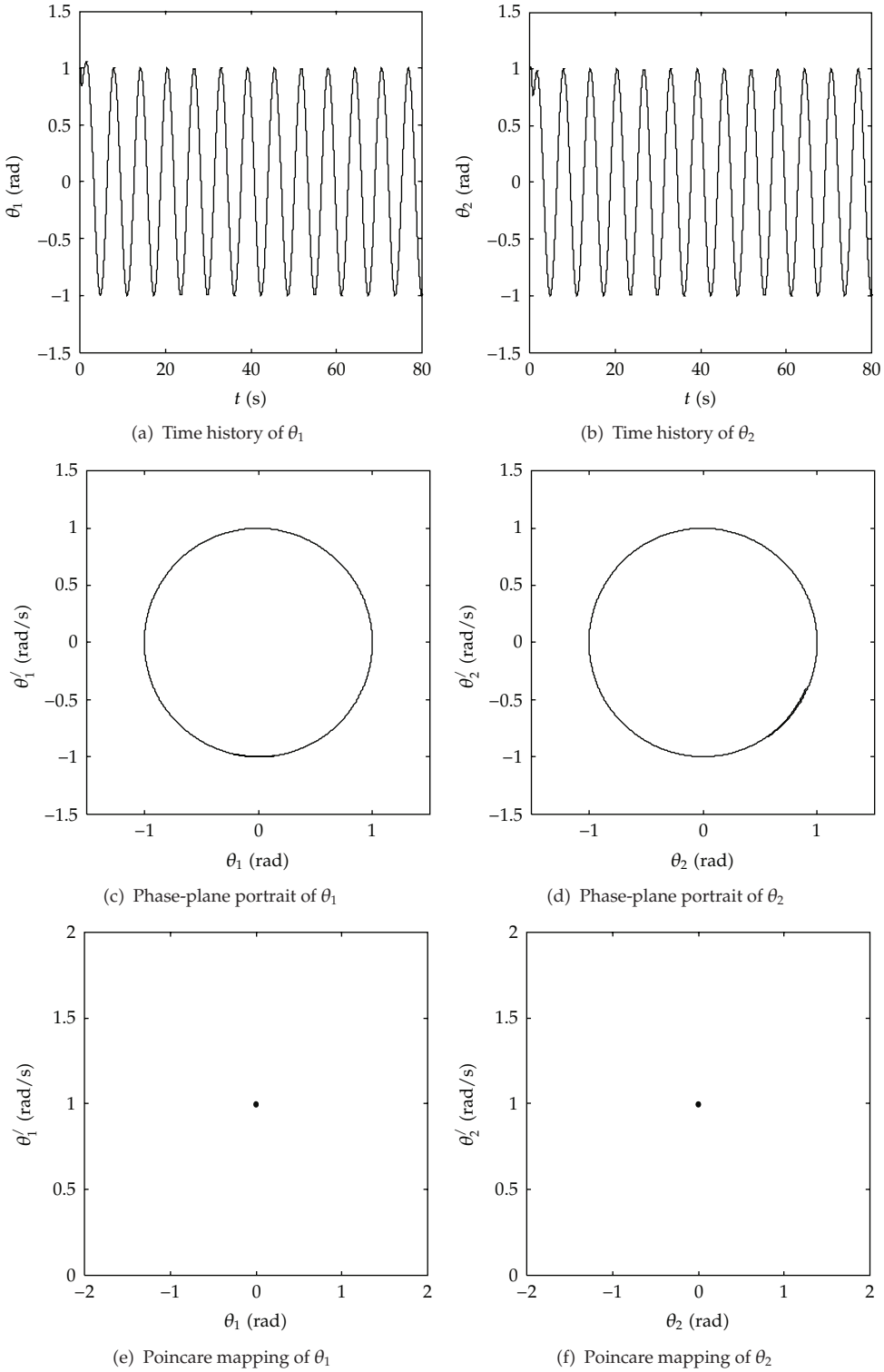

(a) Time history of θ_1

(b) Time history of θ_2

(c) Phase-plane portrait of θ_1

(d) Phase-plane portrait of θ_2

(e) Poincare mapping of θ_1

(f) Poincare mapping of θ_2

Figure 2: Continued.

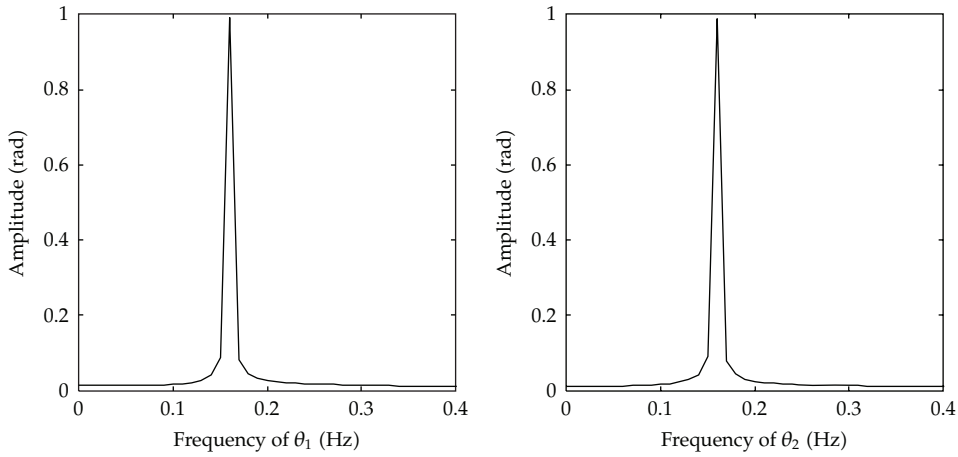

(g) Amplitude spectrum of θ_1 (h) Amplitude spectrum of θ_2

Figure 2: Single-periodic motions.

isolated points. There also exist more than two and four obvious frequency lines, as shown in Figures 3(g) and 3(h), which show that the multiperiodic motions of the two-bar linkage are stable in this case.

3.4. Quasiperiodic Motions

Given $\mathbf{A} = \mathrm{diag}(-16, -16)$ and $\mathbf{B} = \mathrm{diag}(-3, -9)$, the two-bar linkage can realize quasiperiodic motions. The simulated motions of the two joints are shown in Figure 4 with the initial conditions of $\theta_1 = 1$, $\dot{\theta}_1 = 0$, $\theta_2 = 1$, and $\dot{\theta}_2 = 0$.

It can be seen from Figure 4 that the motions of θ_1 and θ_2 are complex. Both the time histories and the phase plane portraits of θ_1 and θ_2 are difficult to distinguish the motion type rather than traditional harmonics. The Poincare mapping portrait of each, shown in Figures 4(e) and 4(f), is the concentrated stick-like area. More than six and eight frequency lines appear in the corresponding frequency spectra of θ_1 and θ_2 shown in Figures 4(g) and 4(h). The simulations can also show that the motions of the two-bar linkage are quasiperiodic in this case.

3.5. Chaotic Motions

Given $\mathbf{A} = \mathrm{diag}(-2.5, -2.5)$ and $\mathbf{B} = \mathrm{diag}(-7, -7)$, the two-bar linkage can realize chaos motions. The simulated chaotic motions are shown in Figure 5, in the case of the initial conditions of $\theta_1 = 1$, $\dot{\theta}_1 = 0$, $\theta_2 = 1$, and $\dot{\theta}_2 = 0$.

From Figures 5(a) and 5(b), the simulated responses of θ_1 and θ_2 are irregular without obvious periods. The two phase plane portraits (shown in Figures 5(c) and 5(d)) and the Poincare mapping (shown in Figures 5(e) and 5(f)) of θ_1 and θ_2 illustrate irregular shape or strange attractors. Their corresponding amplitude spectra also unfold multifrequency lines and explicit broadband ranges. According to the qualitative theory of chaos, these motions are chaotic in this case.

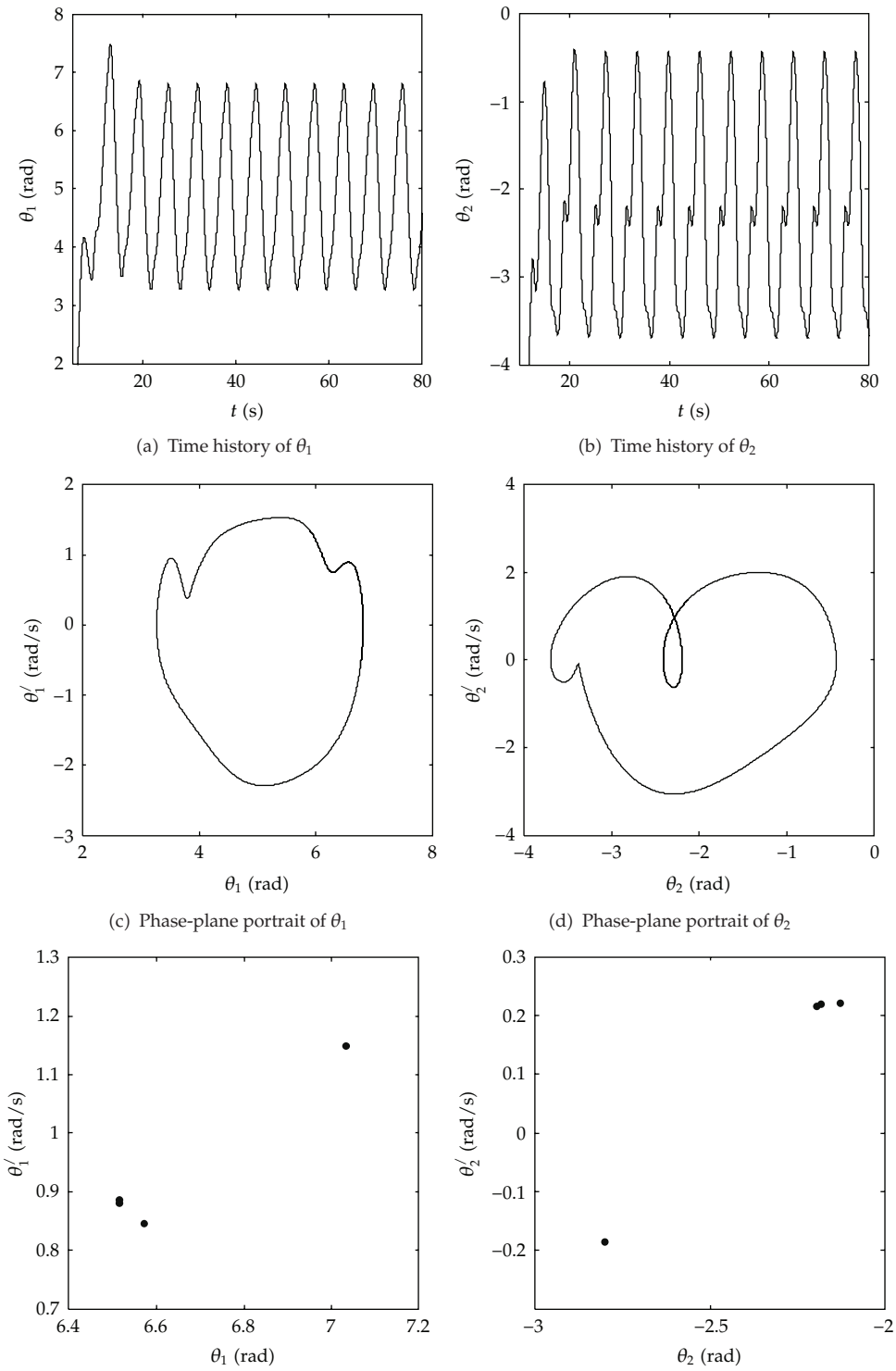

(a) Time history of θ_1

(b) Time history of θ_2

(c) Phase-plane portrait of θ_1

(d) Phase-plane portrait of θ_2

(e) Poincare mapping of θ_1

(f) Poincare mapping of θ_2

Figure 3: Continued.

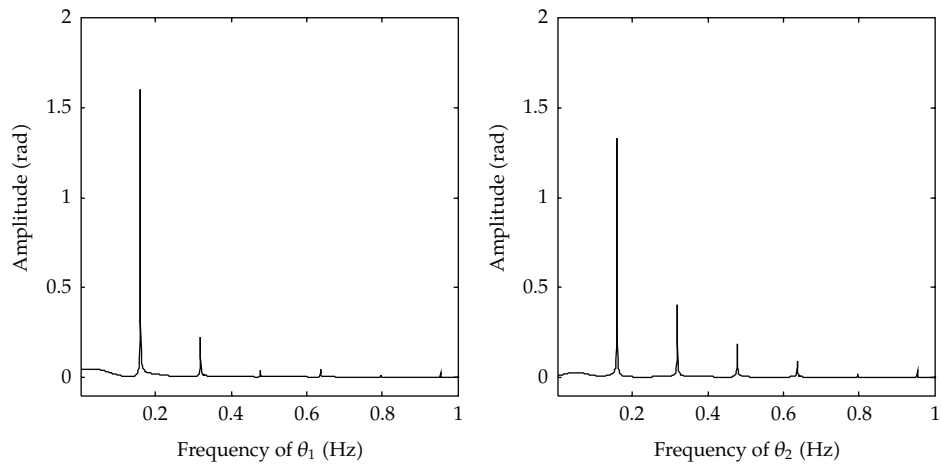

(g) Amplitude spectrum of θ_1 (h) Amplitude spectrum of θ_2

Figure 3: The simulated multiple-periodic motions.

Table 3: The Lyapunov exponents of the simulated chaotic motions of Figure 5.

	First	Second	Third	Fourth	Fifth
θ_1	0.5496	0.0960	−0.0027	−0.1008	−2.0600
θ_2	0.1431	−0.0371	−0.0787	−0.1567	−2.4240

According to the above simulation results, even for the same initial conditions, controlled behaviors vary with the parameters in the controllers. This is because the basins of entrainment, whose counterparts in maps are addressed in [9, 10], depend on the parameters of controller.

4. Discussion on the Simulated Chaotic Motions

In order to quantitatively describe the simulated chaotic motions of the two-bar linkage, Lyapunov exponent and the hypothesis possibility with surrogate data method are used based on nonlinear theory [14–17]. The first five order Lyapunov exponents of the time series of θ_1 and θ_2 are calculated according to algorithm in [14] and shown in Table 3. The calculated hypothesis possibilities with the surrogate data method [17] for the time series of θ_1 and θ_2 are shown in Table 4.

As shown in Table 3, the maximum Lyapunov exponents of the motions of angle θ_1 and θ_2 are 0.5496 and 0.1431, respectively. The positive values indicate that the motions of the two angles are chaotic.

From the calculated hypothesis possibilities with the surrogate data method for the motions of θ_1 and θ_2, that is, 6.3252×10^{-6} and 3.8644×10^{-19}, it is demonstrated that both of them are chaotic due to the checking possibility values which are smaller than .05, referring to an empirical value in [17].

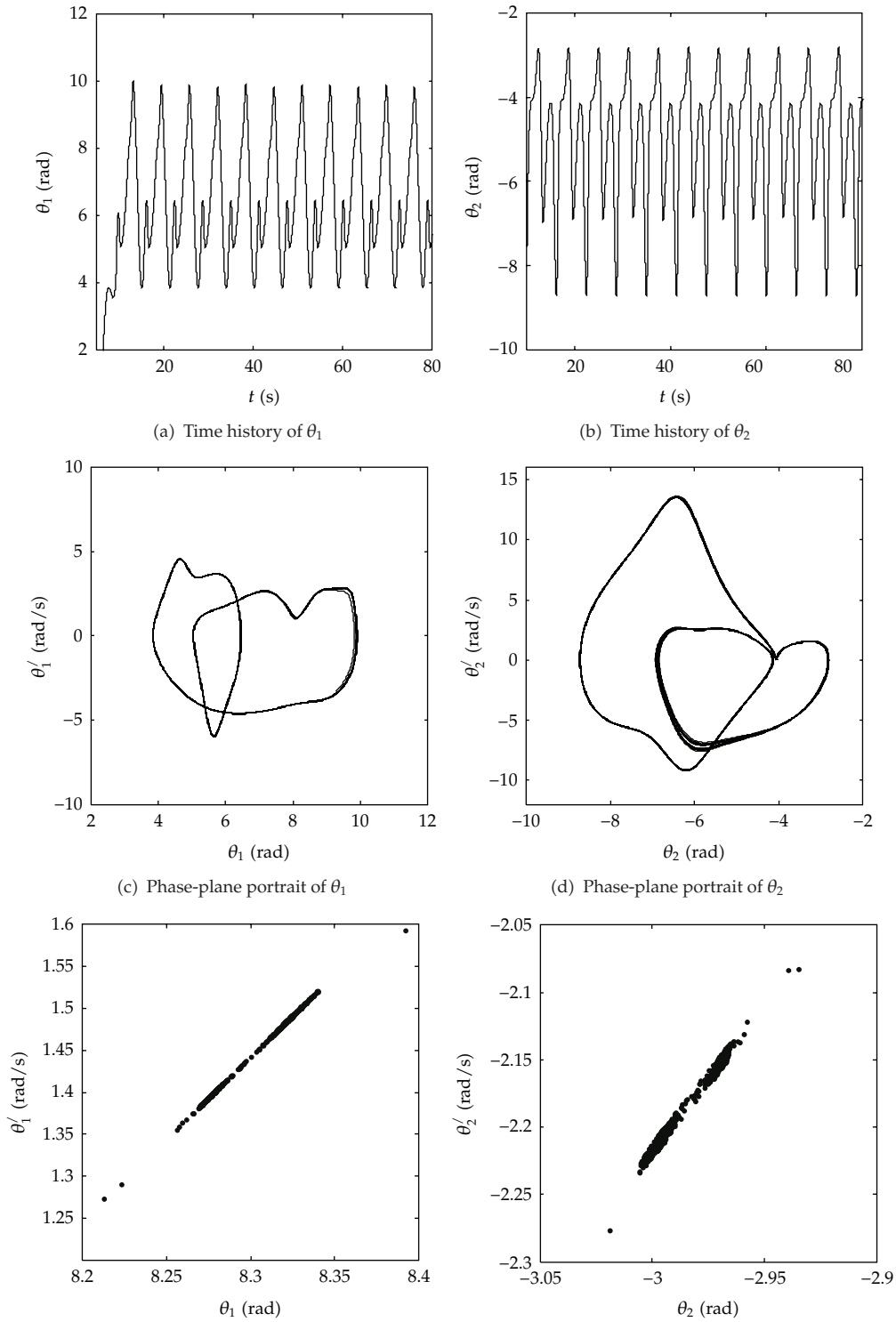

(a) Time history of θ_1

(b) Time history of θ_2

(c) Phase-plane portrait of θ_1

(d) Phase-plane portrait of θ_2

(e) Poincare mapping of θ_1

(f) Poincare mapping of θ_2

Figure 4: Continued.

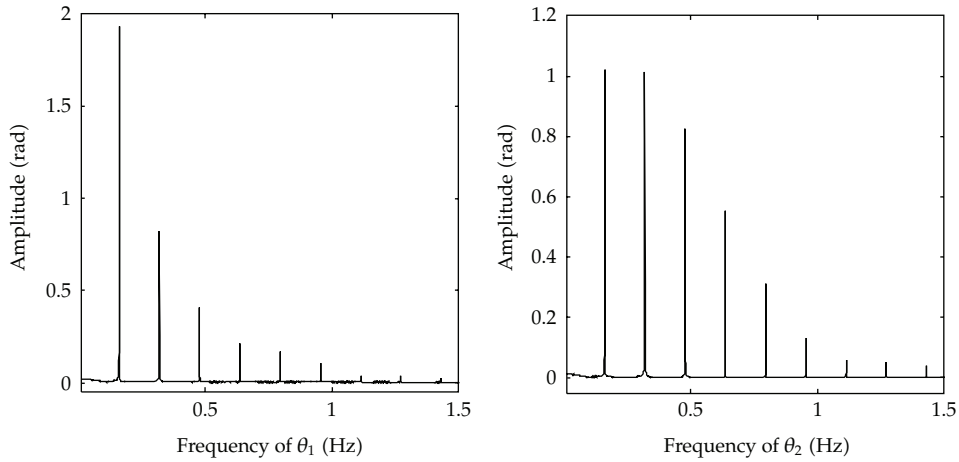

(g) Amplitude spectrum of θ_1 (h) Amplitude spectrum of θ_2

Figure 4: The simulated quasiperiodic motion.

Table 4: The calculated values with surrogate data method for chaotic motions.

	Q_D	μ_s	χ	P
θ_1	5.5241	1.5851	4.5152	6.3252×10^{-6}
θ_2	8.9715	1.5561	8.9408	3.8644×10^{-19}

5. Conclusions

In this paper, the dynamical model of a two-bar linkage with OPCL controller is proposed in order to obtain different motions. It is verified that the OPCL controlled system is asymptotically stable based on the Lyapunov theory, when the control coefficient matrices of **A** and **B** are diagonal and with negative real parts of eigenvalues. It is reliable to force a two-bar linkage to achieve different stable motions of θ_1 and θ_2.

Numeral simulations are conducted to demonstrate that the two-bar linkage can achieve single-periodic, multiple-periodic, quasiperiodic, and chaotic motions by changing the control parameters of **A** and **B** of the OPCL controller for θ_1 and θ_2 successfully. The proposed OPCL approach works on the given conditions.

Furthermore, for the simulated chaotic motions, the maximum Lyapunov exponents are positive, that is, 0.5496 and 0.1431, respectively. The calculated hypothesis possibilities of them with the surrogate data method for the same chaotic motions are 6.3252×10^{-6} and 3.8644×10^{-19}, smaller than .05.

Acknowledgment

The authors gratefully acknowledge that the work was supported by the Key Project of Science and Technology Research Funds of Chinese Ministry of Education (Grant no. 108037).

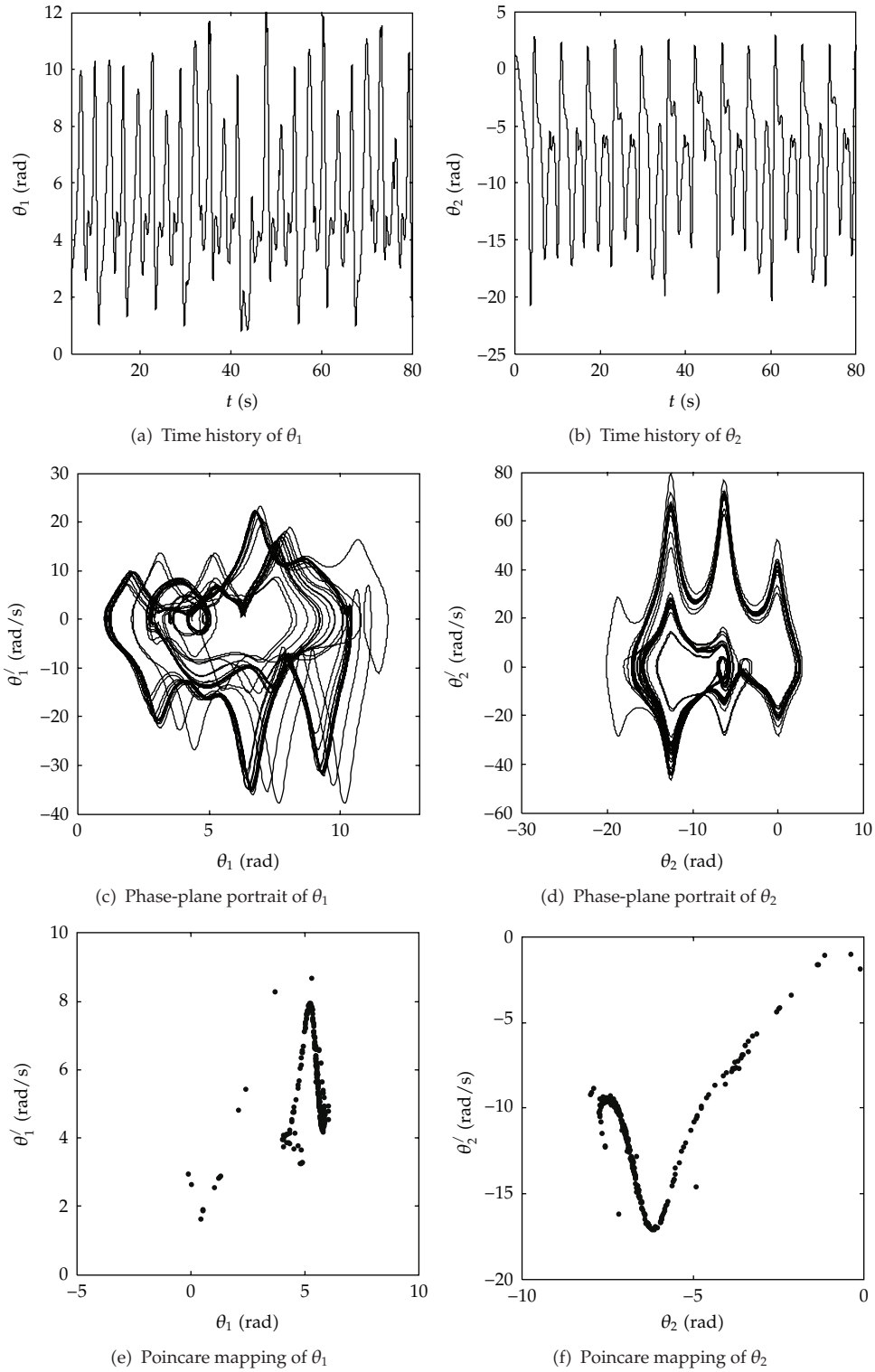

(a) Time history of θ_1

(b) Time history of θ_2

(c) Phase-plane portrait of θ_1

(d) Phase-plane portrait of θ_2

(e) Poincare mapping of θ_1

(f) Poincare mapping of θ_2

Figure 5: Continued.

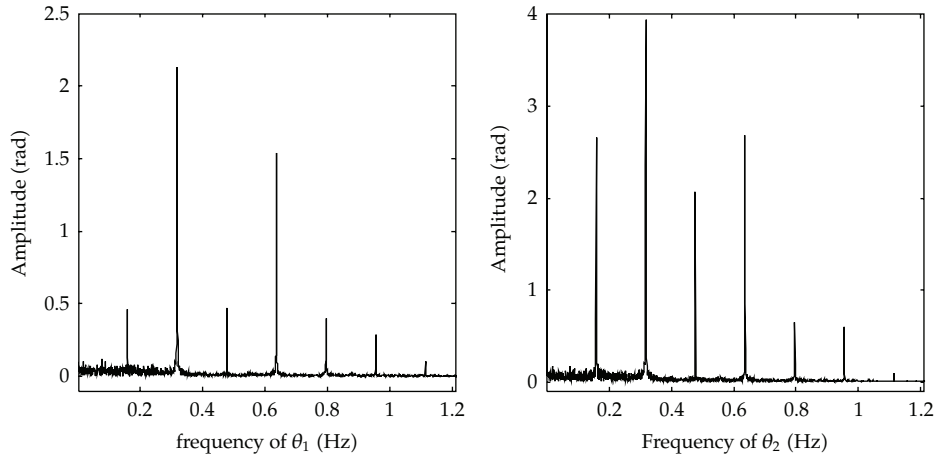

(g) Amplitude spectrum of θ_1 (h) Amplitude spectrum of θ_2

Figure 5: The simulated chaotic motions.

References

[1] K. Matsuoka, N. Ohyama, A. Watanabe, and M. Ooshima, "Control of a giant swing robot using a neural oscillator," in *Proceedings of the 1st International Conference on Natural Computation (ICNC '05)*, vol. 3611 of *Lecture Notes in Computer Science*, pp. 274–282, August 2005.

[2] Q. Han, Z. Qin, X. Yang, and B. Wen, "Rhythmic swing motions of a two-link robot with a neural controller," *International Journal of Innovative Computing, Information and Control*, vol. 3, no. 2, pp. 335–342, 2007.

[3] S. Lankalapalli and A. Ghosal, "Possible chaotic motions in a feedback controlled 2R robot," in *Proceedings of the 13th IEEE International Conference on Robotics and Automation*, pp. 1241–1246, IEEE, April 1996.

[4] A. S. Ravishankar and A. Ghosal, "Nonlinear dynamics and chaotic motions in feedback-controlled two- and three-degree-of-freedom robots," *International Journal of Robotics Research*, vol. 18, no. 1, pp. 93–108, 1999.

[5] F. Verduzco and J. Alvarez, "Bifurcation analysis of A 2-DOF robot manipulator driven by constant torques," *International Journal of Bifurcation and Chaos in Applied Sciences and Engineering*, vol. 9, no. 4, pp. 617–627, 1999.

[6] K. Li, L. Li, and Y. Chen, "Chaotic motion of a planar 2-dof robot," *Machine*, vol. 29, no. 1, pp. 6–8, 2002 (Chinese).

[7] E. A. Jackson and I. Grosu, "An open-plus-closed-loop (OPCL) control of complex dynamic systems," *Physica D*, vol. 85, no. 1-2, pp. 1–9, 1995.

[8] L.-Q. Chen and Y.-Z. Liu, "A modified open-plus-closed-loop approach to control chaos in nonlinear oscillations," *Physics Letters A*, vol. 245, no. 1-2, pp. 87–90, 1998.

[9] L.-Q. Chen, "An open-plus-closed-loop control for discrete chaos and hyperchaos," *Physics Letters A*, vol. 281, no. 5-6, pp. 327–333, 2001.

[10] L.-Q. Chen and Y.-Z. Liu, "An open-plus-closed-loop approach to synchronization of chaotic and hyperchaotic maps," *International Journal of Bifurcation and Chaos*, vol. 12, no. 5, pp. 1219–1225, 2002.

[11] Q.-K. Han, X.-Y. Zhao, and B.-C. Wen, "Synchronization motions of a two-link mechanism with an improved OPCL method," *Applied Mathematics and Mechanics*, vol. 29, no. 12, pp. 1561–1568, 2008.

[12] L.-Q. Chen, "The parametric open-plus-closed-loop control of chaotic maps and its robustness," *Chaos, Solitons and Fractals*, vol. 21, no. 1, pp. 113–118, 2004.

[13] Y.-C. Tian, M. O. Tadé, and J. Tang, "Nonlinear open-plus-closed-loop (NOPCL) control of dynamic systems," *Chaos, solitons and fractals*, vol. 11, no. 7, pp. 1029–1035, 2000.

[14] A. Wolf, J. B. Swift, H. L. Swinney, and J. A. Vastano, "Determining Lyapunov exponents from a time series," *Physica D*, vol. 16, no. 3, pp. 285–317, 1985.

[15] A. A. Tsonis and J. B. Elsner, "Nonlinear prediction as a way of distinguishing chaos from random fractal sequences," *Nature*, vol. 358, no. 6383, pp. 217–220, 1992.
[16] M. T. Rosenstein, J. J. Collins, and C. J. De Luca, "A practical method for calculating largest Lyapunov exponents from small data sets," *Physica D*, vol. 65, no. 1-2, pp. 117–134, 1993.
[17] J. Theiler, S. Eubank, A. Longtin, B. Galdrikian, and J. Doyne Farmer, "Testing for nonlinearity in time series: the method of surrogate data," *Physica D*, vol. 58, no. 1–4, pp. 77–94, 1992.

Hindawi Publishing Corporation
Mathematical Problems in Engineering
Volume 2010, Article ID 294102, 10 pages
doi:10.1155/2010/294102

Research Article

Design Optimization of a Natural Gas Substation with Intensification of the Energy Cycle

Arcangelo Pellegrino and Francesco Villecco

Department of Mechanical Engineering, Faculty of Engineering, University of Salerno, Via Ponte Don Melillo, 84084 Fisciano, Italy

Correspondence should be addressed to Francesco Villecco, fvillecco@unisa.it

Received 9 March 2010; Accepted 3 September 2010

Academic Editor: Carlo Cattani

Natural gas is currently the natural substitute of petroleum as an energy source, since the foreseen ending up of this latter in the next decades. As a matter of fact, natural gas is easier to handle, less dangerous to be transported, somehow environmentally more friendly. The gas ducts operate with large flow rates over very long distances at high pressures, which are usually lowered in proximity of the final substations by lamination valves which, in fact, dissipate energy. However, a careful management of the pressure reduction may allow an energy recovery while using the gas expansion to operate a turbine. In this case, gas must be preheated to compensate for the energy required by the expansion. A proper control of all the parameters involved becomes crucial to an intelligent use of these resources. In this paper, the possibility of using a pre-heating system has been examined as a way to intensify the energy cycle in an expansion substation of the city gas network. Fuzzy logic has been used to optimize the natural gas expansion in a turbine to produce electrical energy. A fuzzy system has been designed and realized to control the whole process of gas expansion, from the gas pre-heating to the pressure reduction. The system operates over the whole year, accounting for the pressure, temperature, and gas flow rate variations experienced in the gas line. The exit values of the latter and the inlet value of the gas pressure are selected as input variables, being the output variable the temperature of the pre-heating water at the heat exchanger inlet.

1. Introduction: The Quest for Energy

It is a fact that the world has changed in the last 20 years. In the 70s and 80s, industries were somehow coal and nuclear oriented, the greenhouse effect was not scaring the earth, and Chernobyl disaster was far on the horizon. Today, petroleum is claimed to be over, biomasses are then particularly considered, wind-operated generators are more and more installed [1]. In this new scenery, every possibility of saving energy, either improving a process efficiency or reusing the waste, is appreciated.

Natural gas ducts—substations system can be seen as the current largest network of energy microgenerators in the world. It reaches almost every place, is easy to operate, does not need specialized personnel, and it is relatively safe.

Gas is transported by the pressure gradient necessary to accomplish the equation energy. Detailed first principles modelling based upon fundamental mass, momentum, and energy balances is reported by Fawke [2] and Schobeiri [3]. At the substations where the gas is withdrawn, pressure has to be decreased. This is usually done by simply dissipating the pressure energy in a lamination valve. Gas pressure and, consequently, temperature decrease as an effect of the isoenthalpic expansion, according to the Joule-Thomson coefficient value. Sometimes, gas needs to be preheated to compensate for the temperature decrease occurring [4, 5].

Apparently, there is no way to improve the process, nor to recover anything out of it. However, at a more accurate analysis of the energy balance, something can be done. Actually, velocity of the expanded gas increases during lamination, and turbulence phenomena occur. Part of the energy is thus lost in a useless noisy flux. On the other hand, pressures in the ducts range from 70 to 40 bars, down to 20 in the local distribution, whereas 5 bars are typically requested as a final value in a city network. Variability of pressure associates with similar behaviours of gas temperature and flow rate. All of them change either during the day and in the course of the whole year, without any reproducibility.

Note that the gas final pressure has to be kept stable and the final temperature under 5 centigrades not to have formation of methane hydrates, whatever the temperature, pressure, and flow rate of the inlet gas. An intelligent design of the plant expansion process used to drive a turbine and to produce electrical energy could lead to an energy recovery as large as 15% without interfering with the required stability of the exit pressure [6–15].

It is aim of this paper to design the optimal gas expansion process to achieve the objective of transforming a gas substation in an energy generator.

2. The Real Case

The gas substation selected for this paper has to respect some crucial requirements to be eligible for a case study.

(1) The power production has to be at least as large as 50 kW.

(2) The pre-heater system available has to be large enough to support the pretreatment necessary for the gas turboexpansion.

(3) The substation itself has to be large enough to allow the installation of a turbine.

(4) The access points of the National Electricity Board where to send the electrical energy produced have to be near.

Based on data available from the Gas Company, the substation named F in the list supplied by the Company was selected, serving the east side of the city.

For this substation, the gas flow rate ranges during the day as shown in Figures 1 and 2, for a summer and a winter day, respectively. The data point out that differences of an order of magnitude are experienced during the year. As a matter of fact, the gas flow rate ranges in a year from about 400 to 12000 m^3h^{-1}.

The behaviour of gas temperature is not different, even if on a less dramatic range of variability.

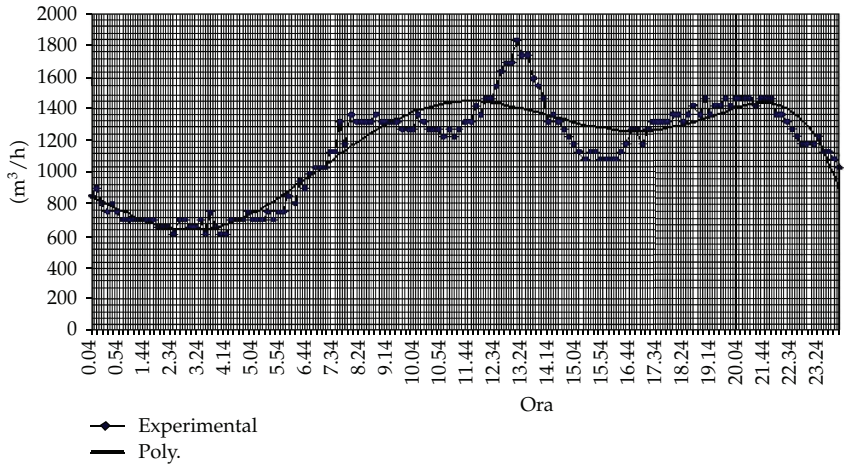

Figure 1: Variability of gas flow rate during a day in summer.

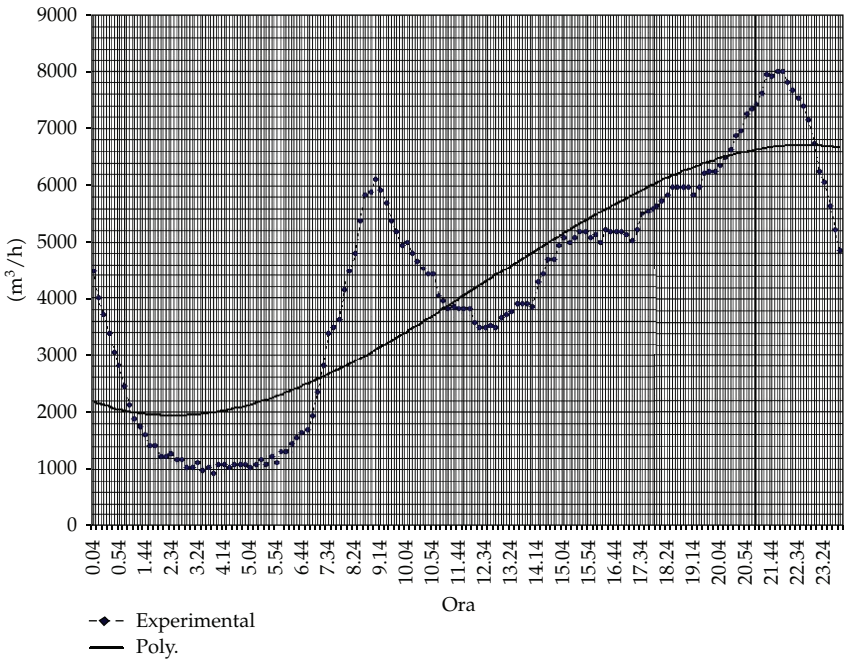

Figure 2: Variability of gas flow rate during a day in winter.

Moreover, in the case study input pressure of natural gas, far from being constant at an expected value of 24 bar, ranges from 22 to 25 bar, whereas input temperature varies between 5 and 30°C .

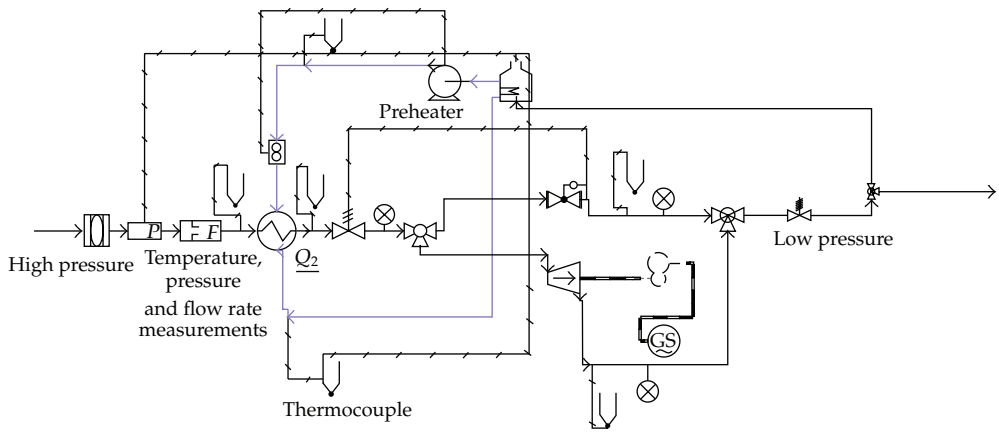

Figure 3: Flow diagram of the natural gas substation.

3. The Approach to the Optimal Design

In this paper an analysis of the city gas distribution net together with data of operative conditions of the substations is used to investigate the thermodynamic and economic feasibility of applying a turboexpander for energy recovery by designing and building-up a controlled gas substation. The control system had to ensure that both temperature and pressure of natural gas at the exit are constant whatever the pressures and temperatures at the inlet and whatever the gas flow rate. An intelligent connection between heaters and input values of gas temperature, pressure, and flow rates will save energy [16].

4. The Plant and the Alternatives

The original scheme of the expansion section of the plant before the intervention described in the present paper consisted only of a lamination valve. This is the most frequent arrangement as is the less expensive. However, no energy recovery is planned nor gas temperature or pressure control is installed. This, as above reported, may even lead to methane hydrates formation.

The first alternative examined in this paper is based on the use of a pre-heater section in the gas line. On the scale pan are put the pre-heater cost, the relevant operating costs, the money-saving deriving from the gas better quality due to the absence of methane hydrates.

Finally, the introduction of a turbine to recover energy during the gas expansion and of a fuzzy controller to manage the gas pre-heating before expansion certainly increases the fixed costs, especially when compared to the investments for the typical scale of the gas substations, but allows a significant saving in the plant operating costs, even leading to the sale of the recovered energy.

5. The Plant

The plant in its final arrangement is sketched in Figure 3. The pre-heater section of the plant includes an industrial boiler that burns natural gas from the station and provides hot water at a temperature based on the pressure drop caused by the gas lamination.

A control system has to be designed for the plant, as it is necessary to easy decide whether to increase or decrease the pre-heating temperature and of what amount, to have the maximum electricity production with a minimum output temperature of 5°C and a maximum output pressure of 5 bars. This will also guarantee the electrical energy production stability

In conventional applications, operative variables depend on mathematical models related to gas combustion, heat transfer, and turbine fluid dynamics, that are all fairly complicated, especially in systems where a large number of parameters is either hidden or has to be accounted for. The ability to use simple linguistic variables rather than numerical variables in order to work more easily with systems too complex for mathematical modeling is the main objective of fuzzy logic-based controllers.

6. The Fuzzy System

It is a while that fuzzy logic is successfully used in the process industry. Whatever the reason, either its ability to model imprecise and subjective notions or the easiness of building up controllers that do not need mathematical modeling of the process, fuzzy logic is nowadays applied in virtually all sectors of industry and science in the western world.

The basis of a fuzzy logic controller is the representation of linguistic descriptions as membership functions indicating the degree to which a value belongs to the class labeled by linguistic description. In fuzzy logic control algorithms, degree of membership serves as inputs. The determination of appropriate degree of membership is the part of the design process. Once the membership functions are defined, the actual input values are transformed to degree of membership (varying from 0 to 1) of linguistic descriptors. This process is called fuzzification. The resulting fuzzified data is passed through an inference mechanism that contains the rules for the output. After the rules are applied, the combined effect of all rules will be evaluated according to a proper weightage for each rule. The weightage will be generally used to fine-tune the fuzzy controller and this process is defuzzification [17–19].

Examples of applications can be found in literature, ranging from aircraft engine control to locomotive wheel sleep control, steam turbine start-up, SEP (symbol error probability) of HS-MRC (hybrid selection/maximal-ratio combining power supplier controller), up to domestic or industrial scale microwave ovens. Fuzzy logic is even used to the fed-batch cultures of microorganisms and for the on-line control of feeding rate of substrate [20].

Gas turbines controlled via neurofuzzy systems have been used in biomasses-based electric power plants and adaptive fuzzy logic controller developed for turbine generator systems [5].

In the fuzzy system designed for this plant, as input variables gas temperature, pressure, and flow rate will be considered, whereas the output variable will be the pre-heating water temperature T^* at the heat exchanger inlet, that will range from 75 to 95°C. The controlled parameters are the output temperature T, the gas flow rate Q, and the gas input pressure P.

As for any fuzzy control, the rules adopted are logical rather than mathematical. Seven labels have been used to define the conditions of the system. The state of a variable is described as follows:

(i) NL : negative large,

(ii) NM: negative medium,

(iii) NS: negative small,

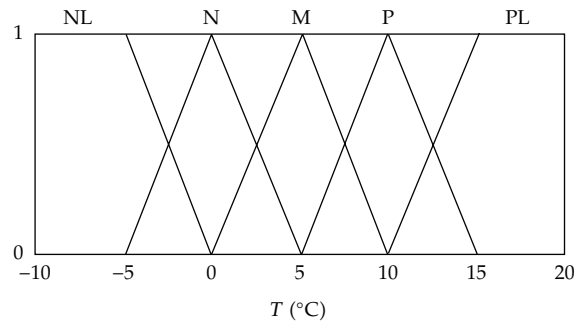

Figure 4: Membership functions of variable T (°C).

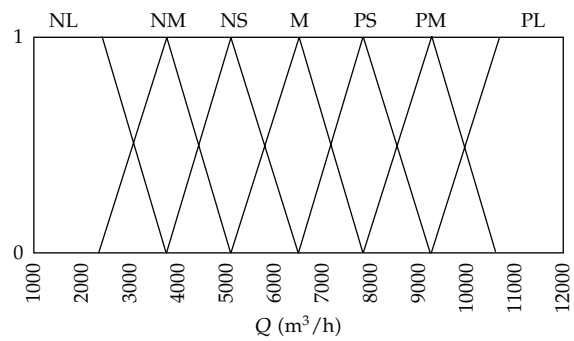

Figure 5: Membership functions of variable Q (m^3/h).

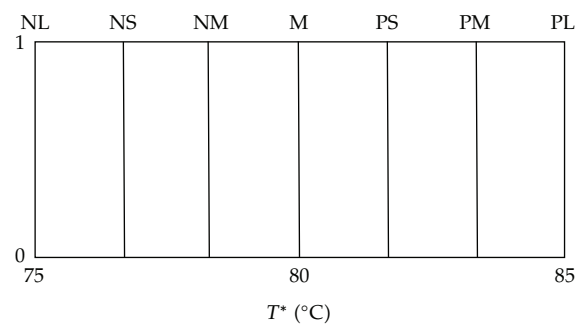

Figure 6: Membership functions of variable T^* (°C).

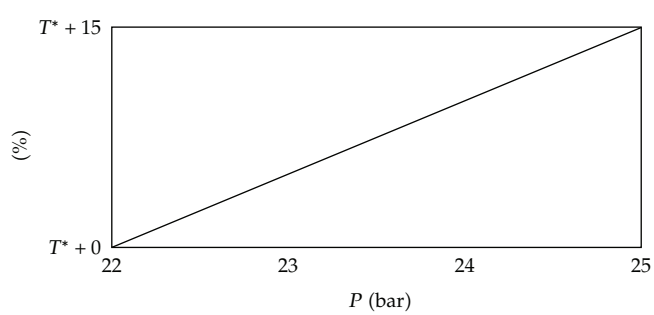

Figure 7: Correction of range of T^* as function of P (bar).

Table 1: FAM (Fuzzy Associative Memory) matrix.

T				Q			
	NL	**NM**	**NS**	**M**	**PS**	**PM**	**PL**
NL	PS	PS	PM	PM	PM	PL	PL
N	M	M	PS	PS	PS	PS	PM
M	NS	M	M	M	M	PS	PS
P	NM	NM	NM	NS	NS	M	M
PL	NL	NL	NM	NM	NS	NS	NS

(iv) M : medium,

(v) PS: positive small,

(vi) PM: positive medium,

(vii) PL: positive large.

A triangular membership function (MF) has been used for the input variables, having experienced that this simple shape is satisfyingly accurate. The membership function of the output variable is a singleton, that is, a series of unit pulses, since in this way the center of gravity can be easier calculated when defuzzyfying [21, 22].

The input and output variation intervals are.

(i) $10° < T < 20°$ [°C];

(ii) $1000 < Q < 12000$ [m^3/h];

(iii) $22 < P < 25$ [bar];

(iv) $75° < T^* < 95°$ [°C].

Seven membership functions are assigned to Q and T^*. Five functions are instead assigned to T. Functions overlap is necessary to let the system to have a fuzzy rather than a boolean behavior. Figures 4, 5, and 6 report the membership functions of T, Q, and T^*, respectively.

In Figure 7 is reported the correction of the range of variability of temperature as a function of inlet gas pressure P. As P changes, the temperature range, that is, the subject of the fuzzy membership functions, has to be modified to best accomplish the energy balance.

In this system, 7 MFs have been adopted for Q and 5 MFs for T. We could thus have 35 input combinations and 245 different rules, using 7 output functions. Actually, the number of necessary rules is quite smaller. In our case, an FAM (Fuzzy Associative Memory) matrix has been used. In the matrix, first line and first column report the input variables, whereas the output variable is derived according to the rule

$$T \text{ and } Q \longrightarrow T^* \tag{6.1}$$

The matrix is reported in the above table.

7. Results

As previously pointed out, the gas outlet temperature is the crucial variable and the one monitored as marker of the efficacy of the control system designed. It has to be outlined that

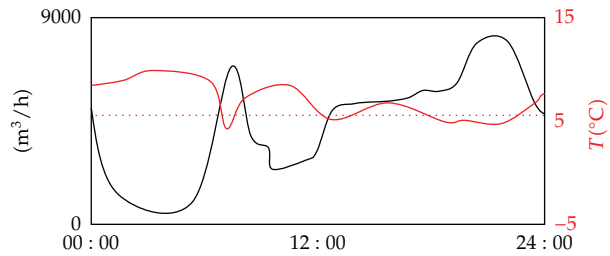

Figure 8: Variability of gas flow rate (black line) and temperature (red line) in a winter day.

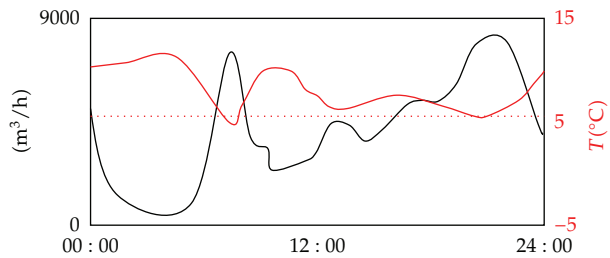

Figure 9: Variability of gas flow rate (black line) and temperature (red line) in a winter day with the pre-heating system.

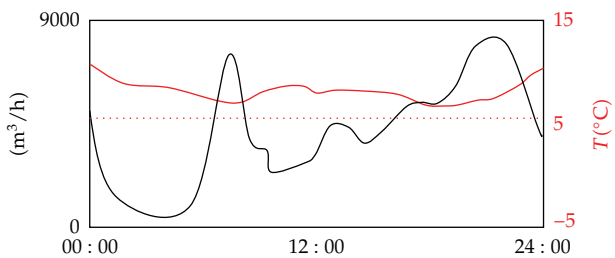

Figure 10: Variability of gas flow rate (black line) and temperature (red line) in a winter day with the pre-heating system and a fuzzy control.

each of the parameters considered concurs to complicate the whole picture: variability of the gas flow rate interferes with the plant energy balance as much as environmental conditions and adduction gas ducts temperature themselves.

Figure 8 shows that the outlet temperature continuously changes during a winter day when no control systems are applied to the plant. Figures 9 and 10 show the effect of introducing the pre-heating system and eventually the fuzzy control to manage the gas expansion.

It is remarkable the effect of the optimization performed in smoothing the outlet gas temperature, that tends to flatten on the 5°C value desired.

Note that the more the outlet temperature approaches 5°C from the above, the larger is the amount of energy saved, the better is the efficiency of the fuzzy control realized.

8. Conclusions

The radial flow turbine selected for this work can handle a large flow rate variability at variable inlet gas temperature at an affordable price. The investment costs of the fuzzy system are negligible, being basically related to the measurement equipments, whereas the energy recovery is larger than 15%. The fuzzy control system also helps in decreasing the maintenance costs of about 15% and allows to save up to 3 T.E.P. in a year, producing up to 450000 kWh. The payback of the investment cost is reached in less than 8 years, against an expected 25 years life-cycle. The turboexpander driven by fuzzy logic as above allows to recover and to sell to the National Electricity Board up to 450,000 kWh per year.

When considering that the size of the substation selected for this case study is considered representative of the Italian gas net, the existing network of gas distribution substations once fuzzy controlled becomes a network of electricity generators of 200 to 500 kW.

Combined use of fuzzy logic and neural networks would lead to autoadaptive intelligent systems, which actually appear to be the future.

References

[1] R. Shinnar and F. Citro, "A road map to U.S. decarbonization," *Science*, vol. 313, no. 5791, pp. 1243–1244, 2006.

[2] A. J. Fawke, H. I. H. Saravanamuttoo, and M. Holmes, "Experimental verification of a digital computer simulation method for predicting gas turbine dynamic behaviour," *Proceedings of the Institution of Mechanical Engineers*, vol. 186, no. 27, pp. 323–329, 1972.

[3] T. Schobeiri, "Digital computer simulation of the dynamic operating behaviour of gas turbines," *Brown Boveri Review*, vol. 74, no. 3, pp. 161–173, 1987.

[4] M. Lown, E. Swidenbank, and B. W. Hogg, "Adaptive fuzzy logic control of a turbine generator system," *IEEE Transactions on Energy Conversion*, vol. 12, no. 4, pp. 394–399, 1997.

[5] F. Jurado, M. Ortega, A. Cano, and J. Carpio, "Neuro-fuzzy controller for gas turbine in biomass-based electric power plant," *Electric Power Systems Research*, vol. 60, no. 3, pp. 123–135, 2002.

[6] A. Hussain and H. Seifi, "Dynamic modeling of a single shaft gas turbine," in *Proceedings of the IFAC Symposium on Control of Power Plants and Power Systems*, IFAC Symposia Series, pp. 43–48, Pergamon Press, Munich, Germany, March 1992.

[7] W. W. Hung, "Dynamic simulation of gas-turbine generating unit," *IEE Proceedings C: Generation Transmission and Distribution*, vol. 138, no. 4, pp. 342–350, 1991.

[8] W. I. Rowen, "Simplified mathematical representations of heavy duty gas turbines," *Journal of Engineering for Power*, vol. 105, no. 4, pp. 865–869, 1983.

[9] A. Cleveland, "Power Generation with Turbo Expanders," ASME 90-DT-2, 1992.

[10] R.A.C.I. s.r.l., Settore Progettazione, "Schede Tecniche-Prestazioni Termodinamiche di impianti di turboespansione," ST 1042200, 2002.

[11] H. E. RohliK, "Analytical determination of radial inflow turbine geometry for maximum efficiency," Tech. Rep. TN D-4384, NASA, 1968.

[12] S. K. Ghosh, "Computation of velocity, pressure and temperature profiles in a cryogenic turboexpander," in *Proceedings of the 18th National & 7th ISHMT-ASME Heat and Mass Transfer Conference*, IIT Guwahati, January 2006.

[13] "Application of turboexpanders for pressure letdown energy recovery in the natural gas industry," American Gas Association, 1987.

[14] M. P. Boyce, *Gas Turbine Engineering Handbook*, Gulf Professional, Butterworth, Malaysia, 2nd edition, 2002.

[15] L. C. Kun, "Expansion turbine and refrigeration for gas separation and liquefaction," *Advances in Cryogenic Engineering*, vol. 33, pp. 963–973, 1988.

[16] O. E. Balje, *Turbomachines—A Guide to Design, Selection and Theory*, John Wiley & Sons, New York, NY, USA, 1981.

[17] B. Kosko, *Il Fuzzy Pensiero. Teoria e Applicazioni della Logica Fuzzy*, Baldini e Castoldi Milano, 2002.

[18] S. Cammarata, *Sistemi a logica fuzzy—come rendere intelligenti le macchine*, Etas Libri, 2nd edition, 1997.
[19] H. J. Zimmermann, *Fuzzy Set Theory and Its Applications*, Kluver Academic Publishers, Boston, Mass, USA, 2009.
[20] P. P. Bonissone, V. Badami, K. H. Chiang, P. S. Khedkar, K. W. Marcelle, and M. J. Schutten, "Industrial applications of fuzzy logic at general electric," *Proceedings of the IEEE*, vol. 83, no. 3, pp. 450–465, 1995.
[21] M. Pappalardo, A. Pellegrino, M. d'Amore, and F. Villecco, "Design of a fuzzy control for a microwave monomode cavity to soot trap filter regeneration," in *Intelligence in a Small World—Nanomaterials for the 21st Century*, CRC- Press, Boca Raton, Fla, USA, 2003.
[22] M. Pappalardo, A. Pellegrino, R. Carmando, F. Villecco, R. Ametrano, and M. d'Amore, "A fuzzy controller for the indoor atmosphere of a pharmaceutical plant," in *Proceedings of the 5th International Conference on Intelligent Processing and Manufacturing of Materials*, July 2005.

Hindawi Publishing Corporation
Mathematical Problems in Engineering
Volume 2010, Article ID 124148, 13 pages
doi:10.1155/2010/124148

Research Article

Influence of Asymmetric Mesh Stiffness on Dynamics of Spiral Bevel Gear Transmission System

Li Yinong, Li Guiyan, and Zheng Ling

The State Key Laboratory of Mechanical Transmission, Chongqing University, Chongqing 400044, China

Correspondence should be addressed to Li Yinong, ynli@cqu.edu.cn

Received 13 January 2010; Accepted 26 March 2010

Academic Editor: Carlo Cattani

An 8-DOF (degrees-of-freedom) nonlinear dynamic model of a spiral bevel gear pair which involves time-varying mesh stiffness, transmission error, backlash, and asymmetric mesh stiffness is established. The effect of the asymmetric mesh stiffness on vibration of spiral bevel gear transmission system is studied deliberately with numerical method. The results show that the mesh stiffness of drive side has more effect on dynamic response than those of the coast side. Only double-sided impact region is affected considerably by mesh stiffness of coast side while single-sided impact and no-impact regions are unchanged. In addition, the increase in the mesh stiffness of drive side tends to worsen the dynamic response of the transmission system especially for light-load case.

1. Introduction

Spiral bevel gear has been widely used in many power transmission systems due to its considerable technical advantages. Owing to backlash, time-varying mesh stiffness, and many other nonlinear factors, gear transmission system produces complex dynamic behavior which has aroused wide attention from scholars around the world. Since the first gear dynamic model was proposed by Tuplin in 1950s, considerable progress has been made in parallel axis gear dynamics [1–4]. However, the dynamics of a spiral bevel-geared system is lack of investigations when compared with the parallel system. Liangyu et al. [5] derived a twelve-degrees-of-freedom vibration model of a pair of Spiral bevel gears. Meanwhile an 8-DOF and a 2-DOF simplified model and a modified model with mesh error are given, which provides a theoretical foundation for studying dynamic response

of Spiral bevel gears. Gosselin et al. [6] proposed a general formula and applied it to analyze the load distribution and transmission error of spiral bevel gear pair and hypoid gear pair. Bibel et al. [7] studied the three-dimensional stress of a spiral bevel gear pair with finite element method. Fujii et al. [8] carried out analysis of dynamic behaviors of straight bevel-geared shaft supported on tapered roller and angular contact bearings, respectively, and then they measured the torsional and bending vibrations of the geared rotor and the vibrating displacement in the axial direction under a constant transmitted torque by using straight and skew bevel gears with a power circulating-type bevel-gear testing machine [9]. Xu et al. [10] analyzed the coupled lateral-torsional vibration behavior of the rotors with the engagement of spiral bevel gears by means of the transfer matrix method, which neglected the relationships of the generalized displacements between two bevel gears. Donley et al. [11] developed a dynamic model of a hypoid gear set for use infinite element analysis of gearing systems. In their gear mesh model, the mesh point and line-of-action are time invariant. Fang [12] developed a lumped parameter vibration model of a spiral bevel gear transmission to compute dynamic load and gear response. His mesh model is based on the classical gear mesh force equations that produce a simple unidirectional gear-mesh-coupling vector. Cheng and Lim [13] proposed a hypoid gear dynamic model based on exact gear geometry for analyzing gear mesh mechanism and applied the corresponding linear dynamic model to study the hypoid gear pair dynamics with transmission error excitation. In recent years, spiral bevel gear dynamics has gained extensive attention from many scholars and many relevant investigations have been published [14–17].

Unlike spur or helical gears, the mesh couplings in spiral bevel gears are not symmetric, due to the complex curvilinear features of the spiral bevel gear tooth geometry. That is, their mesh parameters for the drive and coast sides are very different. Most of the previous studies on the dynamics of spiral bevel gear transmissions focus on backlash and time-varying mesh stiffness, assuming symmetric mesh parameters for simplicity.

In this paper, we focus mainly on the dynamics of high-speed, precision spiral bevel gear pairs often used in automotive and aerospace power transmission systems. An 8-DOF nonlinear dynamic model of a spiral bevel gear pair which involves time-varying mesh stiffness, transmission error, backlash, and mesh stiffness asymmetry is proposed. Compared to mesh stiffness, the mesh damping with time-varying and asymmetric has less effect on dynamic response. Therefore, the study focuses on the effect of the asymmetric mesh stiffness on the vibration characteristics of spiral bevel gear transmission system, and the mesh damping parameter is assumed to be constant as in references [13, 14].

2. Dynamic Model

The proposed nonlinear dynamic model of a spiral bevel gear pair is shown in Figure 1. Three-dimensional Cartesian coordinate is set up, which uses the theoretical intersection of the two bevel gear axis for the origin. The two gear bodies are considered as rigid cone disks and bending rotation can be neglected for the bearing layout in Figure 1. Then the model includes transverse and torsion coordinates as shown in Figure 1.

The coordinate vector of the system can be expressed with $[X_1, Y_1, Z_1, \theta_{1x}, X_2, Y_2, Z_2, \theta_{2y}]^T$.

The normal dynamic load of pinion and its components along axis can be calculated as

$$\begin{aligned}
F_n &= \overline{k}_h\left(\overline{\lambda}_n\right) f\left(\overline{\lambda}_n\right) + c_h \dot{\overline{\lambda}}_n, \\
F_x &= F_n\left(\sin\alpha_n \sin\delta_1 + \cos\alpha_n \sin\beta_m \cos\delta_1\right), \\
F_y &= -F_n\left(\sin\alpha_n \cos\delta_1 - \cos\alpha_n \sin\beta_m \sin\delta_1\right), \\
F_z &= -F_n \cos\alpha_n \cos\beta_m,
\end{aligned} \tag{2.1}$$

$$\begin{aligned}
\overline{k}_h\left(\overline{\lambda_n}\right) &= \begin{cases} \overline{k}_{h1}, & \overline{\lambda_n} > \overline{b}, \\ 0, & -\overline{b} \le \overline{\lambda_n} \le \overline{b}, \\ \overline{k}_{h2}, & \overline{\lambda_n} < -\overline{b}, \end{cases} \\
\overline{k}_{h1} &= \overline{k}_{hm1} + \sum_{r=1}^{\infty} k_{har1} \cos\left(r\overline{\omega_h}\overline{t} + \phi_{hr1}\right), \\
\overline{k}_{h2} &= \overline{k}_{hm2} + \sum_{r=1}^{\infty} k_{har2} \cos\left(r\overline{\omega_h}\overline{t} + \phi_{hr2}\right), \\
f\left(\overline{\lambda_n}\right) &= \begin{cases} \overline{\lambda_n} - \overline{b}, & \overline{\lambda_n} > \overline{b}, \\ 0, & -\overline{b} \le \overline{\lambda_n} \le \overline{b}, \\ \overline{\lambda_n} + \overline{b}, & \overline{\lambda_n} < -\overline{b}, \end{cases}
\end{aligned} \tag{2.2}$$

where $\overline{k}_{h1}$, $\overline{k}_{h2}$—mesh stiffness of drive side and coast side, respectively; $\overline{\lambda}_n$—Dynamic transmission error; $\overline{k}_h(\overline{\lambda_n})$, $f(\overline{\lambda}_n)$—Nonlinear displacement function; c_h—Mesh damping coefficient; α_n—Normal surface pressure angle; δ_1—Pitch cone angle of the pinion; β_m—Helix angle at meshing point; $\overline{k}_{hm1}$, $\overline{k}_{hm2}$—Mean mesh stiffness of drive side and coast side, respectively; k_{har1}, k_{har2}—Fourier series coefficients; $\overline{b}$—Half of the gear backlash.

Dynamic transmission error can be defined with

$$\overline{\lambda}_n = (-X_1 + X_2)a_1 + (Y_1 - Y_2)a_2 + \left(Z_1 - Z_2 + r_{m1}\theta_{1x} - r_{m2}\theta_{2y}\right)a_3 + \overline{e}\left(\overline{t}\right), \tag{2.3}$$

where

$$\begin{aligned}
a_1 &= \sin\alpha_n \sin\delta_1 + \cos\alpha_n \sin\beta_m \cos\delta_1, \\
a_2 &= \sin\alpha_n \cos\delta_1 - \cos\alpha_n \sin\beta_m \sin\delta_1, \\
a_3 &= \cos\alpha_n \cos\beta_m,
\end{aligned} \tag{2.4}$$

$\overline{e}(\overline{t})$ is the static transmission error on normal direction of meshing surface. It can be expressed in a Fourier series form: $\overline{e}(\overline{t}) = \sum_{r=1}^{\infty} \overline{e}_r \sin(r\overline{\omega_h}\overline{t} + \phi_{er})$, where r_{m1}, r_{m2}—mean radius at meshing point; $\overline{e}_r$—amplitude of the r-order harmonic; ϕ_{er}—phase angle of the r-order harmonic.

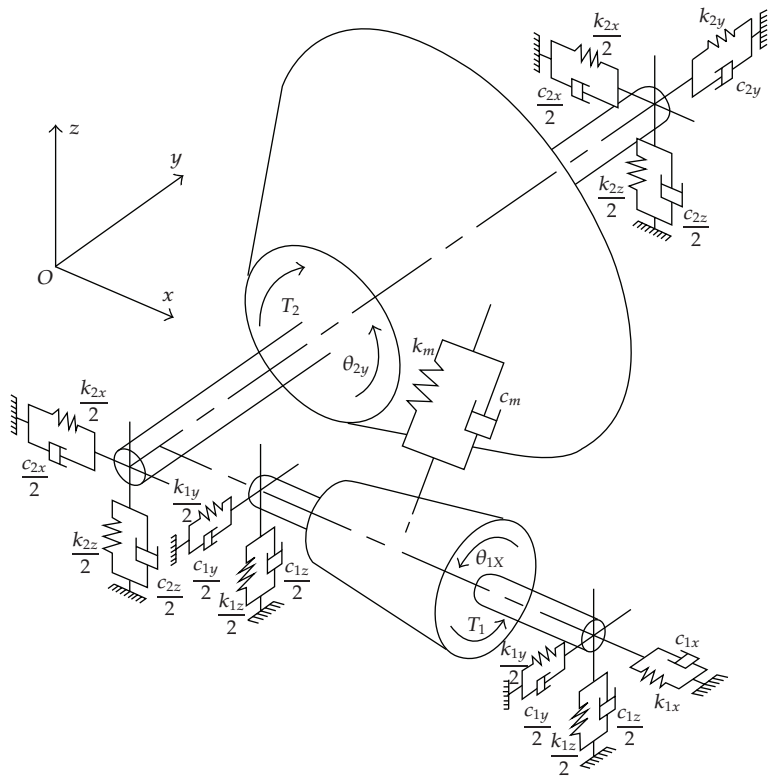

Figure 1: Dynamic model of a spiral bevel gear pair.

The equations of the dynamic model can be described as

$$\begin{gathered}
m_1\ddot{X}_1 + C_{1x}\dot{X}_1 + K_{1x}X_1 = F_x, \\
m_1\ddot{Y}_1 + C_{1y}\dot{Y}_1 + K_{1y}Y_1 = F_y, \\
m_1\ddot{Z}_1 + C_{1z}\dot{Z}_1 + K_{1z}Z_1 = F_z, \\
I_{1x}\ddot{\theta}_{1x} = T_1 + F_z r_{m1}, \\
m_2\ddot{X}_2 + C_{2x}\dot{X}_2 + K_{2x}X_2 = -F_x, \\
m_2\ddot{Y}_2 + C_{2y}\dot{Y}_2 + K_{2x}Y_2 = -F_y, \\
m_2\ddot{Z}_2 + C_{2z}\dot{Z}_2 + K_{2z}Z_2 = -F_z, \\
I_{2y}\ddot{\theta}_{2y} = -T_2 - F_z r_{m2},
\end{gathered} \tag{2.5}$$

$$T_1 = T_{1m} + T_{1v}, \qquad T_2 = T_{2m}, \tag{2.6}$$

where m_1, m_2—Mass of pinion and gear, respectively; I_{1x}, I_{2y}—Mass moments of inertias of pinion and gear, respectively; K_{ij}, C_{ij}—Bearing stiffness and damping along the three coordinate axis, respectively; T_1, T_2—Load torques on pinion and gear, respectively; T_{1m}, T_{2m}—Mean load torques on pinion and gear, respectively; T_{1v}—Ripple torque on pinion.

Using $\overline{\lambda}_n$ as a new freedom degree, the two rigid-body rotation equations of the original model can be changed into a single one:

$$\begin{gathered}
m_e a_1 \ddot{X}_1 - m_e a_2 \ddot{Y}_1 - m_e a_3 \ddot{Z}_1 - m_e a_1 \ddot{X}_2 + m_e a_2 \ddot{Y}_2 + m_e a_3 \ddot{Z}_2 \\
+ m_e \ddot{\overline{\lambda}}_n + c_h a_3^2 \dot{\overline{\lambda}}_n + \overline{k}_h\left(\overline{\lambda}_n\right) a_3^2 f\left(\overline{\lambda}_n\right) = a_3 (F_{1m} + F_{1v}) + m_e \ddot{\overline{e}}_n\left(\overline{t}\right), \\
m_e = \frac{I_{1x} I_{2y}}{\left(I_{1x} r_{m2}^2 + I_{2y} r_{m1}^2\right)}, \\
F_{1m} = \frac{T_{1m}}{r_{m1}} = \frac{T_{2m}}{r_{m2}}, \\
F_{1v} = \frac{T_{1v} r_{m1} m_e}{I_{1x}} = \sum_{r=1}^{\infty} F_r \cos\left(r\omega_{T1} t + \phi_{T1r}\right),
\end{gathered} \tag{2.7}$$

where m_e—Equivalent mass of the gear pair; F_{1v}, F_{1m}—Ripple and mean force on pinion, respectively.

Next, introducing the parameters

$$x_i = \frac{X_i}{l}, \quad y_i = \frac{Y_i}{l}, \quad z_i = \frac{Z_i}{l}, \quad b = \frac{\overline{b}}{l},$$

$$\lambda_n = \frac{\overline{\lambda}_n}{l}, \ \omega_n = \sqrt{\frac{k_{hm}}{m_e}}, \quad \omega_{ij} = \sqrt{\frac{k_{ij}}{m_i}},$$

$$\varsigma_{ij} = \frac{c_{ij}}{(2 m_i \omega_n)}, \quad \varsigma_{ih} = \frac{c_h}{(2 m_i \omega_n)},$$

$$k_{ij} = \frac{\omega_{ij}^2}{\omega_n^2}, \quad k_{ih} = \frac{\overline{k}_h\left(\overline{\lambda}_n\right)}{\left(m_i \omega_n^2\right)},$$

$$t = \omega_n \overline{t}, \quad \omega_h = \frac{\overline{\omega_h}}{\omega_n}, \quad \omega_T = \frac{\overline{\omega}_T}{\omega_n},$$

$$k_{hm} = \frac{\left(\overline{k}_{hm1} + \overline{k}_{hm2}\right)}{2},$$

$$g_1 = \frac{\overline{k}_{h1}}{k_{hm}} = k_{hm1} + \sum_{r=1}^{\infty} k_{hr1} \cos\left(r\omega_h t + \phi_{hr1}\right),$$

$$g_2 = \frac{\overline{k}_{h2}}{k_{hm}} = k_{hm2} + \sum_{r=1}^{\infty} k_{hr2} \cos\left(r\omega_h t + \phi_{hr2}\right),$$

$$g(\lambda_n) = \begin{cases} g_1, & \lambda_n > b, \\ 0, & -b \le \lambda_n \le b, \\ g_2, & \lambda_n < -b, \end{cases}$$

$$f(\lambda_n) = \begin{cases} \lambda_n - b, & \lambda_n > b, \\ 0, & -b \le \lambda_n \le b, \\ \lambda_n + b, & \lambda_n < -b, \end{cases}$$

$$f_{1m} = \frac{F_{1m}}{m_e l \omega_n^2}, \quad f_{1v} = \frac{F_{1v}}{m_e l \omega_n^2},$$

$$f_e = \sum_{r=1}^{\infty} F_{hr} (r\omega_h)^2 \cos(r\omega_h t + \phi_{er}), \tag{2.8}$$

where $i = 1, 2$; $j = x, y, z$.

The dimensionless form of (2.5) can be obtained as

$$\begin{gathered}
\ddot{x}_1 + 2\varsigma_{1x}\dot{x}_1 + k_{1x}x_1 - 2a_1\varsigma_{1h}\dot{\lambda}_n - a_1 k_{1h} f(\lambda_n) = 0, \\
\ddot{y}_1 + 2\varsigma_{1y}\dot{y}_1 + k_{1y}y_1 + 2a_2\varsigma_{1h}\dot{\lambda}_n + a_2 k_{1h} f(\lambda_n) = 0, \\
\ddot{z}_1 + 2\varsigma_{1z}\dot{z}_1 + k_{1z}z_1 + 2a_3\varsigma_{1h}\dot{\lambda}_n + a_3 k_{1h} f(\lambda_n) = 0, \\
\ddot{x}_2 + 2\varsigma_{2x}\dot{x}_2 + k_{2x}x_2 + 2a_2\varsigma_{2h}\dot{\lambda}_n + a_2 k_{2h} f(\lambda_n) = 0, \\
\ddot{y}_2 + 2\varsigma_{2y}\dot{y}_2 + k_{2y}y_2 - 2a_2\varsigma_{2h}\dot{\lambda}_n - a_2 k_{2h} f(\lambda_n) = 0, \\
\ddot{z}_2 + 2\varsigma_{2z}\dot{z}_2 + k_{2z}z_2 - 2a_3\varsigma_{2h}\dot{\lambda}_n - a_3 k_{2h} f(\lambda_n) = 0, \\
a_1\ddot{x}_1 - a_2\ddot{y}_1 - a_3\ddot{z}_1 - a_1\ddot{x}_2 + a_2\ddot{y}_2 + a_3\ddot{z}_2 + \ddot{\lambda}_n + 2a_3^2\varsigma_h\dot{\lambda}_n + a_3^2 g(\lambda_n) f(\lambda_n) = a_3 f_{1m} + a_3 f_{1v} + f_e.
\end{gathered} \tag{2.9}$$

3. Numerical Results

As there is no analytical method existing for (2.9), the equation is solved by applying the explicit Runge-Kutta integration routine with variable step that is generally applicable to strong nonlinear equation. The effect of tooth mesh stiffness asymmetry on dynamic response of spiral bevel gear system for both light and heavy loads is studied here. For subsequent numerical study, the baseline data used are

$$Z_1 = 36, \quad Z_2 = 40, \quad \alpha_n = 20^\circ, \quad \beta_m = 35^\circ, \quad \bar{b} = 35\,\mu\text{m}. \tag{3.1}$$

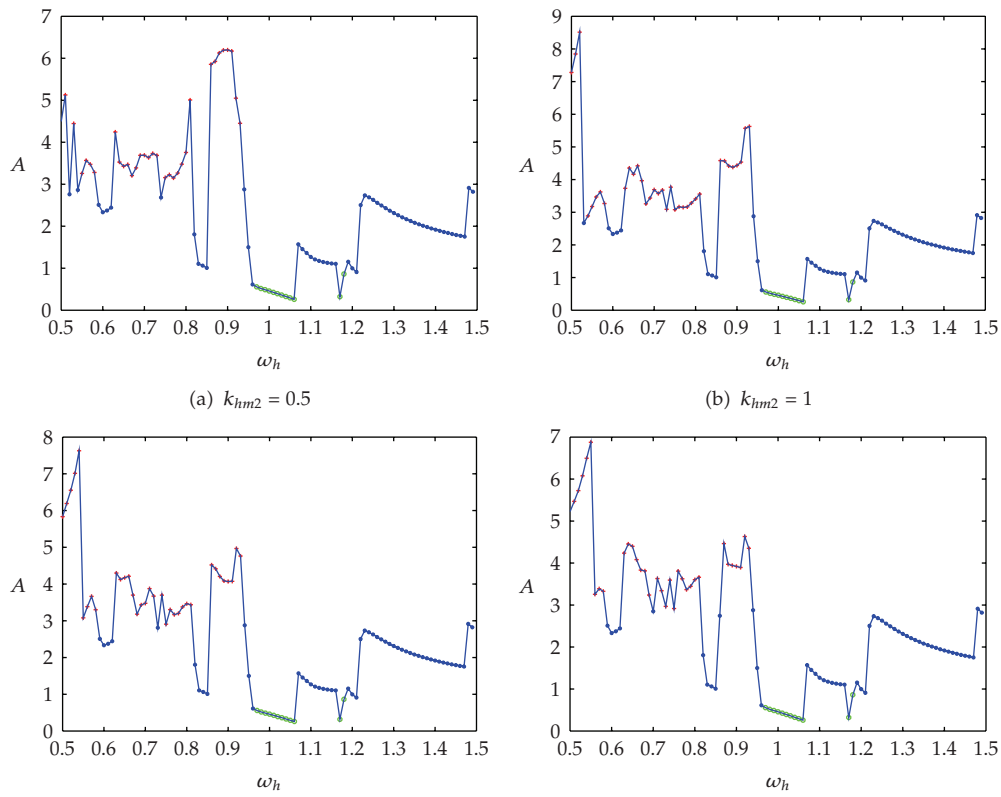

(a) $k_{hm2} = 0.5$ (b) $k_{hm2} = 1$

(c) $k_{hm2} = 1.5$ (d) $k_{hm2} = 2$

Figure 2: Effect of mean mesh stiffness of coast side for lightly loaded case. ∗—single-sided impact ∘—no impact +—double-sided impact.

In this part, it is focused on effect of mean mesh stiffness k_{hm1}, k_{hm2}, assuming that $k_{hr1} = k_{hr1}$, $\phi_{hr1} = \phi_{hr2}$ for simplicity.

3.1. Effect of Mesh Stiffness Asymmetry for Lightly Loaded Case

Dimensionless dynamic parameters set in the system are as follows:

$$\begin{gathered}
\varsigma_{ij} = 0.01, \qquad \varsigma_{ih} = 0.0125, \qquad \varsigma_{ih} = 0.0125, \\
k_{ih} = 0.25, \qquad k_{hr1} = k_{hr2} = 0.2, \\
\phi_{hr1} = \phi_{hr2} = 0, \\
f_{1m} = 0.25, \qquad f_{1v} = 0 \quad \omega_h = 0.7, \\
f_e = 0.5\omega_h^2 \cos \omega_h t, \quad i = 1, 2, \ j = x, y, z.
\end{gathered} \tag{3.2}$$

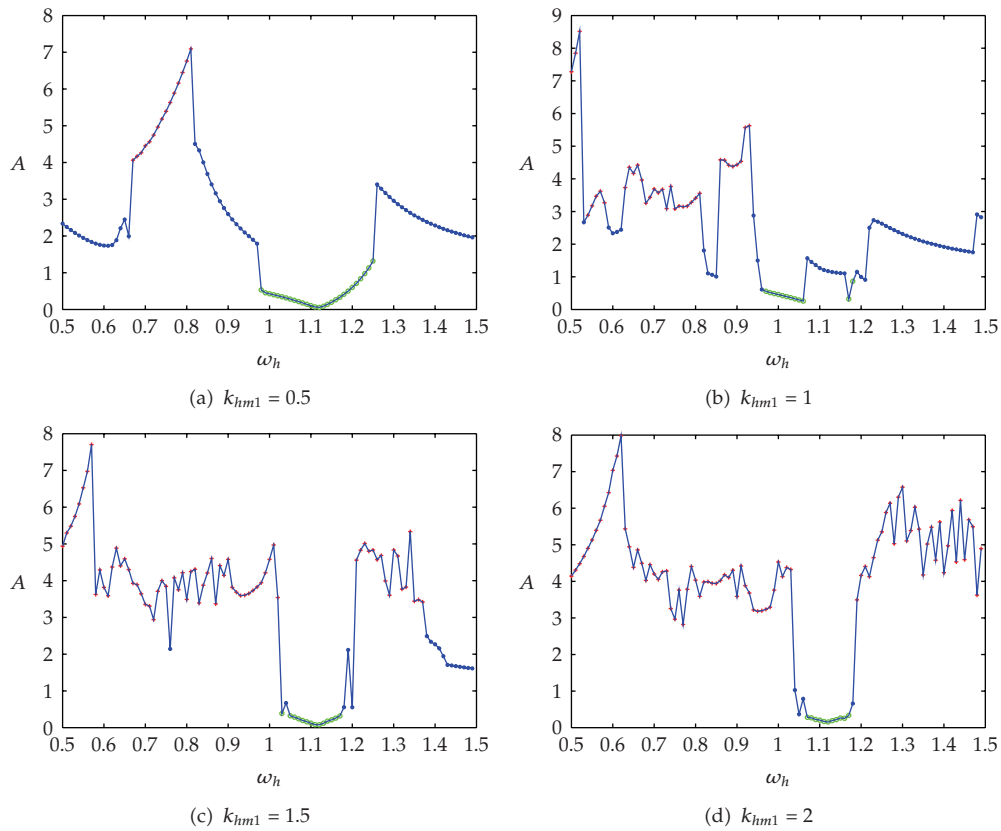

Figure 3: Effect of mean mesh stiffness of drive side for lightly loaded case. ∗—single-sided impact ∘—no impact +—double-sided impact.

The effect of the mean mesh stiffness of coast side on dynamic response for lightly loaded case is shown in Figure 2. The horizontal axis represents excitation frequency ω_h and the vertical axis represents peak-peak value of the dynamic transmission error A. As shown in Figure 2(a), when $k_{hm2} = 0.5$, single-sided impact response and double-sided impact response alternate in the low-frequency regions. And the max of A occurs at $\omega_h = 0.9$. In the region $\omega_h \in [0.96, 1.06]$, there are no impact responses, and the gear pair running smoothly as k_{hm2} is increased to 1 in Figure 2(b); the max of A 8.5 moves to the frequency $\omega_h = 0.52$. The dynamic response in no-impact and single-sided impact regions $\omega_h \in [0.96, 1.5]$ keeps unchanged. When k_{hm2} is increased further to 1.5 and 2, the peak-peak value A in double-sided impact region changes obviously while the location and vibration response of single-sided impact and no-impact regions are nearly unchanged. The above results show that the mesh stiffness of coast side only affects double-sided tooth impact region.

Figure 3 shows the effect of mean mesh stiffness of drive side for lightly loaded case. It can be seen from Figure 3(a) that double-sided impacts dominate the range $\omega_h \in [0.67, 0.79]$. And four response jump discontinuities can be seen at frequency $\omega_h = 0.67, 0.79, 0.97, 1.25$. It can be observed that response jump discontinuities appear at these frequencies. As k_{hm1} is increased to 1, it can be observed that more double-sided impacts appear and the location of each impact region shifts obviously. As k_{hm1} is further increased to 1.5 and 2, both response

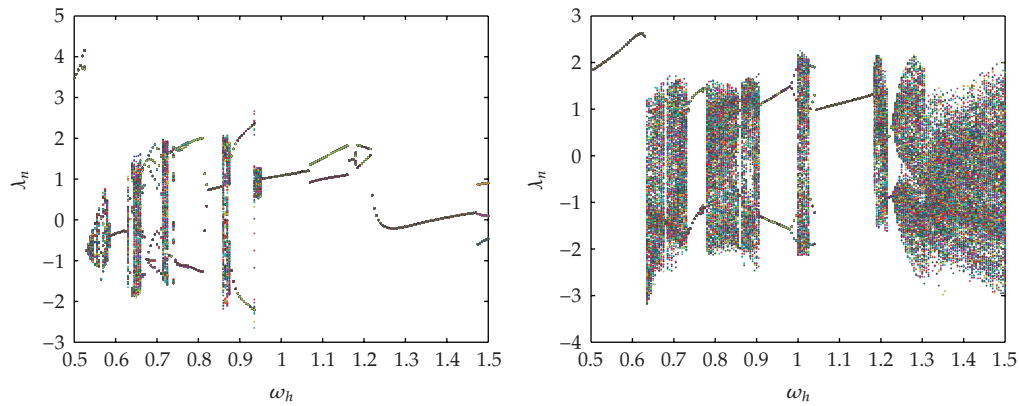

(a) $k_{hm1} = 1$ (b) $k_{hm1} = 2$

Figure 4: Bifurcation diagram for lightly loaded case.

jumps and single-sided impacts increased considerably, and response in the whole excitation frequency areas changes significantly. As can be seen in Figure 3(c), except the two narrow bands $\omega_h \in [1.03, 1.17]$ and $\omega_h \in [1.36, 1.5]$, the rest excitation frequencies are all double-sided impact regions. When $k_{hm1} = 2$, width of double-sided tooth impact region is further increased.

To further explain the effect of the mean mesh stiffness of drive side on dynamic response, bifurcation diagram is introduced in Figure 4. For the current light-load case, it can be observed that, as k_{hm1} is increased from 1 to 2, chaotic motion regions increase considerably. From above observations, it can be concluded that the mesh stiffness of drive side affects dynamic response greatly in the whole excitation frequency region. Furthermore, the increase of drive side mesh stiffness tends to worsen dynamic response.

3.2. Effect of Mesh Stiffness Asymmetry for Heavily Loaded Case

Dimensionless dynamic parameters set in this part are as follows:

$$\begin{gathered}\varsigma_{ij} = 0.01, \qquad \varsigma_{ih} = 0.0125, \qquad \varsigma_{ih} = 0.0125, \qquad k_{ih} = 0.25, \qquad k_{hr1} = k_{hr2} = 0.2, \\ \phi_{hr1} = \phi_{hr2} = 0, \qquad f_{1m} = 1, \qquad f_{1v} = 0, \qquad f_e = 0.5\omega_h^2 \cos \omega_h t, \\ i = 1, 2, \quad j = x, y, z.\end{gathered} \tag{3.3}$$

When $k_{hm1} = 1$, the effect of k_{hm2} for heavy-load case is shown in Figure 5. No-impact region $\omega_h \in [0.74, 1.18]$ is far wider than double-sided impact region $\omega_h \in [0.5, 0.61]$ in Figure 5(a). And the max of $A = 15.9$ which comes at $\omega_h = 0.52$ is much larger than that of 6 for light-load case. There are three single-sided impact regions $\omega_h \in [0.62, 0.73]$, $\omega_h \in [1.19, 1.27]$, and $\omega_h \in [1.32, 1.5]$, and little response jump can be seen. As k_{hm2} is increased to 1, dynamic response in double-sided impact region changes greatly while responses in single-sided impact and no-impact regions remain the same. And the max of A is increased to 24. As k_{hm2} is increased further to 1.5 and 2, only double-sided impact region is affected. The results show that double-sided impact region becomes obviously narrower

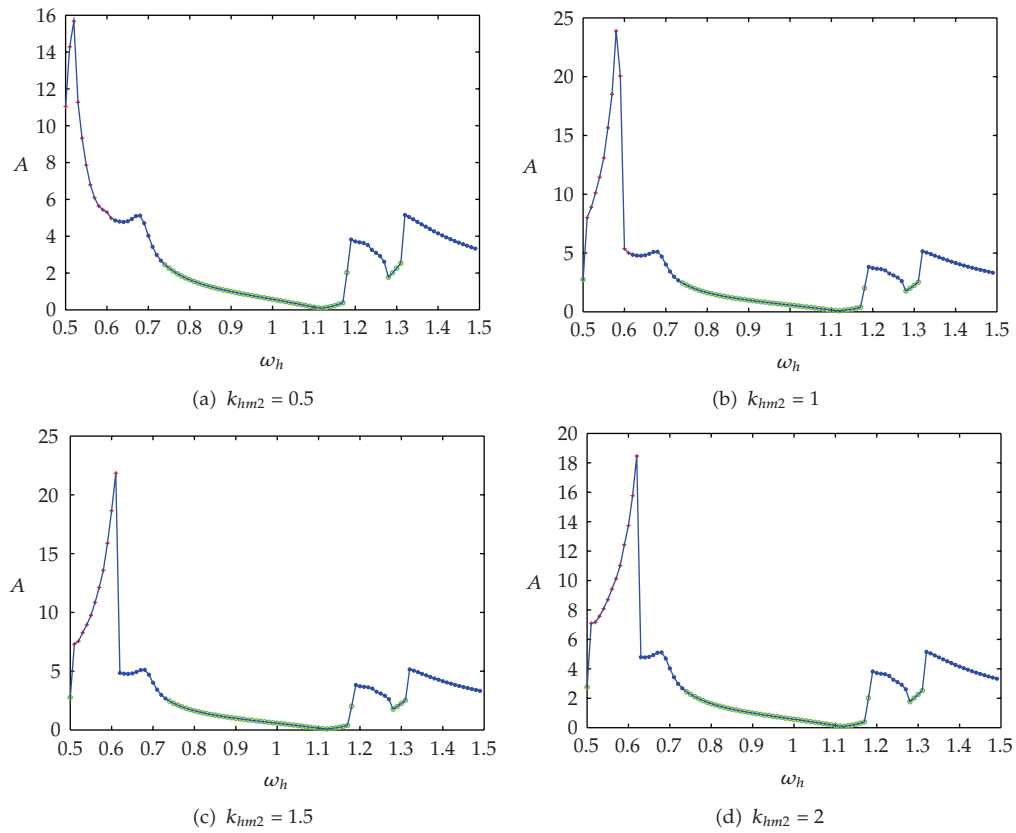

Figure 5: Effect of mean mesh stiffness of coast side for heavily loaded case. ∗—single-sided impact ∘—no impact +—double-sided impact.

and response jumps diminish considerably for heavily loaded case. Although the peak-peak value of dynamic transmission error in double-sided impact region is larger than that of light-load case, response jump discontinuities and double-sided tooth impacts for heavily loaded case are far fewer. As light-load condition, only double-sided impact region is affected considerably by mesh stiffness of coast side. This is because k_{hm2} only takes effect for double-sided impact condition.

Figure 6 shows dynamic response for different mean mesh stiffness of drive side while leaving mean mesh stiffness of coast side unchanged. In Figure 6(a), there are three no-impact regions $\omega_h \in [0.98, 1.33]$, $\omega_h \in [0.57, 0.79]$, and $\omega_h \in [1.44, 1.5]$, one double-sided impact region $\omega_h \in [0.8, 0.91]$, and three response jump frequencies $\omega_h = 0.8$, $\omega_h = 0.91$, and $\omega_h = 0.97$. The max of $A = 32$ occurs at $\omega_h = 0.92$. As k_{hm1} is increased to 1, no-impact regions are reduced to two $\omega_h \in [0.74, 1.18]$ and $\omega_h \in [1.28, 1.31]$, and the location of each impact region changes significantly. For $k_{hm1} = 1.5$ in Figure 6(c), the number of double-sided impact region is increased to two $\omega_h \in [0.57, 0.76]$ and $\omega_h \in [1.31, 1.41]$, and more response jumps appear. When k_{hm1} is increased to 2, double-sided impact region becomes wider and response in double-sided impact region takes significant changes from Figure 6(c).

Figure 7 shows response bifurcation for different k_{hm1}, while k_{hm2} is fixed to 1. For $k_{hm1} = 1$ in Figure 7(a), no chaotic motion can be seen. However, as k_{hm1} is increased to 2,

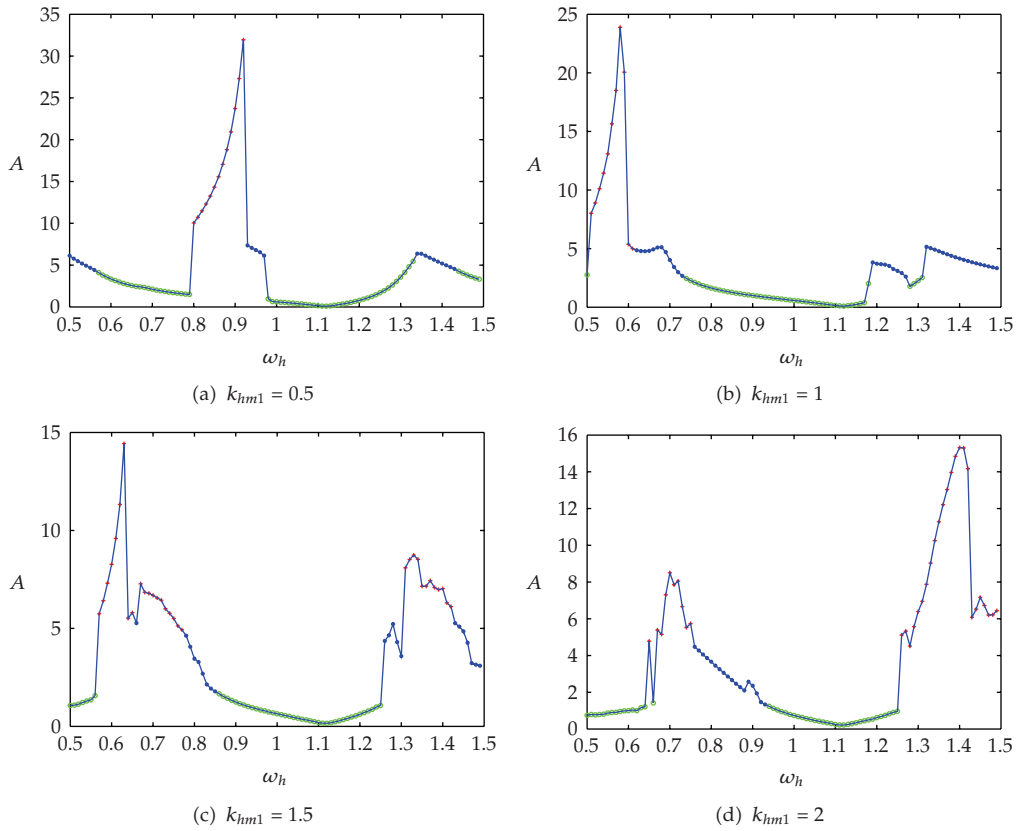

Figure 6: Effect of mean mesh stiffness of drive side for heavily loaded case. ∗—single-sided impact ∘—no impact +—double-sided impact.

there are two obvious chaotic motion areas. Comparing with Figure 4, it can be seen that chaotic motion areas diminish considerably in Figure 7. From these results we can conclude that mesh stiffness of drive side also affects dynamic response greatly for heavy-load case. In addition, the increase of k_{hm1} will worsen the dynamic response of the system especially for light-load case. Compared with light-load condition, the degree of gear backlash nonlinearity is lower for heavy-load case. This is because mesh force under heavy-load condition is large and hence mesh teeth are difficult to separate.

4. Conclusions

A nonlinear dynamic model of a spiral bevel gear pair which involves time-varying mesh stiffness, transmission error, backlash, and mesh stiffness asymmetry is proposed. The effect of tooth mesh stiffness asymmetry on vibration of spiral bevel gear transmission system is studied deliberately. Some important conclusions are obtained.

Firstly, the mesh stiffness for drive side has more effect on dynamic response than those of the coast side. Only double-sided impact region is affected considerably by mesh stiffness of coast side while single-sided impact and no-impact regions are unchanged.

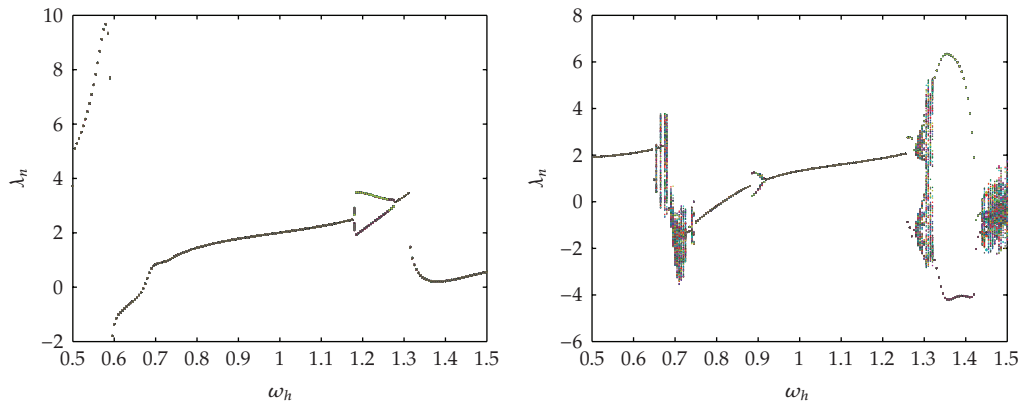

(a) $k_{hm1} = 1$ (b) $k_{hm1} = 2$

Figure 7: Bifurcation diagram for heavily loaded case.

Secondly, the dynamic response of the system is very sensitive to mesh stiffness of drive side. The change of mesh stiffness of drive side will affect response in the whole excitation frequency areas. Furthermore, the increase of drive side mesh stiffness tends to worsen dynamic response especially for lightly loaded case.

Thirdly, the vibration characteristic for heavily loaded case is far better than that for lightly loaded case. And the mesh stiffness asymmetry affects the dynamic response more compared with heavy-load case.

Acknowledgments

This paper is supported by National Natural Science Foundation of China (Grant no. 50875270), Key Scientific Projects of Ministry of Education of China (Grant no. 108108) and Natural Science Foundation of Chongqing (CSTC, 2008BA6025).

References

[1] L. Runfang and W. Jianjun, *Dynamics of Geared System—Vibration, Impact, Noise*, Science Publishing House, Beijing, China, 1997.

[2] A. Kahraman and R. Singh, "Non-linear dynamics of a spur gear pair," *Journal of Sound and Vibration*, vol. 142, no. 1, pp. 49–75, 1990.

[3] A. Kahraman and R. Singh, "Non-linear dynamics of a geared rotor-bearing system with multiple clearances," *Journal of Sound and Vibration*, vol. 144, no. 3, pp. 469–506, 1991.

[4] W. Jianjun, L. Qihan, and L. Runfang, "Research advances for nonlinear vibration of gear transmission system," *Advances In Mechanics*, vol. 35, no. 1, pp. 37–51, 2005 (Chinese).

[5] C. Liangyu, C. Chunyuan,, and E. Zhongkai, "A vibration model spiral bevel gears," *Journal of Northeast University of Technology*, vol. 14, no. 2, pp. 146–149, 1993 (Chinese).

[6] C. Gosselin, L. Cloutier, and Q. D. Nguyen, "A general formulation for the calculation of the load sharing and transmission error under load of spiral bevel and hypoid gears," *Mechanism and Machine Theory*, vol. 30, no. 3, pp. 433–450, 1995.

[7] G. D. Bibel, A. Kumar, S. Reddy, and R. Handschuh, "Contact stress analysis of spiral bevel gears using finite element analysis," *Journal of Mechanical Design*, vol. 117, no. 2 A, pp. 235–240, 1995.

[8] M. Fujii, Y. Nagasaki, M. Nohara, and Y. Terauchi, "Effect of bearing on dynamic behaviors of straight bevel gear," *Transactions of the Japan Society of Mechanical Engineers. Part C*, vol. 61, no. 581, pp. 234–238, 1995 (Japanese).

[9] M. Fujii, Y. Nagasaki, and M. Nohara, "Differences in dynamic behavior between straight and skew bevel gears," *Transactions of the Japan Society of Mechanical Engineers. Part C*, vol. 63, no. 613, pp. 3229–3234, 1997 (Japanese).

[10] l. Z. Xu, M. Zhao, P. Z. Ren, and W. D. Chai, "Method for analyzing the vibration behavior of rotor with the engagement of spiral bevel gears," *Mechanical Science and Technology*, vol. 16, pp. 668—673, 1997.

[11] M. G. Donley, T. C. Lim, and G. C. Steyer, "Dynamic analysis of automotive gearing systems," *Journal of Passenger Cars*, vol. 101, no. 905, pp. 77–87, 1992.

[12] Z. D. Fang, "Dynamic analysis of spiral bevel gears in assembly," in *Proceedings of the International Gearing Conference*, vol. 43, pp. 389–392, Newcastle, UK, 1994.

[13] Y. Cheng and T. C. Lim, "Vibration analysis of hypoid transmissions applying an exact geometry-based gear mesh theory," *Journal of Sound and Vibration*, vol. 240, no. 3, pp. 519–543, 2001.

[14] J. Wang, T. C. Lim, and M. Li, "Dynamics of a hypoid gear pair considering the effects of time-varying mesh parameters and backlash nonlinearity," *Journal of Sound and Vibration*, vol. 308, no. 1-2, pp. 302–329, 2007.

[15] S. Wang, Y. Shen, and H. Dong, "Nonlinear dynamical characteristics of a spiral bevel gear system with backlash and time-varying stiffness," *Chinese Journal of Mechanical Engineering*, vol. 39, no. 2, pp. 28–32, 2003.

[16] L. Wang, Y. Huang, R. Li, and T. Lin, "Study on nonlinear vibration characteristics of spiral bevel transmission system," *China Mechanical Engineering*, vol. 18, no. 3, pp. 260–264, 2007 (Chinese).

[17] M. Li and H. Y. Hu, "Dynamic analysis of a spiral bevel-geared rotor-bearing system," *Journal of Sound and Vibration*, vol. 259, no. 3, pp. 605–624, 2003.

Hindawi Publishing Corporation
Mathematical Problems in Engineering
Volume 2010, Article ID 379472, 21 pages
doi:10.1155/2010/379472

Research Article

Analysis of a Nonlinear Aeroelastic System with Parametric Uncertainties Using Polynomial Chaos Expansion

Ajit Desai and Sunetra Sarkar

Department of Aerospace Engineering, IIT Madras, Chennai 600036, India

Correspondence should be addressed to Sunetra Sarkar, sunetra.sarkar@gmail.com

Received 10 January 2010; Revised 30 April 2010; Accepted 14 June 2010

Academic Editor: Carlo Cattani

Aeroelastic stability remains an important concern for the design of modern structures such as wind turbine rotors, more so with the use of increasingly flexible blades. A nonlinear aeroelastic system has been considered in the present study with parametric uncertainties. Uncertainties can occur due to any inherent randomness in the system or modeling limitations, and so forth. Uncertainties can play a significant role in the aeroelastic stability predictions in a nonlinear system. The analysis has been put in a stochastic framework, and the propagation of system uncertainties has been quantified in the aeroelastic response. A spectral uncertainty quantification tool called Polynomial Chaos Expansion has been used. A projection-based nonintrusive Polynomial Chaos approach is shown to be much faster than its classical Galerkin method based counterpart. Traditional Monte Carlo Simulation is used as a reference solution. Effect of system randomness on the bifurcation behavior and the flutter boundary has been presented. Stochastic bifurcation results and bifurcation of probability density functions are also discussed.

1. Introduction

Fluid-structure interaction can result in dynamic instabilities like flutter. Nonlinear parameters present in the system can stabilize the diverging growth of flutter oscillations to a limit cycle oscillation (LCO). Sustained LCO can lead to fatigue failure of rotating structures such as wind turbine rotors. Hence, it is an important design concern in aeroelastic analysis. Moreover, there is a growing interest in understanding how system uncertainties in structural and aerodynamic parameters and initial conditions affect the characteristics of such dynamical response.

Uncertainty quantification in a stochastic framework with stochastic inputs has traditionally been analyzed with Monte Carlo simulations (MCSs). To apply this procedure

one should use the distribution of the input parameters to generate a large number of realizations of the response. Probability density function (PDF) and other required statistics are then approximated from these realizations; however, it is computationally expensive, especially for large complex problems. Hence, there is a need to develop alternate approaches which are computationally cheaper than direct MCS procedure. Perturbation method is a fast tool for obtaining the response statistics in terms of its first and second moments [1]. The statistical response is determined by expanding the stochastic parameters around their mean via a Taylor series [2]. The application of this method is, however, limited to small perturbations and does not readily provide information on high-order statistics [3, 4]. The resulting system of equations becomes extremely complicated beyond second-order expansions as shown in the literature. Sensitivity method is a more economical approach, based on the moments of samples, but it is less robust and depends strongly on the modeling assumptions [5]. Another approach based on expanding the inverse of the stochastic operator in a Neumann series is also limited to small fluctuations only; even combining with the Monte Carlo method also seems to result in a computationally prohibitive algorithm for complex systems [4].

Polynomial chaos expansion (PCE) is a more effective approach, pioneered by Ghanem and Spanos [4], proposed first in the structural mechanics finite elements area. It is a spectral representation of the uncertainty in terms of orthogonal polynomials. The stochastic input is represented spectrally by employing orthogonal polynomial functionals from the Askey scheme as basis in the random space. The original homogeneous PCE was based on Hermite polynomials from the Askey family [6]. It can give optimal exponential convergence for Gaussian inputs [7]. A standard Galerkin projection is applied along the random dimensions to obtain the weak form of the equations. The resulting deterministic systems are solved using standard techniques to solve for each random mode [8]. Galerkin polynomial chaos expansion (Galerkin PCE) based approaches have been examined extensively with different basis functions to model several uncertain flow and flow-induced instability problems [9, 10].

Galerkin PCE (also called intrusive approach) modifies the governing equations to a coupled form in terms of the chaos coefficients. These equations are usually more complex and arriving at them is quite often a tedious task for some choices of the uncertain parameters. In order to avoid these, several uncoupled alternatives have been proposed. These are collectively called nonintrusive approaches. In a nonintrusive polynomial chaos method a deterministic solver is used repeatedly as in Monte Carlo simulation. The Probabilistic Collocation (PC) method is such a nonintrusive polynomial chaos method in which the problem is collocated at Gauss quadrature points in the probability space [11, 12]. The deterministic solutions are performed at these collocation points. The nonintrusive polynomial chaos method proposed by Walters and coworkers [13–15] is based on approximating the polynomial chaos coefficients. A similar approach called nonintrusive Spectral Projection has been used by Reagan et al. [16]. Pettit and Beran [17, 18] have also used a stochastic projection technique to compute the chaos expansion coefficients in an aeroelastic system. When multiple uncertain parameters are involved the collocation grids are constructed using tensor products of one-dimensional grids. Thus, the number of collocation points and therefore the number of required deterministic solutions increases rapidly. As an alternative, sparse grid collocation approaches can be implemented [19–21].

The intrusive and nonintrusive PCE approaches and their implementation to an aeroelastic model with structural nonlinearity are discussed in detail in the subsequent sections.

2. Nonlinear Aeroelastic Model

Figure 1 shows a schematic plot of the two degree-of-freedom pitch-plunge aeroelastic system and also the notations used in the analysis. The aeroelastic equations of motion for the linear system have been derived by Fung [22]. For nonlinear restoring forces such as with cubic springs in both pitch and plunge, the mathematical formulation is given by Lee et al. [23] as follows:

$$\begin{aligned} &\varepsilon'' + x_\alpha \alpha'' + 2\zeta_\varepsilon \frac{\overline{\omega}}{U}\varepsilon' + \left(\frac{\overline{\omega}}{U}\right)^2 \left(\varepsilon + \beta_\varepsilon \varepsilon^3\right) = -\frac{1}{\pi\mu} C_L(\tau), \\ &\frac{x_a}{r_\alpha^2}\varepsilon'' + \alpha'' + 2\frac{\zeta_\alpha}{U}\alpha' + \frac{1}{U^2}\left(\alpha + \beta_\alpha \alpha^3\right) = \frac{2}{\pi\mu r_\alpha^2} C_M(\tau). \end{aligned} \tag{2.1}$$

The above equations are shown in the nondimensional form. The nondimensional parameters are given below. The plunge deflection is considered positive in the downward direction and the pitch angle about the elastic axis is denoted positive nose up. Elastic axis is located at a distance $a_h b$ from the midchord where b is the half chord. Let us also use v as the wind velocity h as the plunge deflection. Among the nondimensional quantities, $\varepsilon = h/b$ = nondimensional displacement of the elastic axis point; $\tau = vt/b$ = nondimensional time; $U = v/(b\omega_\alpha)$= the nondimensional velocity (also called reduced velocity); $\overline{\omega} = \omega_\varepsilon/\omega_\alpha$, ω_ε and ω_α are the natural frequencies of the uncoupled plunging and pitching modes respectively. In the structural part, ζ_ε and ζ_α are the damping ratios in plunge and pitch respectively, r_α is the radius of gyration about the elastic axis, and μ is the airfoil mass ratio defined as $m/(\pi\rho v)$. β_α and β_ε denote coefficients of cubic spring in pitch and plunge respectively. For incompressible, inviscid flow, Fung [22] gives the expressions for unsteady lift and pitching moment coefficients, $C_L(\tau)$ and $C_M(\tau)$:

$$\begin{aligned} C_L(\tau) &= \pi\left(\varepsilon'' - a_h\alpha'' + \alpha'\right) + 2\pi\left\{\alpha(0) + \varepsilon'(0) + \left[\frac{1}{2} - a_h\right]\alpha'(0)\right\}\phi(\tau) \\ &\quad + 2\pi\int_0^\tau \phi(\tau-\sigma)\left[\alpha'(\sigma)\varepsilon''(\sigma) + \left[\frac{1}{2} - a_h\right]\alpha''(\sigma)\right]d\sigma, \\ C_M(\tau) &= \pi\left[\frac{1}{2} + a_h\right] \times \left\{\alpha(0) + \varepsilon'(0) + \left[\frac{1}{2} - a_h\right]\alpha'(0)\right\}\phi(\tau) \\ &\quad + \pi\left[\frac{1}{2} + a_h\right] \times \int_0^\tau \phi(\tau-\sigma)\left\{\alpha'(\sigma) + \varepsilon''(\sigma) + \left[\frac{1}{2} - a_h\right]\alpha''(\sigma)\right\}d\sigma \\ &\quad + \frac{\pi}{2}a_h\left(\varepsilon'' - a_h\alpha''\right) - \left[\frac{1}{2} - a_h\right]\frac{\pi}{2}\alpha' - \frac{\pi}{16}\alpha'' \end{aligned} \tag{2.2}$$

The Wagner function $\phi(\tau)$ is given by:

$$\phi(\tau) = 1 - \varphi_1 e^{-\epsilon_1\tau} - \varphi_2 e^{-\epsilon_2\tau}. \tag{2.3}$$

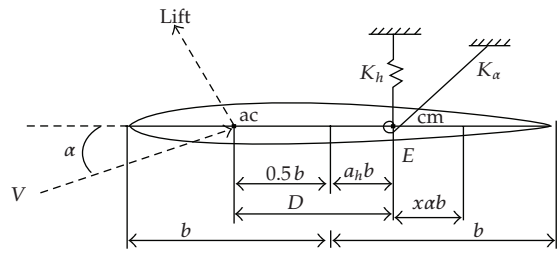

Figure 1: The schematic of a symmetric airfoil with pitch and plunge degrees-of-freedom.

Values for the constants are, $\psi_1 = 0.165$, $\psi_2 = 0.335$, $\epsilon_1 = 0.0455$ and $\epsilon_2 = 0.3$ [24]. Introducing the following new variables w_1, w_2, w_3, and w_4 [23], the original integrodifferential equations for aeroelastic system given by (2.1) are reformulated:

$$\begin{aligned} w_1 &= \int_0^\tau e^{-\epsilon_1(\tau-\sigma)}\alpha(\sigma)d\sigma, \\ w_2 &= \int_0^\tau e^{-\epsilon_2(\tau-\sigma)}\alpha(\sigma)d\sigma, \\ w_3 &= \int_0^\tau e^{-\epsilon_1(\tau-\sigma)}\varepsilon(\sigma)d\sigma, \\ w_4 &= \int_0^\tau e^{-\epsilon_2(\tau-\sigma)}\varepsilon(\sigma)d\sigma. \end{aligned} \tag{2.4}$$

Now a set of autonomous differential equations of the form $\mathbf{X}' = f(\mathbf{X})$ are obtained as, $\mathbf{X} = \{x_1, x_2, x_3, x_4, x_5, x_6, x_7, x_8\} = \{\alpha, \alpha', \varepsilon, \varepsilon', w_1, w_2, w_3, w_4\}$.

Explicitly, the system looks like,

$$\begin{aligned} x_1' &= x_2, \\ x_2' &= \frac{(c_0 N - d_0 M)}{(c_1 d_0 - c_0 d_1)}, \\ x_3' &= x_4, \\ x_4' &= \frac{(-c_1 N + d_1 M)}{(c_1 d_0 - c_0 d_1)}, \\ x_5' &= x_1 - \epsilon_1 x_5, \\ x_6' &= x_1 - \epsilon_2 x_6, \\ x_7' &= x_3 - \epsilon_1 x_7, \\ x_8' &= x_3 - \epsilon_2 x_8, \end{aligned} \tag{2.5}$$

where

$$\begin{aligned} M &= c_2 x_4 + c_3 x_2 + c_4 x_3 + c_5 x_3^3 + c_6 x_1 + c_7 x_5 + c_8 x_6 + c_9 x_7 + c_{10} x_8 - f(\tau), \\ N &= d_2 x_2 + d_3 x_1 + d_4 x_1^3 + d_5 x_4 + d_6 x_3 + d_7 x_5 + d_8 x_6 + d_9 x_7 + d_{10} x_8 - g(\tau). \end{aligned} \tag{2.6}$$

The coefficients $c_0 \cdots c_{10}$ and $d_0 \cdots d_{10}$ depend on the system parameters, and their expressions along with $f(\tau)$ and $g(\tau)$ are given in the appendix.

3. Uncertainty Quantification and Polynomial Chaos Expansion

It is increasingly being felt among the aeroelastic community that aeroelastic analysis should include the effect of parametric uncertainties. This can potentially revolutionize the present design concepts with higher rated performance and can also reshape the certification criteria. Nonlinear dynamical systems are known to be sensitive to physical uncertainties, since they often amplify the random variability with time. Hence, quantifying the effect of system uncertainties on the aeroelastic stability boundary is crucial. Flutter, a dynamic aeroelastic instability involves a Hopf bifurcation where a damped (stable response) oscillation changes to a periodic oscillatory response at a critical wind velocity. In a linear system the post flutter response can grow in an unbounded fashion [22]. System parametric uncertainties can significantly affect the onset and properties of bifurcation points. The importance of stochastic modeling of these uncertainties is that they quantify the effect of the uncertainties on flutter and bifurcation in a probabilistic sense and gives the response statistics in a systematic manner.

The original homogeneous polynomial chaos expansion [4] is based on the homogeneous chaos theory of Wiener [6, 25]. This is based on a spectral representation of the uncertainty in terms of orthogonal polynomials. In its original form, it employs Hermite polynomials as basis from the generalized Askey scheme and Gaussian random variables. Spectral polynomial chaos-based approaches with other basis functions have also been used in the recent past in various unsteady flow and flow-structure interaction problems of practical interest [8, 26, 27].

3.1. Classical Galerkin Polynomial Chaos Approach

In the classical Galerkin-PCE approach, the polynomial chaos expansion of the system response is substituted into the governing equation and a Galerkin error minimization in the probability space is followed. This results in a set of coupled equations in terms of the polynomial chaos coefficients. The resulting system is deterministic, but it is significantly modified to a higher order and complexity depending on the order of chaos expansion and system nonlinearity. After solving this set of coefficient equations, they are substituted back to get the system response.

As per the Cameron-Martin theorem [28], a random process $X(t,\theta)$ (as function of random event θ) which is second-order stationary can be written as

$$\begin{aligned} X(t,\theta) = \widehat{a}_0\psi_0 &+ \sum_{i_1=1}^{\infty}\widehat{a}_{i_1}\psi_1(\xi_{i_1}(\theta)) + \sum_{i_1=1}^{\infty}\sum_{i_2=1}^{i_1}\widehat{a}_{i_1 i_2}\psi_2(\xi_{i_1}(\theta),\xi_{i_2}(\theta)) \\ &+ \sum_{i_1=1}^{\infty}\sum_{i_2=1}^{i_1}\sum_{i_3=1}^{i_2}(\widehat{a}_{i_1 i_2 i_3})\psi_3(\xi_{i_1}(\theta),\xi_{i_2}(\theta),\xi_{i_3}(\theta)) + \cdots, \end{aligned} \tag{3.1}$$

where $\psi_n(\xi_{i_1},\xi_{i_2},\ldots,\xi_{i_n})$ denotes the Hermite polynomial of order n in terms of n-dimensional independent standard Gaussian random variables $\boldsymbol{\xi} = (\xi_{i_1},\xi_{i_2},\ldots,\xi_{i_n})$ with zero mean and

unit variance. The above equation is the discrete version of the original Wiener polynomial chaos expansion, and the continuous integrals are replaced by summations. For notational convenience equation (3.1) can be rewritten as

$$X(t,\theta) = \sum_{j=0}^{\infty} a_j(t)\Phi_j(\boldsymbol{\xi}(\theta)). \tag{3.2}$$

There is an one-to-one relationship between the ψ's and Φ's and also $\widehat{a}_j$'s and a_j's in (3.1) and (3.2). In the original form, chaos expansion uses Hermite polynomials (ψ_ns). The form of the one-dimensional Hermite polynomials is given as follows.

$$\begin{aligned}
\psi_0 &= 1,\\
\psi_1 &= \xi,\\
\psi_2 &= \xi^2 - 1,\\
\psi_3 &= \xi^3 - 3\xi,\\
\psi_4 &= \xi^4 - 6\xi^2 + 3,\\
\psi_n &= \xi\psi_{n-1} - (n-1)\psi_{n-2}.
\end{aligned} \tag{3.3}$$

One can also use orthogonal polynomials from the generalized Askey scheme for some standard nonGaussian input uncertainty distributions such as gamma and beta [8]. For any arbitrary input distribution, a Gram-Schmidt orthogonalization can be employed to generate the orthogonal family of polynomials [29].

Any stochastic process $\alpha(t,\boldsymbol{\xi}(\theta))$, governed by Gaussian random variables $\boldsymbol{\xi}$ (ξ can always be normalized as a standard Gaussian one), can be approximated by the following truncated series:

$$\alpha(t,\boldsymbol{\xi}(\theta)) = \sum_{j=0}^{p} \widehat{\alpha}_j(t)\Phi_j(\boldsymbol{\xi}(\theta)) \tag{3.4}$$

Note that, here the infinite upper limit of (3.2) is replaced by p, called the order of the expansion. For n number of random variable and polynomial order n_p, p is given by the following [26]:

$$p = \frac{(n+n_p)!}{n!n_p!} - 1. \tag{3.5}$$

We demonstrate the Galerkin-PCE approach for a generalized dynamical system for a single random variable case, that is, with a random cubic stiffness. Let us write the governing equation with cubic nonlinearity in the following form [27]:

$$\pounds[\alpha(t,\theta)] + \beta_\alpha[\alpha(t,\theta)]^3 = 0, \tag{3.6}$$

here £ is a linear differential operator.

Equation (3.4) is now rewritten for a single random variable ξ as

$$\alpha(t,\xi(\theta)) = \sum_{j=0}^{p} \widehat{\alpha}_j(t)\Phi_j(\xi(\theta)). \tag{3.7}$$

Here Φ_j's are now Hermite polynomials ψ_j as shown in (3.3).

If the cubic spring constant β_α is assumed to be a Gaussian random variable with mean $\overline{\beta}_\alpha$ and standard deviation $\widetilde{\beta}_\alpha$, it can be characterized by

$$\beta_\alpha = \overline{\beta}_\alpha + \xi\widetilde{\beta}_\alpha = \sum_{l=0}^{1} \beta_{\alpha l}\Phi_l, \tag{3.8}$$

with, $\beta_{\alpha 0} = \overline{\beta}_\alpha$ and $\beta_{\alpha 1} = \widetilde{\beta}_\alpha$.

Substituting the chaos expansion terms, (3.7) and (3.8) in (3.6),

$$\pounds\left[\sum_{j=0}^{p} \widehat{\alpha}_j(t)\Phi_j\right] + \sum_{l=0}^{1} \beta_{\alpha l}\Phi_l \left[\sum_{j=0}^{p} \widehat{\alpha}_j(t)\Phi_j\right]^3 = 0. \tag{3.9}$$

The cubic nonlinear function can be expressed in the following form:

$$\left[\sum_{j=0}^{p} \widehat{\alpha}_j(t)\Phi_j\right]^3 = \sum_{i=0}^{p}\sum_{m=0}^{p}\sum_{n=0}^{p} \widehat{\alpha}_i\widehat{\alpha}_m\widehat{\alpha}_n\Phi_i\Phi_m\Phi_n. \tag{3.10}$$

Substituting (3.10) into (3.9) and simplifying, we get,

$$\pounds\left[\sum_{j=0}^{p} \widehat{\alpha}_j(t)\Phi_j\right] + \sum_{l=0}^{1} \beta_{\alpha l}\Phi_l \left[\sum_{i=0}^{p}\sum_{m=0}^{p}\sum_{n=0}^{p} \widehat{\alpha}_i\widehat{\alpha}_m\widehat{\alpha}_n\Phi_i\Phi_m\Phi_n\right] = 0. \tag{3.11}$$

Using Galerkin projection on (3.11) by taking $\langle\cdot,\Phi_k\rangle$, for $k = 0,1,\ldots,p$,

$$\pounds[\widehat{\alpha}_k(t)] + \frac{1}{\langle\Phi_k^2\rangle}\left[\sum_{l=0}^{1}\sum_{i=0}^{p}\sum_{m=0}^{p}\sum_{n=0}^{p} \beta_{\alpha l}\widehat{\alpha}_i\widehat{\alpha}_m\widehat{\alpha}_n\langle\Phi_l\Phi_i\Phi_m\Phi_n\Phi_k\rangle\right] = 0. \tag{3.12}$$

The expected value operator $\langle\cdot\rangle$, called the inner product, is defined as,

$$\langle\Phi_l\cdots\Phi_k\rangle = \int_{-\infty}^{\infty} \Phi_l\cdots\Phi_k\,\omega(\xi)\mathrm{d}\xi. \tag{3.13}$$

Table 1

$\langle \Phi_1\Phi_1 \rangle = 1$	$\langle \Phi_0\Phi_0\Phi_0\Phi_0\Phi_0 \rangle = 1$
$\langle \Phi_2\Phi_2 \rangle = 2$	$\langle \Phi_0\Phi_0\Phi_1\Phi_1\Phi_2 \rangle = 2$
$\langle \Phi_3\Phi_3 \rangle = 6$	$\langle \Phi_0\Phi_1\Phi_1\Phi_2\Phi_2 \rangle = 10$
$\langle \Phi_4\Phi_4 \rangle = 24$	$\langle \Phi_0\Phi_1\Phi_2\Phi_2\Phi_3 \rangle = 48$

For Hermite polynomials the weighting function $\omega(\xi)$ is the Gaussian probability density function. For single random variable case it is given as

$$\omega(\xi) = \left(\frac{1}{\sqrt{2\pi}}\right) e^{-((1/2)\xi^2)}. \tag{3.14}$$

The Hermite polynomials are orthogonal with respect to this weighting function in the Hilbert space. The polynomial chaos forms a complete orthogonal basis in the L_2 space of real-valued functions depending on the Gaussian random variables; hence the inner product of two orthogonal polynomial can be replaced by the identity

$$\langle \Phi_l \Phi_k \rangle = \left\langle \Phi_l^2 \right\rangle \delta_{lk}, \tag{3.15}$$

δ_{lk} is the Kronecker delta function, given as:

$$\delta_{lk} = \begin{cases} 1 & \text{if } l = k, \\ 0 & \text{otherwise.} \end{cases} \tag{3.16}$$

The inner product terms in (3.12) $\langle \Phi_l \Phi_i \Phi_m \Phi_n \Phi_k \rangle$ and $\langle \Phi_k^2 \rangle$ can be evaluated analytically before-hand and substituted in the equation. The resulting system becomes a deterministic differential equation in terms of the chaos coefficients. Depending on the type of nonlinearity, the number of random variables and the number of expansion terms, evaluating the inner products could be tedious. In the present study, they are computed by numerical integration by using Gauss-Hermite quadrature rule and verified analytically by using symbolic mathematical solver *Mathematica*. Some typical nonzero inner-products are given in Table 1.

The Galerkin approach is also called the intrusive approach as it modifies the system governing equations in terms of the chaos coefficients. The modification results into a higher order and much more complex form. As a result, this approach may become computationally quite expensive.

3.2. Nonintrusive Projection Method

A number of nonintrusive variants of PCE have been developed to counter the disadvantages of the classical Galerkin method. Stochastic projection is one of them [4, 30]. In the present study, a stochastic projection-based approach is used to evaluate the chaos coefficients. Here, the chaos expansions are not substituted in the governing equations; instead samples of the solutions are used (using low-order deterministic simulations) to evaluate the coefficients

directly using a projection formula. As a result, this approach can utilize the existing deterministic code and hence the name nonintrusive. The random process is approximated by a truncated series, as shown in (3.7).

The Hermite polynomials are statistically orthogonal, that is, they satisfy $\langle \Phi_i \Phi_j \rangle = 0$ for $i \neq j$, hence the expansion coefficients can be directly evaluated as

$$\widehat{\alpha}_j(t) = \frac{\langle \alpha(t, \xi(\theta)) \Phi_j \rangle}{\left\langle \Phi_j^2 \right\rangle}. \tag{3.17}$$

The denominator in (3.17) can be shown to satisfy $\langle \Phi_j^2 \rangle = j!$ for nonnormalized Hermite polynomials [31]. So the key step in projecting $\alpha(t, \xi(\theta))$ along the polynomial chaos basis is the evaluation of $\langle \alpha(t, \xi(\theta)) \Phi_j \rangle$. The inner product is given by the following integral:

$$\langle \alpha(t, \xi(\theta)) \Phi_j \rangle = \int_{-\infty}^{\infty} \alpha(t, \xi(\theta)) \Phi_j \omega(\xi) \mathrm{d}\xi. \tag{3.18}$$

A Gauss-Hermite quadrature will be suitable for evaluating the above as the domain is $(-\infty, \infty)$ and the weight function is Gaussian PDF. The quadrature points are the zeros of the Hermite polynomials of chosen order. A number of deterministic runs are performed at the quadrature points which is much lower than the full Monte Carlo simulations. We refer to this step as a pseudo-Monte Carlo simulation approach. In the pseudo-MCS approach the samples of β_α are generated from the corresponding ξ values which are the Gauss-Hermite quadrature points. The realizations of the system response $\alpha(t, \theta)$ are then used to estimate the deterministic coefficients, $\widehat{\alpha}_j(t)$'s, in (3.17) using the Gauss-Hermite quadrature rule. It should also be noted that for each evaluation of the inner product integral a convergence study is done by gradually increasing the number of quadrature points.

4. Results and Discussions

The main focus of the present study is quantifying the effect of system uncertainties on the bifurcation behavior and the flutter boundary of the nonlinear aeroelastic system. A fourth order variable step Runge-Kutta method is employed for the time integration. The main bifurcation parameter in a flutter system is the nondimensional wind velocity, also called the reduced velocity. In a linear aeroelastic system, the response changes to an exponentially growing solution from a stable damped oscillation at some critical wind velocity, known as the linear flutter speed. Nonlinear aeroelastic system can stabilize the response at the post-flutter regime to limit cycle oscillations [23] and the critical point becomes a Hopf bifurcation point. With a cubic nonlinearity, both supercritical and subcritical Hopf bifurcations are possible [32]. The latter case is observed for a softening cubic spring. Here in the stochastic analysis, we focus on the supercritical case. A deterministic bifurcation diagram with the following parameter values [23] is shown in Figure 2: $\mu = 100, \overline{\omega} = 0.2, a_h = -0.5, x_\alpha = 0.25, \zeta_\alpha = 0, \zeta_\varepsilon = 0, r_\alpha = 0.5, \beta_\alpha = 3, \beta_\varepsilon = 0$. The variation of the limit cycle oscillation (LCO) amplitude is plotted with reduced velocities. Bifurcation occurs at the corresponding linear flutter speed of 6.285, and the observation match well with the earlier results [33]. At the post flutter velocities, limit cycle oscillations are observed and the amplitude of the LCOs increase as the reduced velocity increases.

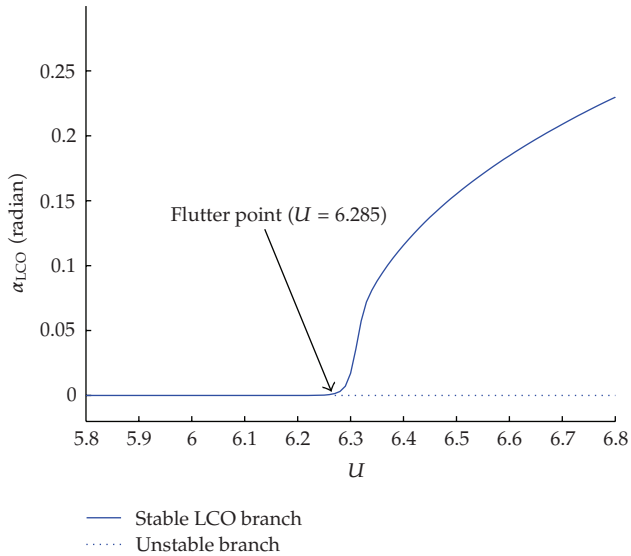

Figure 2: Deterministic flutter and bifurcation diagram with cubic nonlinearity (supercritical Hopf bifurcation).

We now consider random variations in the system parameters and investigate the influence on the overall dynamics. We consider only single uncertain parametric variation in this paper, that is, a single random variable model. First, the hardening cubic spring constant is considered to be a Gaussian random variable with mean $\overline{\beta}_\alpha = 3$ and standard deviation $\widetilde{\beta_\alpha} = 0.3$. All other parameters are assumed to be deterministic. Figure 3 shows bifurcation behavior with the cubic stiffness as random, it now has a range of possible LCO amplitudes for each reduced velocity and the onset of flutter is unaffected. The standard deviation, that is, the amplitude variation range increases as reduced speed increases.

A Galerkin PCE approach is used to quantify the propagation of this uncertainty on the response. The Galerkin approach modifies the 8th-order flutter system to an $8 \times (p + 1)$ order system. It also involves calculating the complex fifth-order inner product terms as shown earlier. As a result, the solution process is computationally intensive for the nonlinear system in question. After solving for the chaos coefficients, in the post processing stage, the coefficients are substituted back to the expansion form to get the stochastic response. Probability density functions (PDFs) and other required statistics can then be readily obtained. The time histories of the first few random modes in pitch are plotted in Figure 4. The zeroth-order mode is the mean; one can also see that the contribution of higher-order random modes is gradually diminishing. A representative PDF is shown in Figure 5 for increasing order of chaos expansion terms. PDFs are calculated at time $t = 7000$ at which the solutions are well past their transients and stationary. The reduced speed considered here is $U = 6.42$, close to the deterministic bifurcation point. The figure also presents results from a standard MCS with 12000 samples as a comparison reference. One can see how increasing the order of expansion the CPU time for the solution is getting magnified. Results are presented up to the 12th order of expansion at which the PCE results match well with that of MCS. However, the simulation time also approaches to that of the reference MCS. While calculating the CPU time for the Galerkin-PCE approach the inner products computation and post processing of results are not taken into account.

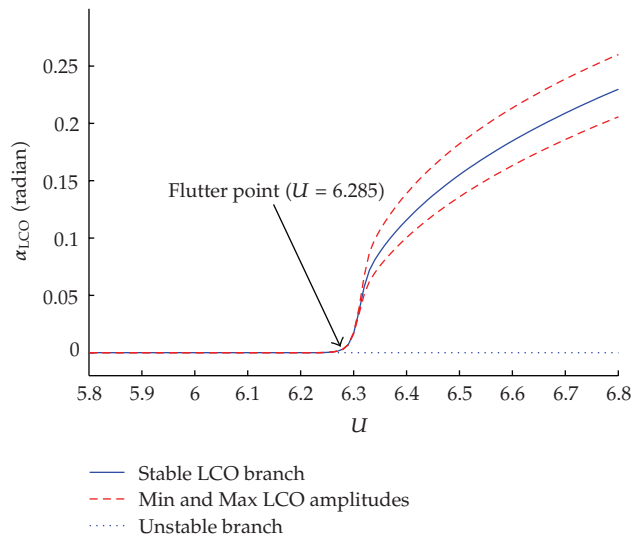

Figure 3: Uncertain nonlinear stiffness: stochastic bifurcation diagram.

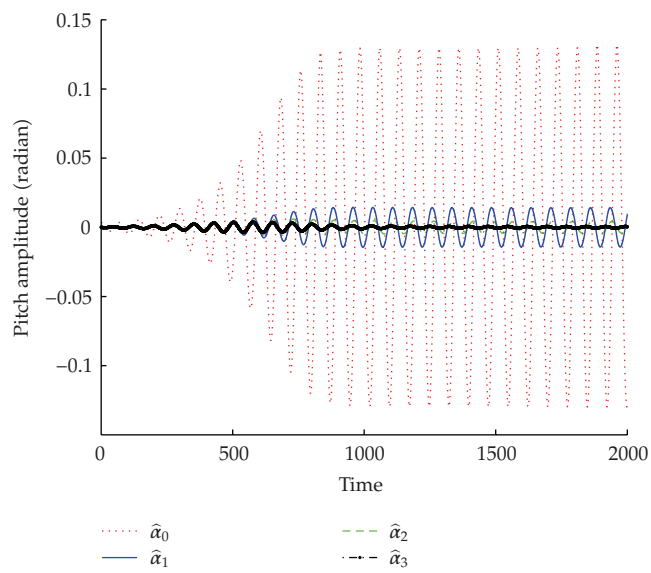

Figure 4: Galerkin-PCE: behavior of the first few random modes.

Now the nonintrusive projection approach is followed using a Gauss-Hermite quadrature. Galerkin-PCE and nonintrusive results are compared in terms of their accuracy and simulation time in Figure 6. A good match with MCS is seen for the 12th order of expansion. Once again a standard MCS with 12000 samples is used as a reference solution (in other cases too we have used a standard 12000 samples MCS as reference). However, nonintrusive approach is seen to be much faster than Galerkin-PCE for the same level of accuracy as indicated in Figure 6. With this, the computational disadvantage of

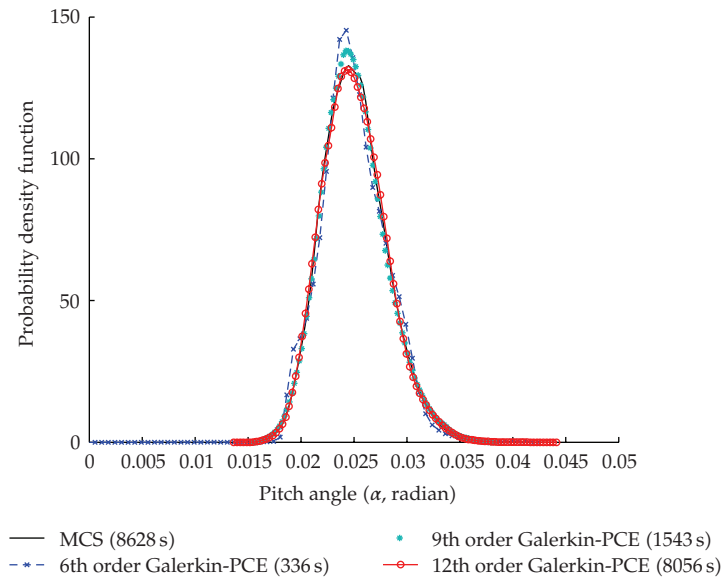

Figure 5: Galerkin-PCE: PDF comparisons for increasing order of chaos expansions, at $t = 7000$ with $U = 6.42$.

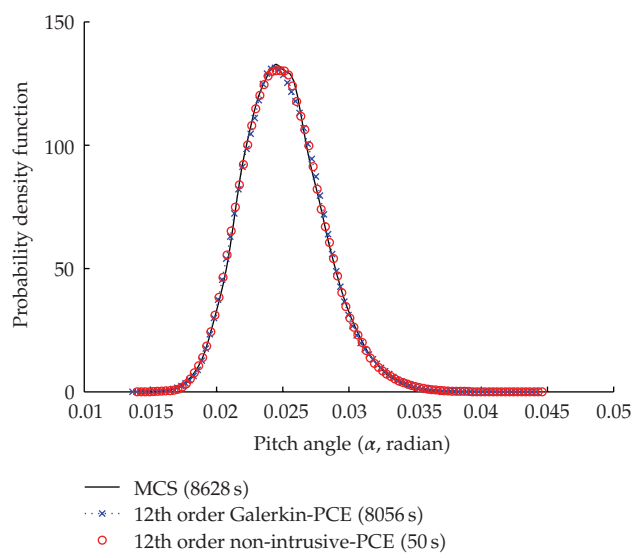

Figure 6: Galerkin-PCE: PDF comparisons for intrusive and nonintrusive PCE, at $t = 7000$ with $U = 6.42$.

the conventional Galerkin based PCE for nonlinear systems is demonstrated. Henceforth, this approach will not be used for further simulations in this paper.

The response realization time histories for a few samples of random variable ξ are plotted in Figure 7. The response time histories show difference in amplitude but not in phase. A typical realization time history obtained with the 12th order PCE along with its deterministic counterpart is compared in Figure 8. The match is perfect even at long time. Amplitude response PDFs as a function of reduced velocities (bifurcation parameter) are

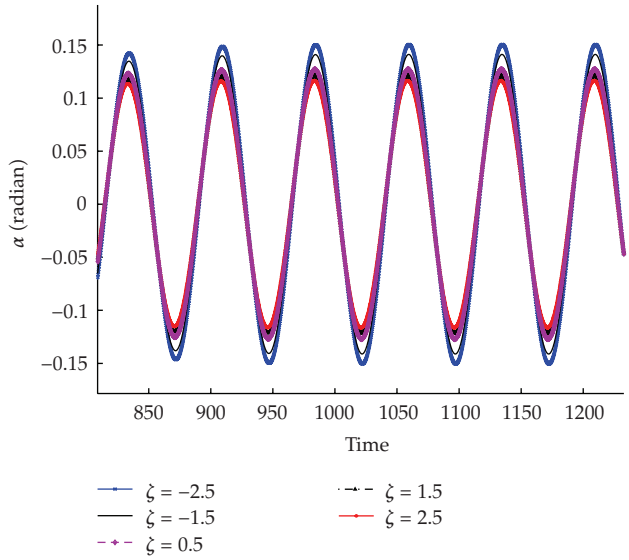

Figure 7: Uncertain nonlinear stiffness: five different realizations time histories at $U = 6.42$.

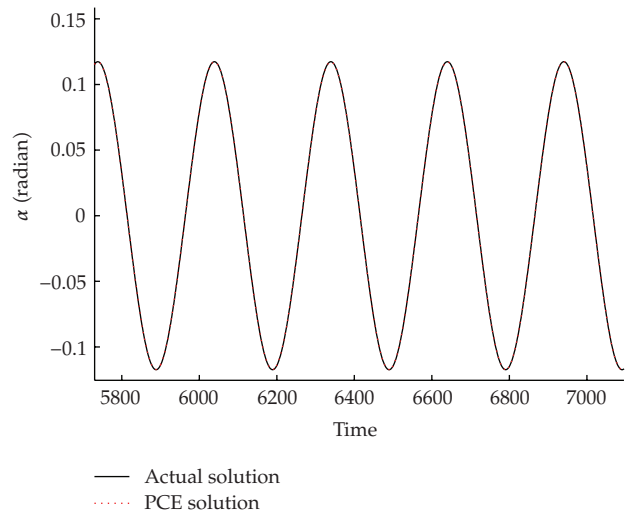

Figure 8: Uncertain nonlinear stiffness: comparison of a typical time history with 12th order PCE and MCS for $\xi = 1.5$ and $U = 6.42$.

shown in Figure 9. They represent single peak monotonic behavior as all the realizations give finite amplitude LCOs. Effectively, the PDFs are not undergoing any qualitative change or bifurcations. Close to $U = 6.4$ the PDF looks sharper and narrower as most realizations are going towards the same limit cycle amplitude. As the speed increases, the PDF is broader and less sharp, indicating that the realization amplitudes are spread over a wider band of amplitudes.

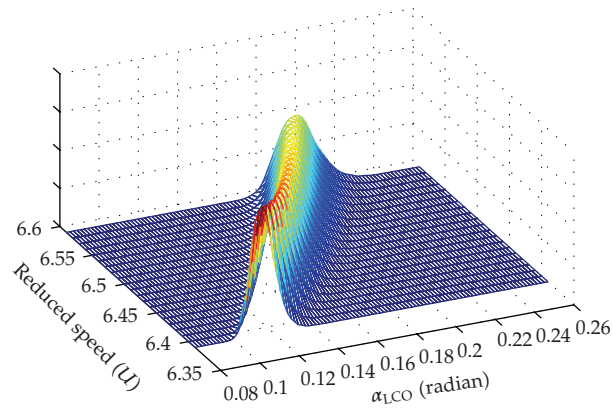

Figure 9: Uncertain nonlinear stiffness: amplitude response PDF as a function of reduced speed.

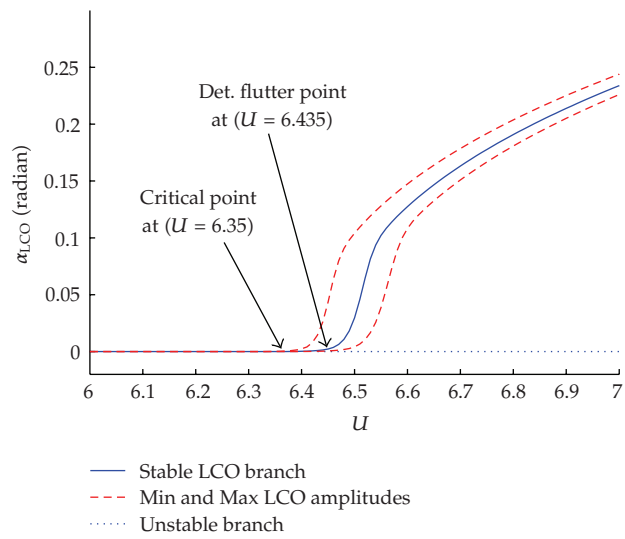

Figure 10: Uncertain viscous damping: stochastic bifurcation diagram.

Next, we consider the viscous damping ratio in pitch (ζ_α) to be uncertain (in the earlier part damping was put to be zero) and all the other parameters deterministic. This case is potentially more interesting than the earlier one. The damping ratio is assumed to be a Gaussian random variable with mean $\bar{\zeta}_\alpha$ =0.1 and standard deviation $\tilde{\zeta}_\alpha$ = 0.01. Figure 10 shows the bifurcation behavior with random damping ratio. The firm line gives the deterministic bifurcation behavior. The other bifurcation branches are for the two different extreme realizations of the random damping. Thus they represent the boundaries of the possible random variations of the bifurcation behavior (stochastic).

The major difference between the uncertain damping and the earlier considered uncertain stiffness is that, variation in damping can show phase shifting behavior in the response realizations. This is presented in Figure 11 where five different realizations are

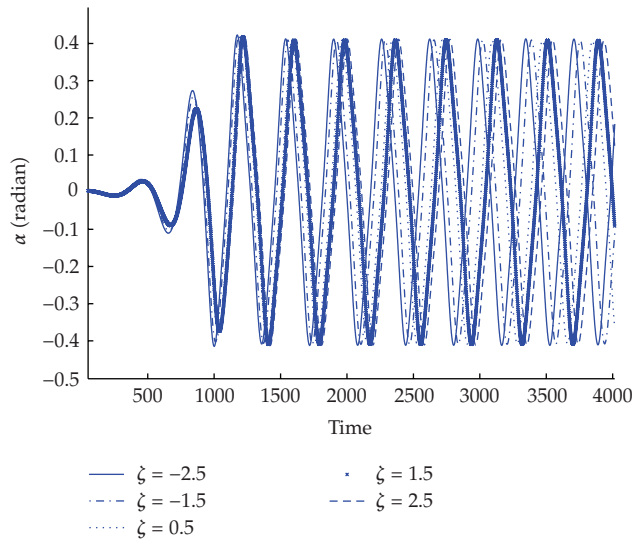

Figure 11: Uncertain viscous damping: five different realizations time history at $U = 6.52$.

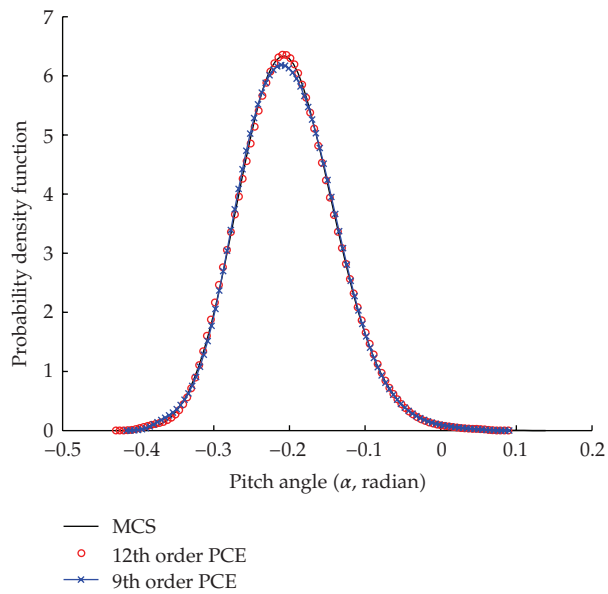

Figure 12: Uncertain viscous damping: comparison of the PDFs with increasing order of PCE at nondimensional time 1400 at $U = 6.52$.

shifted in phase from each other. This behavior becomes more pronounced as time increases. As a result, response PDFs can now show bimodal behavior especially at large times. A few representative PDFs are plotted now at different reduced velocities. Figure 12 shows the response PDF at $U = 6.52$ and time = 1400. Though the time level is past the transients it is not large and the phase shift is not yet very pronounced. The response

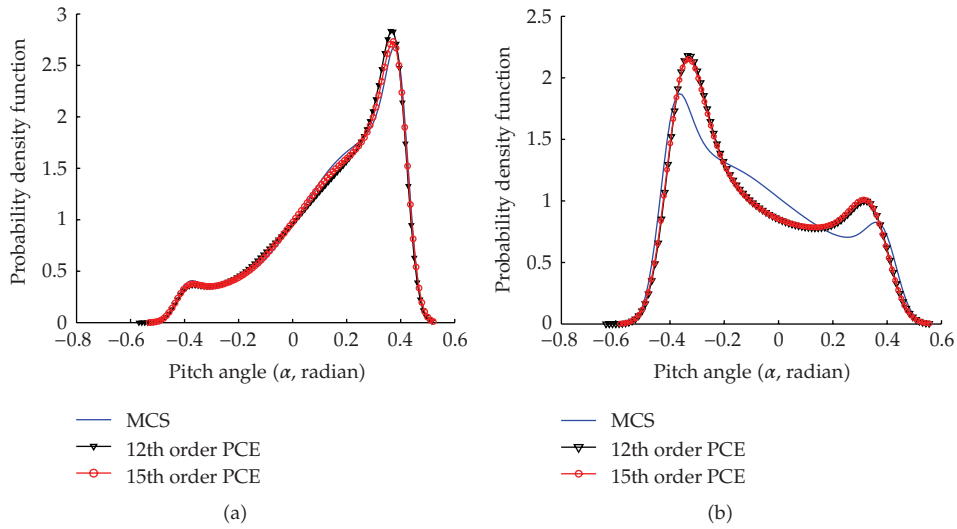

Figure 13: Uncertain viscous damping: comparison of the PDFs with increasing order of PCE at $U = 6.52$ with nondimensional time (a) $t = 5000$, (b) $t = 7800$.

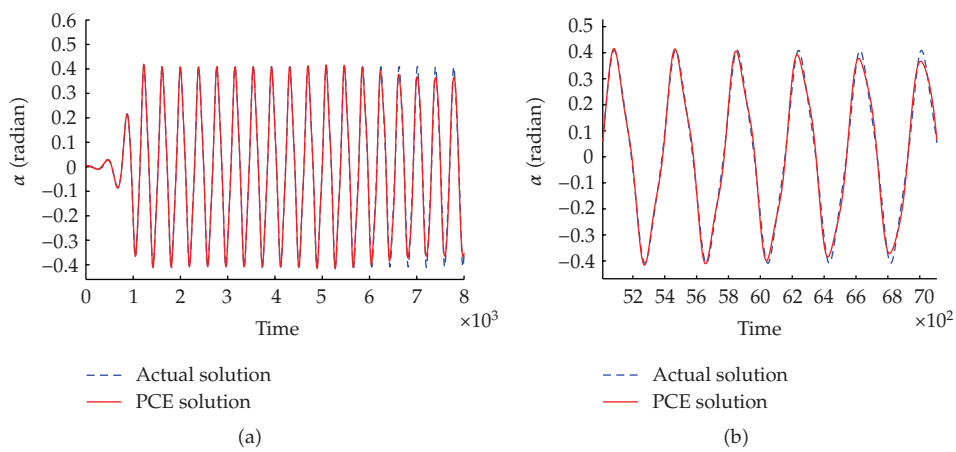

Figure 14: Uncertain viscous damping: a typical time history with (a) The 15th order PCE and MCS at $\xi = 2.3$ and reduced speed $U = 6.52$. (b) A close-up of (a).

PDF shows a single peak pattern. A reasonably good match with MCS is obtained within the 12th order of chaos expansion. However, at higher time levels as the phase shifting becomes stronger, the PDFs start to look distorted from their single peak behavior and goes towards a double peak pattern. Figure 13 shows the PDF at $U = 6.52$ and time 5000 and 7800. In the first case, a double-peak bimodal PDF is just emerging as shown in Figure 13(a). In this case a 12th order expansion is not sufficient to capture the response accurately; a 15th order expansion gives better accuracy. At higher time 7800, the response

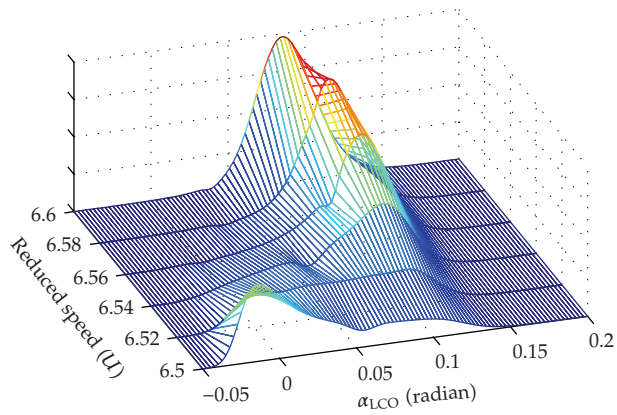

Figure 15: Uncertain viscous damping: amplitude response PDF as a function of reduced velocities.

PDF is more towards a two-peak bimodal shape as is seen in Figure 13(b). However, even a 15th order chaos expansion does not give the required accuracy. If one considers a different reduced velocity, the bimodal behavior can appear at some different time levels. The important observations from these figures are two-fold. First is the gradual double-peak behavior with increasing time. The second one is the apparent mismatch between the MCS and PCE results which seems to be increasing again with time. The reason for the first is nothing but the increasing phase shifting between the realizations time histories. However, for the second, the reason for the mismatch is the long time degeneracy which is shown in Figure 14. This mismatch can be improved by using higher order chaos expansions.

A typical realization time history with PCE along with its deterministic counterpart are presented in Figure 14. One can clearly see a degeneracy in the time history which starts around time levels close to 6000. PCE can show such type of degenerate behavior in capturing LCO response [17], especially at large times. As a counter measure, one can increase the order of the chaos expansion. However, this can only push the degeneracy to a later time but can not solve it entirely. Nonpolynomial based chaos approaches have been attempted in the recent past towards this end [17]. An unsteady adaptive stochastic finite elements method, developed by Witteveen and Bijl [34–36] has also been used successfully. This approach is based on time-independent parametrization. This achieves a constant accuracy in time with a constant number of samples. In this method interpolation of oscillatory samples is based on constant phase instead of a constant time.

The amplitude response PDFs for the uncertain damping case is shown in Figure 15 for different reduced velocities. Here the LCO amplitudes are captured after the initial transients have died down but before the time degeneracy has started. A nonmonotonic behavior is clearly indicated; some realizations are going to damped oscillation and others give LCO amplitudes scattered within the domain boundary. At $U = 6.5$, the double-peak behavior of the PDF indicates the two different LCO amplitudes around which most of the realizations are concentrated. Towards $U = 6.6$, all realizations give finite amplitude LCO, thus essentially they are of the same type. The PDF shows a single-peak monotonous behavior. Therefore, the PDFs of the response amplitude have clearly gone through a qualitative change here, in other words, a bifurcation.

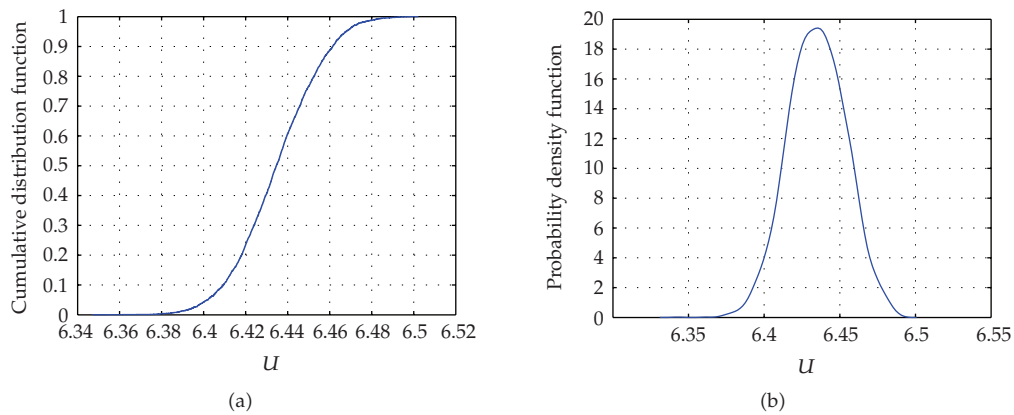

Figure 16: Uncertain viscous damping: (a) CDF, (b) PDF of the critical flutter point.

For the uncertain damping case, we also see that the critical reduced velocity at which flutter can occur, has come down from its corresponding deterministic value. This value can be read off the bifurcation plot (Figure 10) as $U = 6.35$. This is the lowest extrema of the critical points. The cumulative distribution function (CDF) and the PDF of the critical points are shown in Figure 16. The CDF can directly give the probability of flutter (in other words, probability of failure) at any given reduced velocity.

5. Conclusions

The bifurcation behavior of a nonlinear pitch-plunge flutter problem with uncertain system parameters has been studied. The problem is a simple model problem to understand the mechanism of nonlinear flutter in a stochastic framework. The parameters which have been assumed to be random could attribute their uncertainties to laboratory testing conditions. Moreover, a cubic nonlinear stiffness is used for various sources of analytic nonlinearities; they often represent different control mechanisms and could face modeling uncertainties.

The classical Galerkin Polynomial Chaos method and the nonintrusive Projection method are applied to capture the propagation of uncertainty through the nonlinear aeroelastic system. The focus of this work is to investigate the performance of these techniques and to see how the aeroelastic stability characteristics are altered due to the random effects. The Monte Carlo solution is used as reference solution. The computational cost of the Galerkin Polynomial Chaos method is seen to be very high and subsequently only the Projection method based on Gauss-Hermite quadrature is used for the analysis. The effect of uncertain cubic structural nonlinearity and viscous damping parameter are investigated. Uncertainty in the cubic stiffness does not alter the bifurcation (flutter) point, it only affects the amplitudes of the periodic response in the post flutter stage. The PDF behavior also does not show any qualitative changes. On the other hand, uncertainty in damping affects the bifurcation point. It can lower the onset of flutter; the PDF of the response amplitude also undergoes a qualitative change. In other words, a bifurcation of the response PDF takes place. The results highlight the risk induced by parametric uncertainty and importance of uncertainty quantification in nonlinear aeroelastic systems.

The uncertain damping case by polynomial chaos suffer from long time degeneracy, as is also discussed in the literature. The degeneracy can be controlled by using higher order chaos expansions, though this cannot be a permanent solution. For the uncertain nonlinear stiffness, the problem of time degeneracy is not encountered.

Appendix

The coefficients introduced in Section 2 are used from [23] and are reproduced here for the sake of completeness:

$$c_0 = 1 + \frac{1}{\mu}, \quad c_1 = x_\alpha - \frac{a_h}{\mu}, \qquad c_2 = 2\zeta_\varepsilon \frac{\overline{\omega}}{U} + \frac{2}{\mu}\left(1 - \psi_1 - \psi_2\right),$$

$$c_3 = \frac{1 + 2(1/2 - a_h)\left(1 - \psi_1 - \psi_2\right)}{\mu}, \qquad c_4 = \left(\frac{\overline{\omega}}{U}\right)^2 + \frac{2}{\mu}\left(\psi_1\epsilon_1 + \psi_2\epsilon_2\right),$$

$$c_5 = \beta_\varepsilon\left(\frac{\overline{\omega}}{U}\right)^2, \qquad c_6 = \frac{2}{\mu}\left[\left(1 - \psi_1 - \psi_2\right) + \left(\frac{1}{2} - a_h\right)\left(\psi_1\epsilon_1 + \psi_2\epsilon_2\right)\right],$$

$$c_7 = \frac{2}{\mu}\psi_1\epsilon_1\left[1 - \left(\frac{1}{2} - a_h\right)\epsilon_1\right], \qquad c_8 = \frac{2}{\mu}\psi_2\epsilon_2\left[1 - \left(\frac{1}{2} - a_h\right)\epsilon_2\right],$$

$$c_9 = -\frac{2}{\mu}\psi_1\epsilon_1^2, \qquad c_{10} = -\frac{2}{\mu}\psi_2\epsilon_2^2,$$

$$d_0 = \frac{x_\alpha}{r_\alpha^2} - \frac{a_h}{\mu r_\alpha^2}, \qquad d_1 = 1 + \frac{1 + 8a_h^2}{8\mu r_\alpha^2},$$

$$d_2 = 2\frac{\zeta_\alpha}{U} + \frac{1 - 2a_h}{2\mu r_\alpha^2} - \frac{(1 + 2a_h)(1 - 2a_h)\left(1 - \psi_1 - \psi_2\right)}{2\mu r_\alpha^2}$$

$$d_3 = \frac{1}{U^2} - \frac{(1 + 2a_h)\left(1 - \psi_1 - \psi_2\right)}{\mu r_\alpha^2} - \frac{(1 + 2a_h)(1 - 2a_h)\left(\psi_1\epsilon_1 + \psi_2\epsilon_2\right)}{2\mu r_\alpha^2},$$

$$d_4 = \frac{\beta_\alpha}{U^2}, \quad d_5 = -\frac{(1 + 2a_h)\left(1 - \psi_1 - \psi_2\right)}{\mu r_\alpha^2}, \qquad d_6 = -\frac{(1 + 2a_h)\left(\psi_1\epsilon_1 + \psi_2\epsilon_2\right)}{\mu r_\alpha^2},$$

$$d_7 = -\frac{(1 + 2a_h)\left(\psi_1\epsilon_1[1 - (1/2 - a_h)\epsilon_1]\right)}{\mu r_\alpha^2}, \qquad d_8 = -\frac{(1 + 2a_h)\left(\psi_2\epsilon_2[1 - (1/2 - a_h)\epsilon_2]\right)}{\mu r_\alpha^2},$$

$$d_9 = \frac{(1 + 2a_h)\psi_1\epsilon_1^2}{\mu r_\alpha^2}, \qquad d_{10} = \frac{(1 + 2a_h)\psi_2\epsilon_2^2}{\mu r_\alpha^2},$$

$$f(\tau) = \frac{2}{\mu}\left(\left(\frac{1}{2} - a_h\right)\alpha(0) + \varepsilon(0)\right)\left(\psi_1\epsilon_1 e^{-\epsilon_1\tau} + \psi_2\epsilon_2 e^{-\epsilon_2\tau}\right), \qquad g(\tau) = -\frac{(1 + 2a_h)f(\tau)}{2r_\alpha^2}. \tag{A.1}$$

References

[1] M. Kleiber and T. D. Hien, *The Stochastic Finite Element Method: Basic Perturbation Technique and Computer Implementation*, John Wiley & Sons, Chichester, UK, 1992.

[2] T. D. Hien and M. Kleiber, "Computational aspects in structural design sensitivity analysis for statics and dynamics," *Computers and Structures*, vol. 33, no. 4, pp. 939–950, 1989.

[3] R. Ghosh, S. Chakraborty, and B. Bhattacharyya, "Stochastic sensitivity analysis of structures using first-order perturbation," *Meccanica*, vol. 36, no. 3, pp. 291–296, 2001.

[4] R. G. Ghanem and P. D. Spanos, *Stochastic Finite Elements: A Spectral Approach*, Springer, New York, NY, USA, 1991.

[5] R. G. Hills and T. G. Trucano, "Statistical validation of engineering and scientific models: background," May 1999, http://citeseerx.ist.psu.edu/viewdoc/summary?doi=10.1.1.40.1901.

[6] N. Wiener, "The homogeneous chaos," *American Journal of Mathematics*, vol. 60, no. 4, pp. 897–936, 1938.

[7] R. Ghanem, "Stochastic finite elements with multiple random non-Gaussian properties," *Journal of Engineering Mechanics*, vol. 125, no. 1, pp. 26–40, 1999.

[8] D. Xiu and G. E. Karniadakis, "Modeling uncertainty in flow simulations via generalized polynomial chaos," *Journal of Computational Physics*, vol. 187, no. 1, pp. 137–167, 2003.

[9] D. Lucor and G. E. Karniadakis, "Predictability and uncertainty in flow-structure interactions," *European Journal of Mechanics B*, vol. 23, no. 1, pp. 41–49, 2004.

[10] G. Lin, C.-H. Su, and G. E. Karniadakis, "Predicting shock dynamics in the presence of uncertainties," *Journal of Computational Physics*, vol. 217, no. 1, pp. 260–276, 2006.

[11] I. Babuška, F. Nobile, and R. Tempone, "A stochastic collocation method for elliptic partial differential equations with random input data," *SIAM Journal on Numerical Analysis*, vol. 45, no. 3, pp. 1005–1034, 2007.

[12] G. J. A. Loeven, J. A. S. Witteveen, and H. Bijl, "Probabilistic collocation: an efficient non-intrusive approach for arbitrarily distributed parametric uncertainties," in *Proceedings of the 45th AIAA Aerospace Sciences Meeting*, vol. 6, pp. 3845–3858, Reno, Nev, USA, January 2007.

[13] S. Hosder, R. W. Walters, and R. Perez, "A non-intrusive polynomial chaos method for uncertainty propagation in CFD simulations," in *Proceedings of the 44th AIAA Aerospace Sciences Meeting*, vol. 14, pp. 10649–10667, Reno, Nev, USA, January 2006.

[14] R. W. Walters, "Towards stochastic fluid mechanics via polynomial chaos," in *Proceedings of the 41st AIAA Aerospace Sciences Meeting and Exhibit*, Reno, Nev, USA, 2003.

[15] S. Hosder, R. W. Walters, and M. Balch, "Efficient uncertainty quantification applied to the aeroelastic analysis of a transonic wing," in *Proceedings of the 46th AIAA Aerospace Sciences Meeting and Exhibit*, Reno, Nev, USA, 2008.

[16] M. T. Reagan, H. N. Najm, R. G. Ghanem, and O. M. Knio, "Uncertainty quantification in reacting-flow simulations through non-intrusive spectral projection," *Combustion and Flame*, vol. 132, no. 3, pp. 545–555, 2003.

[17] C. L. Pettit and P. S. Beran, "Polynomial chaos expansion applied to airfoil limit cycle oscillations," in *Proceedings of the 45th AIAA/ASME/ASCE/AHS/ASC Structures, Structural Dynamics and Materials Conference*, vol. 3, pp. 1975–1985, Palm Springs, Calif, USA, April 2004.

[18] C. L. Pettit and P. S. Beran, "Spectral and multiresolution Wiener expansions of oscillatory stochastic processes," *Journal of Sound and Vibration*, vol. 294, no. 4, pp. 752–779, 2006.

[19] B. Ganapathysubramanian and N. Zabaras, "Sparse grid collocation schemes for stochastic natural convection problems," *Journal of Computational Physics*, vol. 225, no. 1, pp. 652–685, 2007.

[20] T. Gerstner and M. Griebel, "Numerical integration using sparse grids," *Numerical Algorithms*, vol. 18, no. 3-4, pp. 209–232, 1998.

[21] D. Xiu and J. S. Hesthaven, "High-order collocation methods for differential equations with random inputs," *SIAM Journal on Scientific Computing*, vol. 27, no. 3, pp. 1118–1139, 2005.

[22] Y. C. Fung, *An Introduction to the Theory of Aeroelasticity*, John Wiley & Sons, New York, NY, USA, 1955.

[23] B. H. K. Lee, L. Jiang, and Y. S. Wong, "Flutter of an airfoil with a cubic nonlinear restoring force," *AIAA-98-1725*, pp. 237–257, 1998.

[24] R. T. Jones, "The unsteady lift of a wing of finite aspect ratio," NACA Report 681, NACA, 1940.

[25] N. Wiener, *Nonlinear Problems in Random Theory*, Technology Press Research Monographs, MIT Press and John Wiley & Sons, New York, NY, USA, 1958.

[26] D. Xiu and G. E. Karniadakis, "The Wiener-Askey polynomial chaos for stochastic differential equations," *SIAM Journal on Scientific Computing*, vol. 24, no. 2, pp. 619–644, 2002.

[27] O. P. Le Maître, O. M. Knio, H. N. Najm, and R. G. Ghanem, "A stochastic projection method for fluid flow. I. Basic formulation," *Journal of Computational Physics*, vol. 173, no. 2, pp. 481–511, 2001.
[28] R. H. Cameron and W. T. Martin, "The orthogonal development of non-linear functionals in series of Fourier-Hermite functionals," *Annals of Mathematics*, vol. 48, pp. 385–392, 1947.
[29] J. A.S. Witteveen, S. Sarkar, and H. Bijl, "Modeling physical uncertainties in dynamic stall induced fluid-structure interaction of turbine blades using arbitrary polynomial chaos," *Computers and Structures*, vol. 85, no. 11–14, pp. 866–878, 2007.
[30] D. R. Millman, P. I. King, and P. S. Beran, "A stochastic approach for predicting bifurcation of a pitch and plunge airfoil," in *Proceedings of the 21st AIAA Applied Aerodynamics Conference*, Orlando, Fla, USA, 2003, Paper no. AIAA-2003-3515.
[31] C. L. Pettit and P. S. Beran, "Spectral and multiresolution Wiener expansions of oscillatory stochastic processes," *Journal of Sound and Vibration*, vol. 294, no. 4, pp. 752–779, 2006.
[32] D. S. Woolston, H .L. Runyan, and R. E. Andrews, "Some effects of system nonlinearities in the problem of aircraft flutter," Tech. Rep. TN 3539, NACA, 1955.
[33] H. Alighanbari and S. J. Price, "The post-hopf-bifurcation response of an airfoil in incompressible two-dimensional flow," *Nonlinear Dynamics*, vol. 10, no. 4, pp. 381–400, 1996.
[34] J. A. S. Witteveen and H. Bijl, "Higher period stochastic bifurcation of nonlinear airfoil fluid-structure interaction," *Mathematical Problems in Engineering*, vol. 2009, Article ID 394387, 26 pages, 2009.
[35] J. A.S. Witteveen and H. Bijl, "An alternative unsteady adaptive stochastic finite elements formulation based on interpolation at constant phase," *Computer Methods in Applied Mechanics and Engineering*, vol. 198, no. 3-4, pp. 578–591, 2008.
[36] J. A. S. Witteveen and H. Bijl, "Effect of randomness on multi-frequency aeroelastic responses resolved by unsteady adaptive stochastic finite elements," *Journal of Computational Physics*, vol. 228, no. 18, pp. 7025–7045, 2009.

Hindawi Publishing Corporation
Mathematical Problems in Engineering
Volume 2010, Article ID 579010, 14 pages
doi:10.1155/2010/579010

Research Article

Forecasting of Sporadic Demand Patterns with Seasonality and Trend Components: An Empirical Comparison between Holt-Winters and (S)ARIMA Methods

Rita Gamberini,[1] Francesco Lolli,[1] Bianca Rimini,[1] and Fabio Sgarbossa[2]

[1] *Department of Engineering Sciences and Methods, University of Modena and Reggio Emilia, via Amendola 2, Padiglione Morselli, Reggio Emilia 42100, Italy*
[2] *Department of Management and Engineering, University of Padua, Stradella San Nicola 3, Vicenza 36100, Italy*

Correspondence should be addressed to Rita Gamberini, rita.gamberini@unimore.it

Received 19 March 2010; Accepted 16 June 2010

Academic Editor: Carlo Cattani

Items with irregular and sporadic demand profiles are frequently tackled by companies, given the necessity of proposing wider and wider mix, along with characteristics of specific market fields (i.e., when spare parts are manufactured and sold). Furthermore, a new company entering into the market is featured by irregular customers' orders. Hence, consistent efforts are spent with the aim of correctly forecasting and managing irregular and sporadic products demand. In this paper, the problem of correctly forecasting customers' orders is analyzed by empirically comparing existing forecasting techniques. The case of items with irregular demand profiles, coupled with seasonality and trend components, is investigated. Specifically, forecasting methods (i.e., Holt-Winters approach and (S)ARIMA) available for items with seasonality and trend components are empirically analyzed and tested in the case of data coming from the industrial field and characterized by intermittence. Hence, in the conclusions section, well-performing approaches are addressed.

1. Introduction

In the recent competitive environment, where manufacturing and service companies operate in unstable sectors, managing irregular and sporadic demand patterns represents an increasingly frequent and complex issue. Startup productions, multiechelon supply chains or spare parts production, and selling are some examples of market fields characterized by intermittent demand profiles.

The complexity of dealing with these kinds of demand patterns lies in finding the best tradeoff between negative effects related with high storage levels, such as high amount of space and resources for keeping large warehouse areas, high holding costs, as well as high risks and cost due to items obsolescence, and negative effects related with low storage levels, such as lost demand and customers.

Therefore, when treating irregular and sporadic demand patterns, two relevant issues are discussed:

(i) demand forecasting in the future periods,

(ii) utilization of demand forecasting obtained for managing stocks. Hence issues related with when and how much it costs to create stocks for satisfying the forecasted customers' orders are faced.

The focus of this paper is on the first issue, which represents an unforgettable prerequisite for the second one and could become a needful competitive leverage for companies.

2. Literature Review

Croston [1] has published a pioneer work concerning forecast of irregular and sporadic demand (successively improved by Rao [2]). He observes that single exponential smoothing, even if frequently used for forecasting in inventory control systems, reaches inappropriate results when applied to intermittent demand patterns. Otherwise, computing both the average size of not-null demand occurrences and the average intervals between such occurrences is the intuition of Croston in order to achieve the estimator of mean demand per period. In particular, Croston considers customers' order series with demand occurrences generated by a Bernoulli process and with demand sizes (when not null) following a normal distribution. Then, he applies separately a single exponential smoothing to not-null demand sizes and interdemand intervals. Finally he combines them.

Successively, modifications of Croston's approach are proposed. Johnston and Boylan [3, 4] analyse demand patterns with the order arrival process modelled as a Poisson stream. Therefore, a negative exponential distribution is supposed to represent interorder arrivals. The authors propose a model to estimate the variance of demand and use it in a forecasting demand approach, whose performance is tested by considering a wide variety of operative conditions (i.e., many different average interdemand intervals, negative exponential, Erlang, and rectangular as distributions of order size). Syntetos and Boylan [5] explain the detection of a mistake in Croston's mathematical derivation of the expected estimate of demand per time period and propose an alternative approach, based again on the concept of forecasting demand from its constituent events. Subsequently, Syntetos and Boylan [6] introduce a factor equal to $(1 - \alpha/2)$ applied to Croston's original estimator of mean demand, with α being equal to the smoothing parameter in use for updating the interdemand intervals, in order to obtain a theoretically unbiased estimator. The derivation of the new estimator is based on Croston's assumptions of stationary, identically, independently distributed series of demand sizes and demand intervals, geometrically distributed interdemand intervals, and independence of demand sizes and intervals. Segersted [7] has proposed an alternative Croston's approach modification, adopted in sporadic demand inventory control by coupling it to the computation of probability of stock shortage, supposing demand following an Erlang distribution. An experimental analysis of the reachable performance is reported by Levén and Segersted in [8].

Recently, original contributions are published. Willemain et al. [9] forecast the cumulative distribution of demand over a fixed lead time using a new type of time series bootstrap. Specifically, the hypothesis of demand independence among subsequent time periods is disregarded and the existence of autocorrelation is considered. In the study by Gutierrez et al. in [10] the problem of forecasting lumpy demand series is analysed and a Neural Network (NN) approach is proposed. NN outperforms single exponential smoothing, Croston's approach, as well as Syntetos and Boylan approach in most of the analysed series and forecasting environments. Nevertheless, a consistent amount of data is required for setting the estimator and this is not the case treated in what follows in the paper. Keeping our attention on methodologies requiring a low amount of data to be set (i.e., moving averages, exponential smoothing, Croston's approach, Syntetos and Boylan modifications, as well as time series bootstrap), several works publish results obtained by comparing their performance in a wide variety of alternative operative conditions (i.e., Willemain et al. [11], Johnston and Boylan [3, 4], Sani and Kingsman [12], Strijbosch et al. [13], Willemain et al. [9], Syntetos and Boylan [6], Regattieri et al. [14], and given specifications reported by Syntetos in [15]).

Since Syntetos et al. [16] published their work, experimental analyses on alternative forecasting methods have been carried out by following the steps described in the sequel: firstly data categorization based on characteristics chosen by the management in respect to its needs and then finding the more appropriate forecasting methods for the different categories. Otherwise, Syntetos et al. [16] propose to categorize the demand patterns by following an alternative procedure: firstly analysing the optimal performance areas of several forecasting methods and then categorizing the demand patterns in accordance with results obtained. Even if, on one hand, these pioneering passes in the direction of demand patterns' categorizing are very interesting, on the other hand, the study by Syntetos et al. in [16] is based on assumptions not always confirmed by real-life data (i.e., demand occurring as a Bernoulli process or independence of demand values, as commented by [17–19]). Moreover, the proposed categorization methodology, even if it achieves satisfying results in the applied statistical fitting tests, does not describe the behaviour of the whole of the data series introduced in the experimentation. Hence, when complex data coming from real-life industrial contexts are managed, the definition of a pool of well-performing forecasting techniques still remains an interesting result to be investigated. Specifically, in this paper sporadic and irregular demand patterns with seasonality and trend components are studied.

Forecasting methods for demand patterns with seasonality and trend components are proposed by several authors. The focus in the following brief overview is on two techniques: the Holt-Winters (HW) approach [20], (see [21]), and ARIMA model, which is identified and then applied through the Box-Jenkins procedure [22]. Such a choice is justified by their applicability in real-life environments, mainly due to the great multitude of available statistical commercial softwares and expected good results, justified by past studies cited in the sequel. Furthermore, whilst HW is a useful forecasting tool addressed for its simplicity, (S)ARIMA is a robust approach appreciable due to its applicability to a wide variety of operative conditions.

HW is an extrapolative technique that isolates level, trend, and seasonal components of a time series regardless of the nature of the time series data being collected. It presents both a multiplicative and an additive version. ARIMA model is an integrated technique of auto-regressive (AR) models and moving average models, capable of finding a fitting function in an iterative way through the Box-Jenkins procedure. In the following, the acronym (S)ARIMA is used in place of ARIMA to specify the possibility that seasonality is present in

analysed time series. For a more detailed discussion on the application of (S)ARIMA models see the studies by Jarrett in [23] and Bowerman and O'Connell in [24].

Several authors investigate HW and (S)ARIMA performances in a wide variety of operating conditions [25–28], and [29]. Nevertheless the analysis of reachable forecasting results on irregular and sporadic time series with trend and seasonal components still remains a field to be widely investigated.

Hence, the purpose of the paper is to present results obtained by comparing HW and (S)ARIMA forecasting performances when applied to a set of real-life sporadic and irregular time series with seasonality and trend components.

The paper is organized as described in the sequel. A synthesis of the methodology implemented in the experimental analysis and then the first step of the project, concerning the collection and preliminary analysis of data, are presented, respectively, in Sections 3 and 4. In Section 5 the selection of the best (S)ARIMA model is carried out and then compared in Section 6 with the Holt-Winters method in terms of forecasting performances. Finally, conclusions and some guidance for practitioners are given in Section 7.

3. Framework of the Experimental Analysis

As aforementioned, the aim of the paper is the comparison between the Holt-Winters exponential smoothing with (S)ARIMA in cases of erratic and sporadic demands with seasonal and trend components.

Holt-Winters method manages three components of demand per period: a level component, a trend component, and a seasonal component. Each of them is estimated by exponential smoothing and successively opportunely weighted and combined in order to predict demand. In particular, two versions of HW components compositions are available: additive and multiplicative, but the presence of time periods with null demand does not allow the multiplicative version to be applied in this paper [20] (Winters, 1960) . A linear regression on time values is used to define the initial level and trend components while a dummy-variable regression on detrended time values is used to estimate the initial seasonal component.

While HW is simply applied by commercial softwares (in the sequel EViews 5 is adopted), which allow the solution to be achieved without any intervention of the user, (S)ARIMA models require the optimal definition of a set of parameters in accordance with results obtained in fitting tests. In Figure 1 the Box-Jenkins procedure [22] is briefly depicted and then explained in the sequel.

The flow diagram depicted in Figure 1 is an iterative decisional framework finalized firstly to find a (S)ARIMA model and then to apply it for demand forecasting. The Box-Jenkins procedure starts from the collection of data and preliminary analysis, which allow the identification of the preferable (S)ARIMA model to be achieved quickly. The first step of the preliminary analysis regards the stationarity of the time series, in terms of both mean and variance, required as a prerequisite for the application of the auto-regressive (AR) models and moving average (MA) models [22]. In case of nonstationarity, the procedure suggests the introduction of two differentiation orders, that is, d and D, that are, respectively, the non-seasonal and seasonal differentiation orders. A first order d of differentiation is applied in case of linear trend while a second order makes the time series stationary in case of quadratic trends and so on. In the same way D regards the seasonal component and it can be chosen by several tests, such as the Canova and Hansen test [30].

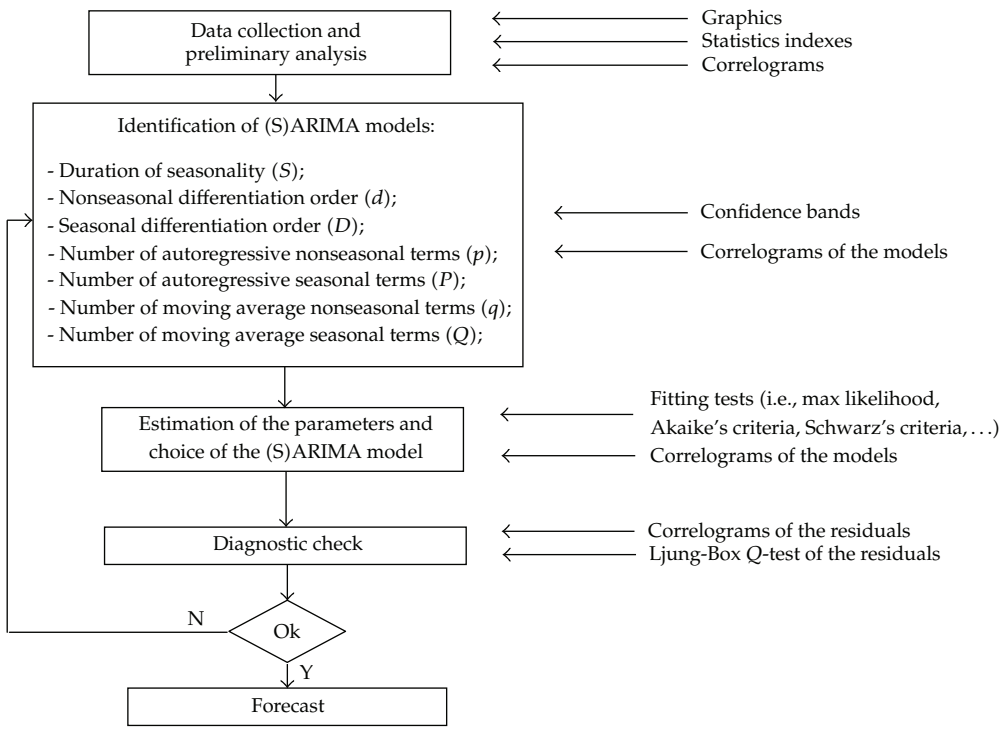

Figure 1: The Box-Jenkins procedure.

Graphics, statistical indexes, and correlograms support this phase. In particular, the more useful indicators are the distribution of the global autocorrelation coefficients (ρ_k, for $k = 1, \ldots, T$ with T being equal to the number of time periods constituting the time series) and the distribution of the partial correlation coefficients, which emerge, respectively, from the analysis of the global correlogram (ACF) and the partial correlogram (PACF). When a time series is stationary, autocorrelation coefficients in ACF and PACF tend to zero after two or three time lags. Some tests are available in order to check the stationarity of the series, such as the Durbin-Watson test and the Ljung-Box Q-test. Moreover, ACF and PACF provide guidance both in extrapolating trend and seasonal components and then in selecting parameters (S, p, q, P, Q) for the complete (S)ARIMA specification in respect of the adherence to theoretical models. In synthesis, the seven parameters (S, d, D, p, q, P, Q) uniquely define each (S)ARIMA model that is suitable for fitting the original time series.

In order to chose the best (S)ARIMA model avoiding overfitting occurrence (the necessity of testing too many parameters), many techniques and methods have been suggested to add mathematical rigor to the search process, including Akaike's criterion [31] or Schwarz's criterion [32]. Each of them works by penalizing models based on the number of their parameters. Anyway, since nowadays statical commercial softwares allow the user to test different (S)ARIMA models very quickly, in the present paper the choice of the best (S)ARIMA model is based on its forecasting performances uniquely. Moreover, the identification of the best (S)ARIMA model throughout the whole application of the Box-Jenkins procedure for decades has required specific statistical knowledge, finalized to define the seven (S)ARIMA parameters by graphics, statistical indexes, and correlograms analysis,

which in real industrial implementations are available rarely. Nevertheless, nowadays, the purpose in the market of commercial softwares quickly testing different (S)ARIMA models guarantees the introduction of such procedure in a wide variety of real-life contexts.

After the identification of the (S)ARIMA model, a diagnostic check must be conducted (see Figure 1) for assessing that the model does not neglect any component. Thus, if residuals are correlated, then the Box-Jenkins procedure restarts from the (S)ARIMA model identification until the residuals are uncorrelated and normally distributed. The Ljung-Box Q-test helps the user to check the uncorrelation of the residuals. Finally, after a positive response given by the diagnostic check, demand forecast via (S)ARIMA can be made.

Several accuracy measures are presented in literature for comparing the performances of forecasting methods. For a more detailed discussion about them, see the study by Makridakis in [33].

Define T as the number of forecasted time periods, F_t as the forecasted demand size in time period t, A as the mean demand size occurring in the forecasted time periods, and D_t as the real demand size occurring in time period t, for $t = 1, \ldots, T$.

Accuracy measures adopted in this paper are described in (3.1), (3.2), and (3.3), in accordance with guidelines reported by Regattieri et al. In [14].

MAD/A

It represents the Mean Absolute Deviation (MAD) divided by the average demand size. This index, by describing the incidence of the mean absolute forecasting error on the mean existing demand, allows the evaluation of forecasting approaches performance on time series with very different mean values, as introduced by Regattieri et al. [14]:

$$\mathrm{MAD}/A = \frac{\sum_{t=1}^{T} |F_t - D_t|/T}{A}. \tag{3.1}$$

MSE/A

It represents the arithmetic Mean of the Sum of the Squares of the forecasting Errors (MSE) divided by the average demand size. Low values of MSE/A address the adoption of forecasting approaches with a high incidence of low errors between true values and estimated ones. Otherwise, high MSE/A indicates that high errors sometimes occur. Specifically, the ratio with A is proposed again in order to compare values obtained in series characterized by consistent differences in the mean demand size:

$$\mathrm{MSE}/A = \frac{\sum_{t=1}^{T} (F_t - D_t)^2/T}{A}. \tag{3.2}$$

ME/A

It represents the Mean Error (ME) divided by the average demand size. This index permits to define the estimation behavior of forecasting methods and specifically to understand whether an overestimation or an underestimation of the prediction data occurs:

$$\mathrm{ME}/A = \frac{\sum_{t=1}^{T} (F_t - D_t)/T}{A}. \tag{3.3}$$

Specifically, in this proposed paper, the goodness of forecasting is evaluated by computing MAD/A, ME/A and MSE/A on 5 and 12 future time periods.

4. Collection and Preliminary Analysis of Data

Twelve data series describing demand of twelve spare parts have been collected from real industrial applications, each of them composed by 36 time periods. In detail, the data are related to several high-value minuteria products, like precision screws and small spare parts for transmission and hydraulic units. They are all characterized by erratic patterns because of their variability in demand sizes while some data series are sporadic too due to the presence of time periods in which demand does not occur. Therefore, two coefficients are computed (CV and ADI) in accordance with definitions reported by Willemain et al. In [11]. Specifically, CV represents the coefficient of variation of not-null demands, while ADI represents the average number of time periods between two successive not-null demands. Alternatively, in accordance with definitions reported by Syntetos and Boylan in [5], CV^2 can be computed, that is, the squared version of CV. Hence CV and ADI establish the marks, respectively, of demand sizes variability and of the intermittence of demand pattern.

In the following sections forecast will concern five and twelve periods ahead; thus CV and ADI are calculated both for 31 time periods, from period 1 to period 31 (CV_{31}, ADI_{31}) and for 24 time periods (CV_{24}, ADI_{24}), from period 1 to period 24. Respectively, 5 and 12 disregarded data are adopted as benchmark for testing the forecasting performance of the analyzed approaches (HW and (S)ARIMA). Moreover, the statistical analysis leads to deny the aprioristic assumption of Croston [1]; in fact demand sizes (when demand occurs) are not normally distributed and they are not mutually independent due to the presence of autocorrelation, as outlined below.

The analysis based on the Box-Jenkins procedure (see Figure 1) begins by investigating the more useful characteristics of time series for the declared purposes, such as firstly the extrapolation both of a trend and of a seasonal and then the identification of an adequate (S)ARIMA model capable of fitting the series. These characteristics are related with the distribution of the global autocorrelation coefficients (ρ_k) and the distribution of the partial correlation coefficients, which emerge, respectively, from the analysis of the global correlogram (ACF) and the partial correlogram (PACF). All demand patterns are generated by nonstationary processes, since their autocorrelation coefficients in ACF and PACF do not tend to zero after two or three time lags. Hence, parameters d and D of the (S)ARIMA models must be achieved for each time series in order to make them stationary. Moreover, some series are mainly influenced by seasonality while others present both seasonality and a consistent trend. In fact, in both cases ρ_k are different to zero or present peeks every S time lag. But, in the former case they are characterized by disregardable increases or decreases by varying time lag, while in the latter case, when both seasonality and a consistent trend are registered, increases or decreases clearly appear.

Table 1 reports the summary of the main characteristics for each time series: CV, ADI, the best distribution functions that are not rejected in fitting demand sizes (ddp), and finally the presence of both seasonality and consistent trend components.

The software AutoFit has been used. It evaluates all the best fitting distribution functions in descending order of ranking. Sometimes it does not find any fitting function. Such cases are traced in column ddp of Table 1, by indicating the label *reject*.

Table 1: Data collection and preliminary analysis.

Series	Group	CV_{31}	ADI_{31}	CV_{24}	ADI_{24}	ddp	Seasonality	Trend
s1		1.80	1.35	1.79	1.26	reject	x	
s2		1.54	1.11	1.45	1.09	Geometric (6.34e − 002)	x	
s3		1.30	1.19	1.35	1.09	Neg. Binomial (1, 4.75e − 002)	x	
s4	1	1.09	1.48	1.01	1.33	Neg. Binomial (3, 7.76e − 002)	x	
s5		1.22	1.19	1.21	1.14	Neg. Binomial (2, 4.11e − 002)	x	
s6		1.25	1	1.30	1	reject	x	
s7		2.40	1.29	2.36	1.33	reject	x	
s8		1.11	1.41	1.33	1.50	reject	x	x
s9		2.38	1.35	1.77	1.14	Neg. Binomial (2, 4.88e − 002)	x	x
s10	2	1.63	1.41	1.69	1.41	Neg. Binomial (1, 9.88e − 002)	x	x
s11		1.28	1	1.42	1	Neg. Binomial (1, 4.7e − 002)	x	x
s12		1.30	1	1.34	1	Neg. Binomial (2, 1.6e − 002)	x	x

Time series are grouped into two sets: Group 1 and Group 2. The former includes series from s1 to s7, mainly characterized by seasonal component, while the latter includes series from s8 to s12, with both seasonal and consistent trend components.

5. Identification of Possible (S)ARIMA Models and Choice of the Best One

The implementation of the Holt-Winters method does not require any discretional intervention of the user because the commercial software adopted in this paper finds the best smoothing parameters in an iterative way. For this reason, the main portion of this section is focused on (S)ARIMA models identification.

In order to reduce the number of tested (S)ARIMA models, the differentiation orders (d and D) are initially set and kept unmodified in the following steps. They represent, respectively, the non seasonal and the seasonal differentiation orders finalized to make the series stationary. By analyzing the patterns, on one hand, only linear trends emerge; therefore a first order of non seasonal differentiation is necessary ($d = 1$). On the other hand, D could be chosen through several tests, such as the Canova and Hansen test [30], but in the proposed experimentation a stable seasonal pattern is always present; thus the seasonality is effectively handled by stationary seasonal AR and MA terms ($D = 0$). Moreover the duration of seasonality of each time series is 4 time periods; hence S is set to 4.

Since a (S)ARIMA model is uniquely defined by seven parameters $(p, d, q) \times (P, D, Q)_S$, the number of possible (S)ARIMA models to be tested is reduced for the assumptions above in the following way: $(p, 1, q) \times (P, 0, Q)_4$, where p, q, P, and Q change from one to three.

Note that each (S)ARIMA model could generate negative forecasted values, which are practically inconsistent. Thus, a null demand is imposed every time a negative value is forecasted.

In order to compare the different (S)ARIMA models, their forecasting performance is evaluated in terms of MAD/A, as underlined in Section 3. In particular, the selection of each (S)ARIMA model is based on the minimization of MAD/A. The selected models for forecasting both 5 and 12 time periods ahead are reported in Table 2.

Table 2: Selected (S)ARIMA models for 5 and 12 time periods ahead.

Series	Group	5 time periods ahead	12 time periods ahead
s1	1	$(3,1,1) \times (2,0,2)_4$	$(2,1,3) \times (2,0,2)_4$
s2		$(2,1,2) \times (3,0,1)_4$	$(1,1,3) \times (2,0,2)_4$
s3		$(3,1,1) \times (3,0,2)_4$	$(3,1,2) \times (2,0,2)_4$
s4		$(1,1,2) \times (2,0,3)_4$	$(1,1,3) \times (2,0,2)_4$
s5		$(2,1,2) \times (2,0,2)_4$	$(3,1,2) \times (2,0,1)_4$
s6		$(1,1,2) \times (2,0,2)_4$	$(3,1,2) \times (2,0,1)_4$
s7		$(2,1,2) \times (3,0,1)_4$	$(1,1,1) \times (3,0,1)_4$
s8	2	$(3,1,2) \times (2,0,2)_4$	$(1,1,1) \times (3,0,1)_4$
s9		$(2,1,2) \times (3,0,1)_4$	$(2,1,2) \times (2,0,1)_4$
s10		$(1,1,2) \times (3,0,1)_4$	$(2,1,3) \times (2,0,1)_4$
s11		$(2,1,2) \times (3,0,3)_4$	$(1,1,1) \times (2,0,2)_4$
s12		$(2,1,2) \times (2,0,1)_4$	$(3,1,2) \times (2,0,1)_4$

Table 3: Comparison between (S)ARIMA and HW based on MAD/A.

Series	Group	MAD/A 5 time periods ahead		MAD/A 12 time periods ahead	
		(S)ARIMA	HW	(S)ARIMA	HW
s1	1	**4.9**%	**4.9**%	9.3%	**8.9**%
s2		**9.7**%	14.2%	**13.8**%	**13.8**%
s3		13.2%	**11**%	33.5%	**21.5**%
s4		7.3%	**6.9**%	**8.9**%	21.1%
s5		**2.3**%	4.8%	**4.7**%	7.6%
s6		**1.4**%	1.8%	4.1%	**2.8**%
s7		1.4%	**0.2**%	**5.3**%	5.5%
s8	2	**14.9**%	21.6%	**35**%	40.9%
s9		**8.3**%	66.7%	**53.6**%	92.9%
s10		**5.3**%	26.7%	**16.5**%	32.5%
s11		**4.0**%	11.1%	**8.5**%	24.6%
s12		10.7%	**10.4**%	**10.4**%	21.7%

Subsequently, selected (S)ARIMA models are also compared with those of HW in terms of MSE/A and ME/A in order to evaluate their capability of often generating low errors along with indicating their potential overestimation or underestimation.

6. Experimental Analysis: Comparison Between (S)ARIMA and HW

The results obtained by HW method are directly comparable with those achieved through selected (S)ARIMA model.

In Table 3 the comparison between HW model and selected (S)ARIMA model is carried out in terms of MAD/A for each time series. In particular, only the lower MAD/A achieved by the two methods are reported in percentage values.

In Figures 2 and 3, the achieved MAD/A values are plotted, respectively, for 5 and 12 time periods ahead, divided into groups defined before for series with seasonal component (Group 1) and for series with both seasonal and consistent trend components (Group 2).

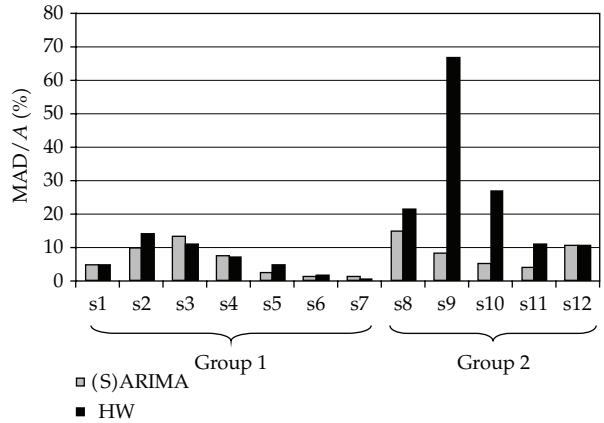

Figure 2: MAD/A values for each time series: forecasts on 5 time periods ahead.

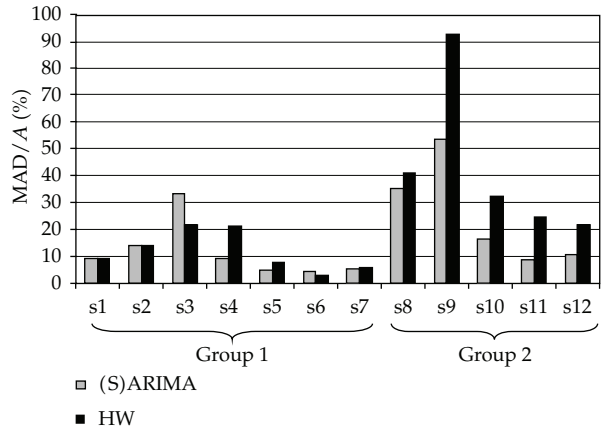

Figure 3: MAD/A values for each time series: forecasts on 12 time periods ahead.

In cases of forecasts on 5 time periods ahead and for time series belonging to Group 1 (from s1 to s7), the Holt-Winters method gives comparable results in respect of the best (S)ARIMA model found. In series s2, s5, s6, (S)ARIMA outperforms; in series s3, s4, s7, HW outperforms; in series s1, the same value of MAD/A is registered. Furthermore, the worst performing approach (HW for series s2, s5, s6 and (S)ARIMA for series s3, s4, s7) gives results not far from the best registered. Otherwise, when both seasonality and consistent trend occur (from s8 to s11), (S)ARIMA model guarantees performances better than those obtained by the Holt-Winters method. Time series s12 is the only case belonging to Group 2 in which Holt-Winters outperforms; however improvement induced is negligible.

Increasing the number of the forecasted time periods from 5 to 12, the same guidelines can be traced. For time series belonging to Group 1, (S)ARIMA outperforms in s4, s5, s7, and HW outperforms in s1, s3, s6. The same MAD/A is reached in s2. Furthermore, except in the case of time series $s3$, best MAD/A registered with HW and (S)ARIMA are comparable. Otherwise, in time series belonging to Group 2, (S)ARIMA outperforms and best MAD/A registered are consistent. In synthesis, the more complex the demand data series become,

Table 4: Comparison between (S)ARIMA and HW based on MSE/A.

Series	Group	MSE/A 5 time periods ahead		MSE/A 12 time periods ahead	
		(S)ARIMA	HW	(S)ARIMA	HW
s1	1	**6.8**%	**6.8**%	27.0%	**22.4**%
s2		**59.3**%	79.6%	**73.0**%	74.2%
s3		**33.0**%	41.8%	469.9%	**111.5**%
s4		35.1%	**28.2**%	**43.8**%	48.9%
s5		**5.1**%	20.2%	**12.9**%	34.5%
s6		**2.6**%	5.1%	22.0%	**7.9**%
s7		434.4%	**3.9**%	**10361.6**%	10675.5%
s8	2	**268.9**%	424.1%	**801.5**%	953.2%
s9		**8.3**%	666.7%	**217.9**%	678.6%
s10		**9.9**%	435.9%	**80.8**%	502.4%
s11		**60.3**%	463.0%	**172.9**%	1424.8%
s12		529.8%	**286.0**%	**439.7**%	1369.8%

Table 5: Comparison between (S)ARIMA and HW based on ME/A.

Series	Group	ME/A 5 time periods ahead		ME/A 12 time periods ahead	
		(S)ARIMA	HW	(S)ARIMA	HW
s1	1	2.9%	**1.0**%	−1.7%	**0.4**%
s2		−4.4%	**1.8**%	**−5.0**%	−6.3%
s3		**2.2**%	−6.6%	**6.7**%	18.7%
s4		0.8%	**0.4**%	**1.3**%	9.5%
s5		−1.7%	**−1.4**%	**−3.5**%	−5.1%
s6		**−0.2**%	−1.8%	**−2.2**%	−2.3%
s7		−1.1%	**−0.2**%	**5.1**%	5.2%
s8	2	1.0%	**0.6**%	**−32.0**%	−32.8%
s9		**0.0**%	33.3%	**−25.0**%	64.3%
s10		**0.8**%	−13.0%	**4.7**%	−5.1%
s11		−0.9%	**0.2**%	**−1.4**%	24.6%
s12		−7.9%	**−0.4**%	**−4.5**%	21.7%

the more useful the application of (S)ARIMA models is. In fact, even if the parsimony of the identified model is an issue dealt with extensively in literature, nowadays the availability of several commercial statistical software programs, which allow the user to test different (S)ARIMA models very quickly, let them become useful tools to be applied in different industrial contexts also for sporadic and irregular time series that present both seasonal and trend components.

Tables 4 and 5 show calculated values of MSE/A and ME/A indices for each time series, for forecasting of both 5 and 12 time periods ahead, divided into the aforementioned groups. Bold values are related with the best-performing approach.

MSE/A values obtained enforce considerations traced by analyzing MAD/A results. Otherwise, ME/A do not address an over- or underestimation. Sometimes the former behavior occurs, sometimes the latter.

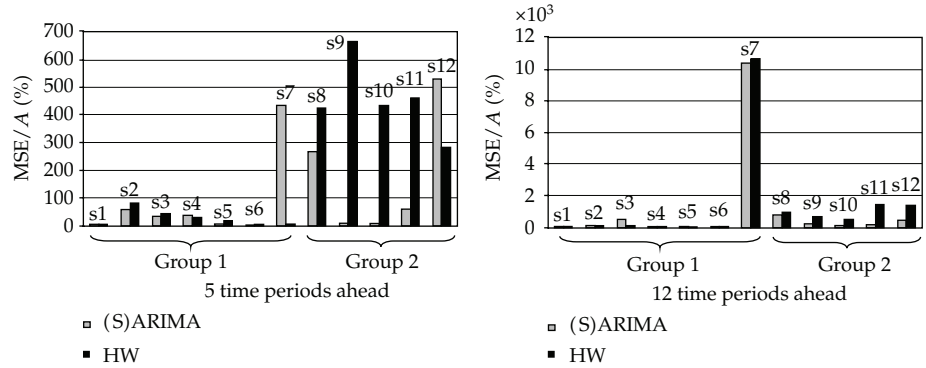

Figure 4: MSE/**A** values for each time series: forecasts on 5 and 12 time periods ahead.

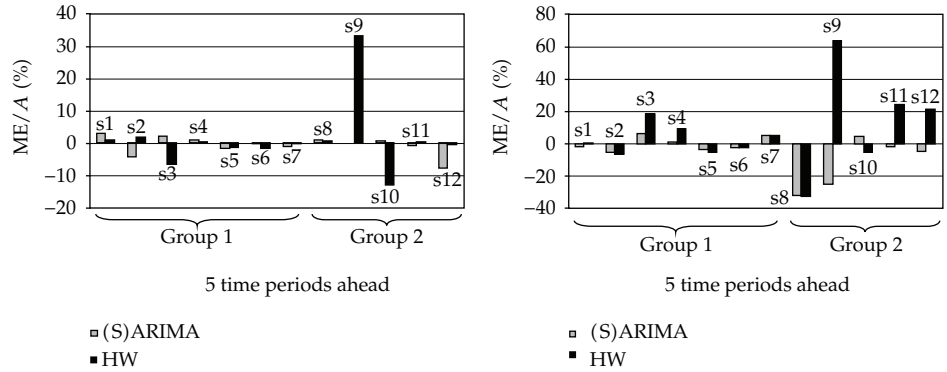

Figure 5: ME/*A* values for each time series: forecasts on 5 and 12 time periods ahead.

The results obtained corroborate the experimental analysis carried out by Bianchi et al. [28], which indicate that ARIMA is better than the best of additive or multiplicative Holt-Winters in more than three-fourths of the sample outcomes, and extend it in cases of sporadic and irregular time series. Specifically, this paper highlights that the performances of the (S)ARIMA models significantly improve when both seasonal and consistent trend components are present in time series.

7. Conclusions

The issue dealt with in the present paper is the comparison between the Holt-Winters method and the (S)ARIMA model for forecasting real life time series. In particular, the analyzed series present a high level of variability in terms of demand size and several null-demand time periods. Moreover, all of the time series reveal a clear seasonality while only several of these present a consistent trend component. On one hand, sporadic and irregular time series are extensively treated in literature, while on the other hand several authors compared the two methods above for seasonal and trendy time series. However, sporadic and irregular time series that present both trend and seasonal components are still neglected. Hence, evaluating the applicability of the (S)ARIMA and the Holt-Winters methods in forecasting sporadic

demand time series with seasonality and trend components is the aim of the present paper in order to establish some useful guidelines for practitioners. The methodology applied consists of testing several (S)ARIMA models and then choosing the best model only in terms of forecasting performances, which is subsequently compared with the Holt-Winters method. In fact, statistical software programs also let the user test a robust and complex method like the (S)ARIMA very quickly and therefore the results from the comparison between the two methods can give a guidance for their applicability.

In particular, in the case of seasonality without a consistent trend component, the best (S)ARIMA model found and the Holt-Winters exponential smoothing model give similar results in terms of MAD/A, but when also a consistent trend component is present, the performances of (S)ARIMA model are more appreciable. These results are enforced by the evaluation of MSE/A. Hence, when the sporadic demand data series structure becomes more complex because of the relevant presence of both seasonal and consistent trend components, the (S)ARIMA model, which is more adaptive than the Holt-Winters method, is also more effective.

This observation represents a useful decision-making guideline in plant management. In fact, several real contexts present these characteristics, such as startup productions, multi-echelon supply chains or spare parts production, and selling, where demand forecasting constitutes an unforgettable prerequisite for an efficient production or selling management and could become a needful competitive leverage for companies.

As underlined in the introduction, when treating sporadic and irregular time series, two relevant issues refer to forecasting and inventory management. Further researches are addressed in the field of order and inventory management when sporadic demand data series with seasonality and consistent trend components are present. Furthermore, a comparative analysis on reachable performances when previously cited methodologies for sporadic demand forecasting with specifical hypothesis (i.e., demand distribution, time periods with zero demand distribution, . . .) are applied to forecasting intermittent series with seasonality and consistent trend components is addressed.

Acknowledgments

The authors wish to thank Eng. L. Biolchini for supporting this research by means of fruitful discussion and constructive criticism.

References

[1] J. D. Croston, "Forecasting and stock control for intermittent demands," *Operational Research Quarterly*, vol. 23, no. 3, pp. 289–303, 1972.
[2] A. Rao, "A comment on "Forecasting and stock control for intermittent demands"," *Operational Research Quarterly*, vol. 24, no. 4, pp. 639–640, 1973.
[3] F. R. Johnston and J. E. Boylan, "Forecasting for items with intermittent demand," *Journal of the Operational Research Society*, vol. 47, no. 1, pp. 113–121, 1996.
[4] F. R. Johnston and J. E. Boylan, "Forecasting intermittent demand: a comparative evaluation of Croston's method. Comment," *International Journal of Forecasting*, vol. 12, pp. 297–298, 1996.
[5] A. A. Syntetos and J. E. Boylan, "On the bias of intermittent demand estimates," *International Journal of Production Economics*, vol. 71, no. 1–3, pp. 457–466, 2001.
[6] A. A. Syntetos and J. E. Boylan, "The accuracy of intermittent demand estimates," *International Journal of Forecasting*, vol. 21, no. 2, pp. 303–314, 2005.
[7] A. Segerstedt, "Forecasting slow-moving items and ordinary items-a modification of Croston's idea,"

Working paper, Industrial logistics, Lulea University of Technology, 2000.
[8] E. Levén and A. Segerstedt, "Inventory control with a modified Croston procedure and Erlang distribution," *International Journal of Production Economics*, vol. 90, no. 3, pp. 361–367, 2004.
[9] T. R. Willemain, C. N. Smart, and H. F. Schwarz, "A new approach to forecasting intermittent demand for service parts inventories," *International Journal of Forecasting*, vol. 20, no. 3, pp. 375–387, 2004.
[10] R. S. Gutierrez, A. O. Solis, and S. Mukhopadhyay, "Lumpy demand forecasting using neural networks," *International Journal of Production Economics*, vol. 111, no. 2, pp. 409–420, 2008.
[11] T. R. Willemain, C. N. Smart, J. H. Shockor, and P. A. DeSautels, "Forecasting intermittent demand in manufacturing: a comparative evaluation of Croston's method," *International Journal of Forecasting*, vol. 10, no. 4, pp. 529–538, 1994.
[12] B. Sani and B. G. Kingsman, "Selecting the best periodic inventory control and demand forecasting methods for low demand items," *Journal of the Operational Research Society*, vol. 48, no. 7, pp. 700–713, 1997.
[13] L. W. G. Strijbosch, R. M. J. Heuts, and E. H. M. van der Schoot, "Combined forecast—inventory control procedure for spare parts," *Journal of the Operational Research Society*, vol. 51, no. 10, pp. 1184–1192, 2000.
[14] A. Regattieri, M. Gamberi, R. Gamberini, and R. Manzini, "Managing lumpy demand for aircraft spare parts," *Journal of Air Transport Management*, vol. 11, no. 6, pp. 426–431, 2005.
[15] A. A. Syntetos, "A note on managing lumpy demand for aircraft spare parts," *Journal of Air Transport Management*, vol. 13, no. 3, pp. 166–167, 2007.
[16] A. A. Syntetos, J. E. Boylan, and J. D. Croston, "On the categorization of demand patterns," *Journal of the Operational Research Society*, vol. 56, no. 5, pp. 495–503, 2005.
[17] L. Shenstone and R. J. Hyndman, "Stochastic models underlying Croston's method for intermittent demand forecasting," *Journal of Forecasting*, vol. 24, pp. 389–402, 2005.
[18] A. V. Kostenko and A. V. Hyndman, "A note on the categorization of demand patterns," *Journal of the Operational Research Society*, vol. 57, pp. 1256–1257, 2006.
[19] A. A. Syntetos, J. E. Boylan, and J. D. Croston, "Reply to Kostenko and Hyndman," *Journal of the Operational Research Society*, vol. 57, pp. 1257–1258, 2006.
[20] C. C. Holt, "Forecasting seasonals and trends by exponentially weighted moving averages," ONR Memorandum 52, Carnegie Institute of Technology, Washington, DC, USA, 1957.
[21] P. R. Winters, "Forecasting sales by exponentially weighted moving averages," *Management Science*, vol. 6, pp. 324–342, 1960.
[22] G. E. P. Box and G. M. Jenkins, *Time Series Analysis: Forecasting and Control*, Holden-Day Series in Time Series Analysis, Holden-Day, San Francisco, Calif, USA, Revised edition, 1976.
[23] J. Jarrett, *Business Forecasting Methods*, Blackwell, Oxford, UK, 1991.
[24] B. L. Bowerman and R. T. O'Connell, *Forecasting and Time Series: An Applied Approach*, Duxbury Press, Belmont, Calif, USA, 1993.
[25] P. Newbold and C. W. J. Granger, "Experience with forecasting univariate time series and the combination of forecasts," *Journal of the Royal Statistical Society. Series A*, vol. 137, pp. 131–165, 1974.
[26] L. Poulos, A. Kvanli, and R. Pavur, "A comparison of the accuracy of the Box-Jenkins method with that of automated forecasting methods," *International Journal of Forecasting*, vol. 3, no. 2, pp. 261–267, 1987.
[27] C. Chen, "Robustness properties of some forecasting methods for seasonal time series: a Monte Carlo study," *International Journal of Forecasting*, vol. 13, no. 2, pp. 269–280, 1997.
[28] L. Bianchi, J. Jarrett, and R. C. Hanumara, "Improving forecasting for telemarketing centers by ARIMA modeling with intervention," *International Journal of Forecasting*, vol. 14, no. 4, pp. 497–504, 1998.
[29] H. Hassani, S. Heravi, and A. Zhigljavsky, "Forecasting European Industrial Production with Singular Spectrum Analysis," *International Journal of Forecasting*. In press.
[30] F. Canova and B. E. Hansen, "Are seasonal patterns constant over time? A test for seasonal stability," *Journal of Business and Economic Statistics*, vol. 13, pp. 237–252, 1995.
[31] H. Akaike, "A new look at the statistical model identification," *IEEE Transactions on Automatic Control*, vol. 19, no. 6, pp. 716–723, 1974.
[32] G. E. Schwarz, "Estimating the dimension of a model," *The Annals of Statistics*, vol. 6, no. 2, pp. 461–464, 1978.
[33] S. Makridakis, "Accuracy measures: theoretical and practical concerns," *International Journal of Forecasting*, vol. 9, no. 4, pp. 527–529, 1993.

Hindawi Publishing Corporation
Mathematical Problems in Engineering
Volume 2010, Article ID 398364, 15 pages
doi:10.1155/2010/398364

Research Article

A New High-Speed Foreign Fiber Detection System with Machine Vision

Zhiguo Chen,[1] Wenbo Xu,[1] Wenhao Leng,[2] and Yi Fu[1]

[1] *School of Information Technology, Jiangnan University, Wuxi 214122, China*
[2] *China Shipbuilding Industry Corporation, No.702 Institute, Wuxi 214082, China*

Correspondence should be addressed to Wenbo Xu, xuwb_sytu@yahoo.cn

Received 22 December 2009; Accepted 22 February 2010

Academic Editor: Carlo Cattani

A new high-speed foreign fiber detection system with machine vision is proposed for removing foreign fibers from raw cotton using optimal hardware components and appropriate algorithms designing. Starting from a specialized lens of 3-charged couple device (CCD) camera, the system applied digital signal processor (DSP) and field-programmable gate array (FPGA) on image acquisition and processing illuminated by ultraviolet light, so as to identify transparent objects such as polyethylene and polypropylene fabric from cotton tuft flow by virtue of the fluorescent effect, until all foreign fibers that have been blown away safely by compressed air quality can be achieved. An image segmentation algorithm based on fast wavelet transform is proposed to identify block-like foreign fibers, and an improved canny detector is also developed to segment wire-like foreign fibers from raw cotton. The procedure naturally provides color image segmentation method with region growing algorithm for better adaptability. Experiments on a variety of images show that the proposed algorithms can effectively segment foreign fibers from test images under various circumstances.

1. Introduction

Before cotton fiber can be spun, the raw cotton must be sorted to remove any foreign particles and fibers. While foreign particles can be clearly distinguished from the raw cotton by color, contrast, and structure, foreign fibers such as polypropylene (PP) or polyethylene (PE) films are often light and transparent, making them difficult to detect using conventional foreign fiber separators. Even very low content of foreign fibers in cotton, such contaminants often appear as a discoloration in the fabric, reducing its value when they end up in finished cotton products, and this may lead to great economic loss for cotton textile enterprises [1].

The nature and extent of foreign fiber contamination are strongly dependent on the origin of the cotton [2]. US and Australian cotton, which are 100% machine picked, do not have significant problems with foreign fiber. Cotton from Turkey contains many red

ribbon-shaped contaminants. In China, mills are battling threads from bleached cotton as well as white fluorescent PP ribbons. Cotton from Central Asia is contaminated with white, nontransparent packaging residues. These are just a few examples.

Currently, foreign fibers are generally eliminated by hand-picking method using human eyes inspection in most Chinese textile mills; this is inefficient and laborious. Various techniques have been developed to implement automatic inspection and elimination of foreign fibers in cotton, including ultrasonic-based inspection, sensor-based inspection, and machine-vision-based inspection [3, 4]. Earlier research work on foreign fiber detection in cotton was designed for cotton grading. The recent research efforts at improving the sensitivity of these systems have generated a few improvements [5, 6]. These include better separation machinery, use of more sophisticated image analysis technique, and more effective sample preparation mechanisms. In the recent years, some machine vision techniques have been applied to textile industries for inspection and elimination of foreign fibers in cotton.

A traditional machine-vision-based foreign fiber detection system mainly consists of line scan camera, frame-grabber, personal computer (PC), and high-pressure gas nozzle [7]. Images of cotton layer are first acquired through camera and then are manipulated to reduce noise and to enhance contrast. After that, images are segmented to distinguish foreign fibers from the cotton background according to the differences of image features. The positions of the foreign fibers in processed images are transmitted to the separator to control the solenoid valves, which switch the high-pressure compressed air on or off to blow the foreign fibers off the cotton tufts. However, this device suffers from fundamental limitation of PC such as central processing unit's (CPU-) long-time overload, and it will frequently lead to undetected foreign fibers in real-time inspection.

Modern manufacturing processes must produce right first time. This is of the highest importance in fiber opening and preparation. In spinning, second-quality or contaminated yarns must be avoided. One obstacle for top-quality yarn is the increasing amount of foreign fibers. This paper, based on experience and information of traditional foreign fiber separator, presents a new high-speed foreign fiber detection system with machine vision to solve the problem of foreign fibers in ginning and spinning.

Image segmentation is the primary stage in image processing of the machine-vision-based foreign fiber detection system. The aim of image segmentation is to partition the image into meaningful connected-components to extract the features of the objects. In the recent years, many segmentation methods have been developed such as segmentation based on fuzzy C means and its variants, mean shift filters, and nonlinear diffusion [8–11].

In our research, a specialized lens with lateral chromatic aberration correction and ultraviolet light illumination for transparent foreign fiber detection were firstly introduced; and then a high-performance embedded controller based on digital signal processor (DSP) and field-programmable gate array (FPGA) was designed to perform all the complex computations of image acquisition and processing freeing the host PC from time-consuming task. A rectangular chute cooperating with specially designed compressed air nozzles perpendicular to it was finally selected to separate foreign fibers from cotton tufts. To overcome disadvantage of the undefined velocity of cotton tufts and foreign objects, some nonlinear control methods should be needed in such circumstance [12–22]. In order to improve detection speed and accuracy, an image segmentation algorithm based on fast wavelet transform is proposed to identify block-like foreign fibers, and an improved canny detector is also developed to segment wire-like foreign fibers from raw cotton. The procedure also provides color image segmentation method with region growing algorithm for better adaptability.

Figure 1: Cameras with specialized lenses.

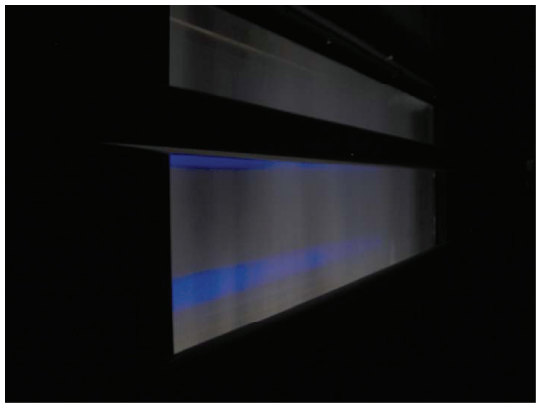

Figure 2: Ultraviolet light.

2. The System

2.1. Sensors

Photo sensors are relatively cheap sensors that are arranged in-line and detect differences in brightness in the passing flow of fibrous tufts. Ultrasonic sensors, also arranged in-line, detect foreign parts with solid, sound-reflecting surfaces but cannot detect foreign fibers, threads, and strings [23].

Color sensors, or 1-CCD (charged couple device) cameras, are line-scan cameras with a single CCD chip. Sensitivity depends on the resolution of these cameras and the scanning width. Because these cameras work with three adjacent scan lines—red, green, and blue—with a certain offset, the color recognition of moving objects is limited and results in a so-called color noise effect.

Much more effective, although more expensive, are 3-CCD cameras. The three basic colors—red, green, and blue—are separated by a prism and simultaneously directed onto three CCD chips [24]. This system is also called a true-color system. Thanks to this simultaneous process, the variable speed of objects in the material flow no longer has

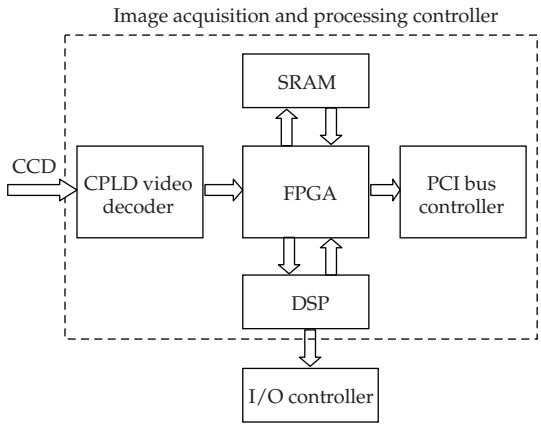

Figure 3: Architecture of image acquisition and processing controller (CCD: charged couple device, CPLD: complex programmable logic device, PCI: peripheral component interconnect, SRAM: static random access memory, FPGA: field-programmable gate array, DSP: digital signal processor, and I/O: input and output).

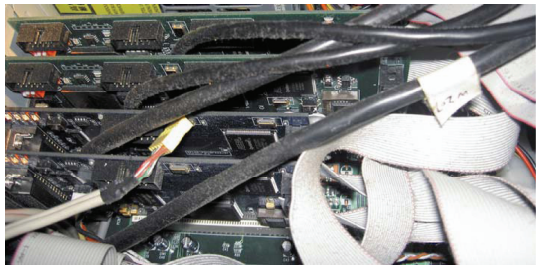

Figure 4: Assembly status of acquisition and processing controllers.

a negative effect. Currently, 3-CCD cameras represent the high-end approach to foreign fiber detection.

To correct for the possible aberrations of the triple-channel prism used in the camera, we used a specialized lens design. Lateral chromatic aberration was minimized by aligning within less than 2 microns. Another central aspect is appropriate color splitting in the triple prism by dielectric color-splitting coatings. To produce high-fidelity color images, two coatings were used in the beamsplitter. While the first coating reflects blue and lets red and green pass, the second reflects red and lets green pass. Figure 1 illustrates mounting location of cameras with specialized lenses.

2.2. Illumination

Another important factor in determining object detectability is the type of illumination. Cameras, as well as the human eye, can detect only objects that distinguish themselves in color, contrast, structure, or luster from cotton tufts. For this reason, the type of illumination applied in foreign fiber detection system plays an essential role. Today's standard is illumination units with fluorescent tubes operating in reflected light mode.

Polarized transmitted light is the ideal system for detecting transparent and semitransparent objects, such as PE foil or PP fabric from bale packaging. To detect such

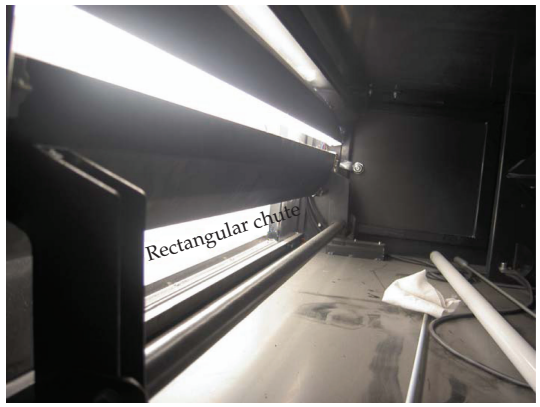

Figure 5: The rectangular chute of tuft flow.

foreign fibers and separate them safely, the raw cotton is illuminated under polarized light, ultraviolet (UV) light, for instance, as showed in Figure 2, making the foreign plastic fibers appear colored. In this way, the foreign fibers can be distinguished from the raw cotton and separated. Such objects may include pieces of polyester (PET), PP, or even bleached cotton treated with optical brighteners [25]. With polarized reflected light and the corresponding camera filters, differences in surface luster of foreign objects can be detected. The system reaches its limits with dull objects. The presence of these particles often results in the dreaded foreign fiber claim.

2.3. Image Acquisition and Processing Controller

High-performance embedded controller, which features a TMS320DM648 DSP (TI Corp) and an XC2S300E-7PQ208C FPGA (Xilinx Corp) is designed to significantly reduce image acquisition and processing times for PC-based platform. With its 8800 MIPS processor, 5 configurable video ports, and 1 GBps total system bandwidth, the embedded controller is ideal for high-speed image acquisition and processing systems in foreign fiber detection. The controller performs all the complex computations of image acquisition and processing, freeing the host PC from this time intensive task. Figure 3 illustrates the architecture of image acquisition and processing controller, and Figure 4 shows the assembly status of controllers in industrial PC (IPC). The detailed designing method will be introduced in another paper.

2.4. Material Presentation

The presentation of the fibrous material to the sensors also affects the performance of foreign fiber separators. Almost all systems on the market monitor the tuft flow in a rectangular chute. One major disadvantage is the undefined velocity of cotton tufts and foreign objects. Because the velocity is not constant, the downstream separation nozzles must be activated for a longer period of time. This inevitably results in an increasing loss of good fibers. However, one advantage that should not be underestimated is the gentle treatment of cotton fibers, which are not mechanically stressed. Systems that feature detection on or close to the surface of a rotating needle roll have three very important advantages. First is the accurately

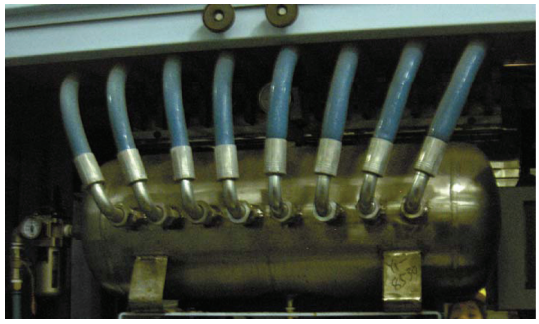

Figure 6: Compressed air tank.

defined material velocity and, hence, the minimal loss of good fibers during removal. Second, accurately detecting the position of foreign objects is advantageous, as there are no problems due to differences in illumination intensity depending on chute depth, as is the case with chute-based systems. The third advantage lies in the high degree of material opening and the associated excellent exposure of the foreign objects. Figure 5 shows the rectangular chute of tuft flow.

2.5. Foreign Fiber Blowing

The designed air scavenging system and a separation device provided with at least eight compressed air nozzles which are perpendicular to pneumatic cotton tufts conveying conduit are successively mounted in a direction of conveyance, wherein said fiber conveying conduit is provided with a removing opening arranged in front of the compressed air nozzles. Contrary to state of the art of actual methods and devices, the foreign fibers are not removed to a substantially pressure-tight separation container. According to our design, the removing opening is connected to a derivation in which a permanent airflow for transporting separated foreign fibers away is maintained. Figure 6 illustrates the compressed air tank, and Figure 7 illustrates the solenoid valves at the right side.

3. Foreign Fiber Detection Methods

3.1. Image Segmentation Algorithm Based on Fast Wavelet Transform

In the original image, cotton can be treated as background, while foreign fibers are expressed as foreground. Consequently, edge detection is a feasible way to our problem. When digital images are to be viewed or processed at multiple resolutions, the discrete wavelet transform (DWT) is the mathematical tool of choice [26–29]. In this paper, the fast wavelet transform (FWT) is adopted to achieve the edge feature extraction. It is defined as

$$\begin{aligned} \varphi(x) &= \sum_n h_\varphi(n)\sqrt{2}\varphi(2x-n), \\ \psi(x) &= \sum_n h_\psi(n)\sqrt{2}\varphi(2x-n), \end{aligned} \tag{3.1}$$

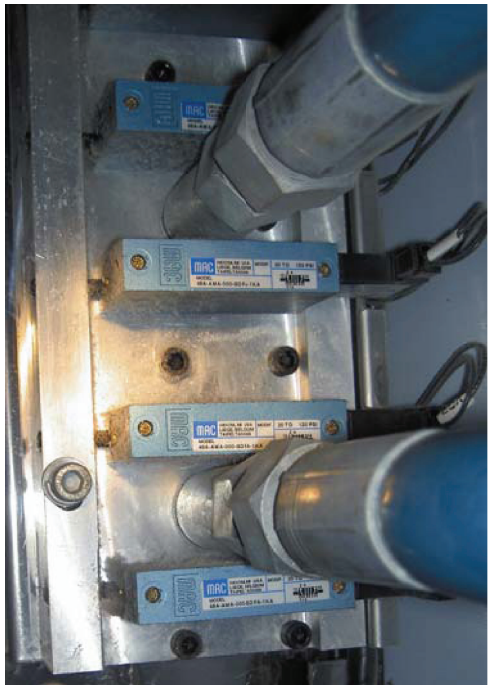

Figure 7: Solenoid valves.

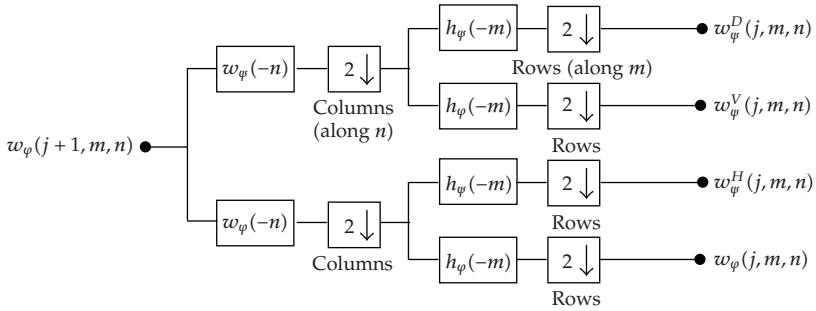

Figure 8: The 2D fast wavelet transform (FWT) filter bank. Each pass generates one DWT scale. In the first iteration, $w_\varphi(j+1,m,n) = f(x,y)$.

where h_φ and h_ψ—the expansion coefficients—are called scaling and wavelet vectors, respectively. They are the filter coefficients of the FWT, an iterative computational approach to the DWT shown in Figure 8.

2D wavelet transform is a direct promotion of 1D wavelet transform [30–32]. It is one of the most prevalent techniques for edge detection and texture extraction. Through the 2D wavelet decomposition, symlets wavelet in this paper, the original cotton image $w_\varphi(j+1,m,n)$ is transformed to 4 parts, $w_\psi^D(j,m,n)$ denotes the detail component in diagonal orientation, $w_\psi^V(j,m,n)$ denotes the detail component in vertical orientation, $w_\psi^H(j,m,n)$ denotes the detail component in horizontal orientation, $w_\varphi(j,m,n)$ denotes the morphology component. In

three detail components, high frequency features are enhanced and the contrast is indicated by the wavelet coefficients.

Here, we propose an algorithm based on FWT to segment foreign fiber from input image. The algorithm can be described as follows.

(1) Input the original input image, denoted as f.

(2) The horizontal, vertical, and directionality of the single-scale wavelet transform of f with respect to "sym4" wavelets, described as f_2.

(3) To merge above information into a single edge image, just zero the approximation coefficients of the generated transform, compute its inverse, and take the absolute value. The resulting edge image is f_3. The inverse FWT uses the equivalent computation as follows:

$$\left[W_{\psi}^{D}(j,m,n)\uparrow^{2m} * h_{\psi}(m)\right]\uparrow^{2n} * h_{\psi}(n) + \left[W_{\psi}^{V}(j,m,n)\uparrow^{2m} * h_{\varphi}(m)\right]\uparrow^{2n} * h_{\psi}(n), \tag{3.2}$$

where $\uparrow^{2m}$ and $\uparrow^{2n}$ denote upsampling along m and n, respectively.

(4) Region growing is used to segment the foreign fiber from f_3. The values of initial seed points S_0 and threshold T_0 are empirical data, in general S_0 is between 10 and 20, and T_0 is between 20 and 40. The resultant image is f_4.

Figure 9 illustrates the segmentation process of the given algorithm.

3.2. An Improved Canny Detector

The canny detector is the most powerful edge detector provided by function edge [33]. Here, the improved edge feature extraction algorithm can be summarized as follows.

(1) Instead of using Gaussian smoothing filter, the improved algorithm carries on the smoothing operation by an adaptive median filter for the characteristics of input image.

(2) The local gradient, $g(x,y) = [G_x^2 + G_y^2]^{1/2}$, and edge direction, $\alpha(x,y) = \tan^{-1}(G_y/G_x)$, are computed at each point. An edge point is defined to be a point whose strength is locally maximum in the direction of the gradient.

(3) The edge points determined in (2) give rise to ridges in the gradient magnitude image. The algorithm then tracks along the top of these ridges and sets to zero all pixels that are not actually on the ridge top so as to give a thin line in the output, a process known as nonmaximal suppression. The ridge pixels are then thresholded using two thresholds, T_1 and T_2, with $T_1 < T_2$. Ridge pixels with values greater than T_2 are said to be "strong" edge pixels. Ridge pixels with values between T_1 and T_2 are said to be "weak" edge pixels.

(4) The algorithm performs edge linking by incorporating the weak pixels that are 8 connected to the strong pixels.

(5) Finally, a modified closing operation in mathematics morphology is applied to fill up gaps in detection result.

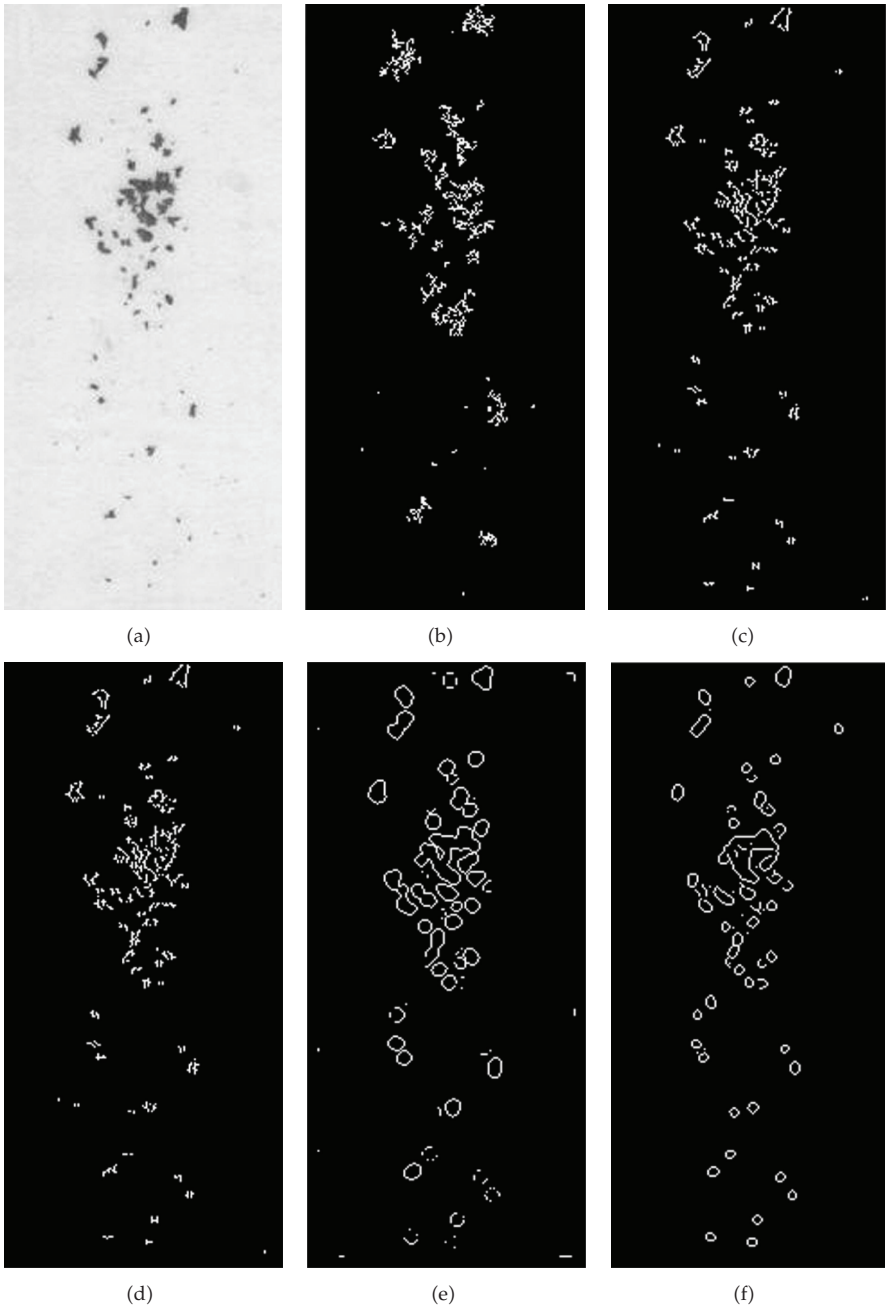

Figure 9: Images segmentation: (a) original image; (b) proposed algorithm in Section 3.1; (c) sobel operator; (d) prewitt operator; (e) log operator; (f) canny operator.

The morphological closing of A by B denoted $A \cdot B$ is a dilation followed by an erosion:

$$A \cdot B = (A \oplus B) \Theta B. \tag{3.3}$$

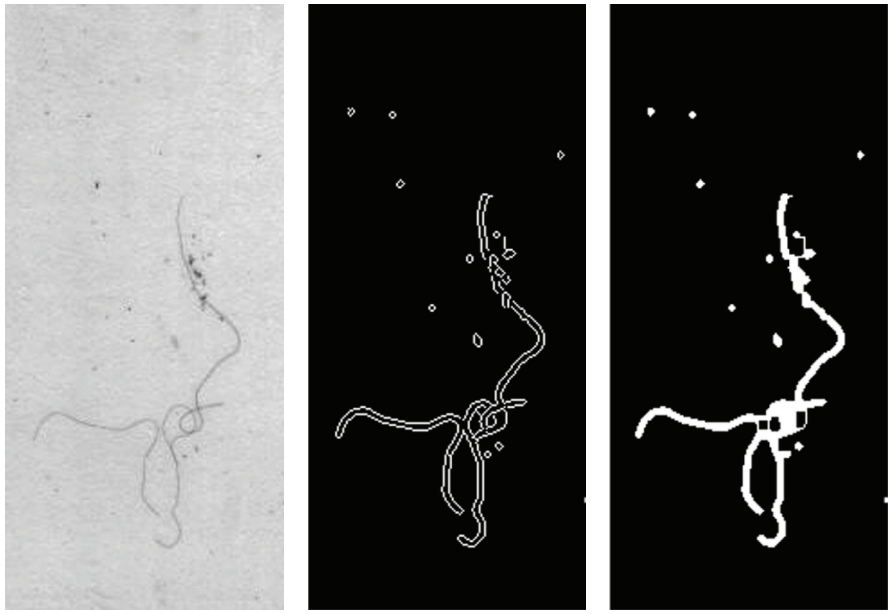

(a) (b) (c)

Figure 10: Images segmentation: (a) original image; (b) canny operator; (c) proposed algorithm in Section 3.2.

Geometrically, $A \cdot B$ is the complement of the union of all translations of B that do not overlap, and it generally joins narrow breaks fills long thin gulfs, and fills holes smaller than the structuring element. However wire-like foreign fibers are relatively difficult to be processed by virtue of their narrow and twining objects. To make the wire-like foreign fibers more clear, a modified closing operation is given by

$$A \cdot B = \left(A \oplus B^L\right) \Theta B^S, \tag{3.4}$$

where B^L is a larger structuring element for dilation and B^S is relatively a smaller one for erosion.

Figure 10 illustrates the result of the above algorithm.

3.3. Region Growing Color Image Segmentation Algorithm

The aim is to segment the color image and extract foreign fiber regions. Suppose that the objective is to segment objects of a specified color range in an RGB image. Given a set of sample color points representative of a color of interest, we obtain an estimate of the "average" or "mean" color that we wish to segmentation. Let this average color be denoted by the RGB pixel in an image as having a color in the specified range or not. To perform this comparison, we need a measure of similarity. One of the simplest measures is the Euclidean distance. Let z denote an arbitrary point in the RGB space. We say that z is similar to m

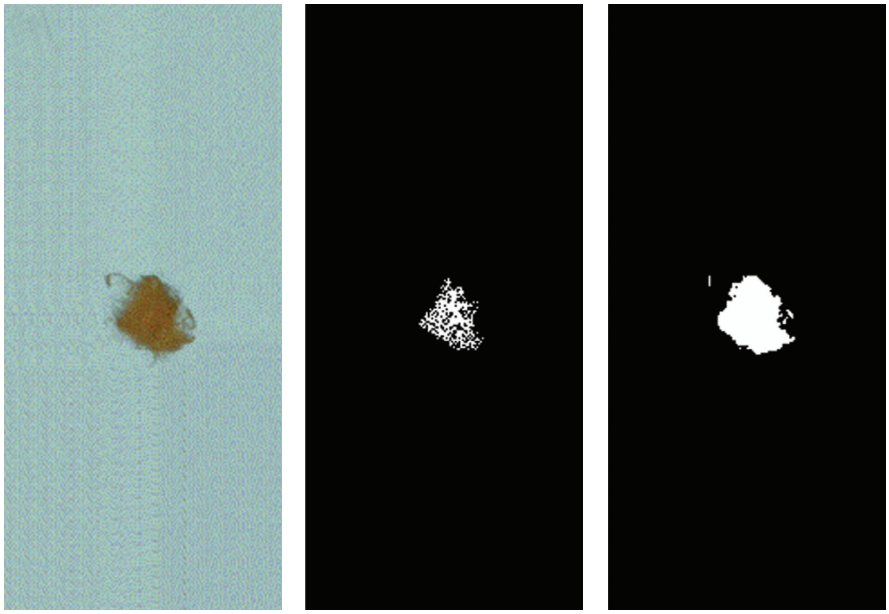

(a) (b) (c)

Figure 11: Processed images using region growing color image segmentation algorithm: (a) original image; (b) $m = 50$; (c) $m = 90$.

if the distance between them is less than a specified threshold, T. The Euclidean distance between z and m is given by [26]

$$\begin{aligned} D(z,m) &= \|z-m\| \\ &= \left[(z-m)^T(z-m)\right]^{1/2} \\ &= \left[(z_R-m_R)^2+(z_G-m_G)^2+\left(z_B-m_B\right)^2\right]^{1/2}, \end{aligned} \tag{3.5}$$

where $\|\cdot\|$ is the norm of the argument, and the subscripts R, G, and B, denote the RGB components of vectors m and z. The locus of points such that $D(z,m) \leq T$ is a solid sphere of radius T. By definition, points contained within, or on the surface of the sphere, satisfy the specified color criterion; points outside the sphere do not.

The algorithm starts with a seed pixel, examines local pixels around it, determines the most similar one, which is then included in the region if it meets certain criteria. This process is followed until no more pixels can be added. The definition of similarity may be set in any number of different ways. Figure 11 illustrates the images segmentation.

4. Results and Discussion

The close examination of the different sensors, illumination systems, and methods of material presentations clearly shows that there is no single ideal system. However, by using systems

precisely adapted to the actual requirements, one can come very close to this ideal. An optimum solution consists of an intelligent combination of different systems.

To balance quality and cost, we used two 3-CCD cameras illuminated by UV lights and two gray cameras with fluorescent lights. Some typical foreign fibers like PP twine, color thread, and hair were selected for the experiments. The foreign fibers were mixed into pure cotton and then made into uniform thin layer. The test images were captured by a 24-bit scanner with nearly 17 million colors offline, and some of them were transformed into gray images before image processing. Matlab 7.04 was used to implement and validate algorithms before the final burn program gets close to real environment. An Intel Pentium IV 2.66 GHz CPU personal computer with 1 GB SDRAM was chosen as the test environment and Windows XP sp2 was selected as the operation system.

4.1. Deficiency of Edge Feature Extraction Algorithms

Three tests were performed to evaluate the segmentation performance of the foreign fiber detection. In test 1 (Section 3.1), the original gray image was used, and segmentation results of the images listed in Figure 9. The results indicated that different segmentation results occurred when different types of algorithms were used. The images of block-like foreign fibers received good segmentation in Figure 9(b) by the proposed algorithm, while the other algorithms did not obtain the expected results. It informs that the proposed algorithm in Section 3.1 is more suitable for block-like foreign fibers detection than the traditional edge detectors.

In test 2 (Section 3.2), the original gray image was processed first by an adaptive median filter, and then it was segmented by the canny operator; finally it was enhanced by the modified closing operation. The result indicates that the canny operator is very useful for wire-like foreign fiber detection. As other edge operators such as sobel and prewitt are not as good as canny operator and the algorithm proposed in Section 3.1 cannot segment wire-like foreign fiber at all; the comparative segment results are not list in this paper.

4.2. About Color Image Segmentation

A large variety of segmentation methods are available at present, but speed and accuracy of an algorithm are key factors for the online visual inspection system [34]. Hence, in addition to ensuring the segmentation accuracy, algorithms with faster speed are more attractive. Therefore, in most cases the methods of foreign fiber detection are not suitable for using the color image segmentation algorithm. However ultraviolet light can make the PE or PP foreign plastic fibers appear colored as the above mentioned in Section 2.2, under such circumstance, color image is very useful and necessary.

Common approaches for color image segmentation are clustering algorithms such as k-means [35] or Mixture of Principal Components [36]; however these algorithms do not take spatial information into account. Furthermore, clustering algorithms require prior information regarding number of clusters, which is a difficult or ambiguous task, requiring the assertion of some criterion on the very nature of the clusters being formed. Some progress has been made on this issue; however much experimentation still needs to be done [37]. An alternative set of algorithms exists which uses color similarity and a region-growing approach to spatial information [38]. Region-growing algorithms have been used mostly in the analysis of grayscale images, and some significant work has been completed

in the color realm by Tremeau and Borel [39]. They discuss the segmentation of color regions which are homogeneous in color (i.e., no illumination effects are considered) thus restricting the application domain. They use a set of thresholds when calculating whether a color pixel is part of a region or not, and the Euclidean distance is used as the measure of similarity between two color vectors. It is well established [40] that the human perception of color similarity is poorly modeled by the Euclidean distance. More researches about color segmentation will be carried out in the future work.

5. Conclusion

A new high-speed foreign fiber detection system has been developed in this research, and images of foreign fibers can be processed more effectively and efficiently using optimal hardware components and appropriate algorithms designing. An image segmentation algorithm based on fast wavelet transform is proposed to identify block-like foreign fibers, and an improved canny detector is also developed to segment wire-like foreign fibers from raw cotton. The color image segmentation with region growing algorithm is introduced for better adaptability. The effectiveness of foreign fiber detection algorithms is demonstrated on a variety of test images. Some quantitative image segmentation methods are used to assess the results.

More rapid and stable foreign-fiber detection methods are now being considered. The useful and effective algorithms will be burned to the designed image acquisition and processing controller soon. A complete system debugging for cotton foreign fibers detection will be carried out very shortly.

Acknowledgment

This work was partly supported by the National Natural Science Foundation of China (NSFC) under the Project Grant nos. 60703106, 60573125, and 60873264.

References

[1] F. M. Shofner and G. F. Williams, "Evolution of the microdust and trash monitor for cotton classification," *Textile Research Journal*, vol. 56, no. 2, pp. 150–156, 1986.

[2] TW, "Optimizing Yarn quality," Special Report, Billian Publishing, 2009, http://www.textileworld.com/Articles/2009/December/Features/Optimizing_Yarn_Quality.html.

[3] K. Kuratani, T. Fujii, M. Tanaka, A. Daito, and T. Murosaki, "Foreign material evaluation equipment: collecting method," in *Proceedings of the SICE Annual Conference*, vol. 1, pp. 376–379, 2003.

[4] A. Daito, T. Murosaki, H. Ito, K. Kuratani, and T. Fujii, "Foreign material evaluation equipment: measurement method," in *Proceedings of the SICE Annual Conference*, vol. 1, pp. 372–375, 2003.

[5] Z. Jiao, L. Song, and X. Wang, "Realization of foreign fiber detecting algorithm based on ADSP-BF533," in *Proceedings of the 9th International Conference on Electronic Measurement and Instruments (ICEMI '09)*, pp. 1-939–1-942, Beijing, China, August 2009.

[6] W. He, L. Han, and X. Zhang, "Study on characteristics analysis and recognition for infrared absorption spectrum of foreign fibers in cotton," in *Proceedings of the IEEE International Conference on Automation and Logistics (ICAL '08)*, pp. 397–400, September 2008.

[7] J.-S. Kwon, J.-M. Lee, and W.-Y. Kim, "Real-time detection of foreign objects using X-ray imaging for dry food manufacturing line," in *Proceedings of the 12th IEEE International Symposium on Consumer Electronics (ISCE '08)*, pp. 1–4, April 2008.

[8] J. C. Bezdek, "A convergence theorem for the fuzzy ISODARA clustering algorithms," *IEEE Transactions on Pattern Analysis and Machine Intelligence*, vol. 2, no. 1, pp. 1–8, 1980.

[9] S. R. Kannan, "A new segmentation system for brain MR images based on fuzzy techniques," *Applied Soft Computing Journal*, vol. 8, no. 4, pp. 1599–1606, 2008.

[10] L. Ma and R. C. Staunton, "A modified fuzzy C-means image segmentation algorithm for use with uneven illumination patterns," *Pattern Recognition*, vol. 40, no. 11, pp. 3005–3011, 2007.

[11] D. Comaniciu and P. Meet, "Mean shift analysis and applications," in *Proceedings of the 7th IEEE International Conference on Computer Vision (ICCV '99)*, vol. 2, pp. 1197–1203, Kerkyra, Greece, September 1999.

[12] K. G. Guseinov, "Approximation of the attainable sets of the nonlinear control systems with integral constraint on controls," *Nonlinear Analysis: Theory, Methods & Applications*, vol. 71, no. 1-2, pp. 622–645, 2009.

[13] A. M. Elaiw, "Multirate sampling and input-to-state stable receding horizon control for nonlinear systems," *Nonlinear Analysis: Theory, Methods & Applications*, vol. 67, no. 5, pp. 1637–1648, 2007.

[14] M. Li, "Fractal time series—a tutorial review," *Mathematical Problems in Engineering*, vol. 2010, Article ID 157264, 26 pages, 2010.

[15] M. Li, "Comparative study of IIR notch filters for suppressing 60-Hz interference in electrocardiogram signals," *International Journal of Electronics and Computers*, vol. 1, no. 1, pp. 7–18, 2009.

[16] G. Toma, "Specific differential equations for generating pulse sequences," *Mathematical Problems in Engineering*, vol. 2010, Article ID 324818, 11 pages, 2010.

[17] E. G. Bakhoum and C. Toma, "Mathematical transform of traveling-wave equations and phase aspects of quantum interaction," *Mathematical Problems in Engineering*, vol. 2010, Article ID 695208, 15 pages, 2010.

[18] G. Toma and F. Doboga, "Vanishing waves on closed intervals and propagating short-range phenomena," *Mathematical Problems in Engineering*, vol. 2008, Article ID 359481, 14 pages, 2008.

[19] Ming Li and Wei Zhao, "Representation of a stochastic traffic bound," *IEEE Transactions on Parallel and Distributed Systems*, 2009.

[20] W.-S. Chen, B. Pan, B. Fang, M. Li, and J. Tang, "Incremental nonnegative matrix factorization for face recognition," *Mathematical Problems in Engineering*, vol. 2008, Article ID 410674, 17 pages, 2008.

[21] C. Cattani, M. Li, and C. Toma, "Short range phenomena: modeling, computational aspects and applications," *Mathematical Problems in Engineering*, vol. 2008, Article ID 761081, 2 pages, 2008.

[22] M. Li, "A method for requiring block size for spectrum measurement of ocean surface waves," *IEEE Transactions on Instrumentation and Measurement*, vol. 55, no. 6, pp. 2207–2215, 2006.

[23] S. Titov, R. Maev, and A. Bogatchenkov, "Wide-aperture, line-focused ultrasonic material characterization system based on lateral scanning," *IEEE Transactions on Ultrasonics, Ferroelectrics, and Frequency Control*, vol. 50, no. 8, pp. 1046–1056, 2003.

[24] J. T. Bosiers, I. M. Peters, C. Draijer, and A. Theuwissen, "Technical challenges and recent progress in CCD imagers," *Nuclear Instruments and Methods in Physics Research, Section A*, vol. 565, no. 1, pp. 148–156, 2006.

[25] M. H. Zohdy, M. B. El Hossamy, A. W. M. El-Naggar, A. I. Fathalla, and N. M. Ali, "Novel UV-protective formulations for cotton, PET fabrics and their blend utilizing irradiation technique," *European Polymer Journal*, vol. 45, no. 10, pp. 2926–2934, 2009.

[26] R. C. Gonzalez and R. E. Woods, *Digital Image Processing*, Prentice-Hall, Upper Saddle River, NJ, USA, 2007.

[27] C. Cattani and J. Rushchitsky, *Wavelet and Wave Analysis as Applied to Materials with Micro or Nanostructure*, vol. 74 of *Series on Advances in Mathematics for Applied Sciences*, World Scientific, Hackensack, NJ, USA, 2007.

[28] C. Cattani, "Harmonic wavelet approximation of random, fractal and high frequency signals," *Telecommunication Systems*, vol. 43, no. 3-4, pp. 207–217, 2010.

[29] C. Cattani, "Harmonic wavelet analysis of a localized fractal," *International Journal of Engineering and Interdisciplinary Mathematics*, vol. 1, no. 1, pp. 35–44, 2009.

[30] C. Cattani, "Shannon wavelets theory," *Mathematical Problems in Engineering*, vol. 2008, Article ID 164808, 24 pages, 2008.

[31] C.-L. Zhang, H. Chen, X.-F. Wang, and D.-H. Fan, "Harmonic wavelet analysis of a localized parabolic partial differential equation," *International Journal of Engineering and Interdisciplinary Mathematics*, vol. 1, no. 1, pp. 45–55, 2009.

[32] W.-S. Chen, "Galerkin-Shannon of Debye's wavelet method for numerical solutions to the natural integral equations," *International Journal of Engineering and Interdisciplinary Mathematics*, vol. 1, no. 1, pp. 63–73, 2009.

[33] L. Ding and A. Goshtasby, "On the Canny edge detector," *Pattern Recognition*, vol. 34, no. 3, pp. 721–725, 2001.

[34] H. Golnabi and A. Asadpour, "Design and application of industrial machine vision systems," *Robotics and Computer-Integrated Manufacturing*, vol. 23, no. 6, pp. 630–637, 2007.

[35] R. J. Schalkoff, *Pattern Recognition: Statistical, Structural and Neural Approaches*, John Wiley & Sons, New York, NY, USA, 1992.

[36] S. Wesolkowski, M. E. Jernigan, and R. D. Dony, "Global color image segmentation strategies: Euclidean distance vs. vector angle," in *Neural Networks for Signal Processing IX*, Y.-H. Hu, J. Larsen, E. Wilson, and S. Douglas, Eds., pp. 419–428, IEEE Press, Piscataway, NJ, USA, 1999.

[37] S. Wesolkowski, S. Tominaga, and R. D. Dony, "Shading and highlight invariant color image segmentation using the MPC algorithm," in *Color Imaging: Device-Independent Color, Color Hardcopy, and Graphic Arts VI*, vol. 4300 of *Proceedings of SPIE*, pp. 229–240, San Jose, Calif, USA, January 2001.

[38] R. M. Haralick and L. G. Shapiro, *Computer and Robot Vision*, vol. 1, Addison-Welsey, Reading, Mass, USA, 1992.

[39] A. Tremeau and N. Borel, "A region growing and merging algorithm to color segmentation," *Pattern Recognition*, vol. 30, no. 7, pp. 1191–1203, 1997.

[40] L. Shafarenko, M. Petrou, and J. Kittler, "Automatic watershed segmentation of randomly textured color images," *IEEE Transactions on Image Processing*, vol. 6, no. 11, pp. 1530–1544, 1997.

Hindawi Publishing Corporation
Mathematical Problems in Engineering
Volume 2010, Article ID 578406, 20 pages
doi:10.1155/2010/578406

Research Article

Design and Lyapunov Stability Analysis of a Fuzzy Logic Controller for Autonomous Road Following

Yi Fu, Howard Li, and Mary Kaye

Department of Electrical and Computer Engineering, University of New Brunswick, Fredericton, NB, Canada E3B 5A3

Correspondence should be addressed to Howard Li, howard@unb.ca

Received 14 September 2009; Accepted 27 January 2010

Academic Editor: Irina N. Trendafilova

Autonomous road following is one of the major goals in intelligent vehicle applications. The development of an autonomous road following embedded system for intelligent vehicles is the focus of this paper. A fuzzy logic controller (FLC) is designed for vision-based autonomous road following. The stability analysis of this control system is addressed. Lyapunov's direct method is utilized to formulate a class of control laws that guarantee the convergence of the steering error. Certain requirements for the control laws are presented for designers to choose a suitable rule base for the fuzzy controller in order to make the system stable. Stability of the proposed fuzzy controller is guaranteed theoretically and also demonstrated by simulation studies and experiments. Simulations using the model of the four degree of freedom nonholonomic robotic vehicle are conducted to investigate the performance of the fuzzy controller. The proposed fuzzy controller can achieve the desired steering angle and make the robotic vehicle follow the road successfully. Experiments show that the developed intelligent vehicle is able to follow a mocked road autonomously.

1. Introduction

Intelligent transportation systems (ITSs) are an emerging global phenomenon benefiting public and private sectors alike. ITSs and intelligent vehicles can relieve congestion, improve safety, and enhance productivity. The field of intelligent vehicles is rapidly growing worldwide. Technologies involved with intelligent vehicles include sensing and control technologies, communications, and computer informatics. Intelligent vehicles offer the potential to significantly enhance safety and operational efficiency. As one component of ITSs, intelligent vehicles use sensing and intelligent algorithms to understand the vehicle's immediate environment, either assisting the driver or fully controlling the vehicle [1]. Intelligent vehicles function at the control layer to enable the driver vehicle subsystem to

operate more effectively. Intelligent vehicles can help drivers in various ways: (1) collision warning—to advise or warn the driver; (2) driver assistance—to partially control the vehicle as an emergency intervention to avoid a collision; (3) automated driving—to fully control the vehicle. Vehicles that can navigate autonomously in everyday traffic will become a reality in a few decades. In this paper, we will focus on the development of embedded systems to realize automated road following for intelligent vehicles.

A lot of highway accidents are caused by deviation from the road. Autonomous road following is one of the major research topics in the area of intelligent vehicles. Because of its potential in preventing accidents caused by human fatigue and performing tasks in environments unreachable by human beings, a lot of road following methods for intelligent vehicles have been proposed in the recent decades. Intelligent vehicles are robotic systems that perceive the driving environment to assist the driver in safe vehicle operation by providing driving assistance or full control of the vehicle. With the proposed research, we will be able to develop an autonomous control system that can be used on cars to assist driving or take the control of driving in order to avoid fatal accidents. Furthermore, the developed intelligent vehicles can be used to perform tasks in an environment that is unreachable by human beings.

Generally speaking, autonomous road following requires two major steps: road feature extraction, and speed/steering control of the vehicles. The success of autonomous road following requires the ability to continuously detect and extract useful road features, to analyze road features, and to perform steering and speed control based on road conditions.

Computer-vision-based road feature extraction has been applied in intelligent vehicles for road following widely because of its advantages in low-power consumption, compact size, availability as a commercial product, cost effectiveness, and robustness [2]. Numerous image processing and feature extraction methods can be found in [3–7].

Control algorithms should be considered as an important issue in road following to ensure safe and smooth rides. Although a lot of researches have been done on this topic, most of them are based on traditional control theories such as PID [2] and nonlinear controllers [8]. The kinematic behavior of autonomous road following is typically nonlinear. Therefore linear models usually fail to describe these systems efficiently. However, it is difficult to analyze nonlinear mathematical models for autonomous road following schemes. Other methods such as neural networks [9, 10] and reinforcement learning (RL) [11] approaches have also been used in road following, but these approaches require learning procedures which consume extra computation time.

Human drivers can drive a car smoothly with their driving expertise rather than knowledge on control theories. This fact leads us to the fuzzy logic solution. Fuzzy logic control is known to be an organized method to emulate human expertise in dealing with imprecise data. It attempts to apply a human-like way of thinking in the application areas and allows intermediate values to be defined with linguistic terms besides conventional evaluations. It has been proven to be an effective and active method in solving control problems during the past decades. Fuzzy logic is a logic much closer to human thinking than traditional logic. It is a precise logic of imprecision and approximate reasoning. Fuzzy logic controllers provide a means of converting a linguistic control strategy based on expert knowledge into an automatic control strategy [12]. In areas where conventional control methods have difficulties because of the lack of precise quantitative data regarding the system inputs and outputs, fuzzy logic controllers can process imprecise data and make rational decisions by emulating human thinking and decision making capabilities. Fuzzy logic control has been applied for intelligent vehicles in many areas such as car parking and vehicle

guidance. Various applications of fuzzy logic control in the field of intelligent vehicles can be found in [13–17].

Safety and reliability are of great importance for intelligent vehicles especially if the vehicles are used for transportation. Therefore, before applying any dynamical systems to intelligent vehicles, the stability of these dynamical systems should be studied to make sure they are stable. Several well-known methods could be used to analyze the stability of a system, such as the Routh-Hurwitz stability criterion, the Lyapunov stability criterion, the Nyquist criterion, finding poles directly, the root locus method, or the Jury stability test for discrete-time control systems. Lyapunov stability theory is probably the most used tool for stability analysis. A dynamic system is Lyapunov stable if all solutions of the system which start near an equilibrium point remain near the point for all time. However, it is difficult to find the suitable Lyapunov functions. There is no general method to construct a Lyapunov function. Trial-and-error or mathematical/physical methods are often used. Some useful approaches for finding Lyapunov functions are Sum of Squares Decomposition [18, 19], convex search for storage functions [20], and variable gradient method [21]. However, these methods do not always lead to a desired Lyapunov function.

In this paper, we will design an autonomous road following embedded system for multiple intelligent vehicles. An intelligent vehicle which is capable of moving between two lines on the road will be designed. A fuzzy logic controller (FLC) will be developed to control the steering wheel of the vehicle for autonomous road following. An FLC on a nonlinear system requires less computational power compared to traditional nonlinear system applications. The resources required for building the embedded system will be significantly reduced. Lyapunov's direct method will be used to analyze the stability of the control system. The "variable gradient" approach proposed in [21] will be used to construct the Lyapunov function of this system. This control system will be implemented on a vision-based intelligent vehicle which is able to perform road following autonomously.

The rest of the paper is organized as follows. The kinematic model of the vehicle is studied in Section 2. Section 3 presents the design of the FLC. Section 4 provides the proof of the stability using Lyapunov's direct method. Experimental setup for the vision-based intelligent vehicle is described in Section 5. Section 6 discusses the simulation and experimental results. The last section of this paper concludes the research.

2. Kinematic Model of the Car

The road following problem of the intelligent vehicle with kinematic constraints in the two-dimensional workspace is studied. A nonholonomic constraint for a robotic vehicle is a nonintegrable equation involving the configuration parameters and their derivatives (velocity parameters) [22]. Such a constraint does not reduce the dimension of the space of configurations attainable by the robot but reduces the dimension of the space of possible motions at any given configuration. Considering the robotic vehicle modeled as Figure 1, the rear wheels are aligned with the vehicle while the front wheels are allowed to pivot about the axes. In a sufficiently large empty space, a robotic vehicle can be driven to any position with any orientation, hence the robot's configuration space has four dimensions, two for translation, one for rotation and one for the steering angle. Let (x, y, ϕ, θ) denote the

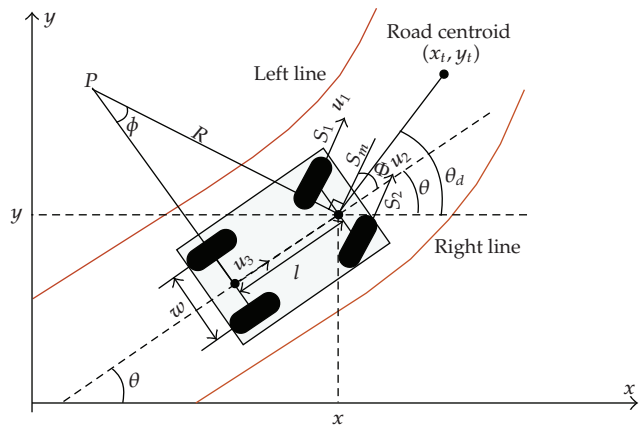

Figure 1: Kinematic model of the car.

configuration of the robot, parameterized by the location of the front wheels. The kinematic model of the robotic vehicle can be represented as

$$\begin{aligned} \dot{x} &= u_3 \cos\theta, \\ \dot{y} &= u_3 \sin\theta, \\ \dot{\theta} &= \frac{u_3}{l} \tan\phi, \end{aligned} \tag{2.1}$$

where u_3 corresponds to the forward velocity of the vehicle and the angle of the vehicle body with respect to the horizontal line is θ, the steering angle with respect to the vehicle body is ϕ, $(x,\ y)$ is the location of the center point of the front wheels, l is the length between the front and the rear wheels.

Since the turn radius of the robot is quite large compared with the radius of the wheels, referring to Figure 1, we have the following relations:

$$\begin{aligned} S_1 &= \left(R - \frac{w}{2}\cos\phi\right)\phi, \\ S_m &= R\phi, \\ S_2 &= \left(R + \frac{w}{2}\cos\phi\right)\phi, \end{aligned} \tag{2.2}$$

where S_1 and S_2 give the displacement (distance traveled) of the front left and front right wheel, respectively, R is the turn radius of the center point of the front wheels, w is the distance between wheels (from center-to-center along the length between the two font wheels or two back wheels), and ϕ is the angle of the turn in radians. S_m is the displacement at the center point of the front wheels. Once we have established the simple geometry for the robotic vehicle system, it is easy to develop algorithms for controlling the robot's steering angle ϕ, thus controlling the robot's orientation θ. As the robot is considered as having a rigid body, to develop a forward kinematic equation for the steering system, we start by specifying a frame of reference in which an arbitrarily chosen point is treated as stationary. All other points in

the system are treated as moving relative to the reference point. Here we treat the center point of the front wheels as the origin of the simulated robot's frame of reference.

For the robotic vehicle that we are modeling, the turn angle of the front wheels has a range of $[-\pi/6,\ \pi/6]$, that is, $-\pi/6 \le \phi \le \pi/6$. By adjusting the steering angle ϕ, we can control the velocity of both the front wheels

$$\begin{aligned} \dot{S}_1 &= \dot{\phi}\left(R - \frac{w}{2}\cos\phi\right) + \frac{w}{2}\phi\dot{\phi}\sin\phi, \\ \dot{S}_2 &= \dot{\phi}\left(R + \frac{w}{2}\cos\phi\right) - \frac{w}{2}\phi\dot{\phi}\sin\phi, \end{aligned} \tag{2.3}$$

so that

$$u_2 - u_1 = \dot{\phi}w(\cos\phi - \phi\sin\phi), \tag{2.4}$$

where u_1 and u_2 correspond to the forward velocity of the front left wheel and the front right wheel, respectively.

The real-time path of the vehicle can be obtained by integrating (2.1). The angle of the vehicle body with respect to the horizontal line at time $(t + \Delta t)$ could be derived first. If $\dot{\phi} \neq 0$, that is, $u_2 \neq u_1$, the angle of the vehicle body with respect to the horizontal line at time $(t + \Delta t)$ is given as

$$\begin{aligned} \theta(t+\Delta t) &= \theta(t) + \frac{u_3}{l}\int_t^{t+\Delta t} \tan\phi dt \\ &= \theta(t) + \frac{u_3}{l\dot{\phi}}\left(-\ln\left|\cos\phi\right|\right)\Big|_t^{t+\Delta t} \\ &= \theta(t) + \frac{u_3}{l\dot{\phi}}\left(-\ln\left|\cos\phi(t+\Delta t)\right| + \ln\left|\cos\phi(t)\right|\right), \end{aligned} \tag{2.5}$$

and if $\dot{\phi} = 0$, that is, $u_2 = u_1$, the angle of the vehicle body at time $(t + \Delta t)$ is given as

$$\theta(t+\Delta t) = \theta(t) + \frac{u_3}{l}\tan\phi\Delta t. \tag{2.6}$$

Next the position of the vehicle at time $(t + \Delta t)$ could be derived. If $\dot{\theta} \neq 0$, that is, $\phi \neq 0$, the position of the moving vehicle at time $(t + \Delta t)$ is given as

$$\begin{aligned} x(t+\Delta t) &= x(t) + \frac{u_3}{\dot{\theta}}(\sin\theta(t+\Delta t) - \sin\theta(t)), \\ y(t+\Delta t) &= y(t) - \frac{u_3}{\dot{\theta}}(\cos\theta(t+\Delta t) - \cos\theta(t)), \end{aligned} \tag{2.7}$$

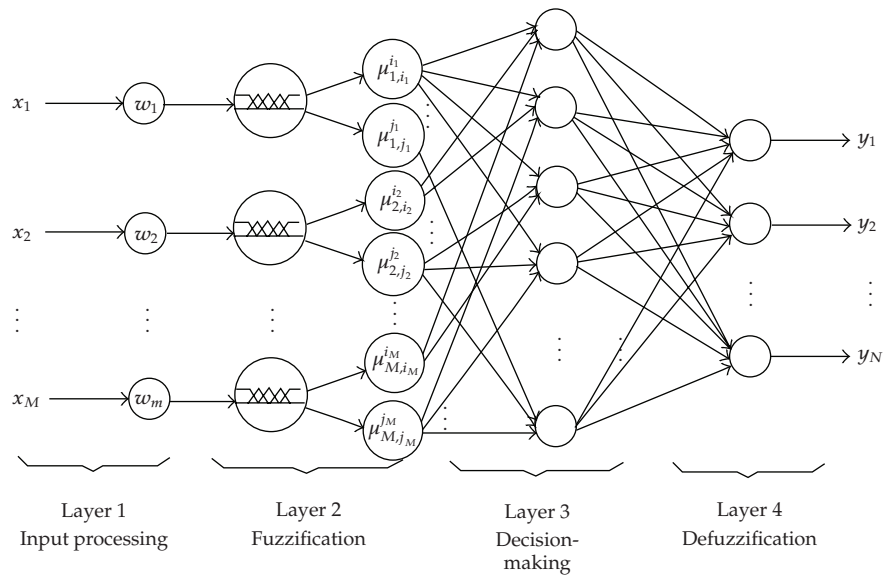

Figure 2: Structure of the FLC.

and if $\dot{\theta} = 0$, that is, $\phi = 0$, the position of the vehicle at time $(t + \Delta t)$ is given as

$$\begin{aligned} x(t + \Delta t) &= x(t) + u_3 \cos\theta \Delta t, \\ y(t + \Delta t) &= y(t) + u_3 \sin\theta \Delta t. \end{aligned} \tag{2.8}$$

3. Design of the FLC

In this section, the general structure of the proposed FLC is presented first. Then based on simulation and experiments, the FLC is designed to perform the road following task. The developed FLC not only enhances performance for road following but also saves computational resources.

3.1. The Structure of the FLC

Figure 2 shows the structure of the proposed FLC which has four layers: input processing layer, fuzzification layer, decision-making layer, and defuzzification layer. These layers form an FLC following the Mamdani model. There are M inputs and N outputs for the FLC. Each rule in the system has the following form:

Rule k: IF x_1 is $S_1^{(k)}$ AND ... AND x_m is $S_m^{(k)}$ ... AND x_M is $S_M^{(k)}$, THEN y_1 is $R_1^{(k)}$ AND ... y_n is $R_n^{(k)}$ ... AND y_N is $R_N^{(k)}$ $\quad (k = 1, 2, \ldots, K)$,

where x_m is the mth input, $m = 1, 2, \ldots, M$, y_n is the nth output, $n = 1, 2, \ldots, N$, $S_m^{(k)}$ is the fuzzy linguistic sets for input x_m, $R_n^{(k)}$ is the fuzzy rule sets for output y_m, and K is the number of rules in the rule base. The design of each layer is presented as follows.

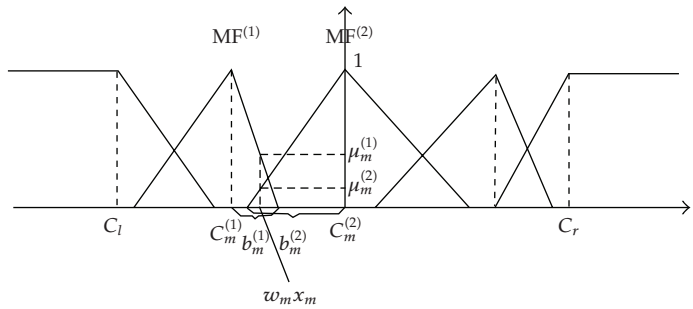

Figure 3: Input MFs.

Input Processing Layer

The inputs of the FCL are crisp values. The input vector can be presented as

$$\begin{bmatrix} x_1 & x_2 & \cdots & x_M \end{bmatrix}. \tag{3.1}$$

Each input is adjusted by a weight factor. Then the input vector can be presented as

$$\begin{bmatrix} w_1 x_1 & w_2 x_2 & \cdots & w_M x_M \end{bmatrix}, \tag{3.2}$$

where $w_1, w_2, \ldots, w_m$ are weight factors.

Fuzzification Layer

It converts the weighted crisp inputs to fuzzy variables. This layer has three nodes for each input: one node defines the fuzzy membership functions (MFs) for the input; the other two nodes represent the two triggered MFs for the input. Triangle MFs are used for fuzzy sets except for the leftmost and the rightmost fuzzy set. The leftmost and rightmost MFs are trapezoidal. Without loss of generosity, MFs for different fuzzy sets can have different triangle or trapezoidal shapes. We constrain the maximum overlapping degree of two MFs to 50%. Therefore the maximum number of triggered MFs is 2 and these two MFs must be adjacent. An example of the MFs with five fuzzy sets is shown in Figure 3. We define $\mathrm{MF}^{(1)}$ and $\mathrm{MF}^{(2)}$ as the first and second triggered MF, and $\mu_m^{(1)}$ and $\mu_m^{(2)}$ as the membership value of the first and second triggered MF of the input x_m, respectively, then $\mu_m^{(1)}$ and $\mu_m^{(2)}$ can be calculated as

$$\begin{gathered}
\mu_m^{(1)} = 1, \quad \mu_m^{(2)} = 0, \quad x_m \le C_l, \\
\mu_m^{(1)} = 0, \quad \mu_m^{(2)} = 1, \quad x_m \ge C_r, \\
\mu_m^{(1)} = \max\left(0, 1 - \frac{w_m x_m - C_m^{(1)}}{b_m^{(1)}}\right), \\
\mu_m^{(2)} = \max\left(0, 1 - \frac{C_m^{(2)} - w_m x_m}{b_m^{(2)}}\right), \quad C_m^{(1)} \le x_m \le C_m^{(2)},
\end{gathered} \tag{3.3}$$

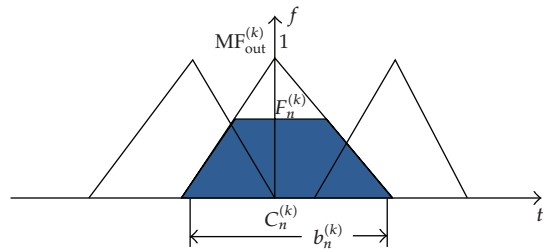

Figure 4: An example of output MFs.

where $C_m^{(1)}$ and $C_m^{(2)}$ are the centers of the two triggered MFs and $C_m^{(1)} < C_m^{(2)}$, C_l and C_r are the leftmost and the rightmost limits, respectively, $b_m^{(1)}$ is the width of the right-half base of $\mathrm{MF}^{(1)}$, and $b_m^{(2)}$ is the width of the left half base of $\mathrm{MF}^{(2)}$. If one of the membership values is zero, the MF with respect to this membership value is not triggered, then there is only one triggered MF. The outputs of this layer are membership values of triggered MFs for all inputs.

Decision-Making Layer

For every output, each node in this layer selects a fuzzy control rule from the rule base of this output and obtains the antecedent value of this rule based on triggered input MFs. Each output has one rule base, which means in the case of N outputs there are N different rule bases in total. For each output, rules are selected according to the predefined rule base corresponding to this output. Thus, each node in this layer selects N rules from N different rule bases. Each control rule is selected based on a combination of MFs. Each of these MFs is one of the triggered MFs of an input. For example, if there are three inputs, two of which have two triggered MFs while the other input has only one triggered MF, the number of selected rules for each output is 4 $(2 \times 2 \times 1)$. The antecedent value of the selected rule k is computed using AND fuzzy logic. Therefore, "min" operation is considered for composition of the FLC:

$$F^{(k)} = \min\left(\mu_1, \mu_2, \ldots, \mu_m, \ldots, \mu_M\right), \tag{3.4}$$

where μ_m is one of the triggered input MFs (either $\mu_m^{(1)}$ or $\mu_m^{(2)}$) of x_m, $k = 1, 2, \ldots, K^*$, and K^* is the number of selected rules.

Defuzzification Layer

This layer converts fuzzy values to crisp values and send them out as control outputs of the FLC. Each node in this layer performs defuzzification for an output. Triangles are used for the output MFs. Figure 4 shows an example of MFs for an output with three fuzzy sets. The center of gravity (COG) algorithm is used to compute output crisp values. Let $C_n^{(k)}$ be the center of the kth triangle. The output y_n can be computed as

$$y_n = \frac{\sum_k C_n^{(k)} \int F_n^{(k)} dt}{\sum_k \int F_n^{(k)} dt}, \tag{3.5}$$

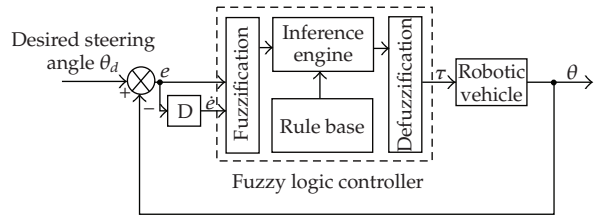

Figure 5: Block diagram of the specified FLC.

where $F_n^{(k)}$ is the antecedent value of the kth selected fuzzy rule for y_n. As all the output MFs are triangles, $\int F_n^{(k)} dt$ can be obtained by computing the area of the trapezoid under the line $f = F_n^{(k)}$. Thus, (3.5) can be modified as

$$y_n = \frac{\sum_k C_n^{(k)} b_n^{(k)} \left(F_n^{(k)} - \left(F_n^{(k)} \right)^2 / 2 \right)}{\sum_k b_n^{(k)} \left(F_n^{(k)} - \left(F_n^{(k)} \right)^2 / 2 \right)} \tag{3.6}$$

where $b_n^{(k)}$ is the base length of the kth output MF. Equation (3.6) simplifies the defuzzification calculation by replacing derivatives with the computation of trapezoid areas.

3.2. The Developed FLC for Road following

A block diagram of the specified FLC for the road following task is shown in Figure 5. The desired orientation of the center line of the car should be aligned with the road centroid. The error is the angle between the desired orientation of the center line and the actual center line of the car. The error is represented by $e = \theta_d - \theta$. To reduce the error to zero, the steering angle should be equal to ϕ. ϕ is determined by the FLC. The error and the change-in-error are calculated and fed into the FLC. The FLC is designed to output control signals corresponding to the control torque to the front steering motor to control the front wheels' steering angle ϕ.

The fuzzification procedure maps the crisp input values to the linguistic fuzzy terms with the membership values between 0 and 1. In this study, we use five MFs for both error $e = \theta_d - \theta$ and change-in-error $\dot{e} = \dot{\theta}_d - \dot{\theta}$ because five MFs can balance between the performance and the complexity of the FLC. The isosceles triangle membership function (MF) is used except for the leftmost and the rightmost input MF which are trapezoidal. Each MF has a 50% overlapping with its neighboring MFs. Figure 6 illustrates the input MFs for e and $\dot{e}$, respectively. Note that the scale for the X coordinate can be changed easily in the program.

The inference engine is responsible for decision making in the control system using approximate reasoning. The fuzzy control rules are designed based on expert knowledge and testing. Furthermore, the control rules also meet the stability requirements derived from Lyapunov's direct method. Table 1 represents abstract knowledge that an expert uses to control the steering angle given information about the error and its derivative. For example, if e is positive large "PL" and is increasing rapidly ($\dot{e}$ is positive large), then the vehicle should turn left sharply, that is, ϕ should be left large (LL). The rule base stores rules which define

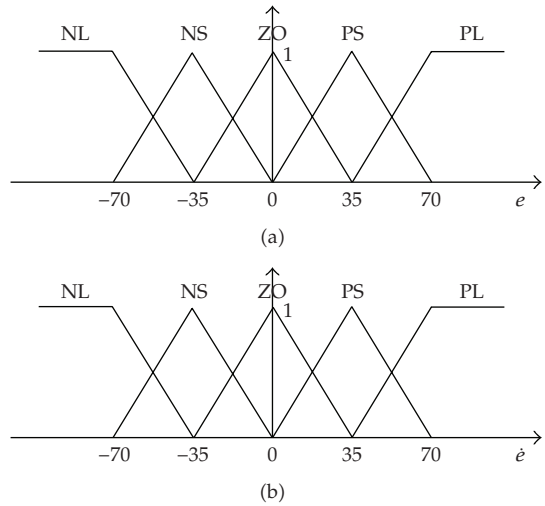

Figure 6: Input Membership functions. (a) Error MF. (b) Change-in-error MF.

Table 1: Fuzzy rule base.

		$\dot{e}_\phi$				
		PL	PS	ZO	NS	NL
	PL	RL	RL	RL	RS	MD
	PS	RL	RL	RS	MD	LS
e_ϕ	ZO	RL	RS	MD	LS	LL
	NS	RS	MD	LS	LL	LL
	NL	MD	LS	LL	LL	LL

Note: PL: Positive Large; PS: Positive Small; ZO: Zero; NS: Negative Small; NL: Negative Large; RL: Right Large (turn right sharply); RS: Right Small (turn right gently); MD: Middle (no turn); LL: Left Large (turn left sharply); LS: Left Small (turn left gently).

the relation between the inputs and the output. Based on the membership functions of the error and the change in error, twenty-five fuzzy rules are obtained.

Figure 7 shows output MFs. All MFs for the output are isosceles triangles with 50% overlap between two neighboring MFs.

The defuzzification procedure maps the fuzzy output from the inference mechanism to a crisp signal. We use the COG defuzzification method to combine the recommendations represented by the implied fuzzy sets from all the rules. The crisp value is computed according to (3.6).

4. Stability Analysis Using Lyapunov's Direct Method

The autonomous road following system can be represented as

$$\begin{aligned} e &= \theta - \theta_d = x_1, \\ \dot{e} &= \dot{\theta} - \dot{\theta}_d = x_2, \end{aligned} \tag{4.1}$$

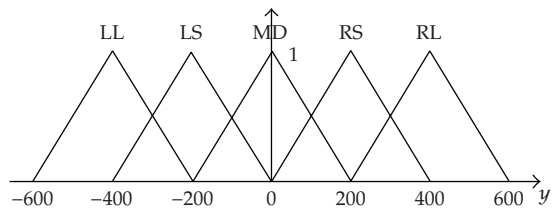

Figure 7: Steering control output MF.

where θ_d is the desired angle, and θ is the actual angle. From (2.1), we know that we need to design the FLC to control the steering wheel so that θ can approach θ_d. The output of the fuzzy controller $\Phi(\cdot)$ is a function of x_1 and x_2 that can be represented by $\Phi(x_1,\ x_2)$. On the intelligent vehicle, the control signal $\Phi(x_1,\ x_2)$ is used to steer the front wheels. We assume that the low-level tracking controller can output the motor torque to steer the front wheels accordingly. Recall (2.1), we have

$$\begin{aligned} \dot{x}_1 &= x_2 = \dot{\theta} - \dot{\theta}_d = \frac{u_3}{l}\tan\phi - \dot{\theta}_d, \\ \dot{x}_2 &= \ddot{\theta} - \ddot{\theta}_d = \frac{u_3}{l}\frac{1}{\cos^2\phi}\dot{\phi} - \ddot{\theta}_d. \end{aligned} \tag{4.2}$$

Assume that at the equilibrium point $e = 0$ and $\dot{e} = 0$, so that the equilibrium is preserved. The main shortcoming of Lyapunov theory is the difficulty associated with the construction of Lyapunov functions [21]. To overcome this problem, we use the "variable gradient" approach proposed in [21] to construct the Lyapunov function. The essence of this method is to assume the gradient of the unknown Lyapunov function $V(\cdot)$ is known up to some adjustable parameters. Then finding $V(\cdot)$ becomes integrating the assumed gradient.

The system can be represented as

$$\dot{x} = f(x) = \begin{bmatrix} \dot{x}_1 & \dot{x}_2 \end{bmatrix}^T = \begin{bmatrix} x_2 & \dot{x}_2 \end{bmatrix}^T. \tag{4.3}$$

We proceed to find a suitable Lyapunov function for this system as follows.

Step 1. Assume that $\nabla V(x) = g(x)$ has the form

$$g(x) = \begin{bmatrix} h_1^1 x_1 + h_1^2 x_2 & h_2^1 x_1 + h_2^2 x_2 \end{bmatrix}. \tag{4.4}$$

Step 2. Impose the symmetry conditions

$$\frac{\partial^2 V}{\partial x_i x_j} = \frac{\partial^2 V}{\partial x_j x_i}, \tag{4.5}$$

or equivalently,

$$\frac{\partial g_i}{\partial x_j} = \frac{\partial g_j}{\partial x_i}. \tag{4.6}$$

In our case, the symmetry condition is

$$\begin{aligned} \frac{\partial g_1}{\partial x_2} &= x_1 \frac{\partial h_1^1}{\partial x_2} + h_1^2 + x_2 \frac{\partial h_1^2}{\partial x_2}, \\ \frac{\partial g_2}{\partial x_1} &= h_2^1 + x_1 \frac{\partial h_2^1}{\partial x_1} + x_2 \frac{\partial h_2^2}{\partial x_1}. \end{aligned} \tag{4.7}$$

To simplify the solution, we assume that g_i's are constant. Then we have

$$\begin{aligned} &\frac{\partial h_1^1}{\partial x_2} = \frac{\partial h_1^2}{\partial x_2} = \frac{\partial h_2^1}{\partial x_1} = \frac{\partial h_2^2}{\partial x_1} = 0, \\ &\frac{\partial g_1}{\partial x_2} = \frac{\partial g_2}{\partial x_1} \Longleftrightarrow h_1^2 = h_2^1 = k \\ &\qquad \Longrightarrow g(x) = \left[h_1^1 x_1 + k x_2 \quad k x_1 + h_2^2 x_2 \right]. \end{aligned} \tag{4.8}$$

If we choose $k = 0$, we have

$$g(x) = \left[g_1 \;\; g_2 \right] = \left[h_1^1 x_1 \;\; h_2^2 x_2 \right]. \tag{4.9}$$

Step 3. Find $\dot{V}$:

$$\begin{aligned} \dot{V}(x) &= \nabla V \cdot f(x) \\ &= g(x) \cdot f(x) \\ &= \left[h_1^1 x_1 \;\; h_2^2 x_2 \right] \begin{bmatrix} x_2 \\ \dot{x}_2 \end{bmatrix} \\ &= h_1^1 x_1 x_2 + h_2^2 x_2 \dot{x}_2. \end{aligned} \tag{4.10}$$

Step 4. Find V from ∇V by integration:

$$\begin{aligned} V(x) &= \int_0^{x_1} g_1(s_1, 0) ds_1 + \int_0^{x_2} g_2(x_1, s_2) ds_2 \\ &= \int_0^{x_1} h_1^1 s_1 ds_1 + \int_0^{x_2} h_2^2 s_2 ds_2 \\ &= \frac{1}{2} h_1^1 x_1^2 + \frac{1}{2} h_2^2 x_2^2. \end{aligned} \tag{4.11}$$

Therefore, we have

$$V(x) = \frac{1}{2}h_1^1 x_1^2 + \frac{1}{2}h_2^2 x_2^2, \tag{4.12}$$

$$\dot{V}(x) = h_1^1 x_1 x_2 + h_2^2 x_2 \dot{x}_2. \tag{4.13}$$

Step 5. Find h_1^1 and h_2^2 that make $V > 0$. From (4.12), $V(x) > 0$ only if $h_1^1,\ h_2^2 > 0$. Let $h_1^1 = h_2^2 = 1$, then we have

$$\dot{V}(x) = x_1 x_2 + x_2 \dot{x}_2 = \left(\dot{\theta} - \dot{\theta}_d\right)\left(\theta + \ddot{\theta} - \theta_d - \ddot{\theta}_d\right). \tag{4.14}$$

Based on the "variable gradient" approach, we can derive the following Lyapunov function:

$$V(x) = \frac{1}{2}\ x_1^2 + \frac{1}{2}x_2^2, \tag{4.15}$$

where $V : B(\epsilon) \to \Re$ for some $\epsilon > 0$, where $B(\epsilon) = \{x \in \Re^2 :\ |x| < \epsilon\}$ is a ball centered at the origin with a radius of ϵ and $|\cdot|$ is a norm on $\Re^2$. Then the gradient of the Lyapunov function is

$$\nabla V(x(t)) = [\ x_1 \quad x_2], \tag{4.16}$$

$$\begin{aligned} \dot{V} &= [\ x_1 \ \ x_2] \begin{bmatrix} x_2 \\ \dot{x}_2 \end{bmatrix} \\ &= x_2(x_1 + \dot{x}_2) \\ &= \left(\dot{\theta} - \dot{\theta}_d\right)\left(\theta + \ddot{\theta} - \theta_d - \ddot{\theta}_d\right) \\ &= \left(\frac{u_3}{l}\tan\phi - \dot{\theta}_d\right)\left(\theta - \theta_d + \frac{u_3}{l}\frac{1}{\cos^2\phi}\dot{\phi} - \ddot{\theta}_d\right). \end{aligned} \tag{4.17}$$

We would like $\dot{V} \le 0$, to prove stability, that is, to show that the fuzzy controller can achieve and maintain the desired θ_d. In (4.17), $u_3/l > 0$, $\cos^2\phi > 0$. We assume that $\dot{\theta}_d$ is bounded, and $\ddot{\theta}_d = 0$. On the RC car, the steering angle $-30° \le \phi \le 30°$.

We can always design the FLC, $\Phi(x_1, x_2)$, to adjust ϕ and $\dot{\phi}$ to achieve the following conditions:

$$\begin{aligned} &\frac{u_3}{l}\frac{1}{\cos^2\phi}\dot{\phi} \ge \theta_d - \theta \quad \text{if } \frac{u_3}{l}\tan\phi - \dot{\theta}_d > 0 \\ &\frac{u_3}{l}\frac{1}{\cos^2\phi}\dot{\phi} \le \theta_d - \theta \quad \text{if } \frac{u_3}{l}\tan\phi - \dot{\theta}_d < 0. \end{aligned} \tag{4.18}$$

Therefore, $\dot{V} \le 0$ can always be achieved and hence the stability holds.

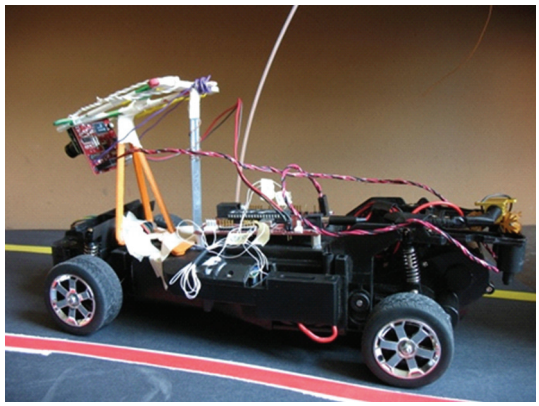

Figure 8: The steering mechanism of the RC car.

5. Experimental Setup

In this section, the hardware setup of the prototype vehicle for autonomous road following is presented. A fully automated robotic system is designed to control a motor vehicle using an on board camera. The hardware system includes a camera associated with a frame grabber. The camera is then connected to a Microchip PIC controller which controls the vehicle motion. This system utilizes the camera with a frame-grabber and a built-in processor to grab pictures of the road and to find the center of the road. Then it calculates the deviation between the center of the car and the center of the road, and sends the result to an FLC. The FLC decides how to turn the vehicle and sends out control signals to control the steering wheel. This is implemented in a way that the vehicle can remain between two lines while simulating highway motion.

5.1. The Remote Control Car

The Audi S4 radio control (RC) car platform is chosen because it offers a fully functional steering and drive system. The control signal for the steering and drive system is generated by the microcontroller which emulates the car's control signals. The speed and steering of the car are controlled by varying the pulse-width modulation (PWM) signals. The steering mechanism of the RC car is shown in Figure 8.

5.2. The Mocked Road

The lane used in this project is the space between two lines as shown in Figure 8. To illustrate the control process, we use a red line and a yellow line. The distance between these two lines is constant.

5.3. Computer Vision

The CMUCam3 camera is chosen for the project. The camera uses a built in microcontroller and a frame grabber to allow postprocessing on each captured image. As the two lines which

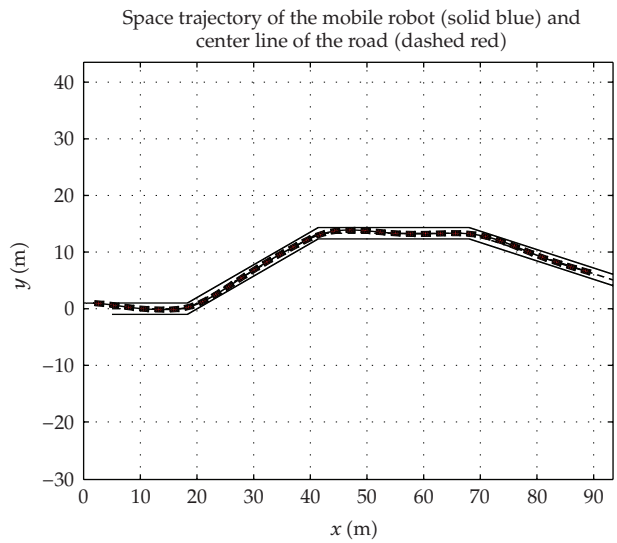

Figure 9: Following a road in Cartesian space.

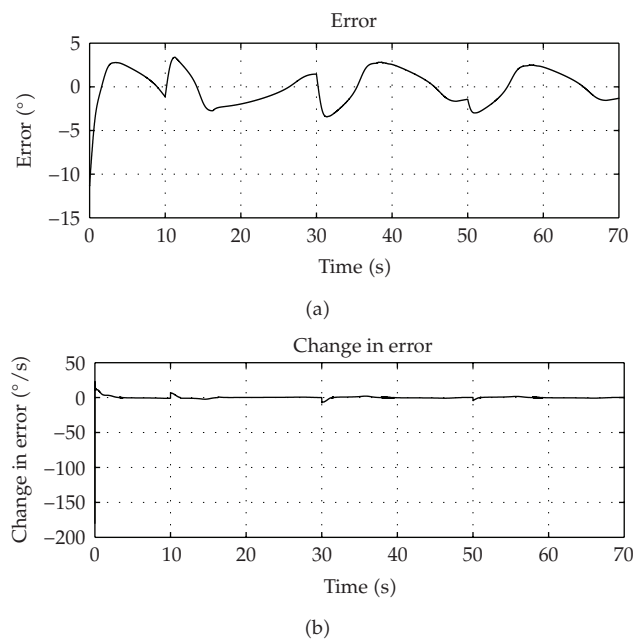

Figure 10: Error e_ϕ and change-in-error $\dot{e}_\phi$.

mark the road are in different colors from the rest of the road, using a multiple color tracking algorithm, we are able to track each line individually. The minimum and maximum RGB values for each line color are set in the camera code. Pixels within the RGB value range are regarded as a part of the line. A filter is applied to filter out noise. The camera finds the location and the width of each colored line in terms of pixels and calculates the centroid of each colored line. The centroid of two colored lines is then used to calculate the position

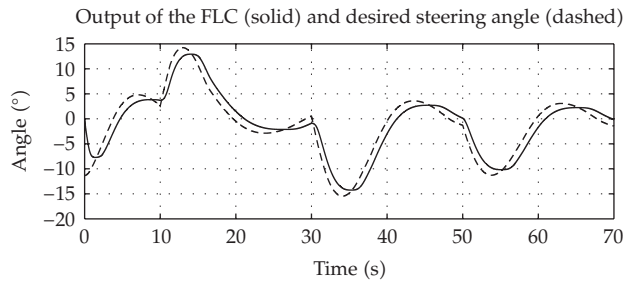

Figure 11: Output of the fuzzy controller.

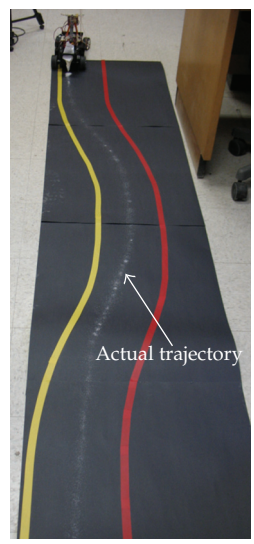

Figure 12: The road following result using the proposed method.

error which is sent to the microcontroller. Since the vehicle is supposed to remain in the center of the two colored lines, error can be calculated if the centroid is not at the center of the image. The camera is programmed using a variation of the C language. The error is calculated according to one of the states described in Table 2. Centroids in the table refer to the x coordinate of the image only. In the table, Cr represents the centroid of the red line, Cy represents the centroid of the yellow line, Cw represents the centroid of the image, C represents the centroid of the two lines, respectively.

5.4. Microcontroller

The PIC18F4431 microcontroller is used to interface with the camera and the car's existing circuitry. It receives the incoming position error from the RS-232 port located on the CMUCam3 board. The microcontroller then uses the error to calculate the appropriate steering signal, using the proposed FLC written in C language. The steering signal is then output to the RC car's circuit.

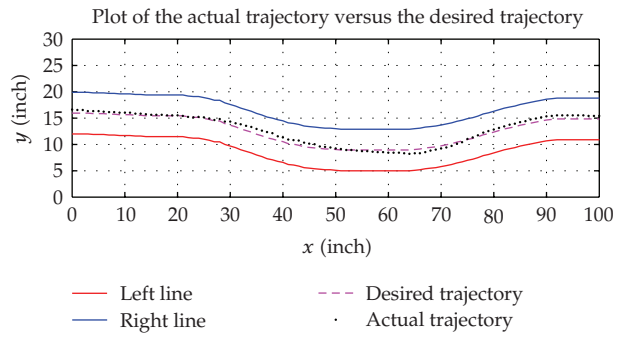

Figure 13: The actual trajectory and the desired trajectory.

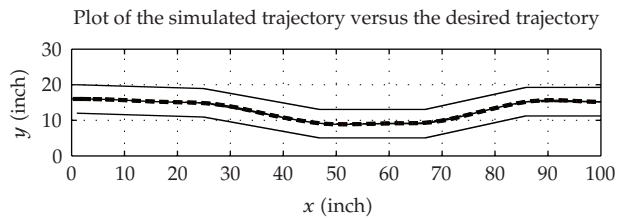

Figure 14: The simulated trajectory and the desired trajectory.

6. Simulation Studies and Experiment Results

In order to verify the performance of the proposed FLC and the system, simulations and experiments have been conducted.

Simulations have been done to test the performance of the fuzzy controller. The results show that the intelligent vehicle is able to follow the road with a speed of 13 m/s. Figure 9 shows the tracking performance of the robotic vehicle in the Cartesian space. The road has two sharp curves and the robot starts from (0, 1) which is off the center of the road. The robot is capable of following the road. It can respond to sudden changes on the road by changing its steering angle accordingly.

Figure 10 shows the steering error and the change-in-error. Figure 11 shows the output of the fuzzy controller. It can be seen that the fuzzy controller can output smooth control signals to sudden changes in e and $\dot{e}$ to make the system stable.

Experiments have been performed to verify the fuzzy logic controller design. In our experiments, we use a mocked road with two lines to guide the navigation of the robot. The actual trajectory of the robot is marked on the road using white powder dropping from a container attached to the rear end of the robot. Figure 12 shows the robot performing the autonomous road following task on the mocked road with curves. The robot moves at a speed of 0.9 m/s. In the figure, the line in the center of the road is the trajectory marked by the powder.

In our experiments, all data, such as errors and mean square errors, are calculated based on four trials. Sample points on the actual trajectories are recorded and compared with the desired trajectory which is the center line of the road. One sample point is taken for every inch along the road. Figure 13 shows the desired trajectory and the actual trajectory we have recorded during the experiment. In the figure, the dashed line represents the desired

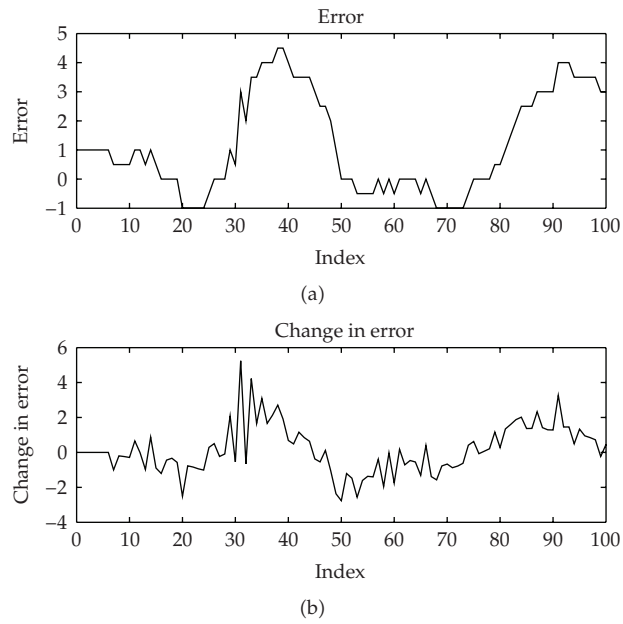

Figure 15: Error and change in error in the experiment.

Table 2: Error calculation table.

Red centroid	Yellow centroid	Error
$Cr! = 0$	$Cy! = 0$	Error = $C - Cw$
$Cr! = 0$	$Cy = 0$	Error = $176 - Cr$
$Cr = 0$	$Cy! = 0$	Error = $0 - Cy$

trajectory while the dotted line represents the actual trajectory. The maximum absolute error between the center line of the road and the actual trajectory of the intelligent vehicle is 1.55 inches. The root mean square error is 0.73 inches which is relatively small compared with the width of the road which is 8 inches.

As a comparison, we also obtained simulation results for the vehicle moving at 0.9 m/s. Figure 14 shows the tracking performance of the vehicle. The desired trajectory is the one used in the experiment. It can be seen that experiment results in Figure 13 match the simulation results in Figure 14 very well. The maximum error in the experiment results is a little larger. This is because in the real world, the camera takes some time to process the raw data in order to obtain the error while in simulation the error is calculated instantaneously.

The error and change in error for both the experiment and the simulation are plotted in Figures 15 and 16. From the figures, it can be seen that the error is larger when there is a curve in the desired trajectory. This is because the desired trajectory is changing while the actual trajectory is deviated from the desired trajectory. The designed fuzzy controller adjusts to the changes and controls the vehicle to follow the trajectory successfully. It is also noted that in the experiment results, the change in error is filtered thus it is smoother than the simulated change in error.

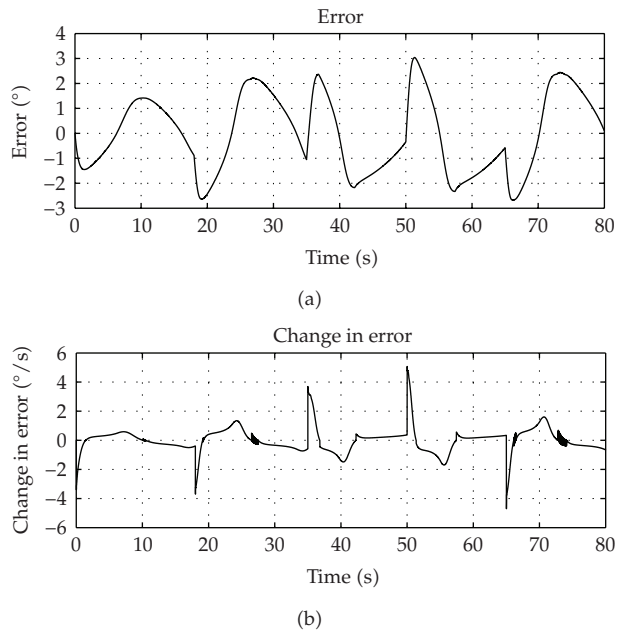

Figure 16: Error and change in error in the simulation.

7. Conclusion

In this paper, an intelligent robotic vehicle which is capable of performing autonomous road following is successfully developed. A vision system installed on the vehicle is used to detect a curved road. An FLC is developed to control the steering wheel of the robotic vehicle according to the deviation from the rods. The deviation of the vehicle from the road is regarded as the error. The error and the change-in-error are used as the input of the FLC. Based on human driving experience and experiments, the FLC makes decision on the steering angle accordingly. An analysis and design of fuzzy control laws for steering control of the nonholonomic robotic vehicle are presented. Lyapunov's direct method is used to guarantee the convergence of the steering error. Simulations using the four degree of freedom nonholonomic robotic vehicle model are also conducted to investigate the performance and stability of the fuzzy controller. Experiments demonstrate that the vehicle with the proposed fuzzy controller can automatically follow the curved road.

Acknowledgment

Peter Miller, Matt Webb, and Chris Desjardins helped with the hardware setup.

References

[1] R. Bishop, "Intelligent vehicle applications worldwide," *IEEE Transactions on Intelligent Systems*, vol. 15, no. 1, pp. 78–81, 2000.

[2] A. M. Zhang and R. A. Russell, "Dominant orientation tracking for path following," in *Proceedings of IEEE/RSJ International Conference on Intelligent Robots and Systems*, pp. 3885–3889, August 2005.

[3] D. Raviv and M. Herman, "A new approach to vision and control for road following," in *Proceedings of the IEEE Workshop on Visual Motion*, pp. 217–225, October 1991.
[4] C. Thorpe, M. H. Hebert, T. Kanade, and S. A. Shafer, "Vision and navigation for the Carnegie-Mellon Navlab," *IEEE Transactions on Pattern Analysis and Machine Intelligence*, vol. 10, no. 3, pp. 362–373, 1988.
[5] D. Raviv and M. Herman, "A unified approach to camera fixation and vision-based road following," *IEEE Transactions on Systems, Man and Cybernetics*, vol. 24, no. 8, pp. 1125–1141, 1994.
[6] Z. Zhu, S. Yang, G. Xu, X. Lin, and D. Shi, "Fast road classification and orientation estimation using omni-view images and neural networks," *IEEE Transactions on Image Processing*, vol. 7, no. 8, pp. 1182–1197, 1998.
[7] R. Chapuis, R. Aufrere, and F. Chausse, "Accurate road following and reconstruction by computer vision," *IEEE Transactions on Intelligent Transportation Systems*, vol. 3, no. 4, pp. 261–270, 2002.
[8] L. Beji and Y. Bestaoui, "An adaptive control method of automated vehicles with integrated longitudinal and lateral dynamics in road following," in *Proceeding of the 2nd International Workshop on Robot Motion and Control*, pp. 201–206, October 2001.
[9] S. Baluja, "Evolution of an artificial neural network based autonomous land vehicle controller," *IEEE Transactions on Systems, Man, and Cybernetics, Part B*, vol. 26, no. 3, pp. 450–463, 1996.
[10] D. Y. Jeong, S. J. Park, S. H. Han, M. H. Lee, and T. Shibata, "A study on neural networks for vision-based road following of autonomous vehicle," *IEEE International Symposium on Industrial Electronics*, vol. 3, pp. 1609–1614, 2001.
[11] S.-Y. Oh, J.-H. Lee, and D.-H. Choi, "A new reinforcement learning vehicle control architecture for vision-based road following," *IEEE Transactions on Vehicular Technology*, vol. 49, no. 3, pp. 997–1005, 2000.
[12] C. C. Lee, "Fuzzy logic in control systems: fuzzy logic controller I," *IEEE Transactions on Systems, Man, and Cybernetics*, vol. 20, no. 2, pp. 404–418, 1990.
[13] T.-H. S. Li, S.-J. Chang, and Y.-X. Chen, "Implementation of human-like driving skills by autonomous fuzzy behavior control on an FPGA-based car-like mobile robot," *IEEE Transactions on Industrial Electronics*, vol. 50, no. 5, pp. 867–880, 2003.
[14] J. L. Arroyabe, G. Aranguren, L. A.L. Nozal, and J. L. Martin, "Autonomous vehicle guidance with fuzzy algorithm," in *Proceedings of 26th Annual Conference of IEEE Industrial Electronics Society (IECON '00)*, vol. 3, pp. 1503–1508, Nagoya, Japan, October 2000.
[15] S. Yasunobu and Y. Murai, "Parking control based on predictive fuzzy control," in *Proceedings of the 3rd IEEE Conference on Fuzzy Systems*, vol. 2, pp. 1338–1341, Orlando, Fla, USA, June 1994.
[16] W. A. Daxwanger and G. K. Schmidt, "Skill-based visual parking control using neural and fuzzy networks," in *Proceedings of the IEEE International Conference on Systems, Man and Cybernetics*, vol. 2, pp. 1659–1664, Vancouver, Canada, October 1995.
[17] M. C. Leu and T.-Q. Kim, "Cell mapping based fuzzy control of car parking," in *Proceedings of IEEE International Conference on Robotics and Automation*, vol. 3, pp. 2494–2499, Leuven, Belgium, May 1998.
[18] P. A. Parrilo, *Structured semidefinite programs and semialgebraic geometry methods in robustness and optimization*, Ph.D. thesis, Caltech, Pasadena, Calif, USA, 2000.
[19] A. Papachristodoulou and S. Prajna, "On the construction of Lyapunov functions using the sum of squares decomposition," in *Proceedings of the 41st IEEE Conference on Decision and Control*, vol. 3, pp. 3482–3487, Las Vegas, Nev, USA, December 2002.
[20] A. Megretski, *Dynamics of Nonlenear Systems*, Lecture Notes, Massachusetts Institute of Technology, Cambridge, Mass, USA, 2003.
[21] H. J. Marques, *Nonlinear Control Systems: Analysis and Design*, John Wiley & Sons, New York, NY, USA, 2003.
[22] Y. Fu, H. Li, and M. Kaye, "Design and stability analysis of a fuzzy controller for autonomous road following," in *Proceedings of IEEE Intelligent Vehicles Symposium*, pp. 66–71, Xi'an, China, June 2009.

Hindawi Publishing Corporation
Mathematical Problems in Engineering
Volume 2010, Article ID 590943, 28 pages
doi:10.1155/2010/590943

Research Article

Modelling and Simulation for Energy Production Parametric Dependence in Greenhouses

Maurizio Carlini[1] and Sonia Castellucci[2]

[1] *CIRDER, University of Tuscia, Via San Camillo de Lellis s.n.c, 01100 Viterbo, Italy*
[2] *DiSAFRi University of Tuscia, Via del Suffragio no.1, 01100 Viterbo, Italy*

Correspondence should be addressed to Sonia Castellucci, sonia.castellucci@libero.it

Received 29 January 2010; Revised 30 June 2010; Accepted 19 August 2010

Academic Editor: Carlo Cattani

Greenhouses crops in Italy are made by using prefabricated structures, leaving out the preliminary study of optical and thermal exchanges between the external environment and the greenhouse, dealing with heating and cooling and the effects of air conditioning needed for plant growth. This involves rather significant costs that directs the interest of designers, builders, and farmers in order to seek constructive solutions to optimize the system of such emissions. This work was done by building a model of gases using TRNSYS software, and these gases then have been checked for compliance. The model was constructed considering an example of a prefabricated greenhouse, located in central of Italy. Aspects of the structural components, and thermal and optical properties are analyzed in order to achieve a representation of reality.

1. Introduction

The aim of this study is to test the response of the software TRNSYS simulation of climate parameters in a greenhouse. To create a template for:

(i) detailed design of structures,

(ii) optimizing resources,

(iii) verifying the use of new energy systems for agricultural activities [1–3].

To simulate the greenhouse, several studies have been proposed in order to obtain forecasts values or simulations of influential variables for protected crops, such as ventilation [4, 5], water temperature for hydroponic systems [6], control of CO_2 for the carbon fertilization [7, 8], moisture budget [9], climate control [10], and heat exchange [11]. Recently,

the thermal behavior of the greenhouses was studied using dynamic thermal simulation tool, TRNSYS 15.1. [12, 13].

Suppose that one has created a model that includes all greenhouse influential variables on microclimate. Values are obtained for climatic parameters representative of reality by allowing the search for optimal solutions for the use of resources [14].

Creating a greenhouse model in the software, one can simulate constructive solutions or air conditioning. One can also create new components to include models that simulate as closely as possible the biological activities of plants.

2. Preliminary Remarks

2.1. Exchange of Heat

The climatic parameters affecting the growth of greenhouse plants are [15]:

(i) radiation entering the greenhouse in the ultraviolet band (290 to 380 nm), visible (380 to 760 nm) and near infrared (760–3000 nm),

(ii) temperature of air, soil and plants,

(iii) air humidity,

(iv) air composition (particularly the concentration of CO_2).

Solar radiation inside the greenhouse is less than the outer coating material which reflects and absorbs solar radiation; one also needs a ventilation system that ensures the movement of air between the plants and facilitates the transpiration; the lower is the air movement, and the smaller is the concentration gradient of CO_2.

One needs to assess the detailed exchange of energy between internal and external and to have accurate values of climatic parameters in the greenhouse. It is necessary to study the temperatures that influence the thermal freight exchange [16]:

(i) air temperature,

(ii) soil temperature (or substrate for soilless),

(iii) plants temperature,

(iv) temperature of the greenhouse cover.

The flow of heat in the greenhouse is a function of time and is calculated using (2.1) which represents the heat balance [17]

$$\frac{\partial Q(t)}{\partial t} = q_{\text{ent}}(t) - q_{\text{usc}}(t) + W_{\text{int}}, \tag{2.1}$$

where Q: flow thermal, t: time, q_{ent}: heat flows in, q_{usc}: heat flows out, and W_{int}: thermal power in the greenhouse.

C_p: heat capacity of the greenhouse, the heat balance of systems (2.1)

$$C_p \frac{\partial T}{\partial t} = q_{\text{ent}}(t) - q_{\text{usc}}(t) + W_{\text{int}}. \tag{2.2}$$

2.2. Thermal Balance

To calculate the heat balance in emissions is necessary to examine the individual energy input [18]:

(1) solar radiation transmittance and reflectance of the cover to the incident radiation,

(2) heat transfer, conduction, convention, and radiation,

(3) condensation heat,

(4) heat of evapotranspiration,

(5) loss of heat of ventilation.

2.2.1. Solar Radiation

The amount of heat which determines the solar radiation [19] depends on:

(i) radiation incident to the ground,

(ii) orientation of the greenhouse,

(iii) type of structure,

(iv) absorption and reflection of the coating material,

(v) share, size, and position of the opaque structure,

(vi) dust on the cover,

(vii) cover condensation.

The incident radiation to the ground, with clear skies, [20] can be calculated with the following relations:

R_b = direct radiation to the ground = $R_e \tau_b \cos\theta_z$ [W/m^2],

R_d = diffuse radiation to the ground = $R_e \tau_d \cos\theta_z$ [W/m^2],

R_g = global radiation to the ground = $R_b + R_d$ [W/m^2],

where R_e = outer radiation [W/m^2], $\cos\theta_z$ = cosine zenith angle = $\operatorname{sen}\phi \operatorname{sen}\delta + \cos\phi \cos\delta \cos\omega$, ϕ = local latitude [°].

Inclination of the sun = $\delta = 23.45 \cdot \operatorname{sen} \cdot [360/365 \cdot (284+n)]$ [°], hour angle $\omega = (360/24) \cdot (12 - h)$ [°], τ_b = transmissivity of the atmosphere [21] to the direct radiation = $A_o + A_1 \times e^{-k/\cos\theta_z}$, τ_d = transmissivity of the atmosphere [21] to the diffuse radiation = $0.271 - 0.294\tau_b$, $A_0 = [0.4237 - 0.00821(6 - A)^2][1 + 0.03\operatorname{sen}(\pi \text{ Error!})]$, $A_1 = [0.5055 + 0.00595(6.5 - A)^2][1 + 0.01\operatorname{sen}(\pi \text{ Error!})]$, $K = [0.2711 + 0.01858(2.5 - A)^2][1.01 - 0.01\operatorname{sen}(\pi \text{ Error!})]$, n = julian day, h = hour days [h], and A = altitude [km].

If the surface is inclined, there will be two angle: Z = inclination of the surface normal with respect to zenith and ψ = angle between the horizontal projection of the surface normal and the south.

The angle between the direction of the sun and the surface normal is

$$\begin{aligned}\cos I = {} & \operatorname{sen}\lambda \operatorname{sen}\delta \cos Z - \cos\lambda \operatorname{sen}\delta \operatorname{sen} Z \cos\psi + \cos\lambda \cos\delta \cos\omega \cos Z \\ & + \operatorname{sen}\lambda \cos\delta \cos\omega \operatorname{sen} Z \cos\psi + \cos\delta \operatorname{sen}\omega \operatorname{sen} Z \operatorname{sen}\psi.\end{aligned} \tag{2.3}$$

The components of radiation are [22]

$R_b I$ = direct radiation on inclined surface = $R_e \tau_b \cos I$,

$R_d I$ = diffuse radiation on inclined surface = $R_e \tau_d \cos I$.

Radiation throughout the cover is

$R_b I$ = direct radiation = $R_e \tau_b$ transmittance (I),

$R_d I$ = diffuse radiation = $R_e \tau_d$ transmittance (I).

To calculate the solar transmittance, I must have the total reflectance of the surface [23]. The reflectance is calculated from the angle of radiation and the angle of refraction of the surface

$$\frac{n_1}{n_2} = \frac{\operatorname{sen}\theta_r}{\operatorname{sen}\theta_i}, \tag{2.4}$$

where s = thick coverture, n = refracting index, k = coefficient absorption, and (ad es.glass: $n = 1.526$ and $K = 0.032\,\mathrm{mm}^{-1}$)

The refractive index of air is approximately 1 [24]; there is $n_2 = n$ (refractive index of the second half): θ_r = refraction angle = $\operatorname{arcsen}(\operatorname{sen}\theta_i/n)$, θ_i: incidence angle of solar radiation as a function of latitude and exposure greenhouse [25].

Surface reflectance = $r_\perp = \operatorname{sen}^2(\theta_r - \theta_i)/\operatorname{sen}^2(\theta_r + \theta_i)$.

Surface reflectance = $r_\parallel = \tan^2(\theta_r - \theta_i)/\tan^2(\theta_r + \theta_i)$.

Total surface reflectance = $r = I_r/I_i = (1/2)(r_\perp + r_\parallel)$.

The transmittance value of the perpendicular component whereas the only loss by reflection

$$\tau_\perp = (1 - r_\perp)^2 \sum_{n=0}^{\infty} r_\perp^{2n} = \frac{(1 - r_\perp)^2}{(1 - r_\perp^2)} = \frac{1 - r_\perp}{1 + r_\perp}. \tag{2.5}$$

Transmittance to the parallel component whereas the only losses for reflection

$$\tau_\parallel = \frac{1 - r_\parallel}{1 + r_\parallel}. \tag{2.6}$$

Transmittance with the only losses for global reflection

$$\tau_r = \frac{1}{2}\left[\frac{1 - r_\perp}{1 + r_\perp} + \frac{1 - r_\parallel}{1 + r_\parallel}\right], \tag{2.7}$$

whereas the overall transmittance only losses for absorption

$$\tau_a = e^{(-K\cdot s)/\cos\theta_r}. \tag{2.8}$$

The transmittance, reflectance, and absorbance of a greenhouse, with the losses by reflection and absorption are determined

$$\begin{gathered}
\tau_{\parallel} = \frac{\tau_a(1-r_{\parallel})^2}{1-(r_{\parallel}\tau_a)^2} = \tau_a \cdot \frac{1-r_{\parallel}}{1+r_{\parallel}} \cdot \frac{1-r_{\parallel}^2}{1-(r_{\parallel}\tau_a)^2} \cong \tau_a \cdot \frac{1-r_{\parallel}}{1+r_{\parallel}}, \\
\tau_{\perp} \cong \tau_a \cdot \frac{1-r_{\perp}}{1+r_{\perp}}, \\
\tau = \frac{1}{2}(\tau_{\parallel}+\tau_{\perp}) \cong \frac{1}{2}\left(\tau_a \cdot \frac{1-r_{\parallel}}{1+r_{\parallel}} + \tau_a \cdot \frac{1-r_{\perp}}{1+r_{\perp}}\right), \\
\tau \cong \tau_a \cdot \frac{1}{2}\left(\frac{1-r_{\parallel}}{1+r_{\parallel}} + \frac{1-r_{\perp}}{1+r_{\perp}}\right) \cong \tau_a \cdot \tau_r.
\end{gathered} \tag{2.9}$$

The global transmittance is

$$\tau \cong \tau_a \cdot \tau_r. \tag{2.10}$$

The reflectance greenhouse is [26]

$$\rho_{\parallel} = r_{\parallel} + \frac{(1-r_{\parallel})^2\tau_a^2 r_{\parallel}}{1-(r_{\parallel}\tau_a)^2} = r_{\parallel}(1+\tau_a\tau_{\parallel}). \tag{2.11}$$

The absorbency is

$$\begin{gathered}
\alpha_{\parallel} = (1-\tau_a)\left(\frac{1-r_{\parallel}}{1-r_{\parallel}\tau_a}\right), \\
\alpha_{\perp} = (1-\tau_a)\left(\frac{1-r_{\perp}}{1-r_{\perp}\tau_a}\right), \\
\alpha = \frac{1}{2}(\alpha_{\parallel}+\alpha_{\perp}).
\end{gathered} \tag{2.12}$$

The transmittance of the diffuse radiation is assumed to be equal to the transmittance of direct radiation with $II = 60^{\circ}$ m.

With the overcast sky [27], one can estimate the average daily radiation (J/m^{2}d) that reaches the earth's surface in a certain place (see Table 1).

Definition:

N_o: the length of day

$$N_o = \frac{2}{15} \cdot \operatorname{arcos}(-tg\phi \cdot tg\delta), \tag{2.13}$$

Table 1: The coefficient depends on a number of factor [30].

	α_i (W/m^{2}K)	In dependency of:
Inside the greenhouse	4–30	Wind Speed ($V_{\text{vento}} < 10\,\text{m/s}$ 3.85 V_{vento})
Outside the greenhouse	2–5	Heating System Temperature coverage
External heating pipes (air)	4.5–9	Pipe diameter Pipe temperature
Internal heating pipes (water)	400–4830	Water speed Pipe diameter

N: hours when the sun is actually visible on the horizon. The ratio N/N_o is called for sunshine or daylight on. The daily global radiation is related all'eliofania on the report of Angstrom

$$\frac{R_g}{R_o} = A + B\frac{N}{N_o},$$

$$R_o = \frac{1367 \cdot 3600 \cdot 24}{\pi} \cdot \left(1 + 0.033 \cdot \cos\frac{360 \cdot n}{365}\right) \cdot \left(\cos\phi \cdot \cos\delta \cdot \operatorname{sen}\omega_s + \frac{\pi \cdot \omega_s}{180} \cdot \operatorname{sen}\phi \cdot \operatorname{sen}\delta\right), \tag{2.14}$$

where ω_s is the hour angle at sunset

$$\cos\omega_s = -\tan\phi \cdot \tan\delta, \tag{2.15}$$

A and B coefficient of the place (see [28]).

The components of direct and diffuse radiation on an inclined surface can be calculated [29] as a function of I and Q multiplied by the transparency measured at normal incident radiation (Table 1). The components of radiation are:

R_bI = direct radiation on the inclined surface = $R_e\tau_b \cos I$,

R_dI = diffuse radiation on the inclined surface = $R_e\tau_d \cos I$.

2.2.2. Thermal Exchange

A contribution to the heat of the greenhouse is the thermal exchange between inside and outside [31].

Heat Conduction

$$Q = \frac{\lambda}{s} \cdot S \cdot (T_1 - T_2), \tag{2.16}$$

where Q = heat [W], s = thick [m], S = surface [m^2], T_1 = inside temperatures of the surface wall, and T_2 = outer temperature surface of the wall.

If the surface S is composed with more elements, the flow through each element is constant

$$\begin{gathered}
Q = \frac{\lambda_1}{s_1} \cdot S \cdot (T_i - T_2) \Longrightarrow Q \cdot \frac{s_1}{\lambda_1} = S \cdot (T_i - T_1), \\
Q = \frac{\lambda_2}{s_2} \cdot S \cdot (T_1 - T_2) \Longrightarrow Q \cdot \frac{s_2}{\lambda_2} = S \cdot (T_1 - T_2), \\
\vdots \\
Q = \frac{\lambda_n}{s_n} \cdot S \cdot (T_{n-1} - T_e) \Longrightarrow Q \cdot \frac{s_n}{\lambda_n} = S \cdot (T_{n-1} - T_e),
\end{gathered} \tag{2.17}$$

adding

$$\begin{gathered}
Q \cdot \left(\frac{s_1}{\lambda_1} + \frac{s_2}{\lambda_2} + \cdots + \frac{s_n}{\lambda_n} \right) = S \cdot (T_i - T_e), \\
Q = \frac{1}{(s_1/\lambda_1 + s_2/\lambda_2 + \cdots + s_n/\lambda_n)} \cdot S \cdot (T_i - T_e),
\end{gathered} \tag{2.18}$$

to $K_t = 1/(s_1/\lambda_1 + s_2/\lambda_2 + \cdots + s_n/\lambda_n)$ $[\mathrm{W/m^2\,K}]$ thermal conductance

$$Q = K_t \cdot S \cdot (T_i - T_e). \tag{2.19}$$

Heat Convection

$$Q = \alpha_i \cdot S \cdot \left(T_{\text{fluido}} - T_{\text{parete}}\right), \tag{2.20}$$

where Q: heat convection, α_i: coefficient convective exchange, S: surface, and T: temperature.

Irradiation

Wien's law for the maximum emission is at a wavelength $\lambda_{\max} = 2885000/T$ (nm).
Temperature

$$\begin{gathered}
T_{vc} = 0.0552 \cdot T_a^{3/2}, \\
T_{vc} = 0.0552 \cdot (T_a + 273.16)^{3/2} - 273.16.
\end{gathered} \tag{2.21}$$

The total radiative flow radiated between two gray surfaces facing for the low Stefan-Boltzman

$$\phi_{\text{rad},12} = \varepsilon_{12} \cdot \Im_{12} \cdot \sigma \cdot \left(T_1^4 - T_2^4\right) \quad \left(\mathrm{W/m^2}\right), \tag{2.22}$$

where $\sigma = 5.6699 \times 10^{-8}$ (W/m^2 K^4), ε_{12} = emissivity between the surface areas 1 and 2; assuming opaque bodies facing a series of reflections between two surfaces leads to

$$\varepsilon_{12} = \frac{1}{1/\varepsilon_1 + 1/\varepsilon_2 - 1}. \tag{2.23}$$

If you think you do not have reflection: $\varepsilon_{12} = \varepsilon_1 \cdot \varepsilon_2 \cdot \Im_{12}$, the view factor is the fraction of the total radiation emitted by a surface that affects surface 2 in many cases, the greenhouse is next to 1.

For a surface issues, one will have

$$\varepsilon + \tau + \zeta = 1, \tag{2.24}$$

where ε = emissivity in the infrared, τ = transmissivity in the infrared, and ρ = reflectivity in the infrared.

Obviously, for opaque bodies, $\tau = 0$, and therefore, $\varepsilon + \zeta = 1$.

Considering a flat wall, thickness s (m), of the surface S (m^2), which defines the interior of a generic building, indoor and outdoor air temperatures are required T_i and T_e different but constant over time (steady) (see Figure 1).

The flow of heat Q_t (W) takes the following path [32]:

(1) adduction

$$Q_t = \alpha_i S(T_i - T_1), \tag{2.25}$$

where α_i = factor adduction internal [W m^{-2} K^{-1}],

(2) conductivity

$$Q_t = \lambda \frac{S}{s}(T_1 - T_2), \tag{2.26}$$

where: λ = Thermal conductivity of wall (W/m K), S = surface wall (m^2), and s = thick (m),

(3) adduction

$$Q_t = \alpha_e S(T_2 - T_e), \tag{2.27}$$

where α_e = factor adduction external (W/m^2 K).

Steady thermal power transmitted in the three steps must be constant; the thermal flows Q_t of the three terms must be equal, and therefore, solving the above equations according to differences in temperature, one has

$$\begin{gathered}(T_i - T_1) = Q_t \frac{1}{\alpha_i S}, \\ (T_1 - T_2) = Q_t \frac{s}{\lambda S}, \\ (T_2 - T_e) = Q_t \frac{1}{\alpha_e S}, \\ \hline (T_i - T_e) = \frac{Q_t}{S}\left(\frac{1}{\alpha_i} + \frac{s}{\lambda} + \frac{1}{\alpha_e}\right),\end{gathered} \tag{2.28}$$

where R = thermal resistance ($\mathrm{m^2\,K/W}$),

$$\begin{gathered}R = \left(\frac{1}{\alpha_i} + \frac{s}{\lambda} + \frac{1}{\alpha_e}\right), \\ (T_i - T_e) = \frac{Q_t}{S} R, \\ Q_t = \frac{S}{R}(T_i - T_e),\end{gathered} \tag{2.29}$$

where $K = 1/R$ global factor transmission ($\mathrm{W/m^2\,K}$),

$$K = \frac{1}{(1/\alpha_i + s/\lambda + 1/\alpha_e)}. \tag{2.30}$$

The flow heat through a flat, steady wall

$$\begin{gathered}Q_t = KS(T_i - T_e), \\ Q_t = KS\Delta_T.\end{gathered} \tag{2.31}$$

The total energy lost ($\mathrm{kJ\,h^{-1}}$) in transmission result in an hour

$$\begin{gathered}E_{\mathrm{tr}} = 3,6 \cdot \sum_{1}^{n} {}_i Q_{t_i}, \\ E_{\mathrm{tr}} = 3,6 \cdot \sum_{1}^{n} {}_i S_i\, k_i (T_i - T_e).\end{gathered} \tag{2.32}$$

2.2.3. Heat of Condensation

To calculate the heat of condensation [33]

$$Q = g \cdot \lambda \cdot A \quad [\mathrm{W}], \tag{2.33}$$

where g = grams of water condensed [$\mathrm{g\,s^{-1}\,m^{-2}}$], λ = latent heat of vaporization [$\mathrm{J\,g^{-1}}$], and A = surface cover [$\mathrm{m^2}$].
The report on the convective exchanges between the air inside and the inside surface of the cover

$$Q = Q' + Q'' = \alpha_{\mathrm{int}} \cdot A \cdot \left(T_{\mathrm{aria\ int}} - T_{\mathrm{parete\ int}}\right) + g \cdot \lambda \cdot A. \tag{2.34}$$

Rearranging the terms

$$\begin{gathered} Q \cdot \frac{1}{\alpha_{\mathrm{int}}} - \frac{g \cdot \lambda \cdot A}{\alpha_{\mathrm{int}}} = A \cdot \left(T_{\mathrm{aria\ int}} - T_{\mathrm{parete\ int}}\right), \\ Q \cdot \frac{1}{K_t} = A \cdot \left(T_{\mathrm{parete\ int}} - T_{\mathrm{parete\,est}}\right), \\ Q \cdot \frac{1}{\alpha_{\mathrm{est}}} = A \cdot \left(T_{\mathrm{parete\,est}} - T_{\mathrm{aria\,est}}\right), \\ \hline Q \cdot \left(\frac{1}{\alpha_{\mathrm{int}}} + \frac{1}{K_t} + \frac{1}{\alpha_{\mathrm{est}}}\right) - \frac{g \cdot \lambda \cdot A}{\alpha_{\mathrm{int}}} = A \cdot \left(T_{\mathrm{aria\ int}} - T_{\mathrm{aria\,est}}\right), \end{gathered} \tag{2.35}$$

with: $K = 1/(1/\alpha_{\mathrm{int}} + 1/K_t + 1/\alpha_{\mathrm{est}})$, we have

$$Q = K \cdot A \cdot \left(T_{\mathrm{aria\ int}} - T_{\mathrm{aria\,est}}\right) + \frac{K}{\alpha_{\mathrm{int}}} \cdot g \cdot \lambda \cdot A. \tag{2.36}$$

2.2.4. Heat Ventilation

The functions of ventilation in a greenhouse are:

(i) replacement of oxygen and CO_2,

(ii) temperature regulation,

(iii) humidity control in greenhouses.

The requirements to be met are as follows [34]:

(i) there must be direct air currents on plants, although there must be good air near the plants,

(ii) incoming air flow should not move immediately on plants,

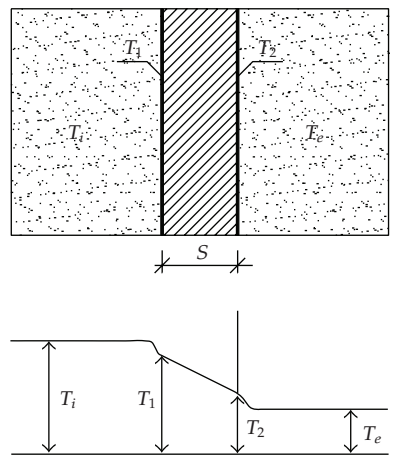

Figure 1

(iii) ventilation equipment should be modular and should be able to seal to hold heat loss,

(iv) fans must be water-resistant,

(v) the construction of the fans should allow operation in all weather conditions,

(vi) the size of the fans must be sufficiently large.

The heat dispersed by ventilation is

$$E_v = V(H_i - H_e). \tag{2.37}$$

3. The Basic Model of Simulation Greenhouse

The simulation of climate parameters of the greenhouse is made with a model that calculates the thermal exchanges in nonstationary [35]. Depending on the parameter, one can highlight energy waste and improve the design of the greenhouse. The created model can be applied in any type of greenhouse changing design parameters in the TYPE 56.

3.1. Model Creation

The greenhouse considered is a prefabricated construction in steel used as a greenhouse for growing flowers and plants. It is covered with glass cover, horizontal beam pattern, and small flat foot north and south.

The approach of the model was carried out by using the program TRNSYS Simulation Studio. It was done starting with the path leading to the construction of a multizone building, which is divided into multiple steps, where the user enters the data on building and its location in space [36]. The data required by the software at this stage will be used for the automatic construction of the project and its connections between the components will be divided into nine steps in which one inserts the following:

(i) the indication of the areas, the number, and the arrangement with each other identify the adjacent walls and their arrangement with respect to north,

(ii) the name of each area and plant size, height of walls and eaves, and length and width of each zone. Software automatically calculates the volume of each zone,

(iii) the percentage of windows on each exterior wall of the building. This indicates the ratio of surface area between the windows and the wall multiplied by one hundred, in addition to adding the rotation angle of the building than the north and the source of meteorological data that will be used in the simulation. This is indeed a link with the Type 109 (Weather Data Processor), and in this case study, the meteorological station of Ancona-Falconara (Airport) was selected.

The meteorological station of Ancona is the weather station of reference for the Air Force Meteorological Service and the World Meteorological Organization concerning the city of Ancona and its coastline. The distance as the crow flies from this weather station and location of the emissions test is about 25 km. With the various components of TRNSYS have been created on the basis of meteorological data coordinates of the site and its features, the availability of measured values within a small radius improves performance [37].

The seepage goes through building walls, values, and modes of natural and mechanical ventilation for the building. These reported values in terms of number of air changes per hour (1/h). The inclusion of these data can still be changed later in the settings of each area. Natural ventilation was set by a temperature sensor that, for given temperature, regulates the process of opening the window (opens and closes at 25°C to 15°C).

The values of heating or cooling include the following. One must put the specific thermal power (W/m^2) component and radiant temperature values for which the process begins and ends. In this case, there has been nothing since the emissions in question does not have such means. These values apply to the whole building and can be changed later in the description of each area [38].

Other values of thermal power for people, accessories, and lighting include the following. The lighting can be managed according to the brightness outside. Even in this case, it was not included at all, because it was not present in the greenhouse test. These values apply to the whole building and can be changed later in the description of each area.

The values of external shading projections for each exterior wall oriented include the following. These projections are divided between the top or side windows. The greenhouse has no such means of external shading.

The values of shading means for shading furniture inside or outside each exterior wall oriented include the following. Their operation is controlled according to the brightness outside. They can also be inserted values for maximum shading external and internal components.

In the window on the last step, we must not put anything but only to confirm data. At this point, the software creates a description of the building in a data file (*.blinds), opens TRNBuild and translates the data file formats needed for the simulation (.bld and .Trn), and finally create a simulation project automatically saving a file (.TMF) and opens in the Simulation Studio. At this point, it is already possible to test the project by running a simulation.

This procedure simplifies the model construction, since the opening of the Simulation Study of climatic data processor [39] (Type 109) is already connected to the components of solar radiation, air temperature, psychrometric data processor, and these in turn are related to the greenhouse. It is also established a conversion system orientation of the greenhouse

(Turn) which is connected to the processor of climatic data for the management of the greenhouse, and they are designed to control artificial lighting and natural ventilation related to each pavilion. There are no regulators of heating and cooling because they were not expected during project creation.

After creating the preliminary draft, changed data is placed within the individual components of the Simulation Study that those inside the TRNBuild were opening directly from the icon building. This work is necessary because the description of the walls and windows of the building is set automatically to a dwelling and not for a greenhouse; in addition, there will be no roof, let alone the calculations of the radiation incident on the roof itself.

To change the initial project, it was started by a description of the greenhouse through the opening of TRNBuild. Through dialog boxes, it was done by adding the orientation of the water and the software automatically included the presence of cover. So, we changed the descriptions of each area. We changed the volume of each zone to also consider the space under the foot and have changed the properties of building walls to fit with those of the greenhouse test [40].

It should be noted that despite the walls and ground that the greenhouse comprises, besides the metal structure, through the windows, they were not included in the description of the external walls but in the windows. This is because the lighting calculations are performed inside the greenhouse through the indices of transmission of solar radiation of their windows, while the walls are not done as thoroughly described in the paragraphs relating to optical properties and thermal windows. Setting windows as external walls would, therefore, lead light inside the greenhouse.

That said, in describing the external walls and ground are included the values of the metal structure. To this end, we created a new type of material (galvanized steel), and its geometric and thermodynamic data are reported by the manufacturer.

Even the windows have created a new type that reflects that of a single-glass greenhouse. The type and properties of glass were in the library of the program, but it was necessary to correct the size and relationship frame/window (the area of the casing split window area) [41].

Regarding the "wall" soil, values of the different layers were included that make up the ground as instructed by the owners of the greenhouse working to run the nursery.

The "wall" soil can also be treated as wall bound (boundary) or linked to soil temperature simulator creating an input to the Type 56.

For each wall must be shown the value of GEOSURF, which may be a fixed value (automatically set as the preliminary description) or an input or a tab. Given the extreme importance that the radiation in this study, it was decided to link data on areas of direct radiation generated by the Type 109 as input to each wall (Figure 2) where weather date: weather generator, Psychrometrics: processor psychrometric, Sky Temp: CPU temperature sky, Radiation: radiation converter, Greenhouse: Greenhouse (Type 56), Nat. Vent. 1 and 2: controllers of ventilation, Turn: unit converters, and Charts: Online Plotter.

For each wall must be shown the value of GEOSURF, which may be a fixed value (automatically set as the preliminary description) or an input or a tab. Given the extreme importance of the radiation in this study, it was decided to link data on areas of direct radiation generated by the Type 109 as input to each wall.

For a correct simulation of humidity inside the greenhouse, one must consider the input of water due to transpiration of plants. Since the calculation of the transpiration of plants is extremely complex, models should be entrusted to a specific type to run which is

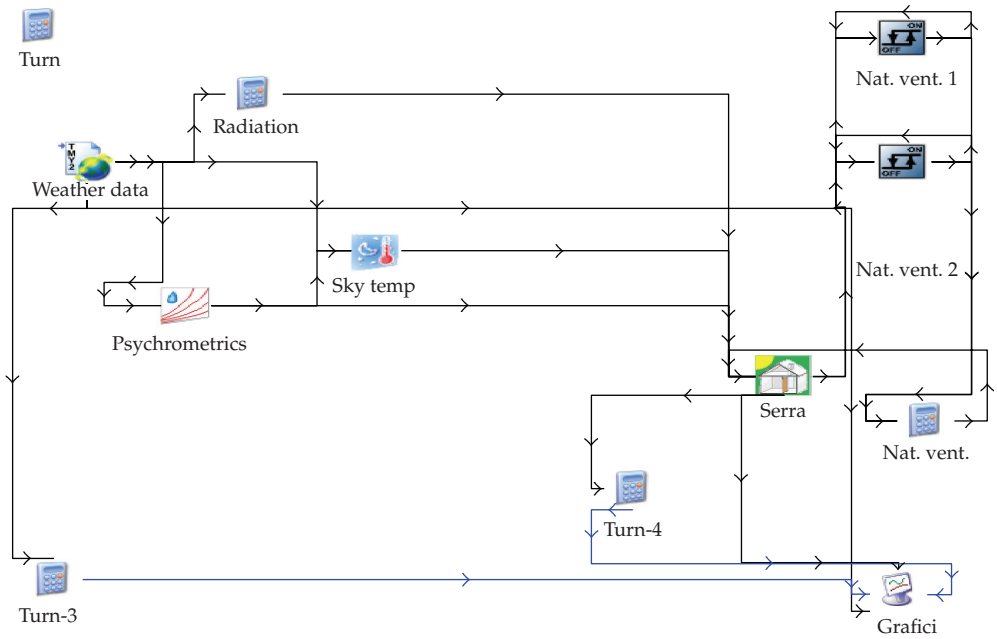

Figure 2: Graphic display of the project.

not one of those available in the program. To simplify the introduction of these constants of transpired water found in the bibliography, the constancy of these values depends on the type of nursery practice and short cycle of the plants.

After finishing the detailed description of the greenhouse, we saved the changes and updated the list of variables (inputs) of the Type 56. This helps to find new items to be served, on the data of solar radiation incident on the slopes of the greenhouse [42].

These data were to be created, however, the Type 109 by inserting two new surfaces on which to assess the components of the radiation, further defining their azimuth and inclination (which is that of water). So, by this component, outputs are automatically generated to ground, which must be connected to the component "Radiation" and then to the greenhouse. Even through the component "Radiation" was necessary to arrange the transfer of this information by creating input and output.

3.2. General Mathematical Description of the Thermal Model

The general case, which does not include the simplified model of the heating and cooling equipment, is presented first. If separate equipment components are used, they can be coupled to the zones as either internal convective gains or ventilation gains [43]. Following this, the simplified method of providing heating and cooling equipment within the TYPE 56 component is described.

Another section will cover the use of a simulation timestep that is not equal to the time base on which the wall transfer function relationships are based. Finally, descriptions of the optical and thermal window model, the way in which solar and internal radiation are distributed within each zone; the moisture balance calculations and the integrated model for thermo-active walls are given (see Figure 3).

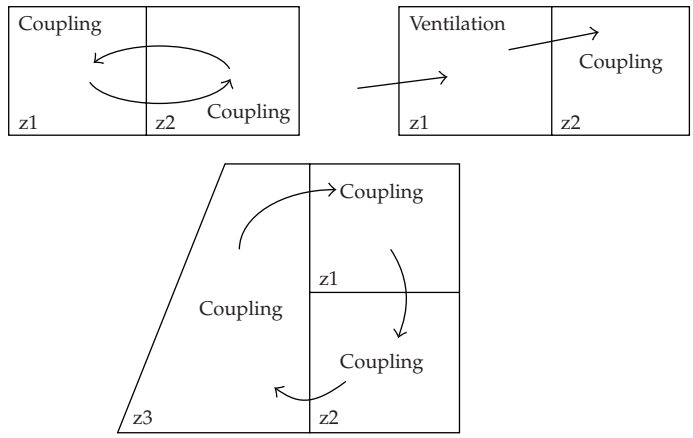

Figure 3: Interzonal air change, cross ventilation, and ventilation circle.

3.2.1. Thermal Zone

The building model in TYPE 56 is a nongeometrical balance model with one air node per zone, representing the thermal capacity of the zone air volume and capacities which are closely connected with the air node (furniture, e.g.) [44]. Thus, the node capacity is a separate input in addition to the zone volume.

Convective Heat Flux to the Air Node

$$Q_i = Q_{\text{surf},i} + Q_{\text{inf},i} + Q_{\text{vent}} + Q_{g,c,i} + Q_{\text{cp lg},i}, \tag{3.1}$$

where $Q_{\text{surf},i}$ = convective heat flow from all inside surfaces, $Q_{\text{surf},i} = U_{w,i} * A_{w,i}(T_{\text{wall},i} - T_{\text{air}})$, $Q_{\text{inf},i}$ = infiltration gains (air flow from outside only), $Q_{\text{inf},i} = V * \rho * c_p(T_{\text{esterna}} - T_{\text{air}})$, Q_{vent} = ventilation gains (air flow from a user defined, source like an HVAC system), $Q_{\text{vent}} = V * \rho * c_p(T_{\text{ventilation},i} - T_{\text{air}})$, $Q_{g,c,i}$ = internal convective gains (by people, equipment, illumination, radiators, etc.), $Q_{g,c,i}$ = [kJ/h], $Q_{\text{cp lg},i}$ = gains due to (connective) air flow from zone i or boundary condition, and $Q_{\text{cp lg},i} = V * \rho * c_p(T_{\text{zone},i} - T_{\text{air}})$.

Coupling

The coupling statement allows the definition an air mass flow a zone receives from another zone, considered as a heat flow from or to the air node. The statement does not automatically define the air flow back to the adjacent zone as would occur in an interzonal air exchange [11]. To consider this return flow, the corresponding coupling must be defined in the adjacent zone to receive the same air flow in return. The reason for this convention is to allow the user to describe cross ventilation or a ventilation circle within 3 or more zones (thermosyphon through a 2-story winter-garden, e.g.).

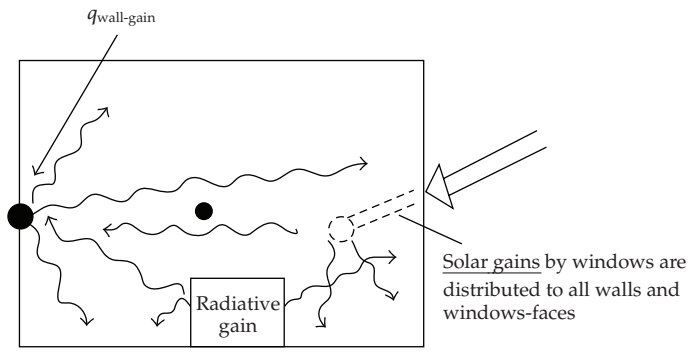

Figure 4: Radiative energy flows considering one wall with its surface temperature node.

Note: There is no air balance check in TYPE 56. The user can empty or overload a zone by couplings. We are sure that the specified air flows into a zone by coupling, ventilation, and infiltration are physically meaningful (see Figure 5).

3.2.2. Radiative Heat Flows (Only) to the Walls and Windows

$$Q_{r,wi} = Q_{r,wi} + Qg_{,r,i,wi} + Q_{\text{sol},wi} + Q_{\text{long},wi} + Q_{\text{wall-gain}}, \tag{3.2}$$

where $Q_{r,wi}$ = radiative gains for the wall surface temperature node [kJ/h], $Qg_{r,i,wi}$ = radiative zone internal gains received by wall [kJ/h], $Q_{\text{sol},wi}$ = solar gains through zone windows received by wall [kJ/h], $Q_{\text{long},wi}$ = long-wave radiation exchange between this wall and all other walls and windows ($\varepsilon_i = 1$) [kJ/h], and $Q_{\text{wall-gain}}$ = surface or window wall the to flow heat specified user [kJ/h].

In the following subsections, [9], the expressions used for the calculation of these energy quantities are given. The procedures for calculating floating temperatures and energy demands follow.

3.2.3. Integration of Walls and Windows

Figure 5 shows the heat fluxes and temperatures [10] that characterize the thermal behavior of any wall or window. The nomenclature used in Figure 4 is defined as follows: $S_{s,i}$ = radiation heat flux absorbed at the inside surface (solar and radiative gains), $S_{s,o}$ = radiation heat flux absorbed at the outside surface (solar gains), $q_{r,s,i}$ = net radiative heat transfer with all other surfaces within the zone, $q_{r,s,o}$ = net radiative heat transfer with all surfaces in view of the outside surface, $q_{w,g,i}$ = user defined heat flux to the wall or window surface, $q_{s,i}$ = conduction heat flux from the wall at the inside surface, $q_{s,o}$ = conduction heat flux into the wall at the outside surface, $q_{c,s,i}$ = convection heat flux from the inside surface to the zone air, $q_{c,s,o}$ = convection heat flux to the outside surface from the boundary/ambient, $T_{s,i}$ = inside surface temperature, $T_{s,o}$ = outside surface temperature, T_i = temperature of zone i (air node), and $T_{a,s}$ = temperature of ambient air at the outer boundary of surface.

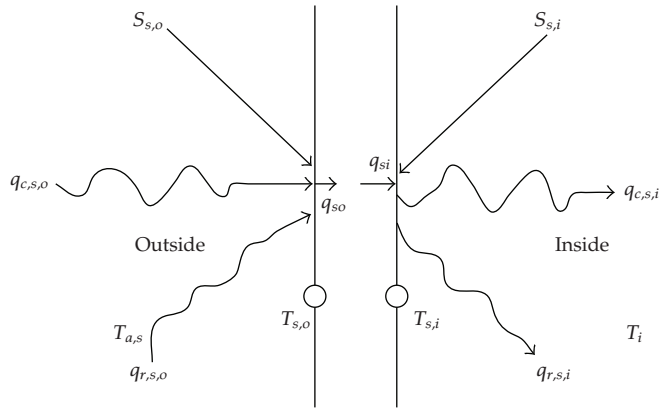

Figure 5: Surface heat fluxes and temperatures.

Table 2: Example wall for calculate the transfer function coefficient.

Material data	Thickness [m]	Conductivity [kJ/h m K]	Capacity [kJ/kg K]	Density [kg/m^3]
Concrete	0.025	7.56	1.0	2400
Mineral wool	0.08	0.144	1.0	40
Gypsum	0.02	2.52	1.0	1400

The walls are modelled according to the transfer function relationships of Mitalas and Arseneault defined from surface to surface. For any wall, the heat conduction at the surfaces are

$$\begin{aligned} \dot{q}_{s,i} &= \sum_{k=0}^{n_{b_s}} b_s^k T_{s,o}^k = \sum_{k=0}^{n_{c_s}} c_s^k T_{s,i}^k = \sum_{k=1}^{n_{d_s}} d_s^k \dot{q}_{s,i}^k, \\ \dot{q}_{s,0} &= \sum_{k=0}^{n_{a_s}} a_s^k T_{s,o}^k = \sum_{k=0}^{n_{b_s}} b_s^k T_{s,i}^k = \sum_{k=1}^{n_{d_s}} d_s^k \dot{q}_{s,o}^k. \end{aligned} \tag{3.3}$$

3.2.4. Transfer Function Method by Mitalas

The method of the transfer function or response factors can be described as the method to tell the "thermal history" of the wall [7]. The wall is considered as a black box. The number of timesteps (k) related to the time base (defined by the user) shows whether the wall is a heavy wall with a high thermal mass (k_20) or if only a few timesteps have to be considered to describe the thermal behavior of this wall. If the time base of the considered wall is higher than the time constant, the calculation of the Transfer-function matrix coefficients is stopped. Therefore, such a "thin" wall can be replaced by a resistance definition neglecting the thermal mass. As an example, Figure 6 shows the different material layers of a wall.

The wall example consists of three layers with concrete, mineral wool, and gypsum from outside to inside (see Tables 2 and 3).

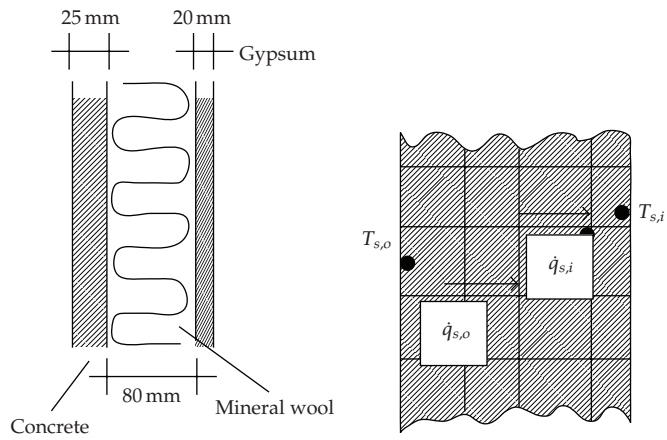

Figure 6: Real wall and black box model of the wall.

Table 3: Thermal conductance, U = 1.76429 KJ/h m^2 K; k-Wert = 0.45239 W/m^2 K.

	Transfer function coefficients			
K	A	B	C	D
0	3.0402072E + 01	8.6597596E − 01	6.2473097E + 01	1.0000000E + 00
1	−2.8791436E + 01	8.7958309E − 01	−6.1044043E + 01	−5.5725114E − 03
2	1.4382785E − 01	8.9032318E − 03	3.2541274E − 01	1.0083948E − 07
3	−1.0589132E − 06	4.0042651E − 07	−4.7183532E − 06	
SUM	1.7544627E + 00	1.7544627E + 00	1.7544627E + 00	9.9442759E − 01

Using the transfer function method, the TRNBUILD program calculates the transfer function coefficients, listed below for the example wall.

For the test wall, the coefficient table looks like that in Table 3. In addition to the transfer function coefficients, the listing contains a calculation of the heat conduction value U of the wall construction and the total heat transfer coefficient k considering a constant combined (convective + radiative) heat transfer (_i, _o) for the inside and outside surface.

3.2.5. The Long-Wave Radiation

The long-wave radiation exchange between the surfaces within the zone and the convective heat flux from the inside surfaces to the zone air are approximated using the star network given by Seem [3] and represented in Figure 7. This method uses an artificial temperature node (T_{star}) to consider the parallel energy flow from a wall surface by convection to the air node and by radiation to other wall and window elements. Comparisons to the detailed building model JOULOTTA from the University of Lund, Sweden, done by S. Holst, ZAE Munich, show a good agreement for the surface temperatures. A single node model using a combined convective and radiative heat transfer coefficient shows much higher differences (IEA Task 13 report)

$$R_{\text{STAR},i} = f(\alpha_i, A_{\text{Surf},i}) = \frac{1}{Q_{\text{surf},i}}(T_{\text{Star}} - T_i). \tag{3.4}$$

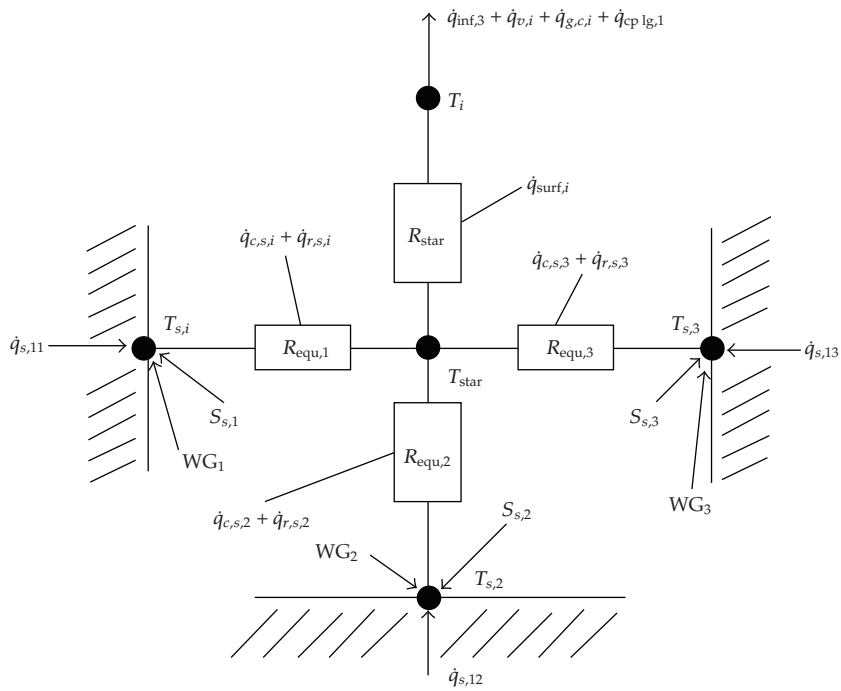

Figure 7: Star network for a zone with three surfaces.

Methods to calculate the resistances $R_{\text{equiv},i}$ and $R_{\text{star},i}$ can be found in reference. Area ratios are used in these calculations to find the absorption factors between all surfaces. The star temperature can be used to calculate a net radiative and convective heat flux from the inside wall surface

$$\dot{q}_{\text{comb},s,i} = \dot{q}_{c,s,i} + \dot{q}_{r,s,i}, \tag{3.5}$$

then,

$$\dot{q}_{\text{comb},s,i} = \frac{1}{R_{\text{equiv},i} A_{s,i}} (T_{s,i} - T_{\text{star}}), \tag{3.6}$$

where $q_{\text{comb},s,i}$ = combined convective and radiative heat flux and $A_{s,i}$ = inside surface area.

For external surfaces the long-wave radiation exchange at the outside surface is considered explicitly using a fictive sky temperature, T_{sky}, which is an input to the TYPE 56 model and a view factor to the sky, f_{sky}, for each external surface. The total heat transfer $q_{\text{comb},s,i}$ is given as the sum of convective and radiative heat transfer

$$\dot{q}_{\text{comb},s,o} = \dot{q}_{c,s,o} + \dot{q}_{r,s,o}, \tag{3.7}$$

with,

$$\begin{aligned} \dot{q}_{c,s,o} &= h_{\text{conv},s,o} \cdot (T_{a,s} - T_{s,o}), \\ \dot{q}_{r,s,o} &= \sigma \cdot \varepsilon_{s,o} \cdot \left(T_{s,o}^4 - T_{f_{\text{sky}}}^4\right), \\ T_{f_{\text{sky}}} &= \left(1 - f_{\text{sky}}\right) \cdot T_{a,s} + f_{\text{sky}} \cdot T_{\text{sky}}, \end{aligned} \tag{3.8}$$

where $q_{\text{comb},s,o}$ = combined convective and radiative heat flux to the surface, $q_{c,s,o}$ = convective heat flux to the surface, $q_{r,s,o}$ = radiative heat flux to the surface, $h_{\text{conv},s,o}$ = convective heat transfer coefficient at the outside surface, f_{sky} = fraction of the sky seen by the outside surface (for a vertical wall with no buildings nearby, a reasonable value for f_{sky} is 0.5. If there are buildings in front of the wall obstructing the view of the sky, the value for f_{sky} would be lower than 0.5. For a horizontal roof with only the sky in view, f_{sky} would be 1.0), T_{sky} = fictive sky temperature used for long-wave radiation exchange, $\varepsilon_{s,o}$ = long-wave emissivity of outside surface (ε = 0.9 for walls, value read from window library for windows), and σ = Stephan-Boltzman costant.

Energy balances at the surfaces give

$$\begin{aligned} \dot{q}_{s,i} &= \dot{q}_{\text{comb},s,i} + S_{s,i} + \text{Wall-gain}, \\ \dot{q}_{s,o} &= \dot{q}_{\text{comb},s,o} + S_{s,o}. \end{aligned} \tag{3.9}$$

For internal surfaces, $S_{s,i}$ can include both solar radiative and long-wave radiation generated form internal objects such as people or furniture.

Wall-gain is a user-defined energy flow to the inside wall or window surfaces. It can describe solar gains changing during the day due to different sun positions or might be used as a simple way to model a floor heating or a ceiling cooling system. For external surfaces, $S_{s,\text{o}}$ consists of solar radiation only.

3.2.6. Infiltration, Ventilation, and Convective Coupling

Infiltration and ventilation rates are given in terms of air changes per hour for each zone. The mass flow rate is the product of the zone air volume, air density, and air change rate. Infiltration occurs always from outdoor conditions, while ventilation occurs from a specified (possibly variable) temperature. Equal amounts of air are assumed to leave the zone at the zone [45] temperature. The energy gains to any zone i due to infiltration and ventilation are

$$\begin{aligned} \dot{Q}_{\text{inf},i} &= \dot{m}_{\text{inf},i} C_p (T_a - T_i), \\ \dot{Q}_{v,i} &= \sum_{k}^{\text{n vent}} \dot{m}_{v,k,i} C_p (T_{v,k} - T_i), \end{aligned} \tag{3.10}$$

where $m_{\text{inf},i}$ = mass flow rate of infiltration air, $m_{v,k,i}$ = mass flow rate of ventilation air of ventilation type k, C_p = specific heat of the air, $T_{v,k}$ = temperature of ventilation air of ventilation type k, and T_a = ambient air temperature.

For each wall or window separating zones of floating temperature or each wall having a known boundary condition, it is possible to specify a convective coupling. This coupling is the mass flow rate that enters the zone across the surface. An equal quantity of air is assumed to leave the zone at the zone temperature. The energy gain due to the convective coupling is the sum of all such gains for all walls or windows in the zone

$$\dot{Q}_{\mathrm{cp\,lg},i} = \sum^{\text{adj zones}} \sum^{\text{surfaces sito } j} \dot{m}_{\mathrm{cp\,lg},s} C_p \left(T_j - T_i\right) + \cdots + \sum^{\text{Known bound}} \dot{m}_{\mathrm{cp\,lg},s} C_p (T_{b,s} - T_i), \tag{3.11}$$

where $m_{\mathrm{cp\,lg},s}$ = the mass flow rate of air *entering* zone i across walls or windows.

3.2.7. Distribution of Solar Radiation

The incoming (primary) direct solar radiation is distributed according to the distribution coefficients (GEOSURF) defined in the building description. These values are distribution factors related to the total direct solar radiation entering the zone and not related to a surface area. The sum of GEOSURF values given for all inside surfaces of a zone should sum up to 1 at all times. The fraction of incoming direct solar that is absorbed by any surface i is given by the product of solar absorptance _s value times the GEOSURF value given for this surface s. If the GEOSURF values for all surfaces of a zone are set to zero, all direct solar radiation entering this zone is treated as diffuse radiation (like in TRNSYS 14.2) and distributed with the absorptance weighted area ratios described below. Note: as for the distribution of primary direct solar radiation there is no dependence on the surface area, it is possible to concentrate all direct solar to a small surface by giving it a high value of GEOSURF. This would result in very high surface temperatures and possible.

Instabilities in Solving the Energy Balance Equations of TYPE 56

After passing the second internal window, all solar radiation is treated as diffuse radiation. To pass direct solar radiation over several zones like in a atria from the top zone to the middle zone to the bottom zone a fictive window between top and bottom zone might be used. The incoming diffuse solar radiation and reflected primary direct solar radiation is distributed according to absorptance-weighted area ratios. The fraction of diffuse solar that is absorbed by any surface s is

$$f_{\mathrm{dif},s,s} = \frac{\alpha_s A_s}{\sum^{\text{surfaces}} \left(1 - \rho_{d,s}\right) A_s}, \tag{3.12}$$

where α_s = the solar absorptance of the surface (defined in the building description), and $\rho_{d,s}$ = the reflectance for diffuse solar of the surface for wall surfaces where $\tau_s = 0$, $\rho_{d,s} = (1 - \alpha_s)$. For windows, the transmission losses are considered by $\tau_s = (1 - \alpha_s - \rho_{d,s})$, and $\rho_{d,s}$ = reflectance for diffuse solar from inside.

3.2.8. Distribution of Long-Wave Radiation

All surfaces are assumed to be black for long-wave radiative exchange and radiative internal gains. These gains are distributed according to area ratios. The fraction of the internal radiative gains for any zone that is adsorbed by a surface s is

$$f_{l,s} = \frac{A_s}{\sum^{\text{surfaces}} A_s}. \tag{3.13}$$

3.2.9. Moisture Balance

In parallel with the sensible energy balance calculation, TYPE 56 calculates a moisture balance considering free floating humidity ratios or humidification/dehumidification to a certain setpoint. In this case, TYPE 56 calculates the latent load. There are two models for the calculation of the moisture balance available in TYPE 56. The first model considers sorption effects with an enlarged moisture capacity of the zone air the second, more sophisticated, model offers a surface and a deep moisture buffer in the walls of the zone.

3.2.10. Effective Capacitance Humidity Model

In the first model, the buffer effect of adsorptive and desorptive materials, soil areas, or plants is considered by an effective moisture capacitance which is defined as the product of the zone air mass and a moisture capacitance ratio [4]

$$M_{\text{eff},i} = \text{Ratio} * M_{\text{air},i}, \tag{3.14}$$

where $M_{\text{eff},i}$ = effective moisture capacitance of the zone, $M_{\text{air},i}$ = the mass of air in the zone, Ratio = multiplication factor generally in the range of 1 to 10, and A moisture balance for any zone results in the following differential equation.

$$M_{\text{eff},i}\frac{d\omega_i}{dt} = \dot{m}_{\text{inf},i}(\omega_a - \omega_i) + \sum_{k}^{\text{n vent}} m_{v,k,i}(\omega_{v,k,i} - \omega_i) + W_{g,i} + \sum^{\text{surfaces } i-j} m_{\text{cp lg},s}(\omega_j - \omega_i), \tag{3.15}$$

where: ω_i = the humidity ratio of the zone, ω_a = the ambient humidity ratio, $\omega_{v,k,i}$ = the humidity ratio of the ventilation air from ventilation type k, $W_{g,i}$ = internal moisture gains, and ω_j = the humidity ratio of an adjacent zone j.

In order to simplify the solution of the simultaneous set of differential equations, the values of ω at the end of the previous timestep are used in the above expression. Subroutine DIFFEQ is then used to independently solve for the final and average values of the humidity ratio over each timestep for each zone. If the average humidity ratio of the zone falls below or rises above a setpoint for humidification or dehumidification, then latent energy is added

or removed to maintain the humidity ratio at the setpoint. It is assumed that the change in zone humidity ratio occurs instantly so that $\omega_i = \omega_i$. In this case,

$$Q_{\mathrm{lat},i} = h_v \left[\dot{m}_{\mathrm{inf},i}\left(\omega_a - \omega_{\mathrm{req},i}\right) + \sum_{k}^{\mathrm{n\,vent}} m_{v,k,i}\left(\omega_{v,k,i} - \omega_{\mathrm{req},i}\right) + W_{g,i} + \sum^{\mathrm{surfaces}\ i-j} m_{\mathrm{cp\,lg},s}\left(\omega_{f,i,M} - \omega_{i,s,M}\right) - \frac{M_{\mathrm{eff},s}\left(\omega_{\mathrm{req},i} - \omega_{i,M}\right)}{\Delta t} \right], \tag{3.16}$$

where $Q_{\mathrm{lat},i}$ = latent energy removed (+dehumidification, −humidification), h_v = the heat of vaporization of water, and $\omega_{\mathrm{req},i}$ = the setpoint for humidification or dehumidification

Between the two setpoints, the humidity ratio is free floating.

3.3. Simulation Result

With the model designed, it is able to simulate the parameters of the greenhouse climate, check the energy required for conditioning the glass or the ideal conditions for the cultivation of a species. Thus, in the planning stages, you can optimize the construction parameters of the greenhouse according to the following:

(i) climatic growing demands identified,

(ii) the climatic parameters of the geographical [46].

With simulation one can find the best building materials for the needs of crops. In particular, the following were simulated:

(i) solar radiation inside a function of incident radiation,

(ii) internal temperature in the outside temperature,

(iii) relative humidity.

3.3.1. Simulation of Annual Solar Radiation Inside the Greenhouse (W/m^2)

The solar radiation arrives in the greenhouse and affects the inside temperature.

In particular, the characteristics constructive of the greenhouse is 97% of the radiation incident reaches the ground and increases the internal temperature (Figure 8).

In Figure 9, we have compared the solar radiation inside with the incident one [47].

Checking on the low resistance of the solar radiation structure, which results to be an advantage during the winter months, with the only problem of a high energetic consumption for the cooling system.

During the cold months, the internal radiation is almost equal to the outside, while in the summer transmission of solar radiation falls on the most important reflection of the glass. This is due to the increased presence of direct radiation and different angles of incidence.

3.3.2. Simulation of Annual Temperature

Blue is outdoor temperature; indoor temperature is red (see Figure 10). During the winter months, the temperature is almost identical to the external light and low thermal capacity of

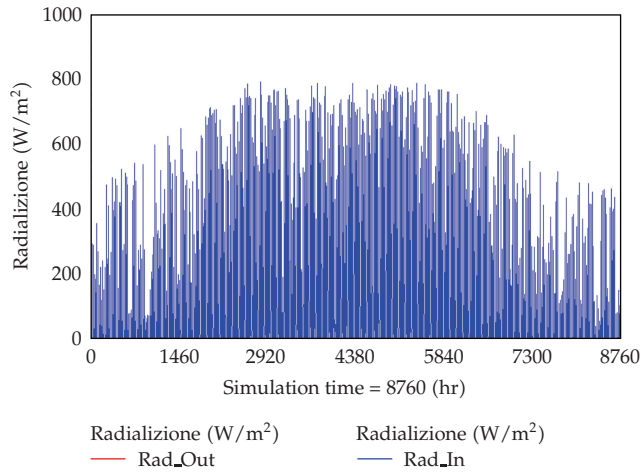

Figure 8: Simulation of annual solar radiation inside the greenhouse (W/m^2).

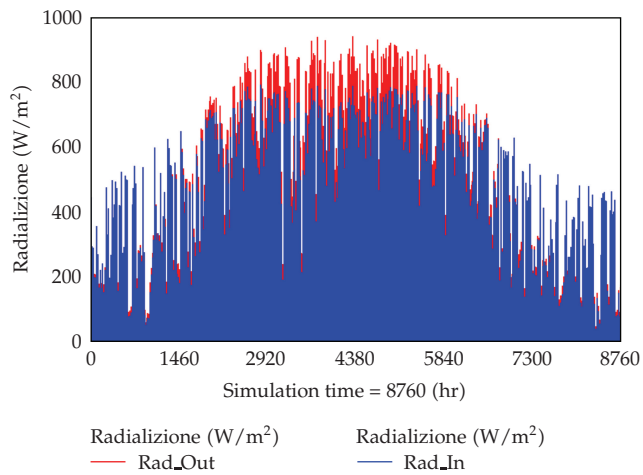

Figure 9: Simulation of annual solar radiation inside the greenhouse (W/m^2) in blue and external red.

the structure (infiltration losses of 1/h). During the warm months, open windows operated with a controller on/of (Type 2) to open windows when the temperature exceeds 30 degrees and provides an air supply of 20/h.

3.3.3. Simulation of Annual Relative Humidity (%)

In red and blue indoor humidity and external, the image is not very representative in the sense that the evapotranspiration is considered constant throughout the year and added to its average value, which is never verifiable as it varies from hour to hour and from day to night, depending the size of the leaves of plants (see Figures 11 and 12).

It is therefore more appropriate to show the graph of a typical day summer crop of tomatoes, with values of daily evapotranspiration inserted into a card.

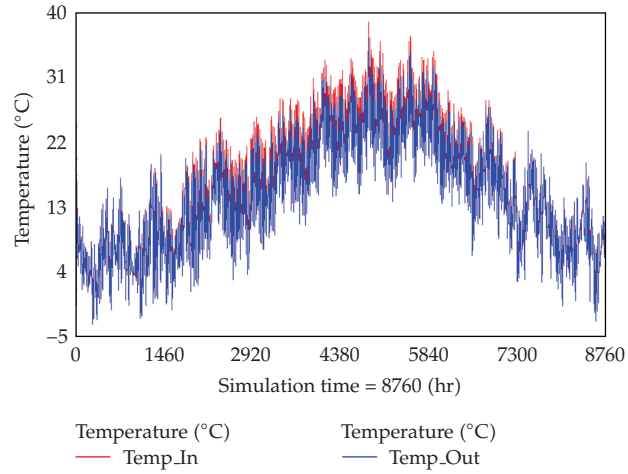

Figure 10: Simulation of annual temperature.

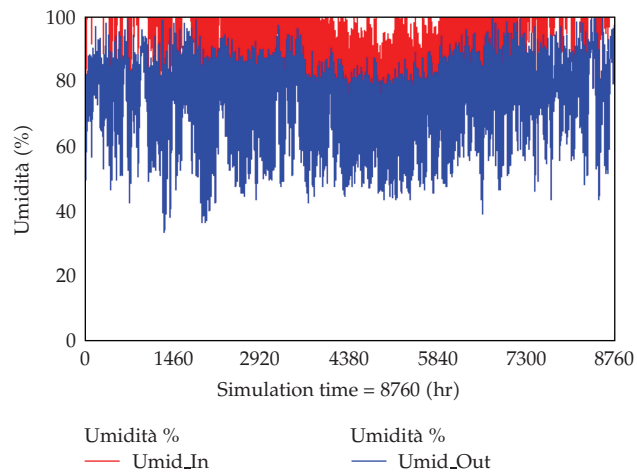

Figure 11: Simulation of annual relative humidity (%).

During the month of June, we have compared the value of internal and external humidity, with a result of superior humidity inside than outside, without considering the evapotranspiration of the plants.

This parameter is important for the plant growth and requires a constant control.

4. Conclusions

TRNSYS software has demonstrated an extreme flexibility to allow development of the project emissions. The construction of the model has been simplified by the procedures explained in a comprehensive manner in the various manuals provided with the software without showing any particular difficulties in communications between the constituent subprograms.

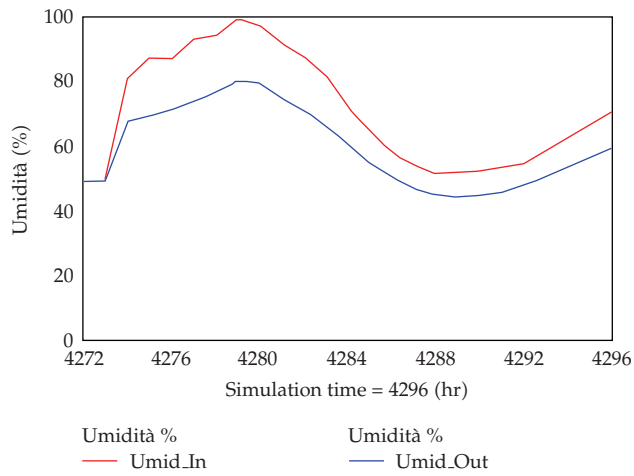

Figure 12: Simulation of relative humidity (%) inside (red) and outside (blue) emissions in the hottest day of the year (July 27).

As for the light component of the simulations, the solution found to allow the passage of long-wave radiation through the windows of the greenhouse modeled as "windows" has perhaps shown a factor critical TRNBuild, or if we do not have the model for reporting light energy to the walls of buildings, this did not affect in any way the results. Moreover, this solution has improved the simulation of moisture for the cold bridge effect. From this model, it might be interesting to continue to work on projects for energy systems applied to agriculture, being able to predict the indoor climatic conditions, and from this starting to figure out which crops are actually achievable [6].

In addition, this program offers many opportunities to improve systems made: insertion of cooling and heating, dehumidification, the total consumption of electricity and machinery for the exercise of individual farming, the heat emitted the various electrical components inside the greenhouse, and everything else necessary to simulate the best situations in the various case studies. In order to build easily new components (type) on variables purely "agricultural" as the evaporator plant transpiration of water from soil.

References

[1] M. Martin and P. Berdahl, "Characteristics of infrared sky radiation in the United States," *Solar Energy*, vol. 33, no. 3-4, pp. 321–336, 1984.

[2] F. Kasten and G. Czeplak, "Solar and terrestrial radiation dependent on the amount and type of cloud," *Solar Energy*, vol. 24, no. 2, pp. 177–189, 1980.

[3] T. Kasuda and P. R. Archenbach, "Earth temperature and thermal diffusivity at selected stations in the United States," *ASHRAE Transactions*, vol. 71, 1965.

[4] J. E. Fernández and B. J. Bailey, "Measurement and prediction of greenhouse ventilation rates," *Agricultural and Forest Meteorology*, vol. 58, no. 3-4, pp. 229–245, 1992.

[5] SOLMET, "Hourly solar radiation surface meteorological observations," Final Report, vol. 2 TD-9724, 1979.

[6] S. Zhu, J. Deltour, and S. Wang, "Modeling the thermal characteristics of greenhouse pond systems," *Aquacultural Engineering*, vol. 18, no. 3, pp. 201–217, 1998.

[7] R. Linker, I. Seginer, and P. O. Gutman, "Optimal CO2 control in a greenhouse modeled with neural networks," *Computers and Electronics in Agriculture*, vol. 19, no. 3, pp. 289–310, 1998.

[8] C. M. Randall, M. E. Whitson et al., "Hourly insolation and meteorological data bases including improved direct insolation estimates," Aerospace Report no. ATR-78(7592)-l, 1977.
[9] O. Jolliet, "HORTITRANS, a model for predicting and optimizing humidity and transpiration in greenhouses," *Journal of Agricultural Engineering Research*, vol. 57, no. 1, pp. 23–37, 1994.
[10] L. Occhipinti and G. Nunnari, "Synthesis of a greenhouse climate controller using Al-based techniques," in *Proceedings of the 8th Mediterranean Electrotechnical Conference (MELECON '96)*, vol. 1, pp. 230–233, May 1996.
[11] G. Beccali, A. Giaccone, and G. Panno, "Modello di calcolo per l'analisi del comportamento termico delle serre," *Energie Alternative HTE*, vol. 4, no. 18, pp. 405–415, 1992, luglio-agosto, pp. 283–289 vol. 4, no. 19, settembre-ottobre.
[12] K. Pavlou and A. Sfakianaki, "Improvement of the energy performance of greenhouses," in *Proceedings of the 2nd PALENC Conference*, 2007.
[13] J. A. Duffie and W. A. Beckman, *Solar Energy Thermal Processes*, John Wiley & Sons, New York, NY, USA, 1974.
[14] ASHRAE Handbook of Fundamentals, American Society of Heating, Refrigerating, and Air-Conditioning Engineers, l972.
[15] J. E. Braun and J. C. Mitchell, "Solar geometry for fixed and tracking surfaces," *Solar Energy*, vol. 31, no. 5, pp. 439–444, 1983.
[16] D. T. Reindl, W. A. Beckman, and J. A. Duffie, "Diffuse fraction correlations," *Solar Energy*, vol. 45, no. 1, pp. 1–7, 1990.
[17] D. T. Reindl, W. A. Beckman, and J. A. Duffie, "Evaluation of hourly tilted surface radiation models," *Solar Energy*, vol. 45, no. 1, pp. 9–17, 1990.
[18] J. E. Hay and J. A. Davies, "Calculation of the solar radiation incident on an inclined surface," in *Proceedings 1st Canadian Solar Radiation Workshop*, pp. 59–72, 1980.
[19] R. Perez, R. Stewart, R. Seals, and T. Guertin, "The development and verification of the perez diffuse radiation model," Sandia Report SAND88-7030, Sandia National Laboratories, Albuquerque, NM, USA, 1988.
[20] K. M. Knight, S. A. Klein, and J. A. Duffie, "A methodology for the synthesis of hourly weather data," *Solar Energy*, vol. 46, no. 2, pp. 109–120, 1991.
[21] K. M. Knight, *Development and validation of a weather data generation model*, M.S. thesis, Solar Energy Laboratory, University of Wisconsin-Madison, Madison, Wis, USA, 1988.
[22] V. A. Graham, *Stochastic synthesis of the solar atmospheric transmittance*, Ph.D. thesis, Department of Mechanical Engineering, University of Waterloo, 1985.
[23] V. A. Graham, K. G. T. Hollands, and T. E. Unny, "Stochastic variation of hourly solar radiation over the day," in *Proceedings of the International Symposium on Empirical Software Engineering (ISESE '87)*, vol. 4 of *Advances in Solar Energy Technology*, Hamburg, Germany, 1987.
[24] L. O. Degelman, "A weather simulation model for building energy analysis," in *Proceedings of the Symposium on Weather Data, ASHRAE Transactions*, pp. 435–447, Seattle, Wash, USA, 1976.
[25] L. O. Degelman, "Monte Carlo simulation of solar radiation and dry bulb temperatures for air conditioning purposes," Tech. Rep. no. 70-9, Department of Architectural Engineering, The Pennsylvania State University, 1970, sponsored by the National Science Foundation under Grant no. GK-2204.
[26] D. G. Erbs, S. A. Klein, and J. A. Duffie, "Estimation of the diffuse radiation fraction for hourly, daily and monthly-average global radiation," *Solar Energy*, vol. 28, no. 4, pp. 293–302, 1982.
[27] D. G. Erbs, *Models and applications for weather statistics related to building heating and cooling loads*, Ph.D. thesis, Solar Energy Laboratory, University of Wisconsin-Madison, Madison, Wis, USA, 1984.
[28] A. Lavagnini, S. Martorelli, and C. Coretti, "Monthly maps of daily global incident solar radiation in Italy," *Il Nuovo Cimento C*, vol. 13, no. 4, pp. 769–782, 1990.
[29] K. G. T. Hollands, L. J. D'Andrea, and I. D. Morrison, "Effect of random fluctuations in ambient air temperature on solar system performance," *Solar Energy*, vol. 42, no. 4, pp. 335–338, 1989.
[30] R. A. Gansler and S. A. Klein, "Assessment of the accuracy of generated meteorological data for use in solar energy simulation studies," in *Proceedings of the 1993 ASME International Solar Energy Conference*, pp. 59–66, Washington DC, USA, April 1993.
[31] R. A. Gansler, *Assessment of generated meterological data for use in solar energy simulations*, M.S. thesis, Solar Energy Laboratory, University of Wisconsin-Madison, Madison, Wis, USA, 1993.
[32] J. A. Duffie and W. A. Beckman, *Solar Engineering of Thermal Processes*, John Wiley & Sons, New York, NY, USA, 1991.
[33] D. G. Stephenson and G. P. Mitalas, "Calculation of heat conduction transfer functions for multi-layer slabs," *ASHRAE Transactions*, vol. 77, pp. 117–126, 1971.

[34] G. P. Mitalas and J. G. Arseneault, *FORTRAN IV Program to Calculate z-Transfer Functions for the Calculation of Transient Heat Transfer Through Walls and Roofs*, Division of National Research Council of Canada, Ottawa, Canada, 1972.
[35] M. Carlini, M. Villarini, S. Esposto, and M. Bernardi, "Performance analysis of greenhouses with integrated photovoltaic modules," in *Proceedings of the International Conference on Computational Science and Its Applications (ICCSA '10)*, vol. 6017 of *Lecture Notes in Computer Science*, pp. 206–214, 2010.
[36] S. Holst, "Heating load of a building model in TRNSYS with different heating systems," ZAE Bayern, Abt. 4, TRNSYS-User Day, Stuttgart, Germany, 1993.
[37] W. Feist, *Thermal Building Simulation, A Critical Review of Different Building Models*, C. F. Müller, Karlsruhe, Germany, 1994.
[38] Th. Lechner, *Mathematical and Physical Fundamentals of the Transfer Function Method*, Institut für Thermodynamik und Wärmetechnik, Universität Stuttgart, 1992.
[39] P. Voit, Th. Lechner, and M. Schuler, "Common EC validation precedure for dynamic building simulation programs—application with TRNSYS," in *Proceedings of the TRANSSOLAR GmbH Conference of International Simulation Societies*, Zürich, Switzerland, 1994.
[40] "WINDOW 4.1, PC Program for Analyzing Window Thermal Performance in Accordance with Standard NFRC Procedures," Windows and Daylighting Group, Building Technologies Program, Energy and Environment Division, Lawrence berkeley Laboratory, Calif, USA, 1994.
[41] M. Koschenz and B. Lehmann, *Design of a Thermal Model for Thermo-Active Construction Element Systems (TABS)*, EMPA, Abteilung Energiesysteme/Haustechnik, Dübendorf, Switzerland, Stefan Holst, TRANSSOLAR, Energietechnik GmbH, Stuttgart, Germany, 2000.
[42] B. Glück, *Strahlungsheizung—Theorie und Praxis*, C. F. Müller, Karlsruhe, Germany, 1982.
[43] M. Koschenz and B. Lehmann, *Handbuch Thermoaktive Bauteilsysteme TABS*, EMPA Abteilung Energiesysteme/Haustechnik, Dübendorf, Switzerland, 2000.
[44] Stender, Merker, *Recknagel Sprenger*, Oldenburg, München, Germany, 1993.
[45] R. Tesi, *Tecniche di Ortoflorofruttocoltura in Ambiente Protetto*, Edagricole-Edizioni Agricole, 1992.
[46] R. Caponetto, L. Fortuna, S. Graziani, and M. G. Xibilia, "Genetic algorithms and applications in system engineering: a survey," *Transactions of the Institute of Measurement and Control*, vol. 15, no. 3, pp. 143–156, 1993.
[47] A. Cavallini and L. Mattarolo, *Applied Thermodynamics*, CLEUP, Padova, Italy, 1992.

Hindawi Publishing Corporation
Mathematical Problems in Engineering
Volume 2010, Article ID 726843, 12 pages
doi:10.1155/2010/726843

Research Article

The Effects of Structure Defects on the Performance of a Micro Comb Resonator

D. Guo and Y. Zhu

State Key Laboratory of Tribology, Department of Precision Instrument, Tsinghua University, Beijing 100084, China

Correspondence should be addressed to D. Guo, guodan26@tsinghua.edu.cn

Received 26 November 2009; Revised 12 April 2010; Accepted 1 May 2010

Academic Editor: Irina N. Trendafilova

A micro comb resonator loaded by alternating electric field is modeled by finite element method, The damping is analyzed by both Couette flow model and Stokes flow model. Structure faults are researched its effects on the dynamic characteristics of the micro comb resonator. The result shows that adhesion fault makes the resonance frequency higher and sensitivity reduction, while crack fault debases the resonance frequency and amplitude. When the crack is located near the end, the stress concentration at the crack location is highest, which is easy to induce the support beam broken.

1. Introduction

With the fabrication processes trending to be more mature, the requirement of reliability and production ability of MEMS increases more. Relative to design, the problems during MEMS fabrication process, especially the problems of defect and fault are serious, which will been the bottleneck of MEMS application. So, simulations and experiments of the movement for microdevices with defects are necessary. Using the stable model of fault and testing method to detect the fault, the quality and reliability of MEMS products can be improved. There are many sources for MEMS defects, such as particle contaminants, adhesion, undersigned bend, insufficient or excess etch, sidewall inclination, and notching [1]. In recent years, the fault simulation of MEMS has been investigated by some researchers. An MEMS affected by particulate contaminations was simulated by Deb and Blanton, the relationship between defect location and performance parameter of structure was analyzed [2]. The structure fault of MEMS was also modeled and simulated by Reichenbach et al. [3]. The broken beam fault and unwanted anchor fault of a micromirror were simulated by Chen et al. [4]. The fault-based testing technology for MEMS was illustrated by Mir et al. [5].

Electrostatic-comb structure has been successfully applied to many microsystems such as microsensors, microaccelerometers, microdrives, due to its simple structure and superior performance [6]. The motion of the devices is greatly influenced by fabricating error, variety of parameters, and deformation as well, especially the faults of structure, which make the kinetic accuracy become reduced [7–9]. In this paper, a dynamic model is built to research the dynamic performance of microcomb resonator under alternating electric field, in which both Couette flow model and Stokes flow model are applied to the damping. Structures with point adhesion or beam crack are analyzed for the dynamic characteristics using finite element method.

2. Dynamic Model of a Microcomb

A typical microcomb resonator usually has two sets of fingers, the one which is connected to the substrate is called fixed fingers (or stationary electrode), and the other which is released from the substrate is called movable fingers (see Figure 1). When two different voltages are applied to these two sets of fingers, the resulting electrostatic force drives the movable fingers toward or apart from the fixed ones. When an alternating voltage is applied, the movable electrode oscillates under the electrostatic force and elastic restoring force, which can be designed for a resonator.

Figure 1 shows the schematic of a typical microresonator. Its finite element dynamic equation is:

$$[M]\{\ddot{u}\} + [C]\{\dot{u}\} + [K]\{u\} = \{F\}\sin\omega t \tag{2.1}$$

where $[K]$, $[M]$ is the structural stiffness matrix and mass matrix, which can be obtained by finite element method. $[C]$ is the air damping matrix, which will be derived later. $\{u\}$ is the node displacement vector. $\{F\}$ is the electrostatic force, which can be derived by the finite element method of electrostatic field. ω is the alternating frequency of electric field.

The electrostatic potential in uniform medium has

$$\nabla^2 V = 0 \tag{2.2}$$

where V is the distribution of electric potential. Equation (2.2) is called Laplace Equation. In the Cartesian coordinate, (2.2) can be write as

$$\frac{\partial^2 V}{\partial x^2} + \frac{\partial^2 V}{\partial y^2} + \frac{\partial^2 V}{\partial z^2} = 0 \tag{2.3}$$

when the V is solved from (2.3), the electric field intensity vector $\{E\}$ can be attained from:

$$\{E\} = -\nabla V. \tag{2.4}$$

Then, the electrostatic force on the movable finger has:

$$F = \varepsilon \int_s (\nabla V)^2 ds \tag{2.5}$$

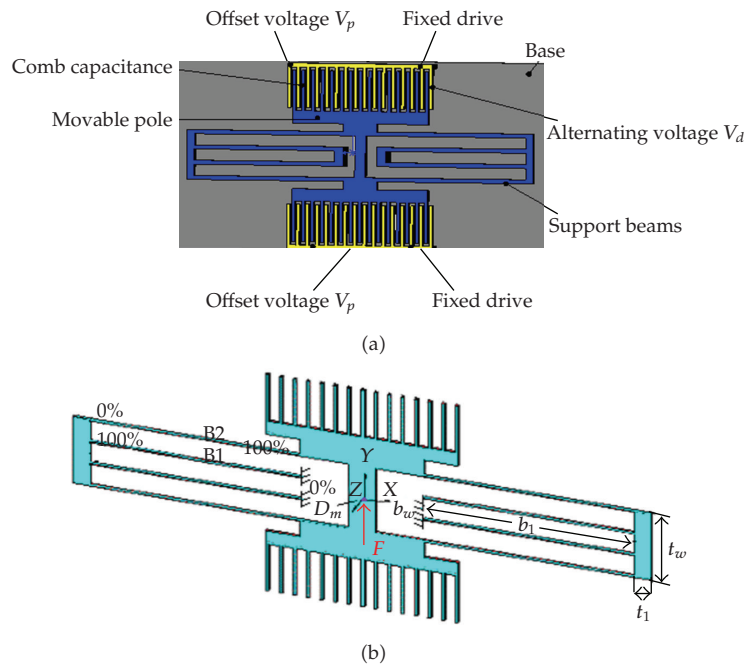

Figure 1: Schematic of microcomb resonator.

where S is the surface of movable finger, and the ε is dielectric coefficient of air, which is 8.854×10^{-6} pF/μm.

The finite element method is applied to analyze the electrostatic field and comb structure. 4-node tetrahedral elements are used to generate meshes. For electrostatic field, the electric potential V at any point can be written as:

$$V = [N]^T [V_e] \tag{2.6}$$

where $[N]$ is the shape function matrix. $[V_e]$ is the node electric potential. According to the principle of minimum potential energy, we have

$$\left\{ \frac{\partial U}{\partial V_e} \right\} = 0 \tag{2.7}$$

where

$$U = \frac{1}{2} \varepsilon \iiint (\nabla V)^2 dx\, dy\, dz. \tag{2.8}$$

Substituting (2.6) into (2.8), combining with (2.7), adding the electric field boundary condition, the $\{V_e\}$ can be solved. Then from (2.5) and (2.6), the electrostatic force at any point can be obtained. For the comb structure, 4-node tetrahedral elements are also used. The electrostatic force is substituting into (2.1), then the subspace iterate method was used

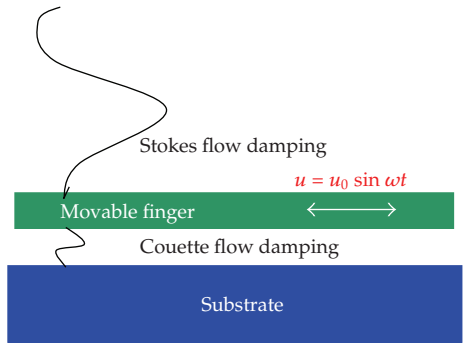

Figure 2: The sketch of damping model.

to obtain the natural frequency and the Newmark integral method was used to obtained vibration response.

Air damping is crucial to the dynamic characteristics of microcomb resonator. For the laterally oscillating resonator, the slide film damping is more significant than the squeeze film damping. So, only the slide film damping is considered here. The air damping of the comb can be divided into three parts, air damping layer (a) between the movable fingers and the base, (b) between the fingers and (c) above the movable fingers. Figure 2 shows the sketch of damping model. For the (a) and (b), air layers are only several microns, so the Couette flow model was applied [10, 11], the damping coefficients can be written as,

$$C_a = \frac{\mu A}{d},$$
$$C_b = \frac{\mu A_c}{g}. \tag{2.9}$$

Because the Couette flow model does not take the media inertial effects into consideration. It can be used under the assumption that the feature distance $\delta = \sqrt{2\mu/\rho\omega}$ is much larger than the gap d between the plate and the substrate [12]. Where μ is viscosity coefficient of air, $\mu = 0.185 \times 10^{-10}\,\mathrm{kg/s/\mu m}$, ρ is the density of air, $\rho = 1.29 \times 10^{-18}\,\mathrm{kg/\mu m^3}$, $h = 2\,\mu\mathrm{m}$ in this paper. So, it can be obtained that the vibration frequency $f = \omega/2\pi$ should be much less than 1×10^6 Hz.

For the (c), air layer is relative thick, so Stokes flow model was applied [11]. The damp coefficient was

$$C_c = \mu\beta A \frac{\sinh(2\beta h) + \sin(2\beta h)}{\cosh(2\beta h) - \cos(2\beta h)},$$
$$\beta = \sqrt{\frac{\pi f}{\nu}} \tag{2.10}$$

where μ is viscosity coefficient of air, $\mu = 0.185 \times 10^{-10}\,\mathrm{kg/s/\mu m}$, f is vibration frequency of the resonator, ν is motion viscous ratio, $\nu = 0.157 \times 10^{-8}\,\mu\mathrm{m^2/s}$, A is the lower surface area of the movable finger structure, A_c is the sum of the fingers' side face area, d is the clearance

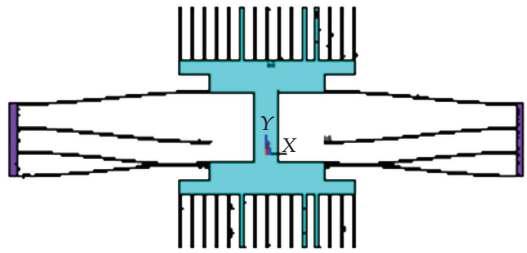

Figure 3: The first vibrational mode of microresonator.

between the microcomb and the base, g is the clearance between the fingers, h is the thickness of the finger. Then the whole damping is the summation of the three parts:

$$C = C_a + C_b + C_c = \frac{\mu A}{d} + \frac{\mu A_c}{g}\mu\beta A\frac{\sinh(2\beta h) + \sin(2\beta h)}{\cosh(2\beta h) - \cos(2\beta h)}. \tag{2.11}$$

3. Dynamic Characteristics Analysis of Faulted Micro-Comb Resonator

Movable structure adhesion and support beam crack are two typical faults of microcomb resonator. Adhesion indicates the movable part fixed, because the clearance in MEMS is very small, during the fabrication process, the movable part is easy to be blocked and stuck by microparticle mass, which leads to the needless structure mounting. The crack usually occurs in the support beam or fingers, which is induced by residual stress or repeated motion. Other defects, such as the mass and stiffness change or asymmetric distribution of the support beam caused by contamination during the fabrication process, perhaps does not bring on the beam cracks or broken, but affect the dynamic performance of the MEMS. In this paper, two typical faults are analyzed their effects on the dynamic performance of microcomb resonator.

3.1. Natural Characteristics of the Micro-Comb Structure

The structural parameters used in this paper are shown in Table 1. The dynamic performance of a microcomb includes natural frequencies, vibration amplitude, response time, quality factor, and so on. From the homogeneous equation of (2.1), by subspace iterative method, the first natural frequency and mode can be obtained, which is the structure's sensitivity work mode. The first natural frequency is $f_n = 11881\,\text{Hz}$, and the 1st mode is shown in Figure 3. For this structure, the damping coefficient can be obtained from (2.11), which is $C = 1.76 \times 10^{-7}\,\text{kg/s}$ at resonator frequency.

When offset voltage $V_p = 50\,\text{V}$ and driven alternating voltage $V_d = 25\sin(2\pi f t)\,\text{V}$ is loaded, where f is the driving frequency, the amplitude frequency response characteristics are analyzed, the maximal amplitude is $A_m = 12.785\,\mu\text{m}$ at natural frequency $f_n = 11881\,\text{Hz}$. The sensitivity of microcomb resonators is defined as the ratio of vibration amplitude of structure and the driven voltage, so at the natural frequency, the sensitivity $s = 0.5114\,\mu\text{m/V}$.

Table 1: The structural parameters of microcomb resonator.

Parameter	Size
Finger gap: g/μm	2.88
Finger length: l/μm	40.05
Finger width: w/μm	2
Gap of comb: c/μm	20.61
Beam length: b_l/μm	151
Beam width: b_w/μm	1.1
Thickness: h/μm	1.96
Area of the lower surface of the movable Finger structure: $A/\mu\text{m}^2$	5.1×10^3
Sum of the fingers' side face area: $A_c/\mu\text{m}^2$	2.35×10^3
Substrate gap: d/μm	2
Truss length: t_l/μm	78
Truss width: t_w/μm	13

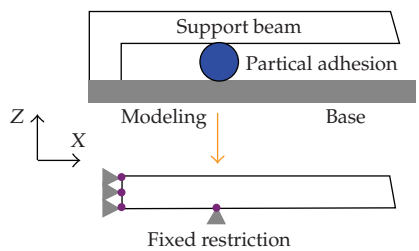

Figure 4: The model of adhesion fault.

3.2. Analysis of Particle Adhesion Fault

The most typical defect which can be encountered in the microcomb resonators is stiction of the suspended beams to the substrate surface. Stiction can mostly occur during MEMS processing (e.g., wet etching). During wet chemical etching, removal of a chip from the liquid etchant often pulls suspended parts towards the substrate surface where they remain stuck due to capillary forces and Van der Waals force. Once in contact, and even after the chip has been dried up, suspended parts may remain stuck due to different types of adhesion forces. In this case, the microresonator will be failure due to the movable part fixed. In this paper, another adhesion case caused by the exterior particle is considered, which will not lead to the failure of the resonator, so is easier to be neglected.

When the exterior particle comes into the structure, rests between the movable part and the fixed part, which will lead to the point adhesion due to the molecular force and so on. Electric particle will cause the resonator short circuit and failure. Insulative particle may not lead the structure entire failure, but may cause the dynamic characteristics change. In this section, the adhesion fault due to insulative particle is analyzed, we assume the particle is rigid, the movable part cannot move relative to the substrate at the adhesion point. Figure 4 shows the simple model of the resonator with an adhesion point.

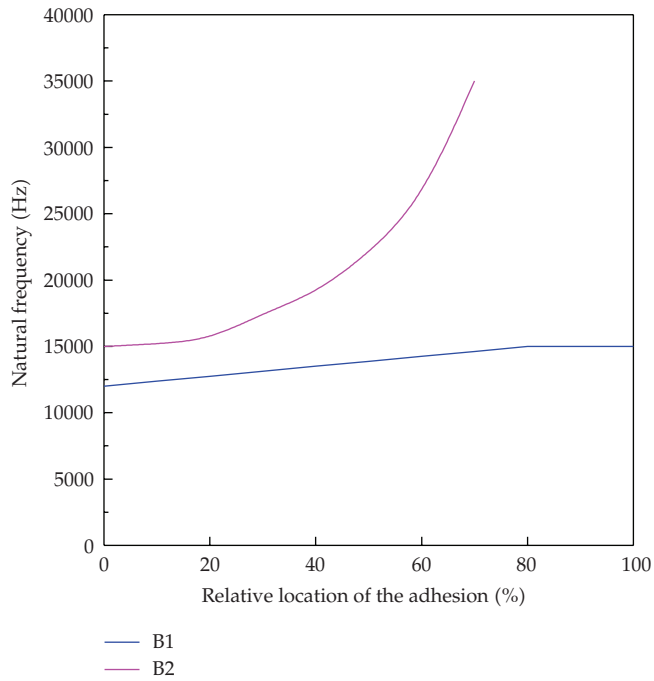

Figure 5: Natural frequencies change with the adhesive locations.

Support beam of the resonator is a folded symmetric structure, where B1 and B2 are two parallel beams of them, as shown in Figure 1(b). One end of B1 is fixed on the substrate. The adhesion at different location of B1 or B2 has different effect on the natural characteristics of the resonator.

Figure 5 shows that the natural frequency change with the location of adhesion, the abscissa is relative location of the adhesion. Where define relative location of adhesion at B1 beam as the ratio of distance from adhesion to the fixed end and the length of B1, and the relative location at B2 is the ratio of distance from adhesion to the folded end and the length of B2, as shown in Figure 1(b). It can be seen from Figure 5 that the natural frequency becomes higher due to the adhesion fault, and increases with the adhesion location ratio growing. Adhesion at B2 has more greatly effect on natural frequency than adhesion at B1. As the relative location ratio at B2 increases, the natural frequency increases more quickly.

Because the adhesion fault is difficult to be predicted in advance, the loaded voltage is usually kept on the faultless resonant frequency $f_n = 11881\,\text{Hz}$, which is called operating frequency. In case the adhesion fault occurs, driving frequency does not change, then the vibration amplitude (working amplitude) changes, lead to reduction of the sensitivity.

When offset voltage 50 V and driven alternating voltage of amplitude 25 V and frequency 11881 Hz is loaded, the relationship of sensitivity and the location of adhesion are shown in Figure 6. It can be seen that the adhesion fault makes the sensitivity lower. As the adhesion relative location ratio at B1 increases, the sensitivity reduces quickly. Adhesion fault at B2 makes the sensitivity reduces too, obviously the resonator is not working on the resonant state here. When the adhesion is located at 10% of B1, sensitivity $s = 0.4144\,\mu\text{m/V}$, however when it is located at 70% of B2, the sensitivity has reduced to $s = 0.0032\,\mu\text{m/V}$.

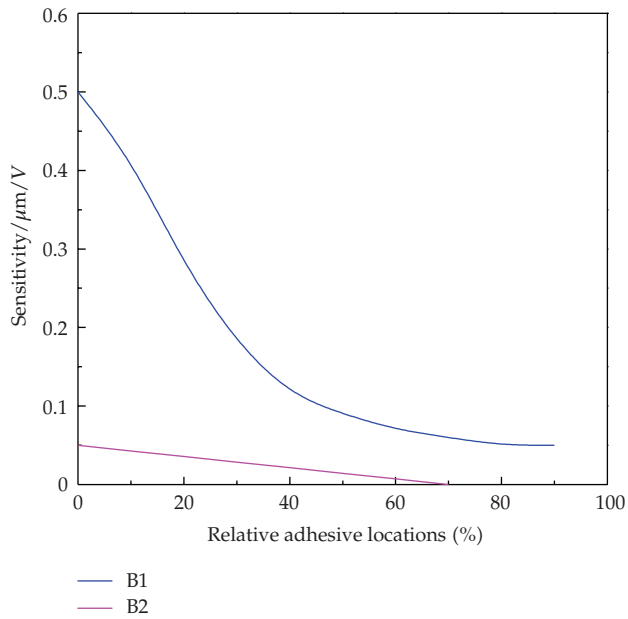

Figure 6: Sensitivity change with the adhesive locations.

3.3. Analysis of the Beam Crack Fault

Crack is a common fault in MEMS. Some microcrack influences not only on the structure performance, but also results in the structure failure when the crack expands with the motion. Beam structure is often used in microresonator. A crack could easily occur due to the stress concentration during fabrication process. In addition, during DRIE process, if the impurity adheres to the etching model, mass lack could occurred, which will cause such faults as crack or perforation.

In this paper, we only analyzed the support beam crack fault, because the support beam stiffness has crucial influence on the dynamic performance of the resonator. The beam crack is simplified as the square groove here. Based on Saint-Venant's Principle, the width of crack is set to $0.1\,\mu$m, which is much smaller than the length of support beam. The depth of crack is set to half of the thickness of the beam. The FEM mesh of cracked beam is shown in Figure 7. 4-node tetrahedral elements are applied here. Figure 8 shows the relationship of resonant frequency and the crack location. The curve for B1 and B2 are similar. The crack causes the resonant frequency lower. The crack located in the middle of B1 and B2 has fewer effect on the resonator frequency, but the crack located near the end of B1 or B2 has more effect on it. The frequency for B2 crack is somewhat higher than that in B1. Comparing with the adhesion fault, the beam crack fault has smaller influence on the resonator frequency. Figure 9 shows the relationship of sensitivity and the crack locations. It can be seen the crack fault causes the sensitivity to be lower, especially for the crack near beam end. When the crack is located in 10% of B1, sensitivity $s = 0.5072\,\mu\text{m/V}$, for crack located in 10% of B2, it is $s = 0.5091\,\mu\text{m/V}$. Comparing with the adhesion fault, crack has smaller effect on the resonator's dynamic performance.

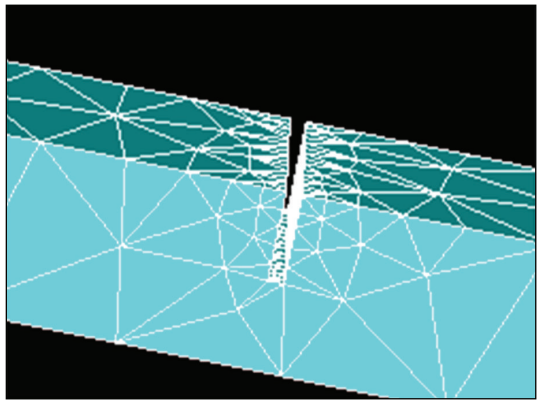

Figure 7: Support beam crack model with FEM.

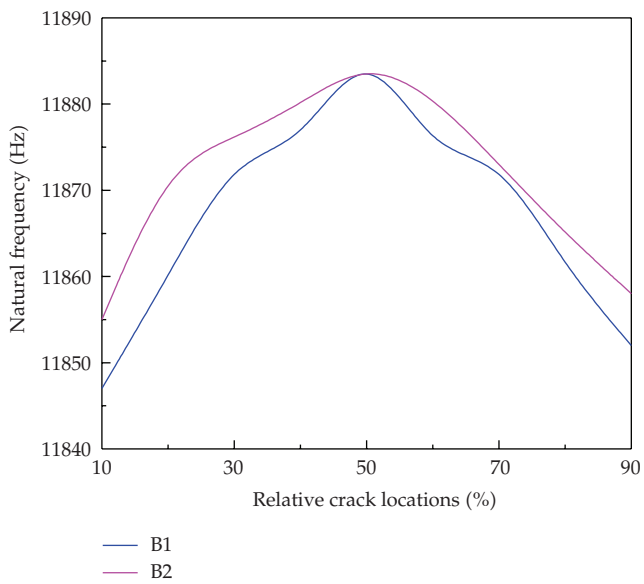

Figure 8: Natural frequencies change with the beam crack locations.

However, crack could cause the stress concentration, sometimes makes the beam broken, and leads to severity failure. Figure 10 shows the maximal stress along B1 and B2, at different crack location. The maximal stress is almost at the crack location. When the crack is located near the end, the maximal stress is highest, which is easy to cause the support beam broken.

4. Conclusion

In this paper, a microcomb resonator with faults was simulated, air damping was considered. The influence of faults on the dynamic performance of microresonator is analyzed. The results

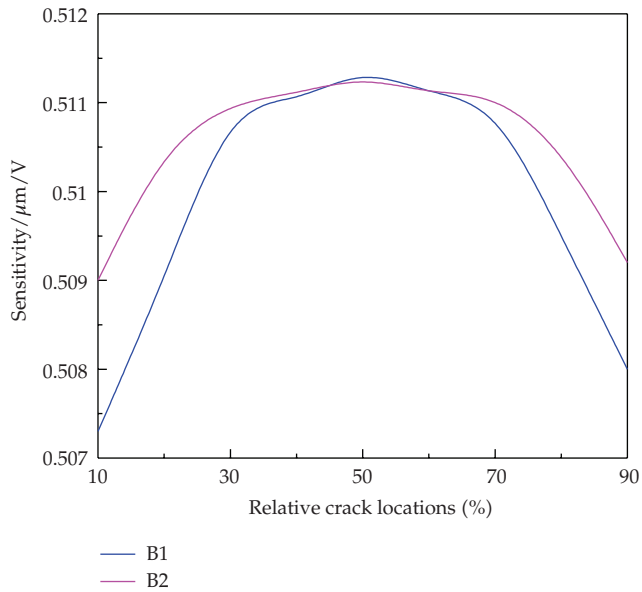

Figure 9: Sensitivity change with the crack locations.

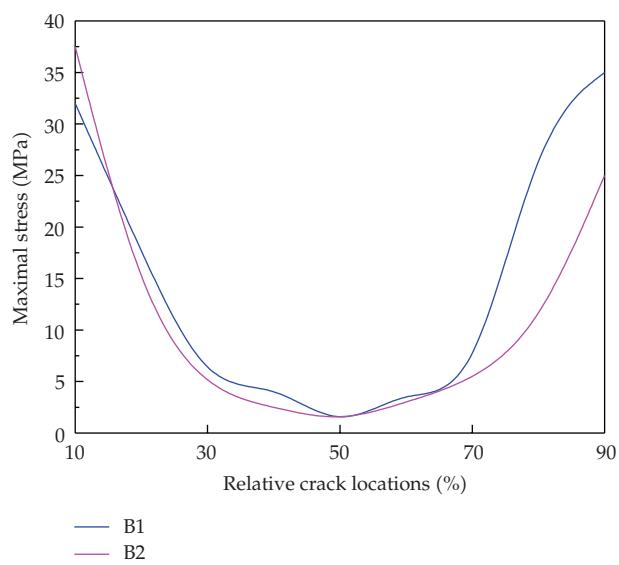

Figure 10: The maximal stresses change with the crack locations.

show that adhesion fault makes the frequency higher, while crack fault reduces the natural frequency. Both faults reduce the sensitivity. The adhesion fault has more obvious effect on the dynamic characteristics than the crack fault, However, if the crack is located near the end, the stress concentration at the crack location is highest, which is easy to cause the support beam broken.

Nomenclature

$[K]$: Structural stiffness matrix
$[M]$: Structural mass matrix
$[C]$: Air damping matrix
$\{u\}$: Node displacement vector
$\{F\}$: The electrostatic force vector
$\{E\}$: Electric field intensity vector
ω: Alternating frequency of electric field
V: Electric potential
ε: Dielectric coefficient of air, pF/μm
μ: Viscosity coefficient of air, kg/s/μm
ρ: Density of air, kg/μm^3
ν: Motion viscous ratio of air, μm^2/s
f: Vibration frequency of the microresonator, Hz
A: The lower surface area of the movable finger structure, μm^2
A_c: The sum of the fingers' side face area, μm^2
d: The clearance between the microcomb and the base, μm
g: The clearance between the fingers, μm
h: The thickness of the finger, μm
l: Finger length, μm
w: Finger width, μm
c: Gap of comb, μm
b_l: Beam length, μm
h: Thickness of comb structure, μm
t_l: Truss length, μm
t_w: Truss width, μm
V_p: Offset voltage, V
V_d: Driven alternating voltage, V
A_m: Maximal vibration amplitude, μm
s: Sensitivity of microcomb resonators, μm/V.

Acknowledgment

This research is supported by National Natural Science Foundation of China (Grant no. 50775121) and the National Natural Science Key Foundation of China (Grant no. 50730007).

References

[1] Kolpekwar, R. D. Blanton, and D. Woodilla, "Failure modes for stiction in surface-micromachined MEMS," in *Proceedings of IEEE International Test Conference (TC '98)*, pp. 551–556, IEEE Computer Society, Washington, DC, USA, October 1998.
[2] N. Deb and R. D. Blanton, "High-level fault modeling in surface-micromachined MEMS," in *Design, Test, Integration, and Packaging of MEMS/MOEMS*, vol. 4019 of *Proceedings of SPIE*, pp. 228–235, Paris, France, May 2000.
[3] R. Reichenbach, R. Rosing, A. Richardson, and A. Dorey, "Finite element analysis to support component level fault modelling for MEMS," in *Design, Test, Integration, and Packaging of MEMS/MOEMS*, vol. 4408 of *Proceedings of SPIE*, pp. 147–158, Cannes-Mandelieu, France, April 2001.
[4] Z. Chen, Y. Y. He, F. L. Chu, and J. Huang, "Dynamic characteristic analysis of the micro-structure with defects," *Chinese Journal of Mechanical Engineering*, vol. 40, no. 6, pp. 23–27, 2004.

[5] S. Mir, B. Charlot, and B. Courtois, "Extending fault-based testing to microelectromechanical systems," *Journal of Electronic Testing: Theory and Applications*, vol. 16, no. 3, pp. 279–288, 2000.
[6] W. C. Tang, T.-C. H. Nguyen, and R. T. Howe, "Laterally driven polysilicon resonant microstructures," *Sensors and Actuators*, vol. 20, no. 1-2, pp. 25–32, 1989.
[7] W. Huang and G. Y. Lu, "Analysis of lateral instability of in-plane comb drive MEMS actuators based on a two-dimensional model," *Sensors and Actuators A*, vol. 113, no. 1, pp. 78–85, 2004.
[8] I. V. Avdeev, M. R. Lovell, and D. Onipede Jr., "Modeling in-plane misalignments in lateral combdrive transducers," *Journal of Micromechanics and Microengineering*, vol. 13, no. 6, pp. 809–815, 2003.
[9] G. Zhou and P. Dowd, "Tilted folded-beam suspension for extending the stable travel range of comb-drive actuators," *Journal of Micromechanics and Microengineering*, vol. 13, no. 2, pp. 178–183, 2003.
[10] C. Young, P. P. Albert, and R. T. Howe, "Viscous damping model laterally oscillating microstructures," *Journal of Microelectromechanical Systems*, vol. 3, no. 2, pp. 81–87, 1994.
[11] W. Ye, X. Wang, W. Hemmert, D. Freeman, and J. White, "Air damping in laterally oscillating microresonators: a numerical and experimental study," *Journal of Microelectromechanical Systems*, vol. 12, no. 5, pp. 557–566, 2003.
[12] E. M. Lifshitz, *Fluid Mechanics*, Pergamon, New York, NY, USA, 2nd edition, 1989.

Hindawi Publishing Corporation
Mathematical Problems in Engineering
Volume 2010, Article ID 749517, 12 pages
doi:10.1155/2010/749517

Research Article

Dynamic Time Warping Distance Method for Similarity Test of Multipoint Ground Motion Field

Yingmin Li,[1] Huiguo Chen,[1,2] and Zheqian Wu[1]

[1] *College of Civil Engineering, Chongqing University, Chongqing 400045, China*
[2] *Department of Architecture & Civil Engineering, Logistics Engineering College, Chongqing 401311, China*

Correspondence should be addressed to Huiguo Chen, chenhg_mail@163.com

Received 1 January 2010; Revised 6 April 2010; Accepted 16 May 2010

Academic Editor: Carlo Cattani

The reasonability of artificial multi-point ground motions and the identification of abnormal records in seismic array observations, are two important issues in application and analysis of multi-point ground motion fields. Based on the dynamic time warping (DTW) distance method, this paper discusses the application of similarity measurement in the similarity analysis of simulated multi-point ground motions and the actual seismic array records. Analysis results show that the DTW distance method not only can quantitatively reflect the similarity of simulated ground motion field, but also offers advantages in clustering analysis and singularity recognition of actual multi-point ground motion field.

1. Introduction

Considerable research studies have shown that nonuniform ground motion input has a significant influence on dynamic response of large scale structures [1, 2]. The influence of multi-point ground motion must be taken into account when analyzing the seismic response of large scale structures. Ground motion records from common stations only reflect one- or multidimension vibration of sites, while multi-point ground motion fields are often obtained from seismic arrays. For lack of actual records of seismic arrays, attenuation rules of actual multi-point ground motion field are usually used to synthesize multi-point ground motions for specific site conditions and distances. In this process, the traveling wave effect and coherence of multi-point ground motions recorded in seismic arrays with various distances are first analyzed, and then the coherence corresponding to various points are obtained through statistical analysis. Finally, the method for synthesizing spatial ground motions with the coherence effect and traveling effect of multi-point earthquake ground motions considered can be established [3–5]. In this method, the variations of ground motions with

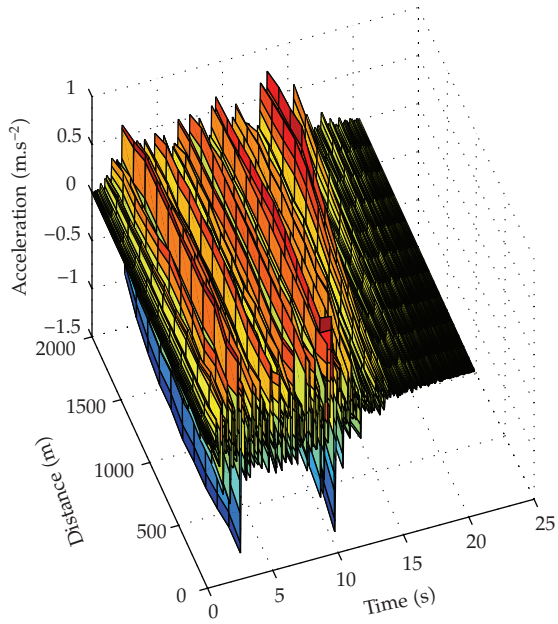

Figure 1: Multi-point ground motion field simulated using actual initial phase.

site conditions and motion propagation can be controlled in a certain range in the extent of engineering scales for both actual array records and artificially synthesized multi-point earthquake ground motions. Multi-point ground motion field in the engineering scale may have a certain degree of similarity. Moreover, if the site condition is homogeneous, the degree of similarity will gradually decrease with the increase in distance [6].

Based on the knowledge that multi-point ground motion fields have similarity in engineering scale, there are at least two issues that can be addressed by determining the similarity of ground motions. First, the reliability of actual array records can be ensured. Since all actual array records are obtained from ground motion recording instruments, the reliability of records from all stations cannot be guaranteed in a particular triggering earthquake. Due to equipment failure or equipment differences some station records may be seriously distorted. When to use seismic array records for analyzing the propagation of multi-point ground motions, the distorted data should be removed to ensure the reasonability of array records and such distorted data can be excluded by using similarity test of actual multi-point ground motions. Second, the reasonability of artificially synthesized multi-point ground motions can also be tested. By judging whether the artificial multi-point ground motion field is similar to actual ground motion field, the efficiency and rationality of the synthesis method for multi-point ground motions can be tested.

For this reason, it is necessary to establish a standardized and efficient similarity test method for multi-point ground motions. For similarity judgment of ground motions, correlation coefficients are frequently used. However, correlation coefficients are mainly defined as a measurement of linear feature of two variables, and they are not suitable for similarity judgment between two sequences with nonlinear correlations. Spatial multi-point earthquake ground motions are often influenced by site conditions, coherence effect and traveling effect, therefore the use of the correlation coefficient is insufficient to reflect the similarity of ground motions. Figures 1 and 2 show two sets of multi-point ground motions

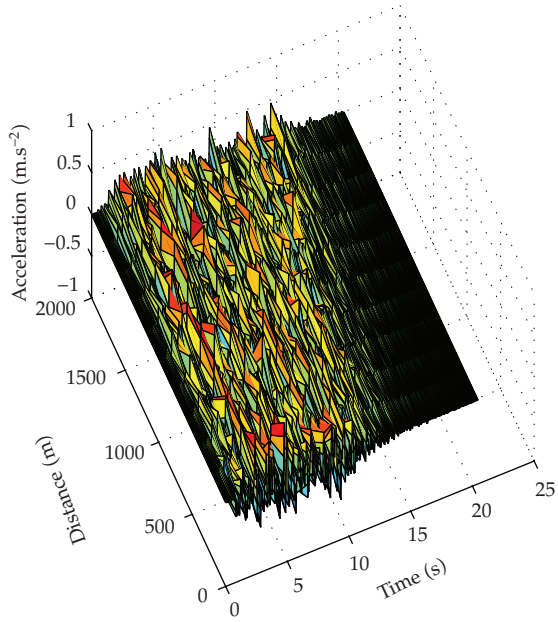

Figure 2: Multi-point ground motion field simulated using random initial phase.

synthesized using the trigonometric series method [7] with two different initial phase values. For condition 1, the initial phase is the actual ground motion phase, and for condition 2, the initial input phase is random. In both cases, the distance interval of synthesized ground motions is 200 m. Figure 3 shows the correlation coefficients between the artificial ground motion and the actual ground motions. For condition 2, due to the impact of the random initial phase value, the nonlinear relationships among ground motions of various points are more prominent, which indicates less correlations among various points. It is clear that in condition 2 the similarity among multi-point ground motions is not correctly presented.

Similarity measurement of time series is an important problem in data mining. By using the basic theory of similarity measurement, it not only can reflect the intrinsic similarity of time series or eigenvectors but also can quantitatively evaluate their similarity features. Similarity measurement has been an important tool in series clustering, pattern matching, classification, rule identification and anomaly detection [8, 9]. Among the methods commonly used for similarity measurement, the dynamic time warping distance (DTW) method proposed by Berndt and Clifford [10] is the most widely used, which can effectively determine the similarity between two series under the circumstances of shift and stretching of amplitude, and the bending of time axis [11]. In this study, the DTW method is applied to the similarity determination and singularity recognition of multi-point ground motions.

2. The Basic Principle of Similarity Measurement Method

In general, the similarity measurement between series means that a function $\mathrm{Sim}(X, Y)$ can be defined where X and Y are two different time series of the same type of data set. The value of the function Sim lies in $(0, 1]$, that is, the bigger the value is, the higher the similarity degree between two series is, and vice versa. In particular, two series are completely similar

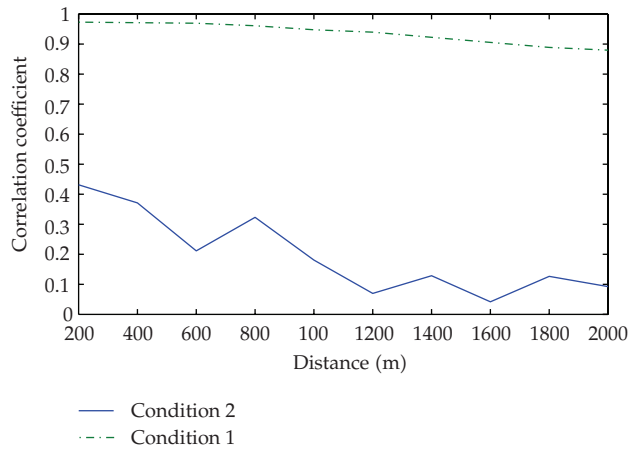

Figure 3: Correlation coefficient of multi-point ground motion field simulated under different conditions.

when Sim = 1. For simple time series, the similarity measurement function can be represented using correlation coefficients or cosine value between two series, while for the complex data, it is difficult to accurately represent the similarity degree using above function. Therefore, the similarity degree between the series is generally represented by defining a specific distance between two series called similarity distance. There are several methods available to define the similarity distance and the Minkowski distance is most frequently used, which is defined as follows:

$$d(X,Y) = \left(\sum_{i=1}^{n} \left| x_i - y_i \right|^P \right)^{1/P}. \tag{2.1}$$

When $P = 2$, the distance between two series is called Euclidean Distance.

Referring to formula (2.1), if two series are equal, their distance is zero, which means two series are completely similar. The larger difference between two series yields larger distance and less similarity. When to calculate the Minkowski distance, it is required that two series have the same length, the values of two series have point-to-point correspondence, and the weight of each pair of difference is equal. Due to such a correspondence, the Minkowski distance cannot be applied to the similarity measurement of complex series with shift and stretching of amplitude. To solve this problem, the dynamic time warping distance method is often used. In this method, the distance is designated to depict the greatest similarity between series by calculating the minimum distance between them, which is defined as follows.

Let $X(x_1, x_2, \ldots, x_n)$ and $Y(y_1, y_2, \ldots, y_m)$ be two series with the length of n and m, respectively, and an $n \times m$ matrix M can be defined to represent the point-to-point correspondence relationship between X and Y, where the element M_{ij} indicates the distance $d(x_i, y_j)$ between x_i and y_j. Then the point-to-point alignment and matching relationship between X and Y can be represented by a time warping path $W = \langle w_1, w_2, \ldots, w_K \rangle, \max(m,n) \leq K < m + n - 1$, where the element $w_k = (i,j)$ indicates

the alignment and matching relationship between x_i and y_j. If a path is the lowest cost path between two series, the corresponding dynamic time warping distance is required to meet

$$\mathrm{DTW}(X,Y) = \min_{W}\left\{\sum_{k=1}^{K} d_k, W = \langle w_1, w_2, \ldots, w_K\rangle\right\}, \tag{2.2}$$

where $d_k = d(x_i, y_j)$ indicates the distance represented as $w_k = (i, j)$ on the path W.

Then the formal definition of dynamic time warping distance between two series is described as

$$\begin{gathered}\mathrm{DTW}(\langle\,\rangle, \langle\,\rangle) = 0,\\ \mathrm{DTW}(X, \langle\,\rangle) = \mathrm{DTW}(\langle\,\rangle, Y) = \infty,\\ \mathrm{DTW}(X,Y) = d(x_i, y_j) + \min\begin{cases}\mathrm{DTW}(X, Y[2:-]),\\ \mathrm{DTW}(X[2:-], Y),\\ \mathrm{DTW}(X[2:-], Y[2:-]),\end{cases}\end{gathered} \tag{2.3}$$

where $\langle\,\rangle$ indicates empty series, $[2:-]$ indicates a subarray whose elements include the second element to the final element in an one-dimension array, $d(x_i, y_j)$ indicates the distance between points x_i and y_j which can be represented by the different distance measurements, for example, Euclidean Distance. The DTW distance of two-time series can be calculated by the dynamic programming method based on accumulated distance matrix [10], whose algorithm mainly is to construct an accumulated distance matrix:

$$r(i,j) = d(x_i, y_j) + \min\{r(i-1,j), r(i,j-1), r(i-1,j-1)\}. \tag{2.4}$$

Any element $r(i, j)$ in the accumulated matrix indicates the dynamic time warping distance between series $X_{1:i}$ and $Y_{1:j}$. Series with high similar complexity can be effectively identified because the best alignment and matching relationship between two series is defined by the dynamic time distance.

3. Similarity Analysis of the Simulated Multi-Point Ground Motions

For structural dynamic analysis, artificial multi-point ground motion field plays a significant role. Current methods of artificial ground motion mainly cover triangular series method and Green function method [3]. According to the general rule of multi-point ground motion field in engineering scale, the multi-point ground motion fields simulated using above methods are of high similarity. Due to site effect, wave propagation and other factors, multi-point ground motions often show relatively more complex nonlinear relationships such as time shift and stretching. The correlation coefficient method shown in Figure 3 cannot accurately represent the similarity of simulated ground motions. For ground motions at the points with different distances, the corresponding dynamic warping time distances between them and the input ground motion can be calculated via the method

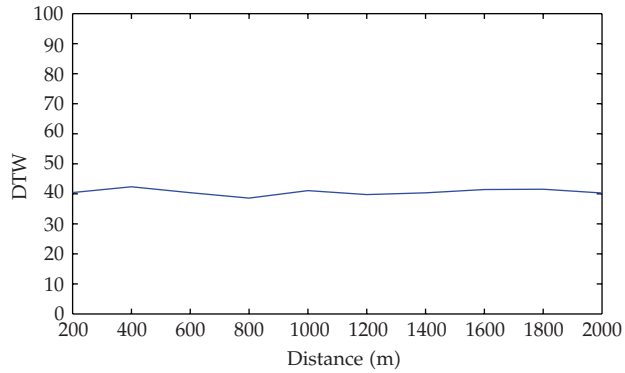

Figure 4: The dynamic warping time distance between the points of the synthesized ground motion in Figure 2 and the input ground motion.

discussed above. Figure 4 shows the dynamic time warping distance between the points and the input ground motion under condition 2 (Figure 2). It can be seen that the dynamic time warping distances between the points and input ground motion is basically around 40, indicating that ground motions of the points have an identical degree of similarity.

However, because different multi-point ground motion fields have different dynamic time warping distances, the degree of similarity between ground motions of various points cannot be intuitively presented. If a maximum distance (or lowest similarity) can be approximately defined between the input ground motion and a assume time series, the similarity degree of ground motions can be calculated numerically. That is to say, if regard the dynamic time warping distance between a particular time series and the input ground motion as a reference standard of maximum distance, the similarity degree of the particular time series and input ground motion can be consider as zero. In this paper, according to the basic understanding that the values of ground motion are not always maintained at the peak value as time increasing, a particular time series can be approximately assumed whose values are constantly the peak value of input ground motion as time increasing. If the dynamic time warping distance between the particular series and the input ground motion is define as D (the maximum distance), then according to the dynamic time warping distance $d(i)$ between the points and input ground motions, the approximate degree of similarity between the points and input ground motions can be calculated as follows:

$$\mathrm{Sim}(a_i, a_1) = 1 - \frac{d(i)}{D}. \tag{3.1}$$

Figure 5 shows the degree of similarity between the points of simulated multi-point ground motion filed in Figure 2 and the input ground motion. By comparing with the results of similarity degree of multi-point ground motion using correlation coefficient as shown in Figure 3, it can be found the degree of similarity via dynamic warping time distance is more reasonable.

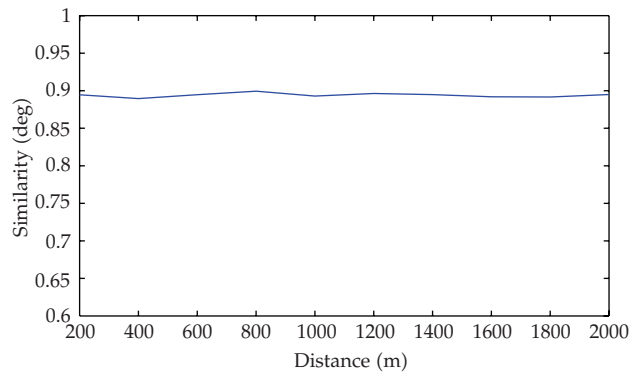

Figure 5: The similar degrees of similarity between the points of the synthesized ground motion filed in Figure 2 and the input ground motion.

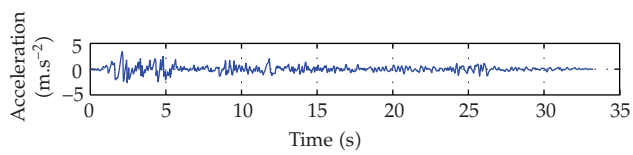

Figure 6: Time history curve of El Centro NS.

4. Clustering Analysis and Singularity Recognition of Multi-Point Ground Motions

More generally, for ground motions in an unknown multi-point ground motion field, if a certain ground motion is seriously distorted, it can also be effectively identified using the dynamic time warping distance. The DTW method provides a basis for clustering analysis and singularity recognition of multi-point ground motion data. To validate the efficiency of this method, the real ground motion (El Centro 1940) recorded at Imperial Valley, California, USA is used whose time history of acceleration is shown in Figure 6.

Firstly, an experiment is performed using the artificially simulated ground motion field with multi-point similarity. Figures 7 and 8 show the time-history curves of artificial ground motions at some points as shown in Figures 1 and 2. By comparing the propagation rule and waveform of El Centro NS and the artificial motions, we can see there are obvious differences. If substitute El Centro wave for the original input seismic wave, a multi-point ground motion field including artificial singular ground motion can be established. Obviously, in this artificially synthesized ground motion field, El Centro wave should be the singular seismic wave. Using the dynamic warping distance method, the similarities of multi-point ground motion field in Figures 1 and 2 are calculated, respectively, and the results are shown in Tables 1 and 2. It can be seen in both Tables the dynamic warping distances between El Centro wave and all other points (indicated in the table as bold characters) show consistent anomalies. It can be concluded that El Centro is the singular seismic wave while the rest are in the same type of ground motion field.

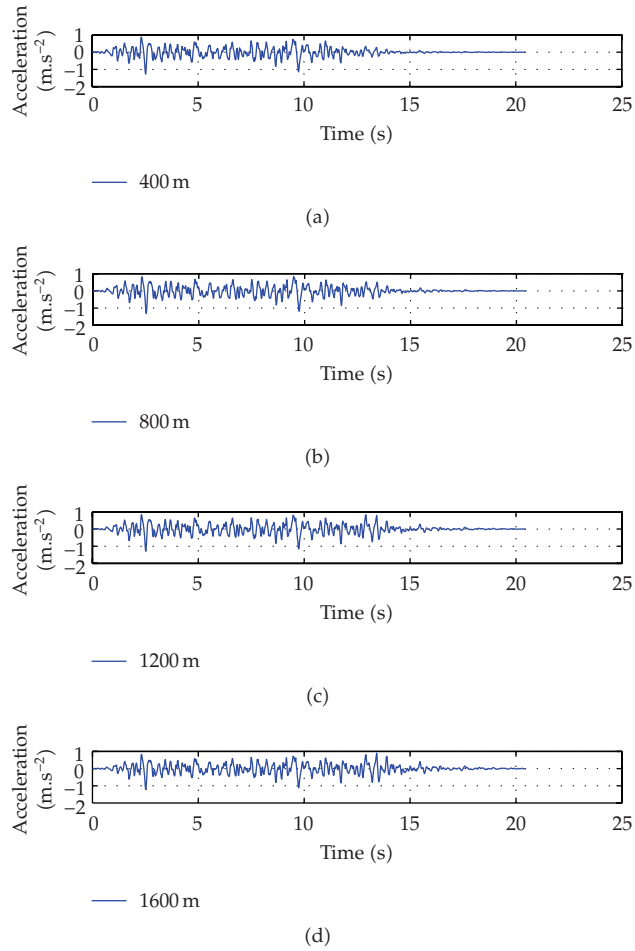

Figure 7: Time history curve of artificial ground motion at some points as shown in Figure 1.

Secondly, the data recorded at the SMART1 Array located in Lotung, Taiwan during Event 40 are used (Figure 9). Similarly, the El Centro wave was introduced in the array records to calculate the dynamic time warping distance between various points. The values are shown in Table 3. It is seen that the singular earthquake ground motion can be accurately determined via dynamic time warping distance calculation.

5. Conclusion

There exists similarity among the ground motions of multi-point ground motion filed and the degree of similarity can be accurately evaluated using the dynamic time warping distance method.

The dynamic time warping distance method is an efficient method for singularity recognition of actual array data, and it can be used in the preprocessing and clustering analysis of actual array data of multi-point ground motion field.

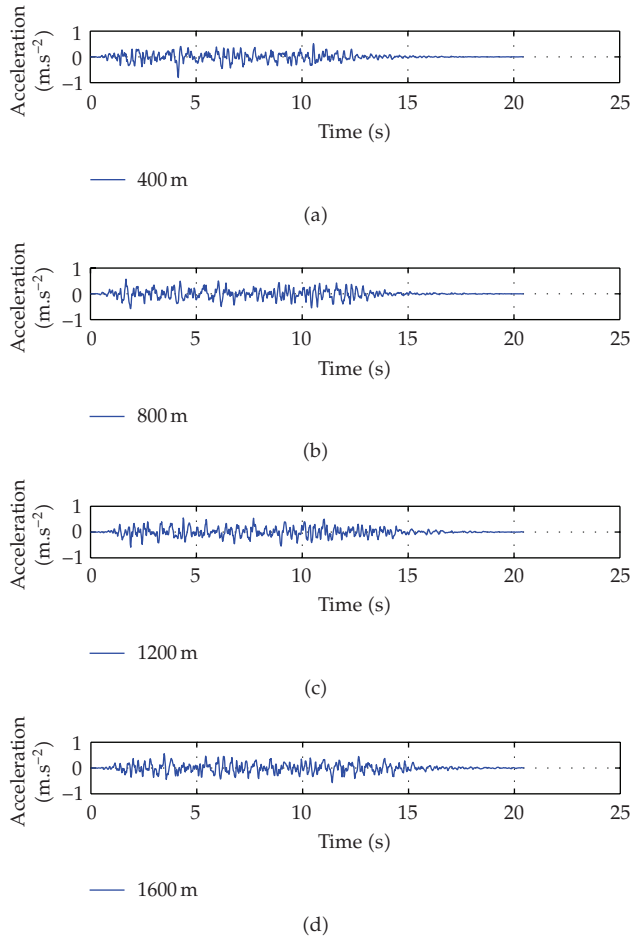

Figure 8: Time history curve of artificial ground motion at some points as shown in Figure 2.

Table 1: The dynamic time warping distance between each point after mixing singular ground motion into the artificial multi-point ground motion field in Figure 1.

DTW distance	El Centro	200 m	400 m	600 m	800 m	1000 m	1200 m	1400 m	1600 m	1800 m	2000 m
El Centro	0	**104**	**106**	**109**	**111**	**114**	**114**	**115**	**115**	**114**	**108**
200 m	**104**	0	28	33	37	45	49	54	56	52	67
400 m	**106**	28	0	21	28	35	38	42	43	57	65
600 m	**109**	33	21	0	19	24	29	31	45	55	64
800 m	**111**	37	28	19	0	18	18	31	40	50	60
1000 m	**114**	45	35	24	18	0	19	25	35	45	58
1200 m	**114**	49	38	29	18	19	0	17	27	38	53
1400 m	**115**	54	42	31	31	25	17	0	19	31	48
1600 m	**115**	56	43	45	40	35	27	19	0	23	41
1800 m	**114**	52	57	55	50	45	38	31	23	0	33
2000 m	**108**	67	65	64	60	58	53	48	41	33	0

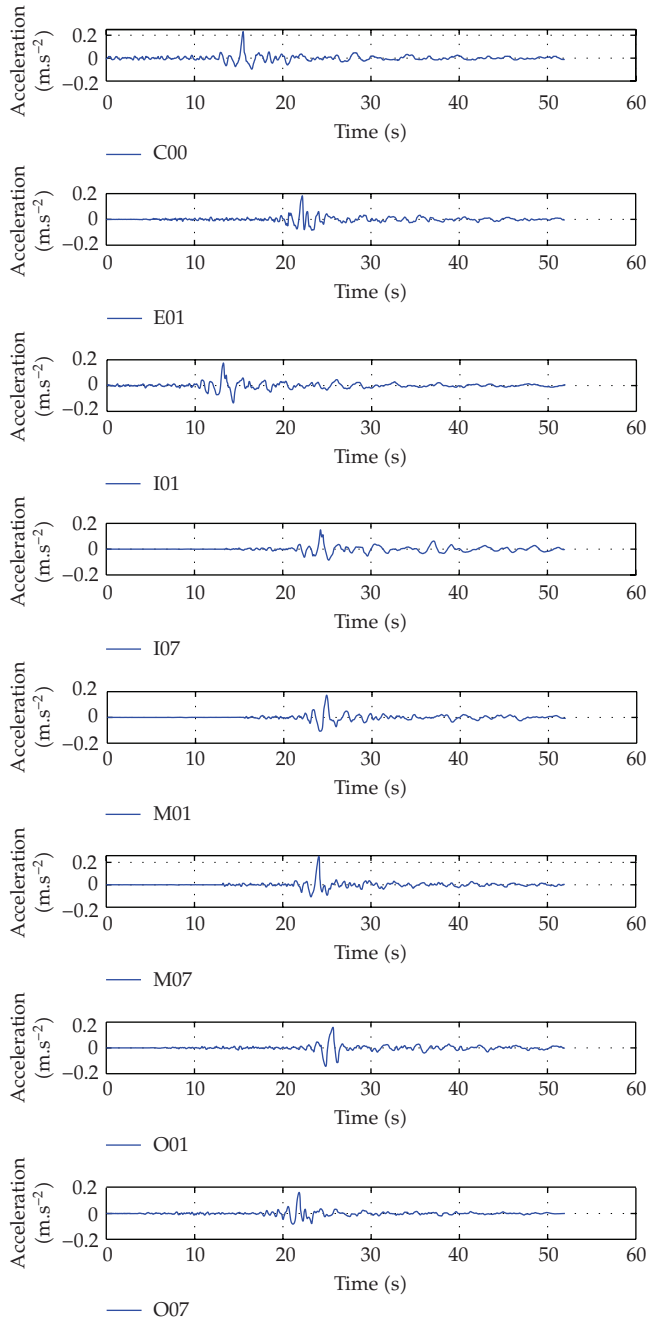

Figure 9: Time history curve of SMART1-40.

Acknowledgment

This work was supported by National Natural Science Foundation of China under Grant no. 90815011 and Program for New Century Excellent Talents in University of China under Grant no. 06-0765.

Table 2: The dynamic time warping distance between each point after mixing singular ground motion into the artificial multi-point ground motion field in Figure 2.

DTW distance	El Centro	200 m	400 m	600 m	800 m	1000 m	1200 m	1400 m	1600 m	1800 m	2000 m
El Centro	0	**75**	**77**	**79**	**78**	**85**	**85**	**84**	**85**	**88**	**83**
200 m	**75**	0	41	41	42	41	41	43	41	41	40
400 m	**77**	41	0	42	43	44	44	45	42	44	43
600 m	**79**	41	42	0	45	45	46	46	45	44	45
800 m	**78**	42	43	45	0	47	50	49	49	49	49
1000 m	**85**	41	44	45	47	0	50	50	52	49	52
1200 m	**85**	41	44	46	50	50	0	52	52	52	51
1400 m	**84**	43	45	46	49	50	52	0	51	52	49
1600 m	**85**	41	42	45	49	52	52	51	0	53	50
1800 m	**88**	41	44	44	49	49	52	52	53	0	51
2000 m	**83**	40	43	45	49	52	51	49	50	51	0

Table 3: The dynamic time warping distance between each point after mixing singular ground motion into SMART1-40 multi-point ground motion field.

DTW distance	C00	E01	I01	I07	M01	M07	O01	O07	El Centro
C00	0	12	9	9	13	10	14	12	**28**
E01	12	0	10	11	9	9	12	8	**22**
I01	9	10	0	9	11	11	12	12	**26**
I07	9	11	9	0	10	11	11	12	**22**
M01	13	9	11	10	0	9	8	7	**19**
M07	10	9	11	11	9	0	10	10	**23**
O01	14	12	12	11	8	10	0	11	**25**
O07	12	8	12	12	7	10	11	0	**18**
El Centro	**28**	**22**	**26**	**22**	**19**	**23**	**25**	**18**	**0**

References

[1] P. Danguang, L. Menglin, and F. Lichu, "Status of seismic response analysis of long-span structures under multiple support excitations," *Journal of Tongji University*, vol. 29, no. 10, pp. 1213–1219, 2001.

[2] M. Berrah and E. Kausel, "Response spectrum analysis of structures subjected to spatially varying motions," *Earthquake Engineering and Structural Dynamics*, vol. 21, no. 6, pp. 461–470, 1992.

[3] H. Yuxian, *Earthquake Engineering*, Seismological Press, Beijing, China, 2006.

[4] H. Hao, C. S. Oliveira, and J. Penzien, "Multiple-station ground motion processing and simulation based on SMART-1 array data," *Nuclear Engineering and Design*, vol. 111, no. 3, pp. 293–310, 1989.

[5] M. K. Berrah and E. Kausel, "A modal combination rule for spatially varying seismic motions," *Earthquake Engineering & Structural Dynamics*, vol. 22, no. 9, pp. 791–800, 1993.

[6] D. Lubo, *Nonlinear analysis of free spanning submarine pipelines subjected to spatially varying earthquake ground motions*, doctoral dissertation, Dalian University of Technology, Dalian, China, 2008.

[7] Q. Tiejun and W. Qianxin, "Simulation of spatial correlative time histories of multi-point ground motion, part I: fundamental formulas," *Earthquake Engineering and Engineering Vibration*, vol. 18, no. 1, pp. 8–15, 1998.

[8] M. Halkidi, Y. Batistakis, and M. Vazirgiannis, "On clustering validation techniques," *Journal of Intelligent Information Systems*, vol. 17, no. 2-3, pp. 107–145, 2001.

[9] G. K. Das, H. Mannila, P. Renganatham, et al., "Rule discovery from time series," in *Proceedings of the 4th International Conference of Knowledge Discovery and Data Mining*, R. Agrawal, S. E. Paul, and P. S. Gregory, Eds., pp. 16–22, AAAI Press, New York, NY, USA, 1998.

[10] D. J. Berndt and J. Clifford, "Finding patterns in time series: a dynamic programming approach," in *Advances in Knowledge Discovery and Data Mining*, pp. 229–248, AAAI/MIT Press, Cambridge, Mass, USA, 1996.

[11] X. Hui, *Similarity search and outlier detection in time series*, doctoral dissertation, Fudan University, Shanghai, China, 2005.